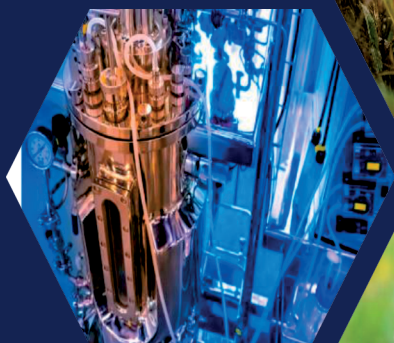
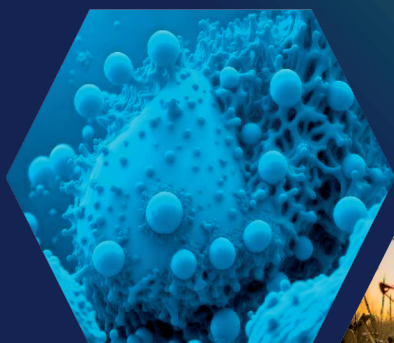


PORTOFOLIU CU LUCRARI STIINTIFICE

1. **Carmen Cîmpeanu**, Andrei Anghel, Ionelia Taranu, Petronela Rosu, *The Power of Microbes: From Byproducts to Efficient and Sustainable Feed*, 2025, ed. Ruse Press, Bulagaria, 104 pag. – pag. 2-107
2. **Cimpeanu, C.**, Predoi, D., Ciobanu, C.S., Iconaru, S.L., Rokosz, K., Predoi, M.V., Raaen, S., Badea, M.L., *Development of Novel Biocomposites with Antimicrobial-Activity-Based Magnesium-Doped Hydroxyapatite with Amoxicillin*. 2024, *Antibiotics*, 13, 963. <https://doi.org/10.3390/antibiotics13100963>. – pag. 108 - 139
3. Spinu, S.M., Cudalbeanu, M.D., Avram, I., Fierascu, R.C., Rosu, P.M., Morosanu, A.M., **Cimpeanu***, C.L. and Babeanu, N. (2024). *Antibacterial and Antitumoral Potentials of Phytosynthesized Silver/Silver Oxide Nanoparticles Using Tomato Flower Waste*. *International Journal of Molecular Sciences*, 25, 9871, pp. 1-24. <https://doi.org/10.3390/ijms25189871> – pag. 140 - 163
4. Iconaru, S.L.; Predoi, D.; Ciobanu, C.S.; Negrilă, C.C.; Trusca, R.; Raaen, S.; Rokosz, K.; Ghegoiu, L.; Badea, M.L.; **Cimpeanu, C.** *Novel Antimicrobial Agents Based on Zinc-Doped Hydroxyapatite Loaded with Tetracycline*. 2024, *Antibiotics* 13, 803. <https://doi.org/10.3390/antibiotics13090803>. – pag.164 - 184
5. Benali, Y.; Predoi, D.; Rokosz, K.; Ciobanu, C.S.; Iconaru, S.L.; Raaen, S.; Negrilă, C.C.; **Cimpeanu, C.**; Trusca, R.; Ghegoiu, L.; et al. *Physico-Chemical Properties of Copper-Doped Hydroxyapatite Coatings Obtained by Vacuum Deposition Technique*. 2024, *Materials*, 17, 3681. <https://doi.org/10.3390/ma17153681>. – pag.185 - 209
6. Predoi, D.; Iconaru, S.L.; Ciobanu, C.S.; Raita, M.S.; Ghegoiu, L.; Trusca, R.; Badea, M.L.; **Cimpeanu***, C. *Studies of the Tarragon Essential Oil Effects on the Characteristics of Doped Hydroxyapatite/Chitosan Biocomposites*. 2023, *Polymers*, 15, 1908. <https://doi.org/10.3390/polym15081908> – pag. 210 - 227
7. Diguta, C.F.; Mihai, C.; Toma, R.C.; **Cîmpeanu, C.**; Matei, F. *In Vitro Assessment of Yeasts Strains with Probiotic Attributes for Aquaculture Use*. 2023, *Foods*, 12, 124. <https://doi.org/10.3390/foods12010124>. – pag. 228 - 242
8. Predoi, G.; Ciobanu, C.S.; Iconaru, S.L.; Predoi, D.; Dreghici, D.B.; Groza, A.; Barbuceanu, F.; **Cimpeanu, C.**; Badea, M.-L.; Barbuceanu, S.-F.; et al. *Preparation and Characterization of Dextran Coated Iron Oxide Nanoparticles Thin Layers*. 2021, *Polymers*, 13, 2351. <https://doi.org/10.3390/polym13142351> – pag. 243 - 260
9. Israel-Roming, F., Gherghina, E., Luta, G., Balan, D., Popa, A., Stefan, R., Cimpeanu, C. and Cornea, C.P., *Studies on biodegradation of tanned leather*. 2012, *Scientific Bulletin, Series F, Biotechnologies*, 16, pp. 1-8. <https://biotechnologyjournal.usamv.ro/pdf/vol.XVI/art22.pdf> – pag. 261 - 265
10. Carmen Cimpeanu, Irina Grebenişan, Tolerance to cadmium and phytochelatins synthesis in *Agrostis tenuis*, 2007, *Research Journal of Agricultural Science*, vol 39, no 2, pp. 85-90. https://www.academia.edu/70560537/Tolerance_to_Cadmium_and_Phytochelatins_Synthesis_in_Agrostis?auto=download – pag. 266 – 271.

The Power of Microbes: From Byproducts to Efficient and Sustainable Feed

**Carmen Cimpeanu
Andrei Anghel
Ionelia Taranu
Petronela Rosu**



2025

Carmen Cimpeanu
Andrei Cristian Anghel
Ionelia Taranu
Petronela Rosu

**The Power of Microbes: From
Byproducts to Efficient and
Sustainable Feed**

Table of Contents

Preface	2
Chapter 1: Feed Efficiency and Fermentation: Enhancing Animal Performance and Economic Viability.....	5
Chapter 2: Enhancing Poultry Nutrition: The Role of Agroindustrial Byproduct Fermentation.....	15
Chapter 3: Microbial Roles and Functional Benefits.....	51
References	70

Preface

It is widely believed that the properties of fermentation were first discovered during the early Neolithic period, initially through the accidental ingestion of fallen fruit and later through deliberate consumption. Due to their high sugar content, these fruits underwent alcoholic fermentation, which improved their taste and imparted inebriating qualities. Other fermentation processes were discovered accidentally as well, notably when grains were buried in the ground for preservation. Because they were not stored in airtight conditions, these grains absorbed moisture from the soil and began fermenting spontaneously, producing what is considered the earliest form of beer. Over time, people observed that leaving various foods in warm, humid environments resulted in natural transformations that enhanced taste and aroma while also preventing contamination by harmful microorganisms, changes once attributed to supernatural forces. This understanding led to the creation of the first fermented dairy products and, subsequently, leavened bread. Around this period, people also began establishing the first farms dedicated to animal husbandry. The earliest domesticated species included sheep, goats, cattle, and pigs, eventually followed by chickens and other poultry. Initially, ruminants primarily consumed locally available resources such as grasses, leaves, straw, and wild plants, as well as root and tuber crops like potatoes, beets, turnips, and carrots, which proved particularly valuable during colder seasons when other vegetation was scarce. For pigs and poultry, staple feeds consisted mainly of cereals such as wheat, barley, oats, and corn, supplemented with household food scraps. To preserve animal feed for winter, people began collecting grasses and other plant residues, storing them in pits. They discovered that this method not only maintained the feed in better condition but also improved its flavor, increasing animals' consumption. Additionally, fermented products offered multiple benefits, including greater resistance to diseases, particularly digestive illnesses, and improved overall health, as evidenced by enhanced vitality and higher yields of milk and eggs. Early fermentation occurred spontaneously, driven by naturally occurring lactic acid bacteria and yeasts in animal feed. However, deliberate, large-scale controlled fermentation practices date back to the 18th century, when modern agricultural methods prompted farmers to adopt purposeful fermentation techniques.

During this time, silage methods were standardized and improved, enabling the preservation of larger quantities of feed. Advances in microbiology in the 19th century facilitated the identification and selection of effective microorganisms for fermentation. Lactic acid bacteria became the preferred starter cultures because of their ability to convert plant sugars into lactic acid, thereby increasing acidity and limiting microbial growth. Concurrently, *Saccharomyces cerevisiae* (baker's yeast) was widely adopted for its capacity to break down complex carbohydrates and proteins, improving feed digestibility, enhancing bioactive compound content, and increasing palatability. Today, feeding fermented products to farm animals is a widespread practice supported by well-established methods and microbial cultures. Modern objectives emphasize using microorganisms to enrich agro-industrial byproducts, degrade anti-nutritional factors, and supply bioactive substances, thereby enhancing overall feed quality. Incorporating fermented feeds into animal diets promotes a circular economy and reduces reliance on medications. This paper explores the most commonly used microorganisms for animal feed fermentation, highlights their beneficial effects on feed, and outlines their primary advantages for farm animal health.

Chapter I: Feed Efficiency and Fermentation: Enhancing Animal Performance and Economic Viability

Nutrition across farm animal species

Proper nutrition is essential for efficient animal growth, as it provides animals with a balanced diet necessary for maintaining health, supporting growth, ensuring optimal production of meat, milk, and eggs, and supplying the energy and nutrients needed for daily activities and reproduction. Malnutrition or inadequate feeding immediately manifests as decreased growth rates and productivity, as well as increased susceptibility to diseases and infections due to compromised immunity [1, 2].

Farm animals predominantly include poultry, swine, ruminants, and aquaculture species, each with specific dietary practices based on their nutritional needs [3, 4]. Poultry diets primarily consist of grains such as corn, wheat, or sorghum, providing energy through high carbohydrate content. These diets are supplemented with protein-rich soybeans containing essential oils, vitamins, and minerals [5, 6]. Additionally, poultry feeds are tailored according to species, developmental stages, and production purposes. Broiler chickens, raised for meat, require protein-rich diets to facilitate rapid muscle growth, with protein levels reduced as they approach market weight [7, 8]. Conversely, laying hens require diets enriched with calcium and phosphorus to ensure strong eggshell formation and healthy bone maintenance [9]. Calcium deficiency can lead to decreased egg production, poorer eggshell quality, and inadequate bone mineralization [10]. Swine are commonly fed grain-based blends supplemented with protein meals, typically consisting of corn and soybean meal [11, 12]. Unlike ruminants, pigs do not efficiently digest fibers for protein synthesis; hence, their diets frequently require supplementation with essential amino acids such as lysine, threonine, and methionine, along with vitamins and minerals for optimal growth [13, 14]. Additionally, piglets demand significantly higher protein concentrations compared to adult pigs [15]. Ruminants possess a four-chambered stomach,

enabling effective fiber digestion with assistance from cellulolytic microbiota, thus producing necessary proteins [16-18]. They typically obtain sufficient caloric content, macronutrients, and micronutrients through forage consumption [18, 19].

Nutritional strategies for ruminants vary according to species and production purpose (meat versus milk). Dairy cows require substantial amounts of forage and supplemental feeds high in carbohydrates and proteins (e.g., corn, soybean meal, or canola meal) due to their high energy and protein demands for milk production [20, 21]. In contrast, beef cattle are optimized for efficient forage utilization and usually require supplemental protein only when forage protein is inadequate or during early developmental stages for accelerated growth [22-24]. Sheep and goats have feeding habits similar to cattle and can generally meet their nutritional needs from grass pasture or hay. However, during lactation or pregnancy, farmers must introduce grains or concentrate feeds. These supplements are also necessary for young lambs to increase their growth rate [25, 26]. Mineral balance varies between sheep and goats. Goats tolerate more dietary copper than sheep, so rations must be adjusted to prevent copper build-up in sheep and shortage in goats [27, 28]. In aquaculture, feeds come as nutrient-dense pellets that pack plenty of protein, since aquatic animals have greater protein needs and process fibre poorly [29, 30]. In omnivorous fish such as *Oreochromis niloticus*, *Cyprinus carpio* and *Ictalurus punctatus*, protein requirements sit around 26-45 %, whereas piscivorous species like *Dicentrarchus labrax* and *Sparus auratus* need roughly 40-55 %. Omnivores also thrive on more carbohydrates [31]. By contrast, pigs and poultry generally do well with 18-26 % protein [32, 33].

Fish lean on protein for energy and lose little heat to their surroundings, which explains the higher demand, while mammals and birds spend more energy on keeping warm [34-36]. Aquafeeds also carry more fat, especially for marine fish that rely on lipids as prime fuel [37, 38]. Fish meal, rich in protein and omega-3 fatty acids, stays a staple alongside grains and oilseed meals [39, 40]. Because fish meal is pricey, producers keep testing plant proteins such as soybean, canola and pea meals to trim costs [41]. A typical tilapia ration blends fish meal with soy or corn gluten meal, then tops it up with vitamins, minerals and essential amino acids [42].

Essential feed types for animal nutrition

Feed types can be broadly categorized into grains, forages, and various by-products resulting from agricultural processing. These categories are typically blended in varying proportions according to the nutritional requirements of farm animals, with each category serving a specific function [1, 43]. Grains, including corn, wheat, barley, and oats, provide a primary source of carbohydrates due to their high starch content, which is metabolized into sugars [44-47]. Although grains are palatable and energy-dense, their relatively low protein and mineral content necessitates pairing them with protein-rich feeds [48, 49]. Oilseed meals, such as soybean meal, canola meal, and cottonseed meal, are residues from oil extraction processes and represent significant sources of protein. Soybean meal is globally predominant, accounting for approximately two-thirds of protein feedstuffs used in animal diets, offering around 47–49% crude protein and an optimal amino acid profile [50-53]. Canola meal, derived from rapeseed, typically contains about 35% protein and is routinely included in cattle and pig diets [54].

Other alternatives, such as cottonseed, sunflower, and peanut meals, are utilized depending on local availability [55, 56]. Forages like pasture, hay, and silage consist of plant components (leaves, stems, stalks) high in fiber and supplying essential vitamins and minerals, albeit with lower energy density. They can be provided fresh (pasture or green chop), dried (hay), or fermented (silage/haylage) [1, 57-59]. Young leafy forages or legume hays, such as alfalfa, can supply substantial protein and energy [60]. While pasture grass is the most cost-effective option, allowing direct grazing, hay is used when fresh forage is unavailable, and silage (commonly produced from fermented corn plants or grass) supports year-round feeding, particularly in dairy and beef operations [61-63].

Ruminants require forage for normal digestion, as its fiber content supports beneficial rumen microbiota, with insufficient fiber potentially causing serious digestive complications [64, 65]. Non-ruminants also benefit from fibrous forage in their diets, promoting a healthy gut microbiota [1, 66]. Another category includes by-products such as distillers' grains, brans, crop residues, and certain animal by-products from agriculture and food industries [67]. Utilizing these residues as animal feed is economically and environmentally

beneficial, diverting bioactive-rich materials away from disposal methods that pose environmental risks [68].

Distillers' dried grains (DDG), the leftovers of corn-based ethanol production, offer plenty of protein and fat, making them suitable in diets for cattle, swine, and poultry, with ruminants benefiting the most [69-71]. Wheat and rice bran also find their way into many pig and poultry rations thanks to a solid mix of protein and fibre [72-74]. Highly fibrous seed hulls such as soybean or cottonseed hulls are better suited to ruminant feeds, where the animals' specialised digestion can handle them well [75, 76]. By-products of animal origin, such as blood meal, meat meal, and fish meal, supply rich protein and minerals, though they usually cost more to produce [77]. Whey that remains after cheese making can top up the energy and protein supply for pigs or calves [78, 79]. Occasionally, bakery waste or surplus fruit and vegetables can round out livestock diets [80]. For these reasons, modern feed formulations combine staple ingredients with such by-products to give farm animals a balanced and economical ration [43].

Feed Conversion and Profitability

Feed is the most expensive part of raising farm animals, often taking up 60-70% of the budget. Even small tweaks in how feed is made or in how well an animal absorbs nutrients can yield rapid financial benefits (John D. Lawrence 2008). Enhancing the efficiency of converting feed into meat, milk, or eggs significantly improves farm profitability [81].

Farmers track efficiency with the feed conversion ratio (FCR), which shows how much feed is needed for one unit of product. If a chicken needs only 1.5 kilograms of feed to gain one kilogram, it means that it has an FCR of 1.5:1. The lower the FCR, the lower the production costs for the same amount of food [82]. Although chickens and pigs usually outperform cattle, feed remains the biggest single cost for every species [61]. For poultry, the FCR is near 1.5:1 [83]. For pigs, it is roughly 3:1 [84]. In cattle, it climbs beyond 7.5:1 [85]. A small change can mean a lot. A ten-percent drop in FCR can lift profits by as much as 20% [82]. Lowering the pig FCR from 3.0 to 2.8, saves 0.2 kilograms of feed for every kilogram of growth. By the time a pig reaches 98 kilograms, about 19.6 kilograms of feed are saved. For a barn of 1000 pigs, this results in

nearly 19.6 tonnes of feed savings, substantially reducing overall production costs [86].

Quality matters too. Feeds rich in protein, fat, carbohydrates, vitamins, and minerals are easier to digest and more appealing to animals. They help them grow faster, use feed more efficiently, and stay healthier, which means more of the nutrients end up as body mass, milk, or eggs instead of being wasted [3, 7, 25]. Over the last 50 years, better feed and better genetics have doubled the growth rate of broiler chickens while cutting their FCR in half, reducing the cost of each kilogram of chicken meat and keeping up with demand [87, 88]. Poor feed, in contrast, pushes FCR upward, raises disease risk, and increases vet bills and mortality, all of which negatively impact profitability [1]. Slower growth also lengthens the feeding period, adding more feed and labour costs [89, 90].

Profitability of fermented feed

Fermenting feed is a highly effective method for improving feed quality, reducing production costs, and lowering the feed conversion ratio (FCR). This process involves incubating feed with various microorganisms, most commonly lactic acid bacteria, which break down complex fibers and anti-nutritional factors while simultaneously boosting the population of beneficial bacteria [91-94].

Studies show that pigs on fermented feeds exhibit superior FCR and higher weight gains, as well as reduced diarrhea and mortality rates, resulting in substantial economic benefits [95-98]. Poultry also experience analogous benefits: feeding fermented feed improves FCR, increases broiler weight gains, and enhances egg production in laying hens [99, 100]. In fact, hens consuming a fermented diet have been reported to lay 4% more eggs [101]. Another economic advantage of feed fermentation is the ability to utilize agro-industrial byproducts.

Fermentation upgrades the nutritional quality of these byproducts, transforming them into cost-effective feed ingredients that can maintain or even improve FCR compared to feeds containing more expensive ingredients [102, 103]. Fermentation also makes it possible to replace costly soybean meal with local grains and high-fiber byproducts. For example, substituting 10% of

a poultry basal diet with fermented dried brewer's grains cut feed costs per kilogram of body weight gain by about 16% and boosted gross income margins by 47% [104]. Replacing 50% of goats' feed with fermented cassava peel lowered feed cost per gain by up to 32% [105]. In cattle, providing 0.4 kg of citrus waste per 100 kg of cow body weight per day reduced daily feeding costs from \$4.75 to \$4.14 [106].

These savings stem from improved nutrient availability due to fermentation, which enables the use of a higher proportion of lower-cost ingredients, such as crop residues, rapeseed meal, or field peas, especially advantageous when corn or soybean prices rise [107, 108]. During lactic acid bacteria fermentation, lactic and acetic acid concentrations increase, reducing feed pH and inhibiting harmful bacteria like *Salmonella* and *E. coli* [109, 110]. Once ingested, fermented feed continues to exert antimicrobial effects against pathogenic bacteria in the gut. For instance, incorporating fermented rye in pig feed lowered *Salmonella Typhimurium* levels by 1.5 log¹⁰ CFU/g [111]. When fermented barley was added to pig feed, *Enterobacteriaceae* (including *Escherichia coli*) decreased by 44% compared to controls [112].

Farms that adopt fermented feeds consequently enjoy healthier animals and lower veterinary expenses [113]. One Dutch farming group reported a 58% decline in antibiotic use over six years following the introduction of fermented feeding, thereby reducing medicine costs [114]. Another study found a 7.15% drop in piglet mortality when fermented feed was used, significantly improving profitability [98]. In poultry, fermented diets have been associated with enhanced immune function and disease resistance, evidenced by reduced enterobacteria in the gut, better litter quality, and lower illness rates [94, 101]. As concerns about antibiotic resistance grow, with increasing restrictions on prophylactic antibiotic use as growth promoters, fermented feeds offer a natural alternative for sustaining livestock performance while partially replacing medications [115, 116].

Fermented feed has also proven profitable for small-scale producers. One approach they employ is to soak whole grains or commercial mash in water for 1–3 days, allowing natural *Lactobacillus* bacteria to ferment the feed [117]. Other small-scale methods involve soaking swill or grain in water overnight to achieve mild fermentation, which can enhance palatability and feed intake [118-120].

Commonly fermented products include cassava peelings and rice bran, with fermentation often carried out in pits or barrels to produce inexpensive pig feed that supports improved growth [121, 122]. Although fermenting feed adds some extra costs, it has shown strong profitability, particularly for laying hens [123, 124]. Since fermented feed is wet, it forms clumps and scatters less, thereby reducing waste [125-127]. The fermentation process also generates enzymes that enhance digestibility, helping pigs absorb more nutrients [93, 95]. Better digestion conducted by fermentation often leads to more efficient phosphorus absorption, allowing farmers to spend less on mineral supplements and lower the nutrient load in manure [128, 129].

In cattle production, despite a high FCR, the economic advantage lies in cattle's ability to obtain essential nutrients from very low-cost feed sources, some of which might otherwise be discarded as waste [130-132]. Other profit-boosting strategies include genetic selection (for example, selecting animals with lower residual feed intake so they eat less for the same gain), precision feeding to minimize waste, and fine-tuning diet formulations [133, 134]. Another tactic is to focus on the most cost-effective feed conversion rather than the absolute lowest FCR, which may require prohibitively expensive all-grain diets. While increasing corn in the ration can improve the biological FCR because cattle gain faster on starch, corn can be expensive; adding some forage reduces costs but slightly worsens the FCR. The economically optimal balance maximizes profit instead of simply minimizing feed use [135-139]. For example, University of Nebraska researchers found that substituting corn silage (a fermented forage) for corn grain in feedlot diets slightly lowered feed efficiency but reduced overall feed costs so much that profitability rose. When corn was \$3.50 per bushel, corn silage, despite having only about 75% of corn's energy, was the cheapest energy source on a cost-per-total-digestible-nutrients basis. Although cattle consumed more feed (lower efficiency) with increased silage, the cost per pound of gain decreased, enhancing profit. Thus, both feed efficiency and feed cost must be considered [140-143].

Fermented feed and forage, often corn, grasses, or legumes, can strongly influence feed costs. These forages are chopped and stored anaerobically to undergo lactic acid fermentation and become silage [144, 145]. This process preserves the forage and increases its digestibility compared to dry hay. For instance, producing corn silage can cost less per ton than purchasing corn grain or hay, and despite a higher FCR, silage is frequently the cheapest energy

source [146, 147]. Corn silage and fermented alfalfa (haylage) have also been shown to promote higher milk yields compared with feeding only dry forages, improving feed efficiency through increased nutrient availability [148, 149].

Smallholder dairy and beef farmers are embracing silage-making to boost herd productivity and profitability. In places like Honduras, Costa Rica, Indonesia, Australia, the Udmurt Republic, Vietnam, and Ethiopia, farmers have begun using polythene bags or community silos to ferment surplus grass or maize stalks for dry-season feeding. This practice maintains or improves milk yields during drought, significantly increasing farm income. By fermenting crop residues or fodder, smallholders transform low-value biomass into higher-value feed that can partially replace expensive commercial concentrates. In addition, cattle tend to be healthier and breed back sooner, ultimately producing more calves over their lifetime [150-156].

Improving feed quality through fermentation

Fermented feed is any animal ration deliberately exposed to microbial fermentation before being fed to livestock. By introducing beneficial microorganisms, either those naturally present in the substrate or supplied as starter cultures, the feed's components are partially degraded, yielding a "pre-digested" product enriched with organic acids and live probiotic bacteria. In contrast, conventional feed is provided unfermented [94, 157, 158]. During fermentation, lactic-acid bacteria of the genus *Lactobacillus* predominate, converting sugars to lactic acid, while yeasts, most commonly *Saccharomyces cerevisiae*, produce ethanol and carbon dioxide. These biochemical activities enhance flavor and improve nutrient release [159-162].

Additional organisms are often included to extend the range of enzymatic actions. For instance, *Bacillus subtilis* or members of the Enterobacteriaceae may provide phytases that cleave phytic acid to liberate essential minerals, whereas filamentous fungi like *Aspergillus* and *Rhizopus* assist in fermenting high-fiber substrates [163-166]. Anaerobic conditions must be maintained by mixing feed with water to form a slurry known as "liquid-feed fermentation," or by tightly packing chopped forage into a silo for silage, since oxygen inhibits preferred fermentative organisms [167, 168].

Successful fermentation requires maintaining an oxygen-free environment and sufficient warmth and moisture to suppress spoilage organisms while supporting desirable microbes. Fermentation typically starts with a brief aerobic phase if oxygen is present, quickly transitioning to anaerobic conditions dominated by beneficial flora. Depending on the substrate and method, fermentation may last from a few days for small grain batches to several weeks for ensiled forages [93, 100, 169].

Fermentation significantly reduces anti-nutritional factors. Phytic acid, which binds essential minerals; tannins, which impair taste; and protease inhibitors, such as trypsin inhibitors in raw soybeans, all decline [170-172]. Through phytase activity, lactic-acid bacteria hydrolyze phytic acid, enhancing mineral absorption of phosphorus, iron, and zinc [173]. Fermentation also cleaves tannins into less astringent compounds and reduces levels of trypsin inhibitors and indigestible oligosaccharides in legumes, thus improving protein digestibility and reducing gastrointestinal discomfort [174-176]. This process further mitigates other anti-nutrients. Lectins in raw legumes, saponins in alfalfa, and non-starch polysaccharides such as β -glucans in barley and arabinoxylans in rye are degraded, reducing gut irritation and lowering digesta viscosity in monogastrics [177-182]. Additionally, fermentation decreases oxalates, which otherwise bind calcium, potentially causing mineral imbalances [183].

Crucially, it also lowers mycotoxin concentrations, improving feed safety [184, 185]. Fermentation practices typically involve three main methods. In liquid fermentation, feed is converted to a slurry and fermented for one to three days, primarily for swine and occasionally poultry [110, 186]. Solid-state fermentation adds just enough moisture to enable microbial growth without producing excess liquid, ideal for high-fiber residues and generating a drier, easily handled product [187]. Ensiling involves storing chopped forage in silos or wrapped bales; naturally occurring lactic-acid bacteria ferment plant sugars, creating stable silage with extended shelf life [188, 189].

Throughout these methods, optimal temperature and moisture are critical for promoting beneficial microorganisms and preventing pathogens [190, 191]. Under favorable conditions, these microbes flourish, producing organic acids,

enzymes, and beneficial metabolites, including increased levels of B-vitamins such as folic acid, riboflavin, niacin, and thiamin [192, 193].

For livestock, fermented feed acts as both prebiotic and probiotic, supplying fermentable substrates to gut microbiota and delivering beneficial bacteria directly. Pigs and poultry fed fermented diets often develop taller intestinal villi and a more robust mucosal barrier, enhancing nutrient absorption [194, 195]. Interest in fermented feeds has grown notably over the past two decades as producers seek natural methods to enhance animal performance and feed efficiency [110, 196]. Restrictions on antibiotic growth promoters, notably their 2006 ban in the European Union, have made fermentation an attractive alternative for sustaining gut health, especially in pigs [116, 197]. The antimicrobial effect arises mainly from lactic-acid bacteria that acidify the gut lumen, creating an environment hostile to pathogens [198, 199].

Finally, fermented rations provide environmental benefits. Enhanced digestibility results in livestock excreting lower nitrogen and phosphorus levels, reducing excess nutrient runoff when manure is used as fertilizer and mitigating environmental pollution risks [200, 201].

Chapter 2: Enhancing Poultry Nutrition: The Role of Agroindustrial Byproduct Fermentation

Enhancing Poultry Feed through Fermentation

The global poultry feed market was valued at US\$ 123.5 billion in 2023 and is projected to reach US\$ 228.1 billion by 2033. Over the next ten years, worldwide sales of poultry feed are forecasted to rise at a Compound Annual Growth Rate (CAGR) of 6.3%, indicating consistent demand growth and market development [202].

The most popular poultry categories are broilers (meat chickens) and layers (egg-laying hens), each requiring different nutritional criteria [101, 203]. In the case of broilers, a high-protein starter feed containing 22% total protein is provided during the initial growth period (0–3 weeks). In subsequent weeks (4–6 weeks), the protein content is reduced to 20%, eventually decreasing to 19% during the finisher phase [203, 204]. Additionally, calcium and phosphorus are critical for bone development, with recommended concentrations of 1% calcium and 0.7% phosphorus [204]. In contrast, laying hens require a lower protein intake of around 16%, yet their calcium concentration is more than triple that of broilers, at about 3.5%, to facilitate eggshell formation. Eggshells typically consist of approximately 40% calcium [10, 205].

The most common ingredients in poultry feed are soybean meal and corn meal. Corn provides a rich source of carbohydrates, while soybean meal is a key source of protein [80, 107, 206]. Moreover, fermentation has been shown to improve the nutritional quality of these feed ingredients by reducing antinutritional factors and increasing protein concentration, ultimately enhancing poultry growth performance and productivity [207, 208]. However, corn meal and soybean meal are relatively expensive. In 2021–2022, feed prices spiked in many regions due to heightened corn and soybean costs, influenced by weather challenges and strong demand [80, 107, 206, 209]. Consequently, partially substituting these ingredients with agroindustrial byproducts can offer significant benefits by reducing production costs [208, 210].

Common agroindustrial byproducts include rapeseed meal, palm-kernel cake, olive-mill waste, rice bran, and DDGS [210]. These byproducts are often region-specific; for instance, rice bran is prevalent in Asian feed formulations, while DDGS (a byproduct of corn ethanol production) is widely used in the US [211, 212].

Nevertheless, using agroindustrial byproducts presents certain challenges, as they generally have lower nutritional value (particularly protein content) and contain various antinutritional factors. Their high fiber content also impedes feed intake and reduces carbohydrate availability [70, 213, 214]. For example, olive byproducts contain around 40% lignocellulosic fibers, making them difficult for poultry to digest. Cocoa pod husk likewise has high lignin and non-starch polysaccharide content, limiting its use.

Additionally, crop residues and grasses frequently have low energy and protein values [210, 214, 215]. Cottonseed meal has been reported to harbor high mycotoxin levels, notably aflatoxin, which can lead to serious health and productivity issues, thereby causing economic losses [51]. However, these limitations can be mitigated via fermentation of agroindustrial byproducts, which increases protein levels and reduces antinutritional compounds. Microbial fermentation breaks down large protein molecules into amino acids and peptides, facilitating easier absorption and utilization [216].

Furthermore, microorganisms produce enzymes such as cellulase, pectinase, and hemicellulase, which degrade fibrous components and enhance carbohydrate availability [74, 217]. Microbial fermentation can also lower the risk of mycotoxin contamination, including Aflatoxin B1 and Ochratoxin A, through degradation or sequestration. Additionally, lactic acid bacteria can produce antifungal metabolites that inhibit fungal growth and reduce mycotoxin production [160, 185, 191].

Consequently, incorporating fermented byproducts into poultry feed helps maintain or even improve growth performance compared to conventional diets without fermented components (Table 1) [206].

Table 1- Effects of Fermented Agroindustrial Byproducts on Poultry Growth and Health

No. Crt.	Poultry	Fermented byproduct	Microorganism involved in fermentation	Effect of fermentation	Effect on the animal	Reference
1	broiler chickens	soybean meal	<i>Bacillus subtilis</i>	enhanced surfactin content	improved growth performance improved intestinal morphology improve bone strength	[218, 219]
2	broiler chickens	soybean meal	<i>Bacillus subtilis</i>	reduced antinutritional factors increased crude protein	improved growth performance	[220]
3	broiler chickens	soybean meal	<i>Lactobacillus acidophilus</i> <i>Bacillus subtilis</i>	increased crude protein reduced crude fiber	improved growth performance enhanced intestinal morphology improved immune response	[221]
4	broiler chickens	soybean meal	<i>Aspergillus oryzae</i> <i>Lactobacillus acidophilus</i> <i>Lactobacillus plantarum</i> <i>Bacillus subtilis</i> <i>Aspergillus oryzae</i>	increased the crude protein content lower pH levels	improved growth performance improved intestinal morphology reduced abdominal fat	[222]
5	broiler chickens	feather meal-soybean meal	<i>Bacillus amyloliquefaciens</i> CU33	improved the keratin degradation improved protein content	improved growth performance increased villus height better protein utilization	[223]
6	laying hens	soybean meal	<i>Bacillus</i> spp. <i>Saccharomyces</i> spp. <i>Lactobacillus</i> spp. <i>Clostridium butyricum</i>	increased crude protein reduced antinutritional factors	improved laying performance improved egg quality improved intestinal health	[224]
7	Japanese quail	soybean meal	<i>Lactobacillus plantarum</i> <i>Bacillus subtilis</i> <i>Aspergillus oryzae</i>	increased crude protein reduced crude fiber	improved growth performance improved small intestine morphology lower serum cholesterol	[207]
8	broiler chickens	rapeseed meal	<i>Bacillus subtilis</i>	increase fat	improved body weight	[107]

			fiber content decreased	leg muscles with higher protein content		
9	laying hens	rapeseed meal	<i>Bacillus subtilis</i> 67	reduced anti-nutritional factors increased egg weight improved nutrient digestibility	[107]	
10	broiler chickens	rapeseed meal	<i>Lactobacillus acidophilus</i> (PTCC1643) <i>Bacillus subtilis</i> (PTCC1156) <i>Aspergillus niger</i> (PTCC5010)	reduced anti-nutritional factors decreased <i>Salmonella</i> colonization in the gastrointestinal tract increased weight gain reduced stress markers	[225]	
11	chahua chickens	soybean hulls and rapeseed cake	<i>Aspergillus niger</i>	increased crude protein	improved growth performance	[208]
			<i>Lactobacillus plantarum</i>	reduced crude fiber	enhanced immunity	
			<i>Lactobacillus fermentum</i>		increased antioxidant capacity improved intestinal health	
12	laying hens	mix of corn, cotton seed meal and rapeseed meal	<i>Lactobacillus acidophilus</i> <i>Lactobacillus plantarum</i>	reduced anti-nutritional factors improved body weight improved immunity improved antioxidant capacity	[226]	
13	laying hens	cottonseed meal and coconut meal	<i>Bacillus</i> spp.	increased crude protein	reduced laying performance	[224]
			<i>Saccharomyces</i> spp. <i>Lactobacillus</i> spp. <i>Clostridium butyricum</i>	reduced antinutritional factors	improved intestinal health	
			<i>Lactobacillus acidophilus</i> <i>Bacillus subtilis</i> <i>Candida utilis</i>	increased crude protein	improved production performance improved egg quality	
14	laying hens	corn by-products				[123]
15	broiler chickens	cornmeal	<i>Umbelopsis isabellina</i> CCF 2412	increased gamma-linolenic acid concentration	improved meat quality	[227]
16	broiler chickens	mixture of yellow corn and soybean meal	<i>Bacillus subtilis</i> var. <i>natto</i> <i>Saccharomyces cerevisiae</i>	lower pH levels increased lactic and acetic acid content	increased body weight improved nutrient digestibility	[228]

17	Xuefeng black-bone chickens	corn and soybean meal	<i>Saccharomyces cerevisiae</i> <i>Bacillus subtilis</i> <i>Lactobacillus plantarum</i> <i>Enterococcus faecium</i>	improved the nutritional composition	improved body weight increased villus height improved immunity lower mortality rates	[229]
18	broiler chickens	corn and soybean meal	<i>Bacillus subtilis</i> <i>Lactobacillus plantarum</i>	lower pH levels enhanced nutrient quality	improved growth performance improved gut health lower mortality rates	[230]
19	broiler chickens	corn and soybean meal	<i>Bacillus subtilis</i> var. <i>natto</i> N21 <i>Bacillus coagulans</i> L12 <i>Lactobacillus casei</i> <i>Lactobacillus acidophilus</i> <i>Lactobacillus acidophilus</i> L15 <i>Lactobacillus delbrueckii</i> <i>Lactobacillus reuteri</i> P24	reduced pH	improved growth performance	[231]
20	broiler chickens	corn and soybean meal	<i>Lactobacillus plantarum</i> <i>Bacillus subtilis</i> <i>Saccharomyces cerevisiae</i>	reduced anti-nutritional factors	improved growth performance enhanced immune function	[232]
21	Xuefeng black-bone chickens	corn and soybean meal	<i>Bacillus subtilis</i> <i>Saccharomyces cerevisiae</i> <i>Lactobacillus plantarum</i> <i>Enterococcus faecium</i>	enhanced nutritional composition	improved intestinal morphology	[233]
22	Ross 308 broiler chicks	Wheat bran	<i>Lactobacillus acidophilus</i> (NHB-La13) <i>Bacillus subtilis</i> (NHB-Bs32) <i>Lactobacillus rhamnosus</i> (grx10) <i>Saccharomyces cerevisiae</i> (NHF-Sc9)	increased the crude protein content increased acid-soluble protein fiber content decreased pH dropped significantly from 6.7 to 4.7 levels of lactic acid bacteria and <i>Bacillus subtilis</i> increased	similar growth and digestibility results to the control diet	[234]

23	broiler chickens	barley grains	<i>Lactobacillus plantarum</i> <i>Bacillus subtilis</i> <i>Aspergillus niger</i>	increased the crude protein content fiber content decreased lower pH levels levels of lactic acid bacteria and <i>Bacillus subtilis</i> increased	improved growth performance boosted antioxidant status improved intestinal histomorphology modulated immune responses	[235]
24	broiler chickens	wheat bran	<i>Bacillus cereus</i>	enhanced nutritional availability	increased microbiota diversity	[236]
	broiler chickens	dried brewer's grains	<i>Bacillus subtilis</i> <i>Lactobacillus rhamnosus</i> <i>Saccharomyces cerevisiae</i> Y10	increased protein and lipid content reduced fiber content reduced anti-nutritional factors	improved body weight lowered the cholesterol content	[104]
25	broiler chickens	bran and soybean meal	<i>Bacillus subtilis</i> <i>Bacillus licheniformis</i>	increased crude protein	improved growth performance increased villus height enhanced antioxidant capacity	[237]
26	Landes geese	mixture of corn, soybean meal and wheat bran	<i>Bacillus subtilis</i> var. <i>natto</i> N21 <i>Saccharomyces cerevisiae</i> Y10	reduced sugar increased lactic acid levels	higher body weight gain greater liver weight increases in beneficial bacteria and reductions in pathogenic bacteria enhanced antioxidant enzyme reduced oxidative markers reduced blood cholesterol	[238]
27	broiler chickens	maize, wheat and soybean meal	<i>Lactobacillus plantarum</i>	increased lactic acid levels	improved gut bacteria composition lower mortality rate	[186]
28	laying hens	corn, soybean meal and wheat bran	<i>Bacillus subtilis</i> <i>Saccharomyces cerevisiae</i>	increased crude protein reduced crude fiber	increased laying rate improved egg quality enhanced immune function	[101]
29	broiler chickens	corn, soybean meal and wheat bran	<i>Lactobacillus casei</i>	increased crude protein	improved growth performance	[239]

30	SanHua geese	corn, soybean meal and wheat bran	<i>Bacillus</i> spp., <i>Lactobacillus</i> spp., and yeast	reduced anti-nutritional factors	improved gut morphology improved immune response	[240]
31	Muscovy ducks	corn, soybean meal and wheat bran	<i>Bacillus fragilis</i> <i>Bacillus sphaericus</i> <i>Bacillus subtilis</i> <i>Bifidobacterium</i> spp. <i>Lactobacillus</i> spp. <i>Enterococcus faecium</i>	enhanced nutritional composition reduced anti-nutritional factors	improved growth performance improved intestinal morphology enhanced organic acid production increased amino acid biosynthesis	[241]
32	laying hens	corn, soybean meal and wheat bran	<i>Clostridium butyricum</i> <i>Lactobacillus crispatus</i> <i>Lactobacillus salivarius</i>	reduced crude fiber reduced anti-nutritional factors	improved albumen height enhanced villus height	[242]
33	layer chicks	corn, soybean meal and wheat bran	<i>Bacillus subtilis</i> <i>Candida tropicalis</i> <i>Lactiplantibacillus plantarum</i> <i>Clostridium butyricum</i>	increased crude protein reduced antinutritional factors	improved growth performance improved intestinal health improved metabolic rates enhanced immune function	[243]
34	broiler chickens	mixture of grated cassava roots and palm kernel cake	spontaneous	increased the crude protein content fiber content decreased	increased live weights increased average daily weight gain increased internal organ weights	[244]
35	broiler chickens	cassava roots and palm kernel cake	<i>Aspergillus oryzae</i> <i>Aspergillus niger</i> <i>Rhizopus</i> spp.	increased crude protein reduced crude fiber	lower feed intakes	[245]

Lactobacillus plantarum
Bifidobacterium spp.

36	broiler chickens	palm kernel cake	<i>Lactobacillus plantarum</i>	reduced antinutritional factors	improved growth performance	[246]
			<i>Saccharomyces boulardii</i>	increased crude protein	enhanced immune function	
37	broiler chickens	olive mill waste	<i>Rhizopus oryzae</i> 284	increased the crude protein content decreasing crude fiber	improved metabolizable energy	[210]
38	broiler chickens	olive leaf residues	<i>Aspergillus niger</i> <i>Candida utilis</i>	increased crude protein reduced anti-nutritional factors	improved growth performance	[247]
39	broiler chickens	molasses	<i>Bacillus subtilis</i>	enhanced surfactin content	improved growth performance improved intestinal morphology	[248]
40	broiler chickens	molasses and brown sugar	<i>Saccharomyces cerevisiae</i>	increased bioactive compounds	improved growth performance higher levels of beneficial metabolites	[249]
41	Japanese quail	distillery yeast sludge	<i>Saccharomyces cerevisiae</i>	enhanced B-complex vitamins increased crude protein	improved growth performance	[250]
42	laying hens	wheat, pea and barley	spontaneous	decreased sugar content increased soluble non-starch polysaccharides reduced phytase activity	higher body weight gain improved feed conversion ratio increased egg quality improved intestinal health increased cannibalism	[251]
43	broiler chickens	pea	<i>Bacillus subtilis</i>	reduced anti-nutritional factors	improved feed conversion ratio improved starch digestibility	[252]
44	broiler chickens	<i>Astragalus membranaceus</i>	<i>Lactobacillus plantarum</i>	reduced antinutritional factors increased bioactive compounds	improved growth performance improved antioxidant status improved intestinal health enhanced immune function	[253]

45	laying hens	astragalus	<i>Lactobacillus pentosus</i>	increased bioactive compounds	improved egg quality increased egg-laying rate	[254]
46	broiler chickens	rice bran	<i>Issatchenkia orientalis</i> Y266 <i>Bacillus subtilis</i> B266	lower pH levels	improved gut microflora enhanced immune response	[255]
47	broiler chickens	mixture of fruits, vegetables, and rice bran	<i>Bacillus subtilis</i> <i>Bacillus licheniformis</i> <i>Bacillus megaterium</i>	enhanced the presence of bioactive compounds enhanced the presence of vitamins and minerals	improved body weight enhanced villus height	[256]
48	broiler chickens	<i>Corni fructus</i> (fruit of <i>Cornus officinalis</i>)	<i>Aspergillus oryzae</i> <i>Bacillus subtilis</i>	increased crude protein	reduced growth performance reduced crude fat content reduced H2S emissions	[257]
49	broiler chickens	kelp (<i>Laminaria</i> <i>japonica</i>)	<i>Aspergillus oryzae</i> <i>Bacillus subtilis</i>	increased crude protein	improved oxidative stability	[257]
50	broiler chickens	canola meal	<i>Lactobacillus fermentum</i> <i>Bacillus subtilis</i>	reduced anti-nutritional factors reducing harmful <i>E. coli</i> populations	reduced NH3 emissions increased weight gain increased feed conversion ratios improved growth performance enhanced lipase and amylase activity increased serum antioxidant enzymes lower oxidative stress markers improved immune status improved villus height and a reduction in pathogenic bacteria	[206]
51	broiler chickens	sea mustard (<i>Undaria</i> <i>pinnatifida</i>)	<i>Lactobacillus buchneri</i> <i>Bacillus subtilis</i> <i>Bacillus licheniformis</i>	reduced anti-nutritional factors	increased body weight gain increased breast muscle lightness	[258]

52	broiler chickens	<i>Alisma canaliculatum</i>	<i>Lactobacillus acidophilus</i> <i>Enterococcus faecium</i> <i>Bacillus subtilis</i> <i>Saccharomyces cerevisiae</i>	decreased protein content decreased fat content	improved body weight	[259]
53	broiler chickens	napierrass and pangolagrass	<i>Bacillus subtilis</i> <i>Entrophospora sp. NP1</i>	increased crude protein	similar growth and digestibility results to the control diet	[203]
54	broiler chickens	"Healthy Chicken Powder" (Jian Ji San, JJS)	<i>Bacillus subtilis</i> <i>Bacillus licheniformis</i> <i>Saccharomyces cerevisiae</i> <i>Zygosaccharomyces rouxii</i>	enhanced nutrient quality	improved body weight improved gut bacteria composition	[260]
55	broiler chickens	banana peel meal	<i>Chrysonilia crassa</i> <i>Bacillus subtilis</i>	increased crude protein reduced crude fiber	reduced uric acid concentration improved ileal villi height	[261]
56	broiler chickens	Citri Sarcodactylis Fructus by-products	<i>Lactobacillus plantarum</i> <i>Bacillus subtilis</i> <i>Saccharomyces cerevisiae</i>	reduced crude fiber	improved growth performance enhanced intestinal health improved immune function	[262]
57	laying hens	marine animal resources coffee residues	<i>Bacillus thermoamylovorans</i> <i>Bacillus thermocloacae</i> <i>Bacillus subtilis</i>	enhanced digestibility	increased egg production improved gut metabolism	[263]
58	laying hens	tea	<i>Bacillus subtilis</i> <i>Lactobacillus plantarum</i>	increased crude protein	improved egg-laying enhanced egg quality increased antioxidant capacity reduced ammonia emissions	[264]
59	laying hens	peony seed dreg	<i>Lactobacillus acidophilus</i> <i>Bacillus subtilis</i>	reduced natural anti-nutritional factors increased bioactive compounds	improved egg production and quality enhanced immune function	[205]

Saccharomycetes					enhanced antioxidant capacity	
60	broiler chickens	substrat for <i>Bacillus licheniformis</i>	<i>Bacillus licheniformis</i>	enhanced surfactin content	improved growth performance increased cecal bacterial diversity	[265, 266]
61	Shaoxing ducks	Shanghai Nonghao Feed	<i>Lactobacillus plantarum</i> <i>Bacillus subtilis</i> <i>Bacillus licheniformis</i>	enhanced nutritional composition	improved egg quality improved intestinal morphology	[267]
62	peking duck	Ginkgo biloba leaves	<i>Bacillus coagulans</i>	decreased ginkgolic acid	improved growth performance anti-lipogenic effect	[268]
63	broiler chickens	dandelion	<i>Saccharomyces cerevisiae</i> <i>Lactobacillus plantarum</i>	increased bioactive compounds	increased average daily gain improved antioxidant enzyme activities improved immunity	[217]
64	laying hens	<i>Eucommia ulmoides</i>	<i>Lactobacillus plantarum</i>	improved palatability increased bioavailability of active components	highest laying rate increased daily feed consumption increased beneficial fatty acids of eggs increased the abundance of <i>Lactobacillus</i> enhanced levels of immunoglobulins lowered blood triglycerides	[269]
65	laying hens	paper mulberry (<i>Broussonetia papyrifera</i>)	<i>Lactobacillus plantarum</i>	increased crude protein content reduced fiber content	increased average daily	[270]
66	Cherry Valley ducks	commercial duck feed	<i>Lactobacillus plantarum</i>	lower fiber elevated methionine	improved egg yolk color decreased serum triglyceride improved sensory qualities	[271]
67	Muscovy ducks	<i>Andrographis paniculata</i>	<i>Saccharomycetes</i> spp.	increased bioactive compounds	improved growth performance	[272]

Lactobacillus spp.

68	layer quails	potato pulp	<i>Geotrichum candidum</i>	reduced antinutritional factors	increased breast muscle yield enhanced immune function	[273]
69	broiler chickens	shea nut meal	<i>Aspergillus niger</i>	increased crude protein reduced crude fiber	similar growth and digestibility results to the control diet	
70	broiler chickens	grape seed	<i>Aspergillus niger</i>	reduced anti-nutritional factors enhanced nutritional value increased polyphenolic content reduced anti-nutritional factors elevated the antioxidant activity	improved feed intake increased weight gain enhanced antioxidant defense increases in beneficial bacteria and reductions in pathogenic bacteria lowered the yellowness of breast meat enhanced immunity	[274] [204]
71	broiler chickens	sour cherry kernel	<i>Aspergillus niger</i>	increased the crude protein content reduced crude fiber reduced anti-nutritional factors		[275]
72	broiler chickens	jatropha curcas kernel meal	<i>Aspergillus niger</i>	reduced the levels of anti-nutritional factors	similar growth and digestibility results to the control diet	[276]
73	broiler chickens	pine needle	<i>Aspergillus niger</i>	increased crude protein reduced crude fiber	improved antioxidant status	[277]
74	broiler chickens	<i>Artemisia argyi</i>	<i>Aspergillus niger</i>	reduced crude fiber enhanced nutrient quality	improved growth performance improved meat quality	[278]
75	Japanese quail	faba bean	<i>Aspergillus niger</i>	increased organic acids	improved body weight reduced triglycerides enhanced immunity improved antioxidant status reduced pathogenic intestinal bacteria	[279]
76	Cherry Valley ducks	flaxseed cake	<i>Aspergillus niger</i>	increased crude protein	improved nutrient utilization	[280]

<i>Candida utilis</i>			
77	broiler chickens	EcoVit R Powder	reduced anti-nutritional factors
		<i>Aslbya gossypii</i>	increased the riboflavin content
			improved growth performance higher daily weight lower mortality rates
			[281]
78	broiler chickens	cocoa pod husk	improved the nutritional value
		<i>Pleurotus ostreatus</i>	increased gizzard and intestinal weights decreased abdominal fat
			[215]
79	broiler chickens	sorghum	reduced antinutritional factors
		<i>Limosilactobacillus fermentum</i>	improved the digestibility increased bioactive compounds
			improved growth performance increased villus height
			[282]

Table 1- Overview of various agroindustrial byproducts subjected to microbial fermentation and their effects on poultry performance. The table summarizes the poultry species examined, specific agroindustrial byproducts fermented, microorganisms utilized for fermentation, resulting biochemical and nutritional transformations, and subsequent impacts on poultry growth, health, and productivity.

Soybean meal

Soybean meal is widely recognized as the most common plant protein source utilized in poultry nutrition. Its popularity stems from its high protein content (approximately 47–49%), relatively balanced amino acid profile (though it may be limited in sulfur-containing amino acids), wide availability [207, 252, 283], and high abundance of essential amino acids such as lysine, tryptophan, threonine, isoleucine, and valine [50, 222].

However, a significant limitation of using soybean meal is the presence of various anti-nutritional factors. These include antigenic proteins (β -conglycinin and glycinin), trypsin inhibitors, phytic acid, oligosaccharides (raffinose and stachyose), lectins, and saponins. Such compounds can reduce nutrient absorption and digestion, potentially leading to gastrointestinal issues and diminished animal performance [99, 220, 222, 283–285]. One method of inactivating these anti-nutritional factors is heat treatment during soybean oil extraction.

Additionally, fermenting soybean meal has proven highly effective for reducing levels of trypsin inhibitors, phytic acid, β -conglycinin, glycinin, raffinose, and stachyose. Fermentation also increases protein concentration (up to 58.5%) and improves nutrient and amino acid digestibility compared to unfermented soybean meal [50, 99, 286]. Most studies involving broiler chickens fed fermented soybean meal report improved growth performance and enhanced intestinal morphology.

The microorganisms most commonly used for fermentation are *Bacillus* and *Lactobacillus* species, which increase protein concentration and reduce anti-nutritional factors [218, 219, 221, 222]. Fermentation of soybean meal using *Bacillus subtilis* LYS1 significantly increased surfactin concentration, notably the C14 and C15 isoforms [218]. Incorporating 2.5% of this fermented product into broiler feed resulted in notable improvements in weight gain and feed conversion ratio (FCR).

Additionally, beneficial intestinal morphological changes were observed, characterized by taller villi and deeper crypts [219]. Furthermore, supplementation with 1.6% fermented soybean meal enhanced tibial bone

mineralization through elevated calcium and phosphorus levels [218]. Fermentation of soybean meal with *Bacillus subtilis* ED-3-7 increased crude protein content by 11.68%, substantially reduced allergenic proteins glycinin and β -conglycinin by 82.04% and 88.42%, respectively, and decreased urease activity by 90.10%. Additionally, this fermentation approach improved broiler growth performance by promoting a healthier gut microbiota, indicated by an increased abundance of *Lactobacillus*, a decrease in *Proteobacteria*, and a higher abundance of *Firmicutes* [220].

Moreover, fermenting soybean meal with a consortium including *Lactobacillus acidophilus*, *Lactobacillus plantarum*, *Bacillus subtilis*, and *Aspergillus oryzae* enhanced overall protein content, particularly lysine, phenylalanine, glutamine, and tyrosine [222]. This process reduced coliform counts, phytic acid, trypsin inhibitors, β -conglycinin, and glycinin levels. In broilers, these modifications led to improved body weight gain and FCR, and reduced intestinal *Salmonella Typhimurium* levels. Additionally, the heterophil-to-lymphocyte ratio decreased, indicating diminished stress and improved immune responses [221]. Reduced abdominal fat deposition and lower plasma 3-methylhistidine levels were observed, suggesting decreased muscle protein degradation. Increased activities of amylase and protease enzymes and upregulated hepatic IGF-1 gene expression further contributed to enhanced growth and metabolism [222].

Similarly, fermentation of a soybean meal and feather meal mixture with *Bacillus amyloliquefaciens* resulted in effective keratin degradation and increased protein content, particularly lysine and histidine. Incorporating 5% of this fermented product into broiler diets enhanced growth performance and resulted in improved intestinal morphology, with taller villi and shallower crypts. Better protein utilization was reflected by reduced blood urea nitrogen and increased creatinine levels [223]. Fermenting soybean meal with a consortium including *Clostridium butyricum* and species from *Bacillus*, *Saccharomyces*, and *Lactobacillus* increased concentrations of amino acids such as serine, glycine, cysteine, leucine, lysine, histidine, and arginine, along with organic acids including butyric, citric, and succinic acids. Feeding this fermented product at 4% inclusion to laying hens boosted egg production, egg mass, and feed intake, and enhanced eggshell strength and albumen quality. Additionally, the fermentation improved the digestibility of dry matter, crude

protein, and fiber, supported intestinal health by elevating intestinal protein levels and upregulating stem cell markers, and positively impacted ovarian development through increased ovarian weight, follicle count, and reproductive hormone levels (FSH and LH) [224].

Lastly, fermentation of soybean meal with *Lactobacillus plantarum*, *Bacillus subtilis*, and *Aspergillus oryzae* effectively reduced anti-nutritional factors including phytic acid, β -conglycinin, glycinin, and crude fiber while increasing crude protein content. Including this fermented product in Japanese quail diets led to enhanced weight gain, improved FCR, and a healthier gut microbiota characterized by increased lactic acid bacteria and decreased coliform counts. Quail also exhibited improved intestinal morphology, evidenced by taller villi, a superior villus height-to-crypt depth ratio, and beneficial reductions in total cholesterol and LDL cholesterol levels [207].

Corn meal

Corn is predominantly utilized as the primary energy feed component in poultry diets, commonly constituting up to 70% of total feed composition. Its appeal stems from a high energy density of approximately 3962 kcal/kg, essential for supporting rapid growth in poultry with limited digestive capacity. The palatability of corn further enhances its attractiveness as a feed ingredient [287, 288].

However, the protein concentration of corn meal is low, at only 9.8%, with the main protein source being zein. Zein is rich in proline and glutamic acid but deficient in other essential amino acids, particularly lysine and tryptophan. Therefore, corn meal is often mixed with soybean meal in poultry feed formulations to compensate for the protein deficiency of corn meal and to supplement the feed with other essential amino acids, especially lysine and tryptophan, which are found in optimal quantities in soybean meal [99, 108, 235, 282, 289]. Corn meal contains approximately 4% fat, primarily composed of beneficial unsaturated fatty acids like linoleic, palmitic, and oleic acids, vital for optimal poultry growth and health [290, 291]. Despite its benefits, corn meal includes certain anti-nutritional factors. Phytate, for instance, can bind minerals, reducing their availability for poultry absorption [99]. Additionally, corn is rich in non-starch polysaccharides (NSPs), which poultry typically

struggle to digest due to the absence of specific endogenous enzymes [182]. Fermentation emerges as an effective strategy to enhance the nutritional quality of corn meal. It significantly reduces anti-nutritional factors such as phytates and NSPs, thus enhancing the bioavailability of crucial minerals like zinc, manganese, copper, and cobalt. Enzymes like tannase and phytase, produced during fermentation, are key to this nutritional enhancement. Furthermore, fermentation has been documented to substantially lower mycotoxin levels in contaminated corn, further boosting feed safety and effectiveness [99, 157, 292].

In the case of corn meal, the most used microorganisms for its fermentation are *Bacillus subtilis*, *Saccharomyces cerevisiae*, and species of the *Lactobacillus* genus. Farm birds whose diets included fermented feed exhibited improved growth performance and enhanced gut health [227-233, 293]. Fermentation of cornmeal with *Umbelopsis isabellina* led to an increase in the concentration of γ -linolenic acid and β -carotene, along with a general modification of the fatty acid profile. Including this 10% ferment in broiler feed produced breast meat with notably higher concentrations of γ -linolenic acid, α -linolenic acid, and oleic acid, yielding a significantly improved n-6/n-3 fatty acid ratio. Sensory evaluation revealed that adding the fermented product either maintained or enhanced key meat attributes such as juiciness and flavor, while chemical analysis of the breast muscle demonstrated a decrease in fat content and an increase in protein content [227]. A mix of corn starch residue (9%), distillers dried grains with solubles (10%), distillers dried solubles (30%), and sprayed corn skin (47%), fermented with *Lactobacillus acidophilus*, *Bacillus subtilis*, and *Candida utilis*, led to an increase in the feed's protein concentration and produced organic acids such as lactic, citric, and acetic. Incorporating this fermented feed into the diet of Hy-Line Brown laying hens increased feed intake, leading to improved production performance. As a result, egg production rose, and egg quality also improved, as parameters such as yolk color, albumen height, and Haugh units were enhanced [293]. A mixture of yellow corn and soybean meal, first fermented with *Bacillus subtilis* and then with *Saccharomyces cerevisiae*, produced increased levels of lactic and acetic acids. Broilers whose feed included this fermented product showed better body weight, weight gain, and feed intake [228].

A similar two-stage fermentation (first with *Bacillus subtilis*, then with *Bacillus coagulans*, *Lactobacillus casei*, *Lactobacillus acidophilus*, *Lactobacillus delbrueckii*, and *Lactobacillus reuteri*) provided further benefits. By increasing the concentrations of lactic and acetic acids and boosting digestible amino acids, broiler growth performance improved, with significant gains in body weight and better feed conversion ratios. Moreover, serum lactate dehydrogenase levels were notably lower, and the number of lactic acid bacteria in the intestine increased [231].

The same corn and soybean meal mix, fermented with *Saccharomyces cerevisiae*, *Bacillus subtilis*, *Lactobacillus plantarum*, and *Enterococcus faecium*, also benefitted the birds. After fermentation, protein concentration increased, and including this feed in the diet of Xuefeng black-bone chickens led to higher body weight, average daily gain, and feed conversion ratio, as well as the production of high-quality meat. Furthermore, when ginseng polysaccharide was added, intestinal structure improved, pro-inflammatory markers (TNF- α and IL-6) decreased, IgG levels rose, and both mortality and diarrhea incidence were significantly reduced [229]. Adding ginseng polysaccharides along with corn and soybean meal fermented with *Bacillus subtilis*, *Saccharomyces cerevisiae*, *Lactobacillus plantarum*, and *Enterococcus faecium* in the diet of Xuefeng black-bone chickens showed further benefits for chick growth. At the intestinal level, villus height and the villus height-to-crypt depth ratio increased, while crypts were shallower. Meanwhile, the gastrointestinal microbiota exhibited a rise in beneficial microorganisms of the genus *Sutterella*, *Bacteroides vulgatus*, and *Eubacterium tortuosum*, along with a decline in potentially pathogenic species such as *Mycoplasma gallinarum* and *Asteroleplasma anaerobium* [233].

Fermenting corn and soybean meal with *Lactobacillus plantarum* and *Bacillus subtilis* enhanced nutrient quality by increasing the levels of small peptides, thereby improving digestibility. Including this feed at 10% in broiler diets led to increased body weight and average daily gain, along with improved feed digestibility. Higher concentrations of proteases and amylases contributed to these improvements. Additionally, positive intestinal changes were noted, such as greater villus height and a larger absorptive area in the duodenum and jejunum, as well as a boost in beneficial gut microbes like *Lactobacillus* and *Bifidobacteria*. Pathogenic species such as *Escherichia coli* and *Salmonella*

decreased, and mortality, especially during the starter phase, was reduced [230].

When *Saccharomyces cerevisiae* was added alongside *Lactobacillus plantarum* and *Bacillus subtilis* in the fermentation process, the feed's beneficial properties were further intensified. Including it at 15% in broiler diets led to higher body weights and increased feed intake. Immune function also improved, with a rise in the bursa of Fabricius and higher serum levels of albumin, globulin, immunoglobulins (IgA, IgG, IgM), lysozyme, and complement factors C3 and C4.

Beyond these immune benefits, broilers on the fermented diet showed greater concentrations of volatile fatty acids (acetic, propionic, and butyric acids) and lactic acid in their ceca, alongside reduced skatole and indole (compounds associated with unpleasant odors). In addition, the composition of the cecal microbiota shifted toward more beneficial groups such as *Ruminococcaceae*, *Lactobacillaceae*, and *Clostridiales*, with reductions in *Rikenellaceae*, *Lachnospiraceae*, and *Bacteroidaceae* [232].

Rapeseed meal

Rapeseed meal, a co-product of rapeseed oil extraction, is increasingly studied as an alternative protein source for livestock and poultry diets. Its potential lies in helping to reduce reliance on conventional protein sources like soybean meal, which are subject to environmental and cost-related challenges [51, 294, 295]. Rapeseed meal is notable for its high protein content, typically ranging from 30% to 40% depending on the extraction method, and offers a well-balanced amino acid profile. It is especially rich in sulfur-containing amino acids such as methionine and cysteine. Additionally, it provides minerals like calcium and phosphorus [52, 91, 107, 283, 294]. However, its broader use is limited by the presence of antinutritional factors, particularly glucosinolates, which can reduce palatability and have been linked to hemorrhagic liver and increased mortality at high concentrations [107].

Fermentation is a promising method for enhancing the nutritional value of rapeseed meal. Microorganisms involved in this process can break down glucosinolates, synthesize beneficial bioactive compounds, such as

antioxidants, modify the protein and amino acid profile, and reduce the crude fiber content [157, 252, 283, 295]. The effects on farm birds have been reflected in improved growth performance and immunity, as well as an enhancement in the quality of meat and eggs [107, 208, 224-226, 295]. Fermenting rapeseed meal with *Bacillus subtilis* strain 67 increases fat content while reducing both fiber and glucosinolate levels. Additionally, this strain's notable cellulolytic and xylulolytic capacity further enhances the feed's nutritional properties. When included in the diet of broiler chickens, the fermented feed led to an approximately 100 g higher weight gain compared to the control group. However, the effects on meat quality varied: breast muscle water-holding capacity decreased, while leg muscle protein content rose by about 0.65% compared to the control group, accompanied by a decrease in carnosine in the leg muscles of birds fed FRSM [295]. For laying hens whose diet included fermented rapeseed meal, egg weight increased, although yolk color intensity dropped slightly—likely due to pigment loss during fermentation. More efficient nutrient absorption was evident through better intestinal villi development and lower intestinal content viscosity, with a notable improvement in phosphorus absorption [107].

Using *Lactobacillus acidophilus*, *Bacillus subtilis*, and *Aspergillus niger* in rapeseed meal fermentation reduced tannins, phenolic compounds, phytic acid, and crude fiber, while boosting crude protein. Each microorganism played a specific role: *Lactobacillus acidophilus* produced lactic acid; *Bacillus subtilis* supplied enzymes such as cellulases and phytases; and *Aspergillus niger* generated hemicellulases and phytases to further break down complex feed components. Including this feed in the diet of broiler chicks challenged with *Salmonella Typhimurium* helped prevent pathogen colonization in both the gut and internal organs. This effect was likely due to organic acids produced during fermentation, which create an acidic environment unfavorable to *Salmonella* growth. In addition, microorganisms in the fermented feed compete with pathogens for binding sites, produce bacteriocins, and enhance immune function by reducing corticosterone levels and increasing lymphocyte counts. Birds on the fermented diet also gained weight more efficiently, had a better feed conversion ratio, and showed lower physiological stress (as indicated by the heterophil-to-lymphocyte ratio) [225].

Similarly, a mixture of soybean hulls and rapeseed cake fermented with multiple microorganisms (*Aspergillus niger*, *Lactobacillus plantarum*, and *Lactobacillus fermentum*) showed beneficial effects. Fermentation raised protein content by about 10% and reduced fiber by about 12%. Ether extract, calcium, and total phosphorus all increased as well. When fed to Chahua chickens, this fermented feed improved average daily gain and feed intake, boosted immunity (higher levels of IgA, IgG, and IgM), and enhanced antioxidant status through increased glutathione peroxidase and superoxide dismutase, with reduced malondialdehyde levels. Moreover, these birds exhibited increased villus height, enhanced villus-to-crypt ratios, and a greater abundance of beneficial gut bacteria, particularly *Lactobacillus* and *Faecalibacterium* [208].

A combination of corn, cottonseed meal, and rapeseed meal fermented with *Lactobacillus plantarum* and *Lactobacillus acidophilus* reduced gossypol, phytic acid, and tannins, while increasing levels of probiotics, enzymes, and organic acids. When included in White Leghorn chicks' diets, it led to higher body weight and daily gains. Stronger immune responses were also observed, including enhanced T-cell/B-cell proliferation, higher immunoglobulins (IgA, IgG, IgM), increased Newcastle disease virus antibodies, and elevated cytokine levels (IL-1, IL-2, IL-4, IL-6, and TNF- α). Antioxidant capacity also improved, with higher levels of superoxide dismutase and glutathione peroxidase alongside reduced malondialdehyde. These benefits appear to be mediated through the NF- κ B signaling pathway [226]. Furthermore, a 1:1 mixture of cottonseed meal and coconut meal fermented with *Bacillus*, *Saccharomyces*, *Lactobacillus*, and *Clostridium butyricum* increased the feed's protein content, amino acids (serine, glycine, cysteine, leucine, lysine, histidine, and arginine), and organic acids such as butyric, citric, and succinic, while lowering the fiber content. Including 4% of this fermented mixture in laying hens' diets boosted egg production, egg mass, and feed intake, in addition to improving eggshell quality, albumen height, Haugh units, and yolk color. Digestibility of dry matter, crude protein, and fiber also increased. At the intestinal level, hens exhibited taller villi, deeper crypts, and a higher villus-to-crypt ratio. They also showed higher expression of tight junction proteins (ZO-1, Occludin, Claudin-1) and intestinal stem cell markers (Lgr5, PCNA). Moreover, follicle development and hormone levels (FSH and LH) rose, indicating improved reproductive performance [224].

Wheat bran and barley

Wheat bran is the outer-layer byproduct of wheat milling and is extensively used as an animal feed raw material due to its high energy content and crude protein. Wheat contains multiple nutrients, including vitamins and antioxidative compounds [74, 102, 236]. Wheat bran contains approximately 13–18% protein and relatively high amounts of minerals such as phosphorus, calcium, potassium, iron, manganese, and zinc [102]. Despite its nutritional value, wheat bran has limitations in poultry diets due to its high fiber content and the presence of antinutritional factors, resulting in poor palatability. Poultry, particularly broilers, do not have sufficient endogenous digestive enzymes to degrade wheat bran effectively. Moreover, non-starch polysaccharides in wheat bran can increase intestinal viscosity, reduce intestinal motility, and block nutrient absorption, potentially limiting growth potential in broilers [102, 236].

To overcome these limitations, fermentation is considered a potent method for enhancing the nutritional quality of wheat bran [102]. Fermentation of wheat bran using *Saccharomyces* and *Lactobacillus* species has been shown to elevate the concentration and bioavailability of soluble dietary fiber and total free phenolics while reducing phytic acid levels by over 20% [102].

Barley (*Hordeum vulgare* L.) is considered an alternative cereal that can substitute common cereal grains like corn, being rich in starch and fiber, typically containing >50% starch [12, 15, 235]. As with wheat bran, barley contains antinutritional factors that limit its dietary inclusion in the poultry industry. The primary limitations are high levels of non-starch polysaccharides, particularly β -glucans. High β -glucan content in barley-based diets can lead to increased digesta viscosity in the intestines of birds [99, 235]. Fermentation and exogenous enzymes such as xylanases and β -glucanases can improve barley utilization by degrading non-starch polysaccharides and increasing protein content [102, 235].

Similar to cornmeal, the most commonly used strains for fermenting wheat bran and barley belong to the *Bacillus* and *Lactobacillus* genera. Once introduced into poultry feed, the most common effects are improved growth performance and enhanced intestinal health [104, 234-237]. Fermenting wheat

bran with *Lactobacillus acidophilus*, *Bacillus subtilis*, *Lactobacillus rhamnosus*, and *Saccharomyces cerevisiae* increased its protein concentration by about 2% and acid-soluble protein by about 7%, while fiber content decreased by about 8%. However, including this fermented wheat bran at 25 g/kg or 50 g/kg in poultry feed did not significantly improve growth performance [234].

In contrast, wheat bran fermented with *Bacillus cereus* and introduced into poultry diets boosted duodenal amylase activity and enhanced microbial diversity in the cecum, suggesting a healthier gut environment [236]. When a mixture of wheat bran and soybean meal was fermented with *Bacillus subtilis*, the feed's protein concentration rose by 2 g/kg, and its inclusion in chicks' diets promoted the proliferation of *Lactobacillus crispatus* in the intestinal microbiota. By comparison, fermentation with *Bacillus licheniformis* increased the feed's protein concentration by about 14 g/kg. Incorporating this product in broiler diets led to higher body weight, average daily gain, and improved feed efficiency.

Examination of the small intestine showed longer villi in the jejunum, indicating enhanced nutrient absorption. There was also significantly higher expression of the *mucin 2* and *zonula occludens-1* genes, which support the intestinal barrier, and significantly higher expression of superoxide dismutase genes in the cecum, suggesting stronger antioxidant defenses. Furthermore, genes encoding glycosyltransferase 2 were more highly expressed, potentially aiding nutrient metabolism. A more diverse gastrointestinal microbiota was also observed [237].

In a two-phase fermentation process, barley was first fermented with *Bacillus subtilis* and *Aspergillus niger*, then with *Lactobacillus plantarum*, together with various fibrolytic enzymes (beta-glucanase, beta-xylanase, pectinase, cellulase, and phytase). This process reduced anti-nutritional factors like non-starch polysaccharides (NSPs) and phytic acid, increased protein concentration by about 1%, and decreased fiber content by around 2%. Lignin levels dropped by about 3%, and cellulose content also declined significantly. Fermentation additionally raised non-phytate phosphorus by about 1 g/kg. Including this fermented barley at 10% in broiler diets improved growth performance, as shown by better feed conversion ratios and higher body weight gain. Nutrient

digestion became more efficient, partly due to elevated enzyme activities (lipase, amylase, trypsin) and improved phosphorus availability. Gut health benefits were noted through increased villus height, a higher villus height-to-crypt depth ratio, reduced intestinal viscosity, and elevated levels of immunoglobulins and lysozyme.

Molecular analyses indicated that fermented barley enhanced expression of nutrient transporters (GLUT-1, PepT1, CAT-1) and tight junction proteins (occludin, claudin-1, MUC-2, JAM-2, β -defensin-1), reflecting more efficient nutrient uptake and a stronger gut barrier. Antioxidant activity also rose, owing to higher levels of glutathione peroxidase, superoxide dismutase, and catalase, which helped mitigate oxidative stress and improve tissue health. The birds' lipid profile improved as well, with lower total cholesterol, triglycerides, and LDL-c, and higher HDL-c levels [235]. When dried brewer's grains were fermented with *Bacillus subtilis*, *Lactobacillus rhamnosus*, and *Saccharomyces cerevisiae*, protein and lipid concentrations increased, while fiber and anti-nutritional factors decreased. Including this fermented product at 10% in broiler feed resulted in improved body weight, feed conversion ratio, and dressing percentage, along with reduced cholesterol levels in thigh meat and serum. From an economic standpoint, feed costs decreased and gross margins rose by up to 47% [104].

Mix of corn, soybean meal and wheat

Corn, soybean meal, and wheat are commonly used ingredients in broiler chicken feed. Proper feed formulation for poultry requires a careful balance of energy (mainly from grains such as corn and wheat) and protein (largely from soybean meal). These ingredients are typically combined with other components such as limestone, dicalcium phosphate, salt, vitamin and mineral premixes, and amino acids (including lysine, methionine, and threonine) to create diets that meet specific nutrient requirements [24, 51, 225, 283, 296, 297].

When these components are fermented with bacteria from the *Bacillus* and *Lactobacillus* genera, they offer several benefits for poultry health and performance, including enhanced body weight gain, a more balanced gut microbiota, strengthened immune responses, and reduced mortality rates [101,

186, 238-243]. Fermented moist feed, composed of a mixture of corn, soybean meal, and wheat fermented with *Lactobacillus plantarum*, resulted in an increased pH level and a higher concentration of *Lactobacilli*. When included in the diet of broiler chickens, this feed improved the feed conversion ratio during the finisher phase (days 27–39) and beneficially modulated the intestinal microbiota by increasing *Lactobacilli* counts while reducing coliforms and Streptococci in both the ileum and caeca.

Furthermore, broilers fed fermented moist feed showed greater villus height in the mid-jejunum and mid-ileum, indicating enhanced nutrient absorption and improved intestinal health. The mortality rate also decreased significantly, from 9.3% to 3.6% [186]. Solid-state fermented feed, prepared from the same mixture of corn, soybean meal, and wheat but fermented with *Lactobacillus casei*, yielded beneficial effects by increasing the concentrations of organic acids, including lactic acid (20 mg/g), acetic acid (5 mg/g), succinic acid (7 mg/g), and pyruvate (0.1 mg/g). Fermentation also elevated the crude protein content and reduced antinutritional factors. This fermented feed was included in broiler diets at two levels: 0.3 kg/t (FFL) and 3 kg/t (FFH). Both FFL and FFH groups showed improved weight gain.

Gut morphology analysis revealed increased villus height in the duodenum, jejunum, and ileum, suggesting enhanced nutrient absorption and reduced tissue damage typically associated with pathogenic bacteria. The immune response was also positively modulated: IL-10, an anti-inflammatory cytokine, was elevated in the FFL group, while pro-inflammatory markers IL-1 β and TLR4 were downregulated in both FFL and FFH groups, indicating diminished intestinal inflammation. Additionally, thymus size was reduced in the FFH group, though spleen and bursa weights remained unchanged. Harmful bacterial populations (*Delsulfobacterota*, *Desulfovibrionia*, *Negativicutes*, and *Escherichia coli*) declined in the FFH group, reflecting a healthier gut microbiota. At the same time, beneficial microbial taxa, particularly *Lactobacillaceae*, *Lactobacillus aviarus*, and other *Lactobacillus* species, increased in both FFL and FFH groups, reinforcing the probiotic effects of fermented feed [239].

Fermenting a mixture of corn, soybean meal, and wheat with *Bacillus subtilis* and *Saccharomyces cerevisiae* decreased the pH to 4.2 and elevated the lactic

acid concentration to 18.29 mg/g, while also increasing the number of lactic acid bacteria (LAB) and the crude protein content. Incorporating this fermented feed into the diet of Hy-Line Brown laying hens improved production performance, raising the laying rate from 73.96% to 78.24% and reducing broken eggs from 0.98% to 0.73%. Feed efficiency also improved, with the feed conversion ratio dropping from 2.20 to 2.12. Egg quality was significantly enhanced: albumen height increased from 5.47 mm to 6.04 mm, the Haugh unit rose from 69.01 to 75.82, and yolk color darkened, reflecting better overall quality. Immune function was strengthened, as evidenced by elevated IgA, IgM, and IgG levels, and higher concentrations of IL-2, IL-6, TNF- α , and IFN- γ .

Intestinal morphology also benefited, with increased villus height in the duodenum, jejunum, and ileum. Moreover, the gut microbiota composition shifted favorably, showing higher abundances of *Lactobacillus*, *Megasphaera*, and *Peptococcus*, and lower levels of *Firmicutes* and *Campylobacter* [101]. Feeding Hy-Line Brown layer chicks a similarly composed feed fermented with *Bacillus subtilis*, *Candida tropicalis*, *Lactiplantibacillus plantarum*, and *Clostridium butyricum* resulted in marked increases in essential amino acids (aspartic acid, threonine, serine, glutamic acid, glycine, and alanine) and organic acids (malic, lactic, and acetic).

Fermentation also reduced antinutritional factors, improving the overall nutritional quality of the feed. When included at a 4% level, this fermented feed enhanced average daily weight gain and intestinal health, as evidenced by improved jejunal morphology, increased villus height, and reinforced intestinal barrier integrity. Serum levels of IgA, IgM, and IgG were elevated, indicating strengthened immune function. Additionally, the fermented feed promoted intestinal regeneration by stimulating proliferation and differentiation of intestinal stem cells through activation of the Wnt/ β -catenin signaling pathway [243]. Fermentation of the same mix, this time with *Clostridium butyricum*, *Lactobacillus crispatus*, and *Lactobacillus salivarius*, reduced crude fiber and β -glucan levels while lowering pH, indicating enhanced organic acid production. When included at a 6% level in the diet of laying hens, this mixture improved egg quality, notably increasing albumen height. Hens also showed greater villus height in the duodenum and ileum, suggesting improved nutrient absorption. Microbial diversity rose, with higher abundances of beneficial

bacterial families like *Ruminococcaceae* [242]. Fermentation duration significantly affects feed quality. In diets fermented with *Bacillus subtilis* and *Saccharomyces cerevisiae* for 24 hours (FLF24) or 48 hours (FLF48), higher lactic acid levels were observed after 48 hours. When Landes geese were fed these fermented diets, they showed improved growth performance, including greater body weight gain and increased feed intake. Both FLF diets promoted leg muscle development, while FLF48 also increased liver weight. FLF supplementation positively altered the intestinal microbiota by elevating *Lactobacillus* counts and reducing *Escherichia coli*. Antioxidant capacity was enhanced, especially in the FLF48 group, as evidenced by higher glutathione peroxidase and superoxide dismutase levels, as well as lower malondialdehyde concentrations in heart, liver, and muscle. Both FLF diets helped reduce total and LDL cholesterol, while FLF48 produced the highest HDL cholesterol levels [238].

Fermentation using *Bacillus*, *Lactobacillus*, and yeast improved the nutritional profile of feed by increasing nutrient availability and decreasing antinutritional factors. The resulting fermented product was rich in probiotics, enzymes, and organic acids. When included at 7.5% in SanHua goose diets, it led to significant improvements in body weight and average daily gain. Microbiota analysis revealed a rise in the relative abundance of *Bacteroidetes* and a corresponding decline in *Firmicutes* in the cecum. At the genus level, *Bacteroides* increased, while *Desulfovibrio*, *Phascolarctobacterium*, *Lachnospiraceae*, *Ruminiclostridium*, and *Oscillospira* decreased. The increase in *Bacteroides* was positively correlated with enhanced growth performance, indicating a favorable microbial shift [240].

Fermentation with probiotics isolated from healthy Muscovy ducks (including *Bacillus fragile*, *Bacillus sphaericus*, *Bacillus subtilis*, *Bifidobacterium*, *Lactobacillus*, and *Enterococcus faecium*) enriched the feed by increasing fatty acid levels and short peptides, thereby improving digestion and nutrient absorption. When fed to Muscovy ducks, this fermented feed significantly increased average daily gain and reduced the feed conversion ratio. Lipid metabolism also benefited, with elevated fatty acid concentrations accompanied by reduced phosphatidylethanolamine, phosphatidylcholine, triglycerides, and triacylglycerol. Intestinal morphology improved through increased villus height and elevated expression of tight junction proteins

(Occludin, Claudin-1, and Zo-1), indicating a stronger intestinal barrier. Additionally, the fermented feed shifted gut microbiota toward beneficial genera (*Rothia*, *Lactococcus*, *Limosilactobacillus*, *Lentilactobacillus*, and *Enterococcus*) while reducing pathogenic taxa, including *Campylobacter* and members of *Prevotellaceae*, *Clostridia-vadinBB60*, and *Oscillospira*. Metabolically, higher levels of organic acids such as cholic acid and gallic acid were observed, along with increased biosynthesis of amino acids and fatty acids [241].

Palm and cassava

Palm kernel cake is a byproduct of oil palm processing that is widely produced in tropical countries and is considered cost-effective compared to conventional feed ingredients like corn and soybean meal. It has a high Ether Extract content, ranging from 8.0% to 12.6%, and its crude protein content generally ranges from 16% to 20%. However, its crude fiber content, which typically falls between 12.1% and 23.0%, along with non-starch polysaccharides (60% to 74.3%) and β -mannan (78%), presents anti-nutritional challenges [246].

Despite these limitations, fermentation and enzymatic hydrolysis are commonly employed to boost PKC's nutritional value [246, 275]. Fermenting palm-kernel cake with *Lactobacillus plantarum* and *Saccharomyces boulardii*, along with xylanase and mannanase, decreases anti-nutritional factors, increases crude-protein content, and generates prebiotic compounds. When this fermented product was incorporated at 10% of a broiler diet, it improved growth performance, stimulated feed intake and nutrient absorption, enhanced immune and antioxidant status, and promoted a healthier intestinal ecosystem. This was evidenced by higher abundances of beneficial genera such as *Lactobacillus* and *Subdoligranulum* [246]. Cassava (*Manihot esculenta*) is another tropical plant widely cultivated for its roots, which are processed into products like starch and bioethanol, producing substantial amounts of residues [121, 298]. These agro-industrial by-products contain high fiber and anti-nutritional factors, including hydrogen cyanide and tannins [105, 121, 299].

Consequently, fermentation is a key processing technique for enhancing their nutritional value by breaking down complex components and increasing protein content [105, 121, 280]. Fermenting a blend of cassava roots and palm-

kernel cake with *Aspergillus oryzae*, *Aspergillus niger*, *Rhizopus spp.*, *Lactobacillus plantarum*, and *Bifidobacterium spp.*, supplemented with cellulase and mannanase, raised the crude-protein content from 9.75% to 13.33% and slightly reduced the crude-fiber content from 12.55% to 12.20%. This treatment resulted in a feedstuff with an improved nutrient profile and probiotic qualities.

However, when this product was fed to broilers, they exhibited lower live-weight gains and consumed less feed, though their feed-conversion ratio was comparable to birds on conventional maize-based diets, ultimately reducing the feed cost per kilogram of weight gain [245]. Moreover, replacing maize with a spontaneously fermented cassava-root meal–palm-kernel cake mixture at 25%, 50%, 75%, or even 100% inclusion enabled broilers to reach higher final body weights and average daily gains than those in the control group. Birds on the 100% fermented diet performed as well as those fed maize, whereas broilers whose maize was completely replaced by the unfermented blend lagged significantly behind. As the level of fermented blend increased, feed cost per kilogram of weight gain decreased, making the 100% replacement the most economical option; overall meat quality also improved [244].

Olive

Olive mill waste is a significant by-product derived from olive oil production and olive tree cultivation, predominantly in Mediterranean countries. For instance, Spain, a leading producer, has approximately 2.75 million hectares dedicated to olive cultivation, representing around 70% of EU production and 45% globally. Olive mill waste primarily includes olive leaves, branches, pomace, and oil mill wastewater [247, 300-302]. This waste is characterized by high levels of proteins, essential minerals such as calcium, phosphorus, potassium, and iron, and bioactive compounds including tocopherol and vitamin A.

Notably, olive mill waste contains numerous phenolic compounds, such as protocatechuic acid, p-hydroxybenzoic acid, chlorogenic acid, syringic acid, caffeic acid, p-coumaric acid, vanillic acid, oleuropein, hydroxytyrosol, and verbascoside. These phenolics exhibit various biological properties, including

antioxidant, anti-inflammatory, antimicrobial, antiviral effects, and prebiotic activity beneficially modulating intestinal microbiota [247, 300, 301, 303].

Utilization of olive mill waste in agriculture has shown significant benefits, including applications as biopesticides and providing biological protection against both soil-borne and aerial pathogens. Olive leaf extracts, in particular, have been effectively employed for the green synthesis of nickel oxide nanoparticles, demonstrating potent antiparasitic effects against adult ticks such as *Hyalomma dromedarii*. Moreover, these extracts exhibit robust antimicrobial activity against various pathogens, including bacteria (e.g., *Bacillus cereus*, *Pseudomonas aeruginosa*) and fungi (e.g., *Aspergillus niger*, *Candida albicans*) [302, 303]. Olive waste also notably suppresses *Verticillium dahliae*, a critical soil-borne fungal pathogen responsible for significant agricultural crop losses [302].

Fermentation of olive mill waste using *Rhizopus oryzae* substantially enhances its nutritional profile by increasing crude protein content by 23.4% and reducing crude fiber content by 9.8%. Incorporating 20% of this fermented waste into broiler diets elevates the feed's metabolizable energy by 8.38% [210]. Olive leaves themselves are a substantial by-product obtained during the agricultural phase, particularly from pruning practices. The European Union (EU-28) alone produces over 20 million tons annually from olive tree pruning residues [300]. Olive leaves are notably rich in polyphenolic compounds, particularly flavonoids such as rutin and diosmin [300, 301]. Additionally, these leaves contain significant levels of calcium, approximately 9.409 mg/g in dried material [300].

Fermenting olive leaf residues with *Aspergillus niger* and *Candida utilis* markedly increases crude protein content by 125.45%, decreases tannic acid content by 86.94%, and expands the total amino acid pool by 22%, particularly enhancing glutamic and aspartic acids by over 25.4%. Incorporation of 10% fermented olive leaves into broiler feed results in 120% greater weight gain over 28 days compared to controls and elevates serum levels of superoxide dismutase, total serum protein, and serum albumin, indicating improved antioxidant defense and enhanced protein metabolism [247].

Molasses

Molasses is a dark-brown, viscous liquid by-product derived primarily from sugar extraction processes involving sugarcane or sugar beet, and occasionally citrus fruits [304-306]. Its protein content ranges from 6.7% to 13.5%, depending on the plant source, while its sugar content varies between 40% and 60% [304, 306]. Molasses predominantly contains sucrose, glucose, and fructose, with minor concentrations of other sugars such as galactose, raffinose, arabinose, and xylose [304, 306]. Furthermore, molasses is rich in organic acids, including lactic acid, aconitic acid, and glycolic acid, which positively impact animal health and growth performance [304]. Additionally, it provides essential trace minerals and vitamins such as riboflavin, choline, folic acid, niacin, pantothenic acid, and thiamine [307].

In animal nutrition, molasses serves as an important energy source due to its high sugar content. It enhances feed palatability, thus promoting increased intake, and also helps prevent spoilage or mold growth, especially during warmer periods [304]. Given its low nitrogen content, molasses is frequently supplemented with non-protein nitrogen sources, typically urea, acting as an excellent carrier to evenly distribute urea, mask its taste, and supply carbohydrates readily available for microbial metabolism [307].

Molasses is widely utilized as a substrate for microbial cultivation aimed at biomass production. For example, *Bacillus subtilis* NIU068 cultured on molasses produces surfactin, an antimicrobial compound particularly effective against pathogens like *Escherichia coli*, *Staphylococcus aureus*, *Salmonella Typhimurium*, and *Clostridium perfringens*. Supplementation with molasses fermented by *Bacillus subtilis* NIU068 in broiler diets challenged with *C. perfringens* resulted in improved growth metrics, including increased body-weight gain, enhanced feed-conversion efficiency, and strengthened bone development [248].

A combination of molasses and brown sugar serves effectively as a substrate for cultivating *Saccharomyces cerevisiae* strain JLAU-Borui No. 2012. The yeast culture derived from this fermentation produces beneficial metabolites, such as glycine, inositol, various organic acids, and mannose, significantly enhancing broiler growth performance. Additionally, microbiome analyses

demonstrate shifts in the cecal microbial community, specifically altering the *Firmicutes*-to-*Bacteroidetes* ratio and notably increasing the abundance of *Akkermansia* [249].

Distillery yeast sludge, obtained from fermenting molasses and other carbon sources with *Saccharomyces cerevisiae*, represents a valuable protein-rich by-product. This sludge contains 27–29% crude protein with an essential amino acid profile comparable to soybean or canola meals, vital B-complex vitamins necessary for avian metabolism, and oligomonosaccharides that improve feed palatability and digestibility, and can bind aflatoxins. This bioconversion process transforms an environmental waste into a beneficial feed ingredient, although it also concentrates nucleic acids, which at higher inclusion rates can negatively affect feed acceptance and nutrient absorption. Incorporating distillery yeast sludge into Japanese quail diets at a 3% inclusion rate increased body-weight gain by 4.59% and improved the feed-conversion ratio.

However, higher inclusion levels reduced growth performance due to decreased digestibility of dry matter and crude protein linked to elevated nucleic acid content. Carcass parameters, including dressing percentage, breast-meat yield, and relative organ weights, remained consistent across treatments, with the lowest production costs per 100 g weight gain observed at the optimal 3% inclusion rate, providing economic benefits without negatively impacting carcass quality [250].

Pea

Pea represents a significant legume crop in Europe, serving as a valuable alternative plant protein source to soybean meal in animal nutrition, particularly in areas where soybean cultivation is constrained by environmental factors [252]. Due to their high-quality protein and starch digestibility, peas are highly beneficial components in animal diets. Their crude protein content ranges between 17.9% and 24.1%, with a starch content around 42% [308]. While pea protein is notably rich in lysine, it is deficient in sulfur-containing amino acids and tryptophan. Additionally, the fatty acid profile of peas includes high levels of polyunsaturated fatty acids, particularly omega-3 and omega-6, which positively influence animal health and physiological functions [308].

However, peas also contain heavy metals such as copper, zinc, cadmium, lead, chromium, and nickel, and serve as a phosphorus source, with 1%–25% of total phosphorus found in various root and tuber forms [164, 309]. Furthermore, peas naturally contain antinutritional factors including α -galactosides, pectin, tannins, lectin, phytic acid, and resistant starch. These compounds can impair digestion, particularly in young chicks, leading to pancreatic hypertrophy and increased dietary requirements for sulfur-containing amino acids (F [252]).

Spontaneous fermentation of pea-based feed, predominantly by *Lactobacillus plantarum*, significantly raises lactic and acetic acid levels and reduces dietary sugars by approximately 77%. Additionally, phytase activity decreases by 87%, while soluble non-starch polysaccharides increase by 24%. Incorporating this fermented feed into laying hens' diets results in enhanced body weight gain (473 g vs. 394 g), improved feed conversion efficiency into egg mass, and heavier eggs (61.4 g vs. 60.0 g). Eggshell quality also benefits, indicated by increased average shell weight (6.37 g vs. 6.08 g) and greater shell stiffness. Moreover, coliform counts in the gastrointestinal tract decrease, reflecting improved intestinal health. However, increased mortality rates are observed with fermented feed (4.2% vs. 0.4%), attributed primarily to heightened aggression and cannibalism. Reduced palatability leading to intermittent hunger and frustration in birds necessitates gradual introduction of fermented feed as a practical management strategy [251].

Fermentation of ground peas using *Bacillus subtilis* significantly reduces antinutritional factors, including a 66% reduction in trypsin-inhibitor activity, 77.5% decrease in resistant starch, and 16% reduction in phytic acid content. The process also modestly elevates crude protein levels and lowers crude fat content. Incorporating this fermented ingredient into broiler diets results in improved feed conversion ratios and enhanced starch digestibility [252].

Astragalus

Astragalus (*Astragalus membranaceus*) is a perennial herb extensively used in traditional medicine in various regions, including China, Southeast Asia, Japan, Korea, Iran, Russia, and several European countries, for treating ailments in both humans and animals [253, 310]. It is rich in bioactive compounds such as flavonoids, saponins, proteins, amino acids, and vitamins.

However, the full utilization of these compounds is often limited due to the dense structural components of its cell walls, specifically cellulose and pectin, which tightly bind bioactive substances [253, 310, 311].

Microbial fermentation is a promising solution to these limitations, as it generates enzymes, notably cellulase and pectinase, which greatly enhance the extraction of bioactive compounds from *Astragalus* by breaking down cell wall components. These enzymes and others also facilitate the degradation, modification, or conversion of bioactive compounds into more potent forms [253, 310]. Furthermore, fermentation improves the sensory attributes, enhancing palatability and efficacy, making them more suitable as feed additives [310].

Fermentation of *Astragalus membranaceus* with *Lactobacillus plantarum* significantly degrades cellulose and pectin in the cell wall, hydrolyzing proteins into smaller, easily digestible molecules, and releasing an enriched spectrum of bioactive compounds. This process notably increases levels of functional sugars, calycosin, and formononetin, while also enhancing galactosidase activity, resulting in elevated concentrations of easily digestible monosaccharides, such as D-galactose, D-fructose, and D-arabinose. The incorporation of this fermented *Astragalus* into broiler feed led to a 20.6% increase in body weight, reflecting improved nutrient uptake and palatability.

Additionally, significant boosts in antioxidant capacity were observed, marked by higher glutathione peroxidase and superoxide dismutase activities and reduced malondialdehyde levels. Enhanced immune function was indicated by elevated levels of IgA, IgM, IgG, and reduced pro-inflammatory IL-6, suggesting a more balanced inflammatory response. Improvements in gut morphology included increased intestinal villus height, reduced crypt depth, and higher short-chain fatty acids (SCFAs) concentrations, indicating a healthier gut environment and microbiota balance [253].

Fermentation with *Lactobacillus pentosus* similarly boosted lactic acid content to 15%. Dietary inclusion of this fermented product in laying hens' feed improved several performance parameters, such as lower egg cholesterol levels, greater eggshell strength, improved feed-to-egg conversion ratios, and increased laying rates. Beneficial shifts in intestinal microbiota were observed,

notably higher abundances of *Prevotellaceae* UCG-001 and *Enterococcus*. These microbial changes accompanied enhanced immune responses and improved liver health [254].

Rice bran

Rice bran is a by-product of the rice milling process, constituting approximately 8% to 10% of the total weight of rough rice. It results from polishing brown rice into white rice, during which the bran and germ layers are removed, leaving behind the starchy endosperm.

Rice bran is nutrient-rich, containing substantial amounts of carbohydrates, proteins, fats, dietary fiber, and various bioactive compounds [312-314]. Its macronutrient composition includes crude fat ranging from 18% to 23%, with palmitic, oleic, and linoleic acids being the predominant fatty acids. Crude protein typically constitutes 11% to 16%, and carbohydrates, mainly starch, make up about 50% of the bran [313, 314].

Rice bran is also notable for its bioactive compounds, including tocopherols at concentrations of 100 to 150 mg/kg, predominantly alpha-tocopherol, as well as γ -oryzanol, phytosterols, squalene, γ -aminobutyric acid, anthocyanins, proanthocyanidins, and B-group vitamins, particularly niacin [312-314]. Nevertheless, raw rice bran contains anti-nutritional factors (ANFs), such as phytic acid, trypsin inhibitors, oxalates, saponins, and tannins, which can negatively impact digestibility and nutrient bioavailability [313, 314].

Fermentation significantly enhances the nutritional profile of rice bran, making it more suitable as an animal feed ingredient. This process increases the content of crude protein, digestible amino acids, and fat while reducing anti-nutritional factors, thereby improving mineral bioavailability. Additionally, the antioxidant activity of phenolic compounds present in rice bran is increased through fermentation. Fermentation also improves palatability, enhancing the acceptability of rice bran as animal feed [313].

Fermentation of rice bran using *Issatchenkia orientalis* and *Bacillus subtilis* slightly reduces its pH from 6.6 to 6.0. When incorporated into broiler diets, this fermented product increases the population of *Lactobacillus* spp. in the

small intestine, thereby improving microbial balance. Specifically, the *Salmonella/Lactobacillus* ratio declines to 0.852 in birds fed fermented rice bran, compared to 0.953 observed in those receiving Avilamycin-supplemented feed. Similarly, the *E. coli/Lactobacillus* ratio decreases from 1.024 in controls to 0.921. Immunological benefits are also observed, after Newcastle disease vaccination, antibody titres averaged $8.89 \pm 0.08 \log^2$ in birds receiving fermented rice bran, markedly higher than the $7.27 \pm 0.09 \log^2$ recorded for the Avilamycin group and higher than the $8.10 \pm 0.15 \log^2$ in controls. These outcomes indicate that fermented rice bran stimulates gut-associated lymphoid tissue and macrophage activity, enhancing systemic immunity [255].

Rice bran fermented with bioactive-rich fruits and vegetables, such as grape, apple, banana, peach, persimmon, various citrus fruits, black sugar, rice, beans, sesame, carrot, garlic, seaweed, and honey, using *Lactobacilli*, *Bacillus subtilis*, *B. licheniformis*, *B. megaterium*, and diverse yeasts, effectively suppresses pathogenic microorganisms, including *Salmonella*, *Staphylococcus*, and *Pseudomonas aeruginosa*. This fermentation significantly enriches the bran in beneficial compounds, including isoflavones (genistein, daidzein), carotenoids, vitamins, particularly vitamin B₁₂ (cobalamin), and minerals. When added to broiler diets at inclusion levels of 2% and 4%, this fermented mixture boosts feed intake, body-weight gain, and overall feed efficiency, with only minor increases in total visceral weight. Histological examination reveals substantial elongation and widening of duodenal and jejunal villi, along with pronounced enlargement and outward projection of epithelial cells, indicating enhanced absorptive surface area and improved intestinal functionality [256].

Chapter 3: Microbial Roles and Functional Benefits

Microbial Roles and Benefits in Poultry Feed Fermentation

Among microorganisms involved in animal feed fermentation, bacteria from the genera *Bacillus* and *Lactobacillus*, as well as filamentous fungi of the genus *Aspergillus*, are the most common. These microbial groups offer different benefits, each with distinct nutritional purposes [315-317]. In bacterial fermentation, the primary outcomes are the accumulation of significant amounts of organic acids, notably lactic and acetic acids, accompanied by an increase in short-chain fatty acids, such as acetic, propionic, and butyric acids.

Moreover, bacterial fermentation is effective in neutralizing mycotoxins, either through adsorption or biodegradation processes [253, 317-321]. Upon consumption, bacterial-fermented feed enhances the populations of beneficial *Lactobacillus*, suppresses pathogens, improves immune response, reduces ammonia emissions, and boosts animal growth performance [253, 313, 315, 319, 320, 322].

Fungal fermentation, primarily by filamentous fungi, excels at breaking down lignocellulosic complexes like cellulose and hemicellulose. Furthermore, fermentation increases the feed's crude protein content through the secretion of fungal proteins and the conversion of carbohydrates into fungal biomass [313, 322-327]. *Aspergillus* species notably produce a diverse array of hydrolytic and oxidative enzymes, including β -galactosidase, phytase, manganese peroxidase, laccase, lipases, glucose oxidase, xylanase, and various proteases, which significantly enhance nutrient digestibility [247, 306, 322, 324, 328, 329]. Moreover, fungal metabolism generates valuable metabolites such as xylitol, ethanol, citric acid, polyhydroxyalkanoates, erythritol, and pullulan, which enhance feed aroma and palatability [306, 324, 329-332]. Consequently, animals consuming fungal-fermented diets experience greater weight gains and better feed-conversion efficiency [327, 333, 334].

***Bacillus* genera**

Members of the *Bacillus* genus are gram-positive, rod-shaped, spore-forming bacteria extensively utilized in dietary applications because of their health-promoting properties, frequently serving as probiotics in animal feed formulations [315-317, 319, 333]. Their notable metabolic versatility includes efficient hydrolysis of starch, glucose and citrate, tolerance to high salinity conditions (up to 6.5% NaCl), and gelatinase activity exhibited by certain strains [335].

Upon ingestion, *Bacillus* strains contribute to establishing an anaerobic intestinal environment favorable to lactic acid-producing bacteria. This action significantly elevates *Lactobacillus* populations in the cecum, ileum, and excreta, concurrently suppressing pathogenic bacteria such as *Escherichia coli* and *Salmonella*, with certain strains capable of reducing *Clostridium* populations [315, 316].

Moreover, dietary supplementation with *Bacillus* strains modifies gut morphology by extending villi length in the jejunum and ileum, increasing goblet cell numbers, and upregulating tight junction proteins such as ZO-1, thereby enhancing epithelial barrier integrity and nutrient absorption [319]. *Bacillus* supplementation further stimulates the production of essential short-chain fatty acids (SCFAs), notably acetic and butyric acids, frequently in association with increased populations of SCFA-producing microbial taxa including *Lachnospiraceae*, *Butyricimonas*, *Odoribacter*, *Clostridiaceae*, *Tannerellaceae*, *Ruminococcus*, and *Faecalibacterium* [319, 320].

Complementing these beneficial microbiota shifts, *Bacillus* secretes extracellular enzymes such as protease, lipase, cellulase, xylanase, and phytase, enhancing nutrient digestibility and reducing detrimental emissions, notably ammonia [333]. Finally, the spores produced by *Bacillus* activate macrophages, improve overall immune competence, and modulate cytokine profiles by reducing pro-inflammatory IL-1 β and IL-6 and elevating anti-inflammatory IL-10 levels [313, 315, 320, 333].

It was observed that the fermentation of canola meal with *Lactobacillus fermentum* and *Bacillus subtilis*, along with multiple feed-digestive enzymes,

reduced anti-nutritional factors, enhanced its nutritional value and digestibility, and positively reshaped its microbiological profile by increasing beneficial *Lactobacillus* counts and suppressing pathogenic *Escherichia coli*. Incorporating this fermented meal at 20% in broiler diets resulted in greater body weight gain, improved feed-conversion ratios, increased digestibility of dry matter, crude protein, and ether extract, and enhanced pancreatic lipase and amylase activities. Immunologically, broilers exhibited significantly greater bursa of Fabricius weights and elevated antibody levels against Newcastle disease virus, indicating stronger immune responses. Additionally, antioxidant capacity improved, as evidenced by increased superoxide dismutase activity and decreased malondialdehyde concentrations.

The fermentation also produced a hypocholesterolemic effect, lowering serum cholesterol. Enhanced intestinal morphology was observed, characterized by increased villus height in the small intestine, higher populations of beneficial *Lactobacillus*, and reduced pathogenic *E. coli* counts [206]. Similarly, fermenting canola meal, even without adding feed enzymes, improved broiler performance compared to unfermented controls. Birds fed the fermented meal achieved greater weight gain, better feed-conversion ratios, and significantly higher dry-matter digestibility than birds fed unfermented canola meal. Amylase and lipase activities exceeded those of the control group but remained lower than when fermentation was combined with enzymes. Immune function, antioxidant markers, and intestinal morphology were also superior compared to the control group [206].

Additionally, fermenting *Cornus officinalis* fruit with *Bacillus subtilis* and *Aspergillus oryzae* increased its protein content from 44.9 g/kg to 174 g/kg. However, when incorporated into broiler diets, this fermented product reduced both average daily gain and feed intake, likely due to tannins and saponins that decrease palatability and hinder nutrient absorption. Nonetheless, the additive reduced crude fat content in broiler meat. Environmentally, it decreased hydrogen sulfide emissions during the first week but elevated ammonia emissions in weeks two and four [257].

Besides, fermentation of kelp using *Bacillus subtilis* and *Aspergillus oryzae* increased its protein content from 11 g/kg to 192 g/kg, and its inclusion in broiler diets did not negatively impact growth performance. Beneficial effects

were observed in meat quality, notably through enhanced oxidative stability, as evidenced by reduced malondialdehyde levels. Additionally, environmental monitoring indicated that broilers fed fermented kelp emitted less atmospheric ammonia from their excreta throughout the rearing period, thereby improving air quality within the poultry house [257].

Also, sea-mustard by-product fermented with *Lactobacillus buchneri*, *Bacillus subtilis*, and *Bacillus licheniformis* resulted in reduced anti-nutritional factors and likely enhanced protein digestibility. Incorporating this fermented product at a level of 2 g/kg into broiler diets increased body-weight gain and improved the feed-conversion ratio. Furthermore, beneficial shifts in gut microbiota were observed, characterized by higher *Lactobacillus* counts and reduced levels of *Escherichia coli* in excreta. Meat quality also improved, as indicated by increased breast-muscle lightness [258].

Likewise, fermentation of *Alisma canaliculatum* root using *Lactobacillus acidophilus*, *Enterococcus faecium*, *Bacillus subtilis*, and *Saccharomyces cerevisiae* increased its protein concentration from 7.36% to 12.5% and reduced its fat content from 6.36% to 4.73%. Incorporating this fermented product into broiler diets led to greater final body weights and higher daily weight gains, alongside improved feed-conversion ratios compared to controls. Meat quality also improved, characterized by increased crude-protein content, decreased crude-fat content, enhanced oxidative stability, and a fatty-acid profile favoring a higher proportion of polyunsaturated fatty acids [259].

On top of that, fermentation of Napier grass (*Pennisetum purpureum* Schumacher) with *Bacillus subtilis* and pangola grass (*Digitaria decumbens* Stent) with *Entrophospora* sp. significantly increased their protein concentrations. Specifically, Napier grass protein content rose from 1.42% to 13.9%, whereas pangola grass increased from 2.34% to 11.8%. When fermented Napier grass was included in broiler diets, the birds achieved an average daily gain of 47.1 ± 0.50 g/day and a feed conversion ratio of 1.94 ± 0.07 , comparable to the corn-based control diet (47.2 ± 0.37 g/day and 1.90 ± 0.08 , respectively). In contrast, broilers fed diets containing fermented pangola grass exhibited notably poorer performance, with an average daily gain of 42.8 ± 0.28 g/day and a feed conversion ratio of 2.17 ± 0.07 [203].

A traditional Chinese medicine composed of eight herbs (*Codonopsis Radix*, *Astragali Radix*, *Radix Glycyrrhizae*, *Poria*, Medicated Leaven, Malt, *Crataegu*, and Areca Seed) was separately fermented using five distinct microbial strains: *Bacillus licheniformis*, *Bacillus subtilis*, *Zygosaccharomyces rouxii*, and two different strains of *Saccharomyces cerevisiae*. Each fermented preparation was individually incorporated into broiler feed to assess potential benefits. Fermentation with each microbial strain facilitated the release or activation of bioactive compounds, thus enhancing functional potency. Among these, feed fermented with *Zygosaccharomyces rouxii* provided the most substantial benefits, significantly increasing probiotic genera such as *Bifidobacterium*, *Bacteroides*, *Blautia*, and *Ruminococcaceae*. Feed fermented with *Bacillus subtilis* achieved the highest body-weight gain, 13.1% greater than the control, while feed fermented with *Zygosaccharomyces rouxii* yielded the most favorable feed-conversion ratio, improving feed efficiency by reducing the FCR by 10.68% and consequently lowering overall production costs [260].

Similarly, fermenting banana-peel meal in two stages, initially with *Chrysonilia crassa* followed by *Bacillus subtilis*, raised its crude protein content from 7.96% to 11.8%, reduced crude fiber content from 19.6% to 12.2%, and increased its metabolizable energy from 2,660 to 3,023 kcal/kg. When included in broiler diets, this fermented product effectively decreased coliform bacteria populations in the ileum, improved villus height, and lowered blood uric acid concentrations, indicating enhanced protein utilization by the chickens [261].

Moreover, fermenting *Citri Sarcodactylis Fructus* by-products using a mixed culture of *Lactobacillus plantarum*, *Saccharomyces cerevisiae*, and *Bacillus subtilis* reduced their crude fiber content. When included in the diets of cyan-shank partridge birds, a fast-growing broiler line, the fermented product led to increased average daily gain and improved feed conversion ratios. Additionally, birds fed this diet exhibited healthier intestines characterized by greater villus height, improved gut morphology, and enhanced epithelial barrier integrity, confirmed by increased expression of tight-junction proteins ZO-1 and Occludin. Furthermore, the cecal microbiota composition shifted beneficially, enriching genera such as *Bacteroides* [262].

Alongside this, fermentation with *Bacillus licheniformis* provided notable benefits when the fermented substrate was included in broiler diets at 3 g/kg. These advantages encompassed increased body weight and average daily gain comparable to those achieved using the antibiotic growth promoter enramycin. Additionally, microbiome analysis showed significant changes in fecal bacterial communities: *Lactobacillus* species, particularly *Lactobacillus crispatus* and *Akkermansia muciniphila*, became more abundant, while populations of *Enterococcus*, *Bacteroides fragilis*, and *Faecalibacterium* declined [265, 266]. Regarding antibiotic resistance markers, the fermented product reduced the abundance of several peptide-resistance genes, notably within *Bacteroides* species, and downregulated aminoglycoside and streptogramin resistance genes, though it upregulated macrolide and aminocoumarin resistance genes. In contrast, enramycin elevated the overall abundance of peptide-resistance genes [266].

Furthermore, fermentation of a by-product mixture comprising small fish, crabs, shrimp, and coffee residues was conducted at 70 °C using thermophilic *Bacillus* species including *Bacillus thermoamylovorans*, *Bacillus thermocloacae*, and *Bacillus subtilis*. Incorporation of this fermented product into laying-hen diets increased cumulative egg production, with the most significant benefits observed in older birds. Although there was a slight reduction in egg mass, the eggs remained within the commercial M-size range of 58–64 g. Egg amino acid profiles were unaffected; however, fecal analyses revealed substantial reductions in lactate and ammonium, indicating enhanced intestinal metabolism [263].

In addition, tea residues fermented using *Bacillus subtilis* and *Lactobacillus plantarum* improved the nutritional profile of the feed, increasing crude protein content, reducing sugar levels, and boosting cellulase activity, as well as enhancing amino-acid and fatty-acid compositions. When incorporated into laying hen diets, this fermented product increased egg-laying rates, average egg weight, and overall egg quality, indicated by higher Haugh units and thicker shells. Additionally, hens displayed enhanced antioxidant status, reflected by increased activities of glutathione peroxidase and superoxide dismutase, along with reduced malondialdehyde levels. Furthermore, beneficial shifts occurred in the hens' gut microbiota, particularly in the relative

abundances of *Bacteroidetes* and *Firmicutes*, while ammonia emissions within the poultry house decreased [264].

Besides, peony-seed dreg fermented using a microbial culture consisting of *Lactobacillus acidophilus*, *Bacillus subtilis*, and *Saccharomyces* reduced the natural anti-nutritional factors in the feed, enhanced its palatability and digestibility, and increased its beneficial bioactive compound content. When included in laying hen diets, the fermented product improved egg production and quality, leading to higher laying rates and increased albumen height. Antioxidant status improved as well, indicated by higher glutathione-peroxidase activity and lower malondialdehyde concentrations. Additionally, birds demonstrated stronger immune responses, evidenced by elevated antibody titers against important viral pathogens. Furthermore, their eggs and meat showed healthier lipid profiles, with higher levels of n-3 polyunsaturated fatty acids and reduced saturated fatty acids [205].

Also, the beneficial effects of fermentation using *Lactobacillus plantarum*, *Bacillus subtilis*, and *Bacillus licheniformis* were demonstrated by incorporating substrates fermented with these microbes into duck diets. Positive outcomes were evident through improvements in egg quality, with yolks showing increased concentrations of flavor amino acids, notably aspartate and alanine, along with reduced levels of trimethylamine, significantly decreasing the typical fishy odor of duck eggs. Intestinal health also improved, particularly in the jejunum, as evidenced by increased villus height and a higher villus-to-crypt depth ratio, suggesting enhanced nutrient absorption. Furthermore, gut microbiota analysis indicated elevated abundances of beneficial genera such as *Anaerobiospirillum* and *Alistipes*, which correlated positively with the improved egg flavor profile. Metabolite analysis of eggs additionally confirmed that these changes contributed to a more desirable overall flavor [267].

On top of that, fermenting *Ginkgo biloba* leaves with *Bacillus coagulans* reduced the concentration of cytotoxic ginkgolic acids while simultaneously increasing acetate and L-lactate levels and slightly decreasing flavonoids and terpene lactones. Adding fermented *Ginkgo biloba* to duck diets resulted in greater body weight gain and a lower feed conversion ratio compared to both the non-fermented *Ginkgo biloba* group and the control group. Additionally,

fermented *Ginkgo biloba* enhanced the fatty acid profile of breast meat by reducing saturated fatty acids, primarily palmitic acid, and increasing polyunsaturated fatty acids such as linoleic acid and arachidonic acid. Gene expression analysis revealed an anti-lipogenic profile, with increased expression of leptin and adiponectin and decreased expression of PPAR γ . Despite these metabolic changes, meat color, pH, and overall quality were unaffected [268].

***Lactobacillus* genera**

Lactobacillus is a genus of gram-positive bacteria known for fermenting sugars to produce lactic acid. It is the largest group within the *Lactobacillaceae* family, encompassing over 100 species and subspecies. *Lactobacillus* cells are typically rod-shaped and frequently form chains, thriving in mildly acidic environments with an optimal pH range of 5.5 to 6.5 [317]. *Lactobacilli* are classified according to their carbohydrate-fermentation pathways as either homofermentative, converting sugars primarily into lactic acid, or heterofermentative, producing lactic acid alongside acetic acid, ethanol, and CO₂ [317]. Substrate preferences differ among species; for example, *L. salivarius* efficiently metabolizes a wide range of carbohydrates including maltose, raffinose, sucrose, and glucose, whereas *L. agilis* preferentially utilizes mannose, glucose, L-lactic acid, and mannitol [336].

Lactobacilli produce several organic acids, primarily lactic and acetic acids, significantly enhancing the aroma and flavor of fermented foods. Additionally, they generate short-chain fatty acids (SCFAs), such as acetic, propionic, and butyric acids [253, 316, 318]. Certain *Lactobacillus* strains also secrete hydrolytic enzymes including proteases, amylases, cellulase, and α -/ β -galactosidases, aiding in the digestion of complex carbohydrates like lactose and plant fibers [253, 337].

As probiotics, *Lactobacillus* strains support a balanced intestinal microbiota, enhance weight gain and feed efficiency in livestock, strengthen immune responses, competitively exclude pathogens such as *Salmonella* and *Escherichia coli*, promote nutrient absorption in the lower gastrointestinal tract, produce bacteriocins like acidophilin, lactolin, and acidlin, and degrade

or reduce the bioavailability of mycotoxins [253, 313, 315, 318, 321, 333, 336-339].

Fermentation of *Eucommia ulmoides* leaf extracts using *Lactiplantibacillus* (*Lactobacillus*) *plantarum* significantly enhanced their palatability by effectively reducing inherent bitterness and improving the bioavailability of active compounds through the breakdown of plant cell walls. These biochemical transformations modified the flavor and taste profiles, effectively stimulating hens' appetites. This process notably improved laying performance, achieving the highest laying rate of 93.44%, compared to 91.24% in hens given water-extracted *E. ulmoides* and 89.23% in the control group. Daily feed consumption slightly increased, and egg breakage rates decreased, indicating enhanced eggshell integrity. Additionally, the fermented extracts exhibited improved flavor profiles marked by beneficial alterations in volatile compounds, alongside increased nutritional value evident in enhanced amino acid and fatty acid compositions. Beneficial fatty acids, such as stearic and oleic acids, notably increased. Gut microbiota analysis showed an elevated relative abundance of beneficial *Lactobacillus* species and reduced populations of pathogenic bacteria, including *Romboutsia* and *Subdoligranulum*. Immunological markers indicated improved immune responses, as reflected by increased levels of immunoglobulins IgA and IgM. Furthermore, the extracts significantly lowered blood triglyceride and total cholesterol levels [269].

Besides, sorghum fermented with *Limosilactobacillus fermentum* exhibited improved digestibility by enzymatically breaking down complex macromolecules, including polysaccharides, fats, and proteins, into smaller organic acids. This fermentation process also reduced anti-nutritional factors, facilitating better nutrient absorption, promoted the production of short-chain fatty acids such as acetate, propionate, and butyrate, and increased the content of beneficial bioactive compounds. Incorporating this fermented sorghum at a 20% inclusion rate in broiler diets led to enhanced growth performance, characterized by higher feed intake, body weight, and overall weight gain. Histomorphological examination of the jejunum demonstrated a notable increase in villus height, indicative of an expanded absorptive surface area, while profiling of cecal short-chain fatty acids confirmed elevated concentrations of acetate and propionate. Furthermore, gene expression

analysis revealed an upregulation of the tight junction protein occludin, indicating improved intestinal barrier integrity [282].

Also, fermentation of dandelion with *Saccharomyces cerevisiae* and *Lactobacillus plantarum* increased the content of bioactive compounds, notably elevating flavonoids by 39.54% and polyphenols by 30.68%, while simultaneously enhancing antioxidant properties. These biochemical improvements were attributed to microbial breakdown of dandelion cell walls, thereby increasing the accessibility of bioactive substances. When included in broiler diets at a concentration of 1 g/kg, this fermented product significantly improved growth performance, evident through higher average daily gain and an enhanced feed-to-gain ratio. Additionally, positive effects on immunity were observed, with increased indices of immune organs such as the bursa of Fabricius and spleen, and decreased levels of inflammatory cytokines, specifically IFN- γ and TNF- α . At an inclusion level of 0.5 g/kg, an elevation in antioxidant enzyme activities, including catalase and total superoxide dismutase, was detected in breast muscle tissues, along with reduced drip loss, indicating improved meat quality preservation. Furthermore, beneficial alterations in the intestinal microbiota occurred, characterized by increased populations of advantageous bacteria, particularly *Firmicutes* and *Lactobacillus*, and reductions in harmful bacteria such as *Bacteroidota* and *Cyanobacteria* [217].

Likewise, fermentation of paper mulberry (*Broussonetia papyrifera*) leaves and stems with *Lactobacillus plantarum* increased crude protein content, reduced crude fiber levels, and decreased antinutritional factors. This fermentation also promoted the release of beneficial bioactive compounds, particularly flavonoids. When included at 1% and 5% in diets for laying hens, the fermented material improved average daily feed intake, enhanced feed conversion efficiency, and increased carotenoid absorption, resulting in a richer egg yolk coloration. Additionally, dietary supplementation positively influenced lipid metabolism in hens, as shown by decreased serum triglyceride levels, increased high-density lipoprotein cholesterol, downregulated hepatic expression of lipid-synthesis genes such as acetyl-CoA carboxylase and fatty acid synthase, and upregulated liver X receptor (LXR), a gene crucial for cholesterol transport to the liver. However, inclusion at the 5% level reduced eggshell weight and thickness, while at the 1% inclusion rate, ovarian

development was negatively affected, with fewer developing follicles and reduced expression of ovarian gonadotropin receptor genes including the estrogen receptor and luteinizing hormone receptor [270].

Alongside this, fermentation of commercial duck feed (obtained from Shanghai Nonghao Feed Co., Ltd.) using *Lactobacillus plantarum* decreased phosphorus, crude fiber, neutral detergent fiber, and insoluble dietary fiber contents, reflecting the microbial degradation of complex carbohydrates. In contrast, acid detergent fiber increased, indicating changes in fiber composition. Essential amino acid availability improved, notably with elevated concentrations of methionine. Additionally, over 287 metabolites, including organic acids and amino acid derivatives such as 2-hydroxy-4-methylthiobutanoic acid, 3-[(methoxycarbonyl)amino]-2,2,3-trimethylbutanoic acid, and stabilized ascorbic acid, were significantly upregulated, indicating enhanced nutrient bioavailability. Incorporating this fermented feed into duck diets at a proportion of 40 percent resulted in higher muscle pH, reduced cooking loss, and no adverse effects on meat color. Sensory evaluations, including electronic tongue assessments, showed improvements in tenderness, juiciness, umami, richness, saltiness, and sweetness. Metabolomic profiling of duck muscle tissue further revealed elevated concentrations of 2-aminoadipate, glycine, N-acetylcysteine, glucose, proline, threonine, and niacinamide, correlating these biochemical alterations with observed sensory and textural improvements [271].

On top of that, fermentation of *Andrographis paniculata* using a combined bacterial culture of *Saccharomyces* and *Lactobacillus* increased bioactive compound concentrations, decreased antinutritional factors and toxins, and produced organic acids. When incorporated into duck feed at 10 g/kg and 30 g/kg, the fermented supplement enhanced growth performance and feed conversion ratios, but inclusion at 50 g/kg reduced body weight, likely due to excessive bioactive components interfering with nutrient absorption. Carcass trait analysis indicated that ducks receiving 10 g/kg of fermented product had higher dressed percentages, whereas those fed 30 g/kg of the unfermented herb showed increased breast muscle yield. Additionally, fermentation improved the lung index, suggesting enhanced oxygen uptake and metabolic efficiency. Immune function improved significantly with the fermented supplement, demonstrated by increased indices of immune organs such as the bursa of

Fabricius and thymus, elevated serum lysozyme activity, and higher lymphocyte transformation rates, all indicative of stronger systemic immune responses. Intestinal morphology also notably benefited from supplementation, showing increased villus height, width, and surface area, contributing to better nutrient absorption, along with increased intraepithelial lymphocyte counts reflecting stronger mucosal immunity. Cecal microbiota sequencing indicated that the fermented supplement reduced potentially harmful bacterial genera including *Succinivibrio*, *Succinatimonas*, *Sphaerochaeta*, and *Mucispirillum*, while increasing beneficial taxa like *Rikenellaceae*, *Methanocorpusculum*, *Fournierella*, and *Ruminococcaceae*, known for their roles in lipid digestion and overall intestinal health [272].

Moreover, fermentation of potato pulp with *Geotrichum candidum*, lactic acid bacteria, and yeast resulted in increased crude protein and lipid content, along with reductions in starch and fiber levels, thereby enhancing palatability. Additionally, the naturally occurring toxin solanine was completely eliminated through this process. Incorporating this fermented potato pulp into quail diets showed no differences in performance compared to control birds, nor were there any effects on blood lipid parameters, thus offering economic advantages by reducing feed costs [273].

***Aspergillus* genera**

Aspergillus is a highly diverse genus of filamentous fungi widely recognized for its significant biotechnological and environmental roles, particularly in improving agricultural residues for animal feed applications [323, 324, 340]. Species such as *A. niger* exhibit robust cellulolytic enzyme systems capable of efficiently degrading lignocellulosic biomass, thus liberating nutrients otherwise inaccessible for animal nutrition [274, 324, 327, 328].

Additionally, *A. niger* is well-established in industrial biotechnology due to its capacity to produce organic acids, notably citric and gluconic acids. These acids play crucial roles in enhancing substrate decomposition and improving feed palatability [247, 306, 313, 329, 330, 341]. Beyond its capabilities in lignocellulose breakdown, *A. niger* synthesizes a highly effective phytase enzyme belonging to the histidine acid phosphatase family. This enzyme exhibits optimal functionality under acidic conditions, significantly enhancing

phosphorus bioavailability in animal diets through the hydrolysis of phytic acid [328].

Furthermore, specific strains of *A. niger* contribute to mycotoxin mitigation. For example, *A. niger* FS10 effectively transforms the mycotoxin patulin into the considerably less toxic metabolite ascladiol via intracellular enzymatic reactions, demonstrating its potential for detoxifying contaminated agricultural by-products, such as apple pomace [342]. These diverse functionalities, including lignocellulose degradation, organic acid secretion, phytase production, and mycotoxin detoxification, underscore the potential of *Aspergillus*, particularly *A. niger*, as a versatile organism for converting low-value agro-industrial by-products into safer, more nutritious animal feed.

Fermenting shea nut meal with *Aspergillus niger* reduces anti-nutritional factors, such as total soluble phenolics by 21.9%, proanthocyanidins by 34.5%, and hydrolysable tannins by 52.9%, while simultaneously increasing crude protein content and mitigating the adverse effects associated with tannins. When incorporated into broiler diets, the fermented meal significantly enhanced performance compared to unfermented shea nut meal. Average daily feed intake rose from 103.2 g to 136.4 g per bird, closely approaching the 142.0 g observed in birds fed a wheat-based control diet. By day 36, birds receiving fermented shea nut meal attained a mean live weight of 1.958 kg per bird, compared to 1.661 kg in those fed unfermented meal and 2.163 kg in the wheat-fed control group [274].

Additionally, fermentation of grape seed with *Aspergillus niger* enhanced its nutritional value by increasing beneficial phenolic compounds, decreasing antinutritional factors such as condensed tannins, and strengthening antioxidant properties through modifications in the phenolic profile, particularly by elevating ferulic acid levels. Incorporating fermented grape seed into poultry diets improved growth performance metrics, including body weight and average daily gain. Furthermore, supplementation elevated serum activities of antioxidant enzymes such as glutathione peroxidase and catalase, indicating enhanced antioxidant defenses; notably, it surpassed synthetic antioxidants in increasing catalase activity. Fermented grape seed also positively influenced gut health by promoting beneficial *Lactobacillus* spp.

populations in the cecum, suppressing pathogenic *Staphylococcus aureus*, and reducing breast meat yellowness compared to control birds [204].

Similarly, fermentation of sour cherry kernel with *Aspergillus niger* increased crude protein content from 29.6% to 34.9% and ether extract from 16.6% to 24.6%, while reducing crude fiber from 27.5% to 20.3% and lowering nitrogen-free extract levels. Additionally, this process significantly reduced cyanogenic glycosides, antinutritional compounds known to be detrimental to poultry [275]. Incorporating fermented kernel at a 1% inclusion rate in broiler diets improved both body weight gain and feed conversion ratio. Although carcass yield, abdominal fat deposition, and key meat quality characteristics were not significantly influenced, chickens fed higher levels of fermented sour cherry kernel displayed increased bursa of Fabricius weight, indicative of enhanced immune function, along with greater gut weight and length, suggesting improved digestive tract development [275].

On top of that, fermentation of defatted, heat-treated *Jatropha curcas* kernel meal with the fungus *Aspergillus niger* effectively reduced antinutritional factors including tannins, saponins, phytates, and toxic phorbol esters, while slightly decreasing crude protein and crude fiber contents. Incorporation of this fermented meal at an 8% inclusion level in diets for Ross 308 broiler chicks resulted in feed intake and growth performance comparable to those observed in the control group: average daily weight gain was 12.3 g/day versus 11.7 g/day, live weight averaged 156.1 g compared to 152.7 g, and feed conversion ratios were 2.0 versus 2.1. No adverse effects were reported, and both groups achieved a 100% survival rate [276].

Also, fermentation of *Pinus ponderosa* pine needles with *Aspergillus niger* more than doubled crude protein content, increasing it from 11.04% to 22.98%, and raised total amino acid levels from 8.72% to 16.54%. Enzymatic activities, previously undetectable, rose significantly post-fermentation, reaching 10.26% for cellulase and 119.45% for hemicellulase, indicating substantial fiber breakdown and improved digestibility. When incorporated into broiler diets, the fermented pine needles maintained comparable body weight gain, feed intake, and feed conversion ratio relative to the control group. However, antioxidant status markedly improved: superoxide dismutase and glutathione peroxidase activities increased, total antioxidant capacity was elevated, and

levels of malondialdehyde, a lipid peroxidation marker, significantly decreased, indicating reduced oxidative stress. Furthermore, total nitric oxide synthase activity declined in the groups receiving fermented pine needles, suggesting modulation of nitric oxide-mediated pathways and further alleviation of oxidative challenges [277].

Besides, fermentation of wormwood (*Artemisia argyi*) with *Aspergillus niger* substantially enhanced fiber degradation, thereby improving enzymatic accessibility and overall digestibility. Concurrently, the process released a diverse array of bioactive compounds, including essential oils, flavonoids, and polysaccharides, significantly enhancing the nutritional and functional properties of *A. argyi*. Incorporating this fermented product at 3% in broiler diets notably improved average daily gain and reduced the feed conversion ratio. Additionally, treated birds exhibited increased carcass dressing percentages and higher proportions of breast and thigh muscles. Meat quality was also improved, demonstrated by enhanced tenderness [278].

Moreover, fermentation of agro-industrial residues from faba bean with *Aspergillus niger* resulted in the biosynthesis of seven organic acids: oxalic, ascorbic, maleic, salicylic, lactic, formic, and citric acids. Incorporating this fermented residue into quail diets markedly improved growth performance, as demonstrated by significantly increased body-weight gain and enhanced feed-conversion ratios. Lipid profile assessments showed reductions in triglycerides and levels of low-density and very-low-density lipoproteins, along with elevated concentrations of high-density lipoproteins. Immune status was similarly improved, with elevated serum levels of immunoglobulins (IgG, IgM, and IgA) and increased lysozyme activity. Antioxidant defenses were also strengthened, indicated by enhanced activities of superoxide dismutase and catalase. Furthermore, microbiological analyses of the intestinal tract revealed reduced populations of *Escherichia coli*, coliforms, and *Salmonella* spp., while beneficial *Lactobacillus* spp. increased. Carcass characteristics remained unaffected [279].

Alongside this, fermentation of flaxseed cake, a byproduct from flaxseed oil extraction, with *Aspergillus niger* and *Candida utilis* increased its crude protein content from 37.08% to 42.94%, ether extract from 7.62% to 7.96%, and calcium content from 0.36% to 0.44%. Simultaneously, antinutritional

components decreased substantially, with hydrocyanic acid levels dropping from 397.76 mg/kg to 106.49 mg/kg and crude fiber content reducing from 13.29% to 8.73%. Including fermented flaxseed cake at a level of 150 g/kg in duckling diets favorably altered serum lipid profiles, significantly lowering triglycerides, total cholesterol, low-density lipoproteins, and high-density lipoproteins. Additionally, ducklings receiving the fermented product exhibited increased relative weights of the gizzard and cecum, reflecting enhanced digestive capacity and improved gut development [280].

Ashbya gossypii

Ashbya gossypii (syn. *Eremothecium gossypii*) is a filamentous hemiascomycetous fungus extensively studied and utilized in industrial biotechnology due to its remarkable ability to overproduce riboflavin (vitamin B2) [331, 332, 343]. The organism efficiently grows on readily metabolizable sugars including glucose, fructose, sucrose, starch, maltose, and glycerol, and performs even better on plant oils, significantly enhancing riboflavin yields. In contrast to other fungi, *A. gossypii* cannot metabolize cellulose, pentoses (arabinose and xylose), galactose, or lactose, likely due to the absence of essential catabolic enzymes [332].

Apart from vitamin production, *A. gossypii* naturally synthesizes abundant aroma-active alcohols and esters, imparting distinctive fruity and floral notes: isoamyl alcohol provides a banana-like aroma, while 2-phenylethanol contributes a rose blossom scent. These volatile compounds have the potential to enhance the palatability of animal feeds.

Furthermore, the fungus produces high concentrations of purine nucleosides such as inosine and guanosine, potent umami flavor enhancers with additional antioxidant and immunomodulatory activities, offering further opportunities to enhance feed acceptance and functional value [331, 332].

Birds experiencing riboflavin deficiency display symptoms such as agitation disorders, lameness, "curled-toe paralysis," and subacute sciatic nerve degeneration as early as the second week, resulting in reduced growth and a mortality rate of around 4.5%.

The commercial feed EcoVit R Powder (produced by Agrano GmbH & Co. KG) incorporates a substrate fermented with *Ashbya gossypii*, a fungus known for its exceptional ability to biosynthesize riboflavin at high concentrations. Broilers fed diets supplemented with EcoVit R Powder consistently demonstrated improved performance compared to unsupplemented birds, showing higher body weights, increased daily weight gains, and enhanced feed conversion ratios, especially during the early growth stages when deficiency effects are most critical.

In both trials, birds receiving supplementation at or above the threshold of 4.5 mg/kg attained superior final body weights, exhibited more uniform growth trajectories, and experienced reduced mortality rates ranging from 1.5% to 2.5%, with no recorded deaths linked to deficiency. Additionally, carcass assessments indicated decreased abdominal fat accumulation and lighter liver weights, implying that adequate riboflavin intake may positively affect meat quality [281].

Birds that exhibit riboflavin deficiency show symptoms such as agitation disorders, lameness, “curled-toe paralysis,” and subacute degeneration of the sciatic nerve as early as the second week, leading to reduced growth and a mortality rate of 4.5%. The commercial feed EcoVit R Powder (produced by Agrano GmbH & Co. KG) contains a substrate fermented with *Ashbya gossypii*, characterized by its ability to biosynthesize high levels of riboflavin. Broilers receiving diets supplemented with EcoVit R Powder consistently outperformed unsupplemented birds in terms of body weight, daily weight gain, and feed conversion ratio, particularly during the early growth phase when deficiency impacts were most pronounced. Across both trials, birds fed at or above the 4.5 mg/kg threshold achieved higher final body weights and more uniform growth curves, and mortality fell to between 1.5 % and 2.5 %, with no deficiency-related deaths recorded. Carcass traits showed reduced abdominal fat deposits and lower liver weights, suggesting that adequate riboflavin intake may positively influence meat quality [281].

Pleurotus ostreatus

Pleurotus ostreatus, commonly known as the oyster mushroom, is a white-rot fungus with increasing biotechnological and environmental significance. It is

extensively studied for its ability to convert agricultural byproducts into nutritionally enriched animal feed and for degrading several major mycotoxins [322, 323, 326, 334, 340, 344].

Like other white-rot fungi, *P. ostreatus* effectively breaks down lignin-rich plant materials by secreting a wide range of extracellular enzymes, including lignin peroxidase, manganese peroxidase, versatile peroxidase, laccase, and the hydrolases amylase, cellulase, pectinase, and protease [322, 323, 325, 326, 340, 344]. The fungus grows rapidly on various agro-industrial residues, such as straw, sawdust, paper scraps, spent coffee grounds, corn stover, and deproteinised rapeseed press cake, simultaneously enhancing their protein content [322, 323, 325, 326, 344, 345].

In addition to nutrient enrichment, *P. ostreatus* synthesizes lovastatin, which inhibits methanogenic archaea and thus potentially reduces enteric methane emissions. It also decomposes antinutritional phytate in wheat bran. Significantly, the fungus converts ochratoxin A into the minimally toxic ochratoxin α , adsorbs and detoxifies zearalenone, and degrades aflatoxin B1 and fumonisin B1 through ligninolytic enzymes, notably laccase [322, 340].

The mushroom sporocarps contain a complete set of essential amino acids, and their lipid fraction predominantly consists of linoleic acid (over 75% of total fatty acids), with significant amounts of palmitic and oleic acids [326]. Furthermore, they include bioactive glucans, blazeispirol, and proteoglycans, which exhibit gastrointestinal immune-stimulating properties [334].

Fermentation of cocoa pod husk with *Pleurotus ostreatus* increased crude protein content by 37.3%, while reducing crude fiber by 21.3%, hemicellulose by 31.0% and anti-nutritional tannins by 93%. Inclusion of this fermented material in broiler diets at 200 g/kg improved feed-to-gain ratios; however, levels above this threshold led to a marked decline in growth performance [215].

Acknowledgements

The publication of this monograph was supported by the University of Agronomic Sciences and Veterinary Medicine of Bucharest—Romania, Research Project 846/30.06.2023, acronym EnterGreenFood in the Competition IPC 2023.

References

1. Rangasami SRS, Purnima M, Pushpam R, Ajaykumar R, Thirunavukkarasu M, Sathiya K, et al. Enhancing Animal Nutritional Security Through Biofortification in Forage Crops: A Comprehensive Review. *Indian Journal of Animal Research*. 2024(Of). 10.18805/ijar.B-5466
2. Dotas V, Symeon G, Dublec K. Editorial: Introducing novel trends in the nutrition of monogastric farm animals for the production of high-quality livestock products. *Front Vet Sci*. 2024;11:1514197. 10.3389/fvets.2024.1514197
3. Baris A. Impact of Feed Quality on Livestock Productivity. *Journal of Livestock Policy*. 2023;2(1):1-8. 10.47604/jlp.v2i1.2112
4. Hotea I, Dragomirescu M, Berbecea A, Radulov I. The role of nutrition in enhancing sustainability in sheep production. *Agricultural Sciences: IntechOpen*; 2024.
5. Javed A, Imran M, Saad Hashmi M, Javaid U, Estella Odoh U, Amjad R. Chicken egg: a comprehensive overview regarding feed sources and human health aspects. *Worlds Poult Sci J*. 2025;81(1):169-204. 10.1080/00439339.2024.2439474
6. Vieira V, de Dias IC, dos Santos MC, Senger GC, Moreno FA, Maiorka A, et al. 497 Amylase supplementation influences nutrient digestibility regardless of corn type in broiler chicken diets. *J Anim Sci*. 2024;102(Supplement_3):153-4. 10.1093/jas/skae234.181
7. Barszcz M, Tuśnio A, Taciak M. Poultry nutrition. *Phys Sci Rev*. 2022;0(0). 10.1515/psr-2021-0122
8. Ravindran V. Nutrition of meat animals: Poultry. *Encyclopedia of Meat Sciences: Elsevier*; 2024. p. 8-16.
9. Garcia-Mejia RA, Sinclair-Black M, Blair LR, Angel R, Jaramillo B, Regmi P, et al. Physiological changes in the regulation of calcium and phosphorus utilization that occur after the onset of egg production in commercial laying hens. *Front Physiol*. 2024;15:1465817. 10.3389/fphys.2024.1465817
10. Li X, Uyanga VA, Jiao H, Wang X, Zhao J, Zhou Y, et al. Effects of low dietary calcium and lipopolysaccharide challenges on production performance, eggshell quality, and bone metabolism of laying hens. *Front Physiol*. 2024;15:1396301. 10.3389/fphys.2024.1396301

11. Tokach MD, Goodband RD, DeRouchey JM, Woodworth JC, Gebhardt JT. 19 formulating U.s. swine diets in a time of high energy costs. *J Anim Sci.* 2023;101(Supplement_2):18-9. 10.1093/jas/skad341.020
12. Zijlstra RT, Tan F, Beltranena E, Nyachoti M. 168 evaluation and improvement of the nutritional value of cereal and pulse grains for swine. *J Anim Sci.* 2022;100(Supplement_3):75-6. 10.1093/jas/skac247.148
13. Chae B, Poaty Ditengou JIC, Lee AL, Tak J, Cheon I, Choi NJ. An Estimation of the Requirements of the Standardized Ileal Digestible Tryptophan, Valine, Isoleucine and Methionine on Young Pigs' (Up to 50 kg) Feed Efficiency: A Meta-Regression Analysis. *Animals (Basel).* 2024;14(19). 10.3390/ani14192884
14. Song W, Wu Z, Li W, Li Y, Yang H. Optimal dietary standardized ileal digestible lysine level for pigs during the grower, early and late finisher periods. *BMC Vet Res.* 2022;18(1):447. 10.1186/s12917-022-03557-1
15. Stas EB, DeRouchey JM, Goodband RD, Tokach MD, Woodworth JC, Gebhardt JT. Nutritional guide to feeding wheat and wheat co-products to swine: a review. *Transl Anim Sci.* 2024;8:txae106. 10.1093/tas/txae106
16. Pasquini Neto R, Furtado AJ, da Silva GV, Lobo AAG, Abdalla Filho AL, Brunetti HB, et al. Forage accumulation and nutritive value in extensive, intensive, and integrated pasture-based beef cattle production systems. *Crop Pasture Sci.* 2024;75(5). 10.1071/cp24043
17. Na SW, Zhou M, Chen Y, Bork E, Fitzsimmons CJ, Le Guan LL. 220 assessment of the Rumen bacterial community in beef cows differing in feed efficiency across four feeding and grazing scenarios. *J Anim Sci.* 2023;101(Supplement_3):135-6. 10.1093/jas/skad281.165
18. Saikanth DRK, T G, Roy D, Kumar N, Buch K, Sharma P, et al. Exploring the Nutritional Landscape: A Review of Fodder Options for Livestock. *International Journal of Environment and Climate Change.* 2023;13(10):2481-93. 10.9734/ijecc/2023/v13i102915
19. Patton J, Dineen M, Keady TWJ, McGee M, Waters S. Developments in nutrition for pasture-based cattle and sheep systems in Ireland. *Irish Journal of Agricultural and Food Research.* 2022. 10.15212/ijafr-2020-0148
20. Sadeghi M, Ghasemi E, Sadeghi R, Hashemzadeh F, Kahyani A, Kalantari-Dehaghi S, et al. Dietary macronutrient composition and partial soybean meal replacement with slow-release urea: Effects on performance, digestibility, rumen fermentation, and nitrogen metabolism in dairy cows. *J Dairy Sci.* 2025;108(1):511-26. 10.3168/jds.2024-25129

21. Abdellaoui L, Khelifi-Touhami NA, Mebkhout F, Tarzaali D, Yahiaoui WI, Hamdi TM, et al. Effect of feed on the milk protein and fat composition. *Agricultural Science and Technology*. 2022;14(2):54-61. 10.15547/ast.2022.02.019
22. Robison CA, Pierce KN, Reuter RR, Warner AL, Wilson BK. The effects of receiving diet roughage inclusion on performance, health, and serum metabolite characteristics of newly received beef calves. *Transl Anim Sci*. 2023;7(1):txad039. 10.1093/tas/txad039
23. McGee M, Regan M, Moloney AP, O'Riordan EG, Lenehan C, Kelly AK, et al. Grass-based finishing of early- and late-maturing breed bulls within suckler beef systems: Performance, profitability, greenhouse gas emissions and feed-food competition. *Livest Sci*. 2024;279(105392):105392. 10.1016/j.livsci.2023.105392
24. Greenwood PL. Review: An overview of beef production from pasture and feedlot globally, as demand for beef and the need for sustainable practices increase. *Animal*. 2021;15 Suppl 1:100295. 10.1016/j.animal.2021.100295
25. Huang Y, Liu L, Zhao M, Zhang X, Chen J, Zhang Z, et al. Feeding regimens affecting carcass and quality attributes of sheep and goat meat - A comprehensive review. *Anim Biosci*. 2023;36(9):1314-26. 10.5713/ab.23.0051
26. Ke T, Zhao M, Zhang X, Cheng Y, Sun Y, Wang P, et al. Review of Feeding Systems Affecting Production, Carcass Attributes, and Meat Quality of Ovine and Caprine Species. *Life (Basel)*. 2023;13(5). 10.3390/life13051215
27. Mongini A. Practical small ruminant nutrition: Applied nutrition for veterinarians. *AABP Proceedings*. 2024(56):167-70. 10.21423/aabppro20238890
28. Silva TR, Soares PC, Dantas AFM, Marques AVS, O. Filho EF, Aguiar GMN, et al. Serum and liver copper, iron, molybdenum and zinc concentration in goats and sheep in the state of Paraíba, Brazil. *Pesquisa Veterinária Brasileira*. 2018;38(7):1313-6. 10.1590/1678-5150-pvb-5542
29. Langi S, Maulu S, Hasimuna OJ, Kaleinasho Kapula V, Tjipute M. Nutritional requirements and effect of culture conditions on the performance of the African catfish (*Clarias gariepinus*)

Clarias gariepinus

-): a review. *Cogent Food & Agriculture*. 2024;10(1). 10.1080/23311932.2024.2302642
30. Arora J, Pervez A. Enhancing Fish Feeding Methods and Formulating Nutritious Feed For The Growth Of
- Labeo rohita. *Journal of Mountain Research*. 2024;19(1). 10.51220/jmr.v19-i1.7
31. Zhang Y, Lu R, Qin C, Nie G. Precision nutritional regulation and aquaculture. *Aquaculture Reports*. 2020;18. 10.1016/j.aqrep.2020.100496
32. Rocha GC, Duarte ME, Kim SW. Advances, Implications, and Limitations of Low-Crude-Protein Diets in Pig Production. *Animals (Basel)*. 2022;12(24). 10.3390/ani12243478
33. Olomu JM. Determination of optimum protein and energy levels for broiler chicks in the tropics. *Niger J Anim Prod*. 2021;3(1):177-83. 10.51791/njap.v3i1.2592
34. Smith RR, Rumsey GL, Scott ML. Heat increment associated with dietary protein, fat, carbohydrate and complete diets in salmonids comparative energetic efficiency. *J Nutr*. 1978;108(6):1025-32. 10.1093/jn/108.6.1025
35. Weihe R, Dessen J-E, Arge R, Thomassen MS, Hatlen B, Rørvik K-A. Improving production efficiency of farmed Atlantic salmon (*Salmo salar* L.) by isoenergetic diets with increased dietary protein-to-lipid ratio. *Aquaculture Research*. 2018;49(4):1441-53. 10.1111/are.13598
36. Kaushik SJ, Seiliez I. Protein and amino acid nutrition and metabolism in fish: current knowledge and future needs. *Aquac Res*. 2010;41(3):322-32. 10.1111/j.1365-2109.2009.02174.x
37. Korkmaz K. Determination of Proximate Composition and Fatty Acid Profiles of Commercial Fish Feeds. *Journal of Anatolian Environmental and Animal Sciences*. 2022;7(2):184-90. 10.35229/jaes.1044795
38. Zhang Y, Guo F, Yang X, Liu Y, Bao Y, Wang Z, et al. Insights into the mechanism of growth and fat deposition by feeding different levels of lipid provided by transcriptome analysis of swamp eel (*Monopterus albus*, Zuiew 1793) liver. *Front Immunol*. 2023;14:1118198. 10.3389/fimmu.2023.1118198
39. Evrendilek GA. The effect of aquaculture feed on the nutritional quality of farmed seafood: A review of feed ingredients and their impact on human health. *Food Nutrition Chemistry*. 2024;2(4). 10.18686/fnc287
40. Saputra S, Antoro S, Dhoe SB, Rajamuddin MAL, Setiawati M, Suprayudi MA. Nutrient content of various water-based alternative protein

sources as candidates for raw material feed in aquaculture. IOP Conf Ser Earth Environ Sci. 2024;1410(1):012015. 10.1088/1755-1315/1410/1/012015

41. Rosle S, Mohd Rahim MS, Agustono A, Hassin NH. Alternative Feeds for Sustainable Aquaculture: A Comprehensive Structured Review. Journal of Science, Technology and Innovation Policy. 2024;10(2):1-11. 10.11113/jostip.v10n2.150

42. Bell ME, Davies SJ. Nutritional value of extracted soybean, full fat soya and maize gluten meal proteins in comparison to a fish meal based reference diet for fingerling tilapia (*Oreochromis mossambicus*). bioRxiv. 2023. 10.1101/2023.11.12.566624

43. Vastolo A, Calabrò S, Cutrignelli MI. A review on the use of agro-industrial CO-products in animals' diets. Italian Journal of Animal Science. 2022;21(1):577-94. 10.1080/1828051x.2022.2039562

44. Traughber ZT, He F, Hoke JM, Davenport GM, Rodriguez-Zas SL, Southey BR, et al. Ancient grains as novel dietary carbohydrate sources in canine diets. J Anim Sci. 2021;99(6). 10.1093/jas/skab080

45. Wrigley CW, Taylor JRN. Origin, evolution, production, and utilization of cereals. ICC Handbook of 21st Century Cereal Science and Technology: Elsevier; 2023. p. 1-15.

46. Tobiasz-Salach R, Stadnik B, Bajcar M. Oat as a Potential Source of Energy. Energies. 2023;16(16). 10.3390/en16166019

47. Biel W, Kazimierska K, Bashutska U. Nutritional Value of Wheat, Triticale, Barley and Oat Grains. Acta Scientiarum Polonorum Zootechnica. 2020;19(2):19-28. 10.21005/asp.2020.19.2.03

48. Alomari DZ, Schierenbeck M, Alqudah AM, Alqahtani MD, Wagner S, Rolletschek H, et al. Wheat Grains as a Sustainable Source of Protein for Health. Nutrients. 2023;15(20). 10.3390/nu15204398

49. Poutanen KS, Karlund AO, Gomez-Gallego C, Johansson DP, Scheers NM, Marklinder IM, et al. Grains - a major source of sustainable protein for health. Nutr Rev. 2022;80(6):1648-63. 10.1093/nutrit/nuab084

50. Alarape K, Adeniyi A, Ayodele T, Bello IA, Sarker NC, Clementson C, et al. Extraction and Nutritional Value of Soybean Meal Protein Isolate. Nutraceuticals. 2024;4(4):503-21. 10.3390/nutraceuticals4040029

51. Tao A, Wang J, Luo B, Liu B, Wang Z, Chen X, et al. Research progress on cottonseed meal as a protein source in pig nutrition: An updated review. Anim Nutr. 2024;18:220-33. 10.1016/j.aninu.2024.03.020

52. Khan NM, Qadeer A, Khan A, Nasir A, Sikandar A, Adil M, et al. Alternative Sources of Proteins in Farm Animal Feeding. *Journal of microbiology, biotechnology and food sciences*. 2024;13(5). 10.55251/jmbfs.10605
53. Hadidi M, Tan C, Assadpour E, Jafari SM. Oilseed meal proteins: From novel extraction methods to nanocarriers of bioactive compounds. *Food Chem*. 2024;438(137971):137971. 10.1016/j.foodchem.2023.137971
54. Wanasundara JPD, Kapel R, Albe-Slabi S. Proteins from canola/rapeseed—current status. *Sustainable Protein Sources*: Elsevier; 2024. p. 285-309.
55. Bernard JK. Oilseed and Oilseed Meals. *Reference Module in Food Science*: Elsevier; 2016.
56. Świątkiewicz S, Arczewska-Włosek A, Józefiak D. The use of cottonseed meal as a protein source for poultry: an updated review. *Worlds Poult Sci J*. 2016;72(3):473-84. 10.1017/s0043933916000258
57. Picado-Pérez T, Lemus R, Rivera D, Villalobos-Villalobos LA. Nutritive and Fermentative Traits of African Stargrass (*Cynodon nlemfuensis* Vanderyst) Forage Preserved for Silage and Haylage. *Fermentation*. 2024;10(6). 10.3390/fermentation10060268
58. Gruber T, Lang C, Fliegerova K, Terler G, Zebeli Q, Hartinger T. An In Vitro Nutritional Evaluation of Mixed Silages of Drought-Impaired Grass and Sugar Beet Pulp With or Without Silage Inoculants. *J Anim Physiol Anim Nutr (Berl)*. 2025;109(3):766-76. 10.1111/jpn.14092
59. Daza J, González V, Moldenhauer R, Reyes C, Rivas J, Solís C, et al. Use of spent brewer's yeasts as an additive of pasture silages and its effects on nutritional quality and pH. *Chilean journal of agricultural research*. 2024;84(2):260-6. 10.4067/s0718-58392024000200260
60. Koninger M, von Velsen-Zerweck A, Eiberger C, Löffler C, Topper A, Visscher C, et al. Nutrient Composition and Feed Hygiene of Alfalfa, Comparison of Feed Intake and Selected Metabolic Parameters in Horses Fed Alfalfa Haylage, Alfalfa Hay or Meadow Hay. *Animals (Basel)*. 2024;14(6). 10.3390/ani14060889
61. Instituto Nacional de Investigaciones Forestales AyP, Garay-Martínez JR. Technological options for establishing pastures and increasing yield and nutrient value forage. *Sustainability in agricultural production and natural resource management T-I Biotechnology and Agricultural Sciences*: ECORFAN; 2023. p. 54-61.

62. Undi M, Sedivec K, Bachler J. Assessing supplementing strategies for beef cattle in a bale grazing system using grass hay during variable winter conditions. *Frontiers in Animal Science*. 2024;5. 10.3389/fanim.2024.1415622
63. Meo-Filho P, Hood J, Lee MRF, Fleming H, Meethal ME, Misselbrook T. Performance and enteric methane emissions from housed beef cattle fed silage produced on pastures with different forage profiles. *Animal*. 2023;17(4):100726. 10.1016/j.animal.2023.100726
64. Zhang Z, Li F, Li F, Wang Z, Guo L, Weng X, et al. Influence of Dietary Forage Neutral Detergent Fiber on Ruminal Fermentation, Chewing Activity, Nutrient Digestion, and Ruminal Microbiota of Hu Sheep. *Animals (Basel)*. 2025;15(3). 10.3390/ani15030314
65. Grant RJ, Cotanch KW. Perspective and Commentary: Chewing behavior of dairy cows: Practical perspectives on forage fiber and the management environment. *Applied Animal Science*. 2023;39(3):146-55. 10.15232/aas.2022-02371
66. Ermers C, McGilchrist N, Fenner K, Wilson B, McGreevy P. The Fibre Requirements of Horses and the Consequences and Causes of Failure to Meet Them. *Animals (Basel)*. 2023;13(8). 10.3390/ani13081414
67. Koptelova A, Ducrey A, Lunven B, Koller L, Nagornova N, Appenzeller EW, et al. Waste-to-Taste: Transforming Wet Byproducts of the Food Industry into New Nutritious Foods. *Chimia (Aarau)*. 2024;78(12):824-30. 10.2533/chimia.2024.824
68. Ab Razak AF, Mohamed HN, Abdullah MS, Sulaiman MS, Mohd Basri SN, Ting UH, et al. Waste Agriculture Material in Animal Feed Trend Evaluation: A Bibliometric Analysis. *Journal of Tourism, Hospitality and Environment Management*. 2024;9(38):242-58. 10.35631/jthem.938017
69. Williams PEV, Burton E. Exploitation of biobased co-product streams; Contributing to European protein demands using ethanol plant derived co-products. *Animal Science Cases*. 2024. 10.1079/animalsciencecases.2024.0002
70. Hristakieva P, Mincheva N, Ivanova I, Oblakova M, Ivanov N, Slavov I. Use of Distiller's Dried Grains with Solubles (DDGS) from corn or wheat in broiler diets. *Bulgarian Journal of Animal Husbandry*. 2023;60(5):22-34. 10.61308/yfao2885
71. Aguiéiras ECG, Greco-Duarte J, de Souza CP, Oliveira RA, Pinto TdO, Ramos R, et al. Integrated process for a new sequential valorization of corn

- ethanol production by-products: Production of fermented solid with lipase activity, ethyl esters, and animal feed. *Ind Crops Prod.* 2024;209(118028):118028. 10.1016/j.indcrop.2024.118028
72. Isah S, Okosun J. Nutritional and Anti-nutritional Compositions of Rice Bran as a Potential Animal Feed. *International Research Journal of Pure and Applied Chemistry.* 2023;24(6):1-6. 10.9734/irjpac/2023/v24i6835
 73. Feng Y, Jiao S, Zhang Y, Liu Y, Zhao F, Wang Y, et al. Compositional Variations in Wheat Bran Influence Growth Performance, Nutrient Retention, and Cecal Microbiome in Broilers. *Animals (Basel).* 2024;14(23). 10.3390/ani14233407
 74. Liu H, Ren X, Li Y, Cao Q, Yang L, Jiang S, et al. Effects of different wheat bran fermentation sources on growth performance, nutrient digestibility, serum antioxidant capacity and fecal microbiota in growing pigs. *Front Vet Sci.* 2023;10:1289010. 10.3389/fvets.2023.1289010
 75. Pierce RB, Adeniji YA, Bomberger R, Goodall SR, Harvatine KJ. Effect of feeding increasing levels of whole cottonseed on milk and milk components, milk fatty acid profile, and total-tract digestibility in lactating dairy cows. *J Dairy Sci.* 2024;107(5):2916-29. 10.3168/jds.2023-23944
 76. The Ohio State University USA, Eastridge ML. Assessing alternative fiber sources from by-products. *Burleigh Dodds Series in Agricultural Science: Burleigh Dodds Science Publishing; 2023.* p. 349-62.
 77. Muniasamy S, Rajasekaran B, Subramaniam B, Muniasamy S, Pailan GH. Utilization of fish waste and by-products for fish meal production as a potential feed ingredient, fish waste to valuable products: Recent applications and research update. *Fish Waste to Valuable Products.* Singapore: Springer Nature Singapore; 2024. p. 301-16.
 78. Hung Y-T, Fruge E, Reznik G, Droegmiller J, Lutz T. PSIII-17 evaluation of cheese co-products in comparison with specialty proteins on growth performance of weaned pigs. *J Anim Sci.* 2023;101(Supplement_2):296-7. 10.1093/jas/skad341.337
 79. Miranda MVFGd, Morais MRPTd, Lima RNd, Leite HMdS, Assis APPd, Teófilo TdS, et al. Performance and development of gastric compartments of calves fed with cheese whey and transition milk. *Ciência Rural.* 2019;49(9). 10.1590/0103-8478cr20190308
 80. Patil NP, Sidhu JS, Hundal JS, Kaur J. Utilization of Biscuit Waste in Poultry Diet- A Review. *International Journal of Bio-resource and Stress Management.* 2024;15(Sep, 9):01-7. 10.23910/1.2024.5552

81. Wilkinson JM. Re-defining efficiency of feed use by livestock. *Animal*. 2011;5(7):1014-22. 10.1017/S175173111100005X
82. Stone NM, Engle CR, Kumar G, Li MH, Hegde S, Roy LA, et al. Factors affecting feed conversion ratios in US commercial catfish production ponds. *Journal of the World Aquaculture Society*. 2024;55(3). 10.1111/jwas.13053
83. Rueda MS, Bonilla S, de Souza C, Starkey JD, Starkey CW, Mejia L, et al. Evaluation of particle size and feed form on performance, carcass characteristics, nutrient digestibility, and gastrointestinal tract development of broilers at 39 d of age. *Poult Sci*. 2024;103(3):103437. 10.1016/j.psj.2024.103437
84. Losinger WC. Feed-conversion ratio of finisher pigs in the USA. *Prev Vet Med*. 1998;36(4):287-305. 10.1016/s0167-5877(98)00094-4
85. Davison C, Michie C, Tachtatzis C, Andonovic I, Bowen J, Duthie CA. Feed Conversion Ratio (FCR) and Performance Group Estimation Based on Predicted Feed Intake for the Optimisation of Beef Production. *Sensors (Basel)*. 2023;23(10). 10.3390/s23104621
86. Hermes S, Ludemann CI, Amer PR. Economic weights for performance and survival traits of growing pigs. *J Anim Sci*. 2014;92(12):5358-66. 10.2527/jas.2014-7944
87. Glatz P, Moore M. Production systems. *Poultry. Encyclopedia of Meat Sciences: Elsevier*; 2024. p. 22-31.
88. Zou A, Nadeau K, Wang PW, Lee JY, Guttman DS, Sharif S, et al. Accumulation of genetic variants associated with immunity in the selective breeding of broilers. *BMC Genet*. 2020;21(1):5. 10.1186/s12863-020-0807-z
89. Faustin Evaris E, Sarmiento Franco L, Sandoval Castro C. Slow-growing male chickens fit poultry production systems with outdoor access. *Worlds Poult Sci J*. 2019;75(3):429-44. 10.1017/s0043933919000400
90. Guan R, Li Y, Hu Z, Shi Y, Chen Z, Wu L, et al. Identifying slow-growing commercial pigs using growth performance and health indicators. *Sci Rep*. 2024;14(1):28222. 10.1038/s41598-024-78093-z
91. Shi C, He J, Wang J, Yu J, Yu B, Mao X, et al. Effects of *Aspergillus niger* fermented rapeseed meal on nutrient digestibility, growth performance and serum parameters in growing pigs. *Anim Sci J*. 2016;87(4):557-63. 10.1111/asj.12457
92. Tang X, Liu X, Zhang K. Effects of Microbial Fermented Feed on Serum Biochemical Profile, Carcass Traits, Meat Amino Acid and Fatty Acid

- Profile, and Gut Microbiome Composition of Finishing Pigs. *Front Vet Sci.* 2021;8:744630. 10.3389/fvets.2021.744630
93. Xu B, Zhu L, Fu J, Li Z, Wang Y, Jin M. Overall assessment of fermented feed for pigs: a series of meta-analyses. *J Anim Sci.* 2019;97(12):4810-21. 10.1093/jas/skz350
94. Wang C, Shi C, Zhang Y, Song D, Lu Z, Wang Y. Microbiota in fermented feed and swine gut. *Appl Microbiol Biotechnol.* 2018;102(7):2941-8. 10.1007/s00253-018-8829-4
95. Fan Z, Xia Z, Cozannet P, de Nanclares MP, Xin H, Wang M, et al. Diets Fermented with Bacteria and Enzymes in China Improve Growth Performance and Health of Weaned Piglets. *Agriculture.* 2022;12(12). 10.3390/agriculture12121984
96. Xin H, Wang M, Xia Z, Yu B, He J, Yu J, et al. Fermented Diet Liquid Feeding Improves Growth Performance and Intestinal Function of Pigs. *Animals (Basel).* 2021;11(5). 10.3390/ani11051452
97. Xiao R, Wang L, Tang Z, Qian X, Wang J, Lian Y, et al. Effects of fermented Chinese herbal medicine feed additives on growth performance and intestinal microbiota of piglets. *PLoS One.* 2024;19(10):e0308196. 10.1371/journal.pone.0308196
98. Jiang D, Yang M, Xu J, Deng L, Hu C, Zhang L, et al. Three-stage fermentation of the feed and the application on weaned piglets. *Front Vet Sci.* 2023;10:1123563. 10.3389/fvets.2023.1123563
99. Predescu NC, Stefan G, Rosu MP, Papuc C. Fermented Feed in Broiler Diets Reduces the Antinutritional Factors, Improves Productive Performances and Modulates Gut Microbiome—A Review. *Agriculture.* 2024;14(10). 10.3390/agriculture14101752
100. Sun H, Chen D, Cai H, Chang W, Wang Z, Liu G, et al. Effects of Fermenting the Plant Fraction of a Complete Feed on the Growth Performance, Nutrient Utilization, Antioxidant Functions, Meat Quality, and Intestinal Microbiota of Broilers. *Animals (Basel).* 2022;12(20). 10.3390/ani12202870
101. Guo W, Xu LN, Guo XJ, Wang W, Hao QH, Wang SY, et al. The impacts of fermented feed on laying performance, egg quality, immune function, intestinal morphology and microbiota of laying hens in the late laying cycle. *Animal.* 2022;16(12):100676. 10.1016/j.animal.2022.100676
102. Ma L, Wang H, Qiu Y, Bai Z, Yang Z, Li E, et al. Alternative Uses of Fermented Wheat Bran: A Mini Review. *Fermentation.* 2024;10(12). 10.3390/fermentation10120611

103. Yasmeen R, Ahmad F. Microbial fermented agricultural waste-based broiler feed: a sustainable alternative to conventional feed. *Worlds Poult Sci J*. 2025;81(1):271-87. 10.1080/00439339.2024.2443222
104. Al-Khalaifah HS, Shahin SE, Omar AE, Mohammed HA, Mahmoud HI, Ibrahim D. Effects of graded levels of microbial fermented or enzymatically treated dried brewer's grains on growth, digestive and nutrient transporter genes expression and cost effectiveness in broiler chickens. *BMC Vet Res*. 2020;16(1):424. 10.1186/s12917-020-02603-0
105. Gunun P, Cherdthong A, Khejornsart P, Wanapat M, Polyorach S, Kaewwongsa W, et al. Replacing Concentrate with Yeast- or EM-Fermented Cassava Peel (YFCP or EMFCP): Effects on the Feed Intake, Feed Digestibility, Rumen Fermentation, and Growth Performance of Goats. *Animals (Basel)*. 2023;13(4). 10.3390/ani13040551
106. Suriyapha C, Supapong C, So S, Wanapat M, Cherdthong A. Bioconversion of agro-industrial residues as a protein source supplementation for multiparous Holstein Thai crossbreed cows. *PLoS One*. 2022;17(9):e0273916. 10.1371/journal.pone.0273916
107. Konkol D, Popiela E, Opalinski S, Lipinska A, Tymoszewski A, Krasowska A, et al. Effects of fermented rapeseed meal on performance, intestinal morphology, the viscosity of intestinal content, phosphorus availability, and egg quality of laying hens. *Poult Sci*. 2024;103(1):103256. 10.1016/j.psj.2023.103256
108. Zhang S, Huang Z, Li Q, Zheng X, Liu J. Two-stage solid-state fermentation to increase the nutrient value of corn processing waste and explore its efficacy as a feed protein source. *Food Chem X*. 2024;23:101656. 10.1016/j.fochx.2024.101656
109. van Winsen RL, Lipman LJ, Biesterveld S, Urlings BAp, Snijders JMa, van Knapen F. Mechanism of *Salmonella* reduction in fermented pig feed. *J Sci Food Agric*. 2001;81(3):342-6. 10.1002/1097-0010(200102)81:3<342::aid-jsfa824>3.0.co;2-6
110. Missotten JAM, Michiels J, Ovyn A, De Smet S, Dierick NA. Fermented liquid feed for weaned piglets: impact of sedimentation in the feed slurry on performance and gut parameters. *Czech Journal of Animal Science*. 2015;60(5):195-207. 10.17221/8169-cjas
111. Faba L, Litjens R, Allaart J, van den Hil PR. Feed additive blends fed to nursery pigs challenged with *Salmonella*. *J Anim Sci*. 2020;98(1). 10.1093/jas/skz382

112. Koo B, Bustamante-Garcia D, Kim JW, Nyachoti CM. Health-promoting effects of Lactobacillus-fermented barley in weaned pigs challenged with Escherichia coli K88(). *Animal*. 2020;14(1):39-49. 10.1017/S1751731119001939
113. Rivera GM, Casinillo LF. Which is better, non-fermented or fermented diets?: The case of production of broilers. *Aceh Journal of Animal Science*. 2021;6(3):79-85.
114. Sheldon T. Saving antibiotics for when they are really needed: the Dutch example. *BMJ*. 2016;354:i4192. 10.1136/bmj.i4192
115. Islam R, Pandey A, Saha T. Alternatives to antibiotics in animal farming. *Alternatives to Antibiotics*. Singapore: Springer Nature Singapore; 2022. p. 147-75.
116. Sethiya NK. Review on Natural Growth Promoters Available for Improving Gut Health of Poultry: An Alternative to Antibiotic Growth Promoters. *Asian Journal of Poultry Science*. 2015;10(1):1-29. 10.3923/ajpsaj.2016.1.29
117. Holzer Z, Levy D, Tagari H, Volcani R. Soaking of complete fattening rations high in poor roughage 1. The effect of moisture content and spontaneous fermentation on nutritional value. *Anim Sci*. 1975;21(3):323-35. 10.1017/s0003356100030798
118. Yasar S, Forbes JM. Performance and gastro-intestinal response of broiler chickens fed on cereal grain-based foods soaked in water. *Br Poult Sci*. 1999;40(1):65-76. 10.1080/00071669987854
119. Chaturvedi ML, Singh UB, Ranjhan SK. Effect of feeding water-soaked and dry wheat straw on feed intake, digestibility of nutrients and VFA production in growing zebu and buffalo calves. *J Agric Sci*. 1973;80(3):393-7. 10.1017/s0021859600058032
120. Radzik-Rant A, Rant W, Niżnikowski R, Świątek M, Szymańska Ż, Ślęzak M, et al. The effect of the addition of wet brewers grain to the diet of lambs on body weight gain, slaughter value and meat quality. *Archives Animal Breeding*. 2018;61(2):245-51. 10.5194/aab-61-245-2018
121. Hong T, Van An L, Be P, Lindberg J. Effect of fermented rice bran and cassava waste on growth performance and meat quality of crossbred pigs. *World Journal of Agricultural Research*. 2016;4(5):132-8.
122. Mk O, So A, Va A. Feeding Microbe-Fermented Cassava Tuber Wastes Modulates Gut Microbiota and Faecal Characteristics of Growing Pigs. *Fermentation Technology*. 2017;06(02). 10.4172/2167-7972.1000145

123. Yang R, Khalid A, Khalid F, Ye M, Li Y, Zhan K, et al. Effect of fermented corn by-products on production performance, blood biochemistry, and egg quality indices of laying hens. *J Anim Sci.* 2022;100(5). 10.1093/jas/skac130
124. Maoba S. Production performance and profitability analysis of small scale layer projects supported through CASP in Germiston Region, Gauteng Province. *South African Journal of Agricultural Extension (SAJAE).* 2016;44(1). 10.17159/2413-3221/2016/v44n1a368
125. Chen T, Zhang W, Liu Y, Song Y, Wu L, Liu C, et al. Effects of Wet Fermented Soybean Dregs on Physical and Mechanical Properties of Pellets of Corn Stover. *Animals (Basel).* 2022;12(19). 10.3390/ani12192632
126. Blazer KJ, Shinnors KJ, Kluge ZA, Tekeste MZ, Digman MF. Physical Properties of Moist, Fermented Corn Grain after Processing by Grinding or Milling. *AgriEngineering.* 2024;6(2):908-24. 10.3390/agriengineering6020052
127. Blazer KJ, Shinnors KJ, Kluge ZA, Tekeste MZ, Digman MF. Physical Properties of Moist, Fermented Corn Kernels. *Processes.* 2023;11(5). 10.3390/pr11051351
128. Tabbassum R, Naveed M, Mehboob I, Babar MH, Holatko J, Akhtar N, et al. Comparative Response of Fermented and Non-Fermented Animal Manure Combined with Split Dose of Phosphate Fertilizer Enhances Agronomic Performance and Wheat Productivity through Enhanced P Use Efficiency. *Agronomy.* 2022;12(10). 10.3390/agronomy12102335
129. Nadeem M, Ali MA, Syed Q, Nelofer R, Sahar U. Nutritional upgrading of various feed ingredients through co-culture solid state fermentation / Çeşitli yem içerikleri besin değerlerinin birlikte kültür katı hal fermentasyonu kullanılarak artırılması. *Turkish Journal of Biochemistry.* 2016;41(5):347-53. 10.1515/tjb-2016-0050
130. Cherdthong A. Potential use of rumen digesta as ruminant diet-a review. *Trop Anim Health Prod.* 2020;52(1):1-6. 10.1007/s11250-019-02018-6
131. Niwiska B. Digestion in Ruminants. *Carbohydrates - Comprehensive Studies on Glycobiology and Glycotechnology* 2012.
132. Dou Z, Toth JD, Pitta DW, Bender JS, Hennessy ML, Vecchiarelli B, et al. Proof of concept for developing novel feeds for cattle from wasted food and crop biomass to enhance agri-food system efficiency. *Sci Rep.* 2022;12(1):13630. 10.1038/s41598-022-17812-w

133. Kushwaha R, Singh AK, Kumar M. Residual feed intake-An emerging system for selection of efficient animals: A review. *Agricultural Reviews*. 2016;37(1). 10.18805/ar.v37i1.9267
134. Arthur JP, Herd R. Residual feed intake in beef cattle. *Revista Brasileira de Zootecnia*. 2008;37:269-79.
135. Fischer A, Dai X, Kalscheur KF. Feed efficiency of lactating Holstein cows is repeatable within diet but less reproducible when changing dietary starch and forage concentrations. *Animal*. 2022;16(8):100599. 10.1016/j.animal.2022.100599
136. Ojo AO, Mulim HA, Campos GS, Junqueira VS, Lemenager RP, Schoonmaker JP, et al. Exploring Feed Efficiency in Beef Cattle: From Data Collection to Genetic and Nutritional Modeling. *Animals (Basel)*. 2024;14(24). 10.3390/ani14243633
137. Fukumasu H, Santana MH, Alexandre PA, Ferraz JBS. Systems biology application in feed efficiency in beef cattle. *Systems Biology in Animal Production and Health*, Vol 2. Cham: Springer International Publishing; 2016. p. 79-95.
138. Santiago BM, da Silva FF, Silva RR, Costa EGL, Porto Junior AF, Costa EN, et al. Effect of different roughages sources on performance, milk composition, fatty acid profile, and milk cholesterol content of feedlot feed crossbred cows (Holstein × Zebu). *Trop Anim Health Prod*. 2019;51(3):599-604. 10.1007/s11250-018-1736-y
139. Comerford JW, House RB, Harpster HW, Henning WR, Cooper JB. Effects of forage and protein source on feedlot performance and carcass traits of Holstein and crossbred beef steers. *J Anim Sci*. 1992;70(4):1022-31. 10.2527/1992.7041022x
140. Ovinge LA, Hilscher FH, Boyd BM, Anderson JN, Erickson GE. Effects of varying levels of silage inclusion and Brown Midrib corn silage on finishing performance of steers. 2019.
141. Burken D, Klopfenstein T, Erickson GE. Economics of feeding elevated levels of corn silage in finishing diets containing MDGS. 2013.
142. García-Chávez I, Meraz-Romero E, Castelán-Ortega O, Zaragoza-Esparza J, Osorio-Avalos J, Robles-Jiménez LE, et al. Corn silage, a systematic review of the quality and yield in different regions around the world. *Ciencia y Tecnología Agropecuaria*. 2022;23(3). 10.21930/rcta.vol23_num3_art:2547

143. García-Chávez I, Meraz-Romero E, Castelán-Ortega O, Zaragoza Esparza J, Osorio Avalos J, Robles Jimenez LE, et al. 2020. 10.20944/preprints202010.0094.v1
144. La Guardia Nave R, Corbin MD. Forage Warm-Season Legumes and Grasses Intercropped with Corn as an Alternative for Corn Silage Production. *Agronomy*. 2018;8(10). 10.3390/agronomy8100199
145. Paat PC, Kairupan AN, Polakitan DJ, Silondae H, Joseph GH, Kindangen JG. Legume leaves in improving the quality of feed silage ruminants: Advantages, challenges and strategies. *Innovations in Biological Science Vol 8: B P International*; 2024. p. 96-115.
146. Hildebrand B, Boguhn J, Rodehutschord M. Effect of maize silage to grass silage ratio and feed particle size on protein synthesis and amino acid profile in different microbial fractions in a semi-continuous rumen simulation. *Animal*. 2011;5(4):537-46. 10.1017/S1751731110002156
147. Townsend PW, Blake RW, Holmann FJ, Van Soest PJ, Sniffen CJ, Sisler DG. Low cost feeding strategies for dual purpose cattle in Venezuela. *J Dairy Sci*. 1990;73(3):792-803. 10.3168/jds.s0022-0302(90)78732-2
148. Yan R, Zhang R, Zhang X, Jiang C, Han J-g, Zhang Y-j. Changes in Milk Production and Metabolic Parameters by Feeding Lactating Cows Based on Different Ratios of Corn Silage: Alfalfa Hay with Addition of Extruded Soybeans. *Asian-Australasian Journal of Animal Sciences*. 2011;24(6):800-9. 10.5713/ajas.2011.10390
149. Kok I, Copani G, Bryan KA, Witt KLM, van Straalen WM, do Amaral RC, et al. Effects of feeding an inoculated corn silage with or without a direct-fed microbial on dry matter intake, milk production, and nutrient digestibility of high-producing lactating Holstein cows. *Transl Anim Sci*. 2024;8:txae010. 10.1093/tas/txae010
150. Schoonhoven A, Holmann F, Argel P, Perez E, Ordoñez JC, Chaves J. Estimation and comparison of benefits due to feeding hay and silage during the dry season on commercial dual-purpose cattle production systems in Honduras and Costa Rica. *Livestock Research for Rural Development*. 2006;18(1):art. 15-art. .
151. Sriagtula R, Aini Q, Susanty H, Yetmaneli Y. Application of Sweet Maize Whole Plant Silage (*Zea mays saccharata* Sturt) and *Gliricidia sepium* for Feed of Dairy Cattle. *jwa*. 2024;31(2):411-6. 10.25077/jwa.31.2.411-416.2024

152. Moran JB, Kaiser A, Stockdale CR. The role of maize silage in milk and meat production from grazing cattle in Australia. *Outlook Agric.* 1990;19(3):171-7. 10.1177/003072709001900307
153. Kislyakova EM, Khokhryakov GA. Influence of silage prepared with biological preservatives on productivity of cows. *Kormlenie sel'skhozjajstvennyh zhivotnyh i kormoproizvodstvo* (Feeding of agricultural animals and feed production). 2021(5):28-40. 10.33920/sel-05-2105-04
154. Ba NX, Lane PA, Parsons D, Van NH, Khanh HLP, Corfield JP, et al. Forages improve livelihoods of smallholder farmers with beef cattle in South Central Coastal Vietnam. *Trop Grassl-Forrages Trop.* 2013;1(2):225. 10.17138/tgft(1)225-229
155. Hibebo DK, Heliso MF. Participatory evaluation and demonstration of livestock feed conservation technologies for small scale dairy farmers in Melokoza and Basketo special districts, Southern Ethiopia. *Global J Res Multidiscip Studies.* 2022;1(1):014-21. 10.58175/gjrms.2022.1.1.0024
156. Whitaker DA, Kelly JM, Smith S. Disposal and disease rates in 340 British dairy herds. *Veterinary Record.* 2000;146(13):363-7.
157. Chang Y, Saeed Omer SH, Li G, Lian H, Liu Y. Research Advance on Application of Microbial Fermented Fodder in Broilers Production: A Short Review. *Open Journal of Animal Sciences.* 2022;12(02):200-9. 10.4236/ojas.2022.122015
158. Dai Z, Cui L, Li J, Wang B, Guo L, Wu Z, et al. Fermentation techniques in feed production. *Animal Agriculture* 2020. p. 407-29.
159. Bartkiene E. Possible uses of lactic acid bacteria for food and feed production. *Agric Res Technol.* 2017;4(4). 10.19080/artoaj.2017.04.555644
160. Admassie M. A Review on Food Fermentation and the Biotechnology of Lactic Acid Bacteria. *World Journal of Food Science and Technology.* 2018;2(1). 10.11648/j.wjfst.20180201.13
161. Walker G, Stewart G. *Saccharomyces cerevisiae* in the Production of Fermented Beverages. *Beverages.* 2016;2(4). 10.3390/beverages2040030
162. Nya E, Etukudo O. Industrial Potentials of *Saccharomyces cerevisiae*. *British Journal of Multidisciplinary and Advanced Studies.* 2023;4(2):23-46. 10.37745/bjmas.2022.0152
163. Yao Y, Li H, Li J, Zhu B, Gao T. Anaerobic Solid-State Fermentation of Soybean Meal With *Bacillus* sp. to Improve Nutritional Quality. *Front Nutr.* 2021;8:706977. 10.3389/fnut.2021.706977

164. Pham HH, Kim DH, Nguyen TL. Wide-genome selection of lactic acid bacteria harboring genes that promote the elimination of antinutritional factors. *Front Plant Sci.* 2023;14:1145041. 10.3389/fpls.2023.1145041
165. Matsuzawa T. Plant polysaccharide degradation-related enzymes in *Aspergillus oryzae*. *Biosci Biotechnol Biochem.* 2024;88(3):276-82. 10.1093/bbb/zbad177
166. Peixoto-Nogueira SC, Sandrim VC, Guimaraes LH, Jorge JA, Terenzi HF, Polizeli ML. Evidence of thermostable amylolytic activity from *Rhizopus microsporus* var. *rhizopodiformis* using wheat bran and corncob as alternative carbon source. *Bioprocess Biosyst Eng.* 2008;31(4):329-34. 10.1007/s00449-007-0166-4
167. Lau N, Hummel J, Kramer E, Hunerberg M. Fermentation of liquid feed with lactic acid bacteria reduces dry matter losses, lysine breakdown, formation of biogenic amines, and phytate-phosphorus. *Transl Anim Sci.* 2022;6(1):txac007. 10.1093/tas/txac007
168. Lisowski A, Wójcik J, Klonowski J, Sypuła M, Chlebowski J, Kostyra K, et al. Compaction of chopped material in a mini silo. *Biomass and Bioenergy.* 2020;139. 10.1016/j.biombioe.2020.105631
169. Yang L, Zeng X, Qiao S. Advances in research on solid-state fermented feed and its utilization: The pioneer of private customization for intestinal microorganisms. *Anim Nutr.* 2021;7(4):905-16. 10.1016/j.aninu.2021.06.002
170. Romano N, Kumar V. Phytase in animal feed. *Enzymes in Human and Animal Nutrition: Elsevier*; 2018. p. 73-88.
171. Griffiths DW. The inhibition of digestive enzymes by polyphenolic compounds. *Advances in Experimental Medicine and Biology. Advances in experimental medicine and biology.* Boston, MA: Springer US; 1986. p. 509-16.
172. Jeyakumar E, Lawrence R. Microbial fermentation for reduction of antinutritional factors. *Current Developments in Biotechnology and Bioengineering: Elsevier*; 2022. p. 239-60.
173. Anastasio M, Pepe O, Cirillo T, Palomba S, Blaiotta G, Villani F. Selection and use of phytate-degrading LAB to improve cereal-based products by mineral solubilization during dough fermentation. *J Food Sci.* 2010;75(1):M28-35. 10.1111/j.1750-3841.2009.01402.x
174. Yang F, Chen C, Ni D, Yang Y, Tian J, Li Y, et al. Effects of Fermentation on Bioactivity and the Composition of Polyphenols Contained in

- Polyphenol-Rich Foods: A Review. *Foods*. 2023;12(17). 10.3390/foods12173315
175. Kook M-C, Cho S-C, Hong Y-H, Park H. *Bacillus subtilis* fermentation for enhancement of feed nutritive value of soybean meal. *J Appl Biol Chem*. 2014;57(2):183-8. 10.3839/jabc.2014.030
176. Xue J, Wu J, Ji Y, Sun S, Gao Y, Yang H, et al. Effect of microbial fermentation on the quality of soybean meal. *Int J Food Sci Technol*. 2024;59(1):72-83. 10.1111/ijfs.16817
177. Di D, He S, Zhang R, Gao K, Qiu M, Li X, et al. Exploring the dual role of anti-nutritional factors in soybeans: a comprehensive analysis of health risks and benefits. *Crit Rev Food Sci Nutr*. 2024:1-18. 10.1080/10408398.2024.2430757
178. Arbab Sakandar H, Chen Y, Peng C, Chen X, Imran M, Zhang H. Impact of fermentation on antinutritional factors and protein degradation of legume seeds: A review. *Food Rev Int*. 2021:1-23. 10.1080/87559129.2021.1931300
179. Kendall WA, Leath KT. Effect of saponins on palatability of alfalfa to meadow voles1. *Agron J*. 1976;68(3):473-6. 10.2134/agronj1976.00021962006800030010x
180. Fu J, Zhao J, Shang H. Functions and mechanisms of nonstarch polysaccharides in monogastric animal production. *Int J Biol Macromol*. 2024;281(Pt 1):136488. 10.1016/j.ijbiomac.2024.136488
181. Annison G, Choct M. Anti-nutritive activities of cereal non-starch polysaccharides in broiler diets and strategies minimizing their effects. *Worlds Poult Sci J*. 1991;47(3):232-42. 10.1079/wps19910019
182. Bederska-Łojewska D, Świątkiewicz S, Arczewska-Włosek A, Schwarz T. Rye non-starch polysaccharides: their impact on poultry intestinal physiology, nutrients digestibility and performance indices – a review. *Annals of Animal Science*. 2017;17(2):351-69. 10.1515/aoas-2016-0090
183. Graż M. Role of oxalic acid in fungal and bacterial metabolism and its biotechnological potential. *World J Microbiol Biotechnol*. 2024;40(6):178. 10.1007/s11274-024-03973-5
184. Guan Y, Lv H, Wu G, Chen J, Wang M, Zhang M, et al. Effects of Lactic Acid Bacteria Reducing the Content of Harmful Fungi and Mycotoxins on the Quality of Mixed Fermented Feed. *Toxins (Basel)*. 2023;15(3). 10.3390/toxins15030226

185. Giacomini RX, Acosta ER, Cerqueira MBR, Primel EG, Garda-Buffon J. 2022. 10.21203/rs.3.rs-2062216/v1
186. Missotten JA, Michiels J, Dierick N, Ovyne A, Akbarian A, De Smet S. Effect of fermented moist feed on performance, gut bacteria and gut histomorphology in broilers. *Br Poult Sci.* 2013;54(5):627-34. 10.1080/00071668.2013.811718
187. Bhargav S, Panda BP, Ali M, Javed S. Solid-state fermentation: an overview. *Chemical and Biochemical Engineering Quarterly.* 2008;22(1):49-70.
188. Kim D, Dong Lee K, Choon Choi K. Role of LAB in silage fermentation: Effect on nutritional quality and organic acid production—An overview. *AIMS Agriculture and Food.* 2021;6(1):216-34. 10.3934/agrfood.2021014
189. Weinberg ZG. Preservation of forage crops by solid-state lactic acid fermentation-ensiling. *Current Developments in Solid-state Fermentation.* New York, NY: Springer New York; 2008. p. 443-67.
190. Capozzi V, Fragasso M, Romaniello R, Berbegal C, Russo P, Spano G. Spontaneous Food Fermentations and Potential Risks for Human Health. *Fermentation.* 2017;3(4). 10.3390/fermentation3040049
191. Skowron K, Budzynska A, Grudlewska-Buda K, Wiktorczyk-Kapischke N, Andrzejewska M, Walecka-Zacharska E, et al. Two Faces of Fermented Foods-The Benefits and Threats of Its Consumption. *Front Microbiol.* 2022;13:845166. 10.3389/fmicb.2022.845166
192. Li W, Cheng P, Zhang JB, Zhao LM, Ma YB, Ding K. Synergism of microorganisms and enzymes in solid-state fermentation of animal feed. A review. *Journal of Animal and Feed Sciences.* 2021;30(1):3-10. 10.22358/jafs/133151/2021
193. Masum SM, Satter MA, Shams B, Amin MZ, Azam MZ, Sultana N. Vitamin B and Essential Minerals Contents of Mixed Solid State Fermented Millet (*Sterea italic*) and Bengal Gram by *Rhizopus oligosporus*. *Bangladesh Journal of Scientific and Industrial Research.* 1970;46(1):1-8. 10.3329/bjsir.v46i1.8098
194. Shah AM, Tarfeen N, Mohamed H, Song Y. Fermented Foods: Their Health-Promoting Components and Potential Effects on Gut Microbiota. *Fermentation.* 2023;9(2). 10.3390/fermentation9020118

195. Leeuwendaal NK, Stanton C, O'Toole PW, Beresford TP. Fermented Foods, Health and the Gut Microbiome. *Nutrients*. 2022;14(7). 10.3390/nu14071527
196. Vandenberghe LPS, Pandey A, Carvalho JC, Letti LAJ, Woiciechowski AL, Karp SG, et al. Solid-state fermentation technology and innovation for the production of agricultural and animal feed bioproducts. *Systems Microbiology and Biomanufacturing*. 2020;1(2):142-65. 10.1007/s43393-020-00015-7
197. Papatsiros VG, Katsoulos PD, Koutoulis KC, Karatzia M, Dedousi A, Christodouloupoulos G. Alternatives to antibiotics for farm animals. *CAB Rev Perspect Agric Vet Sci Nutr Nat Resour*. 2014;2013(032):1-15. 10.1079/pavsnmr20138032
198. Wolfe BE. Are fermented foods an overlooked reservoir of antimicrobial resistance? *Curr Opin Food Sci*. 2023;51(101018):101018. 10.1016/j.cofs.2023.101018
199. Vinayamohan PG, Viju LS, Joseph D, Venkitanarayanan K. Fermented Foods as a Potential Vehicle of Antimicrobial-Resistant Bacteria and Genes. *Fermentation*. 2023;9(7). 10.3390/fermentation9070688
200. Li J, Tao L, Zhang R, Yang G. Effects of fermented feed on growth performance, nutrient metabolism and cecal microflora of broilers. *Anim Biosci*. 2022;35(4):596-604. 10.5713/ab.21.0333
201. Wang H, Long W, Chadwick D, Velthof GL, Oenema O, Ma W, et al. Can dietary manipulations improve the productivity of pigs with lower environmental and economic cost? A global meta-analysis. *Agric Ecosyst Environ*. 2020;289(106748):106748. 10.1016/j.agee.2019.106748
202. FACT1808MR. Market Research Survey: 10 Years Historical Data, Analysis and Forecast. Food & Beverage: Fact.MR; 2022 2022/12 <https://www.factmr.com/report/1808/poultry-feed-market>.
203. Hsu PK, Liu CP, Liu LY, Chang CH, Yang SS. Protein enrichment and digestion improvement of napiergrass and pangolagrass with solid-state fermentation. *J Microbiol Immunol Infect*. 2013;46(3):171-9. 10.1016/j.jmii.2012.04.001
204. Gungor E, Altop A, Erener G. Effect of raw and fermented grape seed on growth performance, antioxidant capacity, and cecal microflora in broiler chickens. *Animal*. 2021;15(4):100194. 10.1016/j.animal.2021.100194
205. Wan Y, Ma R, Qi R, Lu J, Wang Z, Ma Q, et al. Effects of dietary fermented peony seed dreg on the laying performance, albumen quality,

antioxidant capacity, and n-3 PUFA-enriching property of laying hens. *Front Vet Sci.* 2022;9:1109869. 10.3389/fvets.2022.1109869

206. Elbaz AM, El-Sheikh SE, Abdel-Maksoud A. Growth performance, nutrient digestibility, antioxidant state, ileal histomorphometry, and cecal ecology of broilers fed on fermented canola meal with and without exogenous enzymes. *Trop Anim Health Prod.* 2023;55(1):46. 10.1007/s11250-023-03476-9

207. Jazi V, Ashayerizadeh A, Toghyani M, Shabani A, Tellez G, Toghyani M. Fermented soybean meal exhibits probiotic properties when included in Japanese quail diet in replacement of soybean meal. *Poult Sci.* 2018;97(6):2113-22. 10.3382/ps/pey071

208. Chen S, Mei H, Xu L, Zhan L, Yang Y, Zhao D, et al. Impact of fermented feed of soybean hulls and rapeseed cake on immunity, antioxidant capacity, and gut microbiota in Chahua chicken. *Poult Sci.* 2024;103(3):103451. 10.1016/j.psj.2024.103451

209. Ibisworld. Price of Feed in the US - Bed Industry Data and Trends. 2025. <https://www.ibisworld.com/us/bed/price-of-feed/745/#:~:text=Price%20of%20Feed%20,to%20IBISWorld%20estimates%2C%20helping>

210. Hamza AA, Abaci Gunyar O. Nutritional value of commercial broiler feed supplemented with olive mill waste fermented with probiotic *Rhizopus oryzae* strains. *J Appl Microbiol.* 2022;133(3):1872-81. 10.1111/jam.15694

211. Sharif MK, Butt MS, Anjum FM, Khan SH. Rice bran: a novel functional ingredient. *Crit Rev Food Sci Nutr.* 2014;54(6):807-16. 10.1080/10408398.2011.608586

212. Buenavista RME, Siliveru K, Zheng Y. Utilization of Distiller's dried grains with solubles: A review. *J Agric Food Res.* 2021;5(100195):100195. 10.1016/j.jafr.2021.100195

213. Lerner AB, Tokach MD, DeRouchey JM, Dritz SS, Goodband RD, Woodworth JC, et al. Effects of corn distillers dried grains with solubles in finishing diets on pig growth performance and carcass yield with two different marketing strategies. *Transl Anim Sci.* 2020;4(2):txaa071. 10.1093/tas/txaa071

214. Shrivastava B, Jain KK, Kalra A, Kuhad RC. Bioprocessing of wheat straw into nutritionally rich and digested cattle feed. *Sci Rep.* 2014;4:6360. 10.1038/srep06360

215. Alemawor F, Oddoye EO, Dzogbefia VP, Oldham JH, Donkoh A. Broiler performance on finisher diets containing different levels of either *Pleurotus ostreatus*-fermented dried cocoa pod husk or dried cocoa pod husk supplemented with enzymes. *Trop Anim Health Prod.* 2010;42(5):933-9. 10.1007/s11250-009-9510-9
216. Jeong JS, Kim IH. Effect of probiotic bacteria-fermented medicinal plants (*Gynura procumbens*, *Rehmannia glutinosa*, *Scutellaria baicalensis*) as performance enhancers in growing pigs. *Anim Sci J.* 2015;86(6):603-9. 10.1111/asj.12331
217. Mao J, Wang Y, Duan T, Yin N, Dong C, Ren X, et al. Effect of fermented dandelion on productive performance, meat quality, immune function, and intestinal microbiota of broiler chickens. *BMC Vet Res.* 2023;19(1):178. 10.1186/s12917-023-03751-9
218. Lee YS, Ku KL, Chu CS, Chen KL. The Optimal Supplementation of Fermented Product Produced by *Bacillus subtilis* Strain LYS1 with High Surfactin Yield for Improving Growth Performance, Intestinal Villi Morphology, and Tibial Bone Strength in Broilers. *Animals (Basel).* 2024;14(14). 10.3390/ani14142079
219. Lee YS, Ku KL, Chen PY, Chen KL. The fermented product of high-yield surfactin strain *Bacillus subtilis* LYS1 improves the growth performance and intestinal villi morphology in broilers. *Poult Sci.* 2023;102(11):102839. 10.1016/j.psj.2023.102839
220. Liu W, Wang W, Li J, Li H, Gao T, Zhu B. Anaerobic fermentation of soybean meal by *Bacillus subtilis* ED-3-7 and its effect on the intestinal microbial community of chicken. *Poult Sci.* 2025;104(1):104564. 10.1016/j.psj.2024.104564
221. Jazi V, Mohebodini H, Ashayerizadeh A, Shabani A, Barekatain R. Fermented soybean meal ameliorates *Salmonella Typhimurium* infection in young broiler chickens. *Poult Sci.* 2019;98(11):5648-60. 10.3382/ps/pez338
222. Soumeh EA, Mohebodini H, Toghyani M, Shabani A, Ashayerizadeh A, Jazi V. Synergistic effects of fermented soybean meal and mannan-oligosaccharide on growth performance, digestive functions, and hepatic gene expression in broiler chickens. *Poult Sci.* 2019;98(12):6797-807. 10.3382/ps/pez409
223. Lee TY, Lee YS, Yeh RH, Chen KH, Chen KL. *Bacillus amyloliquefaciens* CU33 fermented feather meal-soybean meal product

- improves the intestinal morphology to promote the growth performance of broilers. *Poult Sci.* 2022;101(9):102027. 10.1016/j.psj.2022.102027
224. Lu Z, Zeng N, Jiang S, Wang X, Yan H, Gao C. Dietary replacement of soybean meal by fermented feedstuffs for aged laying hens: effects on laying performance, egg quality, nutrient digestibility, intestinal health, follicle development, and biological parameters in a long-term feeding period. *Poult Sci.* 2023;102(3):102478. 10.1016/j.psj.2023.102478
225. Ashayerizadeh A, Dastar B, Shams Shargh M, Sadeghi Mahoonak A, Zerehdaran S. Fermented rapeseed meal is effective in controlling *Salmonella enterica* serovar Typhimurium infection and improving growth performance in broiler chicks. *Vet Microbiol.* 2017;201:93-102. 10.1016/j.vetmic.2017.01.007
226. Zhu F, Zhang B, Li J, Zhu L. Effects of fermented feed on growth performance, immune response, and antioxidant capacity in laying hen chicks and the underlying molecular mechanism involving nuclear factor-kappaB. *Poult Sci.* 2020;99(5):2573-80. 10.1016/j.psj.2019.12.044
227. Marcincak S, Klempova T, Bartkovsky M, Marcincakova D, Zdolec N, Popelka P, et al. Effect of Fungal Solid-State Fermented Product in Broiler Chicken Nutrition on Quality and Safety of Produced Breast Meat. *Biomed Res Int.* 2018;2018:2609548. 10.1155/2018/2609548
228. Chen KL, Kho WL, You SH, Yeh RH, Tang SW, Hsieh CW. Effects of *Bacillus subtilis* var. natto and *Saccharomyces cerevisiae* mixed fermented feed on the enhanced growth performance of broilers. *Poult Sci.* 2009;88(2):309-15. 10.3382/ps.2008-00224
229. Liu J, Wang H, Luo J, Chen T, Xi Q, Sun J, et al. Synergism of fermented feed and ginseng polysaccharide on growth performance, intestinal development, and immunity of Xuefeng black-bone chickens. *BMC Vet Res.* 2024;20(1):13. 10.1186/s12917-023-03859-y
230. Li L, Li WF, Liu SZ, Wang HH. Probiotic fermented feed improved the production, health and nutrient utilisation of yellow-feathered broilers reared in high altitude in Tibet. *Br Poult Sci.* 2020;61(6):746-53. 10.1080/00071668.2020.1801988
231. Yeh RH, Hsieh CW, Chen KL. Screening lactic acid bacteria to manufacture two-stage fermented feed and pelleting to investigate the feeding effect on broilers. *Poult Sci.* 2018;97(1):236-46. 10.3382/ps/pex300
232. Zhu X, Tao L, Liu H, Yang G. Effects of fermented feed on growth performance, immune organ indices, serum biochemical parameters, cecal

- odorous compound production, and the microbiota community in broilers. *Poult Sci.* 2023;102(6):102629. 10.1016/j.psj.2023.102629
233. Xie Y, Liu J, Wang H, Luo J, Chen T, Xi Q, et al. Effects of fermented feeds and ginseng polysaccharides on the intestinal morphology and microbiota composition of Xuefeng black-bone chicken. *PLoS One.* 2020;15(8):e0237357. 10.1371/journal.pone.0237357
234. Zhang AR, Wei M, Yan L, Zhou GL, Li Y, Wang HM, et al. Effects of feeding solid-state fermented wheat bran on growth performance and nutrient digestibility in broiler chickens. *Poult Sci.* 2022;101(1):101402. 10.1016/j.psj.2021.101402
235. Ibrahim D, El-Sayed HI, Mahmoud ER, El-Rahman GIA, Bazeed SM, Abdelwarith AA, et al. Impacts of Solid-State Fermented Barley with Fibrolytic Exogenous Enzymes on Feed Utilization, and Antioxidant Status of Broiler Chickens. *Vet Sci.* 2023;10(10). 10.3390/vetsci10100594
236. Feng Y, Wang L, Khan A, Zhao R, Wei S, Jing X. Fermented wheat bran by xylanase-producing *Bacillus cereus* boosts the intestinal microflora of broiler chickens. *Poult Sci.* 2020;99(1):263-71. 10.3382/ps/pez482
237. Chen YW, Yu YH. Differential effects of *Bacillus subtilis*- and *Bacillus licheniformis*-fermented products on growth performance, intestinal morphology, intestinal antioxidant and barrier function gene expression, cecal microbiota community, and microbial carbohydrate-active enzyme composition in broilers. *Poult Sci.* 2023;102(6):102670. 10.1016/j.psj.2023.102670
238. Chen W, Zhu X, Wang J, Wang Z, Huang Y. Effects of *Bacillus subtilis* var. natto and *Saccharomyces cerevisiae* fermented liquid feed on growth performance, relative organ weight, intestinal microflora, and organ antioxidant status in Landes geese. *Journal of Animal Science.* 2013;91(2):978-85.
239. Peng W, Talpur MZ, Zeng Y, Xie P, Li J, Wang S, et al. Influence of fermented feed additive on gut morphology, immune status, and microbiota in broilers. *BMC Vet Res.* 2022;18(1):218. 10.1186/s12917-022-03322-4
240. Yan J, Zhou B, Xi Y, Huan H, Li M, Yu J, et al. Fermented feed regulates growth performance and the cecal microbiota community in geese. *Poult Sci.* 2019;98(10):4673-84. 10.3382/ps/pez169
241. Li Z, Li C, Lin F, Yan L, Wu H, Zhou H, et al. Duck compound probiotics fermented diet alters the growth performance by shaping the gut

- morphology, microbiota and metabolism. *Poult Sci.* 2024;103(6):103647. 10.1016/j.psj.2024.103647
242. Lv J, Guo L, Chen B, Hao K, Ma H, Liu Y, et al. Effects of different probiotic fermented feeds on production performance and intestinal health of laying hens. *Poult Sci.* 2022;101(2):101570. 10.1016/j.psj.2021.101570
243. Feng Y, Zeng N, Bordbar F, Lu Z, Gao C. Dietary fermented mixed ingredient product enhances growth performance and intestinal stem cell-mediated epithelial regeneration through Wnt/beta-catenin pathway in layer chicks. *Poult Sci.* 2025;104(2):104821. 10.1016/j.psj.2025.104821
244. Chukwukaelo AK, Aladi NO, Okeudo NJ, Obikaonu HO, Ogbuewu IP, Okoli IC. Performance and meat quality characteristics of broilers fed fermented mixture of grated cassava roots and palm kernel cake as replacement for maize. *Trop Anim Health Prod.* 2018;50(3):485-93. 10.1007/s11250-017-1457-7
245. Aladi N, Nwafor E, Odoemelam V, Emenalom O, Okoli I, Okeudo N. Performance, carcass, and organoleptic scores of broiler chickens fed diets containing wet or sun-dried fermented mixture of grated cassava roots and palm kernel cake as replacements for maize. *Tropical Animal Health and Production.* 2021;53:1-7.
246. Liu Y, Liu Y, Cao Y, Wang C. Pretreatment of Palm Kernel Cake by Enzyme-Bacteria and Its Effects on Growth Performance in Broilers. *Animals (Basel).* 2025;15(2). 10.3390/ani15020116
247. Xie PJ, Huang LX, Zhang CH, Zhang YL. Nutrient assessment of olive leaf residues processed by solid-state fermentation as an innovative feedstuff additive. *J Appl Microbiol.* 2016;121(1):28-40. 10.1111/jam.13131
248. Cheng YH, Zhang N, Han JC, Chang CW, Hsiao FS, Yu YH. Optimization of surfactin production from *Bacillus subtilis* in fermentation and its effects on *Clostridium perfringens*-induced necrotic enteritis and growth performance in broilers. *J Anim Physiol Anim Nutr (Berl).* 2018;102(5):1232-44. 10.1111/jpn.12937
249. Sun Z, Wang T, Aschalew ND, Zhao W, Chen X, Zhang XF, et al. Effects of yeast cultures with different fermentation times on the growth performance, caecal microbial community and metabolite profile of broilers. *J Anim Physiol Anim Nutr (Berl).* 2020;104(1):212-23. 10.1111/jpn.13241
250. Sharif M, Shoaib M, Rahman MAU, Ahmad F, Rehman SU. Effect of distillery yeast sludge on growth performance, nutrient digestibility and

- slaughter parameters in Japanese quails. *Sci Rep.* 2018;8(1):8418. 10.1038/s41598-018-26741-6
251. Engberg RM, Hammershoj M, Johansen NF, Abousekken MS, Steinfeldt S, Jensen BB. Fermented feed for laying hens: effects on egg production, egg quality, plumage condition and composition and activity of the intestinal microflora. *Br Poult Sci.* 2009;50(2):228-39. 10.1080/00071660902736722
252. Goodarzi Boroojeni F, Senz M, Kozłowski K, Boros D, Wisniewska M, Rose D, et al. The effects of fermentation and enzymatic treatment of pea on nutrient digestibility and growth performance of broilers. *Animal.* 2017;11(10):1698-707. 10.1017/S1751731117000787
253. Li H, Kang Y, Sun Y, Bian C, Fan M, Zhang H, et al. The role of *Lactobacterium plantarum* in solid-state fermentation of *Astragalus membranaceus* for broiler chicken feed. *AMB Express.* 2025;15(1):26. 10.1186/s13568-025-01823-7
254. Dong W, Fan Z, Li P, Liu J, Sun G, Peng N, et al. Optimizing the scale-up production of fermented astragalus and its benefits to the performance and egg quality of laying hens. *Front Microbiol.* 2023;14:1165644. 10.3389/fmicb.2023.1165644
255. Koh JH, Suh HJ. Biological activities of thermo-tolerant microbes from fermented rice bran as an alternative microbial feed additive. *Appl Biochem Biotechnol.* 2009;157(3):420-30. 10.1007/s12010-008-8311-3
256. Lokaewmanee K, Yamauchi K, Thongwittaya N. Effects of fermented plant product on growth performance, some blood variables, carcass characteristics, and intestinal histology in broilers. *Br Poult Sci.* 2012;53(2):215-23. 10.1080/00071668.2012.665435
257. Ahmed ST, Mun HS, Islam MM, Yang CJ. Effects of fermented corni fructus and fermented kelp on growth performance, meat quality, and emission of ammonia and hydrogen sulphide from broiler chicken droppings. *Br Poult Sci.* 2014;55(6):745-51. 10.1080/00071668.2014.960804
258. Shi H, Kim SH, Kim IH. Effect of dietary inclusion of fermented sea mustard by-product on growth performance, blood profiles, and meat quality in broilers. *J Sci Food Agric.* 2019;99(9):4304-8. 10.1002/jsfa.9663
259. Hossain ME, Ko SY, Kim GM, Firman JD, Yang CJ. Evaluation of probiotic strains for development of fermented *Alisma canaliculatum* and their effects on broiler chickens. *Poult Sci.* 2012;91(12):3121-31. 10.3382/ps.2012-02333

260. Huang P, Wang P, Xu J, Sun M, Liu X, Lin Q, et al. Fermented traditional Chinese medicine alters the intestinal microbiota composition of broiler chickens. *Res Vet Sci.* 2021;135:8-14. 10.1016/j.rvsc.2020.12.021
261. Sugiharto S, Yudiarti T, Isroli I, Widiastuti E, Wahyuni HI, Sartono TA. Growth performance, haematological responses, intestinal microbiology and carcass traits of broiler chickens fed finisher diets containing two-stage fermented banana peel meal. *Trop Anim Health Prod.* 2020;52(3):1425-33. 10.1007/s11250-019-02147-y
262. Zhou X, Zhang H, Li S, Jiang Y, Deng J, Yang C, et al. Effects of different levels of *Citri Sarcodactylis Fructus* by-products fermented feed on growth performance, serum biochemical, and intestinal health of cyan-shank partridge birds. *Sci Rep.* 2023;13(1):20130. 10.1038/s41598-023-47303-5
263. Ito T, Miyamoto H, Kumagai Y, Udagawa M, Shinmyo T, Mori K, et al. Thermophile-fermented compost extract as a possible feed additive to enhance fecundity in the laying hen and pig: Modulation of gut metabolism. *J Biosci Bioeng.* 2016;121(6):659-64. 10.1016/j.jbiosc.2015.10.014
264. Chen X, Zhou X, Li S, Zhang H, Liu Z. Effects of tea residues-fermented feed on production performance, egg quality, antioxidant capacity, caecal microbiota, and ammonia emissions of laying hens. *Front Vet Sci.* 2023;10:1195074. 10.3389/fvets.2023.1195074
265. Chen YC, Yu YH. *Bacillus licheniformis*-fermented products improve growth performance and the fecal microbiota community in broilers. *Poult Sci.* 2020;99(3):1432-43. 10.1016/j.psj.2019.10.061
266. Chen YC, Yu YH. *Bacillus licheniformis*-fermented products and enramycin differentially modulate microbiota and antibiotic resistome in the cecal digesta of broilers. *Poult Sci.* 2022;101(9):102010. 10.1016/j.psj.2022.102010
267. Tian Y, Zhang R, Li G, Zeng T, Chen L, Xu W, et al. Microbial fermented feed affects flavor amino acids and yolk trimethylamine of duck eggs via cecal microbiota-yolk metabolites crosstalk. *Food Chem.* 2024;430:137008. 10.1016/j.foodchem.2023.137008
268. Liu X, Cao G, Zhou J, Yao X, Fang B. The effects of *Bacillus coagulans*-fermented and non-fermented *Ginkgo biloba* on abdominal fat deposition and meat quality of Peking duck. *Poult Sci.* 2017;96(7):2264-73. 10.3382/ps/pex017
269. Yang J, Wang Y, Zheng L, Peng M, Mai Y, Wang X. Comparative Analysis of the Effect of Dietary Supplementation with Fermented and Water-

Extracted Leaf Extracts of *Eucommia ulmoides* on Egg Production and Egg Nutrition. *Foods*. 2024;13(10). 10.3390/foods13101521

270. Niu KM, Wang YF, Liang X, Zhai Z, Liu J, Wang R, et al. Impact of fermented *Broussonetia papyrifera* on laying performance, egg quality, lipid metabolism, and follicular development of laying hens. *Poult Sci*. 2023;102(5):102569. 10.1016/j.psj.2023.102569

271. Xu L, He J, Duan M, Chang Y, Gu T, Tian Y, et al. Effects of lactic acid bacteria-derived fermented feed on the taste and quality of duck meat. *Food Res Int*. 2023;174(Pt 2):113679. 10.1016/j.foodres.2023.113679

272. Liu Z, Lei X, Li J, Zhong Y, Tan D, Zhang Q, et al. Effects of fermented *Andrographis paniculata* on growth performance, carcass traits, immune function, and intestinal health in Muscovy ducks. *Poult Sci*. 2023;102(3):102461. 10.1016/j.psj.2022.102461

273. Wang TY, Wu YH, Jiang CY, Liu Y. Solid state fermented potato pulp can be used as poultry feed. *Br Poult Sci*. 2010;51(2):229-34. 10.1080/00071661003781864

274. Dei HK, Rose SP, Mackenzie AM, Amarowicz R. Growth performance of broiler chickens fed diets containing shea nut (*Vitellaria paradoxa*, Gaertn.) meal fermented with *Aspergillus niger*. *Poult Sci*. 2008;87(9):1773-8. 10.3382/ps.2008-00055

275. Gungor E, Erener G. Effect of dietary raw and fermented sour cherry kernel (*Prunus cerasus* L.) on growth performance, carcass traits, and meat quality in broiler chickens. *Poult Sci*. 2020;99(1):301-9. 10.3382/ps/pez490

276. Nesseim TDT, Benteboula M, Dieng A, Mergeai G, Marechal F, Hornick JL. Effects of partial dietary substitution of groundnut meal by defatted, *Aspergillus niger*-fermented and heated *Jatropha curcas* kernel meal on feed intake and growth performance of broiler chicks. *Trop Anim Health Prod*. 2019;51(6):1383-91. 10.1007/s11250-019-01830-4

277. Wu QJ, Wang ZB, Wang GY, Li YX, Qi YX. Effects of feed supplemented with fermented pine needles (*Pinus ponderosa*) on growth performance and antioxidant status in broilers. *Poult Sci*. 2015;94(6):1138-44. 10.3382/ps/pev013

278. Wang Q, Wang L, Li L, Sun M, Li P, Yu Y, et al. Effects of dietary supplementation of fermented *Artemisia argyi* on growth performance, slaughter performance, and meat quality in broilers. *Poult Sci*. 2024;103(4):103545. 10.1016/j.psj.2024.103545

279. Al-Gheffari HK, Reda FM, Alagawany M, Saleh O, Alhazmi N, Salem HM, et al. The influence of dietary supplementation with fermented agro-industrial residue of faba bean on Japanese quail performance, immunity, gut microbiota, blood chemistry, and antioxidant status. *Poult Sci.* 2024;103(9):103880. 10.1016/j.psj.2024.103880
280. Zhai SS, Zhou T, Li MM, Zhu YW, Li MC, Feng PS, et al. Fermentation of flaxseed cake increases its nutritional value and utilization in ducklings. *Poult Sci.* 2019;98(11):5636-47. 10.3382/ps/pez326
281. Lambertz C, Leopold J, Ammer S, Leiber F, Thesing B, Wild C, et al. Demand-oriented riboflavin supply of organic broiler using a feed material from fermentation of *Ashbya gossypii*. *Animal.* 2021;15(1):100003. 10.1016/j.animal.2020.100003
282. Latue PE, Ariyadi B, Kurniawati A, Al Anas M. Positive effect of fermented sorghum on productivity, jejunal histomorphology, and tight junction gene expression in broiler chickens. *Poult Sci.* 2025;104(1):104548. 10.1016/j.psj.2024.104548
283. Czech A, Grela ER, Kiesz M. Dietary fermented rapeseed or/and soybean meal additives on performance and intestinal health of piglets. *Sci Rep.* 2021;11(1):16952. 10.1038/s41598-021-96117-w
284. Upadhaya SD, Kim IH. Ileal digestibility of nutrients and amino acids in unfermented, fermented soybean meal and canola meal for weaning pigs. *Anim Sci J.* 2015;86(4):408-14. 10.1111/asj.12305
285. Xie Z, Hu L, Li Y, Geng S, Cheng S, Fu X, et al. Changes of gut microbiota structure and morphology in weaned piglets treated with fresh fermented soybean meal. *World J Microbiol Biotechnol.* 2017;33(12):213. 10.1007/s11274-017-2374-7
286. Cheng SS, Li Y, Geng SJ, Hu LS, Fu XF, Han XY. Effects of dietary fresh fermented soybean meal on growth performance, ammonia and particulate matter emissions, and nitrogen excretion in nursery piglets. *J Zhejiang Univ Sci B.* 2017;18(12):1083-92. 10.1631/jzus.B1700180
287. Rodriguez DA, Lee SA, Stein HH. Digestibility of amino acids, but not fiber, fat, or energy, is greater in cold-fermented, low-oil distillers dried grains with solubles (DDGS) compared with conventional DDGS fed to growing pigs. *J Anim Sci.* 2020;98(10). 10.1093/jas/skaa297
288. Dei HK. Assessment of Maize (*Zea mays*) as Feed Resource for Poultry. *Poultry Science: InTech*; 2017.

289. Jeong JS, Kim IH. Comparative efficacy of up to 50% partial fish meal replacement with fermented soybean meal or enzymatically prepared soybean meal on growth performance, nutrient digestibility and fecal microflora in weaned pigs. *Anim Sci J*. 2015;86(6):624-33. 10.1111/asj.12335
290. Goehring DL, Wu F, DeRouchey JM, Goodband RD, Tokach MD, Woodworth JC, et al. The effects of soybean hulls level, distillers dried grains with solubles, and net energy formulation on nursery pig performance. *Transl Anim Sci*. 2019;3(4):1335-48. 10.1093/tas/txz126
291. Barrera-Arellano D, Badan-Ribeiro AP, Serna-Saldivar SO. Corn oil: Composition, processing, and utilization. *Corn*: Elsevier; 2019. p. 593-613.
292. Czech A, Nowakowicz-Debek B, Lukaszewicz M, Florek M, Ossowski M, Wlazlo L. Effect of fermented rapeseed meal in the mixture for growing pigs on the gastrointestinal tract, antioxidant status, and immune response. *Sci Rep*. 2022;12(1):15764. 10.1038/s41598-022-20227-2
293. Yang R, Khalid A, Khalid F, Ye M, Li Y, Zhan K, et al. Effect of fermented corn by-products on production performance, blood biochemistry, and egg quality indices of laying hens. *J Anim Sci*. 2022;100(5). 10.1093/jas/skac130
294. Shuai C, Chen D, Yu B, Luo Y, Zheng P, Huang Z, et al. Effect of fermented rapeseed meal on growth performance, nutrient digestibility, and intestinal health in growing pigs. *Anim Nutr*. 2023;15:420-9. 10.1016/j.aninu.2023.06.011
295. Konkol D, Jonuzi E, Popiela E, Sierzant K, Korzeniowska M, Leicht K, et al. Influence of solid state fermentation with *Bacillus subtilis* 67 strain on the nutritional value of rapeseed meal and its effects on performance and meat quality of broiler chickens. *Poult Sci*. 2023;102(7):102742. 10.1016/j.psj.2023.102742
296. Shi C, Zhang Y, Lu Z, Wang Y. Solid-state fermentation of corn-soybean meal mixed feed with *Bacillus subtilis* and *Enterococcus faecium* for degrading antinutritional factors and enhancing nutritional value. *J Anim Sci Biotechnol*. 2017;8:50. 10.1186/s40104-017-0184-2
297. Schwarz T, Przybylo M, Zapletal P, Turek A, Pabianczyk M, Bartlewski PM. Effects of Using Corn Dried Distillers' Grains with Solubles (cDDGS) as a Partial Replacement for Soybean Meal on the Outcomes of Pig Fattening, Pork Slaughter Value and Quality. *Animals (Basel)*. 2021;11(10). 10.3390/ani11102956

298. Azad MAK, Jiang H, Ni H, Liu Y, Huang P, Fang J, et al. Diets Partially Replaced With Cassava Residue Modulate Antioxidant Capacity, Lipid Metabolism, and Gut Barrier Function of Huanjiang Mini-Pigs. *Front Vet Sci.* 2022;9:902328. 10.3389/fvets.2022.902328
299. Pilajun R, Wanapat M. Growth performance and carcass characteristics of feedlot Thai native x Lowline Angus crossbred steer fed with fermented cassava starch residue. *Trop Anim Health Prod.* 2016;48(4):719-26. 10.1007/s11250-016-1011-z
300. Ronca CL, Duque-Soto C, Samaniego-Sanchez C, Morales-Hernandez ME, Olalla-Herrera M, Lozano-Sanchez J, et al. Exploring the Nutritional and Bioactive Potential of Olive Leaf Residues: A Focus on Minerals and Polyphenols in the Context of Spain's Olive Oil Production. *Foods.* 2024;13(7). 10.3390/foods13071036
301. Jeba RH, Hemada HM, Nadir AA, Mansour ME. Improving stability of frying oils and food quality with addition of dried olive mill wastewater. *NPJ Sci Food.* 2025;9(1):75. 10.1038/s41538-025-00430-x
302. Soultatos SK, Chatzaki A, Karas PA, Papadaki AA, Kalantzakis GS, Psarras G, et al. Biocontrol Potential of Raw Olive Mill Waste Against *Verticillium dahliae* in Vegetable Crops. *Plants (Basel).* 2025;14(6). 10.3390/plants14060867
303. Alghamdi SQ, Alotaibi NF, Al-Ghamdi SN, Alqarni LS, Amna T, Moustafa SMN, et al. High Antiparasitic and Antimicrobial Performance of Biosynthesized NiO Nanoparticles via Wasted Olive Leaf Extract. *Int J Nanomedicine.* 2024;19:1469-85. 10.2147/IJN.S443965
304. Palmonari A, Cavallini D, Sniffen CJ, Fernandes L, Holder P, Fagioli L, et al. Short communication: Characterization of molasses chemical composition. *J Dairy Sci.* 2020;103(7):6244-9. 10.3168/jds.2019-17644
305. Jain R, Venkatasubramanian P. Sugarcane Molasses - A Potential Dietary Supplement in the Management of Iron Deficiency Anemia. *J Diet Suppl.* 2017;14(5):589-98. 10.1080/19390211.2016.1269145
306. Zhang S, Wang J, Jiang H. Microbial production of value-added bioproducts and enzymes from molasses, a by-product of sugar industry. *Food Chem.* 2021;346:128860. 10.1016/j.foodchem.2020.128860
307. PRESTON¹ T. Molasses as an energy source for cattle. *World Review of Nutrition and Dietetics.* 1973;17:250.
308. Reveglia P, Blanco M, Cobos MJ, Labuschagne M, Joy M, Rubiales D. Metabolic profiling of pea (*Pisum sativum*) cultivars in changing

- environments: Implications for nutritional quality in animal feed. *Food Chem.* 2025;462:140972. 10.1016/j.foodchem.2024.140972
309. Plaza A, Gasiorowska B, Rzazewska E. Heavy metal content in the green fodder of field pea/oat mixtures destined for cattle feed. *Environ Monit Assess.* 2019;191(11):680. 10.1007/s10661-019-7874-5
310. Han S, Xu G, Zhang K, Ahmad S, Wang L, Chen F, et al. Fermented Astragalus Powder, a New Potential Feed Additive for Broilers to Improve the Growth Performance and Health. *Animals (Basel).* 2024;14(11). 10.3390/ani14111628
311. Song B, Li P, Yan S, Liu Y, Gao M, Lv H, et al. Effects of Dietary Astragalus Polysaccharide Supplementation on the Th17/Treg Balance and the Gut Microbiota of Broiler Chickens Challenged With Necrotic Enteritis. *Front Immunol.* 2022;13:781934. 10.3389/fimmu.2022.781934
312. Tan BL, Norhaizan ME, Chan LC. Rice Bran: From Waste to Nutritious Food Ingredients. *Nutrients.* 2023;15(11). 10.3390/nu15112503
313. Manlapig JJD, Matsui H. Production and Utilization of Fermented Rice Bran as Animal Feed. *Anim Sci J.* 2025;96(1):e70037. 10.1111/asj.70037
314. Yilmaz Tuncel N. Stabilization of Rice Bran: A Review. *Foods.* 2023;12(9). 10.3390/foods12091924
315. Jeong JS, Kim IH. Effect of *Bacillus subtilis* C-3102 spores as a probiotic feed supplement on growth performance, noxious gas emission, and intestinal microflora in broilers. *Poult Sci.* 2014;93(12):3097-103. 10.3382/ps.2014-04086
316. Ying W, Zhu R, Lu W, Gong L. A new strategy to apply *Bacillus subtilis* MA139 for the production of solid-state fermentation feed. *Lett Appl Microbiol.* 2009;49(2):229-34. 10.1111/j.1472-765X.2009.02647.x
317. Giraffa G, Chanishvili N, Widyastuti Y. Importance of lactobacilli in food and feed biotechnology. *Res Microbiol.* 2010;161(6):480-7. 10.1016/j.resmic.2010.03.001
318. Neves N, De Dea Lindner J, Stockhausen L, Delziovo FR, Bender M, Serzedello L, et al. Fermentation of Plant-Based Feeds with *Lactobacillus acidophilus* Improves the Survival and Intestinal Health of Juvenile Nile Tilapia (*Oreochromis niloticus*) Reared in a Biofloc System. *Animals (Basel).* 2024;14(2). 10.3390/ani14020332
319. Zhang Q, Li J, Wang G, Wang L, Zhang Z, Fang Z, et al. The replacement of bacitracin methylene disalicylate with *Bacillus subtilis* PB6 in the diet of male Cherry Valley Ducks reduces the feed conversion ratio by

- improving intestinal health and modulating gut microbiota. *Poult Sci.* 2022;101(11):102155. 10.1016/j.psj.2022.102155
320. Xu Y, Yu Y, Shen Y, Li Q, Lan J, Wu Y, et al. Effects of *Bacillus subtilis* and *Bacillus licheniformis* on growth performance, immunity, short chain fatty acid production, antioxidant capacity, and cecal microflora in broilers. *Poult Sci.* 2021;100(9):101358. 10.1016/j.psj.2021.101358
321. Ragoubi C, Quintieri L, Greco D, Mehrez A, Maatouk I, D'Ascanio V, et al. Mycotoxin Removal by *Lactobacillus* spp. and Their Application in Animal Liquid Feed. *Toxins (Basel).* 2021;13(3). 10.3390/toxins13030185
322. Khonkhaeng B, Cherdthong A. *Pleurotus Ostreatus* and *Volvariella Volvacea* Can Enhance the Quality of Purple Field Corn Stover and Modulate Ruminal Fermentation and Feed Utilization in Tropical Beef Cattle. *Animals (Basel).* 2019;9(12). 10.3390/ani9121084
323. Assi JA, King AJ. Manganese amendment and *Pleurotus ostreatus* treatment to convert tomato pomace for inclusion in poultry feed. *Poult Sci.* 2008;87(9):1889-96. 10.3382/ps.2007-00376
324. Wang J, Cao F, Su E, Zhao L, Qin W. Improvement of Animal Feed Additives of Ginkgo Leaves through Solid-state Fermentation using *Aspergillus niger*. *International Journal of Biological Sciences.* 2018;14(7):736-47. 10.7150/ijbs.24523
325. Ventura M, Holland ME, Smith MB, Chaparro JM, Prenni J, Patz JA, et al. Suitability of maize crop residue fermented by *Pleurotus ostreatus* as feed for edible crickets: growth performance, micronutrient content, and iron bioavailability. *Front Nutr.* 2023;10:1157811. 10.3389/fnut.2023.1157811
326. Ostbring K, Lager I, Chagas JCC, Ramin M, Ahlstrom C, Hultberg M. Use of oyster mushrooms (*Pleurotus ostreatus*) for increased circularity and valorization of rapeseed residues. *J Environ Manage.* 2023;344:118742. 10.1016/j.jenvman.2023.118742
327. Kamani M, Karimi Torshizi MA, Shariatmadari F. Supplementation with *Aspergillus* fungi strain cultures on wheat bran on low-protein diets on performance, egg quality and blood characteristics of laying hens. *Br Poult Sci.* 2025:1-10. 10.1080/00071668.2025.2479500
328. Maulana H, Widyastuti Y, Herlina N, Hasbuna A, Al-Islahi ASH, Triratna L, et al. Bioinformatics study of phytase from *Aspergillus niger* for use as feed additive in livestock feed. *J Genet Eng Biotechnol.* 2023;21(1):142. 10.1186/s43141-023-00600-y






329. Cui Y, Li J, Deng D, Lu H, Tian Z, Liu Z, et al. Solid-state fermentation by *Aspergillus niger* and *Trichoderma koningii* improves the quality of tea dregs for use as feed additives. *PLoS One*. 2021;16(11):e0260045. 10.1371/journal.pone.0260045
330. Meng J, Chroumpi T, Makela MR, de Vries RP. Xylitol production from plant biomass by *Aspergillus niger* through metabolic engineering. *Bioresour Technol*. 2022;344(Pt A):126199. 10.1016/j.biortech.2021.126199
331. Aguiar TQ, Silva R, Domingues L. New biotechnological applications for *Ashbya gossypii*: Challenges and perspectives. *Bioengineered*. 2017;8(4):309-15. 10.1080/21655979.2016.1234543
332. Aguiar TQ, Silva R, Domingues L. *Ashbya gossypii* beyond industrial riboflavin production: A historical perspective and emerging biotechnological applications. *Biotechnol Adv*. 2015;33(8):1774-86. 10.1016/j.biotechadv.2015.10.001
333. Ruiz Sella SRB, Bueno T, de Oliveira AAB, Karp SG, Soccol CR. *Bacillus subtilis natto* as a potential probiotic in animal nutrition. *Crit Rev Biotechnol*. 2021;41(3):355-69. 10.1080/07388551.2020.1858019
334. Nasir JA, Chand N, Naz S, Alhidary IA, Khan RU, Batool S, et al. Dietary Oyster Mushroom (*Pleurotus ostreatus*) Waste Inhibits Experimentally Induced *Eimeria tenella* Challenge in Japanese Quails Model. *Animals (Basel)*. 2023;13(21). 10.3390/ani13213421
335. Nguyen AT, Nguyen DV, Tran MT, Nguyen LT, Nguyen AH, Phan TN. Isolation and characterization of *Bacillus subtilis* CH16 strain from chicken gastrointestinal tracts for use as a feed supplement to promote weight gain in broilers. *Lett Appl Microbiol*. 2015;60(6):580-8. 10.1111/lam.12411
336. Ren H, Zentek J, Vahjen W. Optimization of Production Parameters for Probiotic *Lactobacillus* Strains as Feed Additive. *Molecules*. 2019;24(18). 10.3390/molecules24183286
337. Palupi R, Lubis FNL, Pratama ANT. Effects of *Lactobacillus*-Fermented Feed on Production Performance and Carcass Quality of Broiler Chickens. *Journal of World's Poultry Research*. 2023. 10.36380/jwpr.2023.14
338. Higginbotham G, Bath D. Evaluation of *Lactobacillus* fermentation cultures in calf feeding systems. *Journal of Dairy Science*. 1993;76(2):615-20.
339. Heres L, Engel B, van Knapen F, de Jong MC, Wagenaar JA, Urlings HA. Fermented liquid feed reduces susceptibility of broilers for *Salmonella enteritidis*. *Poult Sci*. 2003;82(4):603-11. 10.1093/ps/82.4.603

340. Nobre C, Gonzalez A, Losoya C, Teixeira JA, Belmares R, Abrunhosa L. Detoxification of ochratoxin A and zearalenone by *Pleurotus ostreatus* during in vitro gastrointestinal digestion. *Food Chem.* 2022;384:132525. 10.1016/j.foodchem.2022.132525
341. Lu F, Li C, Wang Z, Zhao W, Chu J, Zhuang Y, et al. High efficiency cell-recycle continuous sodium gluconate production by *Aspergillus niger* using on-line physiological parameters association analysis to regulate feed rate rationally. *Bioresour Technol.* 2016;220:433-41. 10.1016/j.biortech.2016.08.062
342. Yang Y, Ji J, Wu S, Ye Y, Sheng L, Zhang Y, et al. Efficient Biodegradation of Patulin by *Aspergillus niger* FS10 and Metabolic Response of Degrading Strain. *Foods.* 2023;12(2). 10.3390/foods12020382
343. Munoz-Fernandez G, Montero-Bullon JF, Martinez JL, Buey RM, Jimenez A. *Ashbya gossypii* as a versatile platform to produce sabinene from agro-industrial wastes. *Fungal Biol Biotechnol.* 2024;11(1):16. 10.1186/s40694-024-00186-1
344. Chen Y, Fan H, Meng F. *Pleurotus ostreatus* decreases cornstalk lignin content, potentially improving its suitability for animal feed. *J Sci Food Agric.* 2017;97(5):1592-8. 10.1002/jsfa.7907
345. Khatib S, Pereman I, Kostanda E, Zdouc MM, Ezov N, Schweitzer R, et al. Olive mill solid waste induces beneficial mushroom-specialized metabolite diversity revealed by computational metabolomics strategies. *Metabolomics.* 2025;21(3):58. 10.1007/s11306-025-02257-9



Article

Development of Novel Biocomposites with Antimicrobial-Activity-Based Magnesium-Doped Hydroxyapatite with Amoxicillin

Carmen Cimpanu ¹, Daniela Predoi ^{2,*}, Carmen Steluta Ciobanu ^{2,*}, Simona Liliana Iconaru ², Krzysztof Rokosz ³, Mihai Valentin Predoi ⁴, Steinar Raaen ⁵ and Monica Luminita Badea ⁶

- ¹ Faculty of Land Reclamation and Environmental Engineering, University of Agronomic Sciences and Veterinary Medicine of Bucharest, 59 Marasti Blvd., 011464 Bucharest, Romania; carmencimpanu@yahoo.com
- ² National Institute of Materials Physics, Atomistilor Street, No. 405A, 077125 Magurele, Romania; simonaiconaru@gmail.com
- ³ Faculty of Electronics and Computer Science, Koszalin University of Technology, Śniadeckich 2, PL 75-453 Koszalin, Poland; rokosz@tu.koszalin.pl
- ⁴ Department of Mechanics, University Politehnica of Bucharest, BN 002, 313 Splaiul Independentei, Sector 6, 060042 Bucharest, Romania; predoi@gmail.com
- ⁵ Department of Physics, Norwegian University of Science and Technology (NTNU), Realfagbygget E3-124 Høgskoleringen 5, NO 7491 Trondheim, Norway; steinar.raaen@ntnu.no
- ⁶ Faculty of Horticulture, University of Agronomic Sciences and Veterinary Medicine, 59 Marasti Blvd., 011464 Bucharest, Romania; badea.artemisla@gmail.com
- * Correspondence: dpredoi@gmail.com (D.P.); ciobanucs@gmail.com (C.S.C.)

Abstract: Background/Objectives: A biocomposite based on magnesium-doped hydroxyapatite and enriched with amoxicillin (MgHApOx) was synthesized using the coprecipitation method and is presented here for the first time. **Methods:** The stability of MgHAp and MgHApOx suspensions was evaluated by ultrasound measurements. The structure of the synthesized MgHAp and MgHApOx was examined with X-ray diffraction (XRD), Fourier transform infrared (FT-IR) spectroscopy and X-ray photoelectron spectroscopy (XPS). The crystalline structure was determined by X-ray diffraction. The FTIR data were collected in the range of 4000–400 cm^{−1}. The morphology of the nanoparticles was evaluated by scanning electron microscopy (SEM). Furthermore, the biocompatible properties of MgHAp, MgHApOx and amoxicillin (Ox) suspensions were assessed using human fetal osteoblastic cells (hFOB 1.19 cell line). The antimicrobial properties of the MgHAp, MgHApOx and Ox suspension nanoparticles were assessed using the standard reference microbial strains *Staphylococcus aureus* ATCC 25923, *Escherichia coli* ATCC 25922 and *Candida albicans* ATCC 10231. **Results:** X-ray studies have shown that the biocomposite retains the characteristics of HAp and amoxicillin. The SEM assessment exhibited that the apatite contains particles at nanometric scale with acicular flakes morphology. The XRD and SEM results exhibited crystalline nanoparticles. The average crystallite size calculated from XRD analysis increased from 15.31 nm for MgHAp to 17.79 nm in the case of the MgHApOx sample. The energy-dispersive X-ray spectroscopy (EDS) and X-ray photoelectron spectroscopy (XPS) analysis highlighted the presence of the constituent elements of MgHAp and amoxicillin. Moreover, XPS confirmed the substitution of Ca²⁺ ions with Mg²⁺ and the presence of amoxicillin constituents in the MgHAp lattice. The results of the in vitro antimicrobial assay demonstrated that MgHAp, MgHApOx and Ox suspensions exhibited good antimicrobial activity against the tested microbial strains. The results showed that the antimicrobial activity of the samples was influenced by the presence of the antibiotic and also by the incubation time. **Conclusions:** The findings from the biological assays indicate that MgHAp and MgHApOx are promising candidates for the development of new biocompatible and antimicrobial agents for biomedical applications.

Keywords: magnesium; hydroxyapatite; amoxicillin; suspensions; antimicrobial activity



Citation: Cimpanu, C.; Predoi, D.; Ciobanu, C.S.; Iconaru, S.L.; Rokosz, K.; Predoi, M.V.; Raaen, S.; Badea, M.L. Development of Novel Biocomposites with Antimicrobial-Activity-Based Magnesium-Doped Hydroxyapatite with Amoxicillin. *Antibiotics* **2024**, *13*, 963. <https://doi.org/10.3390/antibiotics13100963>

Academic Editor: Domenico Schillaci

Received: 13 September 2024

Revised: 7 October 2024

Accepted: 10 October 2024

Published: 12 October 2024



Copyright: © 2024 by the authors. Licensee MDPI, Basel, Switzerland. This article is an open access article distributed under the terms and conditions of the Creative Commons Attribution (CC BY) license (<https://creativecommons.org/licenses/by/4.0/>).

1. Introduction

Recently, significant advancements have been made in the area of biomaterials, leading to the development of new and improved multifunctional materials with excellent biological and reproducible physicochemical properties. Despite the tremendous advancements in designing and safely utilizing materials with specific properties [1–4], there are still significant limitations in the current material design strategies in numerous areas such as biomedical, environmental, engineering and more [5–10]. Over the years, research has been focused on designing novel materials whose primary function is to restore, replace or enhance the function of various organs or tissues [4,8–10]. One of most renowned materials considered for its promising use in the biomedical field is hydroxyapatite (HAp). HAp, having the chemical composition $\text{Ca}_{10}(\text{PO}_4)_6(\text{OH})_2$, is one of the most promising candidates for the development of novel biocomposites. Being the primary inorganic component found in human and animal bones and teeth, HAp is known for its exceptional biological properties, including bioactivity, biocompatibility, osteoconductivity and non-toxicity [11–14]. Over the years, composite materials based on hydroxyapatite have generated great research interest due to their exquisite biological features. According to previously reported studies, the use of various elements as dopants has been shown to enhance both the physicochemical and biological properties of hydroxyapatite nanoparticles, making this material an ideal candidate for the development of novel innovative biocomposites suitable for a large range of biomedical applications [15–18]. Among the ions proposed as dopants for HAp, magnesium (Mg^{2+}) stands out due to its exceptional biological properties. Magnesium is a highly abundant cation in the human body and plays a crucial role in biological processes such as protein synthesis and glycolysis. Also, it is known that it can activate enzyme systems and regulate the crystallization of biological calcium phosphates [18,19]. In their studies, Zhao et al. [20] demonstrated that coating a surface with Mg/HAp had the ability to enhance the osteogenic differentiation of pre-osteoblasts and also helped promote the early bone osseointegration process. More than that, earlier reported studies highlighted that hydroxyapatite composite materials exhibit non-cytotoxic effects when tested on different types of cells such as human colon cancer (HCT-8) and primary osteoblast (hFOB 1.19) cell lines [16]. The incorporation of Mg^{2+} into pulp-capping materials has been suggested as a promising strategy for developing materials that promote dental tissue regeneration by Li et al. [21] based on their findings. Additionally, magnesium in hydroxyapatite-based compounds has been reported to enhance the *in vitro* antimicrobial activity of HAp [22]. On the other hand, antibiotic resistance has emerged as one of the most urgent global health threats, as highlighted by the World Economic Forum. It has been reported that antibiotic-resistant bacteria are responsible for a large number of deaths and excessive healthcare costs annually. In this context, the need for novel antimicrobial agents is one of the principal targets of researcher communities. Amoxicillin is a widely used antibiotic for treating various bacterial infections. It has been reported to be particularly effective against respiratory tract infections, ear infections, sinusitis, and urinary tract infections. It has the ability to inhibit the growth of various bacterial strains, thus helping to alleviate symptoms such as pain, fever, and inflammation. Its broad-spectrum action makes it a valuable choice for both children and adults in combating common infections [23–25]. In this context, the development of a new composite enriched with amoxicillin could represent a valuable candidate as an antimicrobial agent. Thus, the novelty of this paper mainly consists of the development for the first time of magnesium-doped hydroxyapatite composites enriched with amoxicillin (MgHApOx) by an adapted method. Moreover, we report for the first time the results of the novel MgHApOx complex characterization. The development of magnesium-doped hydroxyapatite composites enriched with amoxicillin represents a significant innovation in the field of biomedical materials. These novel materials manage to bring together the enhanced structural properties of magnesium-doped hydroxyapatite with the significant antimicrobial efficacy of amoxicillin. Incorporating magnesium into hydroxyapatite, which is known as a biocompatible and osteoconductive ceramic, can improve its properties and promote better cell adhesion and proliferation,

making it highly suitable for bone tissue engineering applications. Meanwhile, the addition of amoxicillin, a well-known broad-spectrum antibiotic, helps ensure the material's ability to stop the development of potential bacterial infections, which could help reduce the risk of post-operative complications. This dual-functionality approach provides a promising strategy for the future development of advanced bone graft materials that support both rapid osseointegration and localized infection control and will address the current critical challenges in orthopedic and dental procedures.

The aim of this study was to obtain for the first time the magnesium-doped hydroxyapatite composites enriched with amoxicillin (MgHApOx) by the coprecipitation adapted method. In order to give nanohydroxyapatite (HAp) more biological functions and a greater scope of applicability in the biomedical field, this research studied magnesium-doped hydroxyapatite enriched with amoxicillin (MgHApOx) in a suspension for the first time. In this study, the stability, structure, morphology and chemical composition of MgHAp and MgHApOx were investigated by ultrasonic measurements, X-ray diffraction (XRD), scanning electron microscopy (SEM) and energy-dispersive X-ray spectroscopy (EDS), Fourier transform infrared spectroscopy (FTIR) and X-ray photoelectron spectroscopy (XPS). The results showed that the enrichment of MgHAp samples with amoxicillin leads to slight changes in the stability, average crystallite size and morphology.

2. Results and Discussions

Figures 1a and 2a show a superposition of the signals recorded in the case of MgHAp suspensions (1000 signals) and MgHApOx (900 signals), respectively. In both figures, from right to left, they are plotted as water flow, with all these signals covering 5000 (MgHAp) and 4500 (MgHApOx) seconds of process evolution. The rapid initial evolution of the amplitudes in the case of the MgHAp sample is followed by an almost constant amplitudes phase being detailed in Figure 1b. It can be seen that, initially, we have a small decrease in the initial amplitude of the signal, which is followed by a sudden increase to a constant amplitude. In the case of the MgHApOx sample, we observe that the amplitudes of the recorded signals are almost constant during the experiment (Figure 2b). This ultrasonic signal amplitude indicates the global evolution in the time of the suspension, pertaining to its speed of sedimentation and related to stability. The relative amplitude depends on the compressibility coefficient of the diphasic medium compared to that of distilled water. An amplitude slightly higher than one indicates a higher average compressibility coefficient than in pure water.

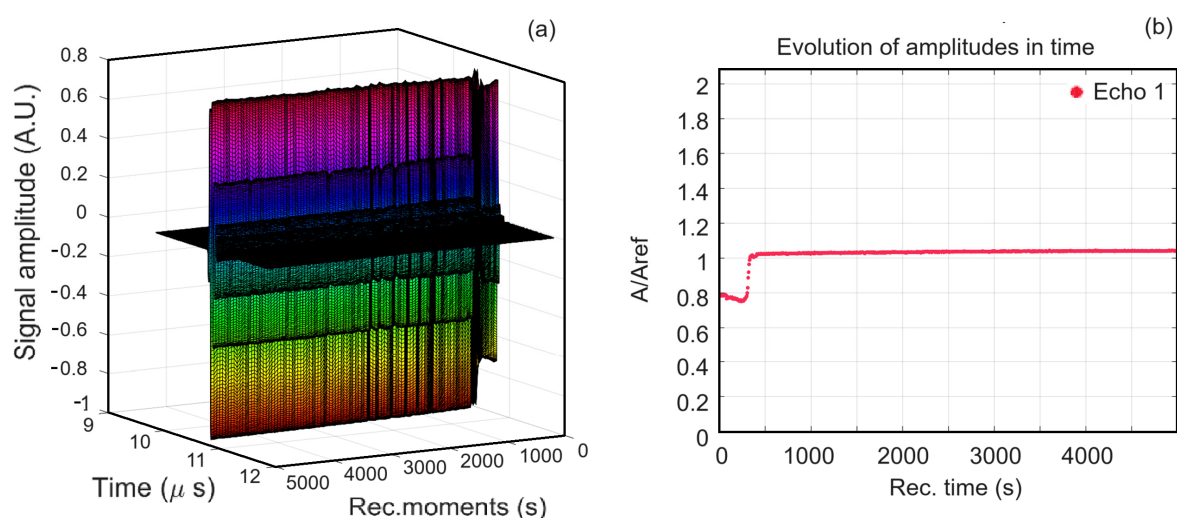


Figure 1. Time evolution of the recorded signals of MgHAp suspension from left to right over 5000 s (a); Recorded signals amplitudes during the experiment for MgHAp suspension (b).

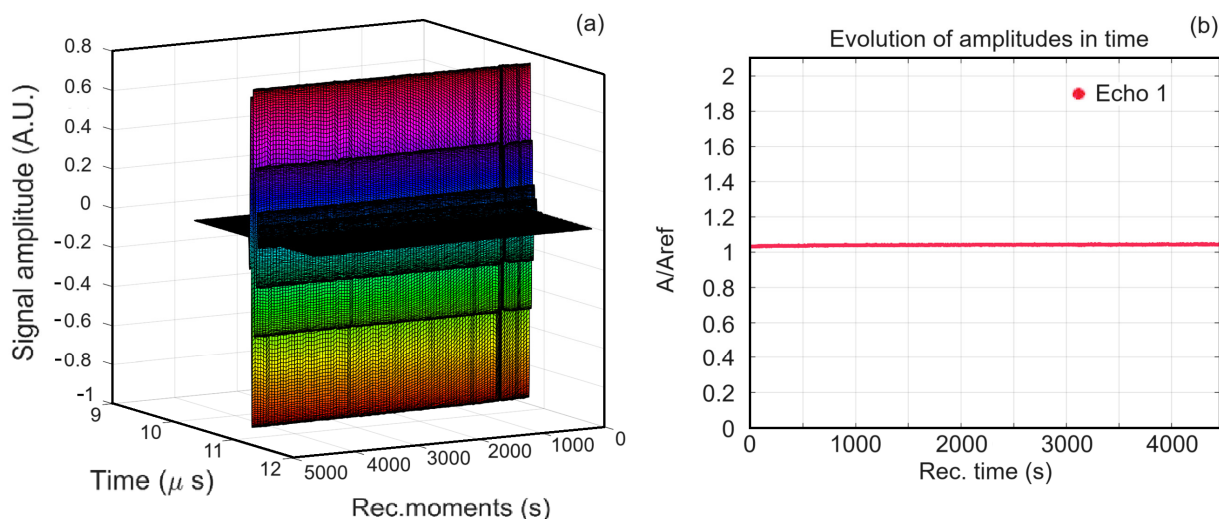


Figure 2. Time evolution of the recorded signals of MgHApOx suspension from left to right over 4500 s (a); Recorded signals amplitudes during the experiment for MgHApOx suspension (b).

The temporal change of properties manifests in the variation of the frequency spectra of all recorded MgHAp and MgHApOx sample signals. These spectra are shown in Figures 3a and 4a. For comparison, the spectrum of the reference liquid (double-distilled water, dotted blue line) was also plotted. The temporal evolution of signal frequency spectra of the MgHAp sample (Figure 3a), which is related to the properties of the suspension in front of the transducers, is represented by two zones of concentration of the 1000 spectral curves. The lower set of spectra corresponds to the initial phase of decreasing amplitudes and shows important differences compared to the spectra of the reference liquid: lower amplitudes in general, only in the 18–20 MHz range, the spectra coincide with that of the reference liquid. The peak for these spectra is at lower frequencies (~22 MHz). Then, during the rapid evolution phase, a few spectra represent the evolution towards the stable state, in which many spectrums get closer to the spectrum of the reference liquid, which has a peak at 26.2 MHz. However, the remaining particles in suspension lead to higher amplitudes compared to the reference liquid, visible in the lower frequencies domain (15–25 MHz). The existence of these two patterns indicates a major modification of the suspension structure, due to the important sedimentation process, from the spectra of larger particles sedimentation to the spectra of the stable suspension of smaller particles.

On the other hand, the signal frequency spectra of the MgHApOx sample (Figure 4a) remain very close together during the experiment. The peak for these spectra is at lower frequencies (~26 MHz) compared to the spectrum of the reference liquid, which has a peak at 26.2 MHz. For frequencies below the peak, the amplitudes of the suspension remain stable above the values for the reference liquid, whereas those corresponding to higher frequencies are practically superposed on the spectrum of the reference liquid. This remark indicates the presence of highly diluted particles with a relatively larger dimension but very stable properties during the experiment, lacking any detectable sedimentation process.

The ultrasonic signals are attenuated by the suspension. The time-averaged attenuation plot is shown in Figures 3b and 4b. Compared to the standard attenuation in the reference liquid (red dotted line), the attenuation is larger for the MgHAp sample (Figure 3b) in the higher frequency ranges, reaching 38 nepper/m at 35 MHz. In the frequency range of 15–25 MHz, the attenuation is lower than the attenuation in the reference liquid. Moreover, compared against the standard attenuation in the reference liquid (red dotted line), the attenuation is larger for the MgHApOx sample (Figure 4b) in the higher frequency ranges, reaching 31 nepper/m at 35 MHz. In the frequency range of 15–30 MHz, the attenuation is lower than the attenuation in the reference liquid.

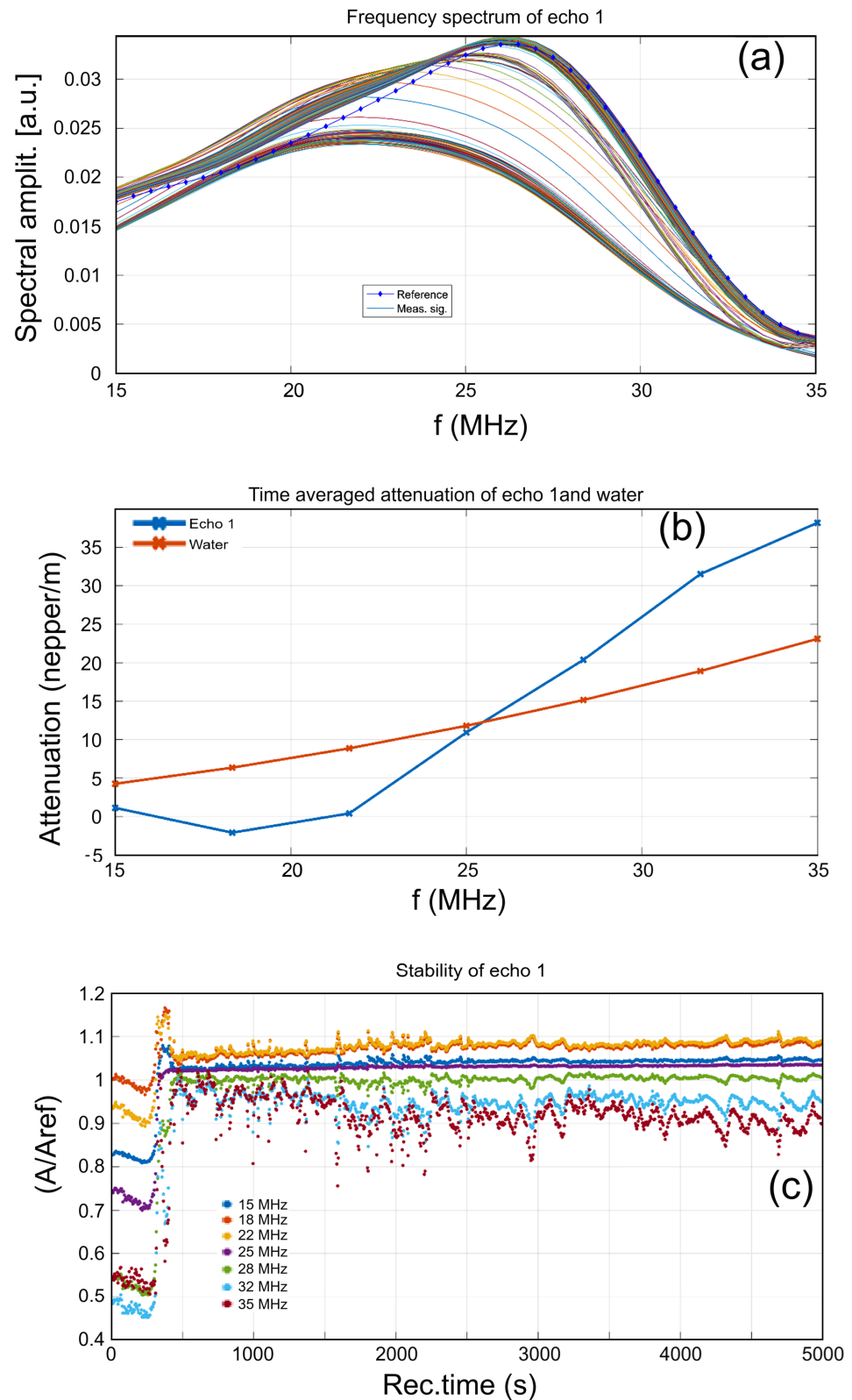


Figure 3. Spectral amplitudes of all recorded signals (a), time-averaged attenuation for the investigated frequency range (b) and relative spectral amplitudes vs. time (c) of MgHAp sample.

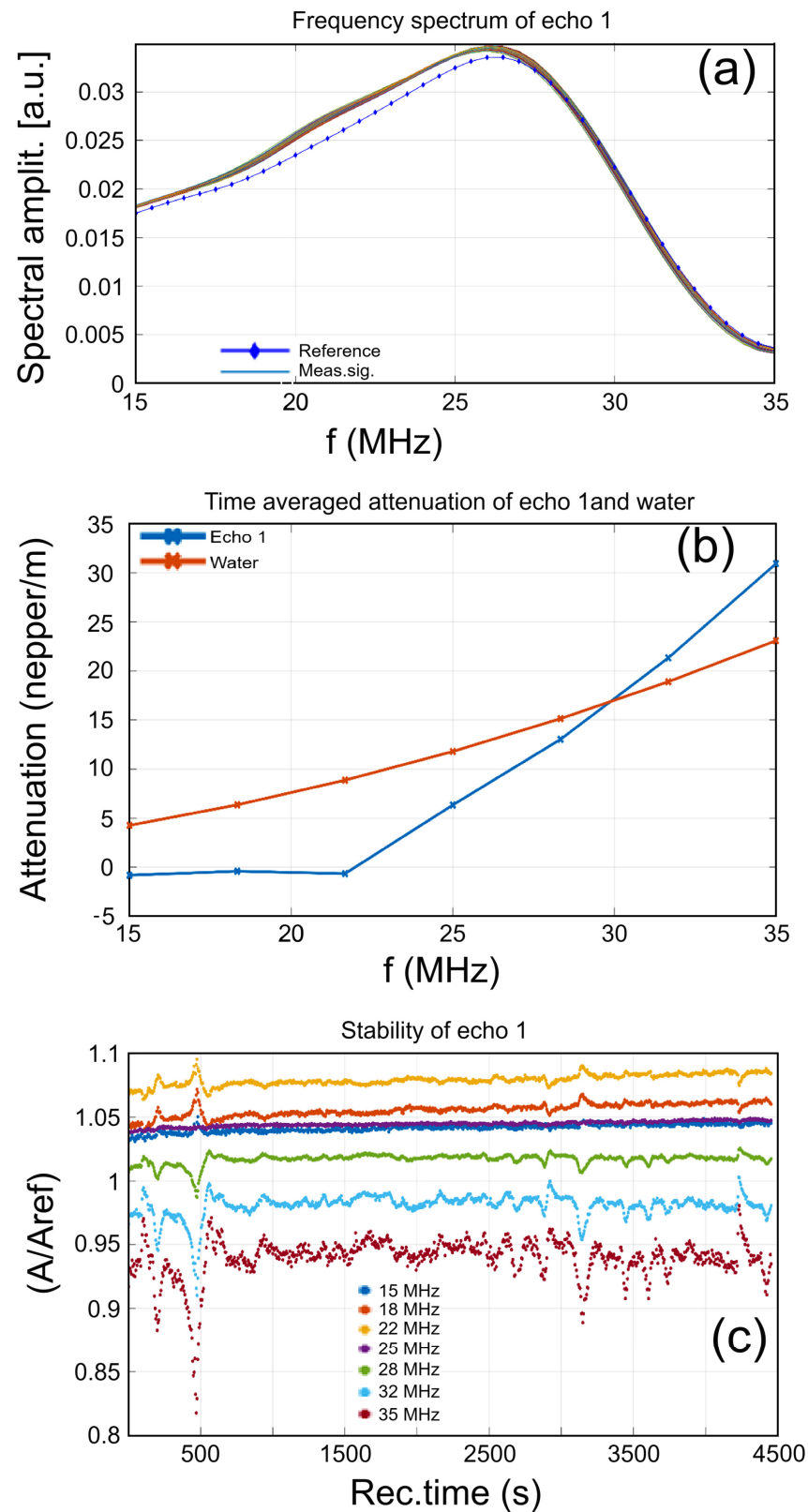


Figure 4. Spectral amplitudes of all recorded signals (a), time-averaged attenuation for the investigated frequency range (b) and relative spectral amplitudes vs. time (c) of MgHApOx sample.

Another MgHAp and MgHApOx suspension characteristic is spectral stability, representing the amplitude of the frequency component of each spectrum, as a function of time

(Figures 3c and 4c). Some remarkable features can be associated with these MgHAp and MgHApOx samples.

In Figure 3c (MgHAp sample), during the first 250 s, all spectral amplitudes decrease slowly, a fact that can be attributed to the settlement of the particles in suspension. Then, at 250 s, the amplitudes rise sharply due to the passage of the sedimentation-free surface in front of the transducers. The suspension remains unstable during the entire experiment. Only the frequency component of 25 MHz shows a stable and slowly increasing amplitude. For all the other frequencies in the spectrums, there are rapid random variations. This indicates that the particles in suspension tend to aggregate and pass in front of the transducers during the entire experiment. In Figure 4c (MgHApOx sample), we can observe that during the first 500 s, the spectral amplitudes of the higher frequencies (28–35 MHz) have two small dips, a fact that can be attributed to the nonuniform settlement of the particles in suspension. Then, these amplitudes continue to exhibit oscillations all along the experiment, being explained by the formation of clusters of the smallest particles in suspension, which are sensitive to higher-frequency components in the ultrasonic signal. On the contrary, the central frequency (25 MHz) of the spectrum keeps a very uniform value of the relative amplitude (1.04) throughout the experiment.

On the contrary, for the lower frequencies (15–22 MHz) of the spectrum, the amplitudes increase with increasing frequency, but they all have peaks before $t = 500$ s, followed by small oscillations throughout the experiment. This relative balance of spectral amplitudes, with some ratios above 1 and others below, explains the overall stable behavior of the suspension. The MgHAp sample becomes relatively stable after the rapid evolution lasting 500 s, as proved by the stability $s = 0.00032 \text{ s}^{-1}$. A is the signal amplitude, with a bar above indicating averaging. The short-lasting variations of amplitudes are averaged, and this fact explains the obtained good stability parameter. The MgHApOx sample is extremely stable overall, as proved by the stability parameter $s = 6.85 \times 10^{-6} \text{ s}^{-1}$. A stability parameter of zero indicates a perfectly stable liquid medium, with no time evolution of the signal amplitude, whereas $S = 0.001$ corresponds to a rather unstable dispersion, with a variation of 0.1% of the averaged signal amplitude in 1 s.

Stability information for the MgHAp and MgHApOx suspensions was obtained through ultrasound measurement (US) and zeta potential (ZP) studies. Ultrasonic measurements on the concentrated suspensions indicated relative stability ($s = 0.00032 \text{ s}^{-1}$) for the MgHAp sample, while the MgHApOx suspension was extremely stable ($s = 6.85 \times 10^{-6} \text{ s}^{-1}$). In order to estimate the zeta potential, the MgHAp and MgHApOx concentrated suspensions were diluted 20 times. The zeta potential measured for the suspension of MgHAp was -14.8 mV , while the potential measured for MgHApOx suspension was -42.6 mV . The low ζ -potential value for the MgHAp sample indicates that the suspension is unstable. In accordance with precedent studies [26–29], colloids with low ζ -potential are prone to flocculation, suggesting early signs of instability. The zeta potential, which indicates the total charge on the nanoparticle surface, is considered optimal for achieving physical colloidal stability when it is around $\pm 30 \text{ mV}$ [30–32]. The results obtained regarding the behavior of the studied samples are in agreement with previous research [26–29,33,34]. Previous studies showed that the zeta potential for suspensions of magnesium-doped hydroxyapatite nanoparticles in dextran matrix was -32.3 mV [33], while for the suspension of magnesium-doped hydroxyapatite ($x_{\text{Mg}} = 0.1$) nanoparticles, the zeta potential was $-17.77 \pm 3.4 \text{ mV}$ [34]. The difference between the zeta potential obtained for the 10MgHAp [34] and 5MgHAp suspensions (which are the object of the present study) could be due to the magnesium concentration. The stability of MgHAp suspensions increases with the concentration of magnesium. In line with previous studies by Suganthi et al. [35], which indicated that a suspension is stable if the absolute zeta potential exceeds 30 mV , it can be concluded that the MgHApOx suspension exhibits very good stability.

The XRD patterns of the MgHAp, MgHApOx and Ox samples are shown in Figure 5. The XRD patterns of the MgHAp sample (Figure 5b) showed reflections due to the planes that correspond to the hydroxyapatite with a hexagonal lattice with a P63/m space group

(JCPDF # 09-0432). On the other hand, the XRD patterns of the MgHApOx sample (Figure 5c) revealed the reflections due to the planes that correspond to the hydroxyapatite (JCPDF # 09-0432) and amoxicillin (JCPDS # 39-1832). The peaks assigned to the (0 0 2), (2 1 1), (1 1 2), (3 0 0), (2 0 2), (3 1 0) and (0 0 4) reflection plans were observed in the both XRD patterns of the MgHAp and MgHApOx. Intense diffraction peaks corresponding to amoxicillin were also observed in the MgHApOx sample. Moreover, the changes in the crystal structure show the substitution effect of amoxicillin in the MgHApOx sample. The diffraction peaks of MgHApOx shifted to a smaller angle than those of MgHAp (Figure 6).

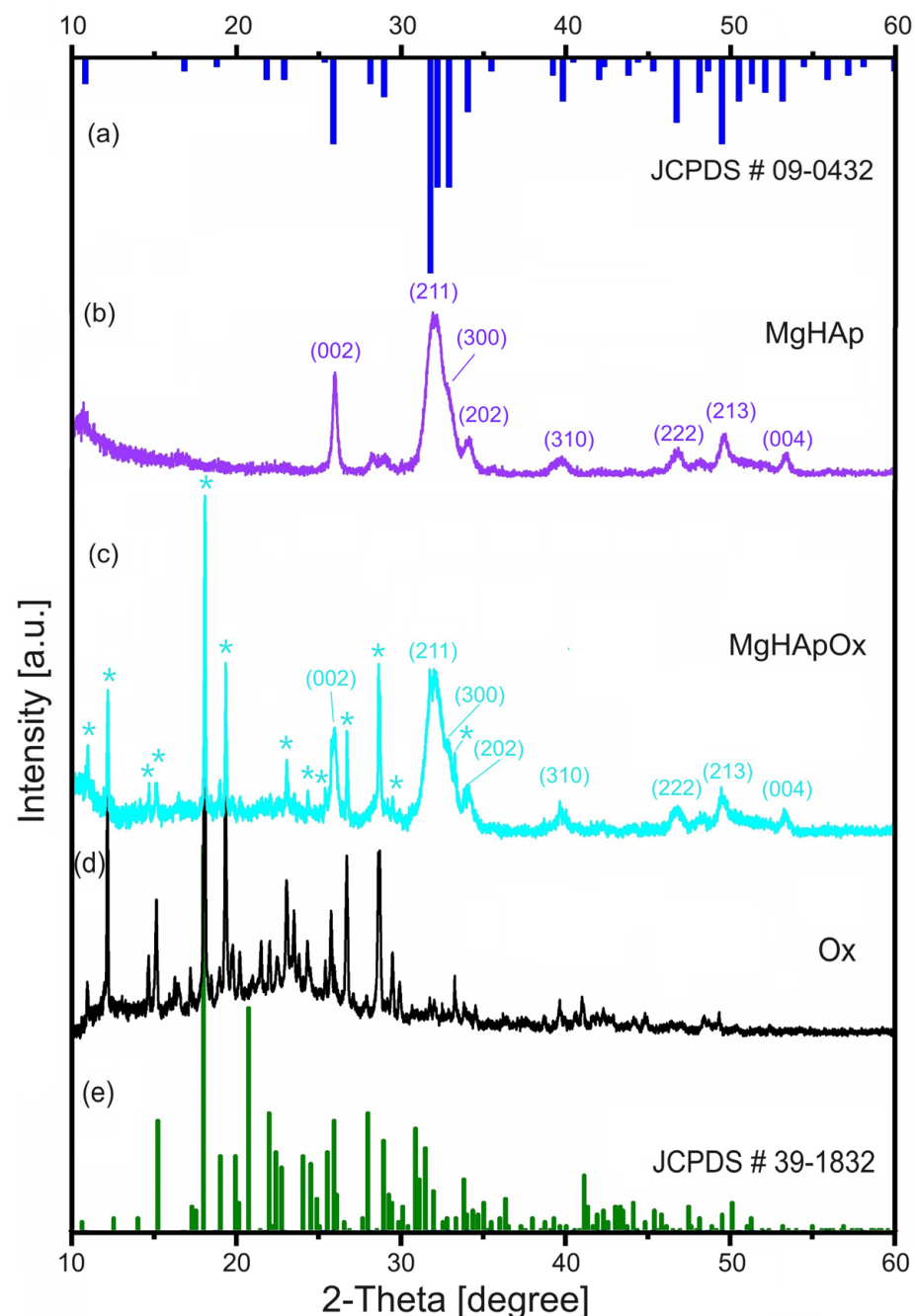


Figure 5. XRD patterns of MgHAp (b), MgHApOx (c) and Ox (d) samples. The JCPDS # 09-0432 of HAp (a) and JCPDS # 39-1832 of Ox (e). The * indicates the maxima associated with amoxicillin structure.

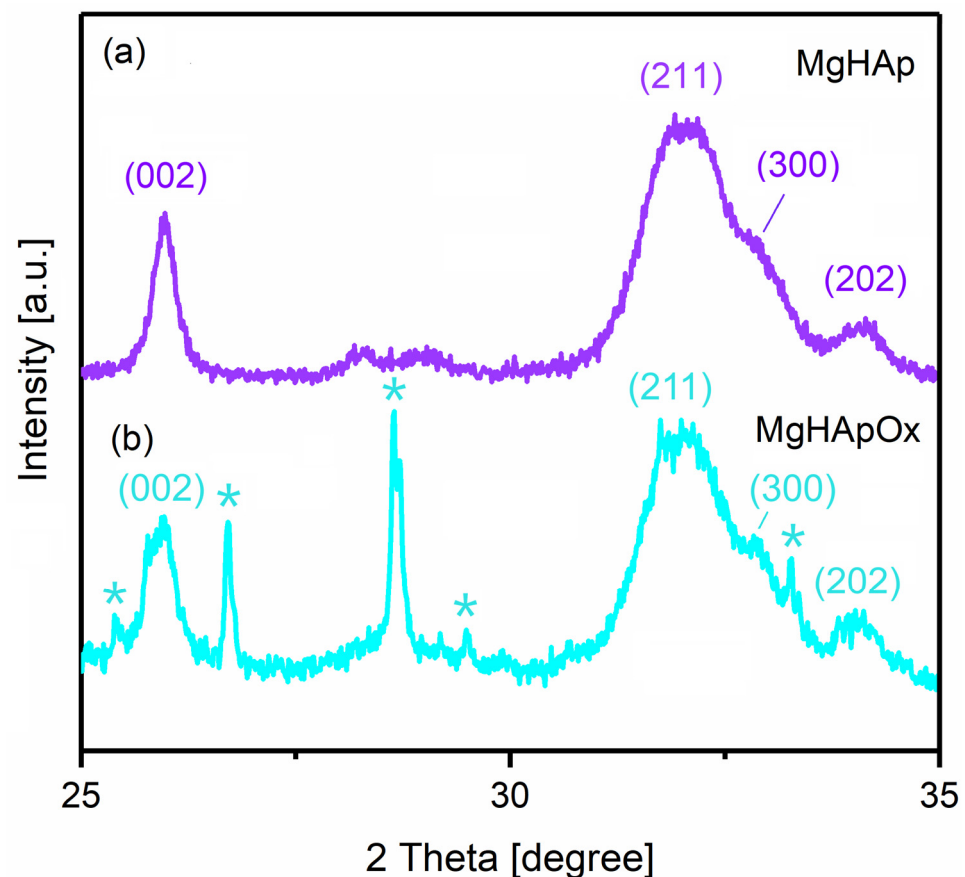


Figure 6. XRD patterns of MgHAp (a), MgHApOx (b) relative shift on 2θ range of 25–35°. The * indicates the maxima associated with amoxicillin structure.

In agreement with previous studies [36], this behavior suggests a significant incorporation of amoxicillin into the MgHAp lattice and an increment in the unit cell of the HAp in the a- and c-axes as well as the unit cell volume. Table 1 presents the average crystallite size calculated using the Scherer equation, d-spacing, lattice parameters and unit cell volume of both analyzed samples.

Table 1. XRD parameters of MgHAp and MgHApOx samples.

Sample	Average Crystal Size (nm)	d-Spacing (nm)	Lattice Parameters (Å)		Unit Cell Volume (Å ³)
			c-Axis	a-Axis	
MgHAp	15.31	3.40	6.85	9.39	605
MgHApOx	17.79	3.43	6.87	9.41	608

It was observed that the average crystallite size increased in the case of the MgHApOx sample. This behavior could be due to the weakening of the hydrogen bonds that lead to the flexibility of amoxicillin and implicitly to a slight increase in the average size of the crystallite. In agreement with previously published results [37], the crystallite size could also be influenced by the intermolecular hydrogen bonds (in our case, the hydrogen bonds from amoxicillin). This behavior is also supported by a slight increase in the distance d, the parameters of the unit cell and the volume of the cell.

Figure 7 depicts both the SEM micrographs and the mean particle diameter distribution obtained for the MgHAp and MgHApOx samples. For both samples, the SEM micrographs were obtained at two different magnifications: $\times 100,000$ (Figure 7a,d) and $\times 200,000$ (Figure 7b,e). Firstly, our results underline that the MgHAp samples consist of

nanoparticles with acicular flake morphology. As can be seen in the SEM micrographs of MgHApOx, the presence of amoxicillin induces some changes in the nanoparticles' morphology. Therefore, the MgHApOx exhibits a well-defined ellipsoidal morphology.

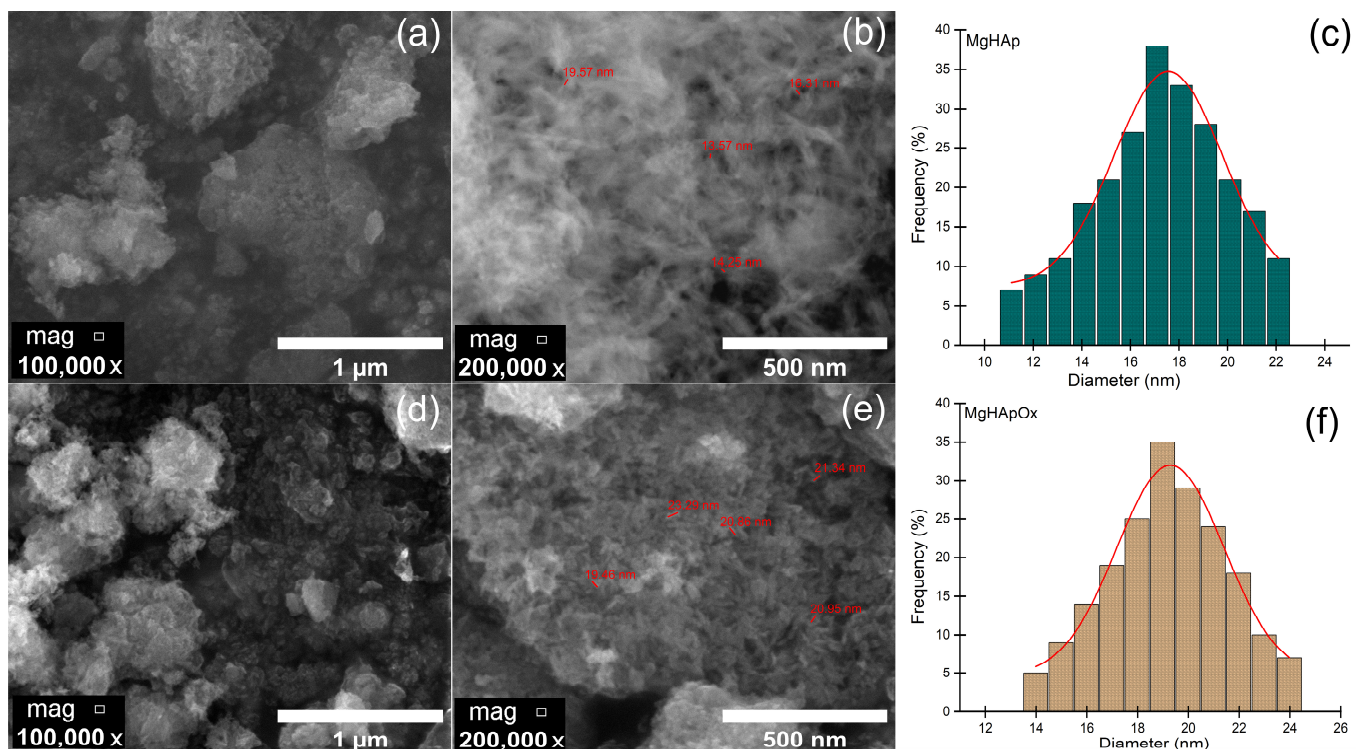


Figure 7. (a,b) SEM micrographs obtained at $\times 100,000$ and at $\times 200,000$ for MgHAp sample; (d,e) SEM micrographs obtained at $\times 100,000$ and at $\times 200,000$ for MgHApOx sample. (c,f) particle size distribution obtained for MgHAp and MgHApOx.

Figure 7c,f reveal the mean particle diameter distribution (from SEM) obtained for the MgHAp and MgHApOx samples. For the MgHAp sample, a mean particle diameter of 17.55 ± 2 nm was obtained. Meanwhile, for the MgHApOx sample, a mean particle diameter of 19.28 ± 2 nm was obtained. Thus, the nanometric dimensions of the MgHAp and MgHApOx samples are sustained and produce SEM results that are in good concordance with the XRD results.

Data about the chemical composition of the studied specimens (MgHAp and MgHApOx) were obtained by EDS studies (Figure 8). In the energy-dispersive X-ray spectroscopy spectra of the MgHAp sample, we observe the presence of lines that are characteristic of calcium (Ca), magnesium (Mg), oxygen (O) and phosphorus (P). These are typical chemical elements characteristic of the MgHAp structure. The energy-dispersive X-ray spectroscopy spectra of the MgHApOx sample confirm the presence of MgHAp and Ox in the sample. In the MgHApOx-EDS spectra, we observe lines that belong to both compounds (Mg, P, O, C, Ca, S and N). In the energy-dispersive X-ray spectroscopy spectra of the MgHApOx sample, we observe lines that appear due to the Ox presence in the sample (sulfur (S) and nitrogen (N)). The obtained EDS spectra testify to the good purity of the MgHAp and MgHApOx samples. The results of the energy-dispersive X-ray spectroscopy studies are in good agreement with the ones obtained by X-ray photoelectron spectroscopy studies (XPS).

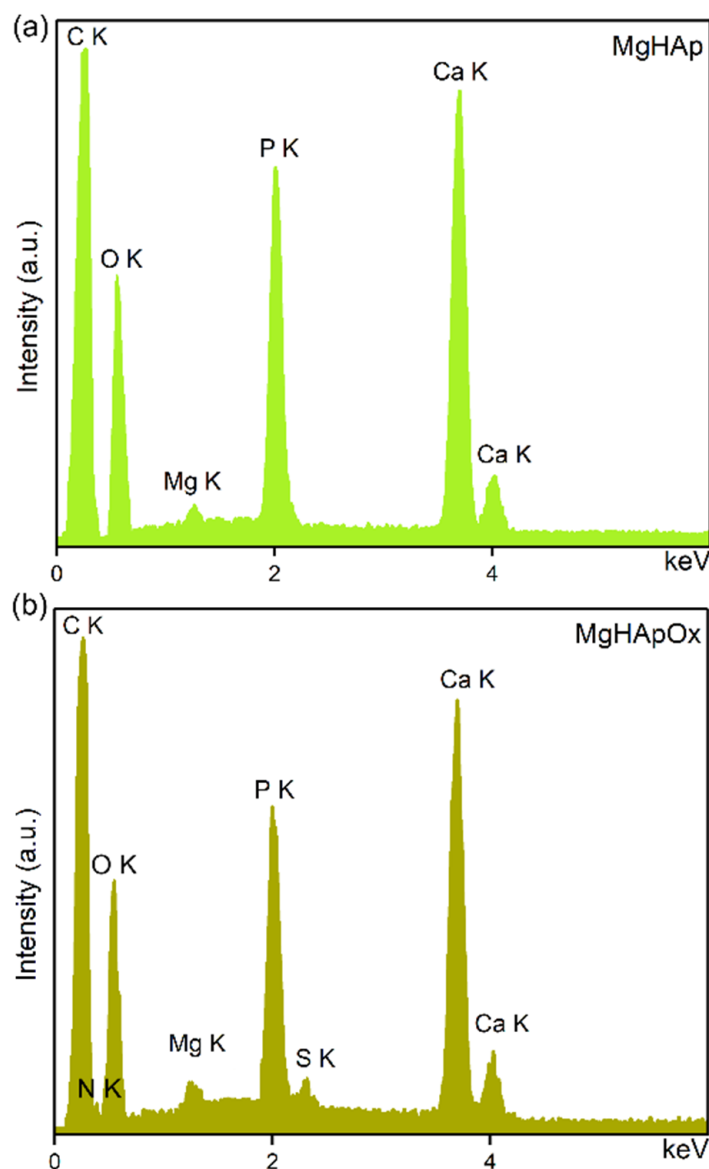


Figure 8. Energy-dispersive X-ray spectroscopy spectra of (a) MgHAp and (b) MgHApOx.

The FTIR spectra obtained for MgHAp, MgHApOx and Ox are revealed in Figure 9. The FTIR spectra of the MgHAp and MgHApOx are dominated mainly by the peaks that are characteristic of the functional groups from HAp. Thus, the peak observed at $\sim 963\text{ cm}^{-1}$ could be attributed to the ν_1 vibration of phosphate groups from HAp [38]. The peaks noticed at $\sim 468\text{ cm}^{-1}$ belong to the ν_2 of phosphate groups. On the other hand, the peaks found at $\sim 563\text{ cm}^{-1}$, $\sim 601\text{ cm}^{-1}$, $\sim 1027\text{ cm}^{-1}$ and around 1091 cm^{-1} are specific to the ν_4 and ν_3 vibrations of the phosphate group from HAp [38]. Furthermore, the shoulder observed at $\sim 876\text{ cm}^{-1}$ could appear due to the carbonate group in the MgHAp sample [38]. In the case of the MgHApOx, we noticed that the HAp peak positions were slightly shifted, probably due to the presence of Ox. Moreover, among the specific peaks of the HAp in the FTIR the MgHApOx are noticed and the specific peaks of Ox. These results indicate that amoxicillin interacts effectively with HAp.

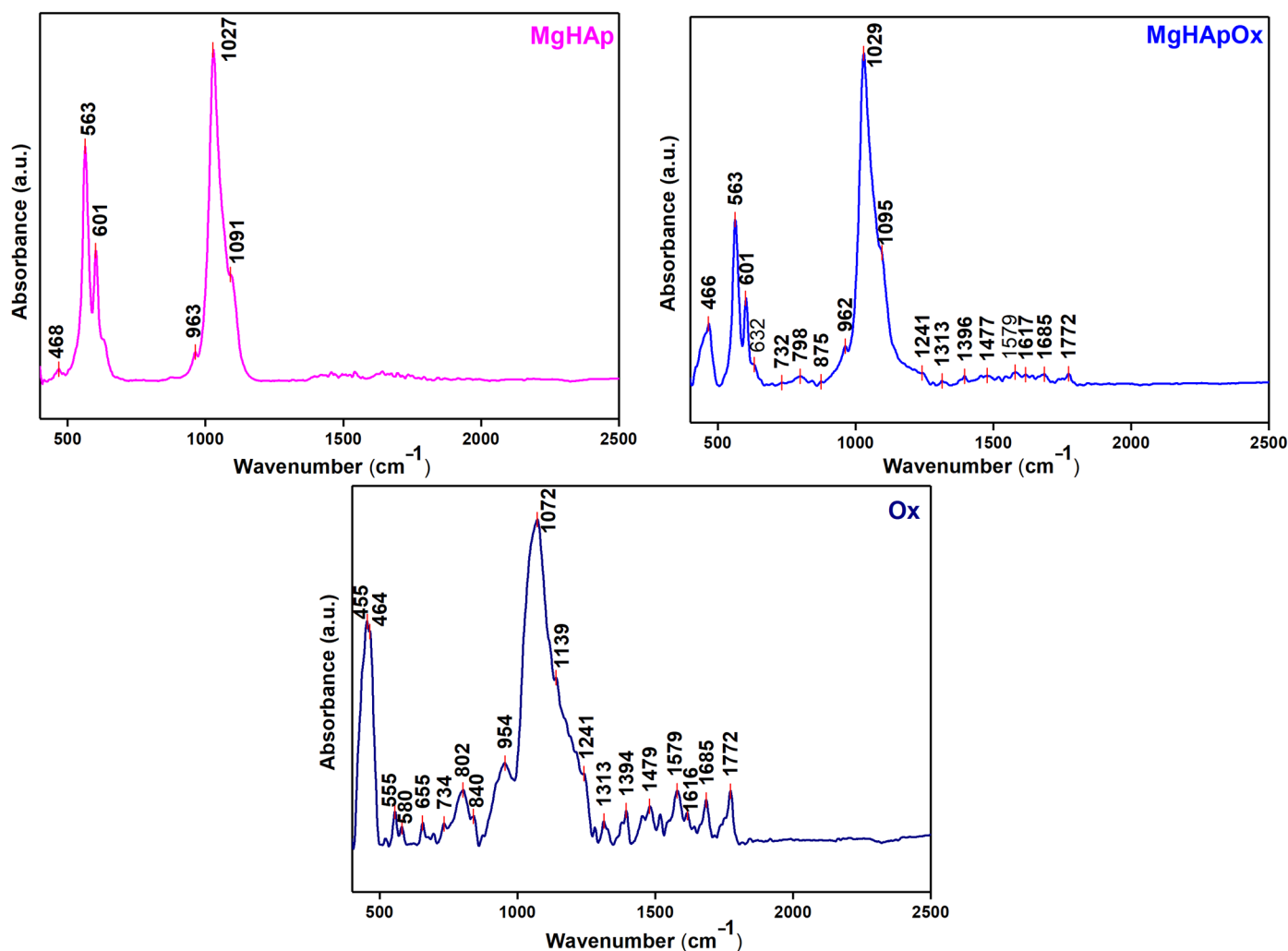


Figure 9. FTIR general spectra of MgHAp, MgHApOx and Ox.

In the FTIR spectra of amoxicillin (Ox) revealed in Figure 9, we noticed maxima that are specific to their structure (amoxicillin). The peak observed at $\sim 1394\text{ cm}^{-1}$ belongs to the NH bend CB stretch combination band and NH_3^+ symmetric deformation of Ox [39]. We also noticed other peaks that are characteristic of Ox at $\sim 1685\text{ cm}^{-1}$ (attributed to $\nu\text{C}=\text{O}$ (amide)), $\sim 1616\text{ cm}^{-1}$ (arise due to $\text{C}=\text{C}$ (aromatic)) and $\sim 1772\text{ cm}^{-1}$ (belongs to $\nu\text{C}=\text{O}$ (β -lactamic ring)) [40–44]. Also, the peak noticed at $\sim 1579\text{ cm}^{-1}$ is characteristic of (vasCOO^-) [41]. The peak observed at $\sim 1072\text{ cm}^{-1}$ could be attributed to C–N stretching vibrations from Ox [42–44]. Furthermore, at $\sim 1394\text{ cm}^{-1}$ and $\sim 1479\text{ cm}^{-1}$ appear peaks that could arise due to the $-\text{CH}_2$ bending and N–H bending vibrations of Ox [42]. The presence of the absorption peaks between the 1800 and 1650 cm^{-1} spectral region of the MgHApOx FTIR spectra clearly indicate the presence of carbonyl ($-\text{C}=\text{O}$) groups, corresponding to both the beta-lactam ring and the amide functional group from amoxicillin.

Figure 10 reveals the second derivative spectra of MgHAp, MgHApOx and Ox samples obtained for the 900 – 1200 cm^{-1} spectral domain. Usually, in the case of the MgHAp sample, the vibration bands (ν_1 and ν_3) that belong to the phosphate groups that form the HAp structure could be found in this spectral domain. Therefore, in the FTIR, the second derivative spectra of the MgHAp are dominated by the intense band observed at $\sim 1027\text{ cm}^{-1}$, which is specific to the ν_3 vibration of the phosphate group. Also, other maxima at $\sim 1004\text{ cm}^{-1}$, $\sim 1045\text{ cm}^{-1}$, $\sim 1070\text{ cm}^{-1}$ and $\sim 1097\text{ cm}^{-1}$ that could be attributed to the ν_3 vibration of the phosphate group from HAp could be observed in the same spectra. Another important peak that belongs to ν_1 vibration of the HAp (phosphate group) was

found at $\sim 963\text{ cm}^{-1}$. The FTIR second derivative spectra of Ox were obtained in order to highlight that the additional peaks observed in the FTIR second derivative spectra of MgHApOx appear due to the Ox presence in the samples. Therefore, in the Ox spectra presented in Figure 10, we observed the presence of various peaks that belong to the vibration of functional groups from Ox. Multiple peaks could be observed between the 1200 and 900 cm^{-1} regions of the Ox FTIR second derivative spectra that correspond to the characteristic in-plane C–H bending vibrations of aromatic compounds [43,44]. In the case of the MgHApOx, it could be noticed that the peaks that are associated with the HAp and Ox vibration are slightly shifted compared with their position in the FTIR second derivative reference spectra (MgHAp and Ox, respectively).

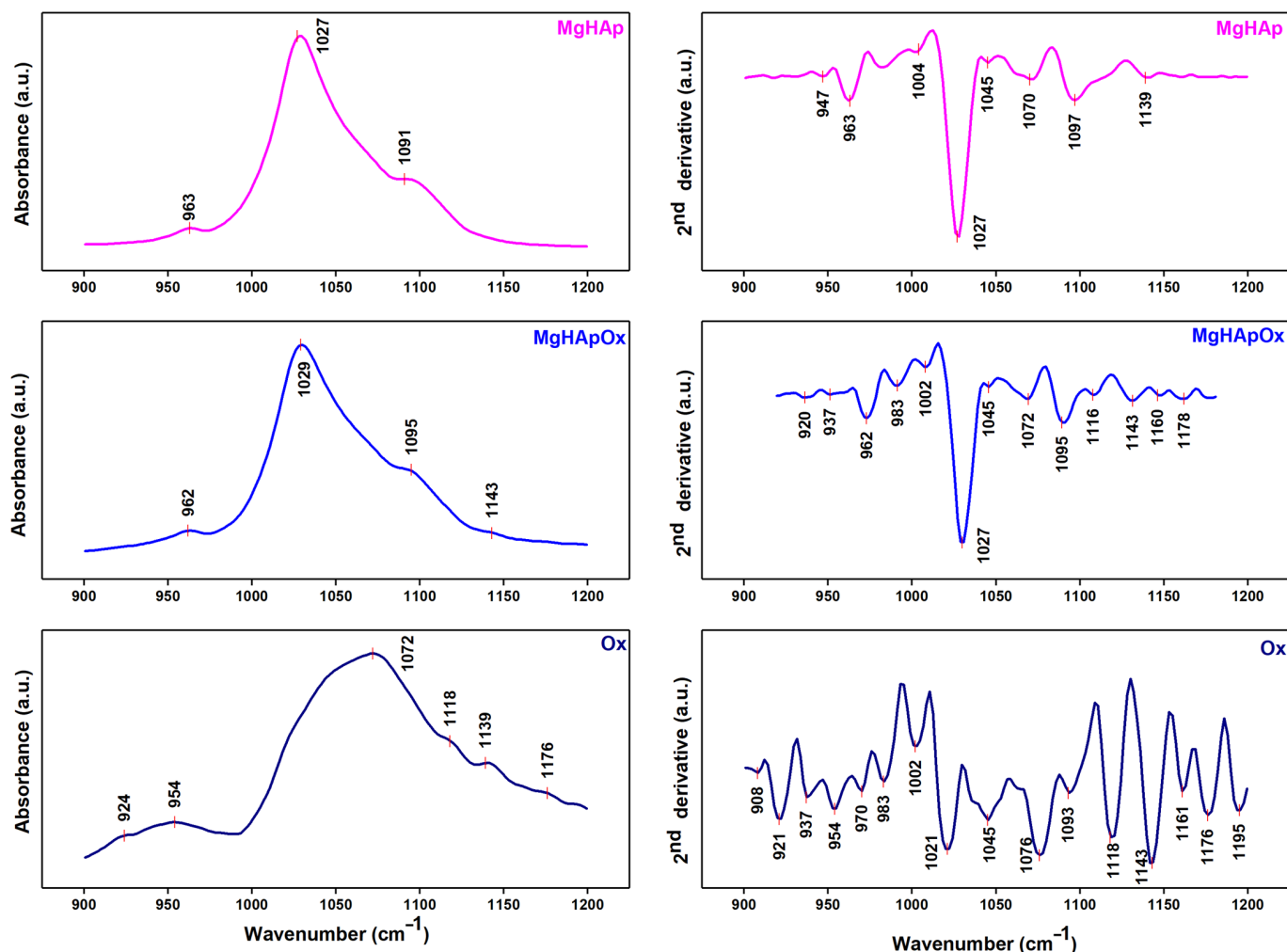


Figure 10. FTIR spectra of MgHAp, MgHApOx and Ox obtained between 900 and 1200 cm^{-1} and their second derivative curve.

Thus, the peaks observed in the second derivative spectra of MgHApOx (Figure 10) are specific to both functional groups from OX and HAp. In this case, the peaks from $\sim 1027\text{ cm}^{-1}$, $\sim 1002\text{ cm}^{-1}$, $\sim 1045\text{ cm}^{-1}$, $\sim 1072\text{ cm}^{-1}$ and $\sim 1095\text{ cm}^{-1}$ are characteristic to the ν_3 vibration of the phosphate group. Meanwhile, the ν_1 vibration peak of the phosphate group could be observed at $\sim 962\text{ cm}^{-1}$ in the second derivative spectra of MgHApOx.

Figure 11 presents the FTIR deconvoluted spectra of MgHAp, MgHApOx and Ox samples obtained for the 900 – 1200 cm^{-1} spectral region. Figure 11 presents the overlay of experimental and calculated data (red line), along with the individual subbands (blue lines) obtained using curve fitting analysis of the MgHAp, MgHApOx and Ox samples between the 900 and 1200 cm^{-1} regions. To obtain a satisfactory fit, we needed 5 subbands

for the MgHAp sample, 13 subbands for the MgHApOx sample and 13 subbands for the Ox sample. The maximums of the five subbands used for the fit of MgHAp are observed at 960 cm^{-1} , 1026 cm^{-1} , 1032 cm^{-1} , 1067 cm^{-1} and 1098 cm^{-1} . Moreover, it can be observed that the main vibrational bands that are found in the MgHApOx spectra in the studied spectral domain are attributed to hydroxyapatite (specifically phosphate groups) and to the Ox structure. Thus, the FTIR studies confirm the presence of both HAp and Ox in the MgHApOx powders, indicating their effective interaction.

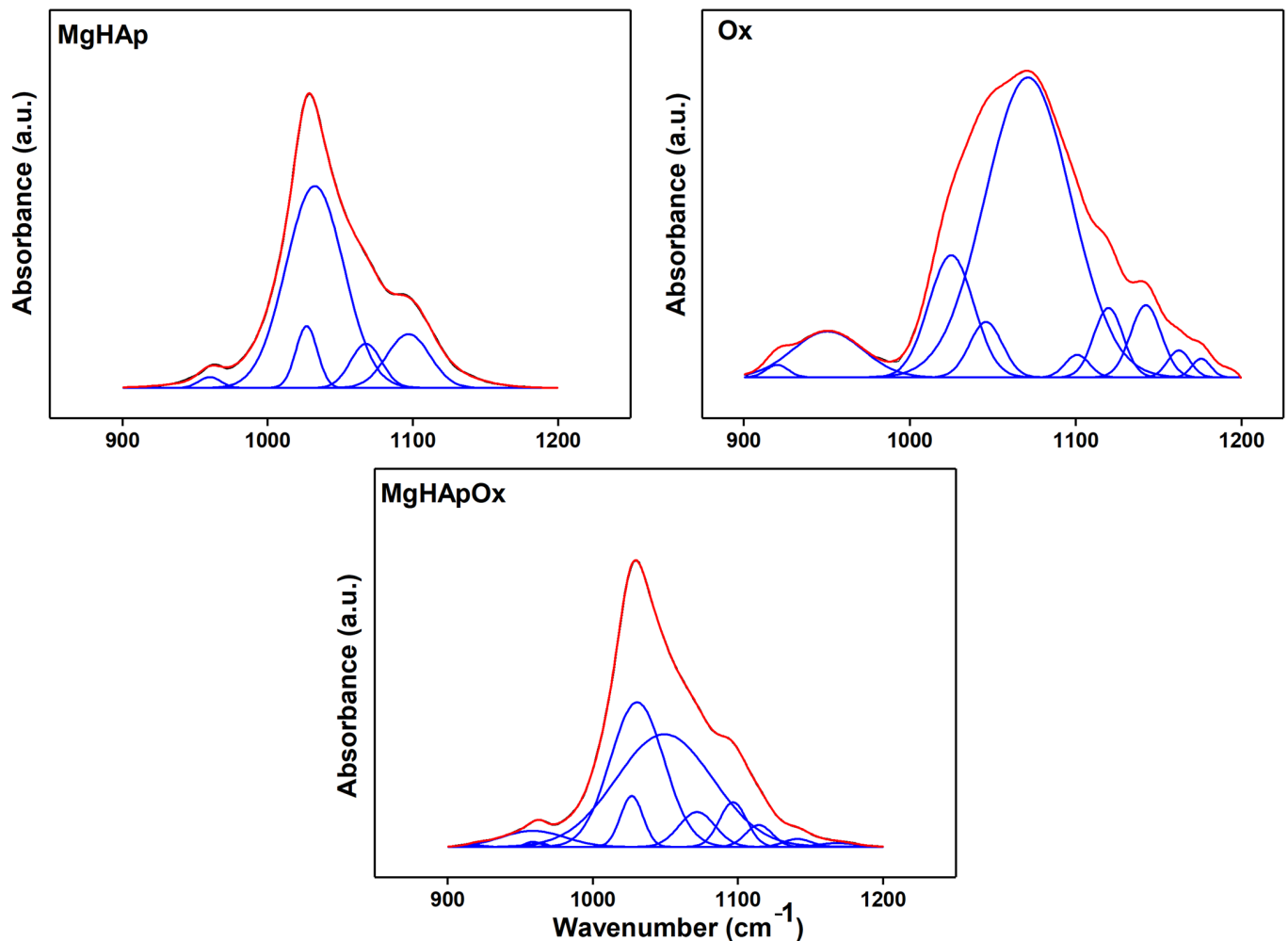


Figure 11. Deconvoluted FTIR spectra of the MgHAp, Ox and MgHApOx obtained in the $900\text{--}1200\text{ cm}^{-1}$ spectral domain.

XPS investigations of MgHAp (Figure 12a) and MgHApOx (Figure 12b) were conducted to confirm the presence of mg and amoxicillin in the HAp lattice. The general XPS spectra of MgHAp and MgHApOx presented in Figure 12a,b highlight the presence of the constituent elements of MgHAp (O, Ca, P and Mg) in both analyzed samples. Also, the constituent elements of amoxicillin (C, N and S) were observed in the general XPS spectrum of MgHApOx, which is presented in Figure 12b. For both analyzed samples, the energy reference was established as the C–C line located at approximately 284.8 eV .

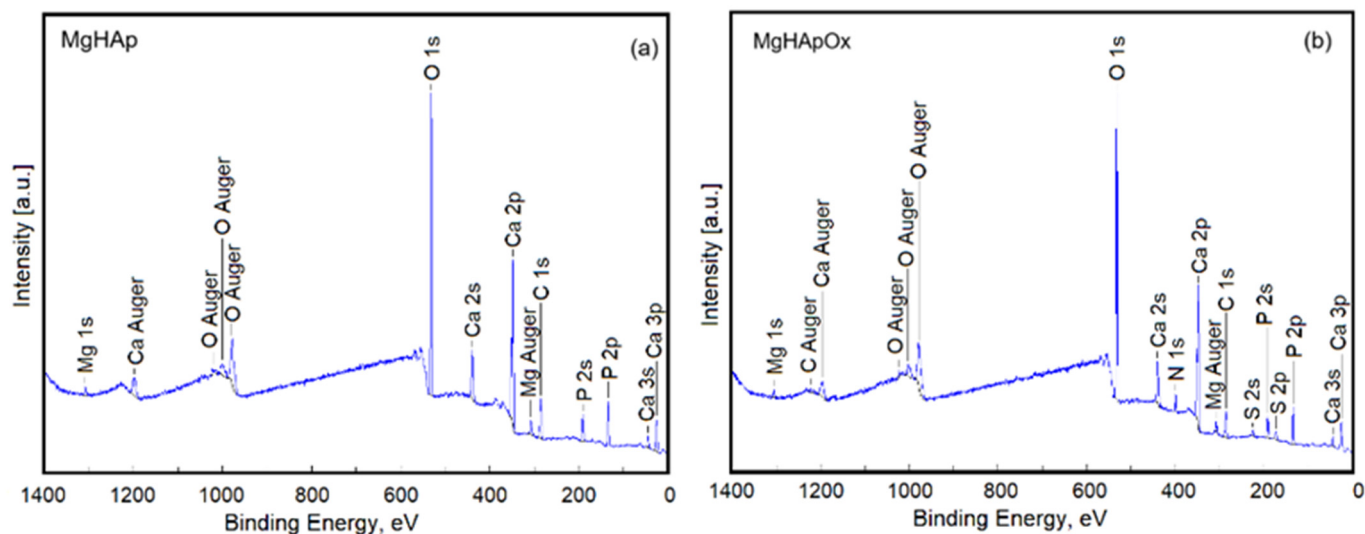


Figure 12. General XPS spectra of MgHAp (a) and MgHApOx (b) samples.

The high-resolution XPS spectra of C 1s, O 1s, Ca 2p and P 2p for MgHAp and MgHApOx samples were presented in Figure 13a–h. The high-resolution XPS spectrum of C 1s for the MgHAp sample (Figure 13a) shows four distinct signals. The four distinct signals in the XPS spectrum of C 1s of the MgHAp sample were identified at the binding energy (BE) of 284.80, 286.10, 287.75 and 288.87 eV, respectively. These bond energies were associated with the single bonds C–C (284.80 eV), C–O (286.10 eV), the double bonds C=C (287.75 eV) and O–C–O (287.75 eV) and –COOR groups (288.87 eV) representing contaminants. The XPS high-resolution spectrum of C 1s for the MgHApOx sample (Figure 13b) showed five distinct signals. The five distinct signals in the XPS spectrum of the C 1s of the MgHApOx sample were identified at the binding energy (BE) of 283.79, 284.81, 285.64, 287.24 and 288.29 eV, respectively. The signal observed at a BE of around 283.79 eV was allocated to C–C and C–S single bonds. The signal observed at a BE of 284.81 eV was assigned to C=C bonds (sp^2 hybridization). The signal identified at 285.64 eV was allocated to C–N and C–O single bonds, while the signal observed at 287.24 eV was assigned to C=O and O–C–O double bonds. The signal observed at 288.29 eV was assigned to –COOR groups representing contaminants.

The high-resolution XPS spectra of O 1s for MgHAp (Figure 13c) and MgHApOx (Figure 13d) samples were presented. For both samples, the high-resolution XPS spectra of O 1s revealed three distinct signals. The first signal revealed at BE of 531.23 eV (MgHAp) and 531.50 eV (MgHApOx) was associated with a Ca–O bond [45] of hydroxyapatite (HAp) and also includes C=O double bonds. On the other hand, previous studies [46–48] have shown that the binding energy of chemisorbed oxygen species (O–) is in the range of 531.0–531.5 eV. The second signal revealed at BEs of 532.4 eV (MgHAp) and 532.6 eV (MgHApOx) could be assigned to the P–O bonds [45] and simple C–O bonds. The third signal observed in the XPS spectra of O 1s was identified at binding energies of 533.90 eV (MgHAp) and 534.01 eV (MgHApOx) and can be allocated to single O–H bonds [49,50].

The high-resolution XPS spectrum of Ca 2p for MgHAp (Figure 13e) and MgHApOx (Figure 13f) showed two distinct signals. The peaks of Ca 2p_{3/2} and Ca 2p_{1/2} for the MgHAp sample were observed at 347.35 and 350.91 eV, respectively, assigned to the tetravalent state (Ca^{2+}). For the MgHApOx sample, the BE of the Ca 2p_{3/2} and Ca 2p_{1/2} states increased slightly to 347.38 and 350.96 eV, respectively. This behavior could be attributed to the presence of amoxicillin (N and S ions) in the MgHAp lattice. For both samples, the Ca 2p doublet with the two specific lines (2p_{3/2} and 2p_{1/2}) are separated by approximately 3.6 eV, with the close area ratio being 2:1. The binding energy is specific to hydroxyapatite in both samples [51].

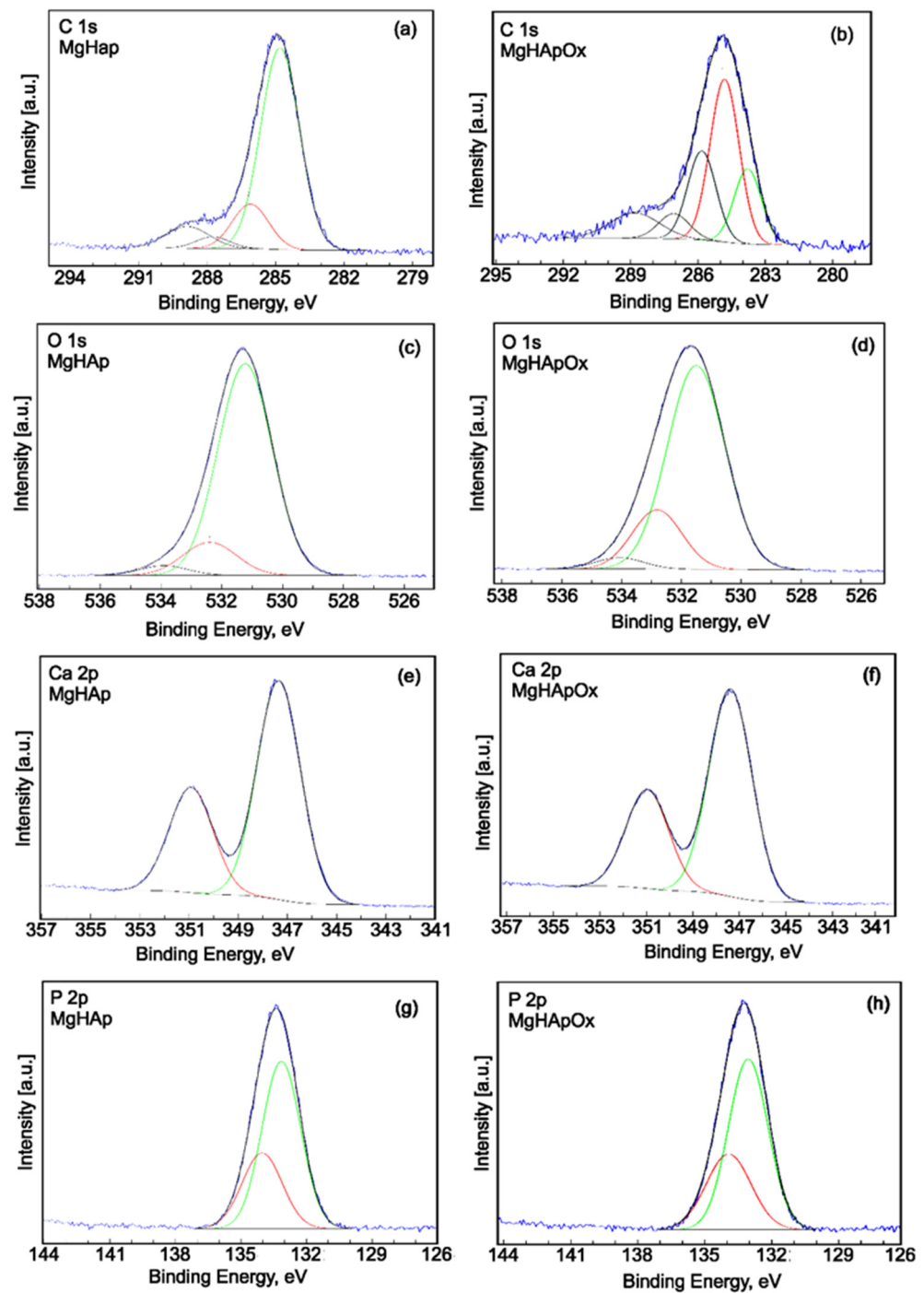


Figure 13. High-resolution XPS spectra and curve-fitting results of C 1s for MgHAp (a) and MgHApOx (b); O 1s for MgHAp (c) and MgHApOx (d); Ca 2p for MgHAp (e) and MgHApOx (f); P 2p for MgHAp (g) and MgHApOx (h).

The high-resolution XPS spectrum of P 2p for MgHAp and MgHApOx are presented in Figures 13g and 13h, respectively. The peaks of P 2p_{3/2} and P 2p_{1/2} for the MgHAp sample were observed at 133.15 and 134.03 eV. For the MgHApOx sample, the peaks of P 2p_{3/2} and P 2p_{1/2} were observed at 133.05 and 133.93 eV. The P 2p doublet with two specific lines (2p_{3/2} and 2p_{1/2}) spaced at approximately 0.9 eV and with an area ratio close to 2:1 was observed in the two analyzed samples (MgHAp and MgHApOx). The binding energy of the doublet is specific to hydroxyapatite [52,53].

The high-resolution XPS spectra of Mg 2p showed one distinct signal for both MgHAp (Figure 14a) and MgHApOx (Figure 14b) samples. Consistent with the findings of S. Ardizzone et al. [54], the binding energy (BE) of Mg 2p at 50.36 eV (MgHAp sample) and 50.34 eV (MgHApOx sample) could indicate the presence of Mg^{2+} bonds with the PO_4^{2-} group. On the other hand, metallic magnesium with a BE of around 49 eV [55] was not detected.

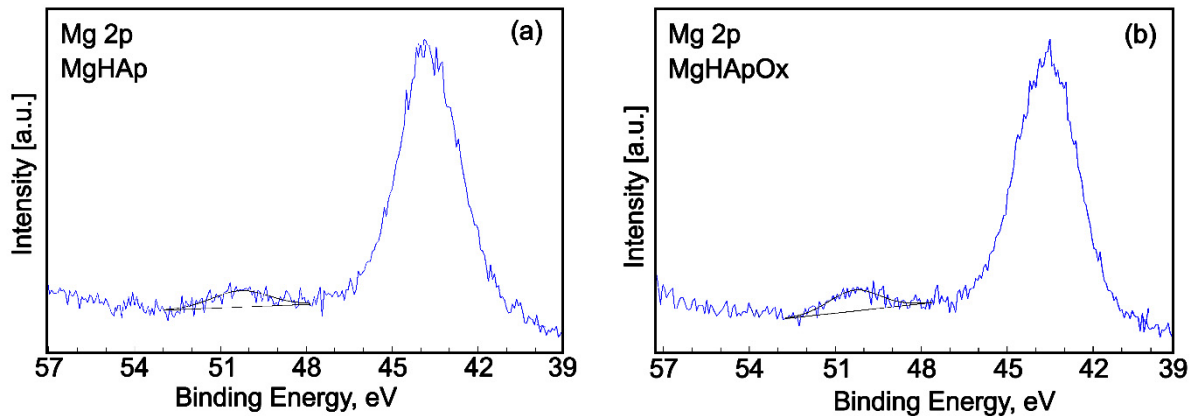


Figure 14. High-resolution XPS spectra and curve-fitting results of Mg 2p for MgHAp (a) and MgHApOx (b).

Figure 15 presents the high-resolution XPS spectra and curve-fitting results of N1s and S 2p for the MgHApOx sample. The high-resolution XPS spectra of N 1s (Figure 15a) showed two distinct signals that were observed at 399.21 and 400.68 eV. The first signal could be assigned to C–N and C–N–C bands. The second signal suggested a protonated N. The high-resolution XPS spectra of S 2p (Figure 15b) showed two distinct signals located at 162.35 and 163.55 eV. The peak of S 2p_{3/2} for the MgHApOx sample was observed at a binding energy of 162.35 while the peak of S 2p_{1/2} was observed at a binding energy of 163.55 eV. The doublet separation (2p_{3/2} – 2p_{1/2}) was equal to 1.2 with a 2:1 area ratio (2p_{3/2}:2p_{1/2}). The two components indicate the presence of C–S bonds [56]. The results of the XPS studies demonstrated that the synthesis method used led to obtaining magnesium-doped hydroxyapatite (MgHAp) and hydroxyapatite doped with magnesium and enriched with amoxicillin (MgHApOx). The results of this study work are in good accordance with the data from the literature [57,58].

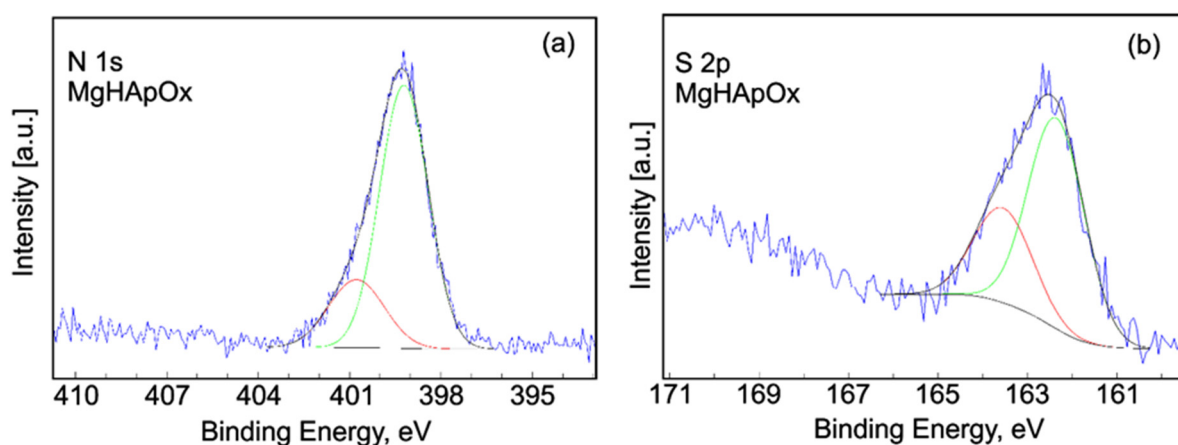


Figure 15. High-resolution XPS spectra and curve-fitting results of N1s (a) and S 2p (b) for MgHApOx sample.

The cytotoxicity of MgHAp, MgHApOx and Ox suspensions was evaluated through hemocompatibility and biocompatibility studies. Hemolysis assays are commonly used to assess the potential hemolytic activity of materials. The results of the hemolysis assays provide significant information about the cytotoxic effects of the tested suspensions. The hemolysis index serves as a key parameter in determining the suitability of materials for biomedical applications. This study aims to identify if the tested materials can produce a rupture of the red blood cells (RBCs), which could lead to hemoglobin release and subsequent hemolysis. A low hemolytic index, having a value of less than 5%, suggests that the tested materials are hemocompatible and safe for biomedical use, while a moderate hemolytic index (5–20%) indicates the need for further testing of the materials to ensure safe use. Conversely, a high hemolytic index, having a value higher than 20%, suggests that the materials could pose significant hemolytic risks, making them unsuitable for use in biomedical applications due to their ability to induce potential damage to RBCs and associated negative physiological effects such as inflammation, thrombosis and organ damage. Materials with a low hemolytic index are preferred for use in biomedical applications due to their minimal risk of adverse reactions and high compatibility with other biological systems. In the case of MgHAp and MgHApOx suspensions, the hemocompatibility assays showed that their hemolytic activity was below 1% for both samples, while the hemolytic activity for the Ox suspensions was between 2.5% and 1.25% depending on the tested concentration. Medical drugs and substances are considered non-hemolytic according to national biological safety standards if the hemolysis rate is below 5%. The results of the hemolytic assays of MgHAp, MgHApOx and Ox suspensions are depicted graphically as mean \pm SD in Figure 16.

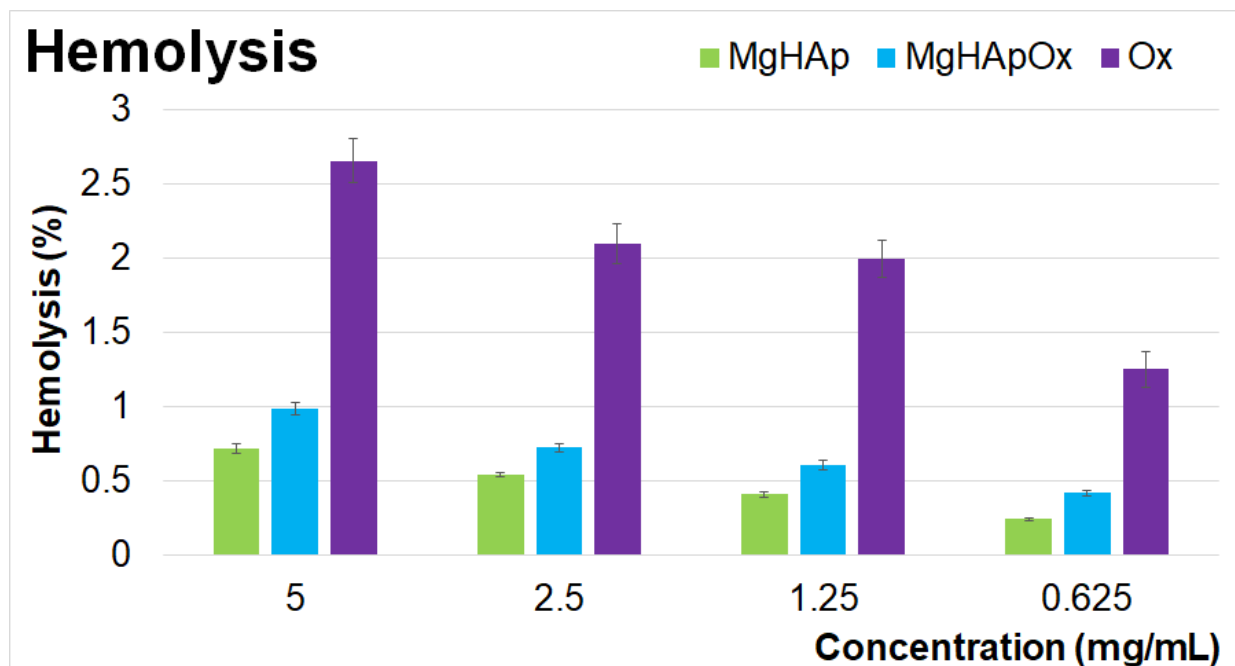


Figure 16. Percentage hemolysis of sheep red blood cells (RBCs) exposed to different concentrations of MgHAp, MgHApOx and Ox suspensions. The statistical analysis of the data was performed using one-way ANOVA. The calculated p -values were $p < 0.002$.

The hemolytic activity studies revealed that none of the tested concentrations of MgHAp, MgHApOx and Ox induced hemolysis. Additionally, the hemolytic index values obtained for MgHAp and MgHApOx were well within the hemocompatibility acceptable limits for biomaterials. Specifically, MgHAp and MgHApOx suspensions exhibited a hemolytic index with a value below 1%. On the other hand, the results revealed that the hemolysis index of all the samples increased with the sample's concentration. Notably,

MgHAp suspensions demonstrated a lower hemolytic index compared to MgHApOx, likely due to the presence of Ox in the sample. These findings indicate that both MgHAp and MgHApOx nanoparticles have a low hemolytic index, suggesting their potential suitability for being considered for further cytotoxicity assessments in order to confirm their safety for biomedical applications. Further information about the cytotoxicity of MgHAp, MgHApOx and Ox suspensions was attained using the colorimetric MTT assay. For this purpose, the cell viability of hFOB 1.19 cells was assessed following exposure to MgHAp, MgHApOx and Ox suspensions at three distinct time intervals. The results of the MTT assay are presented graphically as mean \pm standard deviation (SD) expressed as percentages of control (100% viability) in Figure 17.

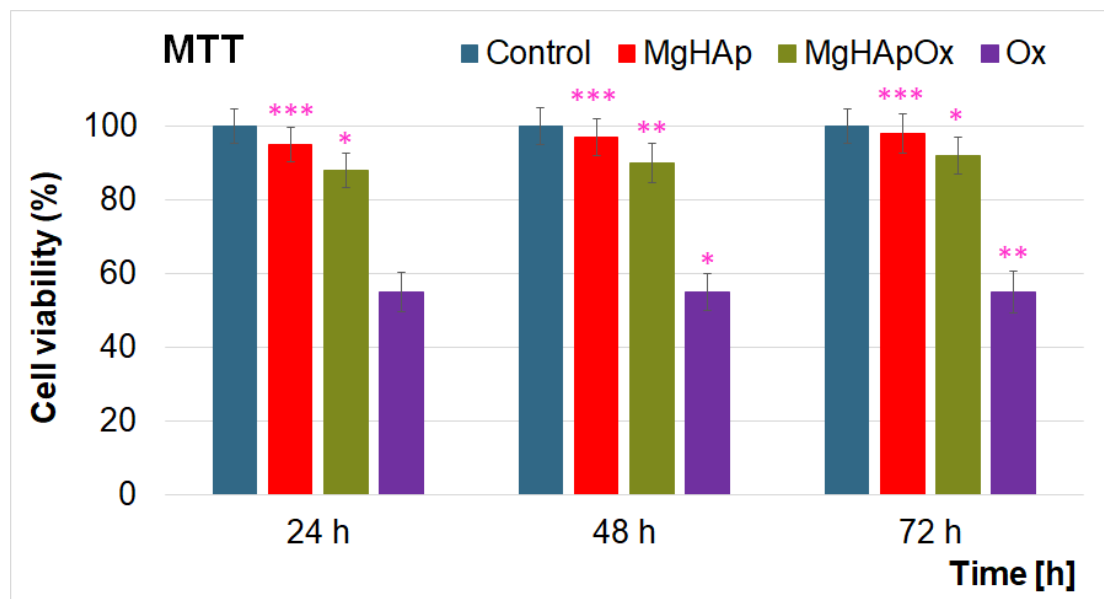


Figure 17. MTT assay of hFOB 1.19 cells incubated with MgHAp, MgHApOx and Ox suspensions for 24, 48 and 72 h. The results are represented as mean \pm standard deviation (SD) and are expressed as percentages of control (100% viability). The statistical analysis of the data was performed using one-way ANOVA. The *p*-values indicated are * $p \leq 0.002$, ** $p \leq 0.001$, *** $p \leq 0.0001$.

The MTT assay results presented in Figure 17 demonstrated that the viability of hFOB 1.19 cells remained above 95% after exposure to MgHAp suspensions for 24, 48 and 72 h. Notably, after 48 and 72 h of exposure, the cell viability increased to 97% and 98%, respectively, when exposed to MgHAp suspensions, revealing their good biocompatibility with hFOB 1.19 cells. These findings align well with previously reported research studies on the biological properties of magnesium-doped hydroxyapatite biocomposites [16,20,59–64]. Moreover, these data suggest that MgHAp suspensions are supportive of human osteoblast cell viability and proliferation and could be considered for future biomedical applications [16,20,59–64]. Furthermore, the data obtained with the aid of the MTT assay emphasized that the MgHApOx suspensions did not exhibit a cytotoxic effect against hFOB 1.19 cells for any of the tested time intervals. The results depicted a cellular viability lower than in the case of MgHAp suspensions but still above 88%, which is a good rate for a biocompatible material. According to the ISO 10993-1: 2018 standard [65–67], biocompatibility is defined as the ability of a material to perform with an appropriate host response in a specific application. Therefore, a viability of over 88% is considered biocompatible due to the fact that it demonstrates a high level of compatibility with living cells, tissues or organisms. The cell viability, in this context, depicts the percentage of cells that remain alive and functional after being exposed to the tested material. A value above 88% indicates that the material does not induce significant cytotoxic effects, meaning it does not damage or induce apoptosis in cells in its vicinity. A viability of over 88% is considered to be a high viability and suggests that

the material does not trigger adverse biological responses, such as inflammation, toxicity or immune rejection. These are the most important factors in determining whether a material can safely be integrated and function within a biological system.

On the other hand, the results revealed a slight increase in the cellular viability of hFOB 1.19 cells with an increase in the exposure time, reaching 92% after 72 h. These results showed that the presence of amoxicillin in the MgHAp suspensions did not greatly influence the toxicity of the sample. Furthermore, the results also highlighted that, when exposed to pure Ox suspensions, hFOB 1.19 cells achieved only 55% cell viability. Also, the data suggest that this did not change significantly with the increase of the exposure time. The obtained results agree well with previously reported data on the toxicity of amoxicillin [23–25]. Due to its broad-spectrum activity and also relatively good biological properties, amoxicillin has been considered a precursor in the development of novel compounds for biomedical applications.

Additional information about the cytotoxic character of the MgHAp, MgHApOx and Ox suspensions was obtained from lactate dehydrogenase (LDH) release studies (Figure 18).

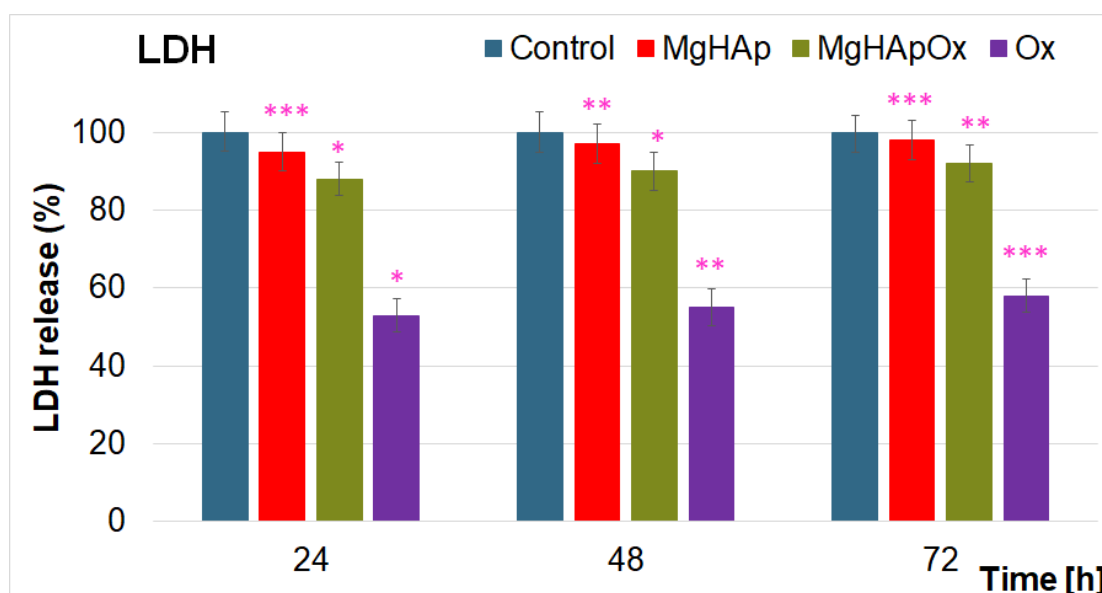


Figure 18. Lactate dehydrogenase (LDH) activity released in the culture medium of hFOB 1.19 cells after the treatment with MgHAp, MgHApOx and Ox suspensions for 24, 48 and 72 h. The results are represented as mean \pm standard deviation (SD). The statistical analysis of the data was performed using one-way ANOVA. The p -values indicated are * $p \leq 0.002$, ** $p \leq 0.001$, *** $p \leq 0.0001$.

LDH assays determine cell cytotoxicity by detecting LDH release from damaged cells into the culture medium. In this context, a low LDH release index indicates low cytotoxicity and high cell viability, while a high LDH release index suggests significant cell damage. The LDH assay results of MgHAp and MgHApOx suspensions showed no significant difference from the control, indicating that these suspensions did not damage the hFOB 1.19 cell membrane or cause cell necrosis. Additionally, the results of the LDH studies also depicted an LDH value of 53% after 24 h of exposure for the pure Ox suspensions and showed a slight increase at about 58% after 72 h. The findings are consistent with the MTT assay results and demonstrate that both MgHAp and MgHApOx suspensions possess great biocompatibility, making them suitable candidates for the development of novel materials with biomedical applications.

In recent years, due to the emergence of antibiotic-resistant microbial strains, the development and understanding of the mechanisms and efficacy of novel antimicrobial agents have been an interest of researchers worldwide. Amoxicillin is an antibiotic that has been widely used due to its effectiveness in treating various bacterial infections and

has become a crucial part of antimicrobial therapy, particularly against Gram-positive and Gram-negative bacteria. In this context, the development of new antimicrobial agents, such as magnesium-substituted hydroxyapatite (MgHAp), represents a significant advancement in the material science field [9,25,57,68–82]. The antimicrobial effects of MgHAp as well as MgHApOx suspensions and pure Ox were evaluated over three different time intervals against one of the most common microbial strains, *Staphylococcus aureus* (*S. aureus*), as well as *Escherichia coli* (*E. coli*) and *Candida albicans* (*C. albicans*). The studies revealed that incorporating amoxicillin into MgHAp had a significant influence in enhancing the antimicrobial effects of MgHAp against *S. aureus*, *E. coli* and *C. albicans*. The results of the in vitro assays are depicted in Figure 19a–c.

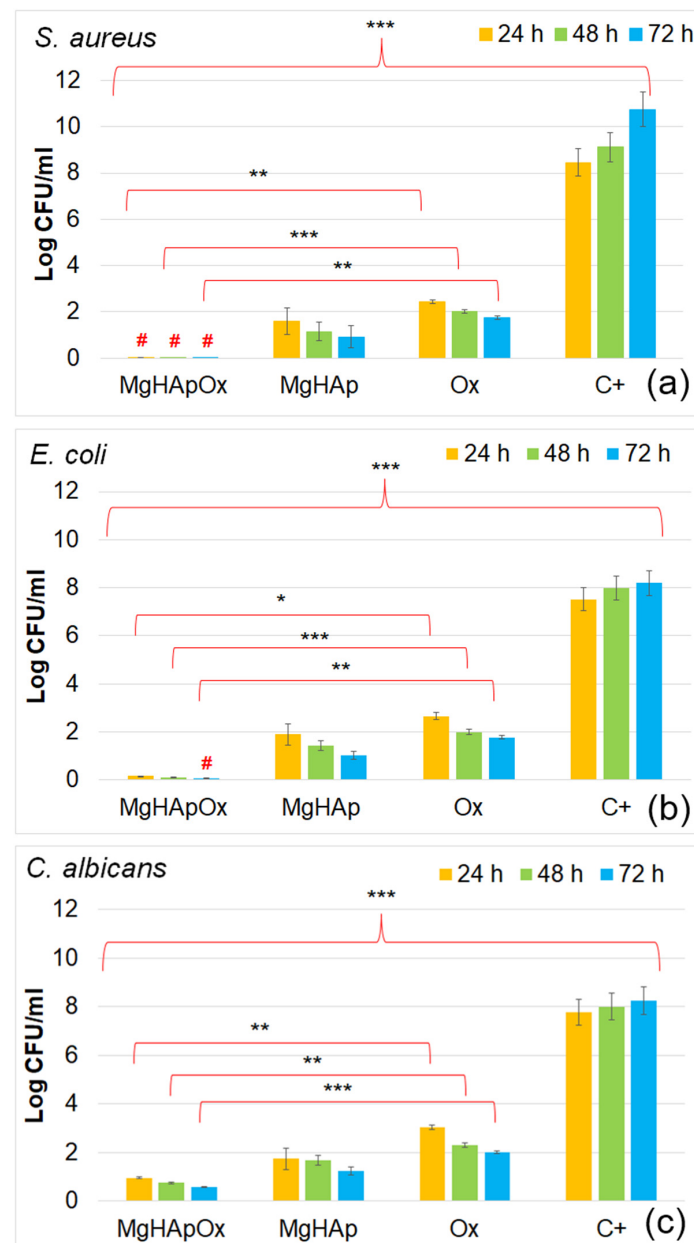


Figure 19. Graphical representation of the logarithmic values of colony forming units (CFU)/mL of *S. aureus* ATCC 25923 (a), *E. coli* ATCC 25922 (b) and *C. albicans* ATCC 10231 (c) microbial strains after 24, 48 and 72 h of exposure to MgHAp, MgHApOx and Ox suspensions. #—depicts the bactericidal properties of the samples. The results are represented as mean \pm standard error. Ordinary one-way ANOVA was used for the statistical analysis. The p -values indicated are * $p \leq 0.002$, ** $p \leq 0.001$, *** $p \leq 0.0001$.

The results depicted that the presence of Ox in the MgHAp suspensions conferred a significant increase in the MgHAp antimicrobial activity for all the tested microbial strains. The data showed that the MgHApOx achieved bactericidal properties against *S. aureus* for all the tested time intervals (Figure 19a). In addition, bactericidal activity was depicted for MgHApOx suspensions after 72 h of exposure in the case of *E. coli* (Figure 19b). These results align well with the data reported in the literature that highlights that amoxicillin is less effective against Gram-negative bacteria than Gram-positive ones and has very poor activity against fungal cells [25]. The data also emphasized that the presence of Ox in the MgHApOx samples increased the inhibitory effects of the MgHAp in the case of *E. coli* and *C. albicans*. The results revealed that the CFU values of the tested microbial strains were decreased by the presence of Ox in the case of MgHApOx compared to the values obtained for MgHAp, as well as for the CFU values of the control sample. Magnesium is well known to be a vital element that has an important function in the fundamental nucleic acid chemistry within the cells of all living organisms [68]. While it is widely recognized and studied for its beneficial contribution to bone health and muscle function, recent research studies have also highlighted that it exhibits antimicrobial properties [57,68–71]. Previously reported studies showed that magnesium-based composites possess important antimicrobial activity against some of the most common pathogens. In this context, magnesium-based composites have been reported to possess antimicrobial properties against *Staphylococcus aureus*, *Pseudomonas aeruginosa*, *Escherichia coli* and *Candida albicans* [57,68–71]. The antimicrobial effects of these compounds were primarily attributed to the release of magnesium ions, which have the ability to inhibit microbial growth by disrupting bacterial cell membranes [57,68–72]. Additionally, strong antifungal properties were also reported in the case of magnesium-based composites [57,68–72]. Research on the effects of magnesium ions against the fungal pathogen *Candida albicans* has revealed that magnesium ions inhibit fungal cell growth and induce the formation of reactive oxygen species, which exert significant toxic effects on fungal cells [57,68–73]. Even though the antimicrobial mechanism of materials is still under investigation, and there is still scarce information in this field, it has been reported that magnesium ions exhibit antimicrobial activity through possible several mechanisms. The primary antimicrobial mechanism reported for magnesium ions is their ability to disrupt the integrity of microbial cell membranes. Another possible mechanism was attributed to magnesium ions' ability to interfere with the lipid bilayer of microbial cells, leading to increased membrane permeability, which causes cell lysis. On the other hand, it has been reported that magnesium ions can inhibit the replication of microbial DNA by binding to nucleotides or enzymes involved in DNA synthesis, thereby preventing microbial growth. Furthermore, magnesium can act as a cofactor for various enzymes that produce reactive oxygen species (ROS), which can damage microbial cells by oxidizing cellular components like proteins, lipids and DNA. These combined effects contribute to the antimicrobial properties of magnesium ions. On the other hand, amoxicillin exhibits its antimicrobial effects by targeting bacterial cell wall synthesis. Being a beta-lactam antibiotic, amoxicillin has the ability to bind to and inhibit penicillin-binding proteins (PBPs) that are important for the cross-linking of peptidoglycan chains, which are a critical component of bacterial cell walls. This inhibition ability leads to the weakening of the cell wall structure, thus leaving bacteria susceptible to the osmotic pressure, causing cell lysis over time and, eventually, death [9,75–77]. Amoxicillin is well known for being particularly effective against a broad spectrum of Gram-positive and some Gram-negative bacteria, making it a widely used antibiotic in the treatment of various bacterial infections [9,75–78]. The results of the in vitro antimicrobial assays are consistent with previously reported studies on the antimicrobial effects of magnesium-based composites and amoxicillin [9,25,57,68–82]. The results demonstrated that the antimicrobial activity of MgHAp and MgHApOx is also dependent on the incubation time and on the type of microbial strain. The data indicated that while the CFU values were low in the early stages of development, their number decreased significantly with exposure time. The superior antimicrobial activity of the MgHApOx suspensions could be attributed both to the release of magnesium ions

from the hydroxyapatite matrix as well as to the presence of amoxicillin. The results have suggested that the synergy between the magnesium ions combined with amoxicillin can significantly enhance the antimicrobial efficacy against the tested microbial strains. Magnesium ions are vital in stabilizing bacterial cell walls and membrane structures. When used in combination with amoxicillin, which is a beta-lactam antibiotic that has the ability to disrupt bacterial cell wall synthesis, magnesium ions can help amplify the antibiotic's effectiveness. This synergistic effect may arise from the ability of magnesium ions to interfere with bacterial defense mechanisms, increasing the cells' vulnerability to amoxicillin. Additionally, magnesium ions might be able to reduce the bacterial resistance to amoxicillin, leading to treatment that has more effective outcomes in infections. In their studies, Enan et al. [82] also concluded that the AgNPs showed synergistic antimicrobial and anti-biofilm activity when combined with amoxicillin. The results of the biological assays suggested that both MgHAp and MgHApOx suspensions exhibit unique properties. Moreover, the results highlighted that the combination of MgHAp with amoxicillin leads to the development of multifunctional biomaterials ideal for biomedical applications such as bone implants and infection management. The properties that magnesium ions confer to HAp, such as biodegradability, biocompatibility and bone-like mechanical properties, allow the novel materials to have a reduced risk of stress shielding and to promote osteogenesis, making it a suitable candidate for biomedical applications that support bone healing. On the other hand, the broad-spectrum antimicrobial activity of amoxicillin helps prevent the apparition of infections. When integrated into magnesium-doped hydroxyapatite, it can provide localized, continuous drug release, thus reducing the risk of infections and also enhancing the healing process. The synergy between the constituents of magnesium-doped hydroxyapatite enriched with amoxicillin could have the ability to accelerate the process of bone regeneration and prevent infection-related complications. Despite all of these beneficial properties, challenges regarding the optimization of release rates and avoiding antibiotic resistance remain critical for future research studies.

Magnesium plays a crucial role in acid-based processes in the biological environment, contributing significantly to bone calcification and decalcification. Given that half of the body's magnesium is in bone tissue, where it plays a crucial role in stimulating the growth of new tissue, the composite of magnesium-doped hydroxyapatite and enriched with amoxicillin (MgHApOx) could significantly help regenerate bone tissue after implantation. Moreover, the presence of amoxicillin in the MgHApOx composite can contribute to significantly reducing the risk of postoperative infection. Controlled ionic substitutions can make the hydroxyapatite composition more similar to natural bone, enhancing bioactivity and bone-forming capacity [83]. In contrast, the inclusion of amoxicillin in the composite material added significant value due to its antibacterial, wound healing and anti-inflammatory properties. The research presented in this paper brings new information to the existing research on the controlled substitution of different ions of apatites [84,85]. This study aligns with the recent interest in the use of Mg^{2+} ions as additives in the development of bone biomaterials [84–88]. Moreover, recent studies [16] showed that the presence of chitosan in the magnesium-doped hydroxyapatite/chitosan composite material could have an important contribution due to its antibacterial, cicatrizing and anti-inflammatory properties. The antimicrobial properties of magnesium and magnesium composites have been attributed to different mechanisms, which are similar to those encountered with other metal ions. Previous results [34] on the antimicrobial activity of 10MgHAp suspensions showed that the magnesium-doped hydroxyapatite suspension has a high efficiency in inhibiting biofilm formation for *P. aeruginosa*, *S. aureus* and *C. albicans* microbial strains, even when used in low concentrations (0.009 mg/mL). Furthermore, the results indicate that the inhibitory effect of MgHAp ($x_{Mg} = 0.1$) suspensions depends on both incubation time and sample concentration. Studies have shown that corrosion products from modern biocompatible magnesium alloys do not significantly impact human metabolic pathways [89,90]. Additionally, current research [91] has demonstrated that magnesium device implantation causes minimal changes in blood composition without harming excretory organs like the

liver or kidneys. Consistent with anterior findings, the colloidal stability of hydroxyapatite suspensions doped with various cations is influenced by different parameters such as hydrodynamic diameters, zeta potential, spectral attenuation and first echo amplitude. Further, the preparation method, the amount of dopant and the surface of the nanoparticles play an important role regarding the stability of hydroxyapatite suspensions doped with different ions [92,93]. At the same time, previous studies [16,33,34,57,58] have shown that the presence of Mg ions in the HAp influences the crystallinity, particle size and the position of the vibration bands associated with phosphate and hydroxyl groups in MgHAp. These characteristics are important for adjusting the properties of nanocomposite materials for use in specific biomedical applications.

The findings from this study suggest that MgHAp and MgHApOsp suspensions could be used in the future development of new antimicrobial agents. The results obtained in this study emphasized that these materials could have significant potential to address the current critical clinical challenges like peri-implantitis and bone defect infections. These novel materials could offer a safe and effective solution in advanced regenerative medicine and implantable medical devices.

3. Materials and Methods

3.1. Materials

The magnesium-doped hydroxyapatite (MgHAp) and magnesium-doped hydroxyapatite enriched with amoxicillin (MgHApOx) suspension were obtained using the following as reagents: diammonium hydrogen phosphate ($(\text{NH}_4)_2\text{HPO}_4$, $\geq 99.0\%$, Sigma Aldrich, St. Louis, MO, USA), calcium nitrate ($\text{Ca}(\text{NO}_3)_2 \cdot 4\text{H}_2\text{O}$, $\geq 99.0\%$, Sigma Aldrich, St. Louis, MO, USA), magnesium nitrate hexahydrate ($\text{Mg}(\text{NO}_3)_2 \cdot 6\text{H}_2\text{O}$, 99.97%, Alpha Aesar, Kandel, Germany) and amoxicillin ($\text{C}_{16}\text{H}_{19}\text{N}_3\text{O}_5\text{S}$, 95.0–102.0%, Sigma Aldrich, St. Louis, MO, USA).

3.2. Synthesis of Magnesium-Doped Hydroxyapatite Enriched with Amoxicillin Suspensions

Both suspensions (MgHAp and MgHApOx) were developed using an adapted co-precipitation method, in agreement with our previous work [34,94]. For both syntheses, the $[\text{Ca} + \text{Mg}]/\text{P}$ ratio was set at 1.67, and the magnesium concentration was $x_{\text{Mg}} = 0.1$ [34,94]. In the following, we will only describe the synthesis method of MgHApOx because this is similar to that of MgHAp. Therefore, the solution containing amoxicillin, magnesium and calcium was obtained by dissolving the specific precursors in a beaker. Then, the obtained solution was added drop by drop in the phosphate solution. Then, the mixture was well stirred (250 rpm) for 12 h at 80 °C on a magnetic stirrer [34,94]. Finally, the obtained mixture was centrifuged using a Hettich Universal 320 centrifuge (Hettich, Tuttlingen, Germany; operated at 6000 rpm for 12 min/cycle) and dispersed in deionized water (4 times). Prior to X-ray diffraction (XRD), energy-dispersive X-ray spectroscopy (EDS), X-ray photoelectron spectroscopy (XPS) and scanning electron microscopy (SEM) analyses, both suspensions were vacuum-dried, and the resulting powders (MgHAp and MgHApOx) were subjected to further analysis.

3.3. Physicochemical Characterization of Samples

3.3.1. Ultrasound Studies

In order to evaluate the stability of the concentrated suspensions of MgHAp and MgHApOx, ultrasound studies were carried out. For this purpose, 100 mL of MgHAp and MgHApOx suspension were stirred continuously at room temperature for 15 min at 700 rpm in order to obtain a good homogeneity of the solid particles. After continuous stirring, the 100 mL were transferred to a container special transparent cubic. Two ultrasonic coaxial transducers were immersed in the suspension and distanced 16 mm face-to-face. The axis of the transducers was 29 mm from the flat bottom of the container box. Immediately after stopping the magnetic stirrer, the acquisition of ultrasonic signals began. In the case of the MgHAp suspension, 1000 ultrasonic signals were acquired, while for the MgHApOx

suspension, 900 ultrasonic signals were acquired, recorded every 5 s from the oscilloscope. Each recorded signal is an average of 32 signals on the oscilloscope, reducing experimental noise. For this study, the US measurements were performed using two identical ultrasonic transducers with a central frequency of 5 MHz (GE's Krautkramer, GE, Boston, MA, USA). One transducer generated and received ultrasonic signals in the fluid, while the second acted solely as a receiver. The signals were amplified and processed with a pulse receiver and a Tektronix DPO 4014B oscilloscope (Tektronix, Inc., Beaverton, OR, USA), while a digital thermometer measured the fluid temperature. All the experimental US data were recorded and analyzed using proprietary software [95–97]. For better accuracy, both the schematics and image of the US experimental setup are revealed in Figure 20 [95].

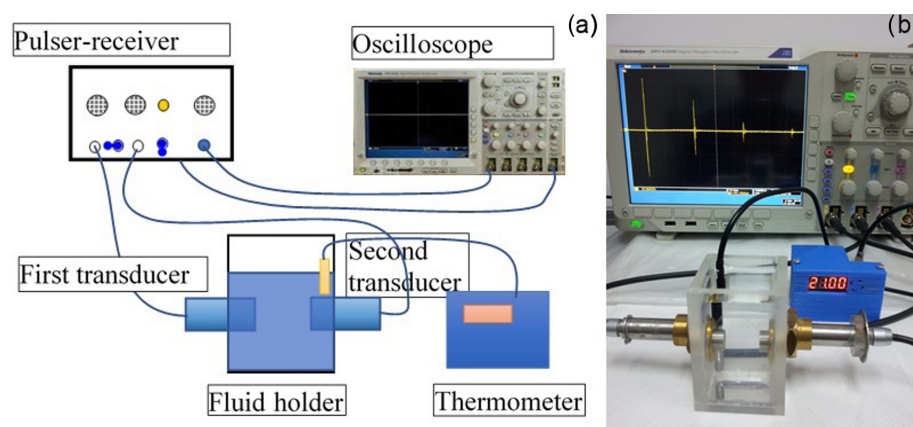


Figure 20. The schematic representation (a) and the image (b) of US experimental setup [95].

3.3.2. Zeta (ζ)-Potential Measurements

Zeta (ζ)-potential studies were performed with the aid of an SZ-100 Nanoparticle Analyzer (Horiba-SAS France, Longjumeau, France) instrument at room temperature. To ensure the accurate characterization of the particle surface charge, prior to measurement, the suspensions were systematically diluted tenfold in deionized water in order to minimize the particle concentration effects on ζ -potential values [32]. For reproducibility and reliability, three independent measurements were performed for each sample.

3.3.3. X-ray Diffraction

X-ray diffraction (XRD) of MgHAp and MgHApOx were investigated using a Bruker D8 Advance diffractometer with CuK α radiation ($\lambda = 1.5418 \text{ \AA}$) (Bruker, Karlsruhe, Germany) equipped with a LynxEye™ 1D high-efficiency one-dimensional linear detector. Data were acquired in the 2θ range of $10\text{--}60^\circ$ with a step size of 0.02° and a time of 5 s per step. JCPDS # 09–432 and JCPDS # 39–1832 were used to confirm the various peaks developed in the apatite and amoxicillin. The average crystallite size (D) of the samples was calculated using Scherrer's formula [98]:

$$D = K\lambda / \beta \cos\theta \quad (1)$$

where K is Scherrer constant, λ is wavelength of the X-rays, β is the full width at half maximum (FWHM) and θ is the diffraction angle of the XRD spectra.

The hexagonal crystal parameters were calculated from the equation of Bragg's reflection [99]. The unit cell volume (\AA^3) was also estimated [100].

3.3.4. Scanning Electron Microscopy

The morphology features of the samples (MgHAp and MgHApOx) were investigated by scanning electron microscopy (SEM) with HITACHI S4500 equipment (Hitachi, Tokyo, Japan) in order to evaluate the influence of amoxicillin on the MgHAp morphology. The parameter values used for the obtaining of SEM images were ETD detector, spot of 3.5 and

an accelerating voltage of 20 kV. Furthermore, the mean particle size was obtained after measuring about 500 nanoparticles. Also, information regarding chemical composition of MgHAp and MgHApOx was obtained by performing energy-dispersive X-ray spectroscopy (EDS) studies. For this purpose, an EDS system was attached to the SEM equipment.

3.3.5. Fourier Transform Infrared Spectroscopy

The Fourier transform infrared (FTIR) spectroscopy in attenuated total reflectance (ATR) mode was employed in order to evaluate the vibrations of functional groups present in MgHAp, MgHApOx and Ox. The FTIR studies were performed with a Perkin Elmer spectrometer equipped with a Universal Diamond/KRS-5 (Waltham, MA, USA). All the FTIR spectra were collected in the 450–2500 cm^{-1} spectral range under ambient conditions. The parameters used for the FTIR measurements were: 32 scans with a resolution of 4 cm^{-1} . The second derivative spectra and the deconvoluted spectra of the MgHAp, MgHApOx and amoxicillin were achieved for the 900–1200 cm^{-1} spectral domain [38].

3.3.6. X-ray Photoelectron Spectroscopy

For this study, the XPS data were collected using a SCIENCE SES 2002 system (Scienta Omicron, Taunusstein, Germany) equipped with a monochromatic Al K α X-ray source ($h\nu = 1486.6$ eV). The binding energy for the sp² carbon (C 1s) peak observed at 284.8 eV was used as reference. The XPS data analysis was performed using Casa XPS version 2.3.14 software.

3.4. In Vitro Biological Assays

3.4.1. Hemolysis Assay

The biological properties of MgHAp, MgHApOx and Ox suspensions were assessed by hemolysis assay using sheep red blood cells (RBCs). The experiments were done according to the previously reported methodology by Miyaji et al. [101] with the modifications described in [95]. For this purpose, various sample concentrations diluted in a 0.9% NaCl solution were mixed with an equal volume of erythrocyte suspension, incubated at a temperature of 37 °C for 30 min and then centrifuged. Triton X-100 and PBS were used as positive and negative controls, respectively. The hemolytic index (HI%) was quantified from the absorbance of the supernatant measured at 540 nm with a FlexStation 3 UV-VIS spectrophotometer (Molecular Devices, San Jose, CA, USA) with the following equation:

$$\text{Hemolysis (\%)} = \frac{V_{\text{ODsample}} - V_{\text{ODnegativecontrol}}}{V_{\text{ODpositivecontrol}} - V_{\text{ODnegativecontrol}}} \times 100 \quad (2)$$

3.4.2. Colorimetric Test Assay 3-(4,5-Dimethylthiazol-2-yl)-2,5-diphenyltetrazolium Bromide (MTT) Assay

The cytotoxicity of MgHAp, MgHApOx and Ox suspensions was determined using human fetal osteoblastic cells (hFOB 1.19) according to the method reported by Ciobanu et al. [95]. For this purpose, the cells were cultured using Dulbecco Modified Eagle's Medium. The culture was grown in a humidified atmosphere with 5% CO₂ at a temperature of 37 °C and seeded at a density of 3×10^4 cells/cm². The cell viability was evaluated after 24, 48 and 72 h exposure intervals with the aid of the colorimetric test assay 3-(4,5-dimethylthiazol-2-yl)-2,5-diphenyltetrazolium bromide (MTT; Sigma-Aldrich, USA). Following each exposure period, the culture medium was removed, and the cells were incubated with 1 mg/mL MTT for 4 h at 37 °C. The absorbance values measured at 595 nm using a FlexStation 3 microplate reader were used to quantify the cell viability. The values of the cell viability were calculated relative to the control sample (set at 100%) and presented graphically as mean \pm SD.

3.4.3. Lactate Dehydrogenase (LDH) Release Measurement

The cytotoxicity of the MgHAp, MgHApOx and Ox suspensions was also assessed through a Lactate dehydrogenase (LDH) release measurement with the aid of Cytotoxicity Detection KitPLUS (Roche, Atlanta, GA, USA). The experiments were performed according to the manufacturer's instructions. After the MgHAp, MgHApOx and Ox suspensions' incubation with the HeLa cells, 50 μ L of the culture supernatant was mixed with 50 μ L of reaction mixture containing the catalyst and dye solution and incubated in the dark for 30 min. The LDH was determined from the absorbance values measured at 485 nm using a Tecan GENios instrument.

3.4.4. In Vitro Antimicrobial Assay

The antimicrobial properties of MgHAp, MgHApOx and Ox were evaluated in vitro using the following common reference strains: *Staphylococcus aureus* ATCC 25923, *Escherichia coli* ATCC 25922, and *Candida albicans* ATCC 10231 (all obtained from ATCC, Old Town Manassas, VA, USA). The antimicrobial testing was conducted as described in [102], with microbial cultures standardized to 0.5 McFarland. The MgHAp, MgHApOx and Ox samples were inoculated with 1.5 mL of microbial suspensions at a concentration of 5×10^6 CFU/mL, prepared in phosphate-buffered saline (PBS) and incubated for 24, 48 and 72 h. The positive control was chosen as the free microbial cultures (C+). Suspensions were collected at 24, 48 and 72 h, plated on LB agar medium and incubated for 24 h at 37 °C to determine the CFU/mL count. All experiments were conducted in triplicate, and the data were presented graphically as mean \pm SD. The statistical analysis was performed using a single-factor ANOVA test.

3.4.5. Statistical Analysis

All the data from the biological assays were presented as mean \pm SD. Unless stated otherwise, the graphs show the average values with error bars representing the standard deviation from at least three replicates per material. Statistical analysis was conducted using ANOVA, with significant differences between groups defined by a p -value of $p < 0.05$.

4. Conclusions

In this study, magnesium-doped hydroxyapatite (MgHAp) and magnesium-doped hydroxyapatite enriched with amoxicillin (MgHApOx) have been successfully synthesized for the first time by an adapted co-precipitation method. The aim of this study was focused on the complex characterization of MgHAp and MgHApOx suspensions from both physico-chemical and biological point of view. The influence of amoxicillin on the stability, structural, morphological and biological features of MgHAp sample was evaluated. The obtained suspensions were analyzed by ultrasound measurements, XRD, XPS, SEM, FTIR and EDS studies. Their in vitro biological features were also evaluated by hemolysis assay, MTT assay, lactate dehydrogenase (LDH) release measurement and antimicrobial assay. The XRD analysis confirms the replacement of Ca^{2+} ions with Mg^{2+} ions in the HAp lattice and a significant incorporation of amoxicillin into the MgHAp lattice. XRD and SEM investigations revealed crystalline nanoparticles. The average crystallite size determined from XRD examination increased from 15.31 nm for MgHAp to 17.79 nm for the MgHApOx sample. The crystallite sizes obtained from SEM were consistent with the XRD results. EDS and XPS certified the presence of Mg in the HAp lattice as well as the presence of amoxicillin constituents in the MgHAp lattice. Furthermore, the FTIR results suggest the presence of functional phosphate groups of HAp in both samples. Moreover, the FTIR results prove the presence of amoxicillin in the MgHApOx. Biological studies revealed that MgHAp and MgHApOx nanoparticles exhibit good biocompatibility towards hFOB 1.19 cells and also antimicrobial properties against *S. aureus*, *E. coli* and *C. albicans*. The hemolysis experiments indicated a hemolytic index of less than 1% for both MgHAp and MgHApOx nanoparticles, and a hemolytic index above 2.5% confirming their suitability for biomedical applications. On the other hand, cell viability studies showed that hFOB 1.19 cells maintained a viability

of over 95% in the case of MgHAp nanoparticles above 88% in the case of the MgHApOx nanoparticles with increased viability observed over the extended incubation periods, while the cell viability of Ox powders was around 55%. Additionally, the LDH studies confirmed that exposure to MgHAp and MgHApOx nanoparticles did not compromise the integrity of the hFOB 1.19 cell membranes. These findings emphasize the potential of MgHAp and MgHApOx nanoparticles in the development of future materials, with applications in the biomedical area. Future research on magnesium-doped hydroxyapatite enriched with amoxicillin should be focused on drug loading, targeted delivery and overcoming antimicrobial resistance while ensuring biocompatibility (in vitro and in vivo) and long-term stability.

Author Contributions: Conceptualization, D.P., C.C. and C.S.C.; methodology, D.P., C.C., S.L.I., C.S.C. and M.V.P.; software, D.P., S.L.I., C.S.C., M.V.P., S.R. and K.R.; validation, D.P., C.C., S.L.I. and C.S.C.; formal analysis, D.P., S.L.I., C.S.C., M.V.P., S.R., K.R. and C.C.; investigation, D.P., S.L.I., C.S.C., M.V.P., S.R., K.R., M.L.B. and C.C.; resources, D.P., S.R. and K.R.; data curation, D.P., M.V.P., S.L.I. and C.S.C.; writing—original draft preparation, D.P., C.C., S.L.I., C.S.C. and M.V.P.; writing—review and editing, D.P., S.L.I., C.S.C., M.V.P., S.R., K.R., M.L.B. and C.C.; visualization, D.P., S.L.I., C.S.C., M.V.P., S.R., K.R., M.L.B. and C.C.; supervision, D.P. and C.C.; project administration, D.P., C.C. and C.S.C.; funding acquisition, D.P. All authors have read and agreed to the published version of the manuscript.

Funding: This work is funded by the Core Program of the National Institute of Materials Physics, granted by the Romanian Ministry of Research, Innovation and Digitalization through Project PC1-PN23080101.

Institutional Review Board Statement: Not applicable.

Informed Consent Statement: Not applicable.

Data Availability Statement: The original contributions presented in the study are included in the article, further inquiries can be directed to the corresponding authors.

Conflicts of Interest: The authors declare no conflicts of interest. The funders had no role in the design of the study; in the collection, analyses, or interpretation of data; in the writing of the manuscript; or in the decision to publish the results.

References

1. Mehrabani, M.G.; Karimian, R.; Mehramouz, B.; Rahimi, M.; Kafil, H.S. Preparation of biocompatible and biodegradable silk fibroin/chitin/silver nanoparticles 3D scaffolds as a bandage for antimicrobial wound dressing. *Int. J. Biol. Macromol.* **2018**, *114*, 961–971. [[CrossRef](#)] [[PubMed](#)]
2. Chan, B.; Leong, K. Scaffolding in tissue engineering: General approaches and tissue specific considerations. *Eur. Spine J.* **2008**, *17*, 467–479. [[CrossRef](#)] [[PubMed](#)]
3. Salem, R.M.; Zhang, C.; Chou, L. Effect of Magnesium on Dentinogenesis of Human Dental Pulp Cells. *Int. J. Biomater.* **2021**, *2021*, 6567455. [[CrossRef](#)] [[PubMed](#)]
4. Cross, L.M.; Thakur, A.; Jalili, N.A.; Detamore, M.; Gaharwar, A.K. Nanoengineered biomaterials for repair and regeneration of orthopedic tissue interfaces. *Acta Biomater.* **2016**, *42*, 2–17. [[CrossRef](#)] [[PubMed](#)]
5. Subramanian, S.; Kamaraj, Y.; Kumaresan, V.; Kannaiyan, M.; David, E.; Ranganathan, B.; Selvaraj, V.; Balupillai, A. Green synthesized zinc oxide nanoparticles induce apoptosis by suppressing PI3K/Akt/mTOR signaling pathway in osteosarcoma MG63 cells. *Glob. Transl. Med.* **2022**, *1*, 34. [[CrossRef](#)]
6. Vallet-Regi, M.; González-Calbet, J.M. Calcium phosphates as substitution of bone tissues. *Prog. Solid State Chem.* **2004**, *32*, 1–31. [[CrossRef](#)]
7. Siddiqui, N.; Madala, S.; Parcha, S.R.; Mallick, S.P. Osteogenic differentiation ability of human mesenchymal stem cells on Chitosan/Poly(Caprolactone)/nano beta Tricalcium Phosphate composite scaffolds. *Biomed. Phys. Eng. Express* **2020**, *6*, 015018. [[CrossRef](#)]
8. Abutalib, M.M.; Yahia, I.S. Novel and facile microwave-assisted synthesis of Mo-doped hydroxyapatite nanorods: Characterization, gamma absorption coefficient, and bioactivity. *Mater. Sci. Eng. C* **2017**, *78*, 1093–1100. [[CrossRef](#)]
9. Demurtas, M.; Perry, C.C. Facile one-pot synthesis of amoxicillin-coated gold nanoparticles and their antimicrobial activity. *Gold Bull* **2014**, *47*, 103–107. [[CrossRef](#)]

10. Nikitin, M.P.; Orlov, A.V.; Znoyko, S.L.; Bragina, V.A.; Gorshkov, B.G.; Ksenevich, T.I.; Cherkasov, V.R.; Nikitin, P.I. Multiplex biosensing with highly sensitive magnetic nanoparticle quantification method. *J. Magn. Magn. Mater* **2018**, *459*, 260–264. [CrossRef]
11. Li, Z.; Chu, D.; Gao, Y.; Jin, L.; Zhang, X.; Cui, W.; Li, J. Biomimicry, biomineralization, and bioregeneration of bone using advanced three-dimensional fibrous hydroxyapatite scaffold. *Mater. Today Adv.* **2019**, *3*, 100014. [CrossRef]
12. Ozawa, T.; Mickle, D.A.; Weisel, R.D.; Koyama, N.; Ozawa, S.; Li, R.-K. Optimal biomaterial for creation of autologous cardiac grafts. *Circulation* **2002**, *106*, I-176–I-182. [CrossRef]
13. Zafar, M.S.; Alnazzawi, A.A.; Alrahabi, M.; Fareed, M.A.; Najeeb, S.; Khurshid, Z. Nanotechnology and nanomaterials in dentistry. In *Advanced Dental Biomaterials*; Woodhead Publishing: Sawston, UK, 2019; pp. 477–505. [CrossRef]
14. Nessler, E.; Boyatzis, S.C.; Boukos, N.; Panagiaris, G. Optimizing the biomimetic synthesis of hydroxyapatite for the consolidation of bone using diammonium phosphate, simulated body fluid, and gelatin. *SN Appl. Sci.* **2020**, *2*, 1892. [CrossRef]
15. Morris, H.F.; Ochi, S. Hydroxyapatite-coated implants: A case for their use. *J. Oral Maxillofac. Surg.* **1998**, *56*, 1303–1311. [CrossRef]
16. Predoi, D.; Ciobanu, S.C.; Iconaru, S.L.; Predoi, M.V. Influence of the Biological Medium on the Properties of Magnesium Doped Hydroxyapatite Composite Coatings. *Coatings* **2023**, *13*, 409. [CrossRef]
17. Luo, J.; Mamat, B.; Yue, Z.; Zhang, N.; Xu, X.; Li, Y.; Su, Z.; Ma, C.; Zang, F.; Wang, Y. Multi-metal ions doped hydroxyapatite coatings via electrochemical methods for antibacterial and osteogenesis. *Colloids Interface Sci. Commun.* **2021**, *43*, 100435. [CrossRef]
18. Luque-Agudo, V.; Fernández-Calderón, M.C.; Pacha-Olivenza, M.A.; Perez-Giraldo, C.; Gallardo-Moreno, A.M.; González-Martín, M.L. The role of magnesium in biomaterials related infections. *Colloids Surf. B* **2020**, *191*, 110996. [CrossRef]
19. Ding, H.; Pan, H.; Xu, X.; Tang, R. Toward a detailed understanding of magnesium ions on hydroxyapatite crystallization inhibition. *Cryst. Growth Des.* **2014**, *14*, 763–769. [CrossRef]
20. Zhao, S.; Jiang, Q.; Peel, S.; Wang, X.; He, F. Effects of magnesium-substituted nanohydroxyapatite coating on implant osseointegration. *Clin. Oral Implant. Res.* **2013**, *24*, 34–41. [CrossRef]
21. Li, F.-Y.; Chaigne-Delalande, B.; Kanellopoulou, C. Second messenger role for Mg²⁺ revealed by human T cell immunodeficiency. *Nature* **2011**, *475*, 471–476. [CrossRef]
22. Jenifer, A.; Senthilarasan, K.; Arumugam, S.; Sivaprakash, P.; Sagadevan, S.; Sakthivel, P. Investigation on antibacterial and hemolytic properties of magnesium-doped hydroxyapatite nanocomposite. *Chem. Phys. Lett.* **2021**, *771*, 138539. [CrossRef]
23. Khan, F.; Bai, Z.; Kelly, S.; Skidmore, B.; Dickson, C.; Nunn, A.; Rutledge-Taylor, K.; Wells, G. Effectiveness and Safety of Antibiotic Prophylaxis for Persons Exposed to Cases of Invasive Group A Streptococcal Disease: A Systematic Review. *Open Forum Infect. Dis.* **2022**, *9*, ofac244. [CrossRef] [PubMed]
24. Alsharif, U.; Al-Moraissi, E.; Alabed, S. Systemic antibiotic prophylaxis for preventing infectious complications in maxillofacial trauma surgery. *Cochrane Database Syst. Rev.* **2017**, *2017*, CD012603. [CrossRef]
25. Kaur, S.; Rao, R.; Nanda, S. Amoxicillin: A Broad Spectrum Antibiotic. *Int. J. Pharm. Sci.* **2011**, *3*, 3.
26. Greenwood, R.; Kendall, K. Selection of suitable dispersants for aqueous suspensions of zirconia and titania powders using acoustophoresis. *J. Eur. Ceram. Soc.* **1999**, *19*, 479–488. [CrossRef]
27. O'Brien, R.W.; Midmore, B.R.; Lamb, A.; Hunter, R.J. Electroacoustic studies of moderately concentrated colloidal suspensions. *Faraday Discuss. Chem. Soc.* **1990**, *90*, 301–312. [CrossRef]
28. Hanaor, D.A.H.; Michelazzi, M.; Leonelli, C.; Sorrell, C.C. The effects of carboxylic acids on the aqueous dispersion and electrophoretic deposition of ZrO₂. *J. Eur. Ceram. Soc.* **2012**, *32*, 235–244. [CrossRef]
29. Fairhurst, D. An Overview of the Zeta Potential Part 3: Uses and Applications, American Pharmaceutical Review. 2013. Available online: <https://www.americanpharmaceuticalreview.com/Featured-Articles/139288-An-Overview-of-the-Zeta-Potential-Part-3-Uses-and-Applications/> (accessed on 3 July 2024).
30. Freitas, C.; Müller, R.H. Effect of Light and Temperature on Zeta Potential and Physical Stability in Solid Lipid Nanoparticle (SLN®) Dispersions. *Int. J. Pharm.* **1998**, *168*, 221–229. [CrossRef]
31. Predoi, D.; Iconaru, S.L.; Ciobanu, S.C.; Predoi, S.A.; Țălu, Ș. *Hydroxyapatite: Innovations in Synthesis, Properties, Nanocomposites, Biomedical Applications, and Technological Developments*; Napoca Star Publishing House: Cluj-Napoca, Romania, 2024; ISBN 978-606-062-901-6.
32. Predoi, D.; Iconaru, S.L.; Ciobanu, S.C.; Țălu, Ș.; Predoi, S.A.; Buton, N.; Ramos, G.Q.; da Fonseca Filho, H.D.; Matos, R.S. Synthesis, characterization, and antifungal properties of chrome-doped hydroxyapatite thin films. *Mater. Chem. Phys.* **2024**, *324*, 129690. [CrossRef]
33. Ciobanu, S.C.; Iconaru, S.L.; Predoi, M.V.; Ghogoiu, L.; Badea, M.L.; Predoi, D.; Jiga, G. Physico-Chemical and Antimicrobial Features of Magnesium Doped Hydroxyapatite Nanoparticles in Polymer Matrix. *Macromol. Symp.* **2024**, *413*, 2400022. [CrossRef]
34. Predoi, D.; Iconaru, S.L.; Predoi, M.V.; Stan, G.E.; Buton, N. Synthesis, Characterization, and Antimicrobial Activity of Magnesium-Doped Hydroxyapatite Suspensions. *Nanomaterials* **2019**, *9*, 1295. [CrossRef] [PubMed]
35. Suganthi, K.S.; Rajan, K.S. Temperature induced changes in ZnO–water nanofluid: Zeta potential, size distribution and viscosity profiles. *Int. J. Heat Mass Transf.* **2012**, *55*, 7969. [CrossRef]
36. Mirzaee, M.; Vaezi, M.; Palizdar, Y. Synthesis and characterization of silver doped hydroxyapatite nanocomposite coatings and evaluation of their antibacterial and corrosion resistance properties in simulated body fluid. *Mater. Sci. Eng. C* **2016**, *69*, 675–684. [CrossRef] [PubMed]

37. Teng, S.H.; Lee, E.J.; Yoon, B.H.; Shin, D.S.; Kim, H.E.; Oh, J.S. Chitosan/nanohydroxyapatite composite membranes via dynamic filtration for guided bone regeneration. *J. Biomed. Mater. Res.* **2009**, *88*, 569–580. [\[CrossRef\]](#)
38. Iconaru, S.L.; Motelica-Heino, M.; Predoi, D. Study on europium-doped hydroxyapatite nanoparticles by Fourier transform infrared spectroscopy and their antimicrobial properties. *J. Spectrosc.* **2013**, *2013*, 284285. [\[CrossRef\]](#)
39. Palanikumar, L.; Ramasamy, S.; Hariharan, G.; Balachandran, C. Influence of particle size of nano zinc oxide on the controlled delivery of Amoxicillin. *Appl. Nanosci.* **2013**, *3*, 441–451. [\[CrossRef\]](#)
40. Prasanna, A.P.S.; Venkatasubbu, G.D. Sustained release of amoxicillin from hydroxyapatite nanocomposite for bone infections. *Prog. Biomater.* **2018**, *7*, 289–296. [\[CrossRef\]](#)
41. Lemnaru, G.-M.; Truşcă, R.D.; Ilie, C.-I.; Tiplea, R.E.; Fica, D.; Oprea, O.; Stoica-Guzun, A.; Fica, A.; Diţu, L.-M. Antibacterial Activity of Bacterial Cellulose Loaded with Bacitracin and Amoxicillin: In Vitro Studies. *Molecules* **2020**, *25*, 4069. [\[CrossRef\]](#)
42. Paul, B.; Adimoolam, S.; Qureshi, M.J. Development and Evaluation of Amoxicillin Loaded Carbopol 934P Mucoadhesive Microcapsules for Sustained Drug Release for H. pylori Treatment: Amoxicillin mucoadhesive microcapsules. *Iran. J. Pharm. Res.* **2019**, *15*, 61–80. [\[CrossRef\]](#)
43. Bisson-Boutelliez, C.; Fontanay, S.; Finance, C.; Kedzierewicz, F. Preparation and physicochemical characterization of amoxicillin β -cyclodextrin complexes. *Aaps. Pharmscitech.* **2010**, *11*, 574–581. [\[CrossRef\]](#)
44. Teoh Si Min, N.; Khan, N.H. Comparative Purity Study by UV Spectrophotometric and Fourier-Transform Infrared Spectroscopic (FTIR) Techniques for the Simultaneous Determination of Amoxicillin Tri-hydrate Capsules. *Biomed. J. Sci. Tech. Res* **2020**, *31*, 24219–24235. [\[CrossRef\]](#)
45. Song, F.; Zhang, H.; Wang, S.; Liu, L.; Tan, X.; Liu, S. Atomic Level Design of CoOH+–Hydroxyapatite@C Catalysts for Superfast Degradation of Organics via Peroxymonosulfate Activation. *Chem. Commun.* **2018**, *54*, 4919–4922. [\[CrossRef\]](#) [\[PubMed\]](#)
46. Hegde, M.S.; Ayyoob, M. O₂- and O₁- types of oxygen species on Ni and barium-doped Ni and Cu surfaces. *Surf. Sci.* **1986**, *173*, L635–L640. [\[CrossRef\]](#)
47. Rao, C.N.R.; Vijayakrishnan, V.; Kulkarni, G.U.; Rajumon, M.K. A comparative study of the interaction of oxygen with clusters and single-crystal surfaces of nickel. *Appl. Surf. Sci.* **1995**, *84*, 285–289. [\[CrossRef\]](#)
48. Kulkarni, G.U.; Rao, C.N.R.; Roberts, M.W. Coadsorption of Dioxygen and Water on the Ni(110) Surface: Role of O₁-Type Species in the Dissociation of Water. *Langmuir* **1995**, *11*, 2572–2575. [\[CrossRef\]](#)
49. Guo, J.; Yu, H.; Dong, F.; Zhu, B.; Huang, W.; Zhang, S. High efficiency and stability of Au-Cu/hydroxyapatite catalyst for the oxidation of carbon monoxide. *RSC Adv.* **2017**, *7*, 45420–45431. [\[CrossRef\]](#)
50. Moulder, J.F.; Stickle, W.F.; Sobol, P.E.; Bomben, K.D. *Handbook of X-ray Photoelectron Spectroscopy*; Physical Electronics Inc.: Chanhassen, MN, USA, 1995.
51. Bee, S.-L.; Bustami, Y.; Ul-Hamid, A.; Lim, K.; Abdul Hamid, Z.A. Synthesis of Silver Nanoparticle-Decorated Hydroxyapatite Nanocomposite with Combined Bioactivity and Antibacterial Properties. *J. Mater. Sci. Mater. Med.* **2021**, *32*, 106. [\[CrossRef\]](#)
52. Gomes, G.C.; Borghi, F.F.; Ospina, R.O.; López, E.O.; Borges, F.O.; Mello, A. Nd:YAG (532 nm) pulsed laser deposition produces crystalline hydroxyapatite thin coatings at room temperature. *Surf. Coat. Technol.* **2017**, *329*, 174–183. [\[CrossRef\]](#)
53. Sinulingga, K.; Sirait, M.; Siregar, N.; Abdullah, H. Synthesis and characterizations of natural limestone-derived nano-hydroxyapatite (HAp): A comparison study of different metals doped Haps on antibacterial activity. *RSC Adv.* **2021**, *11*, 15896–15904. [\[CrossRef\]](#)
54. Ardizzone, S.; Bianchi, L.; Fadoni, M.; Vercelli, B. Magnesium salts and oxide: An XPS overview. *Appl. Surf. Sci.* **1997**, *119*, 253–259. [\[CrossRef\]](#)
55. Ley, L.; McFeely, F.R.; Kowalczyk, S.P.; Jenkin, J.G.; Shirley, D.A. Many-body effects in X-ray photoemission from magnesium. *Phys. Rev. B* **1975**, *11*, 600e12. [\[CrossRef\]](#)
56. Fantauzzi, M.; Elsener, B.; Atzei, D.; Rigoldi, A.; Rossi, A. Exploiting XPS for the identification of sulfides and polysulfides. *RSC Adv.* **2015**, *5*, 75953–75963. [\[CrossRef\]](#)
57. Predoi, S.A.; Ciobanu, S.C.; Chifiriuc, C.M.; Iconaru, S.L.; Predoi, D.; Negrila, C.C.; Marinas, I.C.; Raaen, S.; Rokosz, K.; Motelica-Heino, M. Sodium bicarbonate-hydroxyapatite used for removal of lead ions from aqueous solution. *Ceram. Int.* **2024**, *50*, 1742–1755. [\[CrossRef\]](#)
58. Predoi, D.; Ciobanu, C.S.; Iconaru, S.L.; Predoi, S.A.; Chifiriuc, M.C.; Raaen, S.; Badea, M.L.; Rokosz, K. Impact of Gamma Irradiation on the Properties of Magnesium-Doped Hydroxyapatite in Chitosan Matrix. *Materials* **2022**, *15*, 5372. [\[CrossRef\]](#)
59. Yamasaki, Y.; Yoshida, Y.; Okazaki, M.; Shimazu, A.; Kubo, T.; Akagawa, Y.; Uchida, T. Action of FGMgCO₃Ap-collagen composite in promoting bone formation. *Biomaterials* **2003**, *24*, 4913–4920. [\[CrossRef\]](#)
60. Yamasaki, Y.; Yoshida, Y.; Okazaki, M.; Shimazu, A.; Uchida, T.; Kubo, T.; Akagawa, Y.; Hamada, Y.; Takahashi, J.; Matsuura, N. Synthesis of functionally graded MgCO₃ apatite accelerating osteoblast adhesion. *J. Biomed. Mater. Res.* **2002**, *62*, 99–105. [\[CrossRef\]](#) [\[PubMed\]](#)
61. Landi, E.; Logroscino, G.; Proietti, L.; Tampieri, A.; Sandri, M.; Sprio, S. Biomimetic Mg-substituted hydroxyapatite: From synthesis to in vivo behaviour. *J. Mater. Sci. Mater. Med.* **2008**, *19*, 239–247. [\[CrossRef\]](#)
62. Iconaru, S.L.; Ciobanu, C.S.; Predoi, G.; Rokosz, K.; Chifiriuc, M.C.; Bleotu, C.; Stanciu, G.; Hristu, R.; Raaen, S.; Raita, S.M.; et al. Biological and Physico-Chemical Properties of Composite Layers Based on Magnesium-Doped Hydroxyapatite in Chitosan Matrix. *Micromachines* **2022**, *13*, 1574. [\[CrossRef\]](#)

63. Fox, C.; Ramsoomair, D.; Carter, C. Magnesium: Its proven and potential clinical significance. *South Med. J.* **2001**, *94*, 1195–1201. [CrossRef]
64. Geng, F.; Tan, L.L.; Jin, X.X.; Yang, J.Y.; Yang, K. The preparation, cytocompatibility, and in vitro biodegradation study of pure β -TCP on magnesium. *J. Mater. Sci. Mater. Med.* **2009**, *20*, 1149–1157. [CrossRef]
65. ISO 10993-1:2018; Biological Evaluation of Medical Devices—Part 1: Evaluation and Testing within a Risk Management Process. ISO: Geneva, Switzerland, 2018. Available online: <https://www.iso.org/standard/68936.html> (accessed on 3 May 2024).
66. Wątroba, M.; Bednarczyk, W.; Szewczyk, P.K.; Kawalko, J.; Mech, K.; Grünwald, A.; Unalan, I.; Taccardi, N.; Boelter, G.; Banzhaf, M.; et al. In vitro cytocompatibility and antibacterial studies on biodegradable Zn alloys supplemented by a critical assessment of direct contact cytotoxicity assay. *J. Biomed. Mater. Res. B Appl. Biomater.* **2023**, *111*, 241–260. [CrossRef]
67. Sukumaran, A.; Sweet, V.K.; Vikas, B.; Joseph, B. Cytotoxicity and Cell Viability Assessment of Biomaterials. In *Cytotoxicity—Understanding Cellular Damage and Response*; Sukumaran, A., Mahmoud, A.M., Eds.; IntechOpen: London, UK, 2023. [CrossRef]
68. Alshemary, A.Z.; Akram, M.; Goh, Y.F.; Tariq, U.; Butt, F.K.; Abdolahi, A.; Hussain, R. Synthesis, characterization, in vitro bioactivity and antimicrobial activity of magnesium and nickel doped silicate hydroxyapatite. *Ceram. Int.* **2015**, *41*, 11886–11898. [CrossRef]
69. Predoi, D.; Ciobanu, C.S.; Iconaru, S.L.; Raaen, S.; Badea, M.L.; Rokosz, K. Physicochemical and Biological Evaluation of Chitosan-Coated Magnesium-Doped Hydroxyapatite Composite Layers Obtained by Vacuum Deposition. *Coatings* **2022**, *12*, 702. [CrossRef]
70. Veljovic, D.; Matic, T.; Stamenic, T.; Kojic, V.; Dimitrijevic-Brankovic, S.; Lukic, M.J.; Jevtic, S.; Radovanovic, Z.; Petrovic, R.; Janackovic, D. Mg/Cu co-substituted hydroxyapatite—Biocompatibility, mechanical properties and antimicrobial activity. *Ceram. Int.* **2019**, *45*, 22029–22039. [CrossRef]
71. Demishtein, K.; Reifen, R.; Shemesh, M. Antimicrobial Properties of Magnesium Open Opportunities to Develop Healthier Food. *Nutrients* **2019**, *11*, 2363. [CrossRef] [PubMed]
72. Pathania, D.; Kumar, S.; Thakur, P. Essential oil-mediated biocompatible magnesium nanoparticles with enhanced antibacterial, antifungal, and photocatalytic efficacies. *Sci. Rep.* **2022**, *12*, 11431. [CrossRef]
73. Hans, S.; Fatima, Z.; Ahmad, A.; Hameed, S. Magnesium impairs Candida albicans immune evasion by reduced hyphal damage, enhanced α -glucan exposure and altered vacuole homeostasis. *PLoS ONE* **2022**, *17*, e0270676. [CrossRef]
74. de Marco, B.A.; Natori, J.S.H.; Fanelli, S.; Tótolí, E.G.; Salgado, H.R.N. Characteristics, Properties and Analytical Methods of Amoxicillin: A Review with Green Approach. *Crit. Rev. Anal. Chem.* **2017**, *47*, 267–277. [CrossRef]
75. Todd, P.A.; Benfield, P. Amoxicillin/Clavulanic Acid. *Drugs* **1990**, *39*, 264–307. [CrossRef]
76. Bankole, O.M.; Ojibola, K.I.; Adanlawo, O.S.; Adesina, A.O.; Lawal, I.O.; Ogunlaja, A.S.; Achadu, O.J. Amoxicillin Encapsulation on Alginate/Magnetite Composite and Its Antimicrobial Properties Against Gram-Negative and Positive Microbes. *BioNanoScience* **2022**, *12*, 1136–1149. [CrossRef]
77. Weber, D.J.; Tolkoff-Rubin, N.E.; Rubin, R.H. Amoxicillin and Potassium Clavulanate: An Antibiotic Combination Mechanism of Action, Pharmacokinetics, Antimicrobial Spectrum, Clinical Efficacy and Adverse Effects. *Pharmacotherapy* **1984**, *4*, 122–136. [CrossRef] [PubMed]
78. Güncüm, E.; Işıklan, N.; Anlaş, C.; Ünal, N.; Bulut, E.; Bakirel, T. Development and characterization of polymeric-based nanoparticles for sustained release of amoxicillin—An antimicrobial drug. *Artif. Cells Nanomed. Biotechnol.* **2018**, *46* (Suppl. 2), 964–973. [CrossRef]
79. Amin, A.S.; El-Ansary, A.L.; Issa, Y.M. Colorimetric determination of amoxicillin in pure form and in pharmaceutical preparations. *Talanta* **1994**, *41*, 691–694. [CrossRef] [PubMed]
80. Kurtz, G.S.; Ribeiro, F.M.; Vicente, F.L.; Struchiner, C.J. Development and validation of limited-sampling strategies for predicting amoxicillin pharmacokinetic and pharmacodynamics parameters. *Antimicrob. Agents Chemother.* **2001**, *45*, 3029–3036. [CrossRef] [PubMed]
81. Neu, H.C. Antimicrobial activity and human pharmacology of amoxicillin. *J. Infect. Diseases* **1974**, *129*, 123–131. [CrossRef]
82. Enan, E.T.; Ashour, A.A.; Basha, S.; Felemban, N.H.; El-Rab, S.M.G. Antimicrobial activity of biosynthesized silver nanoparticles, amoxicillin, and glass-ionomer cement against Streptococcus mutans and Staphylococcus aureus. *Nanotechnology* **2021**, *32*, 5101. [CrossRef]
83. Bigi, A.; Foresti, E.; Gregorini, R.; Ripamonti, A.; Roveri, N.; Shah, J.S. The role of magnesium on the structure of biological apatites. *Calcif. Tissue Intern.* **1992**, *50*, 439–444. [CrossRef]
84. Ballardini, A.; Montesi, M.; Panseri, S.; Vandini, A.; Balboni, P.G.; Tampieri, A.; Sprio, S. New hydroxyapatite nanophases with enhanced osteogenic and anti-bacterial activity. *J. Biomed. Mater. Res. A* **2018**, *106*, 521–530. [CrossRef]
85. Cazalbou, S.; Eichert, D.; Ranz, X.; Drouet, C.; Combes, C.; Harmand, M.F.; Rey, C. Ion exchanges in apatites for biomedical application. *J. Mater. Sci. Mater. Med.* **2005**, *16*, 405–409. [CrossRef]
86. Boanini, E.; Gazzano, M.; Bigi, A. Ionic substitutions in calcium phosphates synthesized at low temperature. *Acta Biomater.* **2010**, *6*, 1882–1894. [CrossRef]
87. Xiong, G.; Nie, Y.; Ji, D.; Li, J.; Li, C.; Li, W.; Zhu, Y.; Luo, H.; Wan, Y. Characterization of biomedical hydroxyapatite/magnesium composites prepared by powder metallurgy assisted with microwave sintering. *Curr. Appl. Phys.* **2016**, *16*, 830–836. [CrossRef]
88. Staiger, M.P.; Pietak, A.M.; Huadmai, J.; Dias, G. Magnesium and its alloys as orthopedic biomaterials: A review. *Biomaterials* **2006**, *27*, 1728–1734. [CrossRef]

89. Heimann, R.B. Osseointegrative and Corrosion-Inhibiting Plasma-Sprayed Calcium Phosphate Coatings for Metallic Medical Implants. *Metals* **2017**, *7*, 468. [[CrossRef](#)]
90. Heimann, R.B.; Lehmann, H.D. Recent Research and Patents on Controlling Corrosion of Bioresorbable Mg Alloy Implants: Towards Next Generation Biomaterials. *Recent Pat. Mater. Sci.* **2017**, *10*, 2–19. [[CrossRef](#)]
91. Cizek, J.; Matejcek, J. Medicine Meets Thermal Spray Technology: A Review of Patents. *J. Therm. Spray Technol.* **2018**, *27*, 1251–1279. [[CrossRef](#)]
92. Costescu, A.; Ciobanu, C.S.; Iconaru, S.L.; Ghita, R.V.; Chifiriuc, C.M.; Marutescu, L.G.; Predoi, D. Fabrication, characterization, and antimicrobial activity, evaluation of low silver concentrations in silver-doped hydroxyapatite nanoparticles. *J. Nanomater.* **2013**, *2013*, 194854. [[CrossRef](#)]
93. Zhang, E.; Xu, L.; Yu, G.; Pan, F.; Yang, K. In vivo evaluation of biodegradable magnesium alloy bone implants in the first 6 months implantation. *J. Biomed. Mater. Res. A* **2009**, *90*, 882–893. [[CrossRef](#)] [[PubMed](#)]
94. Predoi, D.; Iconaru, S.L.; Ciobanu, S.C.; Predoi, S.-A.; Buton, N.; Megier, C.; Beuran, M. Development of Iron-Doped Hydroxyapatite Coatings. *Coatings* **2021**, *11*, 186. [[CrossRef](#)]
95. Ciobanu, C.S.; Predoi, D.; Iconaru, S.L.; Predoi, M.V.; Rokosz, K.; Raaen, S.; Negrila, C.C.; Buton, N.; Ghegoiu, L.; Badea, M.L. Physico-Chemical and Biological Features of Fluorine-Substituted Hydroxyapatite Suspensions. *Materials* **2024**, *17*, 3404. [[CrossRef](#)]
96. Predoi, S.A.; Ciobanu, S.C.; Chifiriuc, M.C.; Motelica-Heino, M.; Predoi, D.; Iconaru, S.L. Hydroxyapatite Nanopowders for Effective Removal of Strontium Ions from Aqueous Solutions. *Materials* **2023**, *16*, 229. [[CrossRef](#)]
97. Predoi, S.-A.; Ciobanu, C.S.; Motelica-Heino, M.; Chifiriuc, M.C.; Badea, M.L.; Iconaru, S.L. Preparation of Porous Hydroxyapatite Using Cetyl Trimethyl Ammonium Bromide as Surfactant for the Removal of Lead Ions from Aquatic Solutions. *Polymers* **2021**, *13*, 1617. [[CrossRef](#)] [[PubMed](#)]
98. Gross, K.A.; Komarovska, L.; Viksna, A. Efficient zinc incorporation in hydroxyapatite through crystallization of an amorphous phase could extend the properties of zinc apatites. *J. Australas. Ceram. Soc.* **2013**, *49*, 129–135.
99. Rusu, V.M.; Ng, C.H.; Wilke, M.; Tiersch, B.; Fratzl, P.; Peter, M.G. Size- controlled hydroxyapatite nanoparticles as self-organized organic–inorganic composite materials. *Biomater.* **2005**, *26*, 5414–5424. [[CrossRef](#)] [[PubMed](#)]
100. Miyaji, F.; Kono, Y.; Suyama, Y. Formation and structure of zinc-substituted calcium hydroxyapatite. *Mater. Res. Bull.* **2005**, *40*, 209–220. [[CrossRef](#)]
101. Miyaji, F.; Kono, Y.; Suyama, Y. Synthesis of ZnO nanoparticles and evaluation of antioxidant and cytotoxic activity. *Colloids Surf. B Biointerfaces* **2013**, *111*, 556–560. [[CrossRef](#)]
102. Predoi, D.; Iconaru, S.L.; Predoi, M.V.; Motelica-Heino, M.; Guegan, R.; Buton, N. Evaluation of Antibacterial Activity of Zinc-Doped Hydroxyapatite Colloids and Dispersion Stability Using Ultrasounds. *Nanomaterials* **2019**, *9*, 515. [[CrossRef](#)]

Disclaimer/Publisher’s Note: The statements, opinions and data contained in all publications are solely those of the individual author(s) and contributor(s) and not of MDPI and/or the editor(s). MDPI and/or the editor(s) disclaim responsibility for any injury to people or property resulting from any ideas, methods, instructions or products referred to in the content.



Article

Antibacterial and Antitumoral Potentials of Phytosynthesized Silver/Silver Oxide Nanoparticles Using Tomato Flower Waste

Simona Marcu Spinu ^{1,*}, Mihaela Dragoi Cudalbeanu ^{1,*}, Ionela Avram ², Radu Claudiu Fierascu ^{3,4}, Petronela Mihaela Rosu ⁵, Ana-Maria Morosanu ⁶, Carmen Laura Cimpeanu ^{1,*}, Narcisa Babeanu ⁷ and Alina Ortan ¹

- ¹ Faculty of Land Reclamation and Environmental Engineering, University of Agronomic Sciences and Veterinary Medicine of Bucharest, 59 Marasti Blvd., 011464 Bucharest, Romania; simona.spinu@fifim.ro (S.M.S.); alina.ortan@fifim.ro (A.O.)
 - ² Department of Genetics, University of Bucharest, 1-3 Aleea Portocalelor, 060101 Bucharest, Romania; ionela.avram@unibuc.ro
 - ³ National Institute for Research & Development in Chemistry and Petrochemistry–ICECHIM Bucharest, 202 Splaiul Independenței, 060021 Bucharest, Romania; fierascu.radu@icechim.ro
 - ⁴ Faculty of Chemical Engineering and Biotechnology, National University of Science and Technology Politehnica Bucharest, 1-7 Gheorghe Polizu St., 011061 Bucharest, Romania
 - ⁵ Faculty of Veterinary Medicine, University of Agronomic Sciences and Veterinary Medicine of Bucharest, 59 Marasti Blvd., 011464 Bucharest, Romania; petronela.rosu@fmvb.usamv.ro
 - ⁶ Institute of Biology Bucharest, Romanian Academy, 060031 Bucharest, Romania; anamaria.morosanu@ibiol.ro
 - ⁷ Faculty of Biotechnologies, University of Agronomic Sciences and Veterinary Medicine of Bucharest, 59 Marasti Blvd., 011464 Bucharest, Romania; narcisa.babeanu@usamv.ro
- * Correspondence: mcudalbeanu@gmail.com (M.D.C.); carmencimpeanu@yahoo.com (C.L.C.)



Citation: Marcu Spinu, S.; Dragoi Cudalbeanu, M.; Avram, I.; Fierascu, R.C.; Rosu, P.M.; Morosanu, A.-M.; Cimpeanu, C.L.; Babeanu, N.; Ortan, A. Antibacterial and Antitumoral Potentials of Phytosynthesized Silver/Silver Oxide Nanoparticles Using Tomato Flower Waste. *Int. J. Mol. Sci.* **2024**, *25*, 9871. <https://doi.org/10.3390/ijms25189871>

Academic Editors: Chun-Tao Che and Hongjie Zhang

Received: 19 August 2024

Revised: 6 September 2024

Accepted: 10 September 2024

Published: 12 September 2024



Copyright: © 2024 by the authors. Licensee MDPI, Basel, Switzerland. This article is an open access article distributed under the terms and conditions of the Creative Commons Attribution (CC BY) license (<https://creativecommons.org/licenses/by/4.0/>).

Abstract: This study presents the phytosynthesis of silver-based nanoparticles using tomato flower waste extracts for the first time in the literature. The determination of total polyphenolic and flavonoid contents in the extracts showed high gallic acid equivalents (6436–8802 mg GAE/kg dm) and high quercetin equivalents (378–633 mg QE/kg dm), respectively, dependent on the extraction method. By the Ultra Performance Liquid Chromatography technique, 14 polyphenolic compounds were identified and quantified in the tomato flower waste extracts. The abundant phenolic compounds were caffeic acid (36,902–32,217 mg/kg) and chlorogenic acid (1640–1728 mg/kg), and the abundant flavonoid compounds were catechin (292–251 mg/kg) and luteolin (246–108 mg/kg). Transmission electron microscopy of the nanoparticles revealed a particle size range of 14–40 nm. Fourier Transform infrared spectroscopy and X-ray diffraction studies confirmed the phytosynthesis of the silver/silver oxide nanoparticles. These findings hold significant results for the antibacterial and antitumoral potential applications of the obtained nanoparticles, opening new areas for research and development and inspiring further exploration. The impact of this research on the field of metallic nanoparticle phytosynthesis is substantial, as it introduces a novel approach and could lead to significant advancements in the field.

Keywords: tomato waste; phytochemical profile; metallic nanoparticles; pathogenic bacteria; HeLa tumor cells; HT29 tumor cells

1. Introduction

Tomatoes, globally distributed plants, have origins in America (the Aztec city of Tenochtitla—now Mexico City) and have been imported to Europe by Spanish colonists since the 16th century [1]. Today, tomatoes are considered fruits according to botanical classifications, and vegetables according to culinary classifications, being cultivated both in greenhouses and open agricultural lands. Although tomatoes can be found on the market in the form of fresh tomatoes, they are also available in a wide variety of by-products (dried tomatoes, canned tomatoes, tomato pastes, ketchup, tomato purees, tomato juice, etc.).

Globally, between 2018 and 2022, an average of 4,972,265.6 ha of tomato areas were cultivated per year, with an average of 184,940,640.7 tons of tomatoes produced per year [2]. In Europe, 415,163.4 ha of tomato areas were cultivated on average per year, and 22,833,989.89 tons of tomatoes were produced on average per year [2]. The production of tomatoes, at the European level, increased in 2021, followed by a significant decrease in 2022. The European countries with the highest production of tomatoes are Turkey, Italy, and Spain, which are part of the top 10 producing countries at the global level. In Romania, between 2018 and 2022, an average of 438,686 tons of tomatoes were produced per year, and 19,904 ha of land was cultivated [2].

Considering the high production of tomatoes, a significant amount of vegetable waste results from both tomato crops and post-harvest industrial processing. The aerial biomass formed by leaves, suckers, bunches, stems, and dried flowers after the ripening of the fruit constitutes vegetable agricultural waste. The waste from tomato crops that results at the end of the cultivation cycle has become the subject of numerous studies aimed at the valorization of this important resource. For example, Añibarro-Ortega et al. (2020) recently studied the antioxidant and antimicrobial properties of tomato crop residues resulting from cuttings and biomass left after harvesting to point out the direction of their reuse in the agri-food sector [3]. Many studies have proven that through anaerobic digestion of tomato leaves and stems, pollution can be effectively reduced and bioenergy, i.e., biogas, can be produced [4–6]. Moreover, vegetable tomato plant waste is a potential sugar source for biorefineries, an aspect demonstrated by alkali-catalyzed extrusion methods followed by enzymatic hydrolysis [7], because of the high content of carbohydrates, lignin (acid-insoluble and acid-soluble), and ash. Carbohydrates, saponins, tannins, glycosides, phenols, coumarins, alkaloids, flavonoids, resins, and terpenoids are the main biologically active classes of compounds present in both tomato leaves and stems [8]. For maximum utilization of tomato plant waste, they were used as a growing medium [9] and as a substrate (compost) [10,11], indicating favorable results.

A tomato plant has small yellow flowers in the form of clusters, which contain pistils and stamens (male and female reproductive organs). The tomato flower is the key element in the formation of the fruit, and for the maximum production of tomatoes, as few aborted or unfertilized flowers as possible are needed to minimize negative economic effects. In the case of a tomato plant, whose flowers are hermaphrodite, pollination is carried out predominantly with its own pollen and can take place on the same flower as soon as the pollen has been formed. In greenhouses, the pollination of tomato flowers can be achieved by various methods such as insect pollination, artificial pollination, hormonal pollination, and advanced techniques using drones or robots [12].

Metal nanoparticles continue to interest researchers because of their diverse properties [13–15]. There are various studies that attest to the beneficial effect of metal NPs (copper [16,17], zinc [18–20], silver [21–27], selenium [28,29], and iron [30]) in improving tomato plant growth and yield, as well as increasing life span. At the same time, there are various studies that prove the bio-medical applicability of metal NPs phytosynthesized using different parts of tomato plants such as leaves [31,32], fruits [33–39], seeds [36], and entire plants [40]. In these studies, biological activities such as antibacterial, antifungal, antitumoral, antioxidant, and antidiabetic are highlighted.

Silver and silver oxide nanoparticles are known for their unique properties, being used in numerous fields including electrochemistry and electronics (they improve the efficiency and functionality of devices), catalysis (their ability to oxidize makes them valuable for various chemical reactions and industrial processes), energy storage systems and renewable energy (sensors, photovoltaic cells), and optics (integral switching devices and optical data storage systems). In the medical and pharmaceutical field, they can be functionalized to attach to specific biological molecules, chemotherapy, and antibiotic treatment, and in cosmetics, their beneficial properties are used in skin care products [41–46].

The present study proposes a new approach for the valorization of tomato waste produced at the end of the crop cycle, in particular, the dried tomato flowers that remain

after the ripening of the fruit, for the phytosynthesis of silver oxide nanoparticles with therapeutic potential. To date, no studies have focused on the valorization of dried tomato flowers, harvested after the fruit has reached maturity, to our knowledge. In addition, no studies have demonstrated the biological activities of silver-based nanoparticles phytosynthesized using tomato flower waste extracts, specifically from dried tomato flowers left at the end of the development and ripening cycle of the fruits. Therefore, the aim of this study was to demonstrate the therapeutic potential (antibacterial and antitumoral) of phytosynthesized silver-based nanoparticles using tomato flower waste extract.

2. Results

2.1. Effect of Extraction Method on Extract Yield

The tomato plant waste, i.e., dried flowers left after the ripening cycle of *Lycopersicon esculentum* (Cheramy RZ F1 hybrid) fruit, was oven-dried and then subjected to extraction (Figure 1).



Figure 1. Tomato flower waste collected from the University of Agronomic Sciences and Veterinary Medicine of Bucharest (USAMV) Research Greenhouse.

Following the extraction of the plant material through the three selected methods, ultrasound-assisted extraction (UAE), microwave-assisted extraction (MAE), and cascade extraction (CASE), the extraction yield of tomato flower waste (TFW) was determined (Table 1). All the investigated extraction methods showed high values of TFW, varying between approx. 20% for TFWCAS and approx. 27% for TFWMW.

Table 1. Sample coding and extraction yield of tomato flower waste.

Sample Coding	Extraction Method	Yield (%)
TFWUS	UAE	22.57 ± 0.28^b
TFWMW	MAE	26.92 ± 0.92^a
TFWCAS	CASE	20.56 ± 0.49^c

The results are expressed as the average of three samples (mean \pm SD). TFWUS—tomato flower waste extract obtained by UAE, TFWMW—tomato flower waste extract obtained by MAE, and TFWCAS—tomato flower waste extract obtained by CASE. The superscript letter within the same column indicates significant differences detected among the studied samples using ANOVA ($p < 0.05$).

2.2. Effect of the Extraction Method on the Total Polyphenolic Content (TPC) and Total Flavonoid Content (TFC)

Tomato flower waste extracts revealed a significant total polyphenolic content (TPC, Figure 2a) ranging from approx. 6436 mg GAE/kg dm (TFWCAS) up to 8802 mg GAE/kg dm (TFWMW). The highest value was obtained for TFWMW, which is not statistically significant compared to TFWUS, but it was statistically different compared with TFWCAS.

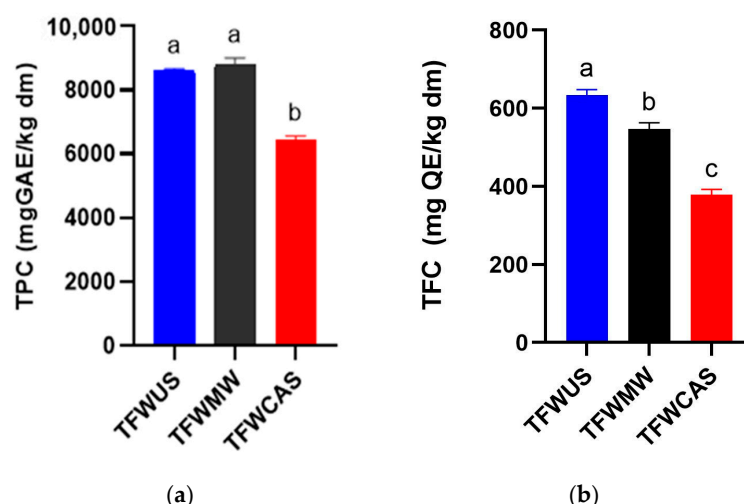


Figure 2. Total phenolic content (a) and total flavonoid content (b) of tomato flower waste extracts obtained by MAE, UAE, and CASE. The letters a–c indicate statistically significant differences detected by ANOVA ($p < 0.05$).

Regarding total flavonoid content (TFC), the TFW extracts revealed values around 378 mg QE/kg dm (TFWCAS) and 633 mg QE/kg dm (TFWUS), as shown in Figure 2b. There were statistically significant differences in the TFC obtained from TFW using all the extraction methods, confirming the influence of the extraction method on both TPC and TFC.

2.3. Quantitative Analysis of Polyphenolic Compounds Present in Tomato Flower Waste Extracts by UPLC

The polyphenolic compounds in all TFW extracts, TFWUS, TFWMW, and TFWCAS, were identified by the Ultra Performance Liquid Chromatography (UPLC) system. Figure 3 shows the UPLC chromatogram of TFW extracts detected at 280 nm, 320 nm, and 370 nm. The polyphenolic compounds detected were initially compared with the Photodiode array (PDA) spectra of targeted reference compounds. The targeted reference polyphenolic compounds were gallic acid, caffeic acid, chlorogenic acid, catechin, epicatechin, p-coumaric acid, ferulic acid, isoquercetin, rosmarinic acid, naringin, myricetin, luteolin, quercetin, and naringenin. A total of 14 polyphenolic compounds were identified in the TFW extracts (Table 2).

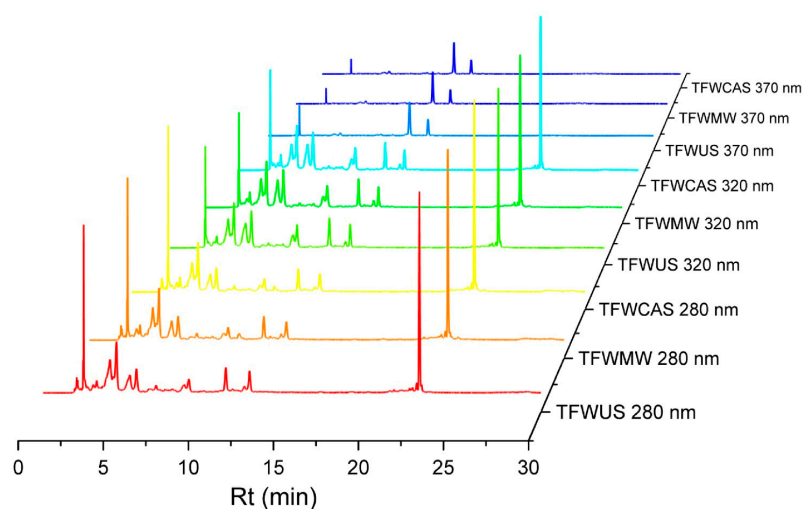


Figure 3. Chromatogram of tomato flower waste extracts obtained by different extraction methods. US, ultrasonic-assisted extraction; MW, microwave-assisted extraction; and CAS, cascade extraction.

Table 2. Quantitative description of the polyphenolic compounds in tomato flower waste extracts by UPLC.

No.	Compound Name	RT (min)	λ_{\max} (nm)	TFWUS (mg/kg)	TFWMW (mg/kg)	TFWCAS (mg/kg)
1	Gallic acid	3.07	280	260.14 ± 2.90 ^b	324.99 ± 23.85 ^a	198.26 ± 1.79 ^c
2	Chlorogenic acid	5.77	320	1640.24 ± 71.77 ^a	106.08 ± 0.57 ^b	1728.51 ± 52.01 ^a
3	Caffeic acid	8.33	320	36,902.34 ± 20.10 ^b	38,720.75 ± 65.48 ^a	32,217.04 ± 30.03 ^c
4	p-Coumaric acid	11.08	320	408.16 ± 22.52 ^b	469.27 ± 2.72 ^a	401.37 ± 7.63 ^b
5	Ferulic acid	12.47	320	338.41 ± 18.14 ^a	367.24 ± 16.64 ^a	329.92 ± 22.79 ^a
6	Rosmarinic acid	15.98	320	21.32 ± 0.38 ^b	27.01 ± 2.39 ^a	22.44 ± 2.25 ^{ab}
7	Catechin	6.29	280	291.98 ± 9.92 ^a	287.49 ± 5.19 ^a	253.21 ± 0.73 ^b
8	Epicatechin	7.86	280	78.11 ± 1.75 ^b	57.95 ± 2.72 ^c	77.10 ± 0.46 ^a
9	Isoquercetin	11.94	370	61.61 ± 4.04 ^a	18.97 ± 0.90 ^b	15.50 ± 1.48 ^b
10	Naringin	13.70	280	45.37 ± 1.33 ^a	28.05 ± 1.54 ^b	26.51 ± 2.89 ^b
11	Myricetin	16.68	370	47.37 ± 0.28 ^b	58.94 ± 0.97 ^a	47.21 ± 0.43 ^b
12	Luteolin	22.20	370	245.95 ± 29.24 ^a	105.07 ± 2.87 ^b	107.99 ± 1.59 ^b
13	Quercetin	22.32	370	62.13 ± 0.49 ^c	84.69 ± 2.55 ^a	67.48 ± 1.82 ^b
14	Naringenin	23.83	280	33.29 ± 0.46 ^c	69.41 ± 2.76 ^a	47.90 ± 1.44 ^b

RT—retention time. Superscript letters within the same row indicate significant differences detected among the studied samples using ANOVA ($p < 0.05$).

The total content of the identified phenolic acids was approx. 39,571 mg/kg, 40,015 mg/kg, and 34,898 mg/kg, in the case of the TFWUS, TFWMW, and TFWCAS extracts, respectively. The compound with the highest content was caffeic acid (over 38,720 mg/kg—TFWMW, 36,902 mg/kg—TFWUS, and 32,217 mg/kg—TFWCAS), followed by chlorogenic acid (1728 mg/kg—TFWCAS and 1640 mg/kg—TFWUS). In comparison with the UAE and CASE extractions, minimal amounts of chlorogenic acid were found in the MAE extraction. The TFWMW extract contained only 106 mg/kg of chlorogenic acid.

The total content of the identified flavonoids was approx. 866 mg/kg, 711 mg/kg, and 643 mg/kg, in the case of TFWUS, TFWMW, and TFWCAS, respectively. The highest content was found to be catechin (approximately 292 mg/kg for TFWUS, 288 mg/kg for TFWMW, and 253 mg/kg for TFWCAS), followed by luteolin, registering approximately 246 mg/kg in the TFWUS extract, 108 mg/kg for TFWCAS, and 105 mg/kg for TFWMW. Similar results were observed for the flavonoids isoquercetin (61.61 mg/kg—TFWUS, 18.97 mg/kg—TFWMW, and 15.50 mg/kg—TFWCAS) and naringin (45.37 mg/kg—TFWUS, 28.05 mg/kg—TFWMW, and 26.51 mg/kg—TFWCAS). Similar to chlorogenic acid, the flavonoid epicatechin minimum content was found in the MAE extraction (TFWMW—57.95 mg/kg, TFWUS—78.11 mg/kg, and TFWCAS—77.10 mg/kg).

Additionally, the TFWMW extract contained the following compounds: gallic acid, p-coumaric acid, ferulic acid, rosmarinic acid, myricetin, quercetin, and naringenin, in slightly higher concentrations than the TFWUS and TFWCAS extracts. The CASE extraction revealed the lowest content of the identified polyphenolic compounds using the UPLC technique.

2.4. Evaluation of the Antioxidant Activity of TFW Extracts

In the present study, the antioxidant activity of TFW extracts was evaluated by three different methods (DPPH, ABTS, and FRAP). The studied TFW extracts demonstrated a high capacity to scavenge the considered free radicals (Table 3).

Table 3. Antioxidant potential of tomato flower waste extracts.

Sample	DPPH (mg AAE/kg dm)	ABTS (mg AAE/kg dm)	FRAP (mg AAE/kg dm)
TFWUS	522.89 ± 1.83 ^b	16,707.68 ± 83.78 ^a	5328.47 ± 67.46 ^b
TFWMW	655.87 ± 0.05 ^a	16,783.85 ± 11.97 ^a	5880.65 ± 83.16 ^a
TFWCAS	518.97 ± 1.83 ^b	15,379.02 ± 95.75 ^b	4594.21 ± 98.35 ^c

The results are expressed as the average of three samples (mean ± SD). The superscript letters within the same column indicate significant differences among the studied samples ($p < 0.05$); dm = dry matter, AAE = Ascorbic Acid Equivalent.

The results of the DPPH assay test, ranging from approx. 519 to 655 mg Ascorbic Acid Equivalent (AAE) per kg of dry matter (dm), showed differences in the antioxidant capacity of the investigated samples, depending on the extraction method used. The DPPH assay results demonstrated significant antioxidant activity of the dried TFW samples.

For ABTS scavenging activity, the results ranged from 15,379 to 16,783 AAE/kg dm. TFWCAS led to statistically significantly lower results than TFWMW. Regarding the FRAP assay, the antioxidant potential ranged from 4594 mg AAE/kg dm for TFWCAS to 5880 mg AAE/kg dm for TFWMW.

After analyzing the correlations among TPC, TFC, and the antioxidant potential tested by the DPPH method, using the Pearson correlation coefficient, direct and indirect relationships among these parameters were observed, as illustrated in the Figure 4.

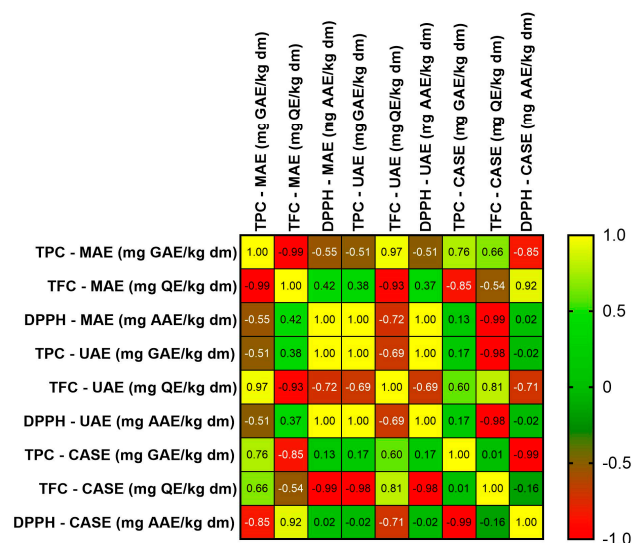


Figure 4. Correlation coefficient matrix among TPC, TFC, and the DPPH assay.

Strong positive correlations were identified between DPPH assay values and TPC (Pearson correlation coefficient = 1.00, $p < 0.01$) in the case of the TFWUS extract. A strong negative correlation was found between TFC and TPC (Pearson correlation coefficient = -0.99) in the case of the TFWMW extract and between DPPH assay values and TPC (Pearson correlation coefficient = -0.99) for the TFWCAS extract.

2.5. Silver-Based Nanoparticles

The phytosynthesis of silver-based nanoparticles was performed using TFW extracts, which served as both reducing and capping agents.

The yield of NPs is presented in Table 4. The TFWMW-NPs sample exhibited the highest yield of NPs, i.e., a yield of 34.8%, followed by the TFWCAS-NPs sample, which exhibited a yield of 32.2%. The TFWUS-NPs sample obtained a lower yield of NPs (29.3%).

Table 4. The yield of NPs formed by tomato flower waste extracts.

Sample Cod	Extract Cod	Extraction Method	Yield (%)
TFWUS-NPs	TFWUS	UAE	29.26 ^c
TFWMW-NPs	TFWMW	MAE	34.81 ^a
TFWCAS-NPs	TFWCAS	CASE	32.22 ^b

UAE—ultrasound-assisted extraction, MAE—microwave-assisted extraction, CASE—cascade extraction. TFW—tomato flower waste. Extract—AgNO₃ ratio 1:10 (v/v), extract concentration 20 mg/mL, AgNO₃ concentration 5 mM, synthesis temperature 70 °C, time 120 min. The superscript letters within the same column indicate significant differences detected among the studied samples using ANOVA ($p < 0.05$).

2.6. Characterization of Silver-Based Nanoparticles

2.6.1. Preliminary Evaluation by UV-Vis Spectrometry

The phytosynthesis of nanoparticles was preliminarily evaluated by UV-Vis spectrometry. This helped to identify the formation of metal nanoparticles because the phenomenon of surface plasmon resonance leads to the appearance of specific peaks of nanoparticles in various states including metal oxides, zero-valent metals, etc. The obtained spectra are presented in Figure 5.

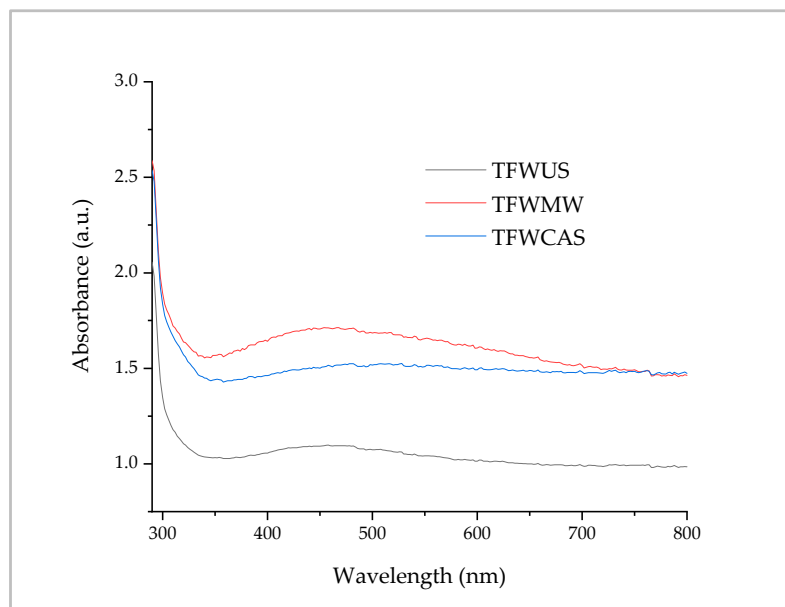


Figure 5. Absorption spectra of the phytosynthesized NPs.

The UV-Vis absorption spectra revealed a relatively low-intensity shoulder in the region of interest (400–500 nm) where AgNPs present specific peaks. The low intensity and the insufficient definition of the peak could be attributed to the presence of silver oxide in the samples (a species that does not exhibit specific maxima in this region).

2.6.2. FTIR Spectroscopy

FTIR spectroscopy analysis was used to compare the TFW extracts (before the reaction, without AgNO_3) with the NPs formed (after the reaction with AgNO_3), and the obtained spectra are presented in Figure 6.

Both FTIR spectra (TFW extracts and NPs) showed two significant stretching bands at $3316\text{--}3347\text{ cm}^{-1}$ (due to the N–H stretching vibration of amines or the O–H stretching vibration of polymeric hydroxyl groups, which are located in close proximity) and at $1635\text{--}1650\text{ cm}^{-1}$ (due to the C=C and C–C stretching vibrations of aromatic rings). The stretching vibrations of Ag–Ag, Ag–O–Ag, Ag–O, and O–Ag–O were observed at peaks between 400 and 600 cm^{-1} (Figure 6b).

Figure 6a shows the absorption spectra of TFW extracts obtained in the range of $4000\text{--}400\text{ cm}^{-1}$. In the region of $2978\text{--}2890\text{ cm}^{-1}$, the $-\text{CH}$, $-\text{CH}_2$, and $-\text{CH}_3$ stretching vibrations are derived from carbohydrates and sugars present in the TFW extracts. In addition, the phenolic C–O stretching vibration was observed at 1276 cm^{-1} . The C–N bond of the amine or the C–O bond of the primary alcohol is caused by stretching vibrations at 1044 cm^{-1} . The peaks between 636 and 1454 cm^{-1} are attributed to C=C–C aromatic ring stretching (1454 cm^{-1}) and several aromatic out-of-plane bending C–H ($636\text{--}948\text{ cm}^{-1}$) and in-plane bending ($948\text{--}1276\text{ cm}^{-1}$).

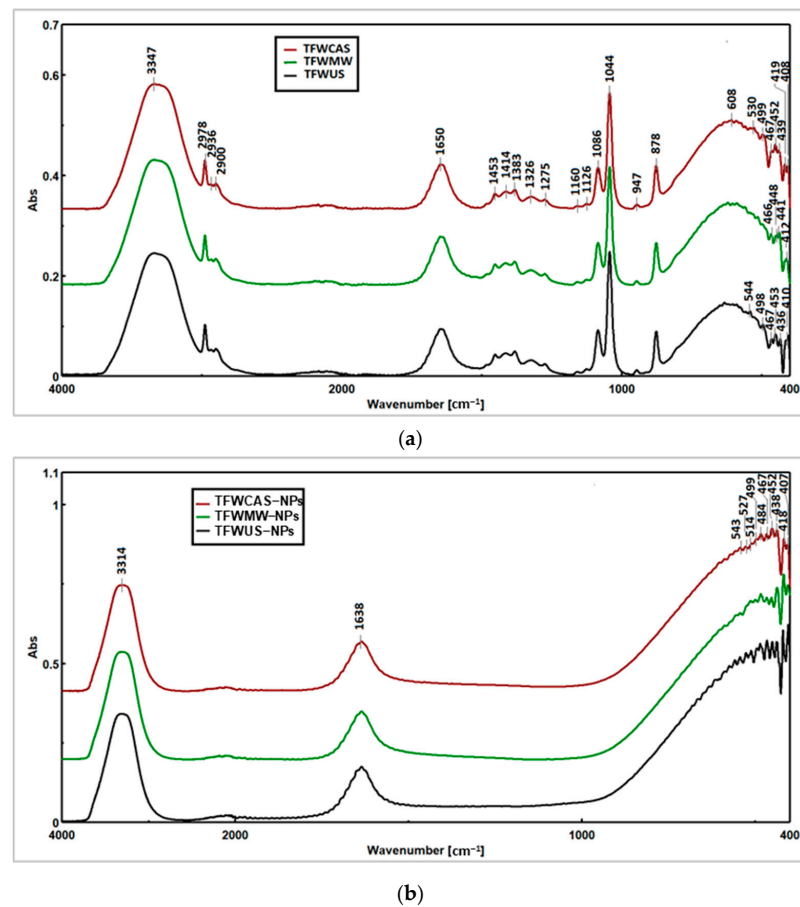


Figure 6. FTIR spectra of (a) TFW extracts and (b) phytosynthesized NPs.

2.6.3. XRD

The XRD technique was used in order to identify the phase composition of the obtained materials. The identification of the diffraction peaks was based on the comparison with ICDD entries 01-071-4613 (Ag) and 01-078-5867 (Ag₂O, marked with # in Figure 7).

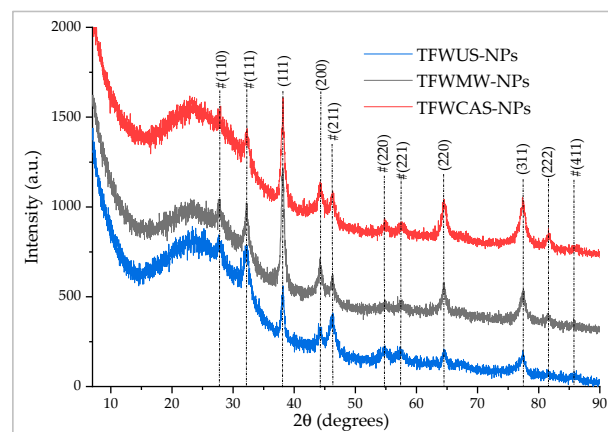


Figure 7. XRD for NPs phytosynthesized by tomato flower waste extracts.

Crystallite size was determined using the Debye–Scherrer equation:

$$D_p = (K \times \lambda) / (\beta \times \cos\theta) \quad (1)$$

where D_p represents the average size of the crystallites, K represents the Scherrer constant (for cubic structures, $K = 0.94$), β represents the width at half-height of the diffraction

maximum, θ represents the Bragg angle, and λ represents the wavelength—1.54059 Å, in our case.

The results for TFW-NPs are presented in Table 5:

Table 5. The crystallite size of the phytosynthesized NPs formed by tomato flower waste extracts.

Sample	Peak Position (Degrees)					FWHM (Degrees) ¹	Crystallite Size (nm) ¹
AgNPs	(111)	(200)	(220)	(311)	(222)		
TFWUS-AgNPs	38.12	44.19	64.62	77.36	81.44	0.57	15.44
TFWMW-AgNPs	38.08	44.34	64.41	77.46	81.39	0.59	14.86
TFWCAS-AgNPs	38.17	44.13	64.49	77.49	81.49	0.65	13.47
Ag ₂ O NPs	(111)	(211)	(220)	(110)			
TFWUS-Ag ₂ O-NPs	32.32	46.17	54.62	27.54		0.68	12.70
TFWMW-Ag ₂ O-NPs	32.10	46.31	54.75	27.72		0.73	11.83
TFWCAS-Ag ₂ O-NPs	32.19	46.09	54.78	27.68		0.85	10.18

¹ Data for the (111) diffraction plane.

The XRD analysis showed the co-existence of the following two phases: silver nanoparticles (AgNPs) and silver oxide nanoparticles (Ag₂O-NPs). Their crystallite sizes, determined using the Scherrer equation, revealed a similar trend for both nanoparticle species, with the TFWUS-NPs leading to the largest crystallites and TFWCAS-NPs to the smallest.

2.6.4. Morphology and Size Distribution of Silver/Silver Oxide Nanoparticles

The morphology and size of the Ag/Ag₂O-NPs formed by TFW extracts were determined by Transmission electron microscopy (TEM) analysis, as shown in Figure 8. The average particle diameters for the TFWUS-NP, TFWMW-NP, and TFWCAS-NP samples were found to be around 40 nm, 22 nm, and 14 nm, respectively. The TEM images (Figure 8a–c) indicate the presence of mostly spherical nanoparticles, with the presence of other morphologies.

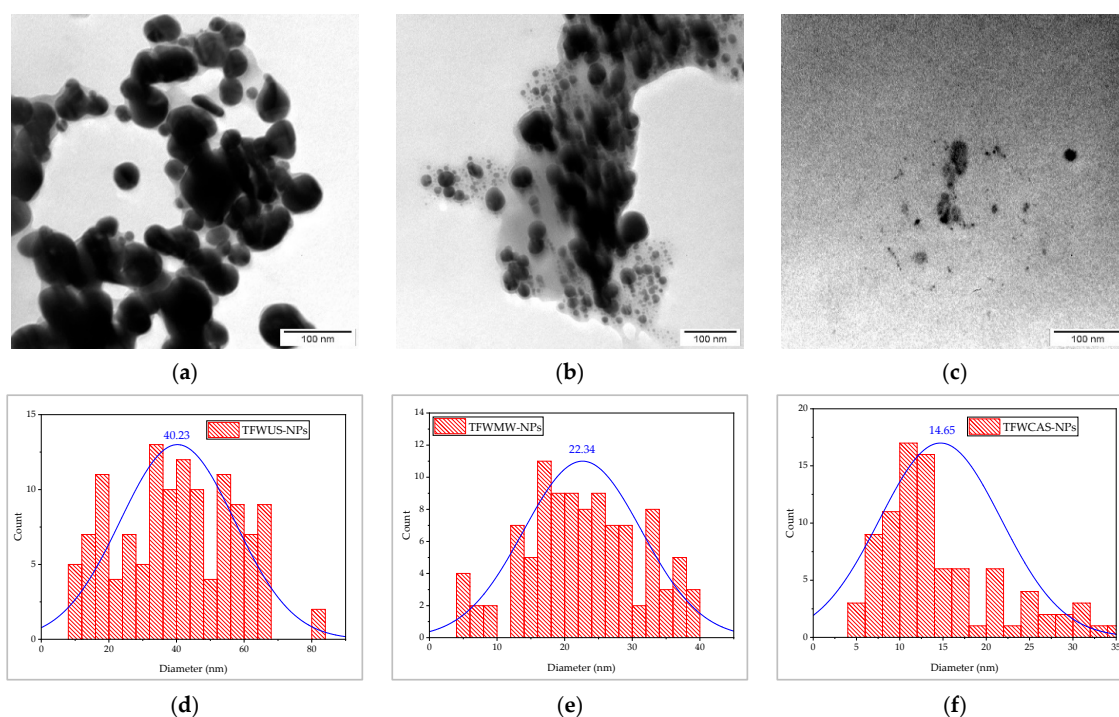


Figure 8. TEM images (a–c) and particle size distribution histograms (d–f) of the TFWUS-NP, TFWMW-NP, and TFWCAS-NP samples.

2.7. Antibacterial Potential of Tomato Flower Extracts and Silver/Silver Oxide Nanoparticles

The antimicrobial activities of the TFW extracts and NPs against pathogenic bacteria, including *E. coli* (Gram-negative) and *S. aureus* (Gram-positive), were carried out through the time-kill kinetics assay. The results showed that both the TFW extracts and NPs exhibited greater antimicrobial potential against *E. coli* than against *S. aureus* (Figure 9). The NPs exhibited higher antimicrobial potential than the TFW extracts. The utilization of TFW extracts in the phytosynthesis of Ag/Ag₂O-NPs was a success. The antimicrobial potential of the Ag/Ag₂O-NPs was significantly higher than if were used only TFW extracts against pathogenic bacteria. The TFW extracts show greater potential against Gram-negative bacteria (*E. coli*) than against Gram-positive bacteria (*S. aureus*). In both cases of antimicrobial potential evaluation of the TFW extracts, TFWUS was more active than the TFWMW and TFWCAS extracts. Regarding the antimicrobial potential of NPs against *E. coli*, TFWUS-NPs and TFWMW-NPs had the highest antimicrobial potential (equal), followed by TFWCAS-NPs. On the other hand, the antimicrobial potential of NPs against *S. aureus* showed the following results: TFWUS-NPs presented the highest antimicrobial potential, followed by TFWMW-NPs and TFWCAS-NPs.

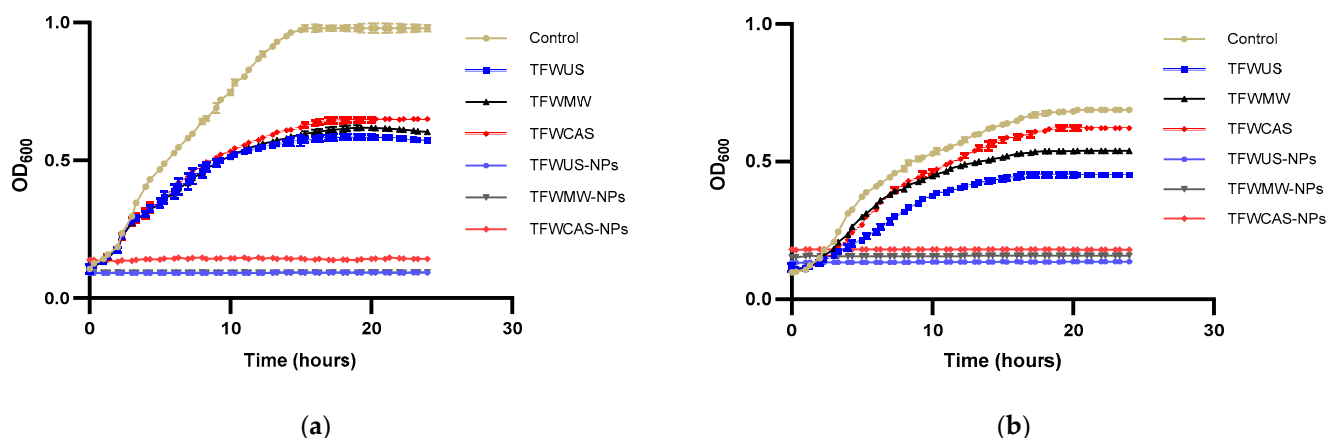


Figure 9. Time-kill kinetics curves of (a) *E. coli* and (b) *S. aureus* treated with the TFW extracts and NPs. Data are presented as means \pm standard deviations ($n = 3$).

2.8. Antitumoral Potential of Tomato Flower Extracts and Silver/Silver Oxide Nanoparticles

Our review of the literature review identified no studies regarding the evaluation of the antitumoral potential of NPs phytosynthesized using TFW extracts in cervical tumor (HeLa) and colon tumor (HT29) cell lines, to our knowledge. The antitumoral potential evaluation of the TFW extracts and NPs showed a significantly reduced viable number of HeLa (Figure 10) and HT29 (Figure 11) cells. For both tumor cell lines studied, the TFW extracts showed similar results, with a cell viability of around 55% (Figures 10a and 11a). Regarding the NP (TFWUS-NPs, TFWMW-NPs, and TFWCAS-NPs) results against the studied tumor cell lines, the NPs showed higher antitumoral potential against HeLa cells (Figure 10b) than against HT29 cells (Figure 11b). The mentioned results could be ascribed to the greater sensitivity of HeLa cells to the silver-based NPs compared with HT29 cells. In both cases, TFWUS-NPs had the highest reduced viable number of tumor cells (50.49%—HeLa, 62.45%—HT29).

Upon microscopic analysis, the HeLa (Figure 12) and HT29 (Figure 13) cells treated with NPs exhibited dead tumor cells, showing cell deformation such as contraction, rounding, and detachment from adjacent cells. In contrast, the untreated (control) cells displayed a normal, round characteristic nucleus.

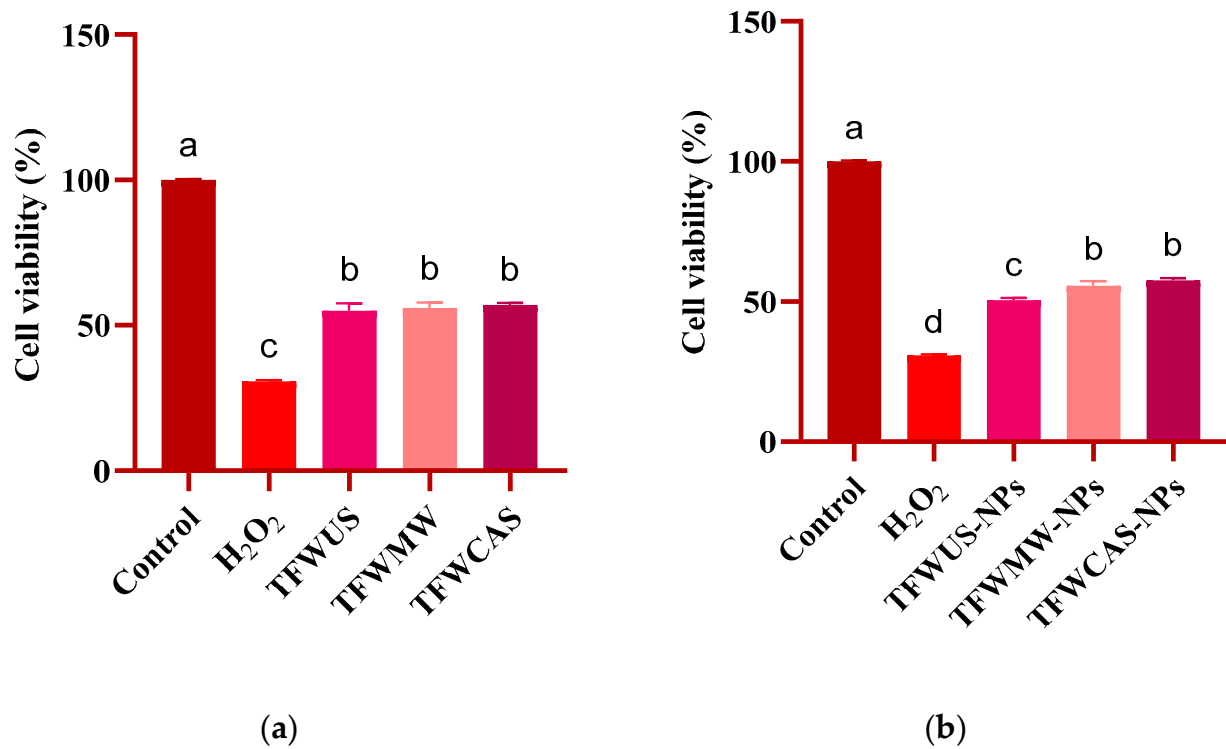


Figure 10. MTT assessment of HeLa cells treated with the (a) TFW extracts and (b) NPs after 24 h. Data are presented as means \pm standard deviations ($n = 3$). a–d indicate a significant difference, $p \leq 0.0001$ compared with the control, calculated using one-way ANOVA.

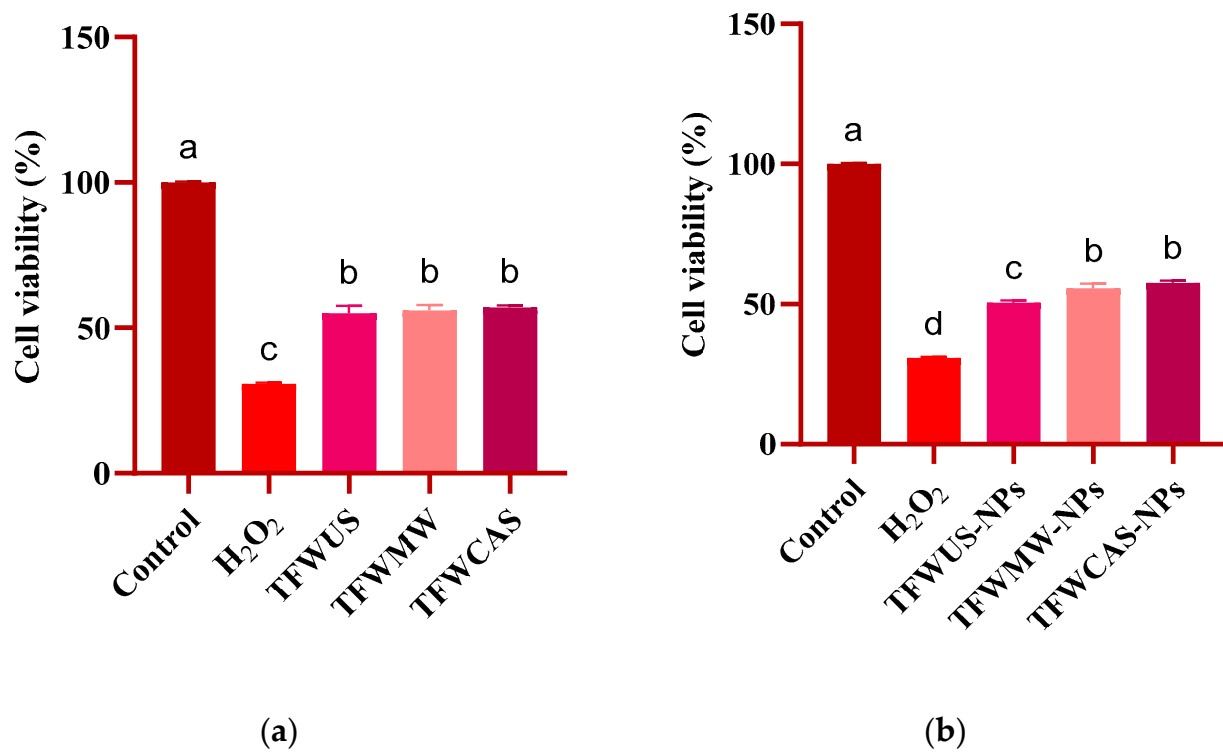


Figure 11. MTT assessment of HT29 cells treated with the (a) TFW extracts and (b) NPs after 24 h. Data are presented as means \pm standard deviations ($n = 3$). a–c indicate a significant difference, $p \leq 0.0001$, compared with the control, calculated using one-way ANOVA.

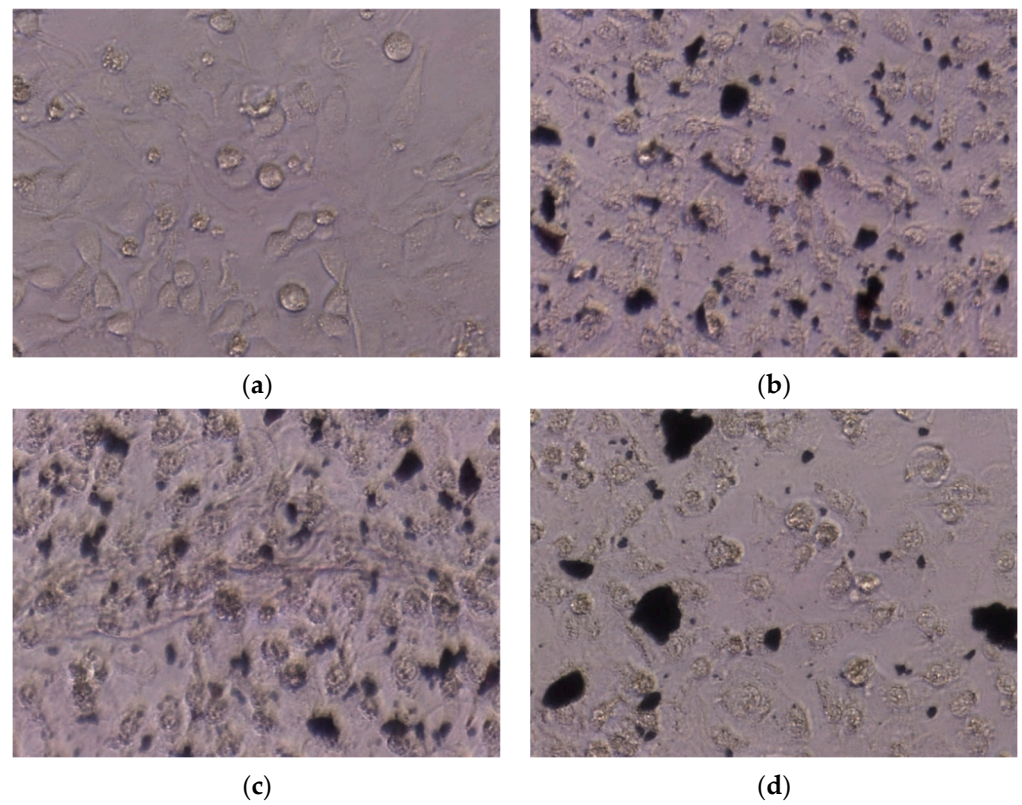


Figure 12. Cell morphology of (a) untreated HeLa cells (control) and HeLa cells treated with (b) TFWUS-NPs, (b,c) TFWMW-NPs, and (d) TFWCAS-NPs.

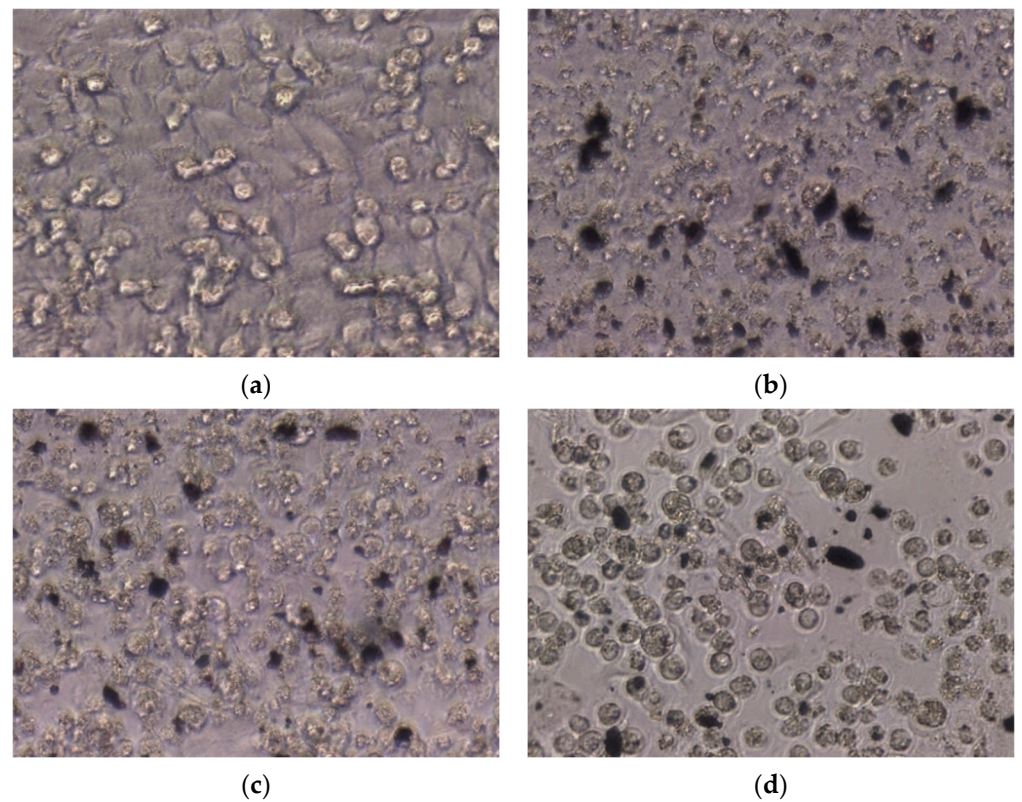


Figure 13. Cell morphology of (a) untreated HeLa cells (Control) and HT29 cells treated with (b) TFWUS-NPs, (b,c) TFWMW-NPs, and (d) TFWCAS-NPs.

3. Discussion

The extraction methods for bioactive compounds are diverse, encompassing conventional as well as advanced methods, such as those employed in this study. Each method is adapted depending on the nature of the compounds of interest and also on the plant material used. Selecting the right extraction method is essential to obtain a high extraction yield and also to ensure the quantity and quality of the compounds of interest. The extraction yield is primarily influenced by temperature, extraction time, and the solvent used for extraction. Comparing the extraction yields for the three methods investigated, MAE led to the highest extraction yield of TFW, followed by UAE and CASE, probably because of its ability to heat the solvent and plant matrix rapidly, therefore enhancing mass transfer, breaking down cell walls, and releasing the bioactive compounds more efficiently. We observed that CASE led to a low yield compared with the other two selected methods, likely because of the sequential application of the two extraction methods, which probably led to partial degradation of sensitive compounds during the extended processing time. As presented in the Materials and Methods Section, in this study, a hydroalcoholic solvent with a 50% (*v/v*) aqueous ethanol concentration was used to maximize the extraction yield across the selected methods. The obtained results are in accordance with the results reported by other researchers. For example, in the case of waste from sugar beet leaves, the extraction yield in the case of MAE was higher than the case of UAE using 50% ethanol as an extraction solvent [47]. At the same time, the extraction yield of TFW is similar, but even higher than the extraction yield obtained by classical ethanolic extraction from the aerial parts of tomatoes such as leaves, stems, and suckers [3].

The evaluation of total polyphenol content and flavonoid content represents the first investigation step for vegetable waste extracts, in an attempt to prove their promising biological activities, such as anti-inflammatory, antioxidant, anti-diabetic, antitumoral, antibacterial, and anti-aging effects [48–51].

Numerous studies have proven the efficiency of MAE for the quantitative extraction of polyphenols, compared with other extraction techniques, in the case of different plant materials. For example, ethanol extracts from jackfruit pulp obtained by microwave-assisted extraction showed significantly better results regarding TPC, DPPH, and ABTS radical scavenging activities compared with those obtained by ultrasound-assisted extraction and ultrasound-microwave-assisted extraction [52]. Afoakwah et al. [53] reported similar results for the same extraction technique, which proved effective in the extraction of polyphenols from the ethanolic extracts of Jerusalem artichoke tubers and also identified a high antioxidant activity compared with the values obtained from liquid–liquid extraction or ultrasound-assisted extraction.

Usually, a high flavonoid content in plant wastes is obtained using ultrasound-assisted extraction [54,55]. For example, Liao et al. [56] reported higher flavonoid content using ultrasound-assisted extraction from peanut shell wastes. These already reported results are in accordance with the higher flavonoid content obtained by ultrasound-assisted extraction compared with microwave-assisted extraction in the present investigation.

The phytochemical screening of TFW extracts, as well as the evaluation of their antioxidant potential, indicated that MAE and UAE proved to be suitable extraction techniques, leading to the highest contents of polyphenols and flavonoids and the best antioxidant activity. The highest content of total phenolic acids was TFWMW (40,015 mg/kg) > TFWUS (39,571 mg/kg) > TFWCAS (approx. 34,898 mg/kg). On the other hand, the highest content of total flavonoids was TFWUS (approx. 866 mg/kg) > TFWMW (711 mg/kg) > TFWCAS (approx. 643 mg/kg).

The TFW hydroalcoholic extracts revealed the capacity to scavenge DPPH radicals, proving their antioxidant activity. TFWMW revealed the highest value of approx. 656 mg AAE/kg dm, indicating that the MAE method is significantly more efficient compared with the UAE and CASE methods. The statistical analysis demonstrated that there were no significant differences between TFWUS (approx. 523 mg AAE/kg dm) and TFWCAS (approx. 519 mg AAE/kg dm) ($p > 0.05$). The TFWMW extract showed higher antioxidant

activity than the TFWUS and TFWCAS extracts, which can be attributed to the higher content of phenolic acids.

Regarding the ABTS assay, the scavenging activity followed the order TFWMW > TFWUS > TFWCAS. There were no statistically significant differences between TFWMW and TFWUS ($p > 0.05$). In the case of the FRAP assay, TFWMW also revealed the highest antioxidant potential; the antioxidant potential varied in the following order TFWMW > TFWUS > TFWCAS. Similar results, comparing the extraction method, regarding DPPH scavenging activity and the FRAP assay were obtained in the case of aerial parts of sea fennel plants, where MAE revealed higher inhibition values than UAE. Moreover, the highest value for free-radical scavenging activity using the FRAP assay was achieved in a study conducted by Veršić Bratinčević et al. when they used MAE extraction at 500 W [57]. Using aqueous ethanol extracts (50%) in the case of *Lavandula* extracts from stems, leaves, and fruit, a higher antioxidant potential was revealed by MAE, compared with UAE, when tested with the ABTS and DPPH assays [58]. These results confirmed the optimal use of the solvent and of the extraction method. Regarding the antioxidant activity assessment by the three different methods investigated (DPPH, ABTS, FRAP), significant differences ($p < 0.05$) were observed in the FRAP assay among all studied extracts.

The present study aimed at the phytosynthesis, characterization, and biological potential evaluation of NPs. The NPs were phytosynthesized by TFW extracts, and the structural characteristics were investigated using a range of analytical techniques such as UV-Vis, FTIR, XRD, and TEM. The preliminary phytochemical screening described above for the TFW extracts showed a high content of polyphenols and flavonoids. Also, the UPLC analysis indicated the presence of the following polyphenolic compounds: gallic acid, caffeic acid, chlorogenic acid, catechin, epicatechin, p-coumaric acid, ferulic acid, isoquercetin, rosmarinic acid, naringin, myricetin, luteolin, quercetin, and naringenin. These compounds, especially flavonoids, present in the TFW extracts can be responsible for the NPs' phytosynthesis and stabilization [59].

The accumulation of phenolic compounds is significantly influenced by tomato cultivars. Environmental factors such as temperature, solar radiation, weather variation and anomalies, light exposure, and agricultural practices such as irrigation methods and nitrogen supply are factors with a role in determining the level of phenolic compound accumulation. The main compound identified in the TFW extracts was caffeic acid followed by chlorogenic acid. These compounds were also identified in several studies targeting tomato plant valorization. Chlorogenic acid was also abundant in tomato leaf extracts of several cultivars [60].

The analysis of the UV-Vis spectra supports the hypothesis of the formation of silver-based NPs, by the presence of the peak associated with the surface plasmonic resonance in the 400–500 nm range. Often, UV-Vis spectrometry can be applied to evaluate the sizes of NPs by determining the position of the specific peak. However, these values should not be considered definitive dimensions, since the position of the specific peaks of phytosynthesized silver-based NPs may undergo a bathochromic shift from its "true" position because of the influence of a series of factors, such as aggregation of NPs into larger clusters and the presence of different phytoconstituents. As such, NP sizes must be further confirmed using other techniques such as XRD or TEM.

FTIR spectroscopy was used to identify the functional groups responsible for the phytosynthesis of NPs. When infrared radiation interacts with TFW extracts or NP samples, the bonds within molecules vibrate at characteristic frequencies, leading to absorption peaks on the FTIR spectrum, each corresponding to specific functional groups. The discovered stretching vibrations of Ag–Ag, Ag–O–Ag, Ag–O, and O–Ag–O were also identified in other studies previously reported in the literature [61–64]. Moreover, the absorption spectra of the TFW extracts were similar and showed characteristic peaks. The identified C–O stretching vibration was attributed to pyran, typical of flavonoid C-rings [65]. The analysis indicated that the functional groups present in the FTIR spectra of the TFW extracts and

absent in the FTIR spectra of the NPs were involved in the reduction of Ag^+ to Ag^0 and stabilization of NPs.

In concordance with TEM analysis, almost all the TFW-NPs were spherical in shape. Few NPs were observed in agglomerated structures, which is a characteristic of phytosynthesized NPs using plant extracts [66]. The TEM morphology and size results are in good concordance with the XRD results.

Numerous studies in the literature describe the antimicrobial and antitumoral potentials of Ag-based NPs phytosynthesized by plant extracts [67–73]. Ag-based NPs disrupt cell membranes and damage intracellular structures [74,75].

In this study, the antimicrobial potential of silver-based NPs was evaluated against *E. coli* and *S. aureus*, and the results presented insignificant differences. NPs inhibited approximately 100% of bacteria cells. NPs showed good antimicrobial potential because of their positive charge and small size [76].

Differences were observed in the antibacterial potential of the TFW extracts. The TFW extracts inhibited approximately 50% of *E. coli* bacteria cells and between 60 and 85% of *S. aureus* bacteria cells. Thus, the TFWUS extract was the most active against *E. coli* and *S. aureus*. This could be attributed to the differences in chemical compositions and the action mechanism. The TFWUS extract contains the highest amount of flavonoids, which confirms the highest antimicrobial potential of both the extract and TFWUS-NPs. Flavonoids may have antimicrobial potential because of their ability to bind with intracellular and soluble proteins and bacterial cell walls [77].

The present study also investigated the antitumoral potentials of the TFW extracts and NPs against HeLa and HT29 tumor cell lines using the MTT assay. The antitumoral potential of the TFW extracts against HT29 cells was similar to the potential against HeLa cells. Mani et al. [78] reported that the HeLa and HT29 tumor cell lines treated with *M. koenigii* and *P. angustifolium* extracts showed similar potential against both tumor cell lines. The antitumoral potential may be attributed to polyphenolic antioxidant compounds, such as caffeic acid, ferulic acid, chlorogenic acid, p-coumaric acid, gallic acid, catechin, isoquercetin, luteolin, and quercetin, which have a significant role in inhibiting tumor cells [79].

The MTT results showed that the NPs were more active against HeLa cells than HT29 cells. Antitumoral potential also depends on NP concentration and the possible interaction with tumor cells. The antitumoral potential assay results evidenced that increasing the concentration of NPs significantly increased the reduced viable number of HeLa and HT29 tumor cells [80]. Also, the microscopic images showed that the NPs tend to agglomerate in the culture medium [81].

4. Materials and Methods

4.1. Tomato Flower Waste Material and Extract Preparation

The plant material used consisted of tomato plant waste and dried flowers left after the ripening cycle of *Lycopersicon esculentum* (Cheramy RZ F1 hybrid) fruit. These wastes from flowers can contain stigmas, styles, and parts of the anther cone. The tomato flower waste was collected from the University of Agronomic Sciences and Veterinary Medicine of Bucharest (USAMV) Research Greenhouse, Bucharest, Romania.

The plant material used was oven-dried and later subjected to grinding and extraction. Tomato flower waste (TFW) extracts were obtained by the following three environmentally friendly extraction methods: microwave-assisted extraction (MAE), ultrasound-assisted extraction (UAE), and cascade extraction (CASE), which is a sequential procedure involving UAE and MAE. All experiments were performed in triplicate. The obtained extracts were separated by filtration using Whatman No. 4 filter paper (Whatman Inc., Florham Park, NJ, USA) under vacuum. The filtrates were concentrated (using a Microvap 118 Nitrogen Evaporator, Organomation®, Berlin, MA, USA) and then subjected to lyophilization until further analysis.

The MAE of the TFW extract was performed using Milestone Ethos Easy equipment (Milestone Srl, Bergamo, Italy). The high power of the microwaves provided by the 2 magnetrons connected to the rotating diffuser offers a very fast heating of the samples, implicitly inducing efficient extraction of the most sensitive compounds [82]. The MAE extraction parameters were as follows: time, 32 min; solvent ethanol–water ratio, 1:1 *v/v*; plant-to-solvent ratio, 1:20 (*w/v*); temperature, 70 °C; power, 750 W; and amplitude, 50% (the sample was encoded as TFWMW). The UAE of TFW extract was performed using an ultrasonic processor (Sonics Vibra-Cell™ VCX 750, SONICS & MATERIALS, INC., Newtown, CT, USA). This high-intensity system, for the extraction of bioactive compounds from plant material, involves the use of a probe that helps to produce the cavitation phenomenon. During cavitation, shock waves are created that release high energy at the level of the sample, thus resulting in an efficient extraction [83,84]. The UAE extraction parameters were as follows: time, 60 min; solvent ethanol–water, 1:1 *v/v*; plant-to-solvent ratio, 1:20 (*w/v*); temperature, 100 °C; and power, 500 W (the sample was encoded as TFWUS). The CASE extraction parameters were as follows: time, 14 min for UAE and 60 min for MAE; solvent ethanol–water ratio, 1:1 *v/v*; plant-to-solvent ratio, 1:20 (*w/v*); temperature, 70 °C for UAE and 100 °C for MAE; power, 750 W for UAE and 500W for MAE; and amplitude, 50% for UAE (the sample was encoded as TFWCAS).

The percentage of the extraction yield was expressed by the lyophilized mass extract related to the initial mass of dried plant material used for extraction.

4.2. Phytochemical Screening in Tomato Flower Waste Extracts

4.2.1. Evaluation of Total Polyphenolic Content (TPC)

In order to determine the total polyphenolic content (TPC) of different crude extracts, the modified Folin–Ciocalteu assay [85] was used, adapted for microspectrophotometry [84]. Aliquots of hydroalcoholic extract were mixed with 1N Folin–Ciocalteu reagent, 20% Na₂CO₃ solution, and ultrapure water (2:1:1:4 volume ratio). The experiments were carried out in triplicate, and the absorbances were read after incubation for 30 min in the dark at room temperature, at 760 nm, using the FLUOstar® Omega microplate reader (BMG LABTECH, Ortenberg, Germany). The results were expressed in milligrams of gallic acid equivalents per kilogram of dry matter (mgGAE/kg).

4.2.2. Evaluation of Total Flavonoid Content (TFC)

The total flavonoid content was determined following the aluminum chloride method adapted for microspectrophotometry [86,87], from TFW, by mixing the hydroalcoholic extracts with 2% AlCl₃ solution (1:1 volume ratio). The experiments were carried out in triplicate, and the absorbance of the samples was read after 15 min of incubation in the dark at room temperature, at 415 nm, using the FLUOstar® Omega microplate reader (BMG LABTECH, Ortenberg, Germany). Using quercetin as standard, the TFC results were expressed in milligrams of quercetin equivalents per kilogram of dry matter (mgQE/kg).

4.3. Identification and Quantification of Polyphenolic Compounds Present in Tomato Flower Waste Extracts by UPLC

Quantitative analysis of TFW extracts was performed using an Ultra Performance Liquid Chromatography (UPLC) System (Waters Acquity UPLC® I Class, Milford, MA, USA) equipped with a binary solvent manager (binary pump), sample manager, column compartment, and PDA detector. In order to perform the analytic separation process, a Zorbax Eclipse Plus C18 chromatographic column (Agilent Technologies, Santa Clara, CA, USA) was used with 4.6 × 150 mm and 5 µm of particle size. The column oven was preset at 30 °C, and the autosampler temperature was 25 °C. The mobile phase consisted of the following two solvents: solvent A containing water and solvent B containing acetonitrile. Both solvents were mixed with 0.1% formic acid. The linear gradient system started with solvent B from 10% to 100% at a flow rate of 0.8 mL/min for 30 min.

The targeted reference polyphenolic compounds were gallic acid, caffeic acid, chlorogenic acid, catechin, epicatechin, p-coumaric acid, ferulic acid, isoquercetin, rosmarinic acid, naringin, myricetin, luteolin, quercetin, and naringenin. Wavelengths of 280 nm, 320 nm, and 370 nm were used to detect the targeted polyphenolic compounds. The samples were carried out in triplicate, and the results were processed in Empower software. The 14 targeted polyphenolic compounds were identified and quantified by comparison with the retention time provided in each compound's spectrum. The calibration curve concentrations ranged from 5 to 150 µg/mL, and the results were expressed in milligrams equivalents per kilogram dried sample (mg/kg).

4.4. Antioxidant Activity Evaluation of Tomato Flower Waste Extracts

4.4.1. DPPH Assay

Antioxidant activity was evaluated using the DPPH (1, 1-Diphenyl-2-Picrylhydrazyl) assay, with few adaptations for the microplate method [88]. The method consisted, in brief, of mixing equal parts of the hydroalcoholic extract with 250 µM DPPH solution (1:1 volume ratio). Absorbance was read after 30 min of incubation in the dark at room temperature, at 517 nm, using the FLUOstar® Omega microplate reader (BMG LABTECH, Ortenberg, Germany). The results obtained were expressed in milligrams of Ascorbic Acid Equivalents per kilogram of dry matter (mgAAE/kg). The experiments were carried out in triplicate.

4.4.2. ABTS Assay

Evaluation of the antioxidant activity using the cationic radical ABTS^{•+} involved the preparation of an ABTS stock solution by mixing equal parts of 2,2'-Azino-bis (3-ethylbenzthiazoline-6-sulfonic acid) diammonium salt 7.8 mM with K₂S₂O₈ 140 mM solution. After 12 h (at room temperature in the dark), the stock solution was diluted with methanol until the absorbance value assessed at 734 nm was 1.1 ± 0.02 arbitrary units. This method was an adapted version of the microplate method [89]. The experiments were carried out in triplicate and consisted of mixing and homogenizing equal parts of ABTS methanolic solution with hydroalcoholic extract (1:1 volume ratio). The reading of their absorbance was performed after incubation in the dark for 30 min at room temperature, at 734 nm, using the FLUOstar® Omega microplate reader (BMG LABTECH, Ortenberg, Germany). The results were expressed in milligrams of Ascorbic Acid Equivalents per kilogram of dry matter (mgAAE/kg).

4.4.3. FRAP Assay

To study the ability of the sample to reduce Fe³⁺ to Fe²⁺ ions, a FRAP solution was prepared consisting of 250 mM acetate buffer solution (pH 3.6), 10 mM 2,4,6-tris (2-pyridyl)-s-triazine (TPTZ) and 20 mM FeCl₃, in a 10:1:1 volume ratio. A modified FRAP method was used, adapted for the microspectrophotometry technique [90]. The experiments consisted of mixing and homogenizing the hydroalcoholic extracts with the FRAP solution in a 1:4 volume ratio, which were left to incubate in the dark for 30 min at room temperature; then, their absorbance was read at 593 nm using the FLUOstar® Omega microplate reader (BMG LABTECH, Ortenberg, Germany). The ferric ion reduction results were expressed in milligrams of Ascorbic Acid Equivalents per kilogram of dry matter (mgAAE/kg).

4.5. Phytosynthesis of Silver-Based Nanoparticles Using Tomato Flower Extracts

The phytosynthesis of silver-based nanoparticles (NPs) consisted of mixing the aqueous extract of tomato flower waste (20 mg/mL) and 5 mM AgNO₃ solution in a 1:10 volume ratio. The mixture obtained was incubated at 70 °C for 2 h. Throughout this process, the solution underwent several color changes, transitioning from colorless to yellowish and then to reddish brown before stabilizing, which confirmed the successful formation of NPs, attributed to the reduction of Ag⁺ to Ag⁰ [91,92] (Figure 14). Then, the samples were centrifuged for 30 min at 12,000 rpm.

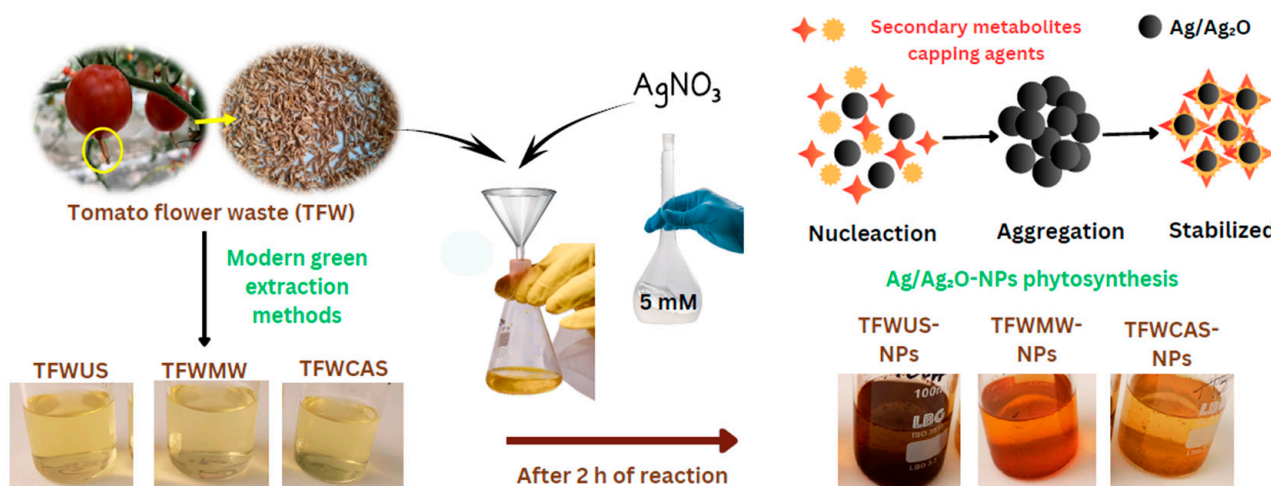


Figure 14. Schematic steps for the formation process of Ag/Ag₂O-NPs.

Repeated washing with ultrapure water followed by centrifugation was performed until the supernatant color completely disappeared. The obtained NPs were lyophilized for further use. Each sample of NPs (5 mg of lyophilized powder) was resuspended in 2 mL of ultrapure water and used in the following analyses.

The yield of NPs formed, expressed as a percentage, was calculated with the following equation:

$$\text{NPs yield (\%)} = m_{\text{NPs}} / m_{\text{Ag}} \times 100 \quad (2)$$

where m_{NPs} represents the mass of NPs formed (g) and m_{Ag} represents the mass of Ag⁺ ions (g) used in phytosynthesis.

4.6. Characterization Techniques of Silver-Based Nanoparticles

4.6.1. Spectrophotometric Analysis of Samples

The nanoparticles were preliminarily evaluated by UV-Vis spectrometry, using a Specord 210 Plus UV-Vis spectrophotometer (Analytik Jena, Jena, Germany, optical resolution 0.5 nm) in the 290–800 nm wavelength range.

4.6.2. FTIR Spectroscopy Analysis

The Fourier transform infrared (FTIR) spectroscopy analysis was performed with a JASCO FT-IR 6300 instrument (Jasco Int. Co., Ltd., Tokyo, Japan), equipped with a Specac ATR Golden Gate (Specac Ltd., Orpington, UK) with a KRS5 lens, in the range of 400 to 4000 cm^{−1}.

4.6.3. XRD Analysis

The lyophilized nanoparticles were subjected to XRD analysis, in order to establish the nature of the obtained nanoparticles.

X-ray diffraction (XRD) analysis was conducted using a 9 kW Rigaku SmartLab diffractometer (Rigaku Corp., Tokyo, Japan). The instrument was operated at 45 kV and 200 mA, utilizing CuKα radiation with a wavelength of 1.54059 Å. Measurements were carried out in scanning mode 2θ/θ, covering a 2θ range from 7° to 90°. PDXL 2.7.2.0 software (Rigaku Corporation, Tokyo, Japan), for peak separation and full-width at half-maximum (FWHM) calculations, was used to analyze the diffraction data. The components were identified by comparing the obtained diffraction patterns with the International Centre for Diffraction Data (ICDD) PDF-5+ database.

4.6.4. TEM Morphological Analysis

TEM studies were performed to investigate the morphology of the obtained NPs. A sample droplet was applied on a 200 mesh formvar-coated grid and allowed to air-dry. The grid sample was then analyzed using a PHILIPS EM208S operated at 80 kV accelerating voltage (Koninklijke Philips N.V., Amsterdam, The Netherlands) and visualized with a Veleta camera (EMSIS GmbH, Münster, Germany).

4.7. Antibacterial Potential Evaluation of Tomato Flower Extracts and Silver-Based Nanoparticles

Using the time-kill kinetics assay, the antibacterial screening of NPs and TFW extracts was carried out against pathogenic bacteria, including *Escherichia coli* (Gram-negative) and *Staphylococcus aureus* (Gram-positive). *E. coli* and *S. aureus* were grown on nutrient agar medium and then incubated for 24 h at 37 °C. A 180 µL inoculum size of approximately 1.0 McFarland diluted in liquid broth was added to each well of a 96-well microtiter plate, and then 20 µL of NPs and TFW extracts were added and incubated at 37 °C for 24 h, while measuring their OD600 every 30 min using a microplate reader (Synergy™ HTX Multi-Mode Microplate Reader, Biotek, Winooski, VT, USA). The control was bacteria without samples. The procedure was carried out in independent triplicates, and the absorbance was plotted against time.

4.8. Antitumoral Potential Evaluation of Tomato Flower Extracts and Silver-Based Nanoparticles

The HeLa (cervical tumor) and HT29 (colon tumor) cell lines were selected for the antitumoral potential assessment of the NPs and TFW extracts, respectively, using the MTT assay. The HeLa and HT29 cell lines were cultivated in DMEM culture medium (Sigma-Aldrich, St. Louis, MO, USA), supplemented with 10% Fetal Bovine Serum (FBS) (Sigma-Aldrich) and 1% penicillin–streptomycin (Sigma-Aldrich, Burlington, MA, USA), exposed to NPs and TFW extracts, respectively, and incubated in 5% CO₂ at 37 °C for 24 h. H₂O₂ was used as a positive control, and ultrapure water was used as a negative control. Following the incubation period, the supernatant was removed, the cells were treated with MTT (Sigma-Aldrich), and the plates were incubated for 4 h at 37 °C. The purple formazan formed was dissolved in 100 µL DMSO, and the optical density was measured at 570 nm using a microplate reader (Synergy™ HTX Multi-Mode Microplate Reader, Biotek, Winooski, VT, USA).

4.9. Statistical Analysis

Statistical analysis of the obtained results was performed using GraphPad software package (v. 10.3.0). Statistical tests selected included analysis of variance (ANOVA) and Tukey's test, both at a significance level of 5% ($\alpha = 0.05$). Also, the correlation between TPC, TFC, and antioxidant activity was determined using the Pearson correlation coefficient.

5. Conclusions

The development of innovative antimicrobial and antitumor products, which provide maximum biocompatibility and prevent the emergence of resistance, is a critical aspect of modern treatments. In this context, the research undertaken in the present study on silver nanoparticles phytosynthesized by ecological methods, using extracts from tomato flower waste, has shown significant promise. These nanoparticles exhibit significant antimicrobial potential against *E. coli* and *S. aureus* pathogenic bacteria and antitumoral potential against HeLa and HT29 tumor cells, offering considerable advantages in terms of sustainability and reducing the negative impact on the environment. Therefore, these findings underline the enormous potential of ecological approaches in the development of advanced therapeutic solutions, showing potential in future medical and industrial applications.

Author Contributions: Conceptualization, S.M.S., N.B. and A.O.; methodology, M.D.C., I.A., R.C.F., A.-M.M., P.M.R. and C.L.C.; software, S.M.S., R.C.F. and M.D.C.; investigation, S.M.S., M.D.C., I.A., R.C.F., P.M.R., A.-M.M. and C.L.C.; data curation, S.M.S., M.D.C., R.C.F. and C.L.C.; writing—original

draft preparation, S.M.S., M.D.C., A.O. and P.M.R.; writing—review and editing, C.L.C., N.B. and A.O.; supervision, N.B. and A.O.; funding acquisition, P.M.R. All authors have read and agreed to the published version of the manuscript.

Funding: S.M.S.: P.M.R., C.L.C. and A.O. gratefully acknowledge the funding provided by the University of Agronomic Sciences and Veterinary Medicine of Bucharest—Romania, Research Project 846/30.06.2023, acronym EnterGreenFood, in the Competition IPC 2023. RCF gratefully acknowledges the support provided by the Ministry of Research, Innovation and Digitization through the INCDCP-ICECHIM Core program PN 23.06.01.01 (AQUAMAT).

Institutional Review Board Statement: Not applicable.

Informed Consent Statement: Not applicable.

Data Availability Statement: All obtained datasets are included in this publication.

Acknowledgments: The authors would like to express their gratitude to Sorin Mănoiu from the National Institute of R&D for Biological Sciences for his assistance with the TEM analysis and to Monica Florentina Raduly from the National Institute for Research and Development in Chemistry and Petrochemistry—ICECHIM Bucharest for her support with the FTIR analysis.

Conflicts of Interest: The authors declare no conflicts of interest.

References

1. van Andel, T.; Vos, R.A.; Michels, E.; Stefanaki, A. Sixteenth-century tomatoes in Europe: Who saw them, what they looked like, and where they came from. *PeerJ* **2022**, *10*, e12790. [CrossRef] [PubMed]
2. Food and Agriculture Organization of the United Nations (2023)—With Major Processing by Our World in Data. Tomato Production—FAO [Dataset]. Food and Agriculture Organization of the United Nations, Production: Crops and Livestock Products [Original Data]. Available online: <https://ourworldindata.org/grapher/tomato-production> (accessed on 15 April 2024).
3. Añibarro-Ortega, M.; Pinela, J.; Ćirić, A.; Martins, V.; Rocha, F.; Soković, M.D.; Ferreira, I.C.F.R. Valorisation of table tomato crop by-products: Phenolic profiles and in vitro antioxidant and antimicrobial activities. *Food Bioprod. Process.* **2020**, *124*, 307–319. [CrossRef]
4. Zhu, Z.; Keesman, K.J.; Yogev, U.; Gross, A. Onsite anaerobic treatment of tomato plant waste as a renewable source of energy and biofertilizer under desert conditions. *Bioresour. Technol. Rep.* **2022**, *20*, 101274. [CrossRef]
5. Almeida, P.V.; Rodrigues, R.P.; Teixeira, L.M.; Santos, A.F.; Martins, R.C.; Quina, M.J. Bioenergy Production through Mono and Co-Digestion of Tomato Residues. *Energies* **2021**, *14*, 5563. [CrossRef]
6. Gioulounta, K.; Matska, M.; Piskilopoulos, A.; Stamatelatu, K. Greenhouse residues' potential for biogas production. *Appl. Sci.* **2023**, *13*, 5445. [CrossRef]
7. Moreno, A.D.; Duque, A.; González, A.; Ballesteros, I.; Negro, M.J. Valorization of Greenhouse Horticulture Waste from a Biorefinery Perspective. *Foods* **2021**, *10*, 814. [CrossRef]
8. Ahmed, S.; Bin, R.F.; Ahmed, S.; Mohammad Shohael, A. Insights into the bioactive compounds, antioxidant potential and TLC profiling of different extracts of tomato plants. *Jahangirnagar Univ. J. Biol. Sci.* **2018**, *7*, 65–77. [CrossRef]
9. Yörük, E.; Eren, E.; Hazneci, E.; Özer, H.; Gülser, C. Potential Use of Postharvest Tomato Wastes as a Growing Media in Soilless Culture. *Compos. Sci. Util.* **2023**, *1*, 1–8. [CrossRef]
10. Rashwan, M.A.; Naser Alkoai, F.; Morsy, M.I.; Blaqueza Fulleros, R.; Nagy Ibrahim, M. Influence of tomato waste compost ratios on plant growth and fruit quality of cucumber and summer squash. *J. Air Waste Manag. Assoc.* **2021**, *71*, 1067–1075. [CrossRef]
11. Tabrika, I.; Azim, K.; Mayad, E.H.; Zaafrani, M. Composting of tomato plant residues: Improvement of composting process and compost quality by integration of sheep manure. *Org. Agric.* **2020**, *10*, 229–242. [CrossRef]
12. Hiraguri, T.; Kimura, T.; Endo, K.; Ohya, T.; Takanashi, T.; Shimizu, H. Shape classification technology of pollinated tomato flowers for robotic implementation. *Sci. Rep.* **2023**, *13*, 2159. [CrossRef] [PubMed]
13. Chang, T.K.; Cheng, T.M.; Chu, H.L.; Tan, S.-H.; Kuo, J.C.; Hsu, P.H.; Su, C.Y.; Chen, H.M.; Lee, C.M.; Kuo, T.R. Metabolic Mechanism Investigation of Antibacterial Active Cysteine-Conjugated Gold Nanoclusters in *Escherichia coli*. *ACS Sustain. Chem. Eng.* **2019**, *7*, 14620–14629. [CrossRef]
14. Ardelean, A.V.; Moroşanu, A.M.; Ardelean, I.; Moisescu, C.; Cornea, C.P. Gold Nanoparticles Synthesis by Green Microalgae and the *Cyanobacterium Synechocystis* PCC 6803 in Light and in Darkness, and Pollutants Degradation by These Nanoparticles in vitro. *AgroLife Sci. J.* **2022**, *11*, 9–17. [CrossRef]
15. Imon, M.A.I.; Toma, S.N.; Sohag, S.M.; Islam, M.J.; Islam, M.M.; Sohag, M.S.U.; Mahmud, I.; Shahria, N.; Dutta, S. Evaluation of Anthelmintic and Antioxidant Efficacy of Green-Synthesized Copper Nanoparticles Derived from *Erioglossum rubiginosum* Leaf and Seed Aqueous Extracts. *Eur. J. Med. Chem. Rep.* **2024**, *12*, 100181. [CrossRef]
16. López-Vargas, E.R.; Ortega-Ortíz, H.; Cadenas-Pliego, G.; De Alba Romenus, K.; Cabrera de la Fuente, M.; Benavides-Mendoza, A.; Juárez-Maldonado, A. Foliar Application of Copper Nanoparticles Increases the Fruit Quality and the Content of Bioactive Compounds in Tomatoes. *Appl. Sci.* **2018**, *8*, 1020. [CrossRef]

17. El-Abeid, S.E.; Mosa, M.A.; El-Tabakh, M.A.M.; Haridy, M.S.A. Antifungal activity of copper oxide nanoparticles derived from *Zizyphus spina* leaf extract against *Fusarium* root rot disease in tomato plants. *J. Nanobiotechnol.* **2024**, *22*, 28. [\[CrossRef\]](#)
18. Iqbal, T.; Raza, A.; Zafar, M.; Afsheen, S.; Kebaili, I.; Alrobei, H. Plant-mediated green synthesis of zinc oxide nanoparticles for novel application to enhance the shelf life of tomatoes. *Appl. Nanosci.* **2022**, *12*, 179–191. [\[CrossRef\]](#)
19. Ahmed, R.; Yusoff Abd Samad, M.; Uddin, M.K.; Quddus, M.A.; Hossain, M.A.M. Recent Trends in the Foliar Spraying of Zinc Nutrient and Zinc Oxide Nanoparticles in Tomato Production. *Agronomy* **2021**, *11*, 2074. [\[CrossRef\]](#)
20. Ahmed, R.; Uddin, M.K.; Quddus, M.A.; Samad, M.Y.A.; Hossain, M.A.M.; Haque, A.N.A. Impact of Foliar Application of Zinc and Zinc Oxide Nanoparticles on Growth, Yield, Nutrient Uptake and Quality of Tomato. *Horticulturae* **2023**, *9*, 162. [\[CrossRef\]](#)
21. Guzmán-Báez, G.A.; Trejo-Téllez, L.I.; Ramírez-Olvera, S.M.; Salinas-Ruiz, J.; Bello-Bello, J.J.; Alcántar-González, G.; Hidalgo-Contreras, J.V.; Gómez-Merino, F.C. Silver Nanoparticles Increase Nitrogen, Phosphorus, and Potassium Concentrations in Leaves and Stimulate Root Length and Number of Roots in Tomato Seedlings in a Hormetic Manner. *Dose-Response* **2021**, *19*, 15593258211044576. [\[CrossRef\]](#)
22. Noori, A.; Donnelly, T.; Colbert, J.; Cai, W.; Newman, L.A.; White, J.C. Exposure of tomato (*Lycopersicon esculentum*) to silver nanoparticles and silver nitrate: Physiological and molecular response. *Int. J. Phytoremediat.* **2020**, *22*, 40–51. [\[CrossRef\]](#) [\[PubMed\]](#)
23. Narware, J.; Singh, S.P.; Chakma, J.; Ranjan, P.; Behera, L.; Das, P.; Manzar, N.; Kashyap, A.S. Enhancing tomato growth and early blight disease resistance through green-synthesized silver nanoparticles: Insights into plant physiology. *S. Afr. J. Bot.* **2024**, *166*, 676–689. [\[CrossRef\]](#)
24. Khatoon, J.; Mehmood, A.; Khalid, A.R.; Khan, M.A.R.; Ahmad, K.S.; Amjad, M.S.; Bashir, U.; Raffi, M.; Proćków, J. Green-fabricated silver nanoparticles from *Quercus incana* leaf extract to control the early blight of tomatoes caused by *Alternaria solani*. *BMC Plant Biol.* **2024**, *24*, 302. [\[CrossRef\]](#) [\[PubMed\]](#)
25. Fares, A.; Mahdy, A.; El-Habbaa, G.; Abdalla, A.; Ahmed, G. A new technique for using gamma irradiation to enhance silver nanoparticles synthesized by chemical reduction and their effect on tomato early blight disease under field conditions. *Biocatal. Agric. Biotechnol.* **2024**, *58*, 103128. [\[CrossRef\]](#)
26. Shendge, V.S.; Magar, S.J.; Somwanshi, S. In vitro Antifungal Efficacy of Silver Nanoparticles against *Fusarium oxysporum* f. sp. *Lycopersici* in Tomato. *Microbiol. Res. J. Int.* **2024**, *34*, 1–9. [\[CrossRef\]](#)
27. Fabyi, O.A.; Olatunji, G.A. Nematicidal potency of silver nanoparticles and extracts from *Borreria verticillata* (L.) G. Mey against *Meloidogyne incognita* on tomato plants. *Indian Phytopathol.* **2024**, *77*, 311–321. [\[CrossRef\]](#)
28. García-Locascio, E.; Valenzuela, E.I.; Cervantes-Avilés, P. Impact of seed priming with Selenium nanoparticles on germination and seedlings growth of tomato. *Sci. Rep.* **2024**, *14*, 6726. [\[CrossRef\]](#)
29. Ahmad, A.; Javad, S.; Iqbal, S.; Shahzadi, K.; Gatasheh, M.K.; Javed, T. Alleviation potential of green-synthesized selenium nanoparticles for cadmium stress in *Solanum lycopersicum* L: Modulation of secondary metabolites and physiochemical attributes. *Plant Cell Rep.* **2024**, *43*, 113. [\[CrossRef\]](#)
30. Tombuloglu, G.; Tombuloglu, H.; Slimani, Y.; Almessiere, M.A.; Baykal, A.; Bostancioglu, S.M.; Kirat, G.; Ercan, I. Effects of foliar iron oxide nanoparticles (Fe₃O₄) application on photosynthetic parameters, distribution of mineral elements, magnetic behaviour, and photosynthetic genes in tomato (*Solanum lycopersicum* var. *cerasiforme*) plants. *Plant Physiol. Biochem.* **2024**, *210*, 108616. [\[CrossRef\]](#)
31. Bharathi, D.; Preethi, S.; Abarna, K.T.; Nithyasri, M.; Kishore, P.; Deepika, K. Bio-inspired synthesis of flower-shaped iron oxide nanoparticles (FeONPs) using phytochemicals of *Solanum lycopersicum* leaf extract for biomedical applications. *Biocatal. Agric. Biotechnol.* **2020**, *27*, 101698. [\[CrossRef\]](#)
32. Vaidehi, D.; Bhuvaneshwari, V.; Bharathi, D.; Pavithra Sheetal, B. Antibacterial and photocatalytic activity of copper oxide nanoparticles synthesized using *Solanum lycopersicum* leaf extract. *Mater. Res. Express* **2018**, *5*, 085403. [\[CrossRef\]](#)
33. Abid, M.A.; Kadhim, D.A.; Aziz, W.J. Iron oxide nanoparticle synthesis using trigonella and tomato extracts and their antibacterial activity. *Mater. Technol.* **2022**, *37*, 547–554. [\[CrossRef\]](#)
34. Chand, K.; Abro, M.I.; Aftab, U.; Shah, A.H.; Lakhan, M.N.; Cao, D.; Mehdi, G.; Mohamed, A.M.A. Green synthesis characterization and antimicrobial activity against *Staphylococcus aureus* of silver nanoparticles using extracts of neem, onion and tomato. *RSC Adv.* **2019**, *9*, 17002–17015. [\[CrossRef\]](#) [\[PubMed\]](#)
35. Shejawal, K.P.; Randive, D.S.; Bhinge, S.D.; Bhutkar, M.A.; Todkar, S.S.; Mulla, A.S.; Jadhav, N.R. Green synthesis of silver, iron and gold nanoparticles of lycopene extracted from tomato: Their characterization and cytotoxicity against COLO320DM, HT29 and Hella cell. *J. Mater. Sci. Mater. Med.* **2021**, *32*, 19. [\[CrossRef\]](#) [\[PubMed\]](#)
36. Zahra, S.; Iqbal, M.S.; Abbas, K.; Qadir, M.I. Synthesis, characterization and evaluation of biological properties of selenium nanoparticles from *Solanum lycopersicum*. *Arab. J. Chem.* **2022**, *15*, 103901. [\[CrossRef\]](#)
37. Ogunyemi, S.O.; Abdallah, Y.; Zhang, M.; Fouad, H.; Hong, X.; Ibrahim, E.; Li, B. Green synthesis of zinc oxide nanoparticles using different plant extracts and their antibacterial activity against *Xanthomonas oryzae* pv. *oryzae*. *Artif. Cells Nanomed. Biotechnol.* **2019**, *47*, 341–352. [\[CrossRef\]](#)
38. Elbrolesy, A.; Abdou, Y.; Elhussiny, F.A.; Morsy, R. Novel Green Synthesis of UV-Sunscreen ZnO Nanoparticles Using *Solanum Lycopersicum* Fruit Extract and Evaluation of Their Antibacterial and Anticancer Activity. *J. Inorg. Organomet. Polym.* **2023**, *33*, 3750–3759. [\[CrossRef\]](#)
39. Ahmed, H.A.; Salama, Z.A.; Salem, S.H.; Aly, H.F.; Nassrallah, A.; Abou-Elella, F.; Aboul-Enein, A.M. Lycopene nanoparticles ameliorate the antioxidants, antimicrobial and anticancer potencies of tomato pomace. *Egypt. J. Chem.* **2021**, *64*, 3739–3749. [\[CrossRef\]](#)

40. Baran, M.F.; Acay, H. Antimicrobial activity of silver nanoparticles synthesized with extract of tomato plant against bacterial and fungal pathogens. *Mid. Blac Sea J. Health Sci.* **2019**, *5*, 67–73. [\[CrossRef\]](#)
41. Muhammad, S.; Ali, A.; Zahoor, S.; Xinghua, X.; Shah, J.; Hamza, M.; Kashif, M.; Khan, S.; Ajat Khel, B.K.; Iqbal, A. Synthesis of Silver oxide nanoparticles and its antimicrobial, anticancer, anti-inflammatory, wound healing, and immunomodulatory activities—A review. *Acta Sci. Appl. Phys.* **2023**, *3*, 33–48.
42. Asif, M.; Iqbal, W.; Fakhar-e-Alam, M.; Hussain, Z.; Saadullah, M.; Hassan, M.; Rehman, J.; Dahlous, K.A.; Al-Qahtani, N.H. Synthesis and Characterization of Chemically and Green-Synthesized Silver Oxide Particles for Evaluation of Antiviral and Anticancer Activity. *Pharmaceuticals* **2024**, *17*, 908. [\[CrossRef\]](#) [\[PubMed\]](#)
43. Shahzad Shirazi, M.; Moridi Farimani, M.; Foroumadi, A.; Ghanemi, K.; Benaglia, M.; Makvandi, P. Bioengineered synthesis of phytochemical-adorned green silver oxide (Ag₂O) nanoparticles via *Mentha pulegium* and *Ficus carica* extracts with high antioxidant, antibacterial, and antifungal activities. *Sci. Rep.* **2022**, *12*, 21509. [\[CrossRef\]](#) [\[PubMed\]](#)
44. Aththanayaka, S.; Thiripuranathar, G.; Ekanayake, S. Microwave-assisted phytogenic Ag/Ag₂O/ZnO nanocomposite as a replacement of Ag/Ag₂O and ZnO nanoparticles: A comparative antioxidant study. *Surf. Interfaces* **2023**, *43*, 103547. [\[CrossRef\]](#)
45. Magdy, G.; Aboelkassim, E.; Abd Elhaleem, S.M.; Belal, F. A Comprehensive Review on Silver Nanoparticles: Synthesis Approaches, Characterization Techniques, and Recent Pharmaceutical, Environmental, and Antimicrobial Applications. *Microchem. J.* **2024**, *196*, 109615. [\[CrossRef\]](#)
46. Sharmin, S.; Rahaman, M.M.; Sarkar, C.; Atolani, O.; Islam, M.T.; Adeyemi, O.S. Nanoparticles as Antimicrobial and Antiviral Agents: A Literature-Based Perspective Study. *Heliyon* **2021**, *7*, e06456. [\[CrossRef\]](#) [\[PubMed\]](#)
47. Maravić, N.; Teslić, N.; Nikolić, D.; Dimić, I.; Šereš, Z.; Pavlić, B. From Agricultural Waste to Antioxidant-Rich Extracts: Green Techniques in Extraction of Polyphenols from Sugar Beet Leaves. *Sustain. Chem. Pharm.* **2022**, *28*, 100728. [\[CrossRef\]](#)
48. Chaves, J.; Mesquita, L.; Strieder, M.; Contieri, L.S.; Pizani, R.S.; Sanches, V.L.; Viganó, J.; Bezerra, R.M.N.; Rostagno, M. Eco-Friendly and High-Performance Extraction of Flavonoids from Lemon Peel Wastes by Applying Ultrasound-Assisted Extraction and Eutectic Solvents. *Sustain. Chem. Pharm.* **2024**, *39*, 101558. [\[CrossRef\]](#)
49. Mikucka, W.; Zielińska, M.; Bułkowska, K.; Witońska, I. Valorization of Distillery Stillage by Polyphenol Recovery Using Microwave-Assisted, Ultrasound-Assisted and Conventional Extractions. *J. Environ. Manag.* **2022**, *322*, 116150. [\[CrossRef\]](#)
50. Ou, H.; Zuo, J.; Gregersen, H.; Liu, X.Y. Combination of Supercritical CO₂ and Ultrasound for Flavonoids Extraction from Cosmos sulphureus: Optimization, Kinetics, Characterization, and Antioxidant Capacity. *Food Chem.* **2024**, *435*, 137598. [\[CrossRef\]](#)
51. Rudrapal, M.; Khairnar, S.J.; Khan, J.; Dukhyil, A.B.; Ansari, M.A.; Alomary, M.N.; Alshabrm, F.M.; Palai, S.; Deb, P.K.; Devi, R. Dietary Polyphenols and Their Role in Oxidative Stress-Induced Human Diseases: Insights into Protective Effects, Antioxidant Potentials, and Mechanism(s) of Action. *Front. Pharmacol.* **2022**, *13*, 806470. [\[CrossRef\]](#)
52. Cheng, M.; He, J.; Wang, H.; Li, C.; Wu, G.; Zhu, K.; Chen, X.; Zhang, Y.; Tan, L. Comparison of Microwave, Ultrasound, and Ultrasound-Microwave Assisted Solvent Extraction Methods on Phenolic Profile and Antioxidant Activity of Extracts from Jackfruit (*Artocarpus heterophyllus* Lam.) Pulp. *LWT-Food Sci. Technol.* **2023**, *173*, 114395. [\[CrossRef\]](#)
53. Afoakwah, N.A.; Zhao, Y.; Tchabo, W.; Dong, Y.; Owusu, J.; Mahunu, G.K. Studies on the Extraction of Jerusalem Artichoke Tuber Phenolics Using Microwave-Assisted Extraction Optimized Conditions. *Food Chem. Adv.* **2023**, *3*, 100507. [\[CrossRef\]](#)
54. Yusoff, I.M.; Mat Taher, Z.; Rahmat, Z.; Chua, L.S. A Review of Ultrasound-Assisted Extraction for Plant Bioactive Compounds: Phenolics, Flavonoids, Thymols, Saponins, and Proteins. *Food Res. Int.* **2022**, *157*, 111268. [\[CrossRef\]](#)
55. Peng, W.; Wang, X.; Wang, W.; Wang, Y.; Huang, J.; Zhou, R.; Bo, R.; Liu, M.; Yin, S.; Li, J. Comparison, Optimization, and Antioxidant Activity of Ultrasound-Assisted Natural Deep Eutectic Solvents Extraction and Traditional Method: A Greener Route for Extraction of Flavonoids from *Moringa oleifera* Lam. Leaves. *Ultrason. Sonochem.* **2024**, *109*, 107003. [\[CrossRef\]](#) [\[PubMed\]](#)
56. Liao, J.; Guo, Z.; Yu, G. Process Intensification and Kinetic Studies of Ultrasound-Assisted Extraction of Flavonoids from Peanut Shells. *Ultrason. Sonochem.* **2021**, *76*, 105661. [\[CrossRef\]](#) [\[PubMed\]](#)
57. Veršić Bratinčević, M.; Kovačić, R.; Popović, M.; Radman, S.; Generalić Mekinić, I. Comparison of Conventional and Green Extraction Techniques for the Isolation of Phenolic Antioxidants from Sea Fennel. *Processes* **2023**, *11*, 2172. [\[CrossRef\]](#)
58. Vilas-Boas, A.A.; Gómez-García, R.; Machado, M.; Nunes, C.; Ribeiro, S.; Nunes, J.; Oliveira, A.L.S.; Pintado, M. *Lavandula pedunculata* Polyphenol-Rich Extracts Obtained by Conventional, MAE and UAE Methods: Exploring the Bioactive Potential and Safety for Use as a Medicine Plant as Food and Nutraceutical Ingredient. *Foods* **2023**, *12*, 4462. [\[CrossRef\]](#)
59. Pradheesh, G.; Suresh, S.; Suresh, J.; Alexramani, V. Antimicrobial and Anticancer Activity Studies on Green Synthesized Silver Oxide Nanoparticles from the Medicinal Plant *Cyathea nilgiriensis* Holttum. *Int. J. Pharm. Investig.* **2020**, *10*, 146–150. [\[CrossRef\]](#)
60. Figueiredo-González, M.; Valentão, P.; Andrade, P.B. Tomato plant leaves: From by-products to the management of enzymes in chronic diseases. *Ind. Crops Prod.* **2016**, *94*, 621–629. [\[CrossRef\]](#)
61. Dharmaraj, D.; Krishnamoorthy, M.; Rajendran, K.; Karuppiah, K.; Annamalai, J.; Durairaj, K.R.; Santhiyagu, P.; Ethiraj, K. Antibacterial and Cytotoxicity Activities of Biosynthesized Silver Oxide (Ag₂O) Nanoparticles Using *Bacillus paramycoides*. *J. Drug Deliv. Sci. Technol.* **2021**, *61*, 102111. [\[CrossRef\]](#)
62. Zagloul, H.; Dhahri, M.; Bashal, A.H.; Khaleil, M.M.; Habeeb, T.H.; Khalil, K.D. Multifunctional Ag₂O/Chitosan Nanocomposites Synthesized via Sol-Gel with Enhanced Antimicrobial and Antioxidant Properties: A Novel Food Packaging Material. *Int. J. Biol. Macromol.* **2024**, *264 Pt 1*, 129990. [\[CrossRef\]](#) [\[PubMed\]](#)
63. Gharibshahi, L.; Saion, E.; Gharibshahi, E.; Shaari, A.H.; Matori, K.A. Structural and Optical Properties of Ag Nanoparticles Synthesized by Thermal Treatment Method. *Materials* **2017**, *10*, 402. [\[CrossRef\]](#) [\[PubMed\]](#)

64. Kayed, K.; Issa, M.; Al-ourabi, H. The FTIR Spectra of Ag/Ag₂O Composites Doped with Silver Nanoparticles. *J. Exp. Nanosci.* **2024**, *19*, 2336227. [\[CrossRef\]](#)
65. Wongsu, P.; Phatikulrungsun, P.; Prathumthong, S. FT-IR Characteristics, Phenolic Profiles and Inhibitory Potential Against Digestive Enzymes of 25 Herbal Infusions. *Sci. Rep.* **2022**, *12*, 6631. [\[CrossRef\]](#) [\[PubMed\]](#)
66. Nawaz, H.Z.R.; Falak, U.; Naz, T.; Baig, M.M.; Mehmood Ahmad, R.T.; Rasheed, A.; Dastgeer, G. Synthesis of Silver/Silver Oxide Heterostructures via Partial Reduction of AgNO₃ Using a Novel Green Reducing Agent. *Ceram. Int.* **2022**, *48*, 37194–37202. [\[CrossRef\]](#)
67. Li, R.; Chen, Z.; Ren, N.; Wang, Y.; Wang, Y.; Yu, F. Biosynthesis of Silver Oxide Nanoparticles and Their Photocatalytic and Antimicrobial Activity Evaluation for Wound Healing Applications in Nursing Care. *J. Photochem. Photobiol. B Biol.* **2019**, *199*, 111593. [\[CrossRef\]](#)
68. Maheshwaran, G.; Nivedhitha Bharathi, A.; Malai Selvi, M.; Krishna Kumar, M.; Mohan Kumar, R.; Sudhahar, S. Green Synthesis of Silver Oxide Nanoparticles Using *Zephyranthes Rosea* Flower Extract and Evaluation of Biological Activities. *J. Environ. Chem. Eng.* **2020**, *8*, 104137. [\[CrossRef\]](#)
69. Yaseen, M.W.; Asghar, M.A.; Bakhsh, E.M.; Akhtar, K.; Khan, S.B.; Iqbal, M. Plant-Mediated Synthesis of Thermally Stable Metal-Polystyrene Nanocomposites for Antioxidant and Antibacterial Food Packaging. *Ind. Crops Prod.* **2024**, *209*, 117959. [\[CrossRef\]](#)
70. Tamanna, N.J.; Hossain, M.S.; Bahadur, N.M.; Ahmed, S. Green Synthesis of Ag₂O & Facile Synthesis of ZnO and Characterization Using FTIR, Bandgap Energy & XRD (Scherrer Equation, Williamson-Hall, Size-Train Plot, Monshi-Scherrer Model). *Results Chem.* **2024**, *7*, 101313. [\[CrossRef\]](#)
71. Masho, T.J.; Arasu, P.T.; Bogale, R.F.; Zerrefa, E.A.; Ramamurthy, S. Green Synthesis, Characterization of Ag₂O/CuO/ZnO Nanocomposites Using Aqueous Extract of *Croton macrostachyus* Leaf for Photodegradation, Antimicrobial, and Antioxidant Activities. *Results Chem.* **2024**, *7*, 101369. [\[CrossRef\]](#)
72. Mathimaran, A.; Pandian, C.J.; Sappanimuthu, P.; Krishnakumar, H.; Amala, M.; Veerapandiyan, M.; Kingsly, J.; Solomon, A.; Sonamuthu, J.; Jeyaraman, J. Synthesis of multifunctional silver oxide, zinc oxide, copper oxide, and gold nanoparticles for enhanced antibacterial activity against ESKAPE pathogens and antioxidant, anticancer activities using *Momordica cymbalaria* seed extract. *Mater. Today Commun.* **2024**, *39*, 108838. [\[CrossRef\]](#)
73. Gevorgyan, S.; Schubert, R.; Falke, S.; Lorenzen, K.; Trchounian, K.; Betzel, C. Structural characterization and antibacterial activity of silver nanoparticles synthesized using a low-molecular-weight *Royal Jelly* extract. *Sci. Rep.* **2022**, *12*, 14077. [\[CrossRef\]](#) [\[PubMed\]](#)
74. Hossain, T.J. Methods for screening and evaluation of antimicrobial activity: A review of protocols, advantages, and limitations. *Eur. J. Microbiol. Immunol. (Bp)* **2024**, *14*, 97–115. [\[CrossRef\]](#) [\[PubMed\]](#)
75. Bruna, T.; Maldonado-Bravo, F.; Jara, P.; Caro, N. Silver Nanoparticles and Their Antibacterial Applications. *Int. J. Mol. Sci.* **2021**, *22*, 7202. [\[CrossRef\]](#)
76. Mohammadi, A.H.; Sobhani-Nasab, A.; Nejati, M.; Hadi, S.; Behjati, M.; Mirzaii-Dizgah, I.; Moradi Hasan-Abad, A.; Karami, M. Preparation and Characterization of CuO, Ag₂O, and ZnO Nanoparticles and Investigation of Their Antibacterial and Anticancer Properties on HCT-116 and C26 Cells. *Inorg. Chem. Commun.* **2023**, *149*, 110404. [\[CrossRef\]](#)
77. Hemeg, H.A.; Moussa, I.M.; Ibrahim, S.; Dawoud, T.M.; Alhaji, J.H.; Mubarak, A.S.; Kabli, S.A.; Alsubki, R.A.; Tawfik, A.M.; Marouf, S.A. Antimicrobial Effect of Different Herbal Plant Extracts Against Different Microbial Populations. *Saudi J. Biol. Sci.* **2020**, *27*, 3221–3227. [\[CrossRef\]](#)
78. Mani, J.; Johnson, J.; Hosking, H.; Walsh, K.; Neilsen, P.; Naiker, M. In Vitro Cytotoxic Properties of Crude Polar Extracts of Plants Sourced from Australia. *Clin. Complement. Med. Pharmacol.* **2022**, *2*, 100022. [\[CrossRef\]](#)
79. Pandey, B.P.; Adhikari, K.; Pradhan, S.P.; Shin, H.J.; Lee, K.E.; Jung, H.J. In-vitro antioxidant, anti-cancer, and anti-inflammatory activities of selected medicinal plants from western Nepal. *Futur. J. Pharm. Sci.* **2020**, *6*, 75. [\[CrossRef\]](#)
80. Ahamed, M.; Khan, M.A.M.; Akhtar, M.J.; Alhadlaq, H.A.; Alshamsan, A. Ag-doping regulates the cytotoxicity of TiO₂ nanoparticles via oxidative stress in human cancer cells. *Sci. Rep.* **2017**, *7*, 17662. [\[CrossRef\]](#)
81. Elyamny, S.; Eltarahony, M.; Abu-Serie, M.; Nabil, M.M.; Kashyout, A.E.-H.B. One-Pot Fabrication of Ag@Ag₂O Core-Shell Nanostructures for Biosafe Antimicrobial and Antibiofilm Applications. *Sci. Rep.* **2021**, *11*, 22543. [\[CrossRef\]](#)
82. Malin, V.; Elez Garofulić, I.; Repajić, M.; Zorić, Z.; Pedisić, S.; Sterniša, M.; Smole Možina, S.; Dragović-Uzelac, V. Phenolic Characterization and Bioactivity of Fennel Seed (*Foeniculum vulgare* Mill.) Extracts Isolated by Microwave-Assisted and Conventional Extraction. *Processes* **2022**, *10*, 510. [\[CrossRef\]](#)
83. Tsiaka, T.; Fotakis, C.; Lantzouraki, D.Z.; Tsiantas, K.; Siapi, E.; Sinanoglou, V.J.; Zoumpoulakis, P. Expanding the Role of Sub-Exploited DOE-High Energy Extraction and Metabolomic Profiling towards Agro-Byproduct Valorization: The Case of Carotenoid-Rich Apricot Pulp. *Molecules* **2020**, *25*, 2702. [\[CrossRef\]](#) [\[PubMed\]](#)
84. Alam, P.; Noman, O.M.; Herqash, R.N.; Almarfadi, O.M.; Akhtar, A.; Alqahtani, A.S. Efficient Extraction of an Anthraquinone Physcion Using Response Surface Methodology (RSM) Optimized Ultrasound-Assisted Extraction Method from Aerial Parts of *Senna occidentalis* and Analysis by HPLC-UV. *Separations* **2022**, *9*, 142. [\[CrossRef\]](#)
85. Martins, G.R.; Monteiro, A.F.; do Amaral, F.R.L.; da Silva, A.S.A. A validated Folin-Ciocalteu method for total phenolics quantification of condensed tannin-rich açai (*Euterpe oleracea* Mart.) seeds extract. *J. Food Sci. Technol.* **2021**, *58*, 4693–4702. [\[CrossRef\]](#) [\[PubMed\]](#)

86. Zhang, L.; Xu, Q.; Li, L.; Lin, L.; Yu, J.; Zhu, J.; Zhang, H.; Xia, G.; Zang, H. Antioxidant and Enzyme-Inhibitory Activity of Extracts from *Erigeron annuus* Flower. *Ind. Crops Prod.* **2020**, *148*, 112283. [[CrossRef](#)]
87. Hafshejani, S.F.; Lotfi, S.; Rezvannejad, E.; Mortazavi, M.; Riahi-Madvar, A. Correlation between Total Phenolic and Flavonoid Contents and Biological Activities of 12 Ethanolic Extracts of Iranian Propolis. *Appl. Sci.* **2023**, *11*, 4308–4325. [[CrossRef](#)]
88. Asem, N.; Abdul Gapar, N.A.; Abd Hapit, N.H.; Omar, E.A. Correlation between total phenolic and flavonoid contents with antioxidant activity of Malaysian stingless bee propolis extract. *J. Apic. Res.* **2019**, *59*, 437–442. [[CrossRef](#)]
89. Chen, Q.; Wang, D.; Tan, C.; Hu, Y.; Sundararajan, B.; Zhou, Z. Profiling of Flavonoid and Antioxidant Activity of Fruit Tissues from 27 Chinese Local Citrus Cultivars. *Plants* **2020**, *9*, 196. [[CrossRef](#)]
90. Johnson, J.B.; Mani, J.S.; Naiker, M. Microplate Methods for Measuring Phenolic Content and Antioxidant Capacity in Chickpea: Impact of Shaking. *Eng. Proc.* **2023**, *48*, 57. [[CrossRef](#)]
91. Shume, W.M.; Murthy, H.C.A.; Zereffa, E. A Review on Synthesis and Characterization of Ag₂O Nanoparticles for Photocatalytic Applications. *J. Chem.* **2020**, *2020*, 5039479. [[CrossRef](#)]
92. Tarighat, M.A.; Naamdar, F. PLSR-colorimetric simultaneous determination of L-Tyrosine and L-Tryptophan in different pharmaceutical and biological samples using one-pot synthesized leaf shape Ag@Ag₂O core-shell nanocomposites modified by β -CD. *J. Pharm. Biomed. Anal.* **2024**, *241*, 115942. [[CrossRef](#)] [[PubMed](#)]

Disclaimer/Publisher's Note: The statements, opinions and data contained in all publications are solely those of the individual author(s) and contributor(s) and not of MDPI and/or the editor(s). MDPI and/or the editor(s) disclaim responsibility for any injury to people or property resulting from any ideas, methods, instructions or products referred to in the content.



Article

Novel Antimicrobial Agents Based on Zinc-Doped Hydroxyapatite Loaded with Tetracycline

Simona Liliana Iconaru ^{1,*}, Daniela Predoi ^{1,*}, Carmen Steluta Ciobanu ¹, Catalin Constantin Negrila ¹, Roxana Trusca ², Steinar Raaen ³, Krzysztof Rokosz ⁴, Liliana Ghegoiu ¹, Monica Luminita Badea ⁵ and Carmen Cimpeanu ⁶

¹ National Institute of Materials Physics, Atomistilor Street, No. 405A, 077125 Magurele, Romania; ciobanucs@gmail.com (C.S.C.); catalin.negrila@infim.ro (C.C.N.); ghegoiuliliana@gmail.com (L.G.)

² National Centre for Micro and Nanomaterials, University Politehnica of Bucharest, 060042 Bucharest, Romania; truscaroxana@yahoo.com

³ Department of Physics, Norwegian University of Science and Technology (NTNU), Realfagbygget E3-124 Høgskoleringen 5, NO 7491 Trondheim, Norway; steinar.raaen@ntnu.no

⁴ Faculty of Electronics and Computer Science, Koszalin University of Technology, Śniadeckich 2, PL 75-453 Koszalin, Poland; rokosz@tu.koszalin.pl

⁵ Faculty of Horticulture, University of Agronomic Sciences and Veterinary Medicine, 59 Marasti Boulevard, 011464 Bucharest, Romania; badea.artemisla@gmail.com

⁶ Faculty of Land Reclamation and Environmental Engineering, University of Agronomic Sciences and Veterinary Medicine of Bucharest, 59 Marasti Boulevard, 011464 Bucharest, Romania; carmencimpeanu@yahoo.com

* Correspondence: simonaiconaru@gmail.com (S.L.I.); dpredoi@gmail.com (D.P.)

Abstract: In this paper, we present for the first time the development of zinc-doped hydroxyapatite enriched with tetracycline (ZnHApTe) powders and provide a comprehensive evaluation of their physico-chemical and biological properties. Various techniques such as X-ray diffraction (XRD), X-ray photoelectron spectroscopy (XPS), scanning electron microscopy (SEM), and Fourier transform infrared spectroscopy (FTIR) were used for the sample's complex evaluation. Moreover, the biocompatibility of zinc-doped hydroxyapatite (ZnHAp) and ZnHApTe nanoparticles was evaluated with the aid of human fetal osteoblastic cells (hFOB 1.19 cell line). The results of the biological assays suggested that these nanoparticles hold great promise as potential candidates for the future development of novel biocompatible and antimicrobial agents for biomedical applications. The antimicrobial properties of the ZnHAp and ZnHApTe nanoparticles were assessed using the standard reference microbial strains *Staphylococcus aureus* ATCC 25923, *Escherichia coli* ATCC 25922, and *Candida albicans* ATCC 10231. The results of the in vitro antimicrobial assay demonstrated that both tested materials exhibited good antimicrobial activity. Additionally, these data also indicated that the antimicrobial effects of the ZnHAp nanoparticles were intensified by the presence of tetracycline (Te). Furthermore, the results also suggested that the antimicrobial activity of the samples increased with the incubation time.

Keywords: zinc; hydroxyapatite; tetracycline; in vitro biological studies; composition; biomedical applications



Citation: Iconaru, S.L.; Predoi, D.; Ciobanu, C.S.; Negrila, C.C.; Trusca, R.; Raaen, S.; Rokosz, K.; Ghegoiu, L.; Badea, M.L.; Cimpeanu, C. Novel Antimicrobial Agents Based on Zinc-Doped Hydroxyapatite Loaded with Tetracycline. *Antibiotics* **2024**, *13*, 803. <https://doi.org/10.3390/antibiotics13090803>

Academic Editor: Marc Maresca

Received: 30 July 2024

Revised: 20 August 2024

Accepted: 23 August 2024

Published: 25 August 2024



Copyright: © 2024 by the authors. Licensee MDPI, Basel, Switzerland. This article is an open access article distributed under the terms and conditions of the Creative Commons Attribution (CC BY) license (<https://creativecommons.org/licenses/by/4.0/>).

1. Introduction

Currently, the prevention of infections and their management (for example, those associated with orthopedic and dental implant procedures/operations) still represent a major challenge for both the medical and the scientific community. The standard treatment for these infections usually involves the systemic administration of antibiotics at high doses for long time periods that come with several important disadvantages (such as high costs and toxicity) [1,2]. On the other hand, the increasing microbial resistance represents a global health problem that requires the funding of new and alternative antimicrobial

agents [3]. The calcium phosphate compounds, specifically hydroxyapatite (HAp), are known as the main inorganic constituent of hard tissues from the human body, such as teeth and bones [4,5]. Synthetic biomaterials based on HAp have attracted the researcher's attention mainly because of their close resemblance to the mineral composition of human bones [4,5]. Moreover, HAp possesses the ability to promote the formation of new bone tissue and exhibit excellent osteoconductive properties [4–6].

Furthermore, the hexagonal structure of stoichiometric hydroxyapatite (HAp) allows substitution with various ions such as zinc, silver, cerium, samarium, and magnesium [7–11]. Among them, zinc is a trace metal that can be found in abundance in bone tissue, enhances bone metabolism and formation, prevents bone loss, and increases bone density [12,13]. In addition, according to previous studies, zinc-doped biphasic calcium phosphate ceramics and zinc-doped HAp have shown excellent bone formation and superior bone-implant attachment in animal studies [14]. Additionally, zinc-containing apatite layers on titanium rods significantly increased the proliferation and differentiation of fibroblastic and osteoblastic cell lines [13].

In addition, zinc is recognized for its antimicrobial activity against various microbial agents, such as *Escherichia coli*, *Pseudomonas aeruginosa*, *Staphylococcus aureus*, *C. albicans*, etc. [15,16]. In the studies previously reported, it was shown that zinc concentration from zinc-doped hydroxyapatite colloids strongly influences their in vitro antimicrobial activity against *Escherichia coli* and *Staphylococcus aureus* [17]. Similar results regarding the antimicrobial activity of zinc-doped hydroxyapatite materials against *Staphylococcus aureus* and *Escherichia* sp. were also reported by Ofudje, E.A., et al. [3]. Moreover, their results highlight that the obtained zinc-doped HAp composites possess excellent bioactive activity [3].

The tetracycline class represents a type of bacteriostatic agent with a broad spectrum of antimicrobial activity. They are effective against both Gram-positive and Gram-negative bacteria, including aerobic and anaerobic types. In addition, tetracyclines are effective in treating infections caused by *Mycoplasma*, *Rickettsiae*, *Chlamydia*, certain protozoa, and spirochetes [18]. Therefore, the development of new biomaterials based on zinc, hydroxyapatite, and tetracycline could represent a proper alternative for the prevention of infection occurrence associated with bone/teeth surgeries/procedures. In a study carried out by Rusu, L.C. [19], the results obtained on new types of bone grafts with antimicrobial properties (obtained by combining hydroxyapatite with a carboxymethylcellulose-collagen gel) used to deliver tetracycline over a long period of time are presented. Their results showed that these grafts could be used to treat infected bone defects [19]. The new types of grafts offer efficient local administration of the antibiotic, which leads to the minimization of systemic side effects [19]. Another study conducted by Rivadeneira, J. et al. [20] reported the development of tetracycline hydrochloride was incorporated into collagen type I membranes coated with bioactive glass to prevent wound infections. The antibiotic was released over 72 h and showed antibacterial activity against *Staphylococcus aureus*. The incorporation of tetracycline was dependent on its initial concentration, but the efficacy in inhibiting bacterial growth was similar across different concentrations, indicating the composite's potential in preventing wound infections [20]. The study reported by Soriano-Souza, C., and collaborators [21] evaluates the hydroxyapatite ceramic microspheres loaded with doxycycline (HADOX) from the physical, chemical, and biological points of view. Their results underline that HADOX microspheres effectively inhibited bacterial growth for up to 7 days and did not significantly affect osteoblast viability compared with non-loaded HA microspheres [21]. In rat socket healing (after tooth extraction) experiments, HADOX facilitated bone formation and controlled inflammation, suggesting its potential as a biomaterial for enhancing bone repair in infected sites [21]. The previous studies conducted by D. Predoi and coworkers [22] revealed that the excellent antimicrobial activity of tetracycline embedded in silver-doped hydroxyapatite suspensions depends on the incubation time [22].

The aim and novelty of this work mainly consist of the development of zinc-doped hydroxyapatite enriched with tetracycline powders for the first time and their complex evaluation from a physicochemical and biological point of view. The obtained powders were evaluated using techniques such as X-ray diffraction (XRD), X-ray photoelectron spectroscopy (XPS), scanning electron microscopy (SEM), and Fourier transform infrared spectroscopy (FTIR). The in vitro biological activity was analyzed using a hemolysis assay, an MTT assay, and a lactate dehydrogenase (LDH) release measurement. Moreover, the in vitro antimicrobial activity of nanopowders was assessed using common reference strains such as *Staphylococcus aureus* ATCC 25923, *Escherichia coli* ATCC 25922, and *Candida albicans* ATCC 10231.

2. Results and Discussions

Figure 1 illustrates the typical XRD patterns of the ZnHAp (Figure 1a), ZnHApTe (Figure 1b), and Te (Figure 1c) samples. The standard database JCPDS #09-0432 (Figure 1e) and JCPDS #39-1987 (Figure 1d) of hydroxyapatite (HAp) and tetracycline (Te) were presented. The diffraction peaks observed in the XRD spectra of the ZnHAp sample correspond to the hexagonal (P63/m) lattice of HAp in agreement with the standard JCPDS database (JCPDS #09-0432). On the other hand, the diffraction peaks observed in the XRD spectra of the ZnHApTe sample (Figure 1b) correspond to the hexagonal lattice of HAp and tetracycline (Te) according with the standard database JCPDS #09-0432 and JCPDS #39-1987. The typical XRD peaks of the HAp structure were identified in Figure 1a. On the other hand, the HAp typical peaks were revealed in Figure 1b. Moreover, the typical peaks of Te were also observed in Figure 1b. Additionally, no zinc oxide, impurities, or secondary phases were detected. XRD analysis confirmed the obtained composite based on hydroxyapatite and tetracycline.

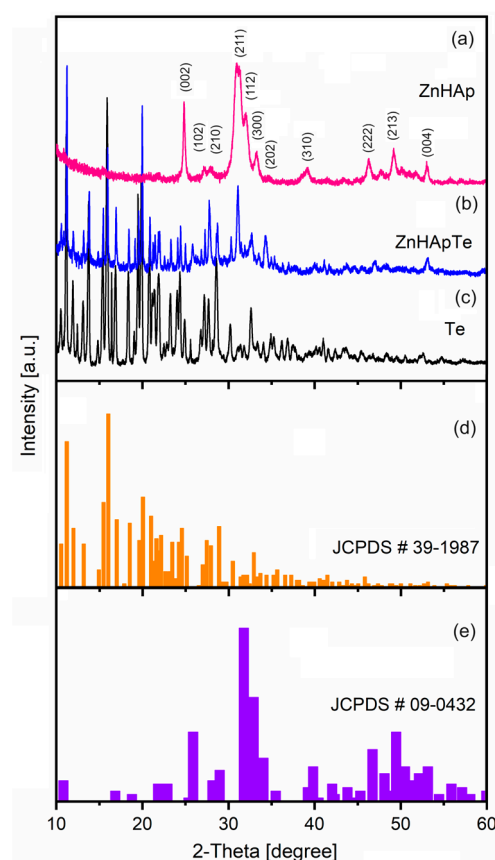


Figure 1. XRD patterns of the ZnHAp (a), ZnHApTe (b), and tetracycline (c) samples and standard database JCPDS #39-1987 (d) and JCPDS #09-0432 (e).

Figure 2 presents the FTIR general spectra obtained for ZnHAp, ZnHApTe, and Te samples. For the ZnHAp samples, the FTIR spectra reveal the presence of the vibrational maxima that are associated with the vibration of functional groups from the hydroxyapatite structure. Therefore, the vibrational maxima centered around 962 cm^{-1} is characteristic of the ν_1 non-degenerate symmetric stretching mode of the P-O bond, indicating the presence of HAp in the studied sample [22]. The vibrational maxima centered around 472 cm^{-1} (ν_2), 560 cm^{-1} (ν_4), 600 cm^{-1} (ν_4), 1021 cm^{-1} (ν_3), and 1095 cm^{-1} (ν_3) are characteristic of the vibration of the PO_4^{3-} group [22,23]. The vibrational maxima centered approximately at 632 cm^{-1} is usually associated with the vibrational modes of structural OH^- groups [22]. Meanwhile, the vibrational maxima centered around 876 cm^{-1} appear because of the presence of carbonate groups in the ZnHAp sample [22].

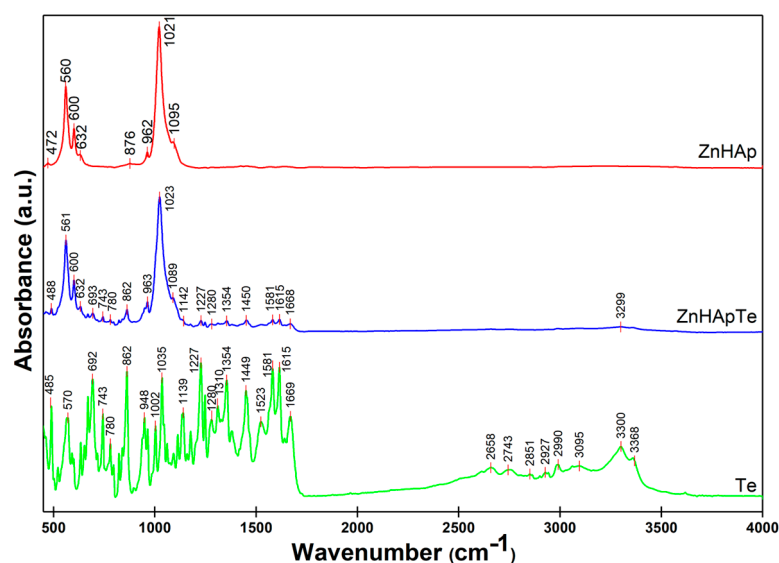


Figure 2. FTIR general spectra obtained for ZnHAp, ZnHApTe, and Te samples.

In the FTIR spectra of tetracycline recorded between 450 and 4000 cm^{-1} , the main vibrational maxima characteristic to the aromatic ring stretching vibrations ($\text{C}=\text{C}$) that are centered between 1449 cm^{-1} and 1669 cm^{-1} [22–25] are observed. In addition, in the FTIR spectra of tetracycline, the vibrational maxima characteristic of the aromatic deformation ($=\text{C}-\text{H}$) are present. These maxima are centered between 669 cm^{-1} and 948 cm^{-1} [22,25]. The vibrational maxima centered around 1354 cm^{-1} could be attributed to either the terminal dimethyl bending vibration mode, symmetric CH_3 bending mode, or C-O stretching [22,24,25]. Additionally, the vibrational maxima centered at 1227 cm^{-1} and 1112 cm^{-1} are attributed to the C-N stretching vibration mode [22,24–26]. In addition, the vibrational maxima specific to the out-of-plane aromatic ring deformation are observed around 485 cm^{-1} , 668 cm^{-1} , and 692 cm^{-1} [22,25]. The vibrational maxima associated with the in-plane ring deformation are centered at 633 cm^{-1} [22,25].

Thus, the FTIR spectra of the ZnHApTe powders clearly highlight the presence of the main vibrational maxima characteristic to the functional groups from both hydroxyapatite and tetracycline molecular structures. The maxima observed in the FTIR spectra of the ZnHApTe powders are slightly shifted compared with the maxima observed in the reference FTIR spectra of the ZnHAp and Te samples. In addition, the additional vibrational maxima that appear in the ZnHApTe sample because of the presence of tetracycline are less intense compared with those in the reference spectra of the antibiotic. These results suggest that the antibiotic interacts well with the hydroxyapatite structure and are in good agreement with the results previously reported by D. Predoi et al. [22].

To obtain valuable information regarding the subtle spectral changes in the ZnHAp, ZnHApTe, and Te samples, the FTIR spectra between 900 cm^{-1} and 1200 cm^{-1} were analyzed using second derivative and curve fitting methods (Figure 3). This spectral

region is characteristic of the ν_1 and ν_3 vibration of PO_4^{3-} (for the ZnHAp sample). The second derivative spectra and deconvoluted spectra of the Te sample are presented to show that the additional maxima that appear in the FTIR spectra of the ZnHApTe sample belong to Te. In the second derivative spectra of the ZnHAp (Figure 3d) sample, the ν_3 main vibrational maxima of the phosphate group are centered around 1020 cm^{-1} , 1023 cm^{-1} , 1039 cm^{-1} , 1043 cm^{-1} , 1071 cm^{-1} , and 1091 cm^{-1} [27,28]. Furthermore, the ν_1 vibrational maxima of the phosphate group is centered around 962 cm^{-1} in Figure 3d. The second derivative spectra of the tetracycline (Figure 3f) reveal the presence of multiple vibrational maxima that are usually associated with the aromatic C-H in-plane deformation (between 1200 and 1000 cm^{-1}) and to C-N stretching (around 965 cm^{-1}) [29]. To better highlight the presence of both ZnHAp and Te in the ZnHApTe composition, FTIR second derivative analysis was conducted (Figure 3f). The obtained spectra revealed that the characteristic maxima of HAp and Te are slightly displaced compared with their position in the reference FTIR spectra. Thus, the vibrational maxima associated with the ν_3 vibration of the phosphate group are centered at about 1023 cm^{-1} , 1034 cm^{-1} , 1045 cm^{-1} , 1071 cm^{-1} , and 1090 cm^{-1} . The presence of HAp in the ZnHApTe was also confirmed by the presence in the second derivative spectra of the intense ν_1 vibration band of the phosphate group at about 963 cm^{-1} . The presence of the tetracycline in the ZnHApTe sample was confirmed by their specific aromatic C-H in-plane deformation and C-N stretching vibrational bands. It was noticed that the main functional groups that conduct the ZnHApTe absorbance in the studied spectral domain are assigned to the hydroxyapatite (namely phosphate groups) and tetracycline structure (C-H in-plane deformation and C-N stretching).

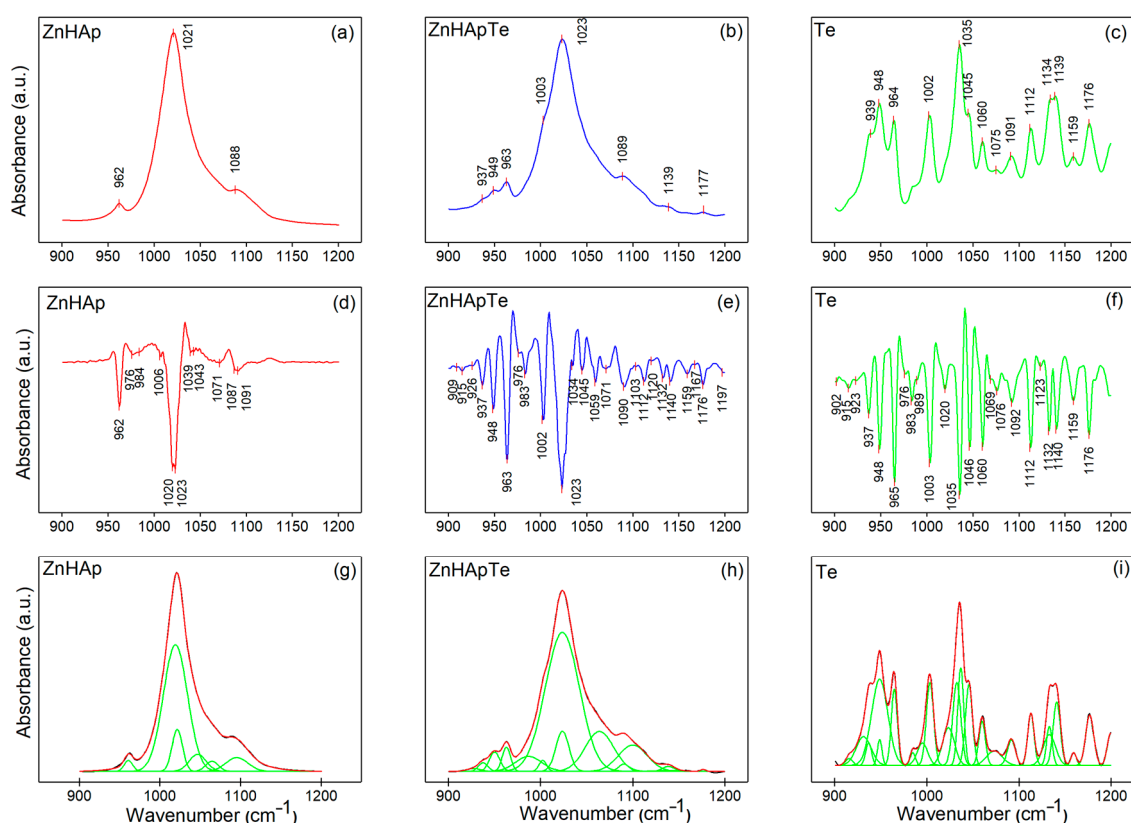


Figure 3. (a–c) FTIR spectra in the $900\text{--}1200\text{ cm}^{-1}$ spectral domain, (d–f) second derivative spectra, and (g–i) deconvoluted FTIR spectra of the ZnHAp, ZnHApTe, and Te samples.

Figure 3g–i shows the experimental and calculated contours overlaid (red) along with the individual subbands (green) identified through curve fitting analysis of the ZnHAp, ZnHApTe, and Te samples in the $900\text{--}1200\text{ cm}^{-1}$ region. Thus, six components were needed to achieve a satisfactory fit for the ZnHAp sample (Figure 3g). The six subbands

are centered at 1022 cm^{-1} , 1019 cm^{-1} , 1047 cm^{-1} , 1095 cm^{-1} , 961 cm^{-1} , and 1065 cm^{-1} . In the case of the ZnHApTe sample, a satisfactory fit was obtained with the aid of fourteen subbands. Moreover, twenty-three subbands were used to obtain a satisfactory fit in the case of the Te sample. Therefore, the results of the FTIR studies demonstrate the presence of both HAp and Te in the analyzed powders and their good interaction.

In order to analyze the surface chemistry and elemental composition of the ZnHAp, Te, and ZnHApTe samples, an XPS study was performed. The general XPS spectra of the samples are presented in Figure 4. The XPS studies highlighted the presence of zinc (Zn), oxygen (O1s), calcium (Ca2p), phosphorus (P2p), and carbon (C1s) in the XPS general spectra of the ZnHAp and ZnHApTe samples (Figure 4a,c). On the other hand, nitrogen (N1s) was observed in the XPS general spectra of the Te and ZnHApTe samples (Figure 4b,c). The presence of N 1s demonstrates the presence of tetracycline in the ZnHApTe sample. In addition, the presence of O1s and C1s also demonstrates the presence of tetracycline in the ZnHApTe sample. It can be observed that the intensities of O1s and C1s peaks are more intense in the case of the ZnHApTe sample (Figure 4c) than in the case of the ZnHAp (Figure 4a) sample. Moreover, the presence of chlorine (Cl1s) in the XPS spectra of the Te and ZnHApTe samples is due to the impurities present in the tetracycline powder.

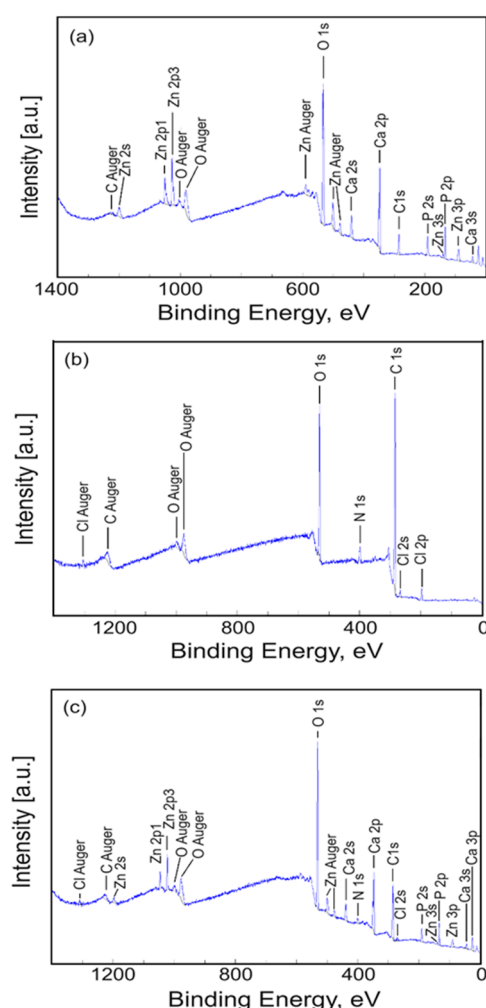


Figure 4. General XPS spectra of the ZnHAp (a), Te (b), and ZnHApTe (c) samples.

XPS high-resolution spectra of constituent elements C1s, O1s, Ca2p, P2p, Zn2p, and N1s of the ZnHApTe sample are presented in Figure 5.

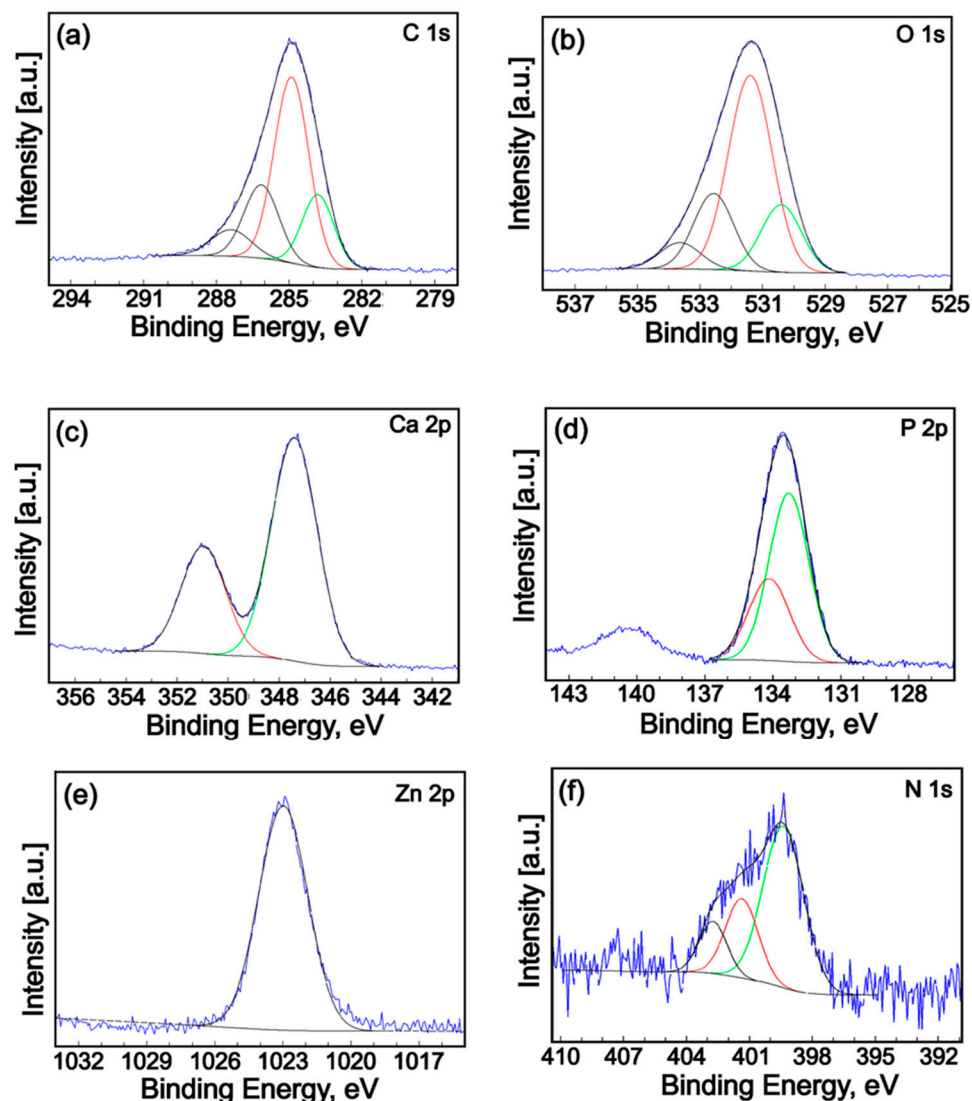


Figure 5. High-resolution XPS spectra and curve-fitting results of C1s (a), O1s (b), Ca2p (c), P2p (d), Zn2p (e) and N1s (f) for ZnHApTe sample.

The high-resolution spectra of C1s of the ZnHApTe (Figure 5a) show a single C-C bond that was identified at a binding energy of 284.9 eV [30]. A peak of about 283.1 eV was also observed for C=C bonds (sp^2 hybridization). The peak observed at 286.14 eV was associated with C-O single bonds. The peak at 287.4 eV allocated to C=C or O-C-O bonds was distinguished. High-resolution XPS spectra of O1s oxygen for the ZnHApTe sample are shown in Figure 5b. The four distinct signals at binding energy at 530.40, 531.31, 532.56, and 533.64 eV were detected. The signal at 530.40 eV was attributed to C=O double bonds with aromatic C. On the other hand, the signal at 530.40 eV can be associated with the bonding of oxygen with calcium (Ca) in agreement with Zhang et al. [31]. The signal identified at 531.31 eV can be ascribed to the Ca-O bond [32] of hydroxyapatite (HAp) and C=O double bonds with aliphatic C. Moreover, in prior studies [33–35], it was shown that the binding energy of chemisorbed oxygen species (O-) is in the range of 531.0–531.5 eV. The signal at 532.56 eV could be attributed to the P-O bond [32] as well as simple C-O bonds with aliphatic C. The signal detected at 533.64 eV can be assigned to O-H [36,37]. The high-resolution XPS spectrum of Ca2p (Figure 5c) shows two specific lines (2p_{3/2} and 2p_{1/2}) spaced at approximately 3.6 eV with an area ratio close to 2:1. The binding energy of the two peaks (347.40 and 350.97 eV) is specific to hydroxyapatite [38]. In the high-resolution XPS spectrum of P2p, two specific lines (2p_{3/2} and 2p_{1/2}) spaced at

approximately 0.9 eV with an area ratio close to 2:1 were observed (Figure 5d). The binding energy of the two peaks (133.29 and 134.16 eV) is specific to hydroxyapatite [39,40]. In Figure 5e, the high-resolution XPS spectrum of Zn2p is presented. After deconvolution, the maximum peak of Zn2p_{3/2} was identified around the binding energy of approximately 1022.5 eV [41]. The obtained results are in good agreement with previously presented data [42]. Moreover, following the replacement of Ca²⁺ ions with Zn²⁺, the valence of zinc did not change. The full width also confirms this fact at half maximum (FWHM) of the 2p_{3/2} signal. The FWHM of the 2p_{3/2} signal was 2.54 eV, which is in agreement with previously obtained results [43]. High-resolution XPS spectra of the N1s peak of ZnHApTe are exhibited in Figure 5f. The N1s peak was deconvoluted in three components. The first component was located at 399.32 eV. The second component was identified at 401.35 eV. The third component was observed at 402.73 eV. The first component could be associated with C-N single bands with aromatic C. The second component located at 401 eV indicates a protonated N. The third component corresponds to the beginning of N-O bond formation.

The transmission electron microscopy studies were used to obtain information about the morphology features of the ZnHAp and ZnHApTe nanoparticles. The results of the TEM studies are presented in Figure 6. As can be observed, both samples possess an acicular morphology. Moreover, the TEM studies also underline the nanometric dimension of the ZnHAp and ZnHApTe nanoparticles and their tendency to form agglomerates.

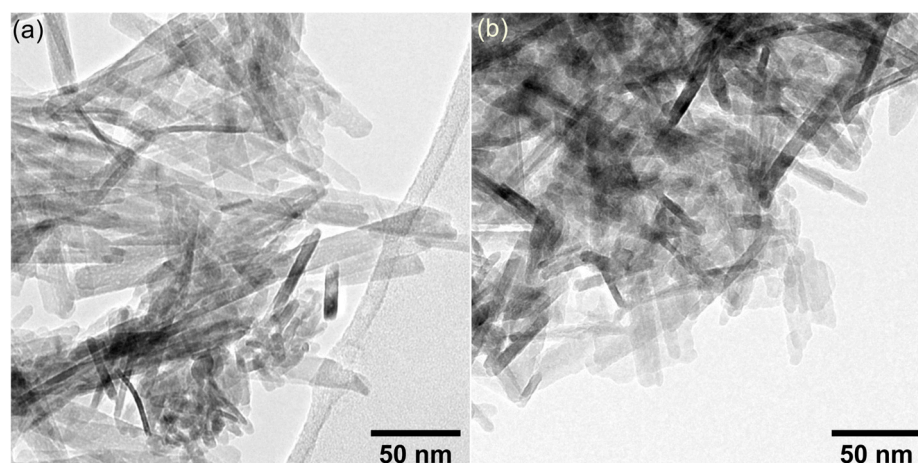


Figure 6. TEM images of ZnHAp (a) and ZnHApTe (b).

Figures 7 and 8 illustrate the SEM images and mean particle diameter of the ZnHAp and ZnHApTe nanoparticles. The SEM images presented in Figures 7 and 8 are recorded at $\times 100,000$ (Figures 7a and 8a) and $\times 200,000$ (inset of Figures 7b and 8b). In the case of the ZnHAp nanoparticles, the SEM images reveal their nanometric dimension and acicular morphology. A slight change in the morphology was noticed for the ZnHApTe nanoparticles. The change in morphology could be attributed to the presence of Te in the sample. For both samples, the SEM images reveal their tendency to form agglomerates. The mean particle diameters determined by SEM analysis were 18.7 ± 2 nm for ZnHAp nanoparticles and 21.3 ± 2 nm for ZnHApTe nanoparticles.

Information about the chemical composition of the ZnHAp, ZnHApTe, and Te samples was obtained through EDS studies. The results of the EDS studies are illustrated in Figure 9.

The EDS spectra of the ZnHAp sample underline the presence of zinc (Zn), calcium (Ca), phosphorus (P), and oxygen (O). All these chemical elements belong to the chemical composition of zinc-doped hydroxyapatite nanoparticles. The EDS spectra of tetracycline reveal the presence of chlorine (Cl), nitrogen (N), and oxygen (O) in the sample. Furthermore, the EDS spectra of ZnHApTe highlight the presence of chemical elements from the ZnHAp and tetracycline samples. Thus, in Figure 9b, the presence of nitrogen (N), oxygen (O), calcium (Ca), chlorine (Cl), zinc (Zn), and phosphorus (P) is underlined. In all the

EDS spectra, a carbon line could be observed because of the carbon tape on which the powders are placed in order to be analyzed. In the case of the Te and ZnHApTe samples, tetracycline also contributed to the C line in the EDS spectrum because of the carbon found in its chemical composition. The results of the EDS studies demonstrate that the analyzed samples are chemically pure based on the absence of additional lines in their EDS spectra.

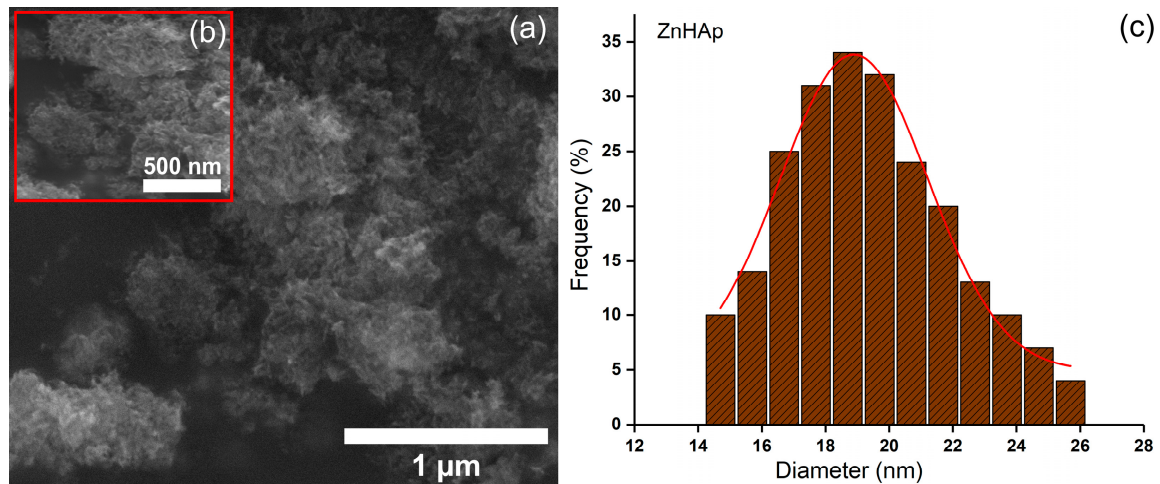


Figure 7. (a,b) SEM images and (c) particle size distribution obtained for the ZnHAp sample.

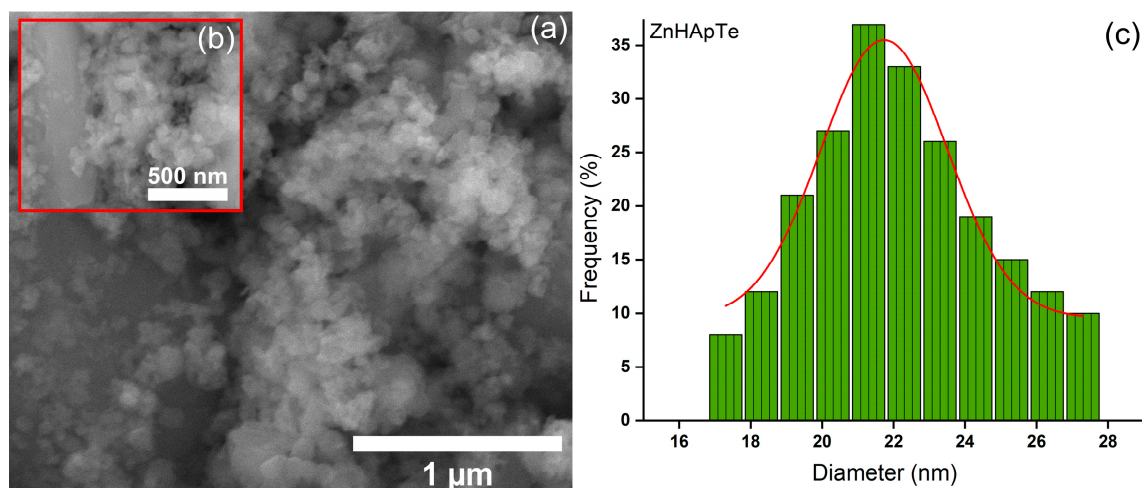


Figure 8. (a,b) SEM images and (c) particle size distribution obtained for the ZnHApTe sample.

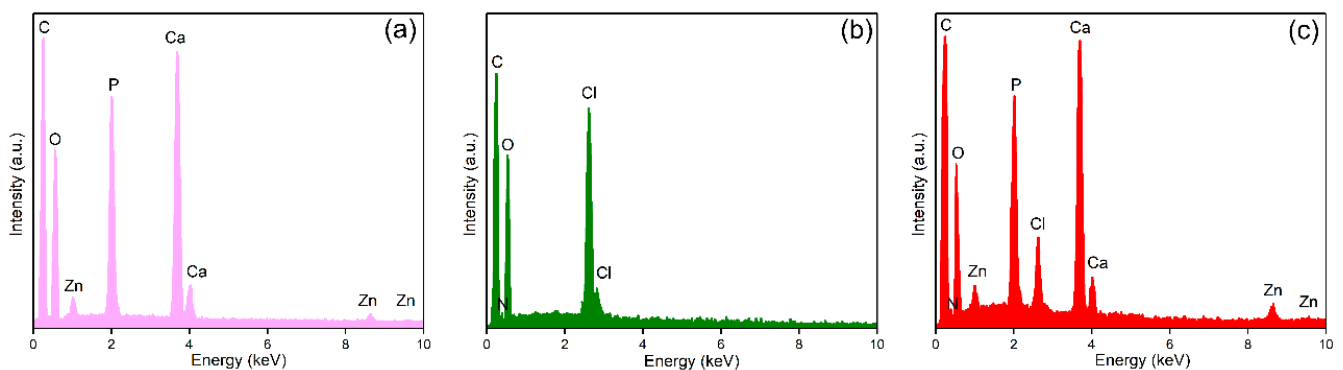


Figure 9. EDS spectra of the ZnHAp (a), Te (b), and ZnHApTe (c) samples.

Furthermore, the EDS quantitative analysis of the ZnHAp and ZnHApTe samples ($x_{\text{Zn}} = 0.1$; $(\text{Ca} + \text{Zn})/\text{P} = 1.67$) was performed, and the results are presented in Table 1.

Table 1. The results of EDS quantitative analyses performed on ZnHAp and ZnHApTe.

Sample	Ca	P	O	Zn	N	Cl
ZnHAp	16.9	10.68	71.49	0.93	-	-
ZnHApTe	20.18	12.65	51.6	0.92	0.95	13.7

The cytotoxicity of the ZnHAp and ZnHApTe nanoparticles was assessed through hemocompatibility and biocompatibility studies. Hemolysis studies are usually used to evaluate the potential hemolytic activity of nanoparticles. The hemolysis assay provides important information about the potential cytotoxic effects of the tested substance. The hemolysis index is a significant parameter when assessing materials for their potential use in biomedical applications. The aim of this assay is to determine whether the tested substances can cause the rupture of red blood cells (RBCs), which can release hemoglobin into the bloodstream and lead to hemolysis. A low hemolytic index ($<5\%$) indicates that the tested substances are hemocompatible and safe for use in biomedical applications, while a moderate hemolytic index ($5\text{--}20\%$) usually signifies the need for further testing to ensure the safety usage of the substance. On the other hand, a high hemolytic index ($>20\%$) indicates that the tested substances may not be safe for biomedical applications because of their significant hemolytic activity. Substances that exhibit a high hemolytic activity can cause damage to red blood cells, release hemoglobin, and provoke various negative physiological responses such as inflammation, thrombosis, and organ damage, rendering them unsuitable for biomedical applications. Contrarily, substances that exhibit a low hemolytic index are suitable for biomedical use because of their minimal risk of possible adverse reactions and their superior compatibility with biological systems. The results of the hemocompatibility assay in the case of the ZnHAp and ZnHApTe nanoparticles revealed that the hemolytic activity was below 1% for both tested samples. The results depicting the hemolytic index obtained for ZnHAp and ZnHApTe nanoparticles are presented graphically as mean \pm SD in Figure 10.

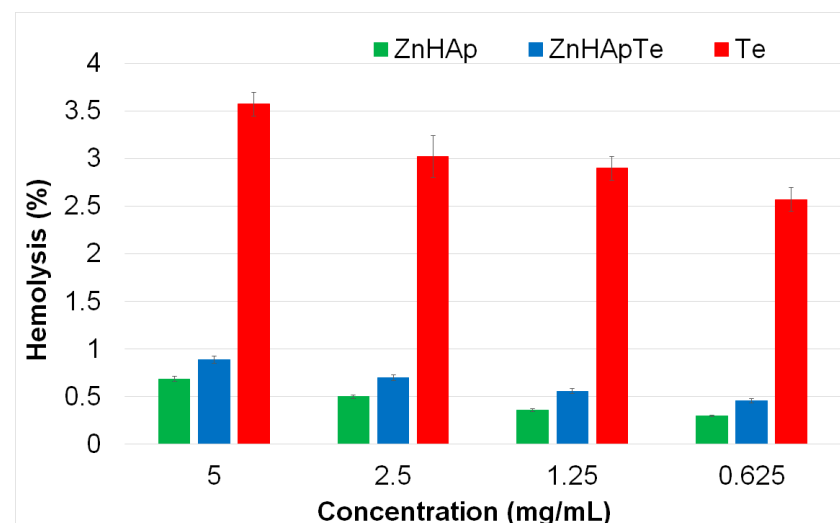


Figure 10. Percentage hemolysis of sheep red blood cells (RBCs) exposed to different concentrations of ZnHAp, ZnHApTe, and Te.

The results of the hemolytic activity highlighted that none of the tested concentrations of ZnHAp, ZnHApTe, and Te caused hemolysis. In addition, the values obtained for the hemolytic index were well within the acceptable hemocompatibility limits for biomaterials. The results showed that the ZnHAp and ZnHApTe nanoparticles exhibited a hemolytic

activity of less than 1%, while the hemolytic index of Te was above 3.5%. On the other hand, these data suggested that the hemolysis index increased with an increase in the concentration. Furthermore, the results showed that the ZnHAp nanoparticles exhibited a lower hemolytic index compared with ZnHApTe. These results could be attributed to the presence of tetracycline in the ZnHAp sample. These findings demonstrated that both ZnHAp and ZnHApTe nanoparticles showed a low hemolytic index, supporting the fact that they could be suitable for further cytotoxicity determinations to confirm their safety for usage in biomedical applications.

Additional information regarding the cytotoxicity of the ZnHAp, ZnHApTe, and Te nanoparticles was obtained with the aid of the colorimetric MTT assay. For this purpose, the cell viability of hFOB 1.19 cells was evaluated after their exposure to different concentrations of the ZnHAp, ZnHApTe, and Te nanoparticles at three different time intervals. The results of the MTT assay are depicted in Figure 11a,b.

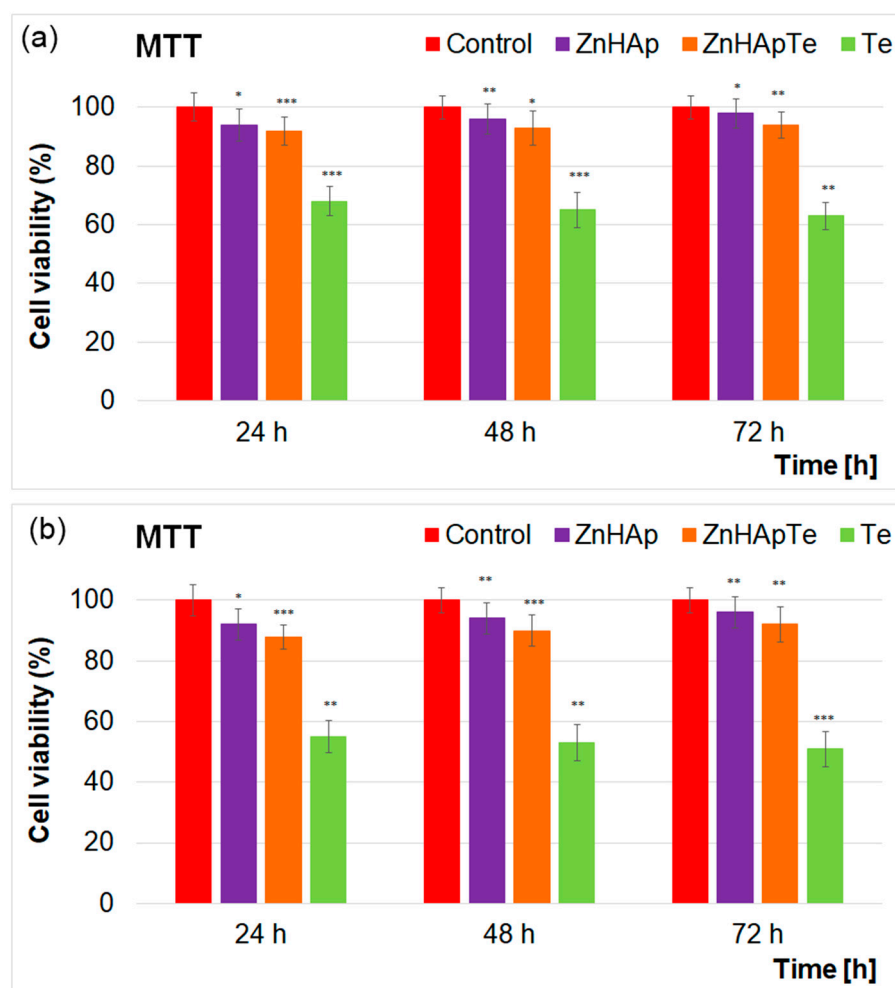


Figure 11. Cell viability of hFOB 1.19 cells incubated with 50 µg/mL (a) and 200 µg/mL (b) of ZnHAp, ZnHApTe, and Te for 24, 48 and 72 h. The results are represented as mean \pm standard deviation (SD) and are expressed as percentages of control (100% viability). The statistical differences between untreated and treated groups were determined by ANOVA, and the results are significant at $p < 0.05$ (*); $p < 0.01$ (**); $p < 0.001$ (***)

The results of the MTT assay depicted in Figure 11a,b revealed that the cell viability of the hFOB 1.19 cells remained above 92% after being exposed to 50 µg/mL ZnHAp and ZnHApTe nanoparticles for 24, 48, and 72 h. In addition, the results of the MTT studies highlighted that after 48 h and 72 h of exposure, the cell viability of the hFOB 1.19 cells exposed to ZnHAp increased, reaching 96% and 98%, respectively, which emphasizes that

the ZnHAp nanoparticles exhibit good biocompatible properties towards hFOB 1.19 cells at a concentration of 50 µg/mL. On the other hand, for a concentration of 200 µg/mL, the cell viability presented a slight decrease for both the ZnHAp and ZnHApTe samples. The results of the MTT assays also highlighted that the Te sample exhibited the lowest degree of biocompatibility for both tested concentrations. The cell viability of hFOB 1.19 cells incubated with 50 and 200 µg/mL Te powders was equal and below 60% for both tested concentrations and for all the incubation periods. These results are in good concordance with other studies reported on the biological properties of zinc-doped hydroxyapatite biocomposites [44–49]. These findings indicated that the ZnHAp nanoparticles exhibited good biological properties when exposed to hFOB 1.19 cells. Studies have shown that ZnHAp supports the viability and proliferation of human osteoblast cells [44], which are essential for bone formation and repair. The presence of zinc ions could enhance the cell's proliferation and differentiation. The results obtained for both the ZnHAp and ZnHApTe nanoparticles are in good agreement with the research of Tank et al., demonstrating the good biocompatibility of ZnHAp with human osteoblast cells (MG-63). Similar results were reported by Thian et al. [44] in their study regarding “*zinc-substituted hydroxyapatite: a biomaterial with enhanced bioactivity and antibacterial properties*”, which highlighted that ZnHAp exhibited very good biocompatible properties against mesenchymal stem cells (MSCs) derived from human adipose tissue. In addition, the biological properties of zinc-doped hydroxyapatite on the MRC-5 fibroblast cells were also reported by Radovanović et al. [47]. Furthermore, in their study, Thian et al. [44] showed that the incorporation of Zn²⁺ ions in the hydroxyapatite matrix could enhance the bioactivity of HAp. The study reported by the present supports our findings and highlights that zinc-doped hydroxyapatite (ZnHAp) exhibits good biocompatibility and could support cell viability and proliferation for numerous cell types, including human osteoblasts, mesenchymal stem cells, and fibroblasts. Furthermore, the results of the MTT assay also emphasized that ZnHApTe did not exhibit any toxic effects on the hFOB 1.19 cells for any tested time interval. The results showed a lower cellular viability than in the case of ZnHAp but still above 92%. In addition, these data also emphasized that the cellular viability of the hFOB 1.19 cells increased with an increase in the incubation time, reaching 94% after 72 h. These results emphasized that the presence of a small amount of tetracycline (5%) in the ZnHAp sample did not induce any cytotoxic effects. These results agree with previously reported data on the toxicity of tetracycline [50–53]. Tetracycline has been reported to exhibit good biological properties in small concentrations. In addition, studies have shown that tetracycline supports osteoblast function, including promoting proliferation, differentiation, and mineralization [53], while providing anti-inflammatory [54] and antioxidant benefits [55], creating a favorable environment for osteoblast function. However, the reported studies stress that insightful consideration should be attributed to the correct dosage necessary to avoid cytotoxic effects. Due to its broad-spectrum action and enhanced biological properties, tetracycline has been utilized in the development of novel compounds with biomedical applications. In their study regarding “controlled release and antibacterial activity of tetracycline hydrochloride-loaded bacterial cellulose composite membranes”, Shao et al. [52] reported that the BC-TCH composite films exhibited good biocompatibility and present effective antibacterial activity. Their results highlighted that TCH did not inhibit the proliferation of HEK293 cells, even at a high concentration [52]. Similar results were obtained by Dayaghi et al. [51], who reported that the presence of tetracycline in the composition of magnesium–zinc scaffolds guaranteed their antimicrobial character while exhibiting good biocompatible properties at small concentrations. Their study revealed that only the scaffolds with tetracycline concentrations of 1% and 5% were biocompatible, whereas the ones possessing higher dosages of tetracycline concentration demonstrated toxicity [51].

Complementary information regarding the cytotoxicity of the ZnHAp and ZnHApTe was obtained with the aid of Lactate dehydrogenase (LDH) release studies (Figure 12a,b).

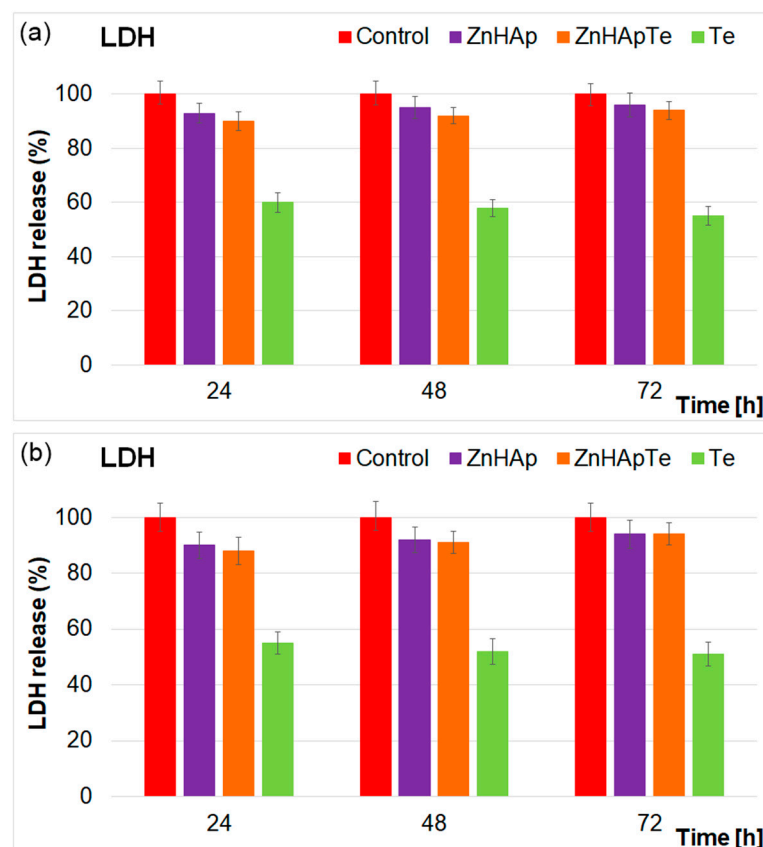


Figure 12. Lactate dehydrogenase (LDH) activity released in the culture medium of hFOB 1.19 cells after the treatment with 50 µg/mL (a) and 200 µg/mL (b) of ZnHAp, ZnHApTe, and Te for 24, 48 and 72 h. The results are represented as mean \pm standard deviation (SD).

The LDH assay is usually used to determine cell cytotoxicity by determining the release of LDH from the damaged cells into the culture medium. In evaluating the cytotoxicity of materials, this investigation can effectively assess the tested materials' impact on cell viability. A low value of LDH release indicates that the tested material exhibits low cytotoxicity, suggesting that the cells remain viable and almost undamaged. On the other hand, a high LDH release is a sign of high cytotoxicity, indicating that the tested materials could cause substantial cell damage and significantly reduce the cell's viability. The results of the LDH assay for the ZnHAp, ZnHApTe, and Te nanoparticles at different concentrations are depicted in Figure 12a,b. LDH activity was quantified in the supernatant of the cells to test the cytotoxicity and membrane integrity. These data were represented graphically as mean \pm SD relative to the control sample, for which the LDH level was set as 100%. The results of the LDH assay emphasized that there were no statistically significant changes from the control for any of the analyzed samples. These findings indicate that exposure to the ZnHAp and ZnHApTe nanoparticles did not damage the hFOB 1.19 cell's membrane, preserving its integrity. The result also indicates the absence of cell necrosis. The results from the LDH activity assay agreed with those obtained from the MTT assays, demonstrating that both the ZnHAp and ZnHApTe nanoparticles exhibited no cytotoxic activity against hFOB 1.19 cells. Data from both assays indicated that these nanoparticles possess good biocompatibility towards hFOB 1.19 cells. These findings emphasized that the ZnHAp and ZnHApTe nanoparticles are promising candidates for future development of biomaterials for biomedical applications.

Tetracycline is a well-known broad-spectrum antibiotic, which was discovered in the late 1940s and has been a fundamental tool in combating various bacterial infections since then. Its use is widespread because of its efficacy against diverse types of microorganisms, such as Gram-positive and Gram-negative bacteria, atypical pathogens, and some protozoa.

The understanding of the antimicrobial range and the action mechanism of tetracycline is crucial for recognizing its clinical value and trying to resolve the emerging issue of antibiotic resistance at a global scale. In this context, the development of novel antimicrobial agents is of great significance worldwide. For this purpose, the antimicrobial effects of tetracycline-enriched ZnHAp were evaluated at three different time intervals using the most common microbial strains, *S. aureus*, *E. coli*, and *C. albicans*. The antimicrobial studies performed on the HAp, Te, ZnHAp, and ZnHApTe nanoparticles revealed that loading ZnHAp with tetracycline determined a complete bactericidal effect against *S. aureus*, increased the bacteriostatic activity against *E. coli*, and enhanced the antifungal activity against *C. albicans* (Figure 13). Furthermore, the studies presented in this paper have demonstrated that *S. aureus* exhibited greater sensitivity to the ZnHAp and ZnHApTe nanoparticles than *E. coli* ATCC 25922 and *C. albicans* ATCC 10231 compared with the control and pure tetracycline. The results of the in vitro antimicrobial assay depicted that HAp nanoparticles did not inhibit the development of any of the tested microbial strains for any given interval. In addition, these data emphasized that the HAp nanoparticles aided the development and proliferation of the microbial cells compared with the control. The results showed a significant increase in the CFU values of the microbial cells exposed to HAp nanoparticles compared with the control.

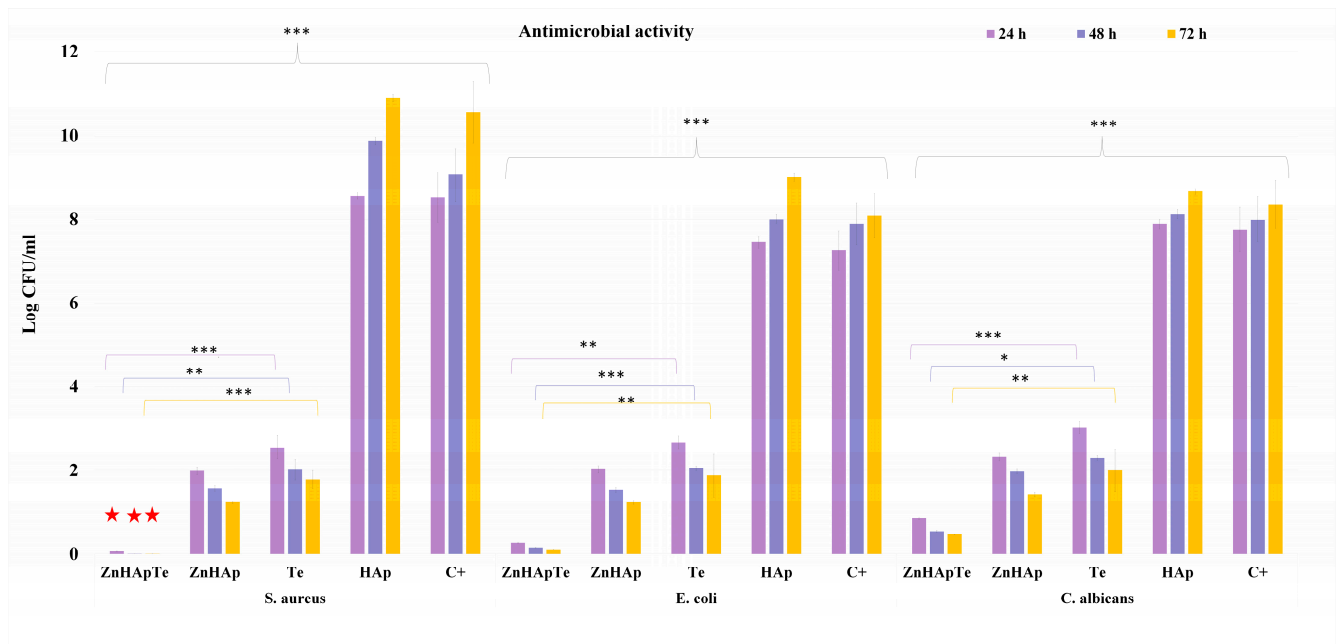


Figure 13. Graphical representation of the logarithmic values of colony forming units (CFU)/mL of *S. aureus* ATCC 25923, *E. coli* ATCC 25922, and *C. albicans* ATCC 10231 microbial strains after 24, 48, and 72 h of exposure to HAp, Te, ZnHAp and ZnHApTe. The results are presented as mean \pm standard error. The statistical analysis was performed by ordinary one-way ANOVA. The p -values indicated are * $p \leq 0.002$, ** $p \leq 0.001$, *** $p \leq 0.0001$. The red stars highlight the bactericidal effects of the samples.

In addition, the results of the in vitro antimicrobial assays have demonstrated that the presence of tetracycline conferred the ZnHApTe biocomposite bactericidal properties against the *S. aureus* bacterial strain.

These results align well with previously reported studies on the antimicrobial effects of tetracycline [56–59]. The findings revealed that the antimicrobial activities of ZnHAp and ZnHApTe are also correlated with the incubation time. The results showed that even though the CFU values are low, even from the early development stage, the CFU values decreased significantly with the incubation time. The antimicrobial activity of the nanoparticles is attributed to both zinc ions from the hydroxyapatite matrix and the presence of tetracycline. Zinc ions (Zn^{2+}) are well known to possess antimicrobial properties through multiple

mechanisms. Zinc ions can compromise the cell's membrane integrity by binding to its negatively charged components, thus increasing its permeability and, in the end, causing cell lysis. They could also inhibit the enzymatic activity by attaching themselves to active sites or by displacing some of the essential metal cofactors and disrupting the critical metabolic functions of the microbial cells. In addition, zinc ions have the ability to inhibit nutrient uptake by competing with the essential metal ions, leading to nutrient deprivation of the microbial cell. On the other hand, zinc ions could generate reactive oxygen species (ROS) that are responsible for inducing oxidative damage to DNA, proteins, and lipids. Zn^{2+} interferes with the processes of DNA replication and transcription by binding to the nucleic acids and other proteins, thus disrupting protein synthesis by interacting with the cell's ribosomal components. Additionally, zinc could enhance the host immune response, aiding in infection clearance [60–63]. These mechanisms are reported to be responsible for zinc ions' effectiveness in various antimicrobial applications, from medical treatments to food preservation [60–67]. On the other hand, it was reported that tetracycline's antimicrobial properties could be attributed to its ability to inhibit protein synthesis in bacteria [68–73]. Tetracycline could also bind to the 30S ribosomal subunit, blocking the attachment of aminoacyl-tRNA to the mRNA-ribosome complex, thereby blocking the addition of new amino acids to the peptide chain and interrupting protein synthesis. This disruption could inhibit bacterial growth and replication. Additionally, tetracycline can compromise the integrity of the bacterial cell membrane. In addition, its broad-spectrum activity makes tetracycline effective against a wide range of Gram-positive and Gram-negative bacteria, as well as some intracellular pathogens. Its ability to pass through the bacterial cells and its bacteriostatic nature, which prevents bacterial multiplication without necessarily killing them, make it a valuable antibiotic for treating numerous infections [68–73]. In this context, the findings obtained from the antimicrobial assays that highlighted that zinc-doped hydroxyapatite enriched with tetracycline demonstrates enhanced antimicrobial properties by combining the effects of zinc ions and tetracycline agree with the existing studies. The combined effects of zinc ions could disrupt microbial cell membranes by binding to negatively charged components, increasing permeability that could cause cell lysis and could inhibit enzymatic activity and generate reactive oxygen species (ROS) and tetracycline, which has the ability to inhibit protein synthesis by binding to the 30S ribosomal subunit, preventing the attachment of aminoacyl-tRNA to the mRNA-ribosome complex, thus blocking the addition of new amino acids and preventing bacterial growth. The synergy between zinc's numerous antimicrobial mechanisms and tetracycline's specific antimicrobial functions contribute considerably to the fact that zinc-doped hydroxyapatite enriched with tetracycline is particularly effective against a wide range of bacteria, including resistant strains, enhancing its use in medical treatments and implants. The results of the in vitro antimicrobial assay highlighted that the synergy between the zinc ions from the HAp matrix, as well as the presence of tetracycline, leads to bactericidal properties against *S. aureus* and confers an increase in the bacteriostatic properties against *E. coli* to the ZnHApTe samples compared with simple ZnHAp and Te samples. In addition, a notable increase in the antifungal activity of the ZnHApTe samples was observed compared with the ZnHAp and Te samples. The findings obtained in this study suggest that the ZnHAp and ZnHApTe nanoparticles could be effectively used to develop novel antimicrobial agents.

3. Materials and Methods

3.1. Materials

For the development of zinc-doped hydroxyapatite (ZnHAp), zinc-doped hydroxyapatite enriched with tetracycline (ZnHApTe) powders were used the next reagents: calcium nitrate ($\text{Ca}(\text{NO}_3)_2 \cdot 4\text{H}_2\text{O}$), diammonium hydrogen phosphate ($(\text{NH}_4)_2\text{HPO}_4$) and zinc nitrate ($\text{Zn}(\text{NO}_3)_6 \cdot 6\text{H}_2\text{O}$) and tetracycline hydrochloride (Te, $\text{C}_{22}\text{H}_{24}\text{N}_2\text{O}_8 \cdot \text{HCl}$).

3.2. Development of Zinc-Doped Hydroxyapatite Enriched with Tetracycline

The zinc-doped hydroxyapatite (ZnHAp) and zinc-doped hydroxyapatite enriched with tetracycline (ZnHApTe) powders were obtained through an adapted co-precipitation method. During the synthesis process, the ratio of $[Ca + Zn]/P$ was equal to 1.67, and the zinc concentration was $x_{Zn} = 0.1$ [74]. The tetracycline solution, together with the zinc, calcium, and phosphate solution, was stirred well for 24 h under ambient conditions. Then, the phosphate solution was added to the calcium and zinc solution and stirred for 72 h. The final concentration of Te in ZnHApTe was 5%. The final mixture was centrifuged, and the resulting precipitate was washed five times with water. After the last centrifugation, the final precipitate was dried in air.

3.3. X-ray Diffraction (XRD)

Information regarding the structure of the obtained samples, including zinc-doped hydroxyapatite (ZnHAp), zinc-doped hydroxyapatite enriched with tetracycline (ZnHApTe), and tetracycline (Te), was achieved using X-ray diffraction (XRD). Measurements were conducted with a Bruker D8 Advance diffractometer, utilizing $CuK\alpha$ radiation ($\lambda = 1.5418 \text{ \AA}$) (Bruker, Karlsruhe, Germany) and equipped with a LynxEye™ 1D high-efficiency linear detector. Data were collected in the 2θ range of $10\text{--}60^\circ$ with a step size of 0.02° and a time of 5 s per step.

3.4. Fourier Transform Infrared Spectroscopy (FTIR)

Fourier evaluated the functional groups present in the ZnHAp, Te, and ZnHApTe samples transform infrared spectroscopy (FTIR). The FTIR spectra were recorded with a Perkin Elmer spectrometer operated in ATR mode (attenuated total reflectance) using a Universal Diamond/KRS-5 (Perkin Elmer, Waltham, MA, USA) within the range of $450\text{--}4000 \text{ cm}^{-1}$. The second derivative spectra were obtained after applying a 5-point smoothing of the original FTIR. The procedure followed for obtaining the deconvoluted spectra in the $900\text{--}1200 \text{ cm}^{-1}$ spectral region was presented in detail in [75].

3.5. X-ray Photoelectron Spectroscopy (XPS)

The XPS analysis of ZnHAp, tetracycline, and ZnHApTe was performed using an X-ray photoelectron spectroscopy (XPS) investigation was conducted using an SES 2002 instrument from Scienta Omicron (Scienta Omicron, Taunusstein, Germany). A monochromatic Al K(alpha) X-ray source with an energy of 1486.6 eV was used. The analysis protocols, as well as the scanning parameters, were used in accordance with previous studies [76]. The CasaXPS 2.3.14 software (utilizing the Shirley background type) was employed [77]. All binding energy (BE) values presented in this study were adjusted to the C1s peak at 284.8 eV for charge correction.

3.6. Transmission Electron Microscopy (TEM)

For the TEM studies, a CM 20 (Philips FEI, Eindhoven, The Netherlands) transmission electron microscope (TEM). The TEM microscope was equipped with a Lab6 instrument.

3.7. Scanning Electron Microscopy (SEM)

The morphology evaluation of the ZnHAp and ZnHApTe nanoparticles was achieved using a scanning electron microscope (SEM, FEI Quanta Inspect F, FEI Company, Hillsboro, OR, USA). Moreover, the SEM microscope was equipped with an energy-dispersive X-ray (EDX) attachment to evaluate the chemical composition of the ZnHAp, Te, and ZnHApTe samples. Prior to the SEM examination, the samples were added to a carbon tape. The mean particle size estimation was performed by numbering approximately 500 nanoparticles.

3.8. Hemolysis Assay

The biological properties of the ZnHAp and ZnHApTe nanoparticles and Te powder were evaluated with the aid of a hemolysis assay. The experiments were performed using

sheep red blood cells (RBCs) following the method described by Das et al. [78] modified as previously reported in [79]. For this purpose, 500 µL of samples of various concentrations in 0.9% NaCl were mixed with 500 µL of erythrocyte suspension. The tubes were mixed and incubated at 37 °C for 30 min. Equal amounts of erythrocyte suspension were added to Triton X-100 (Thermo Fisher Scientific, Waltham, MA, USA) and PBS for the positive and negative controls. After 30 min of incubation, the samples were centrifuged, and the supernatant was carefully transferred to 96-well plates. The absorbance of the supernatant was measured at 540 nm using a FlexStation 3 UV-VIS spectrophotometer (Molecular Devices Company, Sunnyvale, CA, USA) instrument. The hemolytic index (HI%) was calculated using the following equation:

$$\text{Hemolysis (\%)} = \frac{V_{OD \text{ sample}} - V_{OD \text{ negative control}}}{V_{OD \text{ positive control}} - V_{OD \text{ negative control}}} \times 100 \quad (1)$$

3.9. MTT Assay

The cytotoxicity of the ZnHAp, ZnHApTe, and Te nanoparticles was assessed with the aid of human fetal osteoblastic cells (hFOB 1.19 cell line) using a methodology previously described in [79]. For this study, the hFOB 1.19 cells were cultured in Dulbecco Modified Eagle's Medium at 37 °C in a humidified atmosphere with a CO₂ concentration of 5%. The cells were seeded at a density of 3×10^4 cells/cm². The cell viability was determined using the colorimetric test assay 3-(4,5-dimethylthiazol-2-yl)-2,5-diphenyltetrazolium bromide (MTT; Sigma-Aldrich, St. Louis, MO, USA) assay. The viability was evaluated at three different time intervals of incubation, 24, 48, and 72 h, and for two different concentrations of the ZnHAp, ZnHApTe, and Te samples (50 and 200 µg/mL). After each incubation period, the medium was removed, and the cells were incubated using 1 mg/mL MTT and kept for 4 h at 37 °C. The cell viability was quantified based on the absorbance values measured at 595 nm using a microplate reader (Flex Station 3, Molecular Devices, San Jose, CA, USA). The percentage of viable cells was determined relative to the cell viability of the control sample, which was set to 100% viability, and the results were presented graphically as mean ± SD.

3.10. Lactate Dehydrogenase (LDH) Release Measurement

After the three different incubation periods of growth of human fetal osteoblastic cells (hFOB 1.19 cell line), the culture medium was collected, and LDH release was measured using the Cytotoxicity Detection KitPLUS (Roche, Mannheim, Germany) according to the manufacturer's instructions. For this purpose, 50 µL of culture supernatants were mixed with 50 µL of reaction mixture containing the catalyst and dye solution and were incubated for 30 min in the dark. The absorbance was measured at a 485 nm wavelength using a Tecan GENios instrument.

3.11. In Vitro Antimicrobial Activity

The antimicrobial properties of the HAp, ZnHAp, ZnHApTe, and Te nanoparticles were assessed in vitro using one of the most common reference strains, *Staphylococcus aureus* ATCC 25923, *Escherichia coli* ATCC 25922, and *Candida albicans* ATCC 10231 (all from ATCC, Old Town Manassas, VA, USA). The antimicrobial assays followed previously reported methodologies [17] with 0.5 McFarland standard microbial cultures. The samples were inoculated with 1.5 mL microbial suspensions at a density of 5×10^6 CFU/mL, prepared in phosphate-buffered saline (PBS), and incubated for 24, 48, and 72 h. Free microbial cultures served as positive controls (C+). Suspensions were collected at 24, 48, and 72 h, then incubated on LB agar medium for 24 h at 37 °C. The CFU/mL count was determined for each incubated sample. Experiments were performed in triplicate, and data were presented as mean ± SD. Statistical analysis was conducted using the ANOVA single-factor test.

4. Conclusions

The zinc-doped hydroxyapatite enriched with tetracycline (ZnHApTe) powders were obtained for the first time using an adapted coprecipitation method. The results of the XRD studies reveal the presence of the hydroxyapatite and Te in the ZnHApTe sample. The XRD results also underlined the absence of the additional phases. The presence of the functional groups that are characteristics of the HAp and Te structure in the ZnHApTe was highlighted by the FTIR results. The results of the XPS and EDS studies proved the purity of the samples. The antimicrobial assays revealed that both ZnHAp and ZnHApTe nanoparticles exhibited strong inhibitory effects on all the tested microbial strains for all the tested incubation intervals. Furthermore, the results also emphasized that the addition of tetracycline to ZnHAp nanoparticles considerably improved their antimicrobial activity, conferring them bactericidal properties against *S. aureus*, enhanced bacteriostatic activity against *E. coli* and better antifungal properties towards *C. albicans*. These data indicated that the antimicrobial activity was influenced by the incubation time and by the specific type of microbial strain.

The biological assays demonstrated that the ZnHAp and ZnHApTe nanoparticles exhibited good biocompatibility and antimicrobial properties. The hemolysis assay highlighted that the ZnHAp and ZnHApTe nanoparticles had a hemolytic index below 1%, which ensures that they are promising materials for being used in biomedical applications such as bone grafts, dental implants and tissue engineering scaffolds. Furthermore, the cell viability studies depicted that hFOB 1.19 cells maintained cellular viability higher than 94% in the presence of ZnHAp nanoparticles and above 92% in the presence of the ZnHApTe nanoparticles. Moreover, the results have emphasized that the cellular viability of hFOB 1.19 cells increased with an increase in the incubation time. In addition, the LDH assays also showed that exposure to the ZnHAp and ZnHApTe nanoparticles did not damage the hFOB 1.19 cell's membrane, preserving its integrity. The findings of the biological assays depict the potential of the ZnHAp and ZnHApTe nanoparticles to be used in the future for the development of novel biomaterials with biomedical applications.

Author Contributions: Conceptualization, S.L.I., and D.P.; methodology, S.L.I., D.P., and C.S.C.; software, S.L.I., D.P., C.S.C., S.R., and K.R.; validation, S.L.I., D.P., and C.S.C.; formal analysis, S.L.I., D.P., C.S.C., C.C.N., S.R., K.R., and C.C.; investigation, S.L.I., D.P., C.S.C., C.C.N., R.T., S.R., K.R., L.G., M.L.B., and C.C.; resources, D.P., S.R., and K.R.; data curation, S.L.I., D.P., and C.S.C.; writing—original draft preparation, S.L.I., D.P., and C.S.C.; writing—review and editing, S.L.I., D.P., C.S.C., C.C.N., R.T., S.R., K.R., L.G., M.L.B., and C.C.; visualization, S.L.I., D.P., C.S.C., C.C.N., R.T., S.R., K.R., L.G., M.L.B., and C.C.; supervision, S.L.I., and D.P.; project administration, S.L.I., and D.P.; funding acquisition, D.P. All authors have read and agreed to the published version of the manuscript.

Funding: This research received no external funding.

Institutional Review Board Statement: Not applicable.

Informed Consent Statement: Not applicable.

Data Availability Statement: The original contributions presented in the study are included in the article; further inquiries can be directed to the corresponding authors.

Conflicts of Interest: The authors declare no conflicts of interest. The funders had no role in the design of the study, in the collection, analyses, or interpretation of data, in the writing of the manuscript, or in the decision to publish the results.

References

1. Mecu, R.; Cîrțină, D.; Nănescu, V. Hydroxyapatite-antibiotic applications in bone therapy. *JRISS* **2019**, *1*, 121–124. [[CrossRef](#)]
2. Maleki-Ghaleh, H.; Siadati, M.H.; Fallah, A.; Koc, B.; Kavanlouei, M.; Khademi-Azandehi, P.; Moradpur-Tari, E.; Omid, Y.; Barar, J.; Beygi-Khosrowshahi, Y.; et al. Antibacterial and Cellular Behaviors of Novel Zinc-Doped Hydroxyapatite/Graphene Nanocomposite for Bone Tissue Engineering. *Int. J. Mol. Sci.* **2021**, *22*, 9564. [[CrossRef](#)] [[PubMed](#)]

3. Ofudje, E.A.; Adeogun, A.I.; Idowu, M.A.; Kareem, S.O. Synthesis and characterization of Zn-Doped hydroxyapatite: Scaffold application, antibacterial and bioactivity studies. *Heliyon* **2019**, *5*, e01716. [[CrossRef](#)] [[PubMed](#)]
4. Ait Said, H.; Noukrati, H.; Oudadesse, H.; Ben Youcef, H.; Lefeuvre, B.; Hakkou, R.; Lahcini, M.; Barroug, A. Formulation and characterization of hydroxyapatite-based composite with enhanced compressive strength and controlled antibiotic release. *J. Biomed. Mater. Res. A* **2021**, *109*, 1942–1954. [[CrossRef](#)]
5. Jiang, Y.; Yuan, Z.; Huang, J. Substituted hydroxyapatite: A recent development. *Mater. Technol.* **2020**, *35*, 785–796. [[CrossRef](#)]
6. Cinici, B.; Yaba, S.; Kurt, M.; Yalcin, H.C.; Duta, L.; Gunduz, O. Fabrication Strategies for Bioceramic Scaffolds in Bone Tissue Engineering with Generative Design Applications. *Biomimetics* **2024**, *9*, 409. [[CrossRef](#)] [[PubMed](#)]
7. Kim, H.; Mondal, S.; Bharathiraja, S.; Manivasagan, P.; Moorthy, M.S.; Oh, J. Optimized Zn-doped hydroxyapatite/doxorubicin bioceramics system for efficient drug delivery and tissue engineering application. *Ceram. Int.* **2018**, *44*, 6062–6071. [[CrossRef](#)]
8. Lin, K.; Zhou, Y.; Zhou, Y.; Qu, H.; Chen, F.; Zhu, Y.; Chang, J. Biomimetic hydroxyapatite porous microspheres with co-substituted essential trace elements: Surfactant-free hydrothermal synthesis, enhanced degradation and drug release. *J. Mater. Chem.* **2011**, *21*, 16558–16565. [[CrossRef](#)]
9. Sebastianm, S.; Fathima, A.S.L.; Alarifi, S.; Mahboob, S.; Henry, J.; Kavipriya, M.R.; Govindarajan, M.; Nicoletti, M.; Vaseeharan, B. Synthesis and physicochemical characteristics of Ag-doped hydroxyapatite nanoparticles, and their potential biomedical applications. *Environ. Res.* **2022**, *210*, 112979. [[CrossRef](#)]
10. Phatai, P.; Futralan, C.M.; Utara, S.; Khemthong, P.; Kamonwannasit, S. Structural characterization of cerium-doped hydroxyapatite nanoparticles synthesized by an ultrasonic-assisted sol-gel technique. *Results Phys.* **2018**, *10*, 956–963. [[CrossRef](#)]
11. Chen, P.; Wang, F.; Qiao, Y.; Zhang, Z. Luminescence of samarium doped hydroxyapatite containing strontium: Effects of doping concentration. *J. Rare Earths* **2022**, *40*, 398–405. [[CrossRef](#)]
12. Ishikawa, K.; Miyamoto, Y.; Yuasa, T.; Ito, A.; Nagayama, M.; Suzuki, K. Fabrication of Zn containing apatite cement and its initial evaluation using human osteoblastic cells. *Biomaterials* **2002**, *23*, 423–428. [[CrossRef](#)]
13. Wang, X.; Ito, A.; Sogo, Y.; Li, X.; Oyane, A. Zinc-containing apatite layers on external fixation rods promoting cell activity. *Acta Biomater.* **2010**, *6*, 962–968. [[CrossRef](#)]
14. Begam, H.; Mandal, S.; Chanda, A.; Mukherjee, J.; Nandi, S.K. Effect of zinc doping on biological properties of biphasic calcium phosphate ceramics in orthopaedic animal model. *T. Indian. Ceram. Soc.* **2014**, *73*, 284–292. [[CrossRef](#)]
15. Pasquet, J.; Chevalier, Y.; Pelletier, J.; Couval, E.; Bouvier, D.; Bolzinger, M.A. The contribution of zinc ions to the antimicrobial activity of zinc oxide. *Colloids Surf. A Physicochem. Eng. Asp.* **2014**, *457*, 263–274. [[CrossRef](#)]
16. Lallo da Silva, B.; Abuçafy, M.P.; Berbel Manaia, E.; Oshiro Junior, J.A.; Chiari-Andréo, B.G.; Pietro, R.C.R.; Chiavacci, L.A. Relationship between structure and antimicrobial activity of zinc oxide nanoparticles: An overview. *Int. J. Nanomed.* **2019**, *14*, 9395–9410. [[CrossRef](#)] [[PubMed](#)]
17. Predoi, D.; Iconaru, S.L.; Predoi, M.V.; Motelica-Heino, M.; Guegan, R.; Buton, N. Evaluation of Antibacterial Activity of Zinc-Doped Hydroxyapatite Colloids and Dispersion Stability Using Ultrasounds. *Nanomaterials* **2019**, *9*, 515. [[CrossRef](#)] [[PubMed](#)]
18. Klein, N.C.; Cunha, B.A. Tetracyclines. *Med. Clin. North. Am.* **1995**, *79*, 789–801. [[CrossRef](#)] [[PubMed](#)]
19. Rusu, L.C.; Nedelcu, I.A.; Albu, G.; Sonmez, M.; Voicu, M.; Radulescu, G.M.; Ficai, D.; Ficai, A.; Negrutiu, M.L.; Sinescu, C. Tetracycline loaded collagen/hydroxyapatite composite materials for biomedical applications. *J. Nanomater.* **2015**, *2015*, 361969. [[CrossRef](#)]
20. Rivadeneira, J.; Luz, G.M.; Audisio, M.C.; Mano, J.F.; Gorustovich, A.A. Novel antibacterial bioactive glass nanocomposite functionalized with tetracycline hydrochloride. *Biomed. Glas.* **2015**, *1*, 128–135. [[CrossRef](#)]
21. Soriano-Souza, C.; Valiense, H.; Mavropoulos, E.; Martinez-Zelaya, V.; Costa, A.M.; Alves, A.T.; Longuinho, M.; Resende, R.; Mourão, C.; Granjeiro, J.; et al. Doxycycline containing hydroxyapatite ceramic microspheres as a bone-targeting drug delivery system. *J. Biomed. Mater. Res. B Appl. Biomater.* **2020**, *108*, 1351–1362. [[CrossRef](#)] [[PubMed](#)]
22. Predoi, D.; Iconaru, S.-L.; Predoi, M.-V.; Buton, N. Development of Novel Tetracycline and Ciprofloxacin Loaded Silver Doped Hydroxyapatite Suspensions for Biomedical Applications. *Antibiotics* **2023**, *12*, 74. [[CrossRef](#)]
23. Madhumathi, K.; Kumar, T.S. Regenerative potential and anti-bacterial activity of tetracycline loaded apatitic nanocarriers for the treatment of periodontitis. *Biomed. Mater.* **2014**, *9*, 035002. [[CrossRef](#)] [[PubMed](#)]
24. Gunasekaran, S.; Varadhan, S.R.; Karunanidhi, N. Qualitative analysis on the infrared bands of tetracycline and ampicillin. *Proc.-Indian. Natl. Sci. Acad. Part A Phys. Sci.* **1996**, *62*, 309–316.
25. de Sousa, F.B.; Oliveira, M.F.; Lula, I.S.; Sansiviero, M.T.C.; Cortés, M.E.; Sinisterra, R.D. Study of inclusion compound in solution involving tetracycline and β -cyclodextrin by FTIR-ATR. *Vib. Spectrosc.* **2008**, *46*, 57–62. [[CrossRef](#)]
26. Hou, H.; Dai, Z.; Liu, X.; Yao, Y.; Liao, Q.; Yu, C.; Li, D. Reutilization of the expired tetracycline for lithium ion battery anode. *Sci. Total Environ.* **2018**, *630*, 495–501. [[CrossRef](#)] [[PubMed](#)]
27. Popa, C.L.; Groza, A.; Chapon, P.; Ciobanu, C.S.; Ghita, R.V.; Trusca, R.; Ganciu, M.; Predoi, D. Physicochemical analysis of the polydimethylsiloxane interlayer influence on a hydroxyapatite doped with silver coating. *J. Nanomater.* **2015**, *2015*, 250617. [[CrossRef](#)]
28. Predoi, D.; Groza, A.; Iconaru, S.L.; Predoi, G.; Barbuceanu, F.; Guegan, R.; Motelica-Heino, M.S.; Cimpeanu, C. Properties of Basil and Lavender Essential Oils Adsorbed on the Surface of Hydroxyapatite. *Materials* **2018**, *11*, 652. [[CrossRef](#)]

29. Trivedi, M.K.; Patil, S.; Shettigar, H.; Bairwa, K.; Jana, S. Spectroscopic Characterization of Chloramphenicol and Tetracycline: An Impact of Biofield Treatment. *Pharm. Anal. Acta* **2015**, *6*, 395. [\[CrossRef\]](#)
30. Tian, M.; Hu, X.; Qu, L.; Zhu, S.; Sun, Y.; Han, G. Versatile and ductile cotton fabric achieved via layer-by-layer self-assembly by consecutive adsorption of graphene doped PEDOT: PSS and chitosan. *Carbon* **2016**, *96*, 166–174. [\[CrossRef\]](#)
31. Zhang, N.; Xue, H.; Hu, R. The activity and stability of CeO₂@CaO catalysts for the production of biodiesel. *RSC Adv.* **2018**, *8*, 32922–32929. [\[CrossRef\]](#) [\[PubMed\]](#)
32. Song, F.; Zhang, H.; Wang, S.; Liu, L.; Tan, X.; Liu, S. Atomic Level Design of CoOH⁺–Hydroxyapatite@C Catalysts for Superfast Degradation of Organics via Peroxymonosulfate Activation. *Chem. Commun.* **2018**, *54*, 4919–4922. [\[CrossRef\]](#)
33. Hegde, M.S.; Ayyoob, M. O₂- and O₁- types of oxygen species on Ni and barium-doped Ni and Cu surfaces. *Surf. Sci.* **1986**, *173*, L635–L640. [\[CrossRef\]](#)
34. Rao, C.N.R.; Vijayakrishnan, V.; Kulkarni, G.U.; Rajumon, M.K. A comparative study of the interaction of oxygen with clusters and single-crystal surfaces of nickel. *Appl. Surf. Sci.* **1995**, *84*, 285–289. [\[CrossRef\]](#)
35. Kulkarni, G.U.; Rao, C.N.R.; Roberts, M.W. Coadsorption of Dioxygen and Water on the Ni(110) Surface: Role of O1–Type Species in the Dissociation of Water. *Langmuir* **1995**, *11*, 2572–2575. [\[CrossRef\]](#)
36. Guo, J.; Yu, H.; Dong, F.; Zhu, B.; Huang, W.; Zhang, S. High efficiency and stability of Au-Cu/hydroxyapatite catalyst for the oxidation of carbon monoxide. *RSC Adv.* **2017**, *7*, 45420–45431. [\[CrossRef\]](#)
37. Moulder, J.F.; Stickle, W.F.; Sobol, P.E.; Bomben, K.D. *Handbook of X-ray Photoelectron Spectroscopy*; Physical Electronics Inc.: Chanhassen, MN, USA, 1995.
38. Bee, S.-L.; Bustami, Y.; Ul-Hamid, A.; Lim, K.; Abdul Hamid, Z.A. Synthesis of Silver Nanoparticle-Decorated Hydroxyapatite Nanocomposite with Combined Bioactivity and Antibacterial Properties. *J. Mater. Sci. Mater. Med.* **2021**, *32*, 106. [\[CrossRef\]](#)
39. Gomes, G.C.; Borghi, F.F.; Ospina, R.O.; L'opez, E.O.; Borges, F.O.; Mello, A. Nd:YAG (532 nm) pulsed laser deposition produces crystalline hydroxyapatite thin coatings at room temperature. *Surf. Coat. Technol.* **2017**, *329*, 174–183. [\[CrossRef\]](#)
40. Sinulingga, K.; Sirait, M.; Siregar, N.; Abdullah, H. Synthesis and characterizations of natural limestone-derived nano-hydroxyapatite (HAp): A comparison study of different metals doped Haps on antibacterial activity. *RSC Adv.* **2021**, *11*, 15896–15904. [\[CrossRef\]](#) [\[PubMed\]](#)
41. Lou, L.; Nelson, A.E.; Heo, G.; Major, P.W. Surface chemical composition of human maxillary first premolar as assessed by X-ray photoelectron spectroscopy (XPS). *Appl. Surf. Sci.* **2008**, *254*, 6706–6709. [\[CrossRef\]](#)
42. Li, J.; Li, Y.; Zhang, L.; Zuo, Y. Composition of calcium deficient Na-containing carbonate hydroxyapatite modified with Cu (II) and Zn (II) ions. *Appl. Surf. Sci.* **2008**, *254*, 2844–2850. [\[CrossRef\]](#)
43. Biesinger, M.C.; Lau, L.W.M.; Gerson, A.R.; Smart, R.S.C. Resolving surface chemical states in XPS analysis of first row transition metals, oxides and hydroxides: Sc, Ti, V, Cu and Zn. *Appl. Surf. Sci.* **2010**, *257*, 887–898. [\[CrossRef\]](#)
44. Thian, E.S.; Konishi, T.; Kawanobe, Y.; Lim, P.N.; Choong, C.; Ho, B.; Aizawa, M. Zinc-substituted hydroxyapatite: A biomaterial with enhanced bioactivity and antibacterial properties. *J. Mater. Sci. Mater. Med.* **2013**, *24*, 437–445. [\[CrossRef\]](#) [\[PubMed\]](#)
45. Predoi, D.; Iconaru, S.L.; Deniaud, A.; Chevallet, M.; Michaud-Soret, I.; Buton, N.; Prodan, A.M. Textural, Structural and Biological Evaluation of Hydroxyapatite Doped with Zinc at Low Concentrations. *Materials* **2017**, *10*, 229. [\[CrossRef\]](#)
46. Kazimierczak, P.; Benko, A.; Nocun, M.; Przekora, A. Novel chitosan/agarose/hydroxyapatite nanocomposite scaffold for bone tissue engineering applications: Comprehensive evaluation of biocompatibility and osteoinductivity with the use of osteoblasts and mesenchymal stem cells. *Int. J. Nanomed.* **2019**, *14*, 6615–6630. [\[CrossRef\]](#)
47. Radovanović, Ž.; Veljović, D.; Jokić, B.; Dimitrijević, S.; Bogdanović, G.; Kojić, V.; Petrović, R.; Janačković, D. Biocompatibility and antimicrobial activity of zinc(II)-doped hydroxyapatite, synthesized by a hydrothermal method. *J. Serb. Chem. Soc.* **2012**, *77*, 1787–1798. [\[CrossRef\]](#)
48. Badea, M.A.; Balas, M.; Popa, M.; Borcan, T.; Bunea, A.-C.; Predoi, D.; Dinischiotu, A. Biological Response of Human Gingival Fibroblasts to Zinc-Doped Hydroxyapatite Designed for Dental Applications—An In vitro Study. *Materials* **2023**, *16*, 4145. [\[CrossRef\]](#) [\[PubMed\]](#)
49. Ren, F.; Xin, R.; Ge, X.; Leng, Y. Characterization and structural analysis of zinc-substituted hydroxyapatites. *Acta Biomater.* **2009**, *5*, 3141–3149. [\[CrossRef\]](#)
50. Tank, K.P.; Chudasama, K.S.; Thaker, V.S.; Joshi, M.J. Pure and zinc doped nano-hydroxyapatite: Synthesis, characterization, antimicrobial and hemolytic studies. *J. Cryst. Growth* **2014**, *401*, 474–479. [\[CrossRef\]](#)
51. Dayaghi, E.; Bakhsheshi-Rad, H.R.; Hamzah, E.; Akhavan-Farid, A.; Ismail, A.F.; Aziz, M.; Abdolahi, E. Magnesium-zinc scaffold loaded with tetracycline for tissue engineering application: In vitro cell biology and antibacterial activity assessment. *Mater. Sci. Eng. C* **2019**, *102*, 53–65. [\[CrossRef\]](#)
52. Shao, W.; Liu, H.; Wang, S.; Wu, J.; Huang, M.; Min, H.; Liu, X. Controlled release and antibacterial activity of tetracyclinehydrochloride-loaded bacterial cellulose composite membranes. *Carbohydr. Polym.* **2016**, *145*, 114–120. [\[CrossRef\]](#) [\[PubMed\]](#)
53. Gomes, P.S.; Santos, K.D.; Fernandes, M.H. Cell-induced response by tetracyclines on human bone marrow colonized hydroxyapatite and Bonelike. *Acta Biomater.* **2008**, *4*, 630–637. [\[CrossRef\]](#) [\[PubMed\]](#)
54. Higgins, P.; Draper, M.; Nelson, M. Anti-Inflammatory & Anti-Allergy Agents in Medicinal Chemistry. *Former. Curr. Med. Chem.* **2011**, *10*, 132–152. [\[CrossRef\]](#)

55. Kładna, A.; Michalska, T.; Berczyński, P.; Kruk, I.; Aboul-Enein, H.Y. Evaluation of the antioxidant activity of tetracycline antibiotics in vitro. *Luminescence* **2012**, *27*, 249–255. [\[CrossRef\]](#)
56. Sano, T.; Ozaki, K.; Kodama, Y.; Matsuura, T.; Narama, I. Antimicrobial Agent, Tetracycline, Enhanced Upper Alimentarytract Candida Albicans Infection and Its Related Mucosal Proliferation in Alloxan-Induced Diabetic Rats. *Toxicol. Pathol.* **2012**, *40*, 1014–1019. [\[CrossRef\]](#)
57. Heman-Ackah, S.M. Comparison of Tetracycline Action on Staphylococcus Aureus and Escherichia coli by Microbial Kinetics. *Antimicrob. Agents Chemother.* **1976**, *10*, 223–228. [\[CrossRef\]](#)
58. Campbell, P.J.; Heseltine, W.W. An Apparent Growth Stimulant for Candida albicans Released from Tetracycline-Treated Bacterial Flora. *J. Hyg.* **1960**, *58*, 95–97. [\[CrossRef\]](#)
59. Li, B.; Webster, T.J. Bacteria antibiotic resistance: New challenges and opportunities for implant-associated orthopaedic infections. *J. Orthop. Res.* **2018**, *36*, 22–32. [\[CrossRef\]](#)
60. Hemeg, H.A. Nanomaterials for alternative antibacterial therapy. *Int. J. Nanomed.* **2017**, *12*, 8211–8225. [\[CrossRef\]](#)
61. Song, W.; Zhang, J.; Guo, J.; Zhang, J.; Ding, F.; Li, L.; Sun, Z. Role of the dissolved zinc ion and reactive oxygen species in cytotoxicity of ZnO nanoparticles. *Toxicol. Lett.* **2010**, *199*, 389–397. [\[CrossRef\]](#)
62. Li, Y.; Liao, C.; Tjong, S.C. Recent Advances in Zinc Oxide Nanostructures with Antimicrobial Activities. *Int. J. Mol. Sci.* **2020**, *21*, 8836. [\[CrossRef\]](#) [\[PubMed\]](#)
63. Jiang, X.; Tang, X.; Zhang, B.; He, L.; Shi, Y. Antimicrobial activity and synergistic antibacterial mechanism of a combination of zinc and rare-earth scandium against Escherichia coli. *Mater. Technol.* **2019**, *35*, 797–806. [\[CrossRef\]](#)
64. Stafford, S.L.; Bokil, N.J.; Achard, M.E.; Kapetanovic, R.; Schembri, M.A.; McEwan, A.G.; Sweet, M.J. Metal ions in macrophage antimicrobial pathways: Emerging roles for zinc and copper. *Biosci. Rep.* **2013**, *33*, e00049. [\[CrossRef\]](#)
65. Riduan, S.N.; Zhang, Y. Recent Advances of Zinc-based Antimicrobial Materials. *Chem. Asian J.* **2021**, *16*, 2588. [\[CrossRef\]](#)
66. Mendes, C.R.; Dilarri, G.; Forsan, C.F.; Sapata, V.D.M.R.; Lopes, P.R.M.; de Moraes, P.B.; Montagnolli, R.N.; Ferreira, H.; Bidoia, E.D. Antibacterial action and target mechanisms of zinc oxide nanoparticles against bacterial pathogens. *Sci. Rep.* **2022**, *12*, 2658. [\[CrossRef\]](#)
67. Caron, A.J.; Ali, I.J.; Delgado, M.J.; Johnson, D.; Reeks, J.M.; Strzhemechny, Y.M.; McGillivray, S.M. Zinc oxide nanoparticles mediate bacterial toxicity in Mueller-Hinton Broth via Zn²⁺. *Front. Microbiol.* **2024**, *15*, 1394078. [\[CrossRef\]](#) [\[PubMed\]](#)
68. Nguyen, F.; Starosta, A.L.; Arenz, S.; Sohmen, D.; Dönhöfer, A.; Wilson, D.N. Tetracycline antibiotics and resistance mechanisms. *Biol. Chem.* **2014**, *395*, 559–575. [\[CrossRef\]](#) [\[PubMed\]](#)
69. Schnappinger, D.; Hillen, W. Tetracyclines: Antibiotic action, uptake, and resistance mechanisms. *Arch. Microbiol.* **1996**, *165*, 359–369. [\[CrossRef\]](#)
70. Speer, B.S.; Shoemaker, N.B.; Salyers, A.A. Bacterial resistance to tetracycline: Mechanisms, transfer, and clinical significance. *Clin. Microbiol. Rev.* **1992**, *5*, 387–399. [\[CrossRef\]](#)
71. Marily, C. Roberts, Tetracycline resistance determinants: Mechanisms of action, regulation of expression, genetic mobility, and distribution. *FEMS Microbiol. Rev.* **1996**, *19*, 1–24. [\[CrossRef\]](#)
72. Connell, S.R.; Tracz, D.M.; Nierhaus, K.H.; Taylor, D.E. Ribosomal protection proteins and their mechanism of tetracycline resistance. *Antimicrob. Agents Chemother.* **2003**, *47*, 3675–3681. [\[CrossRef\]](#)
73. Grossman, T.H. Tetracycline Antibiotics and Resistance. *Cold Spring Harb. Perspect. Med.* **2016**, *6*, a025387. [\[CrossRef\]](#) [\[PubMed\]](#)
74. Sheykhsaran, E.; Baghi, H.B.; Soroush, M.H.; Ghotaslou, R. An overview of tetracyclines and related resistance mechanisms. *Rev. Med. Microbiol.* **2019**, *30*, 69–75. [\[CrossRef\]](#)
75. Iconaru, S.L.; Motelica-Heino, M.; Predoi, D. Study on europium-doped hydroxyapatite nanoparticles by Fourier transform infrared spectroscopy and their antimicrobial properties. *J. Spectro.* **2013**, *2013*, 284285. [\[CrossRef\]](#)
76. Iconaru, S.L.; Predoi, M.V.; Chapon, P.; Gaiaschi, S.; Rokosz, K.; Raaen, S.; Motelica-Heino, M.; Predoi, D. Investigation of Spin Coating Cerium-Doped Hydroxyapatite Thin Films with Antifungal Properties. *Coatings* **2021**, *11*, 464. [\[CrossRef\]](#)
77. Casa Software Ltd. CasaXPS: Processing Software for XPS, AES, SIMS and More. 2009. Available online: www.casaxps.com (accessed on 1 May 2024).
78. Das, D.; Nath, B.C.; Phukon, P.; Dolui, S.K. Synthesis of ZnO nanoparticles and evaluation of antioxidant and cytotoxic activity. *Colloids Surf. B Biointerfaces* **2013**, *111*, 556–560. [\[CrossRef\]](#)
79. Ciobanu, C.S.; Predoi, D.; Iconaru, S.L.; Predoi, M.V.; Rokosz, K.; Raaen, S.; Negrila, C.C.; Buton, N.; Ghegoiu, L.; Badea, M.L. Physico-Chemical and Biological Features of Fluorine-Substituted Hydroxyapatite Suspensions. *Materials* **2024**, *17*, 3404. [\[CrossRef\]](#)

Disclaimer/Publisher’s Note: The statements, opinions and data contained in all publications are solely those of the individual author(s) and contributor(s) and not of MDPI and/or the editor(s). MDPI and/or the editor(s) disclaim responsibility for any injury to people or property resulting from any ideas, methods, instructions or products referred to in the content.

Article

Physico-Chemical Properties of Copper-Doped Hydroxyapatite Coatings Obtained by Vacuum Deposition Technique

Yassine Benali ¹, Daniela Predoi ^{2,*}, Krzysztof Rokosz ^{3,*}, Carmen Steluta Ciobanu ², Simona Liliana Iconaru ², Steinar Raaen ⁴, Catalin Constantin Negrila ², Carmen Cimpeanu ⁵, Roxana Trusca ⁶, Liliana Ghegoiu ², Coralia Bleotu ^{7,8,9}, Ioana Cristina Marinas ^{8,10}, Miruna Stan ¹¹ and Khaled Boughzala ¹²

- ¹ Faculty of Sciences, University de Gafsa, Route de Tozeur, Gafsa 2112, Tunisia; yassin.bn.ali27@gmail.com
- ² National Institute of Materials Physics, Atomistilor Street, No. 405A, 077125 Magurele, Romania; ciobanucs@gmail.com (C.S.C.); simonaiconaru@gmail.com (S.L.I.); catalin.negrila@infim.ro (C.C.N.); ghegoiuliliana@gmail.com (L.G.)
- ³ Faculty of Electronics and Computer Science, Koszalin University of Technology, Śniadeckich 2, PL 75-453 Koszalin, Poland
- ⁴ Department of Physics, Norwegian University of Science and Technology (NTNU), Realfagbygget E3-124 Høgskoleringen 5, NO 7491 Trondheim, Norway; steinar.raaen@ntnu.no
- ⁵ Faculty of Land Reclamation and Environmental Engineering, University of Agronomic Sciences and Veterinary Medicine of Bucharest, 59 Marasti Blvd, 011464 Bucharest, Romania; carmencimpeanu@yahoo.com
- ⁶ National Centre for Micro and Nanomaterials, University Politehnica of Bucharest, 060042 Bucharest, Romania; truscaroxana@yahoo.com
- ⁷ Department of Cellular and Molecular Pathology, Stefan S. Nicolau Institute of Virology, 030304 Bucharest, Romania; cbleotu@yahoo.com
- ⁸ Research Institute of the University of Bucharest (ICUB), University of Bucharest, 060023 Bucharest, Romania; ioana.cristina.marinas@gmail.com
- ⁹ The Academy of Romanian Scientist, 050711 Bucharest, Romania
- ¹⁰ Department of Microbiology, Faculty of Biology, University of Bucharest, 1-3 Aleea Portocalelor Str., District 5, 060101 Bucharest, Romania
- ¹¹ Department of Biochemistry and Molecular Biology, Faculty of Biology, University of Bucharest, 91-95 Splaiul Independentei, 050095 Bucharest, Romania; miruna.stan@bio.unibuc.ro
- ¹² Higher Institute of Technological Studies of Ksar Hellal, Ksar-Hellal 5070, Tunisia; khaledboughzala@gmail.com
- * Correspondence: dpredoi@gmail.com (D.P.); rokosz@tu.koszalin.pl (K.R.)



Citation: Benali, Y.; Predoi, D.; Rokosz, K.; Ciobanu, C.S.; Iconaru, S.L.; Raaen, S.; Negrila, C.C.; Cimpeanu, C.; Trusca, R.; Ghegoiu, L.; et al. Physico-Chemical Properties of Copper-Doped Hydroxyapatite Coatings Obtained by Vacuum Deposition Technique. *Materials* **2024**, *17*, 3681. <https://doi.org/10.3390/ma17153681>

Academic Editors: Alessia Serena Perna, Antonio Viscusi and Csaba Balázs

Received: 29 May 2024
Revised: 10 July 2024
Accepted: 18 July 2024
Published: 25 July 2024



Copyright: © 2024 by the authors. Licensee MDPI, Basel, Switzerland. This article is an open access article distributed under the terms and conditions of the Creative Commons Attribution (CC BY) license (<https://creativecommons.org/licenses/by/4.0/>).

Abstract: The hydroxyapatite and copper-doped hydroxyapatite coatings ($\text{Ca}_{10-x}\text{Cu}_x(\text{PO}_4)_6(\text{OH})_2$; $x_{\text{Cu}} = 0, 0.03$; HAp and 3CuHAp) were obtained by the vacuum deposition technique. Then, both coatings were analyzed by the X-ray diffraction (XRD), scanning electron microscopy (SEM), atomic force microscopy (AFM), X-ray photoelectron spectroscopy (XPS), Fourier transform infrared spectroscopy (FTIR) and water contact angle techniques. Information regarding the in vitro antibacterial activity and biological evaluation were obtained. The XRD studies confirmed that the obtained thin films consist of a single phase associated with hydroxyapatite (HAp). The obtained 2D and 3D SEM images did not show cracks or other types of surface defects. The FTIR studies' results proved the presence of vibrational bands characteristic of the hydroxyapatite structure in the studied coating. Moreover, information regarding the HAp and 3CuHAp surface wettability was obtained by water contact angle measurements. The biocompatibility of the HAp and 3CuHAp coatings was evaluated using the HeLa and MG63 cell lines. The cytotoxicity evaluation of the coatings was performed by assessing the cell viability through the MTT assay after incubation with the HAp and 3CuHAp coatings for 24, 48, and 72 h. The results proved that the 3CuHAp coatings exhibited good biocompatible activity for all the tested intervals. The ability of *Pseudomonas aeruginosa* 27853 ATCC (*P. aeruginosa*) cells to adhere to and develop on the surface of the HAp and 3CuHAp coatings was investigated using AFM studies. The AFM studies revealed that the 3CuHAp coatings inhibited the formation of *P. aeruginosa* biofilms. The AFM data indicated that *P. aeruginosa*'s attachment and development on the 3CuHAp coatings were significantly inhibited within the first 24 h. Both the 2D and 3D topographies showed a rapid decrease in attached bacterial cells over time, with a significant reduction observed after 72 h of

exposure. Our studies suggest that 3CuHAp coatings could be suitable candidates for biomedical uses such as the development of new antimicrobial agents.

Keywords: copper-doped hydroxyapatite; coatings; vacuum deposition; biocompatibility; antimicrobial activity

1. Introduction

In the last few years, significant efforts have been undertaken by the scientific community in order to enhance the biocompatibility of commonly used implant materials in orthopedics/stomatology. One potential solution purposed involves the deposition of bioactive coatings, such as hydroxyapatite (HAp), on the surface of the implants [1]. Hydroxyapatite is a bioceramic that has attracted researchers' attention because of its structural and chemical resemblance to the main inorganic component of bone tissue. Hydroxyapatite has been used as a coating material for metallic implants due to its excellent cytocompatibility, ability to stimulate cellular functions, and good osteoconductivity [2]. Nonetheless, previous studies have shown that natural hydroxyapatite, which is found in the mineral phases of bone, dentin, and enamel, possesses a chemical composition that is different from synthetic HAp [1–3]. Typically, natural HAp encompasses a wide range of trace elements, such as silicon (Si), fluorine (F), magnesium (Mg), strontium (Sr), zinc (Zn), etc., each possessing distinct biological features [4]. The appearance of post-surgical infections can prevent proper bone integration and cause tissue necrosis, posing serious health risks to patients and altering their quality of life [5–7]. The increase in antibiotic-resistant bacteria is driving research toward new solutions, including the use of metallic ions for their antibacterial properties [5,8]. It is well known that copper (Cu) is a crucial trace element for all organisms and that it is vital for a wide range of physiological functions, including energy production, respiration and tissue development [9,10]. On the other hand, it serves as an enzyme cofactor in many metabolic processes. Furthermore, copper is crucial for bone mineralization and for osteoblast activity [9–15]. Insufficient levels of copper are associated with a range of medical conditions, such as myeloneuropathy, leucopenia, anemia, and Menke's disease [10,13]. Moreover, high levels of Cu are harmful for the human body and lead to Wilson's disease [10,14]. Moreover, copper possesses excellent antimicrobial activity, having been used from ancient times by the Egyptians for maintaining the purity of water [10,15]. Therefore, nowadays, the copper ion is regarded as a promising doping agent due to its pronounced antibacterial activity and low cytotoxicity.

According to the study conducted by Hidalgo-Robatto and coworkers [16], infections related to prosthetic implants and medical devices are mainly caused by certain bacteria, including *Staphylococcus epidermidis* and *Staphylococcus aureus* (Gram-positive), as well as *Escherichia coli* and *Pseudomonas aeruginosa* (Gram-negative). Therefore, the enriching of biomaterials that cover implants/medical devices with antimicrobial agents could represent a promising alternative as a systemic treatment with antibiotics [16]. For example, *Pseudomonas aeruginosa* (*P. aeruginosa*), a Gram-negative bacterium, is known for its multidrug-resistant and extensively drug-resistant strains, which frequently cause severe infections [17]. This fact presents significant challenges in selecting effective antimicrobial treatments due to their resistance [17]. The study reported by Jacobs et al. [5], which was conducted on the copper-doped biphasic calcium phosphate materials, underlined their good antibacterial activity against Gram-positive (methicillin-resistant *Staphylococcus aureus* and methicillin-sensitive) and Gram-negative (*Pseudomonas aeruginosa* and *Escherichia coli*) strains [5]. Other similar studies that have previously been reported revealed that the antibacterial efficiency of copper-doped biomaterials against *Pseudomonas aeruginosa* is dose- and incubation time-dependent [10]. Information about copper-doped hydroxyapatite was provided in various studies conducted by Bazin et al. [18] and Noori et al. [19]. Thus, the in vitro biological studies conducted by Bazin et al. [18] on the MC3T3-E1 cell

line revealed that the incorporation of copper into the sintered hydroxyapatite ceramics did not alter the proliferation and cell adhesion, behavior that confirms the sample's biocompatibility [18]. Furthermore, the results of the studies performed by Noori et al. [19] underlined that copper-doped hydroxyapatite does not disrupt the differentiation of stem cells into osteoblasts, which is a crucial process for the regeneration of bone tissue [19]. Also, the biocompatibility of copper-doped hydroxyapatite is influenced by the copper content [18–20]. Previous studies [20] showed that concentrations of copper up to 5% typically promote cellular growth and functionality, whereas higher levels of copper can lead to toxic effects on cells [20]. The groundbreaking aspect of this work lies in the development of new antimicrobial and biocompatible coatings using 3CuHAp powders through a cost-efficient method: vacuum deposition. Moreover, another aspect underlining the novelty and originality of this work is the achievement (for the first time) of continuous and pure 3CuHAp layers through vacuum deposition.

This study aimed at the development for the first time of copper-doped hydroxyapatite coatings ($\text{Ca}_{10-x}\text{Cu}_x(\text{PO}_4)_6(\text{OH})_2$; $x_{\text{Cu}} = 0.03$; 3CuHAp) by vacuum deposition. Also, this study explored the physico-chemical properties of 3CuHAp coatings, together with their toxic effects on cells and their antibacterial activity. Techniques such as X-ray diffraction (XRD), X-ray photoelectron spectroscopy (XPS), atomic force microscopy (AFM), scanning electron microscopy (SEM), Fourier transform infrared spectroscopy (FTIR) and water contact angle were employed in order to obtain valuable information about the features of the HAp and 3CuHAp coatings. In summary, this work pioneers a novel approach by combining superior physico-chemical and biological properties and cost efficiency in the development of coatings based on HAp and 3CuHAp. These coatings have the potential to improve medical devices/implants, enhancing overall health.

2. Materials and Methods

2.1. Materials

2.1.1. Synthesis of Hydroxyapatite (HAp) and Copper-Doped Hydroxyapatite (3CuHAp)

For the synthesis of undoped hydroxyapatite coatings ($\text{Ca}_{10}\text{Cu}(\text{PO}_4)_6(\text{OH})_2$; Ca/P ratio equal with 1.67; referred to as HAp), the steps described in our previous work [21] were followed. Firstly, two solutions were obtained, containing 0.1 mol of $\text{Ca}(\text{NO}_3)_2 \cdot 4\text{H}_2\text{O}$ (Sigma Aldrich, St. Louis, MO, USA) and 0.06 mol of $(\text{NH}_4)_2\text{HPO}_4$ (Alfa Aesar, Karlsruhe, Germany), respectively. Then, the solution containing $\text{Ca}(\text{NO}_3)_2 \cdot 4\text{H}_2\text{O}$ was slowly added into the $(\text{NH}_4)_2\text{HPO}_4$ solution. During the synthesis, the pH value was maintained at 11. The resulting mixture was stirred at 100 °C for 4 h, then centrifuged and washed for 5 times. Finally, the HAp precipitate was dried at 100 °C and used for the vacuum deposition of the HAp coatings.

A similar procedure was used for obtaining of the copper-doped hydroxyapatite powders (with the chemical formula: $\text{Ca}_{10-x}\text{Cu}_x(\text{PO}_4)_6(\text{OH})_2$; where $x_{\text{Cu}} = 0.03$; referred to as 3CuHAp). During the synthesis, the $[\text{Ca} + \text{Cu}]/\text{P}$ ratio was maintained at 1.67. Briefly, the $\text{Cu}(\text{NO}_3)_2 \cdot 3\text{H}_2\text{O}$ (Alfa Aesar, Karlsruhe, Germany) was dissolved with the $\text{Ca}(\text{NO}_3)_2 \cdot 4\text{H}_2\text{O}$. The next steps were carried out identically to the those described for the hydroxyapatite powders' synthesis. Finally, the 3CuHAp precipitate was dried at 100 °C and used for the vacuum deposition of the 3CuHAp coatings.

2.1.2. Development of Hydroxyapatite (HAp) and Copper-Doped Hydroxyapatite (3CuHAp) Coatings

The deposition of the HAp and 3CuHAp coatings was performed on silicon (Si) substrates. Prior to the vacuum deposition process, the substrates underwent multiple cleanings with acetone and were air-dried at 40 °C. The deposition parameters for the coatings were consistent with the ones presented by Predoi et al. [22]. Briefly, the deposition process took place in a high vacuum environment ($\sim 10^{-6}$ mbar). The powders were thermally evaporated from a W boat, slowly increasing the current through them until the melting state became visible. Afterward, the melt was completely evaporated in

about 120 s. Finally, the HAp and 3CuHAp coatings were thermally treated at 500 °C in air. Figure 1 presents a schematic representation of the synthesis, characterization techniques and key findings of the studies conducted on the HAp and 3CuHAp coatings. Furthermore, the vacuum deposition technique used for the development of the 3CuHAp coatings is a versatile and cost-efficient method. While the setup cost is moderate, the ongoing operation and maintenance costs are manageable. Compared to other deposition techniques, vacuum deposition is cost-effective due to its simplicity and high deposition rate. Other deposition techniques use expensive equipment that requires considerable operation and maintenance costs.

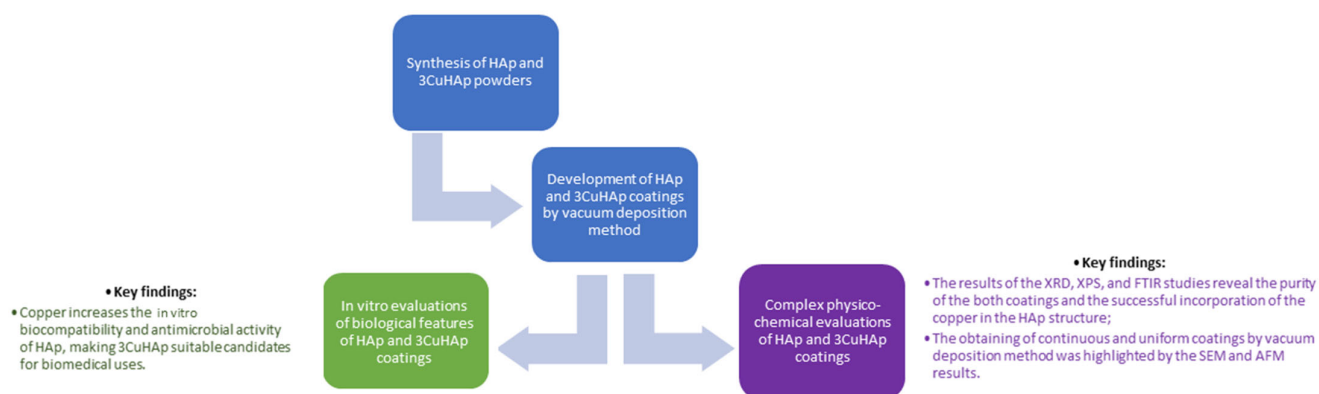


Figure 1. Schematic representation of the synthesis, characterization techniques and key findings.

2.2. Characterizations of 3CuHAp Coatings

2.2.1. X-ray Diffraction (XRD)

The X-ray diffraction (XRD) studies were conducted using a Bruker D8 Advance X-ray diffractometer (manufactured by Bruker in Karlsruhe, Germany). The XRD experimental data were acquired within the 20° to 60° (2θ) range, with a step size of 0.02°, using Cu Kα radiation (wavelength $\lambda = 1.5418 \text{ \AA}$).

2.2.2. Scanning Electron Microscopy (SEM)

The FEI Quanta Inspect F scanning electron microscope (manufactured by FEI Company, Hillsboro, OR, USA) was used in order to evaluate the surface morphology of both coatings. Additionally, the microscope is equipped with an energy-dispersive X-ray (EDS) attachment, which enabled the evaluation of the chemical composition of the HAp and 3CuHAp coatings. More than that, the thickness of both coatings was evaluated using SEM transversal cross-section images. The 3D SEM images were obtained with the aid of ImageJ 1.51j8 software [23].

2.2.3. Atomic Force Microscopy (AFM)

For this study, an atomic force microscope (AFM, NT-MDT NTEGRA Probe NanoLaboratory system, Moscow, Russia) operated in non-contact mode was used to obtain information about the surface features of the HAp and 3CuHAp coatings [24]. The AFM studies were performed using a silicon NT-MDT NSG01 cantilever. The AFM images were recorded on a surface area of $3 \times 3 \mu\text{m}^2$ and Gwyddion 2.55 software was used for their analysis [25].

2.2.4. X-ray Photoelectron Spectroscopy (XPS)

A multimethod SPECS surface analysis system (SPECS GmbH, Berlin, Germany) operating with Al Kα monochromatic radiation (1486.6 eV) was used in order to perform the X-ray photoelectron spectroscopy (XPS) studies. The experimental conditions were reported in previous research conducted by Iconaru et al. [26]. The XPS data were processed

using Spectral Data Processor v. 2.3 (SDP) software. The binding energy of the calibration using C1s was 284.8 eV.

2.2.5. Fourier Transform Infrared Spectroscopy (FTIR)

The PerkinElmer Spectrum 100 FT-IR spectrometer (Waltham, MA, USA) is an instrument widely used for establishing the presence of functional groups in the structure of coatings. Experimental data were collected in the spectral range of 450–1200 cm^{-1} . Additionally, following the procedure detailed in [27], the second derivative spectra of the HAp and 3CuHAp coatings were obtained. The FTIR data were analyzed using the OriginPro 2021b software (OriginLab Corporation, Northampton, MA, USA).

2.2.6. Water Contact Angle Studies

Water contact angle studies were conducted under ambient conditions with the aid of a contact angle goniometer (DSA30 Krüss GmbH, Hamburg, Germany). The sessile drop method was used for the experiments. The HAp and 3CuHAp coatings underwent three repetitions of the contact angle measurement. The mean contact angle values are reported, along with the standard deviation (SD).

2.2.7. In Vitro Antibacterial Activity

The antibacterial properties of the HAp and 3CuHAp coatings were evaluated against the standard *Pseudomonas aeruginosa* 27853 ATCC bacterial strain. The in vitro antibacterial assays were conducted following the protocol outlined in [28]. The antibacterial activity of the 3CuHAp coatings was assessed after 24, 48, and 72 h of incubation with the *P. aeruginosa* 27853 ATCC bacterial suspensions. The quantitative measurements of the bacterial cell survival were recorded at these intervals. For this purpose, *P. aeruginosa* suspensions with a bacterial density of approximately 5×10^6 colony-forming units (CFUs)/mL, derived from 18–24 h cultures, were used in the study. The 3CuHAp coatings were incubated at 37 °C for 24, 48, and 72 h with these bacterial suspensions, and the bacterial growth was monitored over time. For each incubation period, the bacterial suspensions were collected and incubated on LB agar medium. A free bacterial suspension served as a positive control (C+). The CFU count per milliliter (CFU/mL) was determined and graphically represented as the log CFU/mL over time. The antibacterial experiments were conducted in triplicate, and the results are expressed as the mean \pm standard deviation (SD). The qualitative evaluation of the bacterial cell adherence and proliferation on the surface of the 3CuHAp coatings was also studied using the atomic force microscopy (AFM) technique. For these assays, *P. aeruginosa* bacterial cells were cultured on the surface of the 3CuHAp coatings for three different time intervals. After each incubation period, the 3CuHAp coatings were removed from the culture medium, washed using sterile saline solution to remove the unattached bacterial cells, fixed with cold methanol, and prepared for visualization.

2.2.8. In Vitro Biological Evaluation

The cytotoxicity of the HAp and 3CuHAp coatings was assessed using both HeLa (ATCC CRM-CCL2) and osteosarcoma MG63 (ATCC CRL-1427) cells, following a similar methodology to that described by Iconaru et al. [29]. The cells were cultured in Dulbecco's modified Eagle's medium (DMEM) enriched with heat-inactivated fetal bovine serum at 37 °C in an atmosphere containing 5% CO_2 . The HeLa and MG63 cells were seeded at a concentration of 1×10^5 cells/well in complete medium and incubated with the HAp and 3CuHAp coatings for 24, 48, and 72 h. The cytotoxicity was evaluated by measuring the cell viability using the MTT [3-(4,5-dimethylthiazolyl)-2,5-diphenyltetrazolium bromide] reduction assay. After the incubation periods, the cells were washed with phosphate-buffered saline (PBS) and incubated with 1 mg/mL MTT solution for 2.5 h. The cell viability was determined by measuring the optical density of the medium at 595 nm using a TECAN spectrophotometer. The percentage of viable HeLa and MG63 cells was calculated relative to a control sample, which was set to 100% viability. The HeLa and MG63 cells were

seeded at a concentration of 1×10^5 cells/well in complete medium and maintained at 37°C for 72 h. The morphology of the cells maintained together with the HAp and 3CuHAp coatings was observed under visible light using an Axio Observer Inverted microscope (Carl Zeiss, GMBH, Munich, Germany). In addition, the adhesion of the cells on the material was highlighted by fixing them with 70% ethanol, staining them with propidium iodide and photographing them with an Axio Observer D Inverted microscope equipped with a fluorescence module (Carl Zeiss, GMBH, Munich, Germany).

Furthermore, the cells were also visualized with the aid of an inversed trinocular metallographic microscope OX.2153-PLM (Euromex, Arnhem, The Netherlands). The metallographic microscope was equipped with an CMEX digital camera and the images were acquired with ImageFocusAlpha software (v 1.3.7.19728, Euromex, Arnhem, The Netherlands) using the $10\times$ magnification objective. These studies were performed under ambient conditions.

3. Results and Discussion

The samples consisting of the HAp and 3CuHAp coatings obtained by the vacuum deposition process were analyzed from a structural point of view by X-ray diffraction (Figure 2).

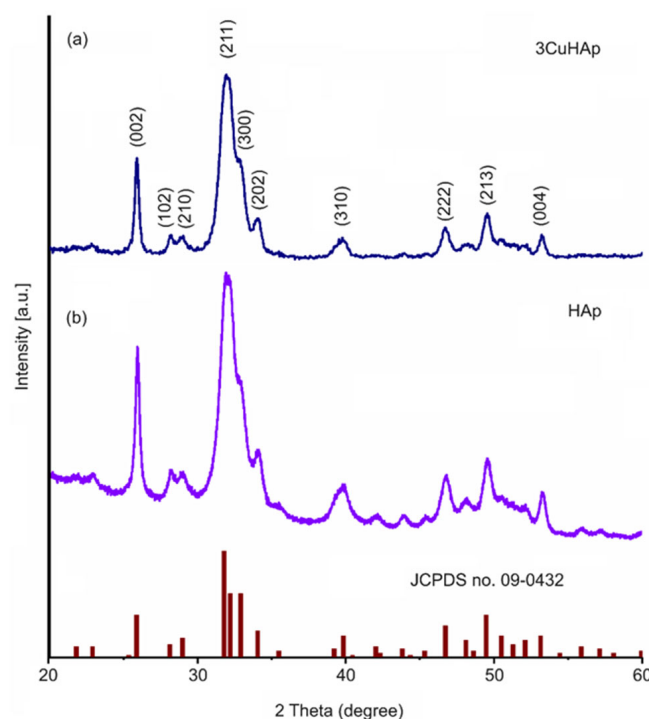


Figure 2. XRD pattern of the HAp (b) and 3CuHAp (a) coatings and JCPDS no. 09-0432.

The X-ray diffraction analysis of the deposited HAp and 3CuHAp coatings revealed the presence of hydroxyapatite (Figure 2a,b). This was highlighted by the diffraction pattern, which exhibited maxima associated with pure hexagonal hydroxyapatite (JCPDS no. 09-0432).

The diffraction peaks corresponded to specific crystallographic planes of the hexagonal HAp structure. These planes were (002), (210), (211), (300), (202), (310), (222), (213), (004), and (322). There were no peaks associated with impurities, indicating that the coatings were composed of a single phase of hydroxyapatite. The calculated lattice parameters were $a = 9.393 \text{ \AA}$ and $b = 6.869 \text{ \AA}$ for the 3CuHAp sample, while for the HAp coatings, the values were $a = 9.416 \text{ \AA}$ and $b = 6.881 \text{ \AA}$. The values of the lattice parameters were lower compared to the values of pure hydroxyapatite ($a = 9.418 \text{ \AA}$ and $b = 6.884 \text{ \AA}$). The cell volume in the case of the 3CuHAp sample was equal of 524.72 \AA^3 , while the cell volume of the HAp

coatings was 528.32 \AA^3 . The cell volume of pure hexagonal HAp is 528.80 \AA^3 . For the HAp ($x_{\text{Cu}} = 0.00$) and 3CuHAp ($x_{\text{Cu}} = 0.03$) samples, the crystallite size was determined using Scherrer's equation [30–32]. The calculated crystallite size for the HAp sample was 19.45 nm, while for the 3CuHAp sample, it was 12.18 nm. The substitution of calcium (Ca) for copper (Cu) at the Ca (II) sites in the hydroxyapatite (HAp) lattice leads to a decrease in the lattice parameters and a contraction of the cell volume. This behavior aligns with findings from prior studies reported by Mariappan et al. [33].

Figure 3 shows the 2D and 3D SEM micrographs, together with the SEM particle size distribution histogram and SEM transversal cross-section image, obtained for HAp. The SEM images (both the 2D and 3D representations) reveal the presence of a continuous coating with no evidence of cracks. Furthermore, the mean particle size obtained by SEM for HAp was 22.1 nm. The transversal cross-section image obtained for the HAp coatings deposited by vacuum deposition on the Si substrate shows that their thickness was around 159.2 nm.

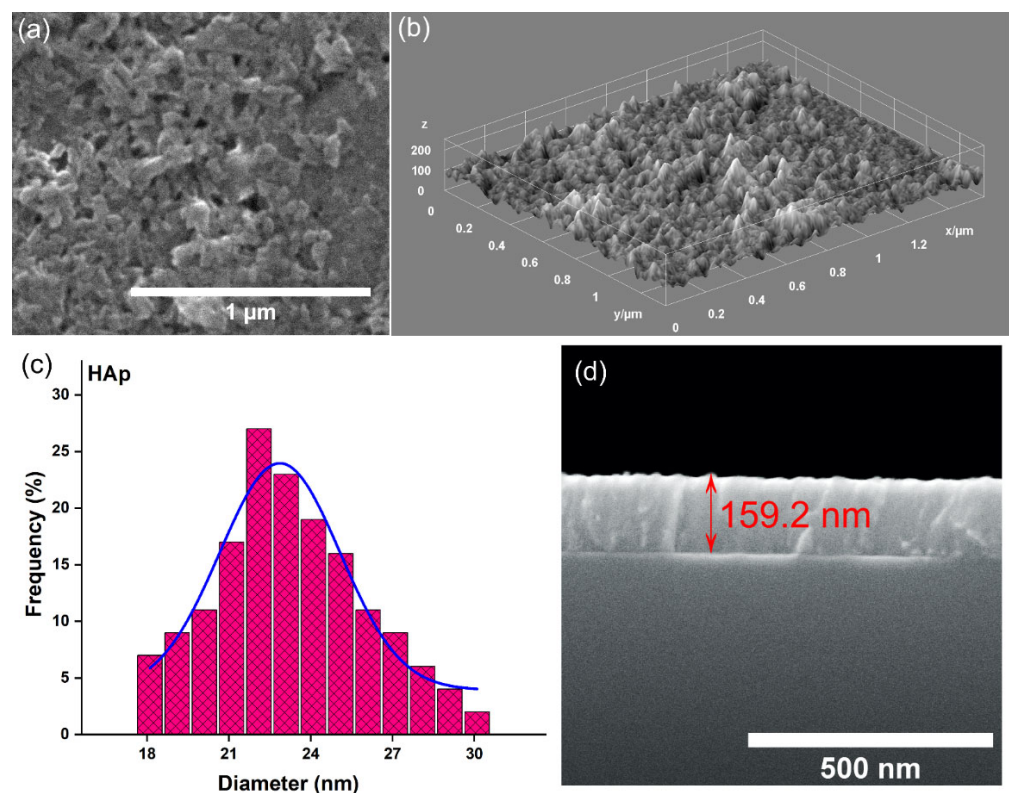


Figure 3. (a) SEM image (2D) of the HAp coatings; (b) SEM image (3D) of the HAp coatings; (c) SEM particle size distribution of the HAp coatings; and (d) SEM transversal cross-section image of the HAp coatings.

Both the 2D and 3D scanning electron microscope images acquired from the 3CuHAp coatings are presented (Figure 4a,b). Notably, the 3CuHAp coatings' surface exhibits an absence of cracks and fissures. Additionally, the SEM images highlight the continuous and homogeneous surface morphology of the 3CuHAp coatings. Importantly, no other surface defects are noticeable in the obtained 2D and 3D SEM images (Figure 4a,b). The mean particle size determined via SEM was 15.8 nm for the 3CuHAp. Moreover, the SEM transversal cross-section image suggests that the thickness of the 3CuHAp coatings was around 158.1 nm.

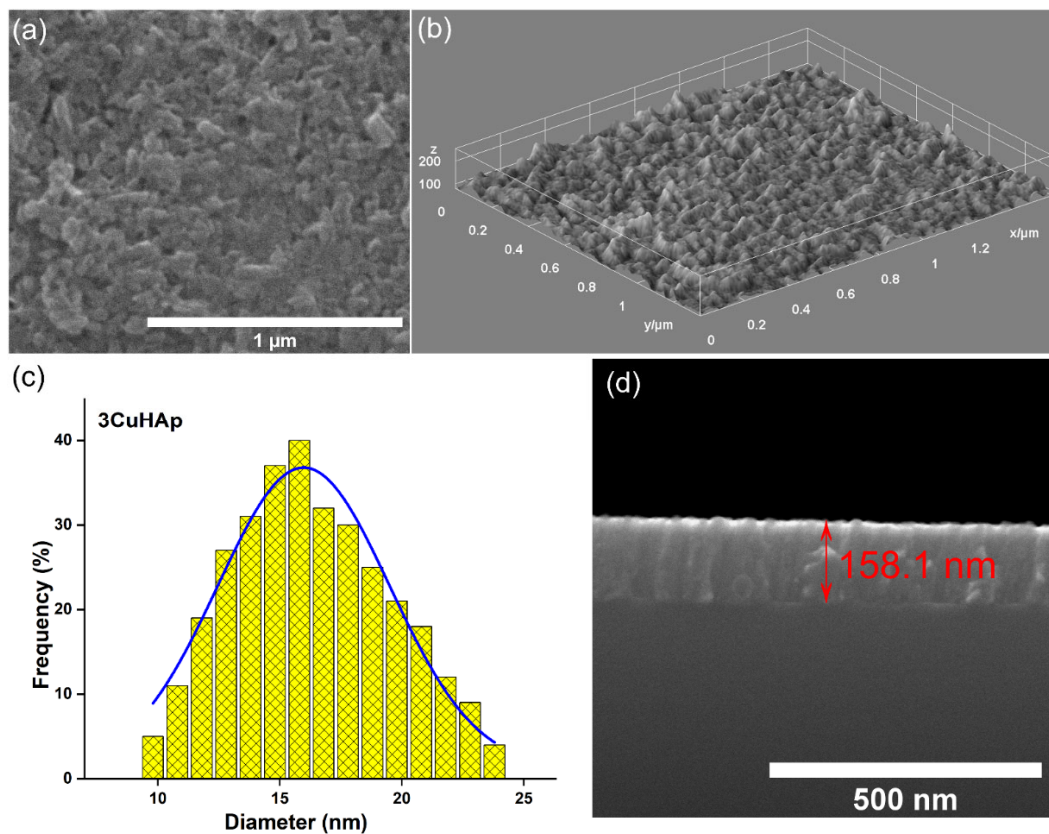


Figure 4. (a) SEM image (2D) of the 3CuHAp coatings; (b) SEM image (3D) of the 3CuHAp coatings; (c) SEM particle size distribution of the 3CuHAp coatings; and (d) SEM transversal cross-section image of the 3CuHAp coatings.

The EDS spectra obtained for the HAp and 3CuHAp coatings deposited on a silicon (Si) substrate by the vacuum deposition coating process are presented in Figure 5a,b. The results indicate that both coatings are pure. This conclusion is based on the absence of maxima in the EDS spectra that could be attributed to contaminants. In the EDS spectra specific to the HAp coatings (Figure 5b), only the lines associated with the next chemical elements that belong to the HAp structure are present: calcium (Ca), oxygen (O) and phosphorus (P). The EDS spectra of the 3CuHAp coatings revealed the presence of calcium (Ca), oxygen (O), phosphorus (P), and copper (Cu) chemicals. These elements collectively contribute to the composition of the $\text{Ca}_{10-x}\text{Cu}_x(\text{PO}_4)_6(\text{OH})_2$ structure. Additionally, both EDS spectra showed an Si line. This Si signal originates from the silicon substrate on which the HAp and 3CuHAp coatings were deposited.

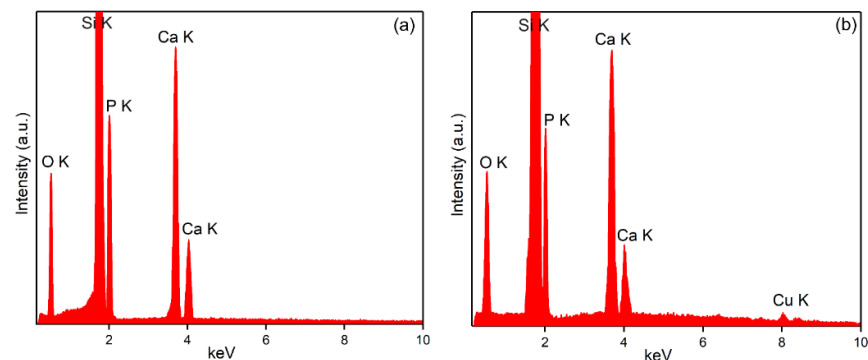


Figure 5. The EDS spectra obtained for the HAp (a) and 3CuHAp (b) coatings.

Atomic force microscopy (AFM) was used to examine the surface topography of the HAp and 3CuHAp coatings. The findings from the AFM studies (2D, together with their 3D representations) are illustrated in Figure 6a–d. The results of the AFM studies obtained for the hydroxyapatite coatings are presented in Figure 6a,b and indicate the presence of a uniform coating consisting of nanoaggregates that are well distributed on the surface. The AFM images (2D and their 3D representations) reveal that no important cracks or fissures could be noticed on the HAp coatings' surface. The value obtained for the roughness parameter (R_{RMS}) by AFM for the HAp coatings was 19.02 nm.

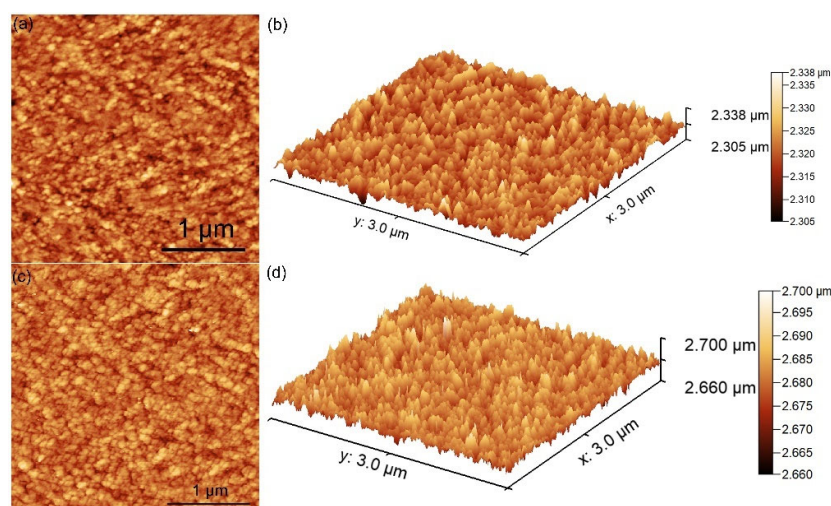


Figure 6. (a) The 2D and (b) 3D AFM images obtained for the HAp coatings; and (c) the 2D and (d) 3D AFM images obtained for the 3CuHAp coatings.

Both the 2D and 3D AFM micrographs reveal the surface topography of the 3CuHAp coatings (Figure 6c,d). The AFM analysis confirms that the studied coating displays a uniform and continuous morphology. Additionally, the 2D surface images clearly show an absence of cracks or fissures, indicating that the nanoaggregates are evenly distributed across the surface of the 3CuHAp coatings. Furthermore, the value obtained from the AFM studies for the roughness parameter (R_{RMS}) was equal to 18.73 nm. As can be seen, the value of R_{RMS} for the 3CuHAp coatings is smaller compared with the value of R_{RMS} obtained for the HAp coatings. This behavior indicates a decrease in roughness in the case of 3CuHAp and could be attributed to the HAp lattice distortion induced by the copper substitution.

Supplementary information about the roughness of the HAp and 3CuHAp coatings was obtained from the AFM images. The values of the roughness parameters (R_a and R_q), were obtained from the AFM images and are presented in Table 1. The value obtained for the roughness average (R_a) parameter was 15.43 nm for HAp and 15.16 nm for 3CuHAp. On the other hand, the values obtained for the root mean square (RMS) roughness (R_q) were nearly equal, with 19.02 nm for HAp and 18.73 nm for 3CuHAp.

Table 1. Roughness parameters of the HAp and 3CuHAp coatings' surface obtained by AFM.

Sample	R_q (nm)	R_a (nm)
HAp	19.02	15.43
3CuHAp	18.73	15.16

Table 2 depicts the values obtained for the roughness parameters (R_a and R_q), as quantified from the SEM images. For the determination of the roughness parameters from the SEM images, the images were first preprocessed and the Z height was correlated from the AFM images. The results obtained from the SEM images concerning the roughness

parameters of the HAp and 3CuHAp coatings are similar and could be correlated with the results determined from the AFM surface topographies.

Table 2. Roughness parameters of the HAp and 3CuHAp coatings' surface obtained by SEM.

Sample	R_q (nm)	R_a (nm)
HAp	19.87	15.45
3CuHAp	18.79	14.78

For the HAp coatings, the value obtained for the roughness average (R_a) parameter was 15.45 nm. Meanwhile for the 3CuHAp, the roughness average (R_a) parameter was 14.78 nm. The root mean square (RMS) roughness (R_q) values were 19.87 nm for HAp and 18.79 nm for 3CuHAp.

The values obtained for the R_a and R_q parameters (from AFM and SEM images) indicate that the studied samples exhibit a low roughness. Moreover, in the case of the 3CuHAp sample, a slight decrease in the roughness parameters could be noticed, a fact that could be attributed to the presence of copper ions in the HAp structure. Furthermore, according to the study reported by Osman et al. [34], a surface with a lower roughness could promote superior biological properties.

To characterize the surface of the HAp and 3CuHAp coatings, X-ray photoelectron spectroscopy was used. Figure 7 presents the XPS survey spectra of the HAp ($x_{Cu} = 0$) coatings. The qualitative analysis revealed the presence of key constituents of hydroxyapatite (Figure 7a), including calcium (Ca), phosphorus (P) and oxygen (O). The presence of copper (Cu) was observed in the general spectrum of 3CuHAp (Figure 7b). The results are in agreement with previous studies [35]. These results align with those achieved from the energy-dispersive X-ray spectroscopy (EDS) analysis, attesting to the presence of copper in the examined samples.

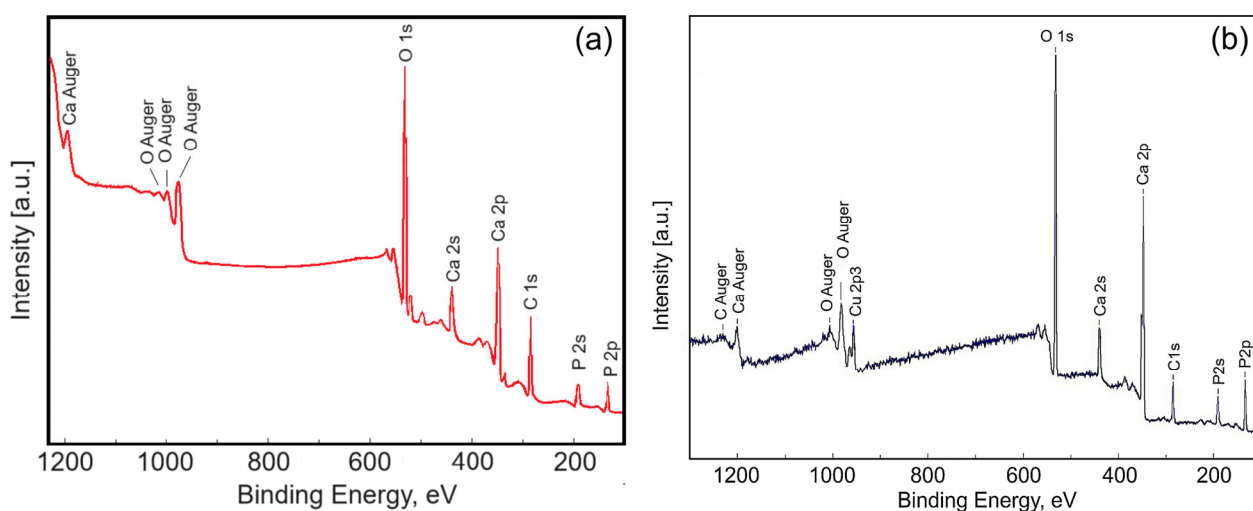


Figure 7. XPS survey scan of the HAp (a) and 3CuHAp (b) coatings obtained by the vacuum deposition process.

High-energy resolution analysis of the individual peaks was performed. Thus, the high-resolution spectra of HAp for carbon, oxygen, calcium and phosphorus are presented in Figure 8. The measured binding energy (EB) scale was referenced to a C 1s at the EB value of 284.8 eV [36]. Figure 8 reveals the high-resolution C 1s spectra for the pure HAp ($x_{Cu} = 0$) coatings. As can be seen, we have only one component that was highlighted at 284.8 eV. This peak is associated with residual or accidental carbon. Serra et al. [37] associated the 284.8 eV peak with C–C and C–H bonds. The high-resolution XPS spectrum of O 1s for the HAp coatings shows one peak located at 531.4 eV (Figure 8b). The peak at

531.4 eV is associated with the hydroxyl groups resulting from the chemisorption of water or oxygen. The results are in line with previous studies by Moulder et al. [38]. The Ca 2p high-resolution spectrum of the HAp coatings exhibited a well-resolved doublet with two components assigned to Ca 2p_{3/2} and Ca 2p_{1/2} (Figure 8c). The peak located at about 347.2 eV shows that the calcium atoms are bound to a phosphate group (PO_4^{3-}). Following the processing of the deconvolution data, the P 2p photoelectron line consists of one single peak at a binding energy of 133.1 eV. In accordance with past XPS studies [39], the binding energy of the photoelectron peaks for Ca and P is characteristic of their full oxidation states (Ca^{2+} and P^{5+}) for hydroxyapatite.

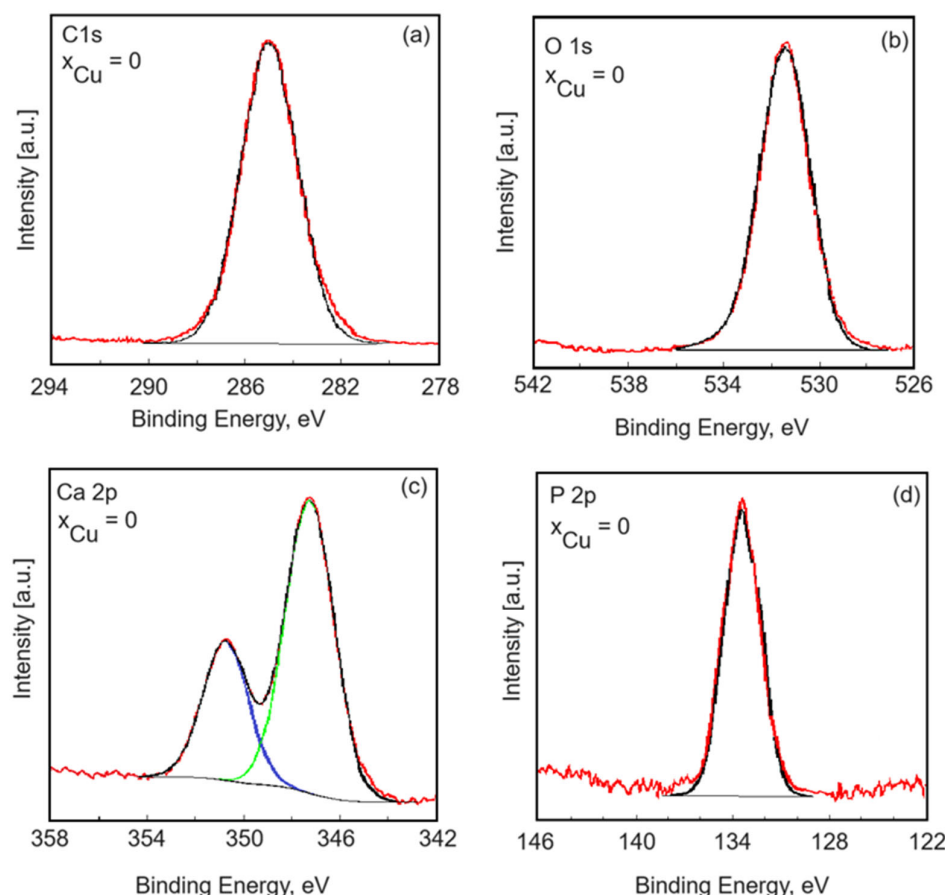


Figure 8. High-resolution XPS spectra of C1s (a), O 1s (b), Ca 2p (c) and P 2p (d) of the HAp coatings obtained by the vacuum deposition process.

The high-resolution spectra of the 3CuHAp sample are presented in Figure 9. The high-resolution XPS spectrum of C 1s of the 3CuHAp sample shows three peaks identified at binding energies of 284.8, 286.4 and 289.2 eV. The peak at 284.8 eV is attributed to C–C and C–H single bonds [40,41]. The peaks at 286.4 eV and 289.2 eV are assigned to C–O–C bonds and O–C=O bonds [40,41]. The high-resolution XPS spectrum of O 1s for the 3CuHAp thin film shows three peaks located at 530.9 eV, 532.3 eV and 533.9 eV (Figure 9b). The peak observed at 530.9 eV is attributed to HAp (the lattice oxygen of the P O species). The peak identified at 532.3 eV is associated with oxygen adsorbed on the HAp surface [42,43]. The peak located at the binding energy of 533.9 eV could be due to possible traces of water. The high-resolution spectrum for calcium (Figure 9c) shows two peaks, Ca 2p_{3/2} and Ca 2p_{1/2}, which are identified at 347.24 eV and 350.79 eV, being associated with the tetravalent state (Ca^{2+}), in agreement with previous studies [42]. The high-resolution spectrum of P2p for the 3CuHAp thin film is presented in Figure 9d. The P 2p_{3/2} and P 2p_{1/2} peaks were located at 133.20 eV and 134.19 eV, respectively. The given information states that

the ratio of the areas is 2:1, and the separation occurs at an energy of 0.9 eV. The bond-binding energy is specific to PO_4 in hydroxyapatite. In Figure 9e, the high-resolution XPS spectra of copper (Cu) reveal three distinct maxima resulting from deconvolution. These peaks occur at specific binding energies of 936.16 eV, 941.79 eV and 945.05 eV. The peak identified at 936.16 eV corresponds to the $\text{Cu}2p_{3/2}$ state. The peaks noticed at 941.79 eV and 945.05 eV are shake-up peaks, suggesting the presence of Cu^{2+} species [44–46]. The peaks associated with Cu^{1+} [47] and CuO at binding energies of 952.3 eV and 933.3 eV [48] were not identified.

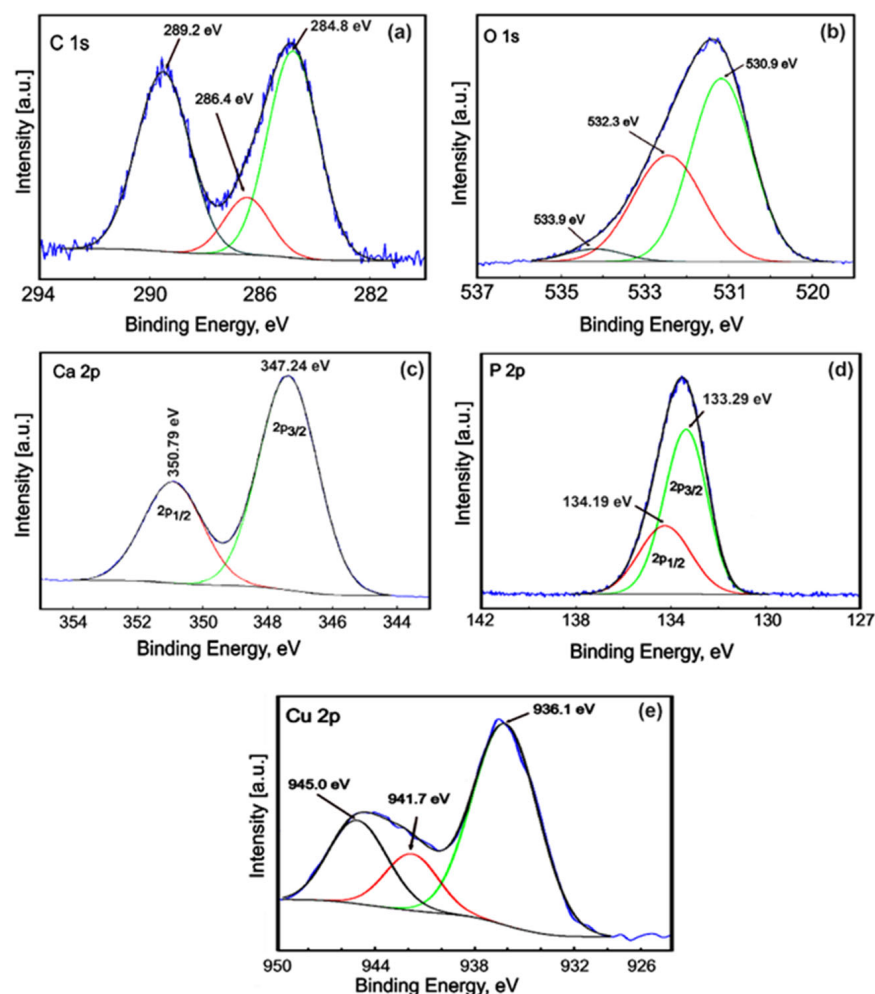


Figure 9. High-resolution XPS spectra of C1s (a), O 1s (b), Ca 2p (c), P 2p (d) and Cu 2p (e) of the 3CuHAp coatings obtained by the vacuum deposition process.

Figure 10 presents the absorption FTIR spectra obtained for the HAp and 3CuHAp coatings. The FTIR spectra of the HAp coatings reveal the presence of the main characteristic vibrational bands of the phosphate and hydroxyl groups from the hydroxyapatite structure. Due to the similarity, in the following, only the maxima noticed in the FTIR spectra of 3CuHAp will be discussed.

The FTIR spectra are dominated by two intense vibrational bands that are centered at $\sim 563\text{ cm}^{-1}$ (ν_4) and $\sim 1030\text{ cm}^{-1}$ (ν_3) and are characteristics of phosphate groups from HAp. Other vibrational bands that are attributed to phosphate groups' vibrations are observed at $\sim 460\text{ cm}^{-1}$ (ν_2), $\sim 605\text{ cm}^{-1}$ (ν_4), $\sim 962\text{ cm}^{-1}$ (ν_1) and $\sim 1096\text{ cm}^{-1}$ (ν_3) [16,27,49–55]. The maxima observed at $\sim 962\text{ cm}^{-1}$ (ν_1) clearly indicate the presence of HAp in the 3CuHAp coatings [16,27,49–55]. On the other hand, the vibration peak specific to OH^- groups from HAp appears at $\sim 631\text{ cm}^{-1}$. Furthermore, in the FTIR spectra obtained for the undoped HAp coatings presented in Figure 10, the presence of maxima could be observed that are

associated with the same vibrational groups as the one observed for the 3CuHAp coatings. Also, the doping of HAp with copper led to a decrease in the FTIR maxima, together with a slight displacement of their position. No other significant vibrational bands are noticed in the FTIR spectra, a fact that indicates the coatings' purity. Therefore, the FTIR results are in concordance with the XRD results.

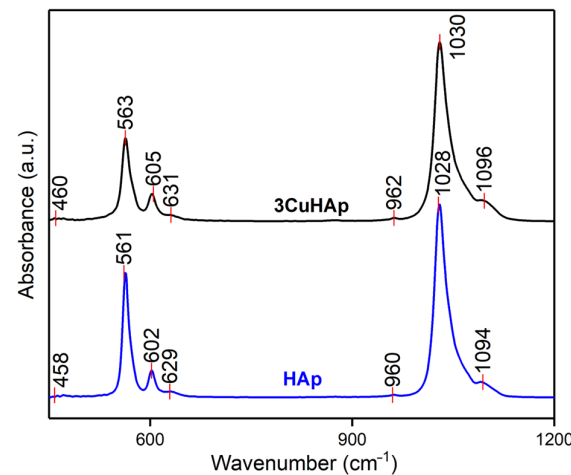


Figure 10. The FTIR spectra of the HAp and 3CuHAp coatings.

To acquire detailed information about the vibrational bands present in the HAp and 3CuHAp samples, we conducted an FTIR second-derivative analysis. The obtained second-derivative spectra (Figure 11), which pertain to the spectral regions characteristic of the ν_4 , ν_3 , ν_2 , and ν_1 phosphate group vibrations, are illustrated in Figure 11. The ν_1 vibration band of the phosphate group could be observed at around 962 cm^{-1} in the second-derivative spectra [16,27,49–55]. Another vibrational band observed in the Figure 11 belongs to the ν_4 (observed at around 563 cm^{-1} , 574 cm^{-1} , 587 cm^{-1} and 605 cm^{-1}) and ν_3 (noticed at about 1030 cm^{-1} , 1041 cm^{-1} , 1059 cm^{-1} and 1096 cm^{-1}) vibrations of the phosphate group [16,27,49–55]. Furthermore, the presence of the vibrational peak associated with the vibration of the hydroxyl group (librational mode) could be noticed in the spectra. Also, the band specific to the ν_2 vibration could be observed in the spectra at around 460 cm^{-1} [16,27,49–55]. Table 3 summarizes the position of the vibrational bands observed in the second-derivative spectra obtained for the HAp and 3CuHAp coatings that are similar to the one observed in the FTIR spectra.

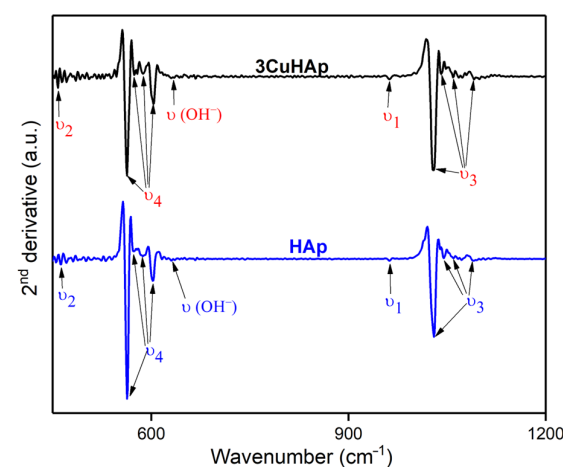


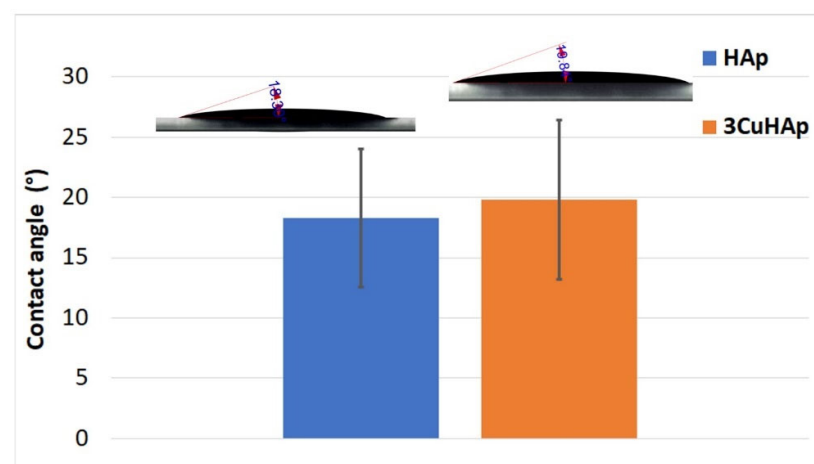
Figure 11. FTIR second-derivative spectra of the HAp and 3CuHAp coatings.

Table 3. IR wavenumber positions (cm^{-1}) specific to the ν_1 , ν_2 , ν_3 , and ν_4 phosphate bands, as identified in the FTIR second-derivative spectra of the HAp and 3CuHAp coatings.

Assignments	Position (cm^{-1})	
	HAp	3CuHAp
Hydroxyl group	629	631
(ν_2) phosphate groups	458	460
(ν_4) phosphate groups	561, 573, 586, 602	563, 574, 587, 605;
(ν_1) phosphate groups	960	962
(ν_3) phosphate groups	1028, 1039, 1057, 1094	1030, 1041, 1059, 1096;

As can be seen in both second-derivative spectra, no intense vibrational bands were observed that could be associated with the presence of a supplementary phase or impurities. These results are consistent with those obtained by the XRD studies.

Wettability is a key property of implant surfaces that affects the cell–material interactions. Research has shown that hydrophilic surfaces promote enhanced mineral deposition and osteoblast cell growth in comparison to hydrophobic surfaces [52,56]. Therefore, in order to obtain valuable information about the wettability properties of the HAp and 3CuHAp coatings, water contact angle studies were performed (Figure 12). The mean value of the contact angle obtained for HAp was equal to $18.30 \pm 5.7^\circ$. Meanwhile, the mean value obtained for the contact angle of the 3CuHAp coatings was $19.84 \pm 6.6^\circ$. These values indicate the presence of a surface with a hydrophilic nature. As can be seen in Figure 12, by doping the hydroxyapatite with copper, a slight increase in the contact angle occurs. This behavior is consistent with the Wenzel's relation for hydrophilic surfaces, which states that increasing the surface roughness will decrease the water contact angle value [57,58]. Such hydrophilic surfaces are known to enhance the biological properties of the materials, including the bioactivity and bone-bonding behavior [52,56]. Moreover, these results suggest that copper-doped hydroxyapatite coatings, when deposited through the vacuum deposition method, hold significant potential for improving the performance and safety of biomedical implants.

**Figure 12.** Water contact angle of the HAp and 3CuHAp coatings.

The cytotoxicity of the HAp and 3CuHAp coatings was assessed using both the HeLa and MG63 cell lines by determining the cell viability with the aid of an MTT assay after 24, 48, and 72 h of incubation with the 3CuHAp coatings. The results of the MTT assays, as illustrated in Figure 13, are presented as the mean \pm standard deviation (SD) from three experiments, with the cell viability expressed as a percentage of the control. The control was considered 100%. Statistical significance was determined using the ANOVA single-factor test, with $p \leq 0.05$ considered to be significant. The data indicated that the viability of the

HeLa and MG63 cells was not significantly different from the control after 24, 48, and 72 h of incubation with the HAp and 3CuHAp coatings, demonstrating good biocompatibility.

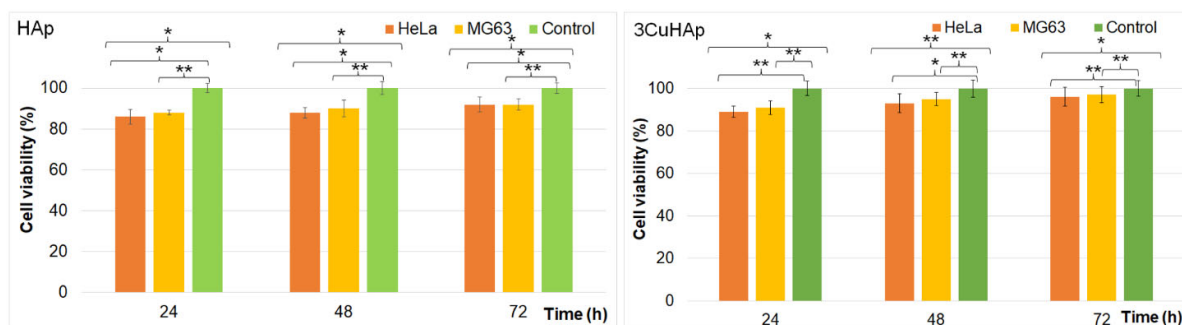


Figure 13. Graphical representation of the cell viability of HeLa and MG63 cells exposed to the HAp and 3CuHAp coatings for 24, 48 and 72 h. The results are depicted as the mean \pm standard deviation (SD) and quantified as percentages of the control (100% viability). The ANOVA single-factor test was used for the statistical analysis and $p \leq 0.05$ was accepted as statistically significant (* $p < 0.03$, ** $p < 0.001$).

The viability of the HeLa and MG63 cells incubated with the HAp coatings was above 86% in the first 24 h and increased with the exposure time, reaching 92% after 72 h of exposure.

In the case of the 3CuHAp coatings, the cell viability remained above 88% after the initial 24 h and increased to 93% after 48 h and 95% after 72 h in the case of the HeLa cells. The result regarding the cell viability obtained for the MG63 cells was above 90% in the first 24 h and increased to 94% after 48 h and 96% after 72 h. These results are consistent with other reported studies regarding the biocompatibility of hydroxyapatite and hydroxyapatite composite coatings [16,18,59–65]. Furthermore, the cell viability of the HeLa and MG63 cells after exposure to the 3CuHAp coatings was consistently above 88%, exceeding the 70% cytotoxicity threshold set by ISO standard 10993-5 [59]. These findings suggest that the 3CuHAp coatings do not present a cytotoxic effect against HeLa and MG63 cells and could be promising candidates for the development of advanced implant materials with good biocompatibility.

Additional information regarding the biocompatibility of the HAp and 3CuHAp was achieved by visual observation of the morphology of the cells exposed to the HAp and 3CuHAp coatings for 72 h. The results revealed that the morphology of the HeLa and MG63 cells remained unchanged when cultured in the presence of both the HAp and 3CuHAp coatings (Figure 14). Moreover, the results also emphasized that the HeLa and MG63 cells seeded on the HAp and 3CuHAp coatings were allowed to proliferate for 72 h without altering their morphology. This observation supports the notion that the HAp and 3CuHAp coatings are biocompatible and could facilitate cell proliferation and tissue regeneration. Moreover, the results revealed that the integration of the implant into the surrounding tissue is possible. These biocompatible properties are attributed to both HAp, which is renowned for its osteoconductive nature and ability to mimic the mineral properties of bones, as well as the presence of the copper ions that form the HAp matrix, which plays an important role in bone growth [1,10,16,18,60–67].

Additional information regarding the adhesion and proliferation of the HeLa and MG63 cells on the surface of the HAp and 3CuHAp coatings was obtained by fluorescence microscopy evaluation. For this purpose, the cells were allowed to grow on the surface of the HAp and 3CuHAp coatings and stained before observation. The images from the fluorescence microscopy studies are shown in Figure 15a–d. Furthermore, metallographic microscopy was used to assess the adherence and proliferation of the cells on the HAp and 3CuHAp coatings. The results of the metallographic microscopy are presented in Figure 15e–h.

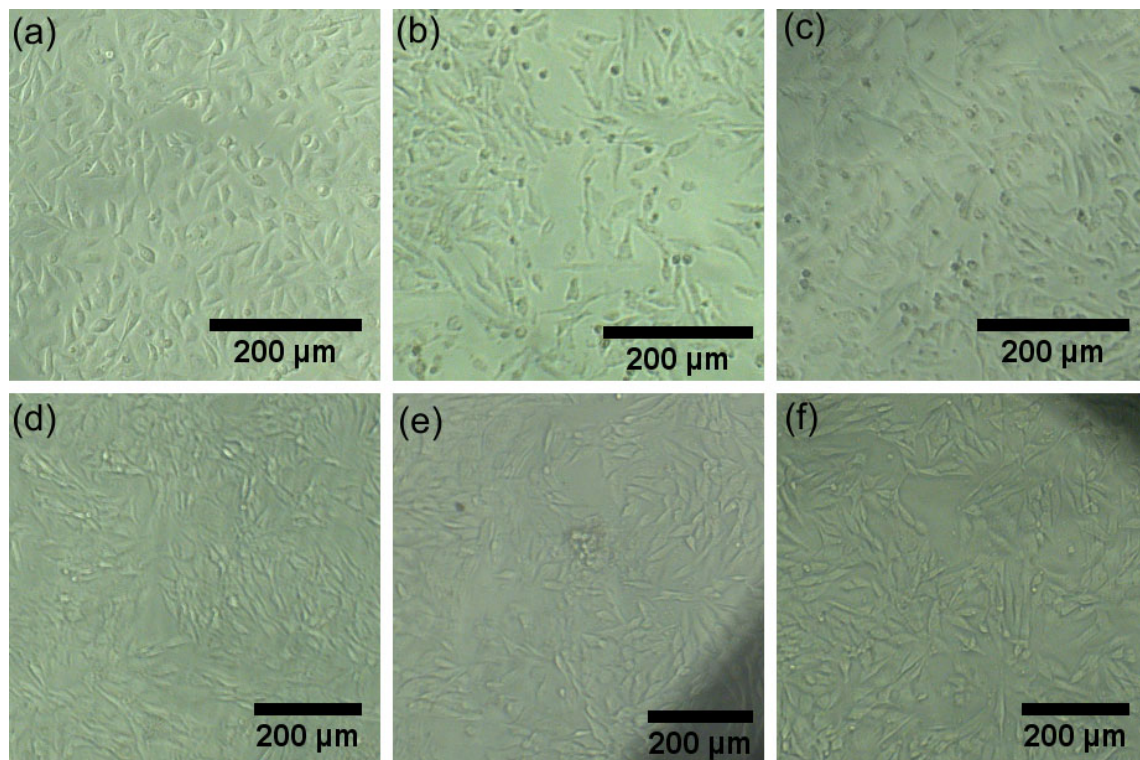


Figure 14. The morphology of HeLa and MG63 cells exposed to the HAp (b,e) and 3CuHAp (c,f) coatings for 72 h. HeLa control cells (a) and MG63 control cells (d).

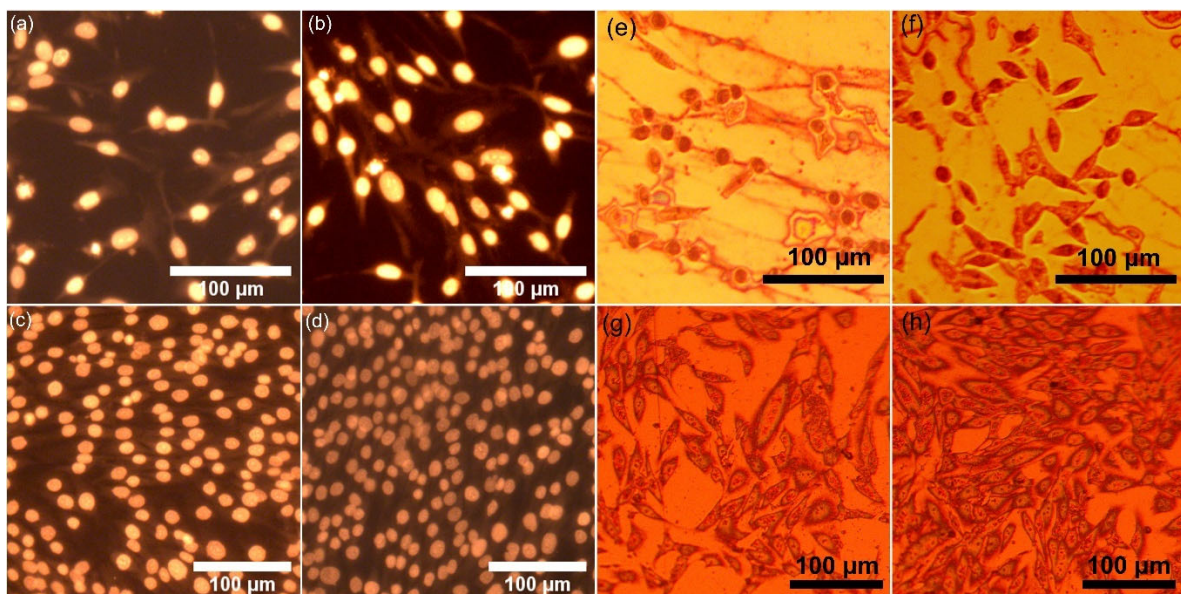


Figure 15. The morphology of HeLa and MG63 cells grown on the HAp coatings (a,c) and 3CuHAp coatings (b,d) visualized by fluorescence microscopy evaluation and the morphology of HeLa and MG63 cells grown on the HAp coatings (e,g) and 3CuHAp coatings (f,h) visualized by metallographic microscopy.

The results of the visual observation revealed that the surfaces of both the HAp and 3CuHAp coatings allowed the studied cells to adhere and to develop. Furthermore, no morphological abnormalities were detected in the HeLa and MG63 cells that adhered to the surface of the coatings. Our studies reveal that the HeLa and MG63 cell viability increases

with the time of exposure (from 24 h to 72 h) to the HAp and 3CuHAp coatings. The cell viability increases over time in the presence of the HAp and 3CuHAp coatings due to their biocompatibility, bioactivity, and ability to support cell adhesion, proliferation, and differentiation. Even though there are several specific mechanisms that are involved in cell adhesion and proliferation, depending on the cell type and the conditions of the experiment, the overall positive interaction between the cells and the HAp and 3CuHAp coatings is a consistent theme. Hydroxyapatite closely resembles the mineral component of bone, making HAp coatings well tolerated by various cells and tissues. They are bioactive, promoting cell adhesion, proliferation, and differentiation, and serve as a source of essential calcium and phosphate ions, enhancing cellular processes. The surface properties of HAp also support cell adhesion and protein adsorption, further enhancing the cell viability. HAp is also known to promote osteogenic differentiation in certain cell types, leading to increased cell function. Additionally, the low toxicity and ability to stabilize cell membranes reduces cell death and improves overall cell health. On the other hand, copper ions could increase the cellular viability by acting as essential cofactors for enzymes involved in various essential biological processes, such as cellular respiration, antioxidant defense, and collagen synthesis. Copper ions have the ability to protect cells from oxidative stress, support ATP production via the mitochondrial electron transport chain, and facilitate collagen and elastin cross-linking, which is crucial for tissue integrity. Furthermore, copper is also reported to be responsible for promoting angiogenesis, enhancing nutrient and oxygen supply. More than that, copper ions support immune function and regulate both the gene expression and signal transduction pathways, all of which collectively enhances cell growth, differentiation, and survival [10–13,68]. In this context, the increase in the HeLa and MG63 cell viability with the incubation time in the presence of the HAp and 3CuHAp coatings could be attributed to several factors: enhanced cell adhesion, improved nutrient exchange, and increased bioactivity, protection against cytotoxic agents, gradual ion release, and reduced oxidative stress. Together, these factors help to create a supportive environment for cells' growth and survival.

Furthermore, to obtain a more comprehensive image of the biological properties of the 3CuHAp coatings, their antibacterial activity was also assessed against *Pseudomonas aeruginosa*, a common Gram-negative bacterial strain that is responsible for infections that are tough to treat in the blood, lungs, or other parts of the body.

The ability of *Pseudomonas aeruginosa* cells to adhere to and develop on the surface of 3CuHAp coatings was investigated with the aid of AFM studies, with the aim of emphasizing the role of copper ions in combating bacterial growth. For this purpose, the AFM topographies of the 3CuHAp coatings were recorded after incubation with a *P. aeruginosa* bacterial suspension at various time intervals (24, 48, and 72 h), under ambient conditions and at room temperature. The 2D surface topographies of the 3CuHAp coatings exposed to the *P. aeruginosa* bacterial suspensions were captured in non-contact mode over an area of $10 \times 10 \mu\text{m}^2$. The 2D AFM images of the 3CuHAp coatings, incubated with *P. aeruginosa* bacterial suspensions for 24, 48, and 72 h, along with their 3D representations, are displayed in Figure 16a–f.

The AFM recordings of the 2D surface topography of the 3CuHAp coatings demonstrated that these coatings effectively inhibited *P. aeruginosa* bacterial cell adherence and growth, even in the early stages of development. The AFM studies further highlighted the coatings' ability to prevent *P. aeruginosa* biofilm formation on their surfaces. The adhered bacterial cells exhibited the characteristic rod-shaped morphology of *P. aeruginosa*, with lengths ranging from 1.03 to 2.57 μm and widths from 0.54 to 0.75 μm . The AFM data indicated that *P. aeruginosa* attachment and development on the 3CuHAp coating surfaces were significantly inhibited even within the first 24 h of incubation. Additionally, both the 2D topography and 3D representations suggested that the antibacterial activity of the coatings is correlated with the incubation time, showing a rapid decrease in the number of attached bacterial cells over time. After 72 h of exposure to the bacterial suspensions, the number of attached bacterial cells decreased significantly. The cell count performed on

the AFM 2D images revealed that after 24 h of exposure, only 16 bacterial cells remained attached to the 3CuHAp surface, while after 48 h, only 9 bacterial cells were still adhered on the surface. After 72 h of incubation, both the 2D AFM topography as well as the 3D representation emphasized the presence of only a few isolated *P. aeruginosa* bacterial cells on the 3CuHAp coatings' surface (the cell count revealed the presence of approximately three isolated bacterial cells). In addition, the AFM studies revealed that the 3CuHAp coatings inhibited *P. aeruginosa* biofilm formation.

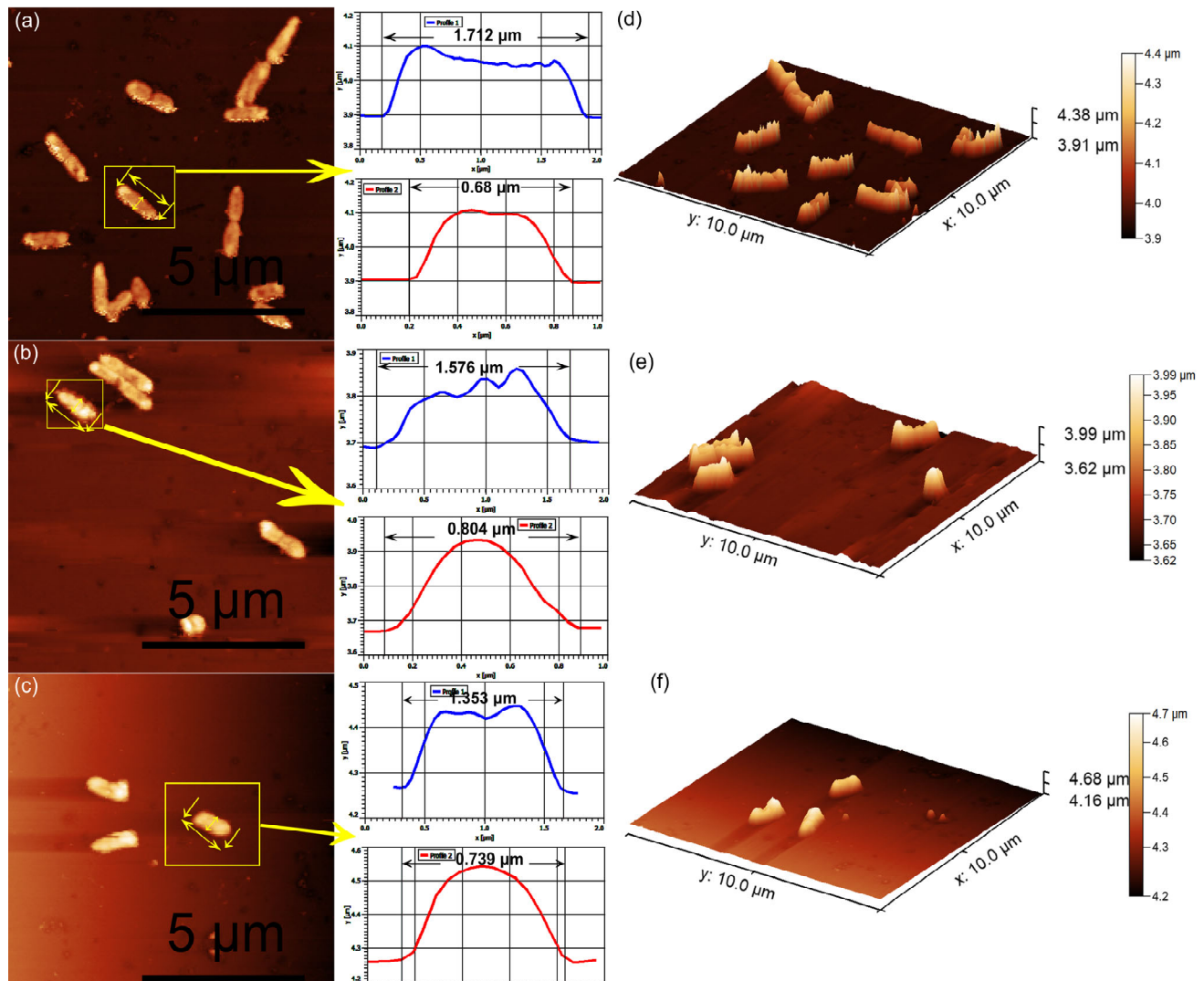


Figure 16. Two-dimensional AFM topography of *Pseudomonas aeruginosa* 27853 ATCC cells attached to the surface of the 3CuHAp coatings after a 24 (a), 48 (b) and 72 h (c) incubation period and their 3D representation (d–f). Individual bacterial cells chosen and their measured profile in width and in length, where the measurement is pointed out by the yellow arrow.

The antibacterial activity of the HAp coatings against *P. aeruginosa* was also evaluated. The results of the AFM topography recorded on the surface of the HAp coatings demonstrated that these coatings promoted the adhesion and development of *P. aeruginosa* on their surface, even from the early stage of the cell's development. Furthermore, the data also showed that the HAp coatings provided the *P. aeruginosa* bacterial cells with an adhesive surface and allowed the development of bacterial biofilm. Also, the data suggested that the development of the bacterial cells on the surface of the HAp coatings increased with the incubation time. The data depicting the 2D topographies as well as the 3D representations of the HAp coatings' surfaces after incubation with *P. aeruginosa* bacterial suspensions for

24, 48 and 72 are presented in Figure 17a–f. The results emphasized that since the HAp coatings did not exhibit any inhibitory activity against the *P. aeruginosa* bacterial cells, the antibacterial activity of the 3CuHAp could be attributed to the copper ions present from the HAp lattice. Furthermore, the data emphasized that the cells adhered to the entire HAp coating's surface.

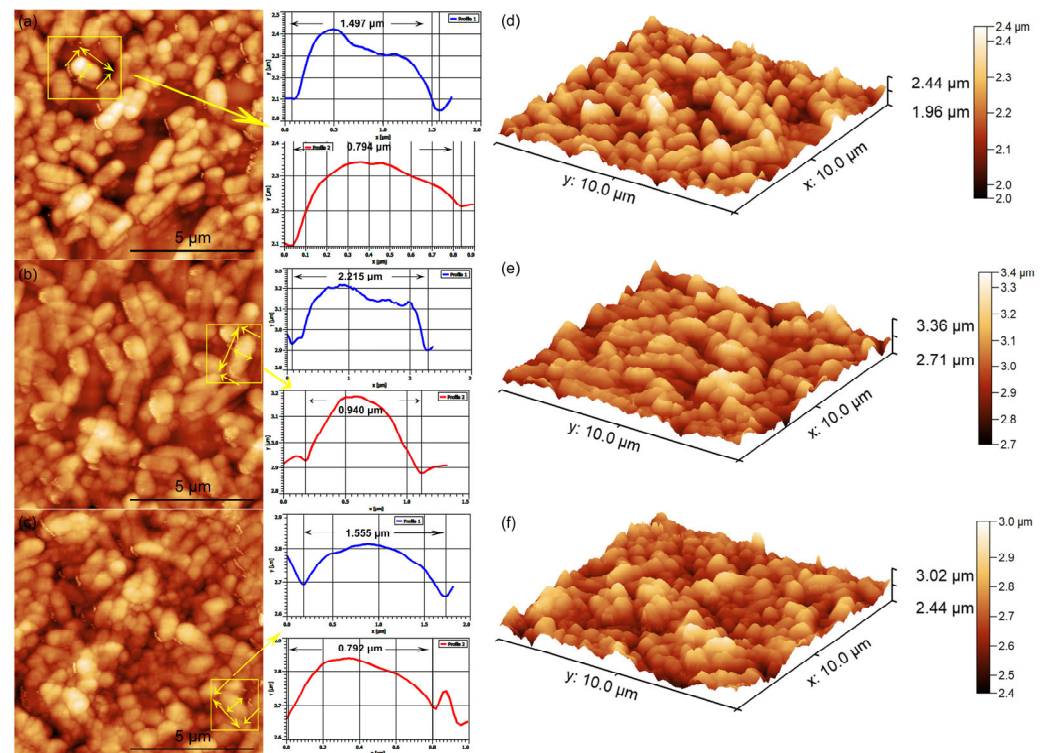


Figure 17. Two-dimensional AFM topography of *Pseudomonas aeruginosa* 27853 ATCC cells attached to the surface of the HAp coatings after a 24 (a), 48 (b) and 72 h (c) incubation period and their 3D representation (d–f). Individual bacterial cells chosen and their measured profile in width and in length, where the measurement is pointed out by the yellow arrow.

An individual analysis was also performed from the AFM data, which provided important quantitative measurements regarding the attached bacterial cell dimensions and surface roughness. The cross-section measurements along the lines depicted in Figures 16 and 17, indicated by the yellow arrows, show information about the individual bacterial cell sizes. The results indicated that the adhered cells were well structured and integrated on the surface of the HAp coatings, and also that they were able to colonize the entire surface of the coatings. On the other hand, the results also emphasized that the bacterial cells were reduced in numbers and that the formation of biofilm was inhibited by the 3CuHAp coatings. From the profile images, the bacterial cells were observed to present the distinctive morphological features of *P. aeruginosa* bacterial cells, being relatively smooth and having lengths between 1.35 μm and 2.25 μm and diameters between 0.68 μm to 0.94 μm.

Additional information regarding the antibacterial activity of the HAp and 3CuHAp coatings was obtained by employing a quantitative in vitro antibacterial assay. The results of the quantitative studies are graphically represented in Figure 18. The quantitative assays depicted in Figure 18 highlighted the antibacterial activity of the 3CuHAp coatings on the adherence to and development of *P. aeruginosa* colony-forming units (CFUs) after exposure periods of 24, 48, and 72 h.

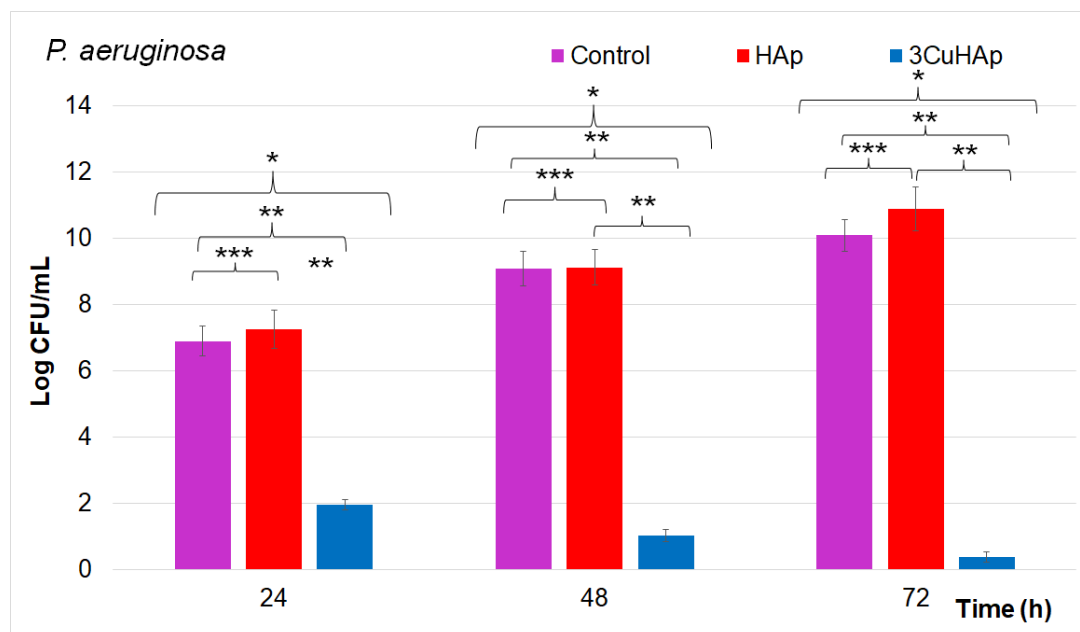


Figure 18. Graphical representation of the log colony forming units (CFUs)/mL of the HAp and 3CuHAp coatings incubated with *Pseudomonas aeruginosa* cells for 24, 48 and 72 h. The ANOVA single-factor test was used for the statistical analysis and $p \leq 0.05$ was accepted as statistically significant (* $p < 0.001$, ** $p < 0.002$, and *** $p < 0.007$).

The antibacterial properties of the HAp and 3CuHAp coatings were examined, using a free *P. aeruginosa* culture as the positive control (C+). The results showed that the HAp coatings promoted the *P. aeruginosa* bacterial cell proliferation and positively influenced their development and adherence across all the tested time intervals. These findings are in good agreement with previous studies emphasizing that hydroxyapatite did not exhibit antibacterial activity [24]. The results of the quantitative antibacterial assays depicted in Figure 18 demonstrated that the development of *P. aeruginosa* CFUs was inhibited early within the first 24 h of exposure to the 3CuHAp coatings compared to the control. The in vitro antibacterial studies indicated a significant reduction in the *P. aeruginosa* colonies within the first 24 h compared to the positive control culture (C+) [69].

The results highlighted the crucial role of copper ions in the antibacterial properties of the 3CuHAp coatings, which were enhanced over time. The data indicated that the 3CuHAp coatings exhibited the strongest antibacterial effect after 72 h of incubation. Over this 72 h exposure period, the coatings, leveraging the antibacterial efficacy of copper ions, effectively inhibited the development of *P. aeruginosa* bacterial cells, significantly reducing the number of bacterial colonies. Even though the exact mechanisms responsible for the antibacterial behavior of the material are still unelucidated, there are several hypotheses. In this case, the most reported mechanism states that the exposure of bacteria to copper ions can interfere and modify the permeability of the cell membrane, leading to the leakage of cellular contents, and eventually, to cell lysis [70].

Another proposed mechanism affirms that copper ions could interfere with protein synthesis and with the DNA replication processes. The antimicrobial activity of copper ions has been attributed to their ability to generate reactive oxygen species (ROS) to inflict damage on bacteria [66]. Gram-negative bacteria have a negatively charged outer layer (lipopolysaccharides), which attracts cations and causes membrane damage. According to various studies [71–74], the anionic surface cell membrane promotes the binding of high concentrations of metal ions, enhancing toxicity. Copper ions can also interact with DNA by interfering with nucleic acid strands and disturb biochemical processes [75]. Copper ions can also generate intracellular hydroxyl radicals, which harm essential proteins [76].

The main mechanism of antimicrobial activity for metal ions is the generation of ROS, whether dependent or independent of Fenton reactions, and mainly leads to damage to cell membranes. Metals such as copper act as catalysts in Fenton-like reactions to generate ROS such as $O_2\bullet$, $OH\bullet$, etc. [77], effects observed in the *E. coli* cell model [78]. Also, the free radicals created can cause damage to the mitochondrial membrane, resulting in cell degradation and ultimately cell death [71]. In addition, copper ions have been found to cause multiple toxic effects; in addition to generating reactive oxygen species, they can also lead to lipid peroxidation and protein oxidation [71], which ultimately lead to the stopping of cell division [79].

Even though the exact mechanisms responsible for the antimicrobial activity are still uncertain, it was hypothesized that the principal and most important of copper's antibacterial mechanisms is attributed to the generation of reactive oxygen species (ROS), which induce oxidative stress that could damage bacterial cells. ROS damage various cellular components, including lipids, proteins, and DNA, leading to bacterial cell dysfunction and eventually death. Furthermore, copper ions have the ability to disrupt the bacterial cell membrane by binding and destabilizing their lipid bilayers, thus increasing the membrane permeability and causing leakage of its cellular contents. It was also reported that copper could interfere with the essential enzyme functions by binding to their active sites, further inhibiting bacterial growth and survival. This multifaceted strategy renders copper highly effective in preventing bacterial attachment, inhibiting biofilm formation, and ultimately, eliminating bacterial infections.

The data from the antibacterial assays are in good agreement with the present data from existing studies [66,67,80]. Furthermore, the results of the biological studies conducted emphasized that 3CuHAp possesses good biocompatibility and also exhibits strong antibacterial activity, making the coating potential candidates for future development in biomedical applications (coatings for various types of implants used in orthopedy and stomatology, medical devices, etc.).

The biocompatibility of the 3CuHAp coatings was thoroughly assessed using the HeLa and MG63 cell lines. The viability of the HeLa and MG63 cells following exposure to the 3CuHAp coatings was consistently above 88%, surpassing the 70% cytotoxicity threshold specified by ISO standard 10993-5. These results indicate that the 3CuHAp coatings exhibit no cytotoxic effects on HeLa and MG63 cells, thereby indicating their potential as promising candidates for the development of advanced implant materials with favorable biocompatibility. Furthermore, the microscopic observation showed that the morphology of the HeLa and MG63 cells remained unchanged when cultured in the presence of the HAp and 3CuHAp coatings. The antibacterial assays against *P. aeruginosa* also emphasized that the 3CuHAp exhibited significant antibacterial activity, even from the first 24 h of incubation. The findings of the AFM studies revealed that the 3CuHAp coatings effectively inhibited the formation of *P. aeruginosa* biofilms. Analysis of the AFM data highlighted a significant inhibition of *P. aeruginosa* attachment and development on the coating's surface within the initial 24 h. Furthermore, both the 2D AFM topography and its 3D representation demonstrated the rapid decline of the attached bacterial cells over time, with a notable reduction observed after 72 h of exposure. The development of the 3CuHAp coatings represents a notable advancement in biomedical applications. The evident suppression of *Pseudomonas aeruginosa* biofilm formation and the notable decrease in bacterial cell attachment demonstrate the potential of these coatings to address infections linked with implantable medical devices.

In summary, our results suggest that the coatings based on HAp and 3CuHAp ($Ca_{10-x}Cu_x(PO_4)_6(OH)_2$; $x_{Cu} = 0, 0.03$), as obtained by the vacuum deposition technique, exhibit structural, chemical, and morphological features that enhance their biological activity. The presence of copper induces good antibacterial activity to HAp. The coatings' surface topography promotes enhanced in vitro biocompatibility. These findings underline that these types of coatings could represent promising candidates for uses in the biomedical field.

On the other hand, this study on copper-doped hydroxyapatite has some limitations, including a narrow range of doping concentrations, use of a single deposition technique and controlled laboratory conditions. Further research is needed and should explore a broader range of copper-doping levels, investigate alternative deposition methods, test long-term stability and analyze the mechanical properties, including in vitro and in vivo behaviors. These improvements will enhance the understanding and practical use of biomaterials based on copper-doped hydroxyapatite.

4. Conclusions

This study reported for the first time the development of copper-doped hydroxyapatite coatings by the vacuum deposition technique. Various techniques were used for the coatings' complex characterization. In summary, the XRD studies confirmed the successful deposition of the HAp and 3CuHAp coatings, both containing pure hexagonal hydroxyapatite without impurities. The results of the AFM and SEM studies confirmed the continuous and homogeneous surface morphology of the coatings. Furthermore, the presence of hydroxyapatite in the studied coatings was proved by the FTIR results. The chemical composition of the HAp and 3CuHAp coatings was analyzed by XPS and EDS measurements. The results highlighted that the 3CuHAp coatings are highly biocompatible with the HeLa and MG63 cell lines, showing over 88% cell viability and no cytotoxic effects, making them suitable for advanced implant materials. Additionally, the in vitro antibacterial assays emphasized that the 3CuHAp coatings exhibit significant antibacterial activity against *Pseudomonas aeruginosa*, effectively inhibiting biofilm formation and bacterial attachment, highlighting their potential to prevent infections in implantable medical devices. Moreover, their proven compatibility with human cells indicates their potential integration into biomedical devices, thereby creating opportunities for the development of safer and more effective medical implants. In conclusion, copper-doped hydroxyapatite represents a promising candidate as a covering biomaterial for implants due to the superior biocompatibility and improved antimicrobial activity.

Author Contributions: Conceptualization, K.R. and D.P.; methodology, K.R., D.P. and S.R.; software, K.R., D.P. and S.R.; validation, Y.B., D.P., K.R., C.S.C., S.L.I., S.R., R.T., L.G., C.B. and K.B.; formal analysis, Y.B., D.P., K.R., C.S.C., S.L.I., S.R., R.T., C.C., I.C.M., M.S., C.C.N., L.G., C.B. and K.B.; investigation, Y.B., D.P., K.R., C.S.C., S.L.I., S.R., R.T., C.C., I.C.M., M.S., C.C.N., L.G., C.B. and K.B.; resources, Y.B., D.P., K.R., C.S.C., S.L.I., S.R., R.T., L.G., C.B. and K.B.; data curation, K.R. and D.P.; writing—original draft preparation, K.R., D.P., S.R., S.L.I., C.S.C. and Y.B.; writing—review and editing, Y.B., D.P., K.R., C.S.C., S.L.I., S.R., R.T., C.C., I.C.M., M.S., C.C.N., L.G., C.B. and K.B.; visualization, Y.B., D.P., K.R., C.S.C., S.L.I., S.R., R.T., C.C., I.C.M., M.S., C.C.N., L.G., C.B. and K.B.; supervision, K.R., D.P. and S.R.; project administration, K.R.; funding acquisition, K.R. and D.P. All authors have read and agreed to the published version of the manuscript.

Funding: This research was funded by the Core Program of the National Institute of Materials Physics, granted by the Romanian Ministry of Research, Innovation and Digitalization through the Project PC1-PN23080101.

Institutional Review Board Statement: Not applicable.

Informed Consent Statement: Not applicable.

Data Availability Statement: The original contributions presented in the study are included in the article, further inquiries can be directed to the corresponding authors.

Conflicts of Interest: The authors declare no conflicts of interest. The funders had no role in the design of the study; in the collection, analyses, or interpretation of data; in the writing of the manuscript; or in the decision to publish the results.

References

1. Furko, M.; Havasi, V.; Kónya, Z.; Grünwald, A.; Detsch, R.; Boccaccini, A.R.; Balázs, C. Development and characterization of multi-element doped hydroxyapatite bioceramic coatings on metallic implants for orthopedic applications. *Bol. Soc. Esp. Ceram. Vidr.* **2018**, *57*, 55–65. [[CrossRef](#)]

2. Huang, Y.; Zhang, X.; Zhao, R.; Mao, H.; Yan, Y.; Pang, X. Antibacterial efficacy, corrosion resistance, and cytotoxicity studies of copper-substituted carbonated hydroxyapatite coating on titanium substrate. *J. Mater. Sci.* **2015**, *50*, 1688–1700. [CrossRef]
3. San Thian, E.; Huang, J.; Barber, Z.H.; Best, S.M.; Bonfield, W. Surface modification of magnetron-sputtered hydroxyapatite thin films via silicon substitution for orthopaedic and dental applications. *Surf. Coat. Technol.* **2011**, *205*, 3472–3477. [CrossRef]
4. Gomes, S.; Vichery, C.; Descamps, S.; Martinez, H.; Kaur, A.; Jacobs, A.; Nedelec, J.M.; Renaudin, G. Cu-doping of calcium phosphate bioceramics: From mechanism to the control of cytotoxicity. *Acta Biomater.* **2018**, *65*, 462–474. [CrossRef] [PubMed]
5. Jacobs, A.; Renaudin, G.; Charbonnel, N.; Nedelec, J.-M.; Forestier, C.; Descamps, S. Copper-Doped Biphasic Calcium Phosphate Powders: Dopant Release, Cytotoxicity and Antibacterial Properties. *Materials* **2021**, *14*, 2393. [CrossRef] [PubMed]
6. Calhoun, J.H.; Manring, M.; Shirliff, M. Osteomyelitis of the Long Bones. *Semin. Plast. Surg.* **2009**, *23*, 59–72. [CrossRef]
7. ter Boo, G.-J.A.; Grijpma, D.W.; Moriarty, T.F.; Richards, R.G.; Eglin, D. Antimicrobial delivery systems for local infection prophylaxis in orthopedic- and trauma surgery. *Biomaterials* **2015**, *52*, 113–125. [CrossRef] [PubMed]
8. Tenover, F.C. Mechanisms of antimicrobial resistance in bacteria. *Am. J. Infect. Control* **2006**, *34*, S3–S10. [CrossRef]
9. Vincent, M.; Duval, R.E.; Hartemann, P.; Engels-Deutsch, M. Contact killing and antimicrobial properties of copper. *J. Appl. Microbiol.* **2018**, *124*, 1032–1046. [CrossRef]
10. Jacobs, A.; Renaudin, G.; Forestier, C.; Nedelec, J.M.; Descamps, S. Biological properties of copper-doped biomaterials for orthopedic applications: A review of antibacterial, angiogenic and osteogenic aspects. *Acta Biomater.* **2020**, *117*, 21–39. [CrossRef]
11. Gérard, C.; Bordeleau, L.J.; Barralet, J.; Doillon, C.J. The stimulation of angiogenesis and collagen deposition by copper. *Biomaterials* **2010**, *31*, 824–831. [CrossRef] [PubMed]
12. Heidenau, F.; Mittelmeier, W.; Detsch, R.; Haenle, M.; Stenzel, F.; Ziegler, G.; Gollwitzer, H. A novel antibacterial titania coating: Metal ion toxicity and in vitro surface colonization. *J. Mater. Sci. Mater. Med.* **2005**, *16*, 883–888. [CrossRef] [PubMed]
13. Hordyjewska, A.; Popiolek, L.; Kocot, J. The many “faces” of copper in medicine and treatment. *BioMetals* **2014**, *27*, 611–621. [CrossRef] [PubMed]
14. Lorincz, M.T. Neurologic Wilson’s disease. *Ann. N. Y. Acad. Sci.* **2010**, *1184*, 173–187. [CrossRef] [PubMed]
15. Grass, G.; Rensing, C.; Solioz, M. Metallic copper as an antimicrobial surface. *Appl. Environ. Microbiol.* **2011**, *77*, 1541–1547. [CrossRef] [PubMed]
16. Hidalgo-Robatto, B.M.; López-Álvarez, M.; Azevedo, A.S.; Dorado, J.; Serra, J.; Azevedo, N.F.; González, P. Pulsed laser deposition of copper and zinc doped hydroxyapatite coatings for biomedical applications. *Surf. Coat. Technol.* **2018**, *333*, 168–177. [CrossRef]
17. Kunz Coyne, A.J.; El Ghali, A.; Holger, D.; Rebold, N.; Rybak, M.J. Therapeutic Strategies for Emerging Multidrug-Resistant *Pseudomonas aeruginosa*. *Infect. Dis. Ther.* **2022**, *11*, 661–682. [CrossRef] [PubMed]
18. Bazin, T.; Magnaudeix, A.; Mayet, R.; Carles, P.; Julien, I.; Demourgues, A.; Gaudon, M.; Champion, E. Sintering and biocompatibility of copper-doped hydroxyapatite bioceramics. *Ceram. Int.* **2021**, *47*, 13644–13654. [CrossRef]
19. Noori, A.; Hoseinpour, M.; Kolivand, S.; Lotfibakhshaiesh, N.; Ebrahimi-Barough, S.; Ai, J.; Azami, M. Exploring the various effects of Cu doping in hydroxyapatite nanoparticle. *Sci. Rep.* **2024**, *14*, 3421. [CrossRef]
20. Li, Q.; Song, S.; Li, J.; Yang, J.; Zhang, R.; Niinomi, M.; Nakano, T. Antibacterial properties and biocompatibility of hydroxyapatite coating doped with various Cu contents on titanium. *Mater. Trans.* **2022**, *63*, 1072–1079. [CrossRef]
21. Motelica-Heino, M.; Predoi, M.V.; Ciobanu, S.C.; Iconaru, S.L.; Predoi, D. Studies of New Layer Formation on the Surface of Zinc Doped Hydroxyapatite/Chitosan Composite Coatings in Biological Medium. *Coatings* **2023**, *13*, 472. [CrossRef]
22. Predoi, D.; Ciobanu, C.S.; Iconaru, S.L.; Raaen, S.; Badea, M.L.; Rokosz, K. Physicochemical and Biological Evaluation of Chitosan-Coated Magnesium-Doped Hydroxyapatite Composite Layers Obtained by Vacuum Deposition. *Coatings* **2022**, *12*, 702. [CrossRef]
23. Image, J. Available online: <http://imagej.nih.gov/ij> (accessed on 28 June 2024).
24. Predoi, D.; Ciobanu, C.S.; Iconaru, S.L.; Predoi, S.A.; Chifiriuc, M.C.; Raaen, S.; Badea, M.L.; Rokosz, K. Impact of Gamma Irradiation on the Properties of Magnesium-Doped Hydroxyapatite in Chitosan Matrix. *Materials* **2022**, *15*, 5372. [CrossRef]
25. Gwyddion. Available online: <http://gwyddion.net/> (accessed on 20 January 2024).
26. Iconaru, S.L.; Ciobanu, C.S.; Predoi, D.; Motelica-Heino, M.; Negrilă, C.C.; Badea, M.L.; Predoi, M.V.; Chifiriuc, C.M.; Popa, M. Nitrogen and Bromide Co-Doped Hydroxyapatite Thin Films with Antimicrobial Properties. *Coatings* **2021**, *11*, 1505. [CrossRef]
27. Iconaru, S.-L.; Motelica-Heino, M.; Predoi, D. Study on Europium-Doped Hydroxyapatite Nanoparticles by Fourier Transform Infrared Spectroscopy and Their Antimicrobial Properties. *J. Spectrosc.* **2013**, *2013*, 284285. [CrossRef]
28. Ciobanu, C.S.; Iconaru, S.L.; Predoi, D.; Truşcă, R.-D.; Prodan, A.M.; Groza, A.; Chifiriuc, M.C.; Beuran, M. Fabrication of Novel Chitosan–Hydroxyapatite Nanostructured Coatings for Biomedical Applications. *Coatings* **2021**, *11*, 1561. [CrossRef]
29. Iconaru, S.L.; Predoi, D.; Ciobanu, C.S.; Motelica-Heino, M.; Guegan, R.; Bleotu, C. Development of Silver Doped Hydroxyapatite Coatings for Biomedical Applications. *Coatings* **2022**, *12*, 341. [CrossRef]
30. Mansour, S.F.; El-dek, S.I.; Ahmed, M.K. Tailoring the structure of biphasic calcium phosphate via synthesis procedure. *Mater. Res. Express* **2017**, *4*, 125015. [CrossRef]
31. Ismail, A.M.; Menazea, A.A.; Kabary, H.A.; El-Sherbiny, A.E.; Samy, A. The influence of calcination temperature on structural and antimicrobial characteristics of zinc oxide nanoparticles synthesized by Sol–Gel method. *J. Mol. Struct.* **2019**, *1196*, 332–337. [CrossRef]
32. Elashmawi, I.S.; Menazea, A.A. Different time’s Nd:YAG laser-irradiated PVA/Ag nanocomposites: Structural, optical, and electrical characterization. *J. Mater. Res. Technol.* **2019**, *8*, 1944–1951. [CrossRef]

33. Mariappan, A.; Pandi, P.; Rani, K.B.; Neyvasagam, K. Study of the photocatalytic and antibacterial effect of Zn and Cu doped hydroxyapatite. *Inorg. Chem. Commun.* **2022**, *136*, 109128. [CrossRef]
34. Osman, M.A.; Alamoush, R.A.; Kushnerev, E.; Seymour, K.G.; Watts, D.C.; Yates, J.M. Biological response of epithelial and connective tissue cells to titanium surfaces with different ranges of roughness: An in-vitro study. *Dent. Mater. Off. Publ. Acad. Dent. Mater.* **2022**, *38*, 1777–1788. [CrossRef] [PubMed]
35. Mavropoulos, E.; Hausen, M.; Costa, A.M.; Alves, G.; Mello, A.; Ospina, C.A.; Mir, M.; Granjeiro, J.M.; Rossi, A.M. The impact of the RGD peptide on osteoblast adhesion and spreading on zinc-substituted hydroxyapatite surface. *J. Mater. Sci. Mater. Med.* **2013**, *24*, 1271–1283. [CrossRef]
36. Lopez, D.A.; Simison, S.N.; De Sanchez, S.R. The influence of steel microstructure on CO₂ corrosion. EIS studies on the inhibition efficiency of benzimidazole. *Electrochim. Acta* **2003**, *48*, 845–854. [CrossRef]
37. Serra, J.; González, P.; Liste, S.; Serra, C.; Chiussi, S.; León, B.; Pérez-Amor, M.; Ylänen, H.O.; Hupa, M. FTIR and XPS studies of bioactive silica based glasses. *J. Non-Cryst. Solids* **2003**, *332*, 20–27. [CrossRef]
38. Moulder, J.F.; Stickle, W.F.; Sobol, P.E.; Bomben, K.D. *Handbook of X-ray Photoelectron Spectroscopy*; Physical Electronics Inc.: Chanhassen, MN, USA, 1995.
39. Battistoni, C.; Casaletto, M.P.; Ingo, G.M.; Kaciulis, S.; Mattogno, G.; Pandolfi, L. Surface characterization of biocompatible hydroxyapatite coatings. *Surf. Interface Anal.* **2000**, *29*, 773–781. [CrossRef]
40. Greczynski, G.; Hultman, L. X-ray photoelectron spectroscopy: Towards reliable binding energy referencing. *Prog. Mater. Sci.* **2020**, *107*, 100591. [CrossRef]
41. Available online: <https://www.thermofisher.com/ro/en/home/materials-science/learning-center/periodic-table/non-metal/carbon.html> (accessed on 30 January 2024).
42. Nagakane, K.; Yoshida, Y.; Hirata, I.; Fukuda, R.; Nakayama, Y.; Shirai, K.; Ogawa, T.; Suzuki, K.; Van Meerbeek, B.; Okazaki, M. Analysis of chemical interaction of 4-MET with hydroxyapatite using XPS. *Dent. Mater. J.* **2006**, *25*, 645–649. [CrossRef] [PubMed]
43. Stranick, M.A.; Root, M.J. Influence of strontium on monofluorophosphate uptake by hydroxyapatite XPS characterization of the hydroxyapatite surface. *Colloids Surf.* **1991**, *55*, 137–147. [CrossRef]
44. Chusuei, C.C.; Brookshier, M.A.; Goodman, D.W. Correlation of relative X-ray photoelectron spectroscopy shake-up intensity with CuO particle size. *Langmuir* **1999**, *15*, 2806–2808. [CrossRef]
45. Zhang, Y.C.; Tang, J.Y.; Wang, G.L.; Zhang, M.; Hu, X.Y. Facile synthesis of submicron Cu₂O and CuO crystallites from a solid metallorganic molecular precursor. *J. Cryst. Growth* **2006**, *294*, 278–282. [CrossRef]
46. Schon, G. ESCA studies of Cu, Cu₂O and CuO. *Surf. Sci.* **1973**, *35*, 96–108. [CrossRef]
47. Kumar, M.; Bhatt, V.; Nayal, O.S.; Sharma, S.; Kumar, V.; Thakur, M.S.; Kumar, N.; Bal, R.; Singh, B.; Sharma, U. CuI nanoparticles as recyclable heterogeneous catalysts for C–N bond formation reactions. *Catal. Sci. Technol.* **2017**, *7*, 2857–2864. [CrossRef]
48. Chen, S.; Brown, L.; Levendorf, M.; Cai, W.; Ju, S.Y.; Edgeworth, J.; Li, X.; Magnuson, C.W.; Velamakanni, A.; Piner, R.D.; et al. Oxidation resistance of graphene-coated Cu and Cu/Ni alloy. *ACS Nano* **2011**, *5*, 1321–1327. [CrossRef] [PubMed]
49. Bai, X.; More, K.; Rouleau, C.M.; Rabiei, A. Functionally graded hydroxyapatite coatings doped with antibacterial components. *Acta Biomater.* **2010**, *6*, 2264–2273. [CrossRef] [PubMed]
50. Shanmugam, S.; Gopal, B. Copper substituted hydroxyapatite and fluorapatite: Synthesis, characterization and antimicrobial properties. *Ceram. Int.* **2014**, *40*, 15655–15662. [CrossRef]
51. Ciobanu, S.C.; Predoi, D.; Chifiriuc, M.C.; Iconaru, S.L.; Predoi, M.V.; Popa, M.; Rokosz, K.; Raaen, S.; Marinas, I.C. *Salvia officinalis*–Hydroxyapatite Nanocomposites with Antibacterial Properties. *Polymers* **2023**, *15*, 4484. [CrossRef]
52. Huang, Y.; Hao, M.; Nian, X.; Qiao, H.; Zhang, X.; Zhang, X.; Song, G.; Guo, J.; Pang, X.; Zhang, H. Strontium and copper co-substituted hydroxyapatite-based coatings with improved antibacterial activity and cytocompatibility fabricated by electrodeposition. *Ceram. Int.* **2016**, *42*, 11876–11888. [CrossRef]
53. Mounika, S.; Ramakrishnan, P. Synthesis and Comparison of Chemical Changes Using FTIR Spectroscopy for Copper Substituted Hydroxyapatite. *E3S Web Conf.* **2024**, *477*, 00083. [CrossRef]
54. Lukaviciute, L.; Karciauskaite, J.; Grigoraviciute, I.; Vasiliauskiene, D.; Sokol, D.; Kareiva, A. Calcium Hydroxyapatite Coatings: Low-Temperature Synthesis and Investigation of Antibacterial Properties. *Coatings* **2023**, *13*, 1991. [CrossRef]
55. Nam, P.T.; Thom, N.T.; Phuong, N.T.; Xuyen, N.T.; Hai, N.S.; Anh, N.T.; Dung, P.T.; Thanh, D.T.M. Synthesis, characterization and antimicrobial activity of copper doped hydroxyapatite. *Vietnam. J. Chem.* **2018**, *56*, 672–678. [CrossRef]
56. Eliaz, N.; Shmueli, S.; Shur, I.; Benayahu, D.; Aronov, D.; Rosenman, G. The effect of surface treatment on the surface texture and contact angle of electrochemically deposited hydroxyapatite coating and on its interaction with bone-forming cells. *Acta Biomater.* **2009**, *5*, 3178–3191. [CrossRef]
57. Ryan, B.J.; Poduska, K.M. Roughness effects on contact angle measurements. *Am. J. Phys.* **2008**, *76*, 1074–1077. [CrossRef]
58. Danish, M. Contact Angle Studies of Hydrophobic and Hydrophilic Surfaces. In *Handbook of Magnetic Hybrid Nanoalloys and their Nanocomposites*; Springer: Cham, Switzerland, 2022. [CrossRef]
59. ISO Standard 10993-5; Evaluation Biologique des Dispositifs Médicaux—Partie 5, Essais Concernant la Cytotoxicité In Vitro. ISO: Geneva, Switzerland, 2009; p. 34.
60. Rodríguez-Valencia, C.; López-Álvarez, M.; Cochón-Cores, B.; Pereiro, I.; Serra, J.; González, P. Novel selenium-doped hydroxyapatite coatings for biomedical applications. *J. Biomed. Mater. Res. A* **2013**, *101*, 853–861. [CrossRef] [PubMed]

61. Marques, C.F.; Olhero, S.; Abrantes, J.C.; Marote, A.; Ferreira, S.; Vieira, S.I.; Ferreira, J.M. Biocompatibility and antimicrobial activity of biphasic calcium phosphate powders doped with metal ions for regenerative medicine. *Ceram. Int.* **2017**, *43*, 15719–15728. [\[CrossRef\]](#)
62. Li, K.; Xia, C.; Qiao, Y.; Liu, X. Dose-response relationships between copper and its biocompatibility/antibacterial activities. *J. Trace Elements Med. Biol.* **2019**, *55*, 127–135. [\[CrossRef\]](#) [\[PubMed\]](#)
63. Gritsch, L.; Lovell, C.; Goldmann, W.H.; Boccaccini, A.R. Fabrication and characterization of copper(II)-chitosan complexes as antibiotic-free antibacterial biomaterial. *Carbohydr. Polym.* **2018**, *179*, 370–378. [\[CrossRef\]](#)
64. Unabia, R.B.; Candidato, R.T., Jr.; Pawłowski, L.; Salvatori, R.; Bellucci, D.; Cannillo, V. In vitro studies of solution precursor plasma-sprayed copper-doped hydroxyapatite coatings with increasing copper content. *J. Biomed. Mater. Res. Part B Appl. Biomater.* **2020**, *108*, 2579–2589. [\[CrossRef\]](#)
65. Tuntun, S.M.; Hossain, M.S.; Uddin, M.N.; Shaikh, M.A.; Bahadur, N.M.; Ahmed, S. Crystallographic characterization and application of copper doped hydroxyapatite as a biomaterial. *New J. Chem.* **2023**, *47*, 2874–2885. [\[CrossRef\]](#)
66. Shen, Q.; Qi, Y.; Kong, Y.; Bao, H.; Wang, Y.; Dong, A.; Wu, H.; Xu, Y. Advances in Copper-Based Biomaterials with Antibacterial and Osteogenic Properties for Bone Tissue Engineering. *Front. Bioeng. Biotechnol.* **2022**, *20*, 795425. [\[CrossRef\]](#)
67. Sahithi, K.; Swetha, M.; Prabakaran, M.; Moorthi, A.; Saranya, N.; Ramasamy, K.; Srinivasan, N.; Partridge, N.C.; Selvamurugan, N. Synthesis and Characterization of Nanoscale Hydroxyapatite-Copper for Antimicrobial Activity Towards Bone Tissue Engineering Applications. *J. Biomed. Nanotechnol.* **2010**, *6*, 333–339. [\[CrossRef\]](#) [\[PubMed\]](#)
68. Hoveidaei, A.H.; Sadat-Shojai, M.; Mosalamiaghili, S.; Salarikia, S.R.; Roghani-Shahraki, H.; Ghaderpanah, R.; Ersi, M.H.; Conway, J.D. Nano-hydroxyapatite structures for bone regenerative medicine: Cell-material interaction. *Bone* **2024**, *179*, 116956. [\[CrossRef\]](#) [\[PubMed\]](#)
69. Mone, N.S.; Syed, S.; Ravichandiran, P.; Kamble, E.E.; Pardesi, K.R.; Salunke-Gawali, S.; Rai, M.; Vikram Singh, A.; Prasad Dakua, S.; Park, B.H.; et al. Synergistic and Additive Effects of Menadione in Combination with Antibiotics on Multidrug-Resistant *Staphylococcus aureus*: Insights from Structure-Function Analysis of Naphthoquinones. *ChemMedChem* **2023**, *18*, e202300328. [\[CrossRef\]](#) [\[PubMed\]](#)
70. Singh, A.V.; Baylan, S.; Park, B.W.; Richter, G.; Sitti, M. Hydrophobic pinning with copper nanowhiskers leads to bactericidal properties. *PLoS ONE* **2017**, *12*, e0175428. [\[CrossRef\]](#) [\[PubMed\]](#)
71. Chatterjee, A.K.; Chakraborty, R.; Basu, T. Mechanism of antibacterial activity of copper nanoparticles. *Nanotechnology* **2014**, *25*, 135101. [\[CrossRef\]](#)
72. Vasiliev, G.; Kubo, A.L.; Vija, H.; Kahru, A.; Bondar, D.; Karpichev, Y.; Bondarenko, O. Synergistic antibacterial effect of copper and silver nanoparticles and their mechanism of action. *Sci. Rep.* **2023**, *13*, 9202. [\[CrossRef\]](#) [\[PubMed\]](#)
73. Nisar, P.; Ali, N.; Rahman, L.; Ali, M.; Shinwari, Z.K. Antimicrobial activities of biologically synthesized metal nanoparticles: An insight into the mechanism of action. *J. Biol. Inorg. Chem.* **2019**, *24*, 929–941. [\[CrossRef\]](#)
74. Ballo, M.K.; Rtimi, S.; Mancini, S.; Kiwi, J.; Pulgarin, C.; Entenza, J.M.; Bizzini, A. Bactericidal activity and mechanism of action of copper-sputtered flexible surfaces against multidrug-resistant pathogens. *Appl. Microbiol. Biotechnol.* **2016**, *100*, 5945–5953. [\[CrossRef\]](#)
75. Slavin, Y.N.; Asnis, J.; Hrífeli, U.O.; Bach, H. Metal nanoparticles: Understanding the mechanisms behind antibacterial activity. *J. Nanobiotechnol.* **2017**, *15*, 65. [\[CrossRef\]](#)
76. Crisan, M.C.; Teodora, M.; Lucian, M. Copper Nanoparticles: Synthesis and Characterization, Physiology, Toxicity and Antimicrobial Applications. *Appl. Sci.* **2022**, *12*, 141. [\[CrossRef\]](#)
77. Salah, I.; Parkin, I.P.; Allan, E. Copper as an antimicrobial agent: Recent advances. *RSC Adv.* **2021**, *11*, 18179–18186. [\[CrossRef\]](#) [\[PubMed\]](#)
78. Gyawali, R.; Ibrahim, S.A.; Abu Hasfa, S.H.; Smqadri, S.Q.; Haik, Y. Antimicrobial Activity of Copper Alone and in Combination with Lactic Acid against *Escherichia coli* O157:H7 in Laboratory Medium and on the Surface of Lettuce and Tomatoes. *J. Pathog.* **2011**, *2011*, 650968. [\[CrossRef\]](#) [\[PubMed\]](#)
79. Gomaa, E.Z.; Housseiny, M.M.; Omran, A.A.A.K. Fungicidal Efficiency of Silver and Copper Nanoparticles Produced by *Pseudomonas fluorescens* ATCC 17397 against Four *Aspergillus* Species: A Molecular Study. *J. Clust. Sci.* **2019**, *30*, 181–196. [\[CrossRef\]](#)
80. Liu, R.; Memarzadeh, K.; Chang, B.; Zhang, Y.; Ma, Z.; Allaker, R.P.; Ren, L.; Yang, K. Antibacterial Effect of Copper-Bearing Titanium alloy (Ti-Cu) against *Streptococcus Mutans* and *Porphyromonas Gingivalis*. *Sci. Rep.* **2016**, *6*, 29985. [\[CrossRef\]](#) [\[PubMed\]](#)

Disclaimer/Publisher’s Note: The statements, opinions and data contained in all publications are solely those of the individual author(s) and contributor(s) and not of MDPI and/or the editor(s). MDPI and/or the editor(s) disclaim responsibility for any injury to people or property resulting from any ideas, methods, instructions or products referred to in the content.

Article

Studies of the Tarragon Essential Oil Effects on the Characteristics of Doped Hydroxyapatite/Chitosan Biocomposites

Daniela Predoi ^{1,*}, Simona Liliana Iconaru ¹ , Carmen Steluta Ciobanu ¹ , Mariana Stefania Raita ², Liliana Ghegoiu ¹, Roxana Trusca ^{3,4}, Monica Luminita Badea ⁵ and Carmen Cimpeanu ^{6,*}

¹ National Institute of Materials Physics, Atomistilor Street, No. 405A, 077125 Magurele, Romania

² Faculty of Veterinary Medicine, University of Agronomic Sciences and Veterinary Medicine of Bucharest, 105 Splaiul Independentei, District 5, 050097 Bucharest, Romania

³ Science and Engineering of Oxide Materials and Nanomaterials, Faculty of Applied Chemistry and Materials Science, University POLITEHNICA of Bucharest, Gh. Polizu 1-7, 011061 Bucharest, Romania

⁴ National Center for Micro and Nanomaterials, University POLITEHNICA of Bucharest, Splaiul Independentei 313, 060042 Bucharest, Romania

⁵ Faculty of Horticulture, University of Agronomic Sciences and Veterinary Medicine, 59 Marasti Blvd., 011464 Bucharest, Romania

⁶ Faculty of Land Reclamation and Environmental Engineering, University of Agronomic Sciences and Veterinary Medicine of Bucharest, 59 Marasti Blvd, 011464 Bucharest, Romania

* Correspondence: dpredoi@gmail.com (D.P.); carmencimpeanu@yahoo.com (C.C.)

Abstract: Due to the emergence of antibiotic-resistant pathogens, the need to find new, efficient antimicrobial agents is rapidly increasing. Therefore, in this study, we report the development of new biocomposites based on zinc-doped hydroxyapatite/chitosan enriched with essential oil of *Artemisia dracuncululus* L. with good antimicrobial activity. Techniques such as scanning electron microscopy (SEM), X-ray diffraction (XRD), energy dispersive X-ray spectroscopy (EDX) and Fourier transform infrared spectroscopy (FTIR) were used in order to evaluate their physico-chemical properties. Our studies revealed that biocomposite materials with nanometric dimension and homogeneous composition could be obtained through an economic and cost-effective synthesis method. The biological assays demonstrated that ZnHA (zinc-doped hydroxyapatite), ZnHACH (zinc-doped hydroxyapatite/chitosan) and ZnHACHT (zinc-doped hydroxyapatite/chitosan enriched with essential oil of *Artemisia dracuncululus* L.) did not exhibit a toxic effect on the cell viability and proliferation of the primary osteoblast culture (hFOB 1.19). Moreover, the cytotoxic assay also highlighted that the cell morphology of the hFOB 1.19 was not altered in the presence of ZnHA, ZnHACH or ZnHACHT. Furthermore, the in vitro antimicrobial studies emphasized that the samples exhibited strong antimicrobial properties against *Escherichia coli* ATCC 25922, *Staphylococcus aureus* ATCC 25923 and *Candida albicans* ATCC 10231 microbial strains. These results are encouraging for the following development of new composite materials with enhanced biological properties that could promote the osteogenic process of bone healing and also exhibit good antimicrobial properties.

Keywords: zinc; hydroxyapatite; tarragon essential oil; chitosan; morphology; biocompatibility; antimicrobial activity



Citation: Predoi, D.; Iconaru, S.L.; Ciobanu, C.S.; Raita, M.S.; Ghegoiu, L.; Trusca, R.; Badea, M.L.; Cimpeanu, C. Studies of the Tarragon Essential Oil Effects on the Characteristics of Doped Hydroxyapatite/Chitosan Biocomposites. *Polymers* **2023**, *15*, 1908. <https://doi.org/10.3390/polym15081908>

Academic Editor: Helena Felgueiras

Received: 28 February 2023

Revised: 6 April 2023

Accepted: 14 April 2023

Published: 16 April 2023



Copyright: © 2023 by the authors. Licensee MDPI, Basel, Switzerland. This article is an open access article distributed under the terms and conditions of the Creative Commons Attribution (CC BY) license (<https://creativecommons.org/licenses/by/4.0/>).

1. Introduction

Lately, the unwanted effects of excessive and uncontrolled use of antibiotics in the curing of various infectious diseases have become more and more evident [1,2]. Thus, an exponential evolution of infectious diseases determined by multi-resistant pathogens was observed, these being difficult to treat, involving higher cost, and becoming an important public health problem [1]. Last but not least, they lead to the alteration of the patients' quality of life. Recently, according to the results of the studies reported by Thompson T. [2], in 2019, over 1.2 million people died due to the diseases developed as a result of

antimicrobial resistance. In this context, in order to ameliorate this public health problem, sustained efforts are being made to find new cheap and effective antimicrobial agents [3–5]. Hydroxyapatite (HA) is one of the commonly used bioceramics in bone tissue engineering, due to its outstanding biological features and similar composition with bone tissue (HA) [6,7]. However, a major disadvantage of hydroxyapatite is its weak antimicrobial activity. Therefore, in order to confer good antimicrobial properties, into the hydroxyapatite structure may be introduced metallic ions, such as zinc, cerium, silver, etc. [8–12]. Among these, zinc ions play an important role in the bone physiology [13] involved in processes such as bone development and DNA replication [7]. In the study made by P. Kazimierzak et al. [14], it was reported that zinc-doped hydroxyapatite biomaterials may support the bone regeneration process and even prevent the occurrence of post-surgery infections due to their outstanding biological properties [14]. Previously, it has been reported that both zinc ($0.01 < x_{Zn} < 0.05$) and chitosan (variation of chitosan concentration between 10 and 20 %wt) concentration play a key role in defining the antimicrobial properties of biomaterials [8,9,15]. In their study, A. Rasyida and collaborators [15] showed that the best antibacterial activity of Zn^{2+} doped HA in chitosan matrix against gram-negative and gram-positive bacterial strains was obtained for a concentration of 10% of chitosan [15]. Moreover, it was shown that the presence of copper and zinc ions in the chitosan/HA scaffolds provided them with good antibacterial activity (against *Escherichia coli* DH5 α and *Staphylococcus aureus*) and also with improved osteoproliferative features [16]. Furthermore, Predoi D. et al. [17] highlighted that zinc and silver co-doped hydroxyapatite in chitosan matrix (coatings and suspension) do not alter the morphology or proliferation of the hFOB 1.19 cell line. Additionally, in our previous studies, it was reported that zinc and silver co-doped hydroxyapatite in chitosan matrix exhibited a good antimicrobial activity against the *Candida albicans* ATCC 90029, *Escherichia coli* ATCC 25922, and *Staphylococcus aureus* ATCC 25923 microbial strains [17].

Other methods, used for the obtaining of desired antimicrobial features, are represented by the incorporation of HA/doped HA in a biopolymeric matrix (such as chitosan, starch, and cellulose) [18] and/or adding natural compounds (e.g., essential oils (EO)) in the HA synthesis process [18]. Tarragon (*Artemisia dracuncululus* L.) is a perennial subshrub member of the Asteraceae family [19]. Tarragon is generally used as a spice, but it also possesses antimicrobial, hepatoprotective and antioxidant properties [19–21]. In previous studies conducted by Fildan, A.P. and collaborators [21], it was underlined that the main components of tarragon essential oils are represented by estragole, limonene, methyleugenol, sabinene, β -ocimene, trans-anethole, α -ocimene, terpinolene, elemicin and terpinen-4-ol [21]. In the studies made by A. Farsanipour et al. [22], it was reported that by coating the *Scomberoides commersonnianus* muscle fillets with chitosan, whey protein isolated and tarragon essential oil were improved, and both the antibacterial activity and antioxidant features of the packaging material were improved. In another study, conducted by Zedan H. and coworkers [23], the authors reported that by adding a concentration of 6% chitosan (high molecular weight) and 20% of tarragon essential oil in yogurt, yogurts with higher shelf life and improved consistency could be obtained.

Taking into consideration all of these important features, the synthesis of a new biocomposite based on Zn^{2+} doped HA in chitosan matrix with essential oil of *Artemisia dracuncululus* L. is of great interest to the bioengineering field. The proposed aim of this work was to obtain, through a cost-effective method (coprecipitation), new biocomposite materials based on zinc-doped hydroxyapatite/chitosan enriched with essential oil of *Artemisia dracuncululus* L. Further, the physico-chemical features of the obtained biocomposite materials were analyzed by scanning electron microscopy (SEM), X-ray diffraction (XRD), energy dispersive X-ray spectroscopy (EDX) and Fourier transform infrared spectroscopy (FTIR). The in vitro biocompatibility of ZnHA (zinc-doped hydroxyapatite), ZnHACH (zinc-doped hydroxyapatite/chitosan), and ZnHACHT (zinc-doped hydroxyapatite/chitosan with essential oil of *Artemisia dracuncululus* L.) was evaluated using a primary osteoblast culture (hFOB 1.19). Finally, the antimicrobial activity of ZnHA, ZnHACH and ZnHACHT

against *Escherichia coli* ATCC 25922, *Staphylococcus aureus* ATCC 25923 and *Candida albicans* ATCC 10231 microbial was investigated.

2. Materials and Methods

2.1. Materials

The synthesis of zinc-doped hydroxyapatite ($\text{Ca}_{10-x}\text{Zn}_x(\text{PO}_4)_6(\text{OH})_2$ with $x_{\text{Zn}} = 0.06$) powder in chitosan matrix (ZnHApCh) enriched with essential oil of *Artemisia dracunculus* L. (ZnHACHT) was obtained through the coprecipitation method using calcium nitrate tetrahydrate, ammonium hydroxide, zinc nitrate hexahydrate of higher purity ($\geq 99.0\%$), diammonium acid phosphate, chitosan ($\text{C}_{12}\text{H}_{24}\text{N}_2\text{O}_9$, low molecular weight: 50,000–190,000 Da; $\geq 75\%$ (deacetylated)), and absolute ethanol procured from Sigma Aldrich, St. Louis, MO, USA. The essential oil of *Artemisia dracunculus* L. was purchased from Florame, Saint Rémy de Provence, France.

Zinc-doped hydroxyapatite suspensions in chitosan with tarragon essential oil were obtained by way of the coprecipitation technique [17,24]. The $[\text{Ca} + \text{Zn}]/\text{P}$ ratio was 1.67. The solutions of $\text{Ca}(\text{NO}_3)_2 \cdot 4\text{H}_2\text{O}$ and $\text{Zn}(\text{NO}_3)_2 \cdot 6\text{H}_2\text{O}$ together with tarragon essential oil (3 mL in 100 mL H_2O) were dropped into the solution of $(\text{NH}_4)_2\text{HPO}_4$ and $\text{C}_6\text{H}_{11}\text{NO}_4$. The pH was maintained constant at 10 throughout the drip. Then, the resulting suspension was stirred continuously for 6 h, after which it was centrifuged and redispersed. The washing procedure was performed 5 times. Subsequent to the last wash, the final precipitate was redispersed in a solution of 1% chitosan and tarragon essential oil (2 mL in 100 mL H_2O) followed by continuous stirring for 12 h. The resulting final suspension (ZnHACHT) was evaluated both from a biological and physico-chemical point of view.

2.2. Characterization Methods

2.2.1. Physico-Chemical Characterization

In order to measure the crystal size in the ZnHAp, ZnHACH and ZnHACHT samples, their X-ray diffraction patterns were measured. The patterns were achieved using a Rigaku SmartLab 3 kW (Rigaku, Tokyo, Japan) diffractometer with $\text{K}\alpha$ Cu radiation ($\lambda = 1.5418 \text{ \AA}$) [24]. The incidence angle was 0.5° [24]. The patterns were recorded in the 2θ range $20\text{--}60^\circ$, with an angle variation of 0.02° , and a detector data acquisition total time of 8.5 s. The crystallite sizes of the samples were obtained by using Scherrer's equation [25]:

$$L = K\lambda / \beta \cdot \cos\theta$$

where L is nano crystallite size, K is dimensionless shape factor, λ (nm) is X-ray wavelength from measuring full width at half maximum of peaks (β) in radian located at any 2θ in the pattern [26].

A scanning electron microscope (FEI Quanta Inspect F) equipped with an energy dispersive X-ray (EDX) device was used to analyze the morphology of samples. For the SEM studies, the powder was placed on a double-adhesive carbon tape without being subsequently covered with Au. The particle size distribution was also obtained from the SEM micrographs. Absorbance FTIR spectra of samples were collected on a SP 100 Perkin Elmer FTIR spectrometer (Waltham, MS, USA). The parameters used for the spectrum acquisition have been described elsewhere [24].

2.2.2. In Vitro Antimicrobial Assay

The antimicrobial properties of the ZnHA, ZnHACH and ZnHACHT samples were assessed in vitro with the aid of reference *Staphylococcus aureus* ATCC 25923 (ATCC, Old Town Manassas, VA, USA), *Escherichia coli* ATCC 25922 (ATCC, Old Town Manassas, VA, USA) and *Candida albicans* ATCC 10231 (ATCC, Old Town Manassas, VA, USA) microbial strains. The in vitro experiments were performed in accordance with the method previously described in [27,28]. The assays were conducted using 0.5 McFarland standard microbial cultures. For this purpose, the biocomposites were inoculated with a volume of 1.5 mL

microbial suspension having a cell density of 5×10^6 CFU/mL (colony forming units/mL), prepared in phosphate-buffered saline (PBS), and afterwards incubated for 24, 48 and 72 h. A free microbial culture was also assessed for 24, 48 and 72 h and used as a positive control (C+). Suspensions of each culture medium were collected at different time intervals (24, 48 and 72 h) and incubated on a LB agar medium for 24 h at 37 °C. The number of CFU/mL was determined for each of the incubated samples with the microbial suspensions. The experiments were performed in triplicate and the data was presented as mean \pm SD.

2.2.3. Cytotoxicity Assay

The biocompatible properties of the ZnHA, ZnHACH and ZnHACHT were determined using a primary osteoblast culture (hFOB 1.19) prepared following the protocol devised by Gallagher et al. [29]. The in vitro cell viability experiments were conducted using the methodology previously described in [30]. For this purpose, for the growth and development of hFOB 1.19 cells, DMEM (Dulbecco's Modified Eagle's Medium) enriched with L-glutamine, sodium pyruvate, non-essential amino acids, sodium bicarbonate and fetal bovine serum was used. Afterwards, the cell cultures were incubated in a 5% CO₂ atmosphere at a temperature of 37 °C. After reaching confluence, the culture was treated with trypsin, DMEM medium with 10% trypsin-inhibiting fetal serum was added to the cell suspension in trypsin and then the medium was centrifuged for 3 min at 1500 rpm. The cells were resuspended in a minimal volume of medium (500 μ L), counted and distributed equally in 3–4 culture plates. The cells were then seeded in Petri plates and incubated with the samples at 37 °C in an atmosphere having 5% CO₂. After 24 h, the cells were visualized under an inverted microscope using an Olympus IX71 microscope (Olympus, Tokyo, Japan). For the microscopic evaluation, the cultures were stained using phalloidin-FITC. For the cell viability assay, the cells were treated with MTT solution [3-(4,5dimethylthiazolyl)-2,5-diphenyltetrazolium bromide] and incubated in an atmosphere with 5% CO₂ at 37 °C, and the optical density of the solubilized formazan at 595 nm was determined using a TECAN spectrophotometer.

2.2.4. Statistical Analysis

The biological assays were performed in triplicate. For the statistical analysis, the t-test and analysis of variance (ANOVA) was used. The difference established between specimens was appreciated to be significant for a value of $p < 0.05$.

3. Results

Figure 1 shows the XRD patterns for ZnHAp, ZnHACH and ZnHACHT. The diffraction patterns of ZnHAp and ZnHACH samples are similar to the pattern for pure hydroxyapatite with the reference hexagonal structure JCPDF 9-432 [24]. In agreement with previous studies [31], in the analyzed ZnHAp and ZnHApCh samples, a single phase of HA was identified. The presence of chitosan led to a slight shift of the peaks to larger angles. The crystallites of the ZnHACH sample are smaller than the crystallites of the ZnHA sample. This fact can also be observed from the width of the diffraction maxima. This behavior is in accord with previous studies [32]. The presence of the essential oil of *Artemisia dracunculus* led to a structural disturbance in the case of the ZnHACHT sample. The diffraction maxima of the ZnHACHT sample corresponds to the reference HA model but are much wider. In this case, the width of the diffraction maxima is due both to the crystallite size, which is smaller than in the case of the ZnHA and ZnHACH samples. The part of the material that becomes amorphous could lead to the formation of a calcium deficient HA.

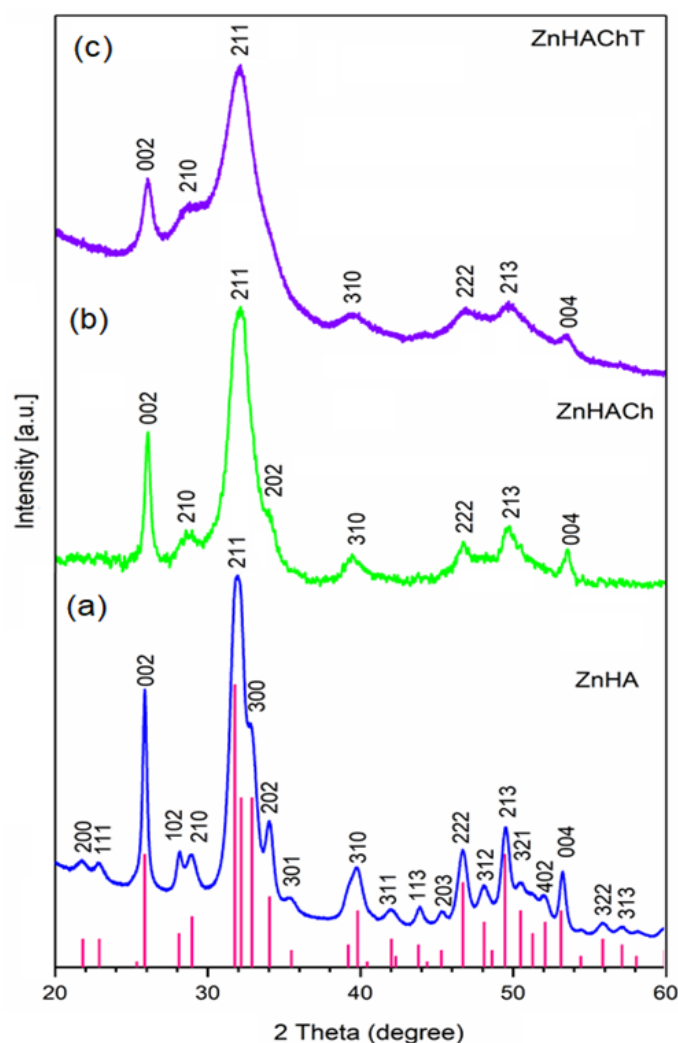


Figure 1. X-ray diffractograms of ZnHA (a), ZnHACH (b) and ZnHACHT (c) powders, and pattern for the reference hexagonal structure JCPDF 9-432 (red lines).

The crystallite sizes of ZnHA, ZnHACH and ZnHACHT samples were 18 nm, 14 and 7 nm, respectively. It is noticed that the size of the particles decreased along with the modification of their surface.

The size of the crystallites was the smallest in the case of the ZnHACHT sample in which an amorphous phase is also present. Our results are in concordance with the studies on “Effect of dilute gelatine on the ultrasonic thermally assisted synthesis of nano-hydroxyapatite” previously reported by Brundavanam, R.K. et al. [33] when gelatine was used.

The SEM micrographs of the samples with ZnHA, ZnHACH and ZnHACHT are presented in Figure 2. The ZnHA sample has an acicular morphology (Figure 2a). In the case of samples synthesized in the presence of chitosan (ZnHACH), the morphology is slightly modified, tending towards the ellipsoidal shape (Figure 2b). The ZnHACHT (Figure 2c) sample in which, in addition to chitosan, the EO of *Artemisia dracuncululus* L. is also present, has two types of morphologies. There are particles with an almost spherical morphology, but also particles that are not well-defined, forming different agglomerated formations that seem not to be well crystallized. This result supports the XRD studies which, in addition to the phase of HA, also highlighted an amorphous phase, in the case of the ZnHACHT sample. In addition to the change in morphology, a variation in the size of the particles was also observed. It is noticed that the particle size decreases from ZnHA to ZnHACHT. As can be observed for all the studied samples, there is a tendency for the

particles to agglomerate. In agreement with previous studies on the “synthesis of nano hydroxyapatite powder that simulate teeth particle morphology and composition” [34] and “biodegradation and bioresorption of calcium phosphate ceramics” [35] the particles tend to aggregate as a result of the small volume and due to the fact that the area/volume ratio is greater than in the case of particles on a submicron or micro scale.

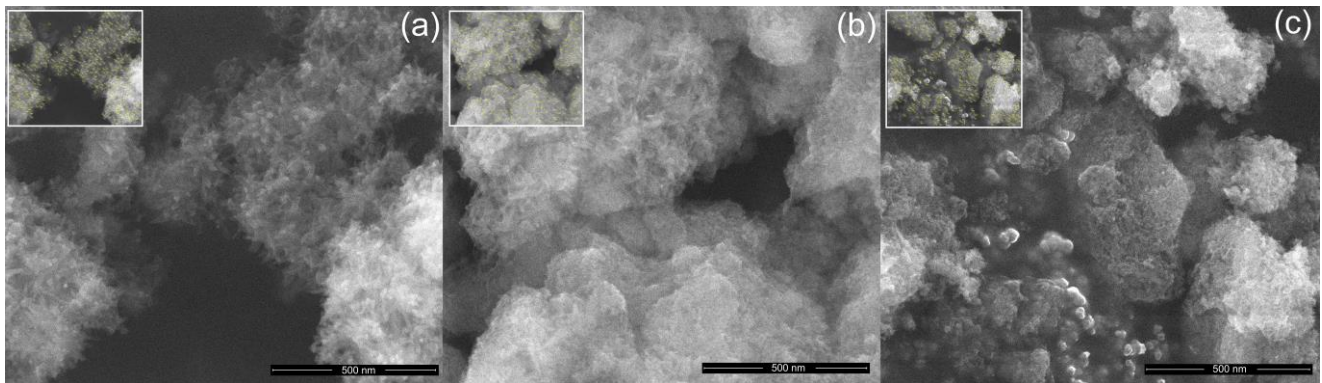


Figure 2. SEM images of the ZnHA (a), ZnHACH (b) and ZnHACHT (c) samples at 100,000× magnification and inset of measured particles used to determine particle size.

The size distributions of the ZnHA, ZnHACH and ZnHACHT samples, which were obtained by counting a number of approximately 400 particles, are presented in Figure 3. It can be observed that the average size in the case of the ZnHA sample was 19 ± 1 nm, while for the ZnHACH sample, it was 15 ± 1 nm. The size distribution in the case of the ZnHACHT sample was obtained by counting the particles with almost spherical morphology, obtaining an average size of 7 ± 2 nm. Particles that are not well-defined and form agglomerated formations were not measured.

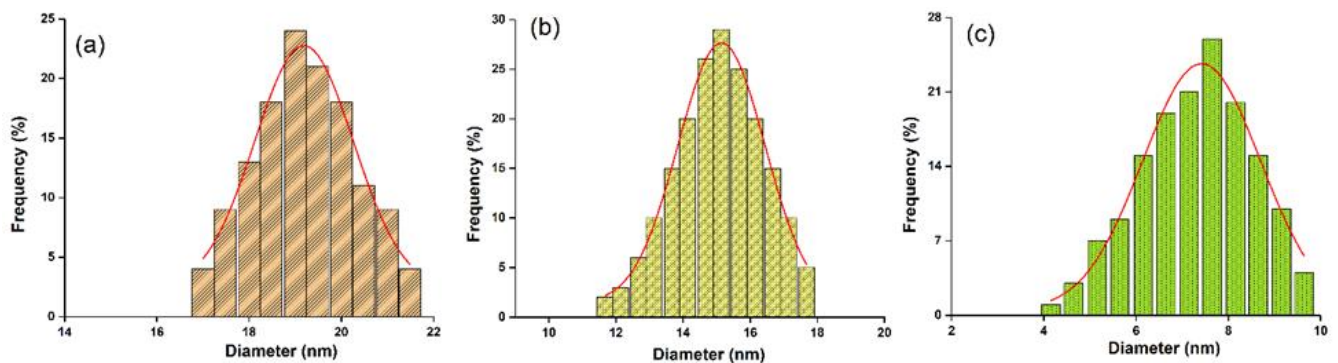


Figure 3. Size distributions of the ZnHA (a), ZnHACH (b) and ZnHACHT (c) samples. The red lines were obtained by fitting the experimental data with a Gaussian function.

The chemical composition of the ZnHA and ZnHACH samples was studied with the aid of EDX analysis, and the results are shown in Figure 4. For the ZnHA powders, the presence of phosphorus (P), calcium (Ca), zinc (Zn) and oxygen (O) can be observed in the EDX spectrum (Figure 4). The carbon (C) line observed in Figure 4 is owed to the presence of double-adhesive carbon tape on which the powders were placed before the SEM analyses. In the case of the ZnHACH sample, the carbon (C) line appears in Figure 4 (left) due to the double-adhesive carbon tape and, on the other hand, due to the presence of chitosan in the studied sample. Furthermore, the presence of chitosan in the ZnHACH powders is also underlined by the presence of the nitrogen (N) line in their specific EDX spectra. In Figure 4 (inset) are presented the results of EDX quantitative analysis.

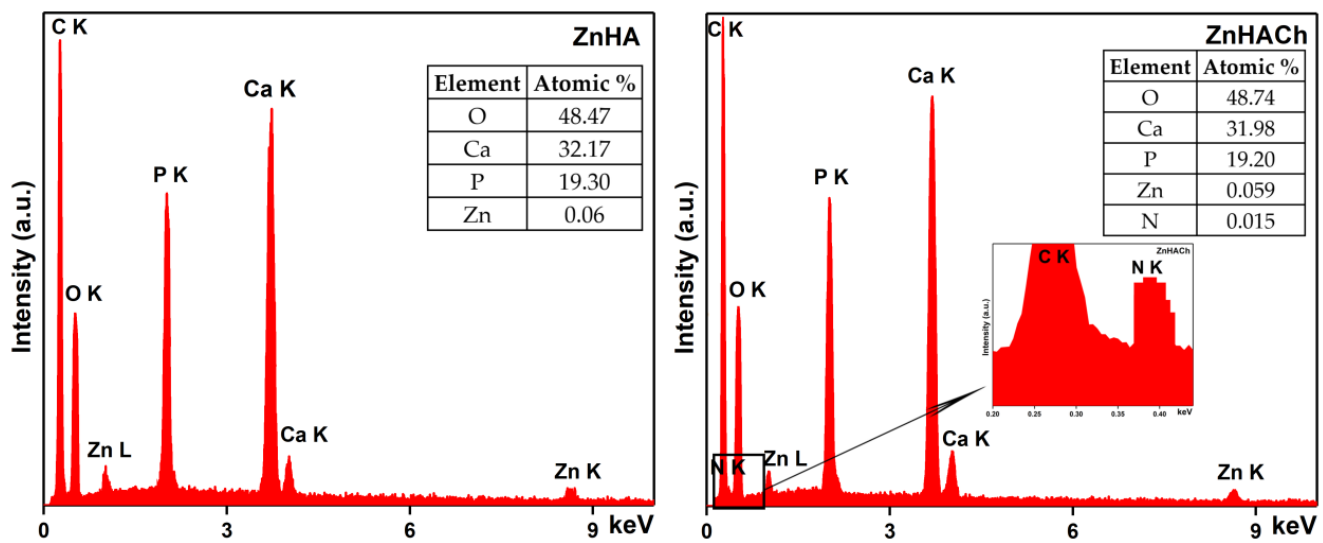


Figure 4. Energy dispersive X-ray spectroscopy (EDX) analysis of ZnHA and ZnHACH samples.

The other lines that are noticed in the EDX spectra of ZnHACH powders belong to the other four chemical elements (calcium, phosphorus, oxygen and zinc) that are specific to ZnHApCh composition. Finally, the results of the studies conducted by energy dispersive x-ray spectroscopy reveal the purity of the obtained samples.

Figure 5 shows the SEM image of ZnHACH with the results of chemical mapping made using SEM. The results of elemental mapping highlight the well spatial distribution of phosphorus (P), calcium (Ca), nitrogen (N), oxygen (O) and zinc (Zn) in the ZnHACH powders. As can be seen in the Figure 5, the mapping images obtained on the studied samples highlight a homogeneous distribution of the main constituents (P, Ca, N, O and Zn).

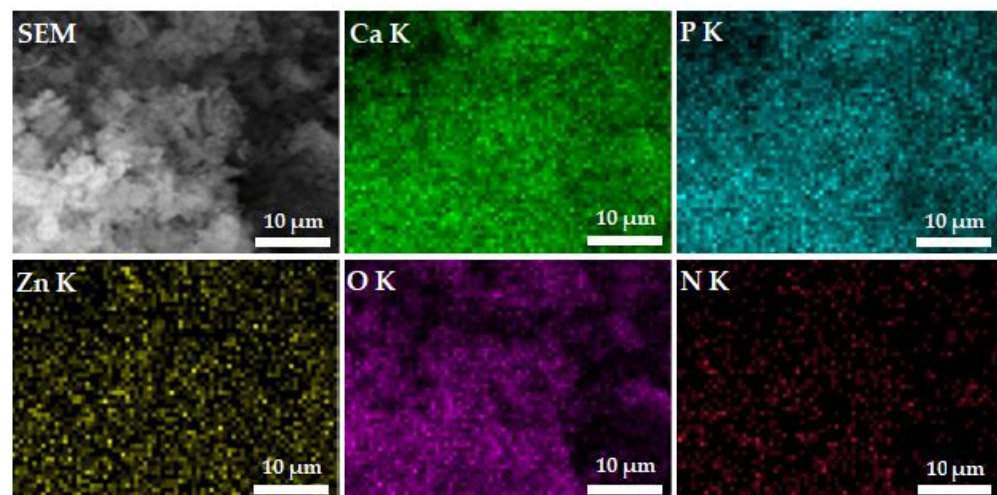


Figure 5. Elemental mapping of ZnHACH powder sample.

The results of FTIR spectral analysis (FTIR spectra and the second derivative spectra in the 450–3650 cm^{-1} spectral region) conducted on ZnHA, ZnHACH and ZnHACHT powders are presented in Figure 6.

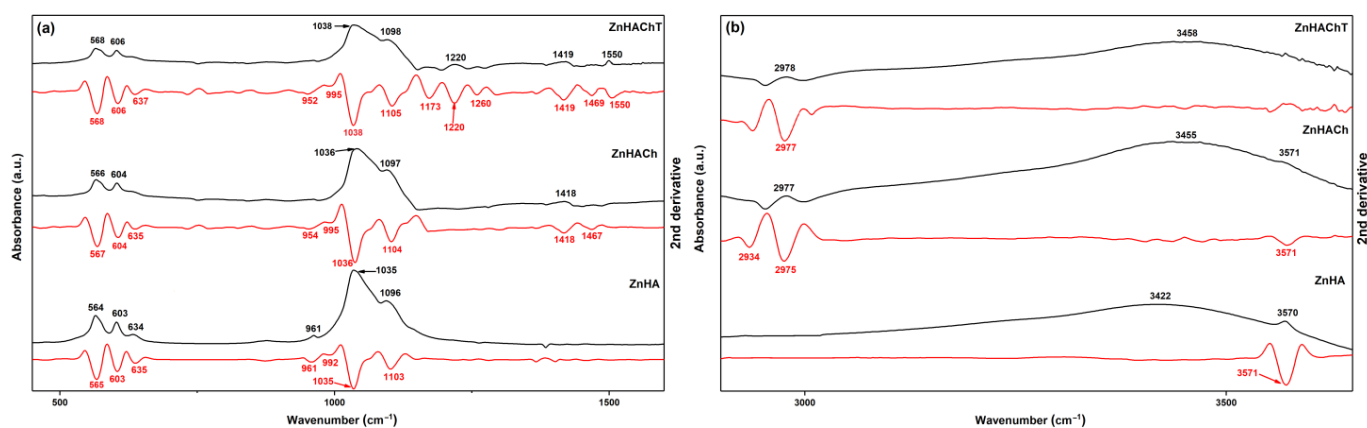


Figure 6. FTIR spectra (black line) and second derivative spectra (red line) characteristic to ZnHA, ZnHACH and ZnHACHT powders in 450–1600 cm^{-1} (a) and 2900–3650 cm^{-1} (b) spectral regions.

In Figure 6, the black line represents the FTIR spectra and the red line represents the second derivative spectra obtained for ZnHA, ZnHACH and ZnHACHT samples. Therefore, the FTIR spectra of ZnHA samples is dominated mainly by the bands that are assigned to the vibrational modes of carbonate, phosphate or hydroxyl groups from the hydroxyapatite (HA) structure. The main bands associated to the bending mode of PO_4^{3-} groups are found at 564 cm^{-1} and 603 cm^{-1} [8,36,37]. The main vibrational band observed at around 634 cm^{-1} belongs to the OH^- librational mode [8]. At around 961 cm^{-1} a maximum that may be attributed to ν_1 vibration of PO_4^{3-} groups [8,36,37] can be noticed. Moreover, in the 1035–1098 cm^{-1} spectral domain peaks characteristic to PO_4^{3-} groups' vibration from the HA structure are present [8,36,37]. At around 873 cm^{-1} could be observed a shoulder specific to the PO_4^{3-} groups' vibration [8,36,37]. In addition, for the ZnHACH sample, besides the presence of the specific vibration bands of ZnHAp presented above, the presence of maxima associated with the presence of chitosan in the 1300–1600 cm^{-1} spectral region is also observed [37]. The presence of the tarragon essential oil in the ZnHACHT powders is underlined by the appearance of new vibration bands (shoulder) around 1220 cm^{-1} and 1550 cm^{-1} that may belong to C–O and C=C stretching in estragole from tarragon essential oil [8,36–40]. Moreover, in the spectral region from 2900 to 3600 cm^{-1} (Figure 6b) can be noticed the presence of maxima that could be associated to the hydroxyl (from HA), amine and C–H vibrations (from chitosan). Therefore, at around 2977 cm^{-1} are observed broad maxima that may be attributed to the C–H asymmetric stretching in CH_3 groups. The large maxima noticed (for all the studied samples) at about 3450 cm^{-1} are specific to the hydroxyl vibration from HA. For the ZnHACH and ZnHACHT samples, the broad maxima specific to the chitosan (N–H vibration) and hydroxyapatite (O–H vibrations) observed between 3300 and 3600 cm^{-1} are overlapped [41].

Furthermore, for a more compressive study of the molecular structure of obtained samples, the second derivative spectra were achieved in the conditions described elsewhere [41]. The red lines from Figure 6 represent the second derivative spectra of ZnHA, ZnHACH and ZnHACHT samples. Between 450 and 1600 cm^{-1} can be observed the maxima that may be attributed to the phosphate groups' vibration (ν_1 , ν_3 and ν_4) [17]. Between 560 and 630 cm^{-1} the maxima that belong to ν_4 of phosphate group are noticed, and between 1000 and 1100 cm^{-1} the presence of maxima associated to the ν_3 vibration of phosphate group is highlighted [41]. Finally, the presence of ν_1 vibration (of phosphate group) is highlighted by the maximum from 961 cm^{-1} . Furthermore, in the case of the second derivative spectra of ZnHACH and ZnHACHT can be noticed the presence of maxima that belong to vibrations specific to chitosan (1300–1600 cm^{-1} , 2934–2977 and around 3571 cm^{-1}) [41] and to tarragon essential oil (at about 1220 cm^{-1} and 1550 cm^{-1}) structure [38–40]. The presence of vibration bands associated with the hydroxyl groups can be noticed at around 637 cm^{-1} and around 3450 cm^{-1} for all the studied samples [8]. It is also observed that

many of the bands specific to the tarragon essential oil structure are overlapped with those of chitosan and even with those of hydroxyapatite. More than that, the presence of chitosan and tarragon essential oil in the samples induce changes in the FTIR spectra. Therefore, it can be noticed that in the case of ZnHACH and ZnHACHT powders, the vibrational bands are wider and less intense compared to those of the ZnHA sample. These features are more pronounced in the case of the ZnHACHT sample. These characteristics of the FTIR spectra obtained for the ZnHACH and ZnHACHT powders suggest that the crystallinity of the ZnHA decreased due to the presence of chitosan and tarragon essential oil in the powders. As can be seen, the results of the FTIR spectral analysis are in concordance with the results of the XRD measurements. Similar behavior (the decrease of the band intensity and their broadening were underlined in the XRD and FTIR spectra) was reported by Danilchenko S.N. et al. [37] in their study entitled “Chitosan–hydroxyapatite composite biomaterials made by a one step co-precipitation method”. All these aspects suggest a decrease in the size of the nanoparticles and, at the same time, a decrease in the degree of crystallinity of the samples due to the chitosan/tarragon essential oil presence in the samples.

Together with the surface, the size of the crystallites have an important role in terms of the response to the bioactivity of the material. Previous studies [42,43] have shown that materials that are less crystalline are more bioresorbable and increase the functions of osteoblasts.

In recent years, due to the increase in pathological conditions of bones, tissue engineering and regenerative medicine were highly employed in the treatment of these conditions [44–50]. For this purpose, over the years, extensive studies were undergone regarding the employment of biocompatible and bioresorbable materials with enhanced biological properties and having controllable degradation and resorption properties in the development of new devices for bone treatment [45,48]. Nowadays, data shows that osteoporosis is a chronic disease that has a strong impact on the general population and is characterized by compromised bone strength that leads to structural changes of the bone that increase the probability of fractures [51–54]. Moreover, even though artificial bone replacement has been used for decades in the treatment of bone defects, the use of prostheses can pose challenges such as infection, aseptic loosening or rejection. Therefore, the research regarding the fabrication of new materials with enhanced biological performance are of great need in order to overcome these challenges [55,56]. Infections associated with implantable devices are one of the main reasons for implant failure and could be caused either by an improper surgical performance or due to the contamination of the surrounding tissues [57]. In this context, the biological characteristics of the ZnHA, ZnHACH and ZnHACHT samples were studied.

The cytotoxicity of the ZnHA, ZnHACH and ZnHACHT was determined using human fetal osteoblast hFOB 1.19 cells by performing in vitro studies. For this purpose, hFOB 1.19 cell suspensions were exposed to the samples for 24 h, and their viability was determined employing the well-known MTT assay. Therefore, the results of the in vitro MTT assays regarding the cell viability of the hFOB 1.19 exposed for 24 h to ZnHA, ZnHACH and ZnHACHT are depicted in Figure 7. The in vitro experiments were done in triplicate and the data was presented as mean \pm Standard Deviation (S.D.). Thus, the results of the MTT studies highlighted that all the investigated biocomposites exhibited strong biocompatible properties after 24 h.

The MTT assay revealed that after 24 h of exposure to the ZnHA, ZnHACH and ZnHACHT samples, the cell viability of the hFOB 1.19 cells was maintained above 92% compared to the control, which emphasizes that the biocomposites present very good biocompatible properties towards hFOB 1.19 cells. Moreover, the results also suggested that the presence of both chitosan and tarragon essential oil as well as the synergies involved in the composite samples contributed to an increase of the cell viability compared to the ZnHA sample. The results are in good concordance with earlier reported studies about the biological properties of hydroxyapatite and hydroxyapatite-based composites [8,58–60].

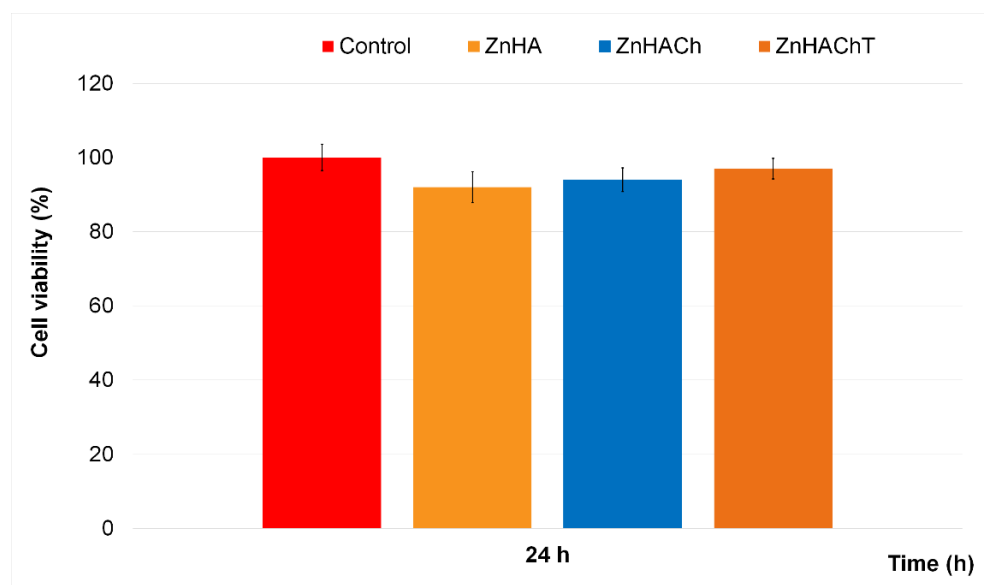


Figure 7. Graphical representation of the MTT assay of the cell viability of hFOB 1.19 cells after 24 h of incubation with ZnHA, ZnHACH and ZnHACHT.

Complex information was also gathered by studying the morphology of the hFOB 1.19 cells exposed for 24 h to ZnHA, ZnHACH and ZnHACHT. The fluorescence microscopy of the hFOB 1.19 cells exposed for 24 h to ZnHA, ZnHACH and ZnHACHT are depicted in Figure 8. The visualization of the hFOB 1.19 cells after 24 h of exposure to ZnHA, ZnHACH and ZnHACHT emphasized that the morphology of the cells was not altered by the presence of the samples. More than that, the fluorescence micrographs also depicted that after 24 h of exposure to the ZnHA, ZnHACH and ZnHACHT biocomposites, the cells still exhibited the normal typical morphology of hFOB 1.19 cells. The results are in agreement with the results provided by the MTT assays which showed that the exposure to the ZnHA, ZnHACH and ZnHACHT for 24 h did not exhibit any toxic effect against the viability of hFOB 1.19 cells. In addition, the fluorescence microscopy images also determined that the investigated samples promoted the proliferation and cell development of hFOB 1.19 cells and also emphasized that the samples favored the cells' spread and their evolution into a layer.

More than that, the results highlighted that the presence of chitosan and tarragon essential oil in the composite materials promoted the cell development and proliferation of hFOB 1.19.

Furthermore, the fluorescence micrographs also showed the presence of both lamellipodia and filopodia, depicted in Figure 8 by green arrows (filopodia) and light blue asterisks (lamellipodia), which strengthen the conclusion that ZnHA, ZnHACH and ZnHACHT possess good biocompatible properties. Usually, the development and proliferation of cells are determined by various parameters such as size and shape of the particles, surface chemistry, roughness, surface chemistry, etc. [61–63]. The initial cell attachment is mediated by thread-like appendages, called filopodia, that extend several micrometers from the cell body to explore the extracellular surface and have the role of anchoring the cell. Filopodia was firstly described in living cells in 1961 by Gustafson and Wolpert [64] and since then have been considered one of the cell's main sensory tools. The presence of lamellipodia and filopodia are strongly correlated with the quality response that cells exhibit to the materials and surface that they were exposed to. Therefore, the presence and extension of numerous lamellipodia and filopodia are typically characteristic of good biocompatibility properties. The results of the cytotoxicity assays as well as the microscopic visualization of the hFOB 1.19 cells exposed for 24 h to ZnHA, ZnHACH and ZnHACHT samples determined that the materials possess high biocompatible properties and that their presence did not induce any morphological changes in the structure of the cells. These results are in concordance with

earlier reported data about the biocompatibility of zinc-doped hydroxyapatite composites materials [65–68]. In their study, Korbut et al. [50], regarding the “three component composite scaffolds based on PCL, hydroxyapatite, and L-lysine obtained in TIPS-SL: bioactive material for bone tissue engineering”, showed that the modification of the scaffolds using hydroxyapatite and L-Lysine conduced to the enhancement of the regenerative potential of the composites and also to an increase of the adhesion of the human osteoblast cells. Moreover, studies conducted by Thian et al. [65] highlighted that the biological properties of hydroxyapatite are influenced by the presence of Zn^{2+} ions in the HA structure. Zinc is a trace element that is actively involved in numerous metabolic processes, and which also activates proteins involved in bone homeostasis [50,68–71]. Zinc is present in a proportion of approximately 30% in bones and plays a key role in bone formation [50,68–71], and bone growth is influenced by the zinc levels present in the bones. The studies performed by Shitole et al. [72] determined that the incorporation of nano-HA and ZnO-NPs into the PCL scaffold greatly improved their osteogenic properties. Moreover, Maimaiti et al. [73] reported that a HA/Zn coating exhibited superior osteogenic properties compared to a pure HA coating. The preliminary results obtained regarding the cytotoxicity of the ZnHA, ZnHACH and ZnHACHT, which correlated with previously reported results, could guide the future development of novel strategies for the obtaining of materials with superior osteogenic activity and improved cytobiocompatibility.

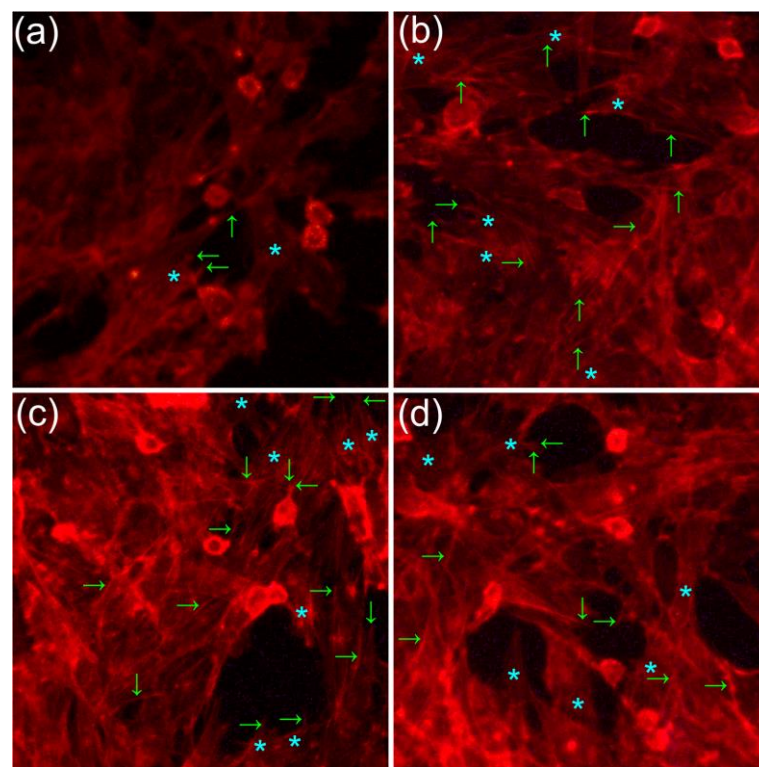


Figure 8. Fluorescence micrographs of primary human osteoblast cells (hFOB 1.19) incubated with ZnHA (b), ZnHACH (c) and ZnHACHT (d) for 24 h comparative to an untreated hFOB 1.19 cell culture used as control (a); green arrows indicate the presence of filopodia and, for the light blue asterisk, the presence of lamellipodia.

In recent years, due to an increase of bone disease affections, mainly caused by population aging and poor medical management of these affections, the incidence of severe cases of infections has increased considerably. The occurrence of implant-related infections is the principal cause of implant failure, and can occur either because of an improper surgical procedure or because of post-operation contamination [74–76], and could lead to great financial burdens to patients, and can cause life-threatening conditions affecting the quality

of life of patients. Therefore, in the last years, there have been tremendous efforts to inhibit at the early stage the microorganism's attachment and proliferation, by developing new materials with antimicrobial properties that might be used as implant coatings. In this context, our study also involved the evaluation of the antimicrobial properties of ZnHA, ZnHACH and ZnHACHT composite materials. The antimicrobial activity of the ZnHA, ZnHACH and ZnHACHT were evaluated against *Escherichia coli* ATCC 25922, *Staphylococcus aureus* ATCC 25923 and *Candida albicans* ATCC 10231 microbial strains. For this aim, the samples were put into contact with the microbial suspensions and their antimicrobial effects were determined after 24, 48 and 72 h. The results of the antimicrobial assays are presented in Figure 9. The data obtained from the antimicrobial assays depicted that all the samples inhibited the development of the microbial strains even after 24 h of incubation. At the same time, the results suggested that the presence of chitosan and tarragon essential oil improved significantly the antimicrobial effects of the biocomposites against the tested microorganisms. The results of the in vitro antimicrobial assays highlighted that the antimicrobial activity of the samples was affected by the incubation time as well as the tested microbial strain. The data showed that the best inhibitory effects were present after 72 h of incubation for both ZnHA and ZnHACH samples. More than that, the results highlighted that the presence of chitosan increased the antimicrobial activity of ZnHA samples.

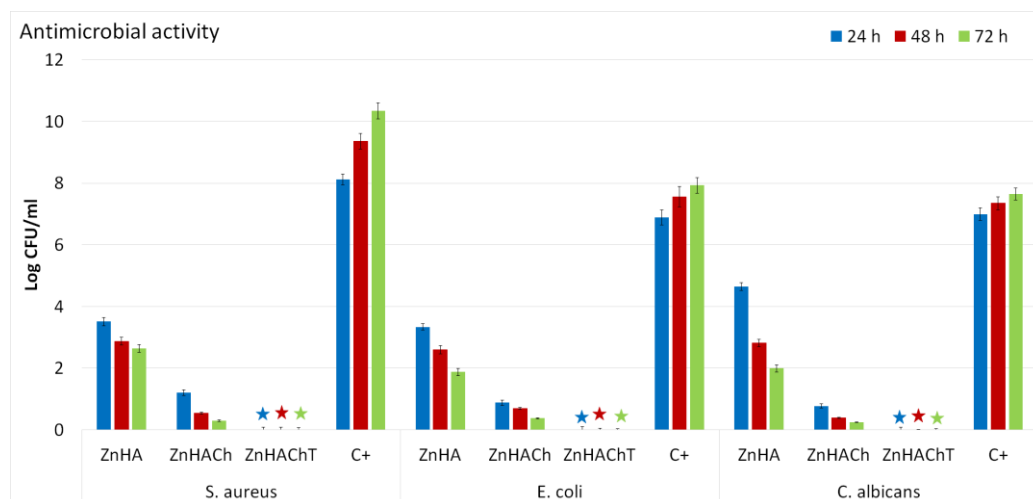


Figure 9. Graphical representation of the antimicrobial activity of ZnHA, ZnHACH and ZnHACHT after 24, 48 and 72 h of exposure to *Staphylococcus aureus* ATCC 25923, *Escherichia coli* ATCC 25922 and *Candida albicans* ATCC 10231.

Furthermore, the results depicted that the presence of chitosan and tarragon essential oil conferred the sample bactericidal and fungicidal effects being able to completely eradicate the microbial strains for all the tested time intervals. The results reported in this paper are in concordance with early reported studies regarding the antimicrobial properties of composite materials and coatings based on hydroxyapatite, zinc ions, chitosan and tarragon essential oils [77–82]. Even though antimicrobial materials have been extensively studied, the exact mechanism responsible for their antimicrobial activity are not yet fully understood. Moreover, the antimicrobial properties of materials are attributed to the properties of their chemical constituents as well as the synergies that appear between them. In addition, the antimicrobial activity is also influenced by numerous parameters such as the type of the microorganism, the shape and size of the particles, the surface chemistry, the state of the material, etc. Furthermore, the metabolism and species of bacteria can also strongly affect the antimicrobial behaviors of various materials. In the case of the ZnHA, ZnHACH and ZnHACHT composites, the antimicrobial properties could be ascribed to the presence of zinc ions, chitosan and tarragon essential oil as well as the synergies that appear in the composite materials due to their constituents. In the case of zinc-doped hydroxyapatite

materials, it is well known that zinc ions play an important role in their antimicrobial properties due to the fact that Zn^{2+} could interfere with cell membrane permeability by combining with functional proteins. If the Zn^{2+} concentration increases in the intracellular space, the interaction that takes place with the thiol group of the enzyme is increased. This phenomenon could disturb the bacterial enzymatic reactions, thus weakening glycolysis and could induce bacterial cell death [83]. Chitosan is a well-known natural polymer that has been proven to possess antimicrobial properties as well as bactericidal activity and was deemed by the United States Food and Drug Administration (FDA) as being GRAS (Generally Recognized as Safe by FDA) [82,84,85]. One of the principal mechanisms deemed to be responsible for the antimicrobial activity of chitosan has been reported as being rendered by the fact that the positive charges resulting from the amino groups of chitosan could interact electrostatically with the negatively charged components of the microbial membranes [86]. In addition to this, other mechanisms by which chitosan molecules could inhibit the growth of microorganisms were also described. One of the accepted possible mechanisms is the ability of chitosan to bind to trace elements and to actively interrupt the nutrients necessary for the growth of microbial cells. Another accepted mechanism insinuates that chitosan molecules could pass through the wall of microbial cells and suppress the synthesis of mRNA by binding to the DNA [87,88]. Furthermore, the antimicrobial properties of plants and plant extracts as well as essential oils are not usually attributed to an individual constituent, but rather to the interaction of the compounds present in their composition. There are reports that indicated there is evidence that the antimicrobial activity of extracts is attributed to the fact that they could make changes to the structure and function of the cell membrane. Studies revealed that extracts and essential oils have the ability to increase the microbial cell's membrane diffusivity, eventually leading to cell death [89]. The mechanism by which essential oil have the ability to inhibit the growth of microorganisms include different modes of action and are mainly attributed to their hydrophobicity. Because of their hydrophobicity, they could easily pass into the lipid bilayer of the microbial cell's membrane, making it more permeable, which usually leads to a leakage of vital cell contents and eventually to cell death [90,91]. Furthermore, another potential antimicrobial mechanism of essential oils was attributed to the fact that the essential oils have the ability to disrupt bacterial enzyme systems [90,91]. In addition, the antimicrobial activity of the essential oils is also defined by their chemical constituents. Essential oils are complex natural mixtures composed of about 20–60 chemical constituents with different concentrations [91]. Usually, essential oils are characterized by two or maybe three major chemical components found in high concentrations (approx. 20–70%) compared to the other chemical components that are present only in trace amounts [91]. Generally, biological properties of the essential oils are determined by their major chemical constituents [92,93]. In the case of our study, the essential oil used to prepare ZnHACHT was French tarragon (*Artemisia dracunculus* L.) and the major chemical constituents of tarragon essential oil were reported to be estragole, sabinene, methyleugenol, *trans*-anethole, limonene, terpinolene, β -ocimene, terpinen-4-ol, α -ocimene and elemicin [19,94–96]. Estragole, also known as methyl chavicol, has been reported to exhibit a broad spectrum of antifungal activities against *Mucor mucedo*, *Aspergillus niger*, *Botryodiplodia theobromae*, *Fusarium solani*, *Candida albicans*, *Rhizopus solani* and *Microsporum gypseum* which were observed to be achieved by causing the disruption of fungal membrane [97]. In the study conducted by Petrosyan et al. [98], the data showed that the tarragon essential oils exhibited stronger antimicrobial effects against gram-positive bacteria and yeasts than against gram-negative ones. Furthermore, in their studies, Raeisi et al. [99] reported that *S. aureus* is more sensitive than *E. coli* to tarragon essential oil. Reza Sharafati Chaleshtori et al. [100], in their studies about the “the evaluation of the antibacterial and antioxidant activity of tarragon (*Artemisia Dracunculus* L.) essential oil and its chemical composition”, determined that the essential oil exhibited different degrees of inhibitory activity against the growth of the tested bacterial strains. Their study concluded that bacterial strains belonging to gram-negative bacteria, especially *Sh. dysenteriae* and *S. marcescens*, were the most sensitive, while *S. aureus* and *L. monocytogenes*, belonging to

gram-positive bacteria, were the most resistant against this essential oil [100]. The preliminary results obtained in our study are in good agreement with previously reported data and also strengthen the hypothesis that the antimicrobial mechanisms of the samples could be influenced both by the constituent chemical elements as well as by the synergies that appear in the composite material. More than that, even if further future complex in vitro and in vivo studies as well as clinical trials are needed to verify the prospective use of composite materials based on hydroxyapatite, zinc, chitosan and tarragon essential as antimicrobial agents, our findings are encouraging and could represent an important stepping stone in the future development of new antimicrobial agents with reduced toxicity, specific antimicrobial mechanism and good osteogenic properties.

4. Conclusions

In this work, we report the synthesis of new biocomposite materials based on zinc-doped hydroxyapatite/chitosan enriched with essential oil of *Artemisia dracuncululus* L. The properties of the obtained samples were investigated using scanning electron microscopy (SEM), X-ray diffraction (XRD), Fourier transform infrared spectroscopy (FTIR) and energy dispersive X-ray spectroscopy (EDX). The XRD results revealed the presence of HA in the samples. The nanometric dimension of the ZnHA was highlighted by the results of both XRD and SEM studies. The purity of the analyzed specimens was demonstrated by the results of EDX analyses. The maxima found in the FTIR spectra belong mainly to the vibration characteristic to the functional groups from HA, chitosan and tarragon essential oil structure.

The cytotoxic activity of the ZnHA, ZnHACH and ZnHACHT was assessed with the aid of the hFOB 1.19 cell line. The results of the MTT assays depicted that the in vitro cell viability was above 92% and reached as high as 97% after 24 h of exposure to the ZnHA, ZnHACH and ZnHACHT. Moreover, the fluorescence micrographs also showed that the samples did not induce any morphological changes in the hFOB 1.19 cells after 24 h of exposure. Furthermore, the fluorescence micrographs showed that after 24 h of exposure to the ZnHA, ZnHACH and ZnHACHT samples, the presence of lamellipodia and filopodia was observed which is characteristic to a good biocompatibility of the tested sample. In addition, the antimicrobial activity of the ZnHA, ZnHACH and ZnHACHT was also evaluated against *Escherichia coli* ATCC 25922, *Staphylococcus aureus* ATCC 25923 and *Candida albicans* ATCC 10231. The results of the antimicrobial assays depicted that all the samples own a strong inhibitory effect against all the tested microbial strains for all the tested time intervals. Moreover, the data suggested that the antimicrobial activity was influenced by both the incubation time as well as the tested microbial strains and the sample. The results highlighted that in the case of ZnHApChT, a bactericidal and fungicidal effect was achieved. These results are promising data for the future development of novel composite materials with enhanced biological properties that could promote the osteogenic process of bone healing and also exhibit antimicrobial properties.

Author Contributions: Conceptualization, D.P. and C.C.; methodology, D.P.; software, D.P., C.S.C. and S.L.I.; validation, D.P., C.S.C., C.C. and S.L.I.; formal analysis, D.P., C.S.C. and S.L.I.; investigation, D.P., C.S.C., S.L.I., R.T., L.G., M.L.B. and M.S.R.; resources, C.C.; data curation, D.P., C.S.C., S.L.I., R.T., L.G., M.L.B. and M.S.R.; writing—original draft preparation, D.P., C.S.C. and S.L.I.; writing—review and editing, D.P., C.S.C., S.L.I., R.T., L.G., M.L.B. and M.S.R.; visualization, D.P., C.C., C.S.C., S.L.I., R.T., L.G., M.L.B. and M.S.R.; supervision, D.P. and C.C.; project administration, D.P.; funding acquisition, C.C. All authors have read and agreed to the published version of the manuscript.

Funding: This research was funded by Faculty of Land Reclamation and Environmental Engineering, University of Agronomic Sciences and Veterinary Medicine of Bucharest.

Institutional Review Board Statement: Not applicable.

Data Availability Statement: Not applicable.

Acknowledgments: The authors would like to thank Faculty of Land Reclamation and Environmental Engineering, University of Agronomic Sciences and Veterinary Medicine of Bucharest for its support with the biological experiments.

Conflicts of Interest: The authors declare no conflict of interest.

References

- Correia, D.M.; Fernandes, L.C.; Fernandes, M.M.; Hermenegildo, B.; Meira, R.M.; Ribeiro, C.; Ribeiro, S.; Reguera, J.; Lanceros-Méndez, S. Ionic Liquid-Based Materials for Biomedical Applications. *Nanomaterials* **2021**, *11*, 2401. [\[CrossRef\]](#) [\[PubMed\]](#)
- Thompson, T. The staggering death toll of drug-resistant bacteria. *Nature*, 2022, *ahead of print*. [\[CrossRef\]](#)
- Gupta, A.; Pratt, R.; Mishra, B. Physicochemical characterization of ferric pyrophosphate citrate. *Biometals* **2018**, *31*, 1091–1099. [\[CrossRef\]](#) [\[PubMed\]](#)
- Subramanian, S.; Kamaraj, Y.; Kumaresan, V.; Kannaiyan, M.; David, E.; Ranganathan, B.; Selvaraj, V.; Balupillai, A. Green synthesized zinc oxide nanoparticles induce apoptosis by suppressing PI3K/Akt/mTOR signaling pathway in osteosarcoma MG63 cells. *Global Transl. Med.* **2022**, *1*, 34. [\[CrossRef\]](#)
- Karahan, M.; Karahan, N.; Ozkan, F.; Yildirim, K. Characterization of Natural Reinforcements and their Composites. *J. Compos. Biodegrad. Polym.* **2021**, *9*, 17–34. [\[CrossRef\]](#)
- Zhao, H.; Jin, H.; Cai, J. Preparation and characterization of nano-hydroxyapatite/chitosan composite with enhanced compressive strength by urease-catalyzed method. *Mater. Lett.* **2014**, *116*, 293–295. [\[CrossRef\]](#)
- Wu, S.; Ma, S.; Zhang, C.; Cao, G.; Wu, D.; Gao, C.; Lakshmanan, S. Cryogel biocomposite containing chitosan-gelatin/cerium-zinc doped hydroxyapatite for bone tissue engineering. *Saudi J. Biol. Sci.* **2020**, *27*, 2638–2644. [\[CrossRef\]](#) [\[PubMed\]](#)
- Predoi, D.; Iconaru, S.L.; Deniaud, A.; Chevallet, M.; Michaud-Soret, I.; Buton, N.; Prodan, A.M. Textural, Structural and Biological Evaluation of Hydroxyapatite Doped with Zinc at Low Concentrations. *Materials* **2017**, *10*, 229. [\[CrossRef\]](#)
- Maleki-Ghaleh, H.; Siadati, M.H.; Fallah, A.; Koc, B.; Kavanlouei, M.; Khademi-Azandehi, P.; Moradpur-Tari, E.; Omid, Y.; Barar, J.; Beygi-Khosrowshahi, Y.; et al. Antibacterial and Cellular Behaviors of Novel Zinc-Doped Hydroxyapatite/Graphene Nanocomposite for Bone Tissue Engineering. *Int. J. Mol. Sci.* **2021**, *22*, 9564. [\[CrossRef\]](#)
- Paterson, T.E.; Shi, R.; Tian, J.; Harrison, C.J.; De Sousa Mendes, M.; Hatton, P.V.; Li, Z.; Ortega, I. Electrospun Scaffolds Containing Silver-Doped Hydroxyapatite with Antimicrobial Properties for Applications in Orthopedic and Dental Bone Surgery. *J. Funct. Biomater.* **2020**, *11*, 58. [\[CrossRef\]](#)
- Franco, D.; Calabrese, G.; Petralia, S.; Neri, G.; Corsaro, C.; Forte, L.; Squarzone, S.; Guglielmino, S.; Traina, F.; Fazio, E.; et al. Antimicrobial Effect and Cytotoxic Evaluation of Mg-Doped Hydroxyapatite Functionalized with Au-Nano Rods. *Molecules* **2021**, *26*, 1099. [\[CrossRef\]](#)
- Vinicius Beserra dos Santos, M.; Bastos Nogueira Rocha, L.; Gomes Vieira, E.; Leite Oliveira, A.; Oliveira Lobo, A.; de Carvalho, M.A.M.; Antevelli Osajima, J.; Cavalcanti Silva-Filho, E. Development of Composite Scaffolds Based on Cerium Doped-Hydroxyapatite and Natural Gums—Biological and Mechanical Properties. *Materials* **2019**, *12*, 2389. [\[CrossRef\]](#)
- Nenen, A.; Maureira, M.; Neira, M.; Orellana, S.L.; Covarrubias, C.; Moreno-Villoslada, I. Synthesis of antibacterial silver and zinc doped nano-hydroxyapatite with potential in bone tissue engineering applications. *Ceram. Int.* **2022**, *48*, 34750–34759. [\[CrossRef\]](#)
- Kazimierzczak, P.; Golus, J.; Kolmas, J.; Wojcik, M.; Kolodnynska, D.; Przekora, A. Noncytotoxic zinc-doped nanohydroxyapatite-based bone scaffolds with strong bactericidal, bacteriostatic, and antibiofilm activity. *Biomater. Adv.* **2022**, *139*, 213011. [\[CrossRef\]](#)
- Rasyida, A.; Wicaksono, S.T.; Pradita, N.N.; Ardhyana, H.; Purnomo, A. Effect of chitosan addition to characteristic and antimicrobial activity of zinc doped hydroxyapatite. *IOP Conf. Ser. Mater. Sci. Eng.* **2017**, *223*, 012063. [\[CrossRef\]](#)
- Tripathi, A.; Saravanan, S.; Pattnaik, S.; Moorthi, A.; Partridge, N.C.; Selvamurugan, N. Bio-composite scaffolds containing chitosan/nano-hydroxyapatite/nano-copper–zinc for bone tissue engineering. *Int. J. Biol. Macromol.* **2012**, *50*, 294–299. [\[CrossRef\]](#) [\[PubMed\]](#)
- Predoi, D.; Iconaru, S.L.; Predoi, M.V. Fabrication of Silver- and Zinc-Doped Hydroxyapatite Coatings for Enhancing Antimicrobial Effect. *Coatings* **2020**, *10*, 905. [\[CrossRef\]](#)
- Muñoz-Bonilla, A.; Echeverria, C.; Sonseca, Á.; Arrieta, M.P.; Fernández-García, M. Bio-Based Polymers with Antimicrobial Properties towards Sustainable Development. *Materials* **2019**, *12*, 641. [\[CrossRef\]](#)
- Hazarika, U.; Kovács, Z.; Bodor, Z.; Gosztola, B. Phytochemicals and organoleptic properties of French tarragon (*Artemisia dracunculus* L.) influenced by different preservation methods. *LWT* **2022**, *169*, 114006. [\[CrossRef\]](#)
- Liu, T.; Lin, P.; Bao, T. Essential oil composition and antimicrobial activity of *Artemisia dracunculus* L. var. *qinghaiensis* Y. R. Ling (Asteraceae) from Qinghai-Tibet Plateau. *Ind. Crops Prod.* **2018**, *125*, 1–4. [\[CrossRef\]](#)
- Fildan, A.P.; Pet, I.; Stoin, D.; Bujanca, G. *Artemisia dracunculus* essential oil chemical composition and antioxidant properties. *Rev. Chim.* **2019**, *70*, 59–62. [\[CrossRef\]](#)
- Farsanipour, A.; Khodanazary, A.; Hosseini, S.M. Effect of chitosan-whey protein isolated coatings incorporated with tarragon *Artemisia dracunculus* essential oil on the quality of *Scomberoides commersonianus* fillets at refrigerated condition. *Int. J. Biol. Macromol.* **2020**, *155*, 766–771. [\[CrossRef\]](#) [\[PubMed\]](#)
- Zedan, H.; Hosseini, S.M.; Mohammadi, A. The effect of tarragon (*Artemisia dracunculus*) essential oil and high molecular weight chitosan on sensory properties and shelf life of yogurt. *LWT* **2021**, *147*, 111613. [\[CrossRef\]](#)

24. Predoi, S.A.; Ciobanu, S.C.; Chifiriuc, M.C.; Motelica-Heino, M.; Predoi, D.; Iconaru, S.L. Hydroxyapatite Nanopowders for Effective Removal of Strontium Ions from Aqueous Solutions. *Materials* **2023**, *16*, 229. [\[CrossRef\]](#) [\[PubMed\]](#)
25. Wang, H.; Yuan, L.; An, J. Crystallographic Characteristics of Hydroxylapatite in Hard Tissues of *Cololabis saira*. *Crystals* **2017**, *7*, 103. [\[CrossRef\]](#)
26. Monshi, A.; Foroughi, M.R.; Monshi, M.R. Modified Scherrer equation to estimate more accurately nano-crystallite size using XRD. *World J. Nano Sci. Eng.* **2012**, *2*, 154–160. [\[CrossRef\]](#)
27. Predoi, D.; Iconaru, S.L.; Buton, N.; Badea, M.L.; Marutescu, L. Antimicrobial activity of new materials based on lavender and basil essential oils and hydroxyapatite. *Nanomaterials* **2018**, *8*, 291. [\[CrossRef\]](#)
28. Predoi, D.; Iconaru, S.-L.; Predoi, M.-V.; Buton, N. Development of Novel Tetracycline and Ciprofloxacin Loaded Silver Doped Hydroxyapatite Suspensions for Biomedical Applications. *Antibiotics* **2023**, *12*, 74. [\[CrossRef\]](#)
29. Gallagher, A.J.; Gundle, R.; Beresford, N.J. Isolation and culture of bone forming cells (osteoblasts) from human bone. *Hum. Cell Cult. Protoc.* **1996**, *2*, 233–263.
30. Predoi, D.; Iconaru, S.L.; Predoi, M.V. Bioceramic Layers with Antifungal Properties. *Coatings* **2018**, *8*, 276. [\[CrossRef\]](#)
31. Sudarsanan, K.; Young, R.A. Significant precision in crystal structural details. Holly Springs hydroxyapatite. *Acta Crystallogr. Sect. B Struct. Crystallogr. Cryst. Chem.* **1969**, *25*, 1534–1543. [\[CrossRef\]](#)
32. Kittel, C. *Introduction to Solid State Physics*, 7th ed.; Wiley: Brisbane, Australia, 1996.
33. Brundavanam, R.K.; Jiang, Z.T.; Chapman, P.; Le, X.T.; Mondinos, N.; Fawcett, D.; Poinern, G.E.J. Effect of dilute gelatine on the ultrasonic thermally assisted synthesis of nano hydroxyapatite. *Ultrason. Sonochem.* **2011**, *18*, 697–703. [\[CrossRef\]](#)
34. Sanosh, K.P.; Chu, M.C.; Balakrishnan, A.; Lee, Y.J.; Kim, T.N.; Cho, S.J. Synthesis of nano hydroxyapatite powder that simulate teeth particle morphology and composition. *Curr. Appl. Phys.* **2009**, *9*, 1459–1462. [\[CrossRef\]](#)
35. LeGeros, R.Z. Biodegradation and bioresorption of calcium phosphate ceramics. *Clin. Mater.* **1993**, *14*, 65–88. [\[CrossRef\]](#)
36. Tiji, S.; Lakrat, M.; Rokni, Y.; Mejdoubi, E.M.; Hano, C.; Addi, M.; Asehraou, A.; Mimouni, M. Characterization and Antimicrobial Activity of *Nigella sativa* Extracts Encapsulated in Hydroxyapatite Sodium Silicate Glass Composite. *Antibiotics* **2022**, *11*, 170. [\[CrossRef\]](#) [\[PubMed\]](#)
37. Danylchenko, S.M.; Kalinkevich, O.V.; Pogorelov, M.V. Chitosan–hydroxyapatite composite biomaterials made by a one step co-precipitation method: Preparation, characterization and in vivo tests. *J. Biol. Phys. Chem.* **2009**, *9*, 119–126. [\[CrossRef\]](#)
38. Osanloo, M.; Sedaghat, M.M.; Sereshti, H.; Rahmani, M.; Saeedi Landi, F.; Amani, A. Chitosan nanocapsules of tarragon essential oil with low cytotoxicity and long-lasting activity as a green nano-larvicide. *J. Nanostruct.* **2019**, *9*, 723–735.
39. Yilmaz, M.T.; Ispirli, H.; Taylan, O.; Dertli, E. A green nano-biosynthesis of selenium nanoparticles with *Tarragon* extract: Structural, thermal, and antimicrobial characterization. *LWT* **2021**, *141*, 110969. [\[CrossRef\]](#)
40. Osanloo, M.; Firoozian, S.; Abdollahi, A.; Hatami, S.; Nematollahi, A.; Elahi, N.; Zarenezhad, E. Nanoemulsion and nanogel containing *Artemisia dracunculus* essential oil; larvicidal effect and antibacterial activity. *BMC Res. Notes* **2022**, *15*, 276. [\[CrossRef\]](#) [\[PubMed\]](#)
41. Predoi, D.; Ciobanu, C.S.; Iconaru, S.L.; Predoi, S.A.; Chifiriuc, M.C.; Raaen, S.; Badea, M.L.; Rokosz, K. Impact of Gamma Irradiation on the Properties of Magnesium-Doped Hydroxyapatite in Chitosan Matrix. *Materials* **2022**, *15*, 5372. [\[CrossRef\]](#)
42. LeGeros, R.Z. Calcium phosphates in oral biology and medicine. *Monogr. Oral. Sci.* **1991**, *15*, 1–201.
43. Prabakaran, K.; Rajeswari, S. Spectroscopic investigations on the synthesis of nano-hydroxyapatite from calcined eggshell by hydrothermal method using cationic surfactant as template. *Spectrochim. Acta A Mol. Biomol. Spectrosc.* **2009**, *74*, 1127–1134. [\[CrossRef\]](#)
44. Howard, D.; Buttery, L.D.; Shakesheff, K.M.; Roberts, S.J. Tissue engineering: Strategies, stem cells and scaffolds. *J. Anat.* **2008**, *213*, 66–72. [\[CrossRef\]](#) [\[PubMed\]](#)
45. Yang, C.; Gao, X.; Younis, M.R.; Blum, N.T.; Lei, S.; Zhang, D.; Luo, Y.; Huang, P.; Lin, J. Non-invasive monitoring of in vivo bone regeneration based on alkaline phosphatase-responsive scaffolds. *Chem. Eng. J.* **2021**, *408*, 127959. [\[CrossRef\]](#)
46. Szustakiewicz, K.; Gazinska, M.; Kryszak, B.; Grzymajło, M.; Pięłowski, J.; Wigłusz, R.J.; Okamoto, M. The influence of hydroxyapatite content on properties of poly(L-lactide)/hydroxyapatite porous scaffolds obtained using thermal induced phase separation technique. *Eur. Polym. J.* **2019**, *113*, 313–320. [\[CrossRef\]](#)
47. Yu, J.; Xu, L.; Li, K.; Xie, N.; Xi, Y.; Wang, Y.; Zheng, X.; Chen, X.; Wang, M.; Ye, X. Zinc-modified calcium silicate coatings promote osteogenic differentiation through TGF- β /Smad pathway and osseointegration in osteopenic rabbits. *Sci. Rep.* **2017**, *7*, 3440. [\[CrossRef\]](#)
48. Gazinska, M.; Krokos, A.; Kobielarz, M.; Włodarczyk, M.; Skibinska, P.; Stepak, B.; Antończak, A.; Morawiak, M.; Płocinski, P.; Rudnicka, K. Influence of hydroxyapatite surface functionalization on thermal and biological properties of poly(L-lactide)- and poly(L-lactide-co-glycolide)-based composites. *Int. J. Mol. Sci.* **2020**, *21*, 6711. [\[CrossRef\]](#) [\[PubMed\]](#)
49. Korbut, A.; Włodarczyk, M.; Rudnicka, K.; Szwed, A.; Płociński, P.; Biernat, M.; Tymowicz-Grzyb, P.; Michalska, M.; Karska, N.; Rodziejewicz-Motowidło, S.; et al. Three Component Composite Scaffolds Based on PCL, Hydroxyapatite, and L-Lysine Obtained in TIPS-SL: Bioactive Material for Bone Tissue Engineering. *Int. J. Mol. Sci.* **2021**, *22*, 13589. [\[CrossRef\]](#)
50. Li, Y.; Yang, Y.; Qing, Y.A.; Li, R.; Tang, X.; Guo, D.; Qin, Y. Enhancing ZnO-NP antibacterial and osteogenesis properties in orthopedic applications: A review. *Int. J. Nanomed.* **2020**, *15*, 6247–6262. [\[CrossRef\]](#)
51. El-Rashidy, A.A.; Roether, J.A.; Harhaus, L.; Kneser, U.; Boccacini, A.R. Regenerating bone with bioactive glass scaffolds: A review of in vivo studies in bone defect models. *Acta Biomater.* **2017**, *62*, 1–28. [\[CrossRef\]](#) [\[PubMed\]](#)



52. Vidal, L.; Kampleitner, C.; Brennan, M.Á.; Hoornaert, A.; Layrolle, P. T Reconstruction of Large Skeletal Defects: Current Clinical Therapeutic Strategies and Future Directions Using 3D Printing. *Front. Bioeng. Biotech.* **2020**, *8*, 61. [\[CrossRef\]](#)
53. Miyakoshi, N. Effects of parathyroid hormone on cancellous bone mass and structure in osteoporosis. *Curr. Pharm. Des.* **2004**, *10*, 2615–2627. [\[CrossRef\]](#)
54. Paterson, A.H. Evaluating bone mass and bone quality in patients with breast cancer. *Clin. Breast Cancer.* **2005**, *5*, S41–S45. [\[CrossRef\]](#) [\[PubMed\]](#)
55. Bose, S.; Sarkar, N. Natural medicinal compounds in bone tissue engineering. *Trends Biotechnol.* **2020**, *38*, 404–417. [\[CrossRef\]](#) [\[PubMed\]](#)
56. Agarwal, R.; Garcia, A.J. Biomaterial strategies for engineering implants for enhanced osseointegration and bone repair. *Adv. Drug. Deliv. Rev.* **2015**, *94*, 53–62. [\[CrossRef\]](#) [\[PubMed\]](#)
57. Abad, C.L.; Haleem, A. Prosthetic joint infections: An update. *Curr. Infect. Dis. Rep.* **2018**, *20*, 15. [\[CrossRef\]](#)
58. Kazimierczak, P.; Benko, A.; Nocun, M.; Przekora, A. Novel chitosan/agarose/hydroxyapatite nanocomposite scaffold for bone tissue engineering applications: Comprehensive evaluation of biocompatibility and osteoinductivity with the use of osteoblasts and mesenchymal stem cells. *Int. J. Nanomed.* **2019**, *14*, 6615–6630. [\[CrossRef\]](#) [\[PubMed\]](#)
59. Yang, C.; Liu, J.; Ren, Q.; Liu, Y.; Zhou, P.; Li, H. Development of Novel Thermal Sprayed Hydroxyapatite-Rare Earth (HA-Re) Coatings for Potential Antimicrobial Applications in Orthopedics. *J. Therm. Spray. Tech.* **2021**, *30*, 886–897. [\[CrossRef\]](#)
60. Ren, F.; Xin, R.; Ge, X.; Leng, Y. Characterization and structural analysis of zinc-substituted hydroxyapatites. *Acta Biomater.* **2009**, *5*, 3141–3149. [\[CrossRef\]](#)
61. Rouahi, M.; Gallet, O.; Champion, E.; Dentzer, J.; Hardouin, P.; Anselme, K. Influence of hydroxyapatite microstructure on human bone cell response. *J. Biomed. Mater.* **2006**, *78*, 222–235. [\[CrossRef\]](#)
62. Ponche, A.; Bigerelle, M.; Anselme, K. Relative influence of surface topography and surface chemistry on cell response to bone implant materials. Part 1: Physico-chemical effects. *Proc. Inst. Mech. Eng. H* **2010**, *224*, 1471–1486. [\[CrossRef\]](#)
63. Mann, V.; Grimm, D.; Corydon, T.J.; Krüger, M.; Wehland, M.; Riwaltdt, S.; Sahana, J.; Kopp, S.; Bauer, J.; Reseland, J.E.; et al. Changes in Human Foetal Osteoblasts Exposed to the Random Positioning Machine and Bone Construct Tissue Engineering. *Int. J. Mol. Sci.* **2019**, *20*, 1357. [\[CrossRef\]](#)
64. Gustafson, T.; Wolpert, L. Cellular mechanisms in the morphogenesis of the sea urchin larva. The formation of arms. *Exp. Cell Res.* **1961**, *22*, 509–520. [\[CrossRef\]](#)
65. Thian, E.S.; Konishi, T.; Kawanobe, Y.; Lim, P.N.; Choong, C.; Ho, B.; Aizawa, M. Zinc-substituted hydroxyapatite: A biomaterial with enhanced bioactivity and antibacterial properties. *J. Mater. Sci. Mater. Med.* **2013**, *24*, 437–445. [\[CrossRef\]](#) [\[PubMed\]](#)
66. Radovanović, Ž.; Veljović, D.; Jokić, B.; Dimitrijević, S.; Bogdanović, G.; Kojić, V.; Petrović, R.; Janačković, D. Biocompatibility and antimicrobial activity of zinc(II)-doped hydroxyapatite, synthesized by a hydrothermal method. *J. Serb. Chem. Soc.* **2012**, *77*, 1787–1798. [\[CrossRef\]](#)
67. Tank, K.P.; Chudasama, K.S.; Thaker, V.S.; Joshi, M.J. Pure and zinc doped nano-hydroxyapatite: Synthesis, characterization, antimicrobial and hemolytic studies. *J. Cryst. Growth* **2014**, *401*, 474–479. [\[CrossRef\]](#)
68. Kambe, T.; Tsuji, T.; Hashimoto, A.; Itsumura, N. The physiological, biochemical, and molecular roles of zinc transporters in zinc homeostasis and metabolism. *Physiol. Rev.* **2015**, *95*, 749–784. [\[CrossRef\]](#) [\[PubMed\]](#)
69. Yamaguchi, M. Role of nutritional zinc in the prevention of osteoporosis. *Mol. Cell Biochem.* **2010**, *338*, 241–254. [\[CrossRef\]](#)
70. Huang, T.; Yan, G.; Guan, M. Zinc Homeostasis in Bone: Zinc Transporters and Bone Diseases. *Int. J. Mol. Sci.* **2020**, *21*, 1236. [\[CrossRef\]](#)
71. Lin, W.; Li, D. Zinc and zinc transporters: Novel regulators of ventricular myocardial development. *Pediatr. Cardiol.* **2018**, *39*, 1042–1051. [\[CrossRef\]](#)
72. Shitole, A.A.; Raut, P.W.; Sharma, N.; Giram, P.; Khandwekar, A.P.; Garnaik, B. Electrospun polycaprolactone/hydroxyapatite/ZnO nanofibers as potential biomaterials for bone tissue regeneration. *J. Mater. Sci. Mater. Med.* **2019**, *30*, 51. [\[CrossRef\]](#)
73. Maimaiti, B.; Zhang, N.; Yan, L.; Luo, J.; Xie, C.; Wang, Y.; Ma, C.; Ye, T. Stable ZnO-doped hydroxyapatite nanocoating for anti-infection and osteogenic on titanium. *Colloids Surf. B Biointerfaces* **2020**, *186*, 110731. [\[CrossRef\]](#)
74. Cassone, A.; Cauda, R. Candida and candidiasis in HIV-infected patients: Where com-mensalism, opportunistic behavior and frank pathogenicity lose their borders. *AIDS* **2012**, *26*, 1457–1472. [\[CrossRef\]](#)
75. Dall, T.M.; Gallo, P.D.; Chakrabarti, R.; West, T.; Semilla, A.P.; Storm, M.V. An aging population and growing disease burden will require a large and specialized health care workforce by 2025. *Health Aff.* **2013**, *32*, 2013–2020. [\[CrossRef\]](#)
76. Papon, N.; Courdavault, V.; Clastre, M.; Bennett, R.J. Emerging and emerged pathogenic Candida species: Beyond the Candida albicans paradigm. *PLoS Pathog.* **2013**, *9*, e1003550. [\[CrossRef\]](#)
77. Król, A.; Pomastowski, P.; Rapińska, K.; Railean-Plugaru, V.; Buszewski, B. Zinc oxide nanoparticles: Synthesis, antiseptic activity and toxicity mechanism. *Adv. Colloid. Interface Sci.* **2017**, *249*, 37–52. [\[CrossRef\]](#) [\[PubMed\]](#)
78. Hirota, K.; Sugimoto, M.; Kato, M.; Tsukagoshi, K.; Tanigawa, T.; Sugimoto, H. Preparation of zinc oxide ceramics with a sustainable antibacterial activity under dark conditions. *Ceram. Int.* **2010**, *36*, 497–506. [\[CrossRef\]](#)
79. Pasquet, J.; Chevalier, Y.; Pelletier, J.; Couval, E.; Bouvier, D.; Bolzinger, M.-A. The contribution of zinc ions to the antimicrobial activity of zinc oxide. *Colloids Surf. A* **2014**, *457*, 263–274. [\[CrossRef\]](#)
80. Zhang, H.; Liang, Y.; Li, X.; Kang, H. Effect of chitosan-gelatin coating containing nano-encapsulated tarragon essential oil on the preservation of pork slices. *Meat Sci.* **2020**, *166*, 108137. [\[CrossRef\]](#)

81. Behbahani, B.A.; Shahidi, F.; Yazdi, F.T.; Mortazavi, S.A.; Mohebbi, M. Antioxidant activity and antimicrobial effect of tarragon (*Artemisia dracunculus*) extract and chemical composition of its essential oil. *J. Food Meas. Charact.* **2017**, *11*, 847–863. [\[CrossRef\]](#)
82. Yan, D.; Li, Y.; Liu, Y.; Li, N.; Zhang, X.; Yan, C. Antimicrobial Properties of Chitosan and Chitosan Derivatives in the Treatment of Enteric Infections. *Molecules* **2021**, *26*, 7136. [\[CrossRef\]](#) [\[PubMed\]](#)
83. Happy, A.; Soumya, M.; Venkat Kumar, S.; Rajeshkumar, S. Mechanistic study on antibacterial action of zinc oxide nanoparticles synthesized using green route. *Chem. Biol. Interact.* **2018**, *286*, 60–70. [\[CrossRef\]](#)
84. Garg, U.; Chauhan, S.; Nagaich, U.; Jain, N. Current Advances in Chitosan Nanoparticles Based Drug Delivery and Targeting. *Adv. Pharm. Bull.* **2019**, *9*, 195–204. [\[CrossRef\]](#) [\[PubMed\]](#)
85. Mo, X.; Cen, J.; Gibson, E.; Wang, R.; Percival, S.L. An open multicenter comparative randomized clinical study on chitosan. *Wound Repair Regen.* **2015**, *23*, 518–524. [\[CrossRef\]](#)
86. Sahariah, P.; Másson, M. Antimicrobial Chitosan and Chitosan Derivatives: A Review of the Structure-Activity Relationship. *Biomacromolecules* **2017**, *18*, 3846–3868. [\[CrossRef\]](#) [\[PubMed\]](#)
87. Elsabee, M.Z.; Abdou, E.S. Chitosan based edible films and coatings: A review. *Mater. Sci. Eng. C Mater. Biol. Appl.* **2013**, *33*, 1819–1841. [\[CrossRef\]](#) [\[PubMed\]](#)
88. Riaz Rajoka, M.S.; Mehresh, H.M.; Wu, Y.; Zhao, L.; Arfat, Y.; Majeed, K.; Anwaar, S. Chitin/chitosan derivatives and their interactions with microorganisms: A comprehensive review and future perspectives. *Crit. Rev. Biotechnol.* **2020**, *40*, 365–379. [\[CrossRef\]](#)
89. Inouye, S.; Takizawa, T.; Yamaguchi, H. Antibacterial activity of essential oils and their major constituents against respiratory tract pathogens by gaseous contact. *J. Antimicrob. Chemother.* **2001**, *47*, 565–573. [\[CrossRef\]](#)
90. Juven, B.J.; Kanner, J.; Schved, F.; Weisslowicz, H. Factors that interact with antimicrobial action of thyme essential oil and its active constituents. *J. Appl. Bacteriol.* **1994**, *76*, 626–631. [\[CrossRef\]](#)
91. Shaaban, H.A. Essential oil as antimicrobial agents: Efficacy, stability, and safety issues for food application. In *Essential Oils-Bioactive Compounds, New Perspectives and Applications*; de Oliveira, M.S., Silva, S., Da Costa, W.A., Eds.; IntechOpen: London, UK, 2020; pp. 1–33. [\[CrossRef\]](#)
92. Pichersky, E.; Noel, J.P.; Dudareva, N. Biosynthesis of plant volatiles: Nature’s diversity and ingenuity. *Science* **2006**, *311*, 808–811. [\[CrossRef\]](#)
93. Betts, T.J. Chemical characterisation of the different types of volatile oil constituents by various solute retention ratios with the use of conventional and novel commercial gas chromatographic stationary phases. *J. Chromatogr. A* **2001**, *936*, 33–46. [\[CrossRef\]](#)
94. Mousavi, M.; Maroufpoor, N.; Valizadegan, O. Fumigant toxicity of tarragon (*Artemisia dracunculus* L.) and dill (*Anethum graveolens* L.) essential oils on different life stages of *Trialeurodes vaporariorum* (Westwood). *Acta Phytopathol. Entomol. Hung.* **2018**, *53*, 29–42. [\[CrossRef\]](#)
95. Obolskiy, D.; Pischel, I.; Fiestel, B.; Glotov, N. *Artemisia dracunculus* L. (tarragon): A critical review of its traditional use, chemical composition, pharmacology, and safety. *J. Agric. Food Chem.* **2011**, *59*, 11367–11384. [\[CrossRef\]](#)
96. Rajabian, A.; Khayyat, M.H.; Emami, S.A.; Tayarani-Najaran, Z.; Oskooie, R.R.; Asili, J. Phytochemical evaluation and antioxidant activity of essential oil, and aqueous and organic extracts of *Artemisia dracunculus*. *J. Nat. Pharm. Prod.* **2017**, *12*, 323–325. [\[CrossRef\]](#)
97. Kumar, V.; Marković, T.; Emerald, M.; Dey, A. Herbs: Composition and Dietary Importance. In *Encyclopedia of Food and Health*; Caballero, B., Finglas, P.M., Toldra, F., Eds.; Elsevier: Amsterdam, The Netherlands, 2016; Volume 3, pp. 332–337.
98. Petrosyan, M.; Sahakyan, N.; Trchounian, A. Chemical composition and antimicrobial potential of essential oil of *Artemisia dracunculus* L., cultivated at high altitude armenian landscape. *Proc. Yerevan State Univ. Chem. Biol.* **2018**, *52*, 116–121. [\[CrossRef\]](#)
99. Raeisi, M.; Tajik, H.; Razavi, R.S.; Maham, M.; Moradi, M.; Hajimohammadi, B.; Naghili, H.; Hashemi, M.; Mehdizadeh, T. Essential oil of tarragon (*Artemisia dracunculus*) antibacterial activity on *Staphylococcus aureus* and *Escherichia coli* in culture media and Iranian white cheese. *Iran. J. Microbiol.* **2012**, *4*, 30–34.
100. Chaleshtori, R.S.; Rokni, N.; Razavilar, V.; Kopaei, M.R. The Evaluation of the Antibacterial and Antioxidant Activity of Tarragon (*Artemisia dracunculus* L.) Essential Oil and Its Chemical Composition. *Jundishapur J. Microbiol.* **2013**, *6*, e7877. [\[CrossRef\]](#)

Disclaimer/Publisher’s Note: The statements, opinions and data contained in all publications are solely those of the individual author(s) and contributor(s) and not of MDPI and/or the editor(s). MDPI and/or the editor(s) disclaim responsibility for any injury to people or property resulting from any ideas, methods, instructions or products referred to in the content.

Article

In Vitro Assessment of Yeasts Strains with Probiotic Attributes for Aquaculture Use

Camelia Filofteia Diguță ^{1,†}, Constanța Mihai ^{2,*}, Radu Cristian Toma ^{1,†} , Carmen Cîmpeanu ² and Florentina Matei ¹ 

¹ Faculty of Biotechnologies, University of Agronomic Sciences and Veterinary Medicine of Bucharest, 59, Mărăști Blvd., District 1, 011464 Bucharest, Romania

² Faculty of Land Reclamation and Environmental Engineering, University of Agronomic Sciences and Veterinary Medicine of Bucharest, 59, Mărăști Blvd., District 1, 011464 Bucharest, Romania

* Correspondence: mihai_tania@yahoo.com

† These authors contributed equally to this work.

Abstract: This study aimed to investigate *in vitro* the probiotic potential of three yeasts strains (BB06, OBT05, and MT07) isolated from agro-food natural sources. Screening was performed, including several functional, technological, and safety aspects of the yeast strains, in comparison to a reference *Saccharomyces boulardii*, to identify the ones with suitable probiotic attributes in aquaculture. The yeast strains were identified by 5.8S rDNA-ITS region sequencing as *Metschnikowia pulcherrima* OBT05, *Saccharomyces cerevisiae* BB06, and *Torulaspora delbrueckii* MT07. All yeast strains were tolerant to different temperatures, sodium chloride concentrations, and wide pH ranges. *S. cerevisiae* BB06 showed a strong and broad antagonistic activity. Moreover, the *S. cerevisiae* strain exhibited a high auto-aggregation ability ($92.08 \pm 1.49\%$) and good surface hydrophobicity to hexane as a solvent (53.43%). All of the yeast strains have excellent antioxidant properties (>55%). The high survival rate in the gastrointestinal tract (GIT) can promote yeast isolates as probiotics. All yeast strains presented a resistance pattern to the antibacterial antibiotics. Non-hemolytic activity was detected. Furthermore, freeze-drying with cryoprotective agents maintained a high survival rate of yeast strains, in the range of 74.95–97.85%. According to the results obtained, the *S. cerevisiae* BB06 strain was found to have valuable probiotic traits.

Keywords: *Saccharomyces*; non-*Saccharomyces*; probiotic properties; safety issue



Citation: Diguță, C.F.; Mihai, C.; Toma, R.C.; Cîmpeanu, C.; Matei, F. In Vitro Assessment of Yeasts Strains with Probiotic Attributes for Aquaculture Use. *Foods* **2023**, *12*, 124. <https://doi.org/10.3390/foods12010124>

Academic Editors: Arun K. Bhunia, Joana S. Amaral, Derek V. Byrne, Theodoros Varzakas, Esther Sendra and Benu P. Adhikari

Received: 10 November 2022

Revised: 18 December 2022

Accepted: 22 December 2022

Published: 26 December 2022



Copyright: © 2022 by the authors. Licensee MDPI, Basel, Switzerland. This article is an open access article distributed under the terms and conditions of the Creative Commons Attribution (CC BY) license (<https://creativecommons.org/licenses/by/4.0/>).

1. Introduction

Fish production in farm aquaculture has increased significantly in the past years. Nevertheless, semi-intensive or intensive production systems have exposed the fish to prolonged stressful conditions with a negative impact on their well-being by suppressing their immunity, thereby increasing the fish's susceptibility to pathogens, all of which can translate into low performance [1–3]. However, the uncontrolled and prolonged application of antibacterial antibiotics to treat bacterial diseases that occur most frequently in the fish leads to significant changes in the microflora of the fish, their accumulation in the tissues [4,5], a decrease in immunity, and the appearance of antibiotic-resistant bacteria, which represent a serious threat [6–9]. The consumption of contaminated fish products could have a negative impact on human health [10,11]. Currently, the use of probiotics has been promoted as a viable, safe alternative method for sustainable aquaculture [5,12–19]. Probiotics are viable microorganisms which, when administered in adequate amounts, provide health benefits to the host [20,21]. Lactic bacteria and *Bacillus* spp. have been the most researched probiotics and widely administered in aquaculture via diet or water, either by themselves, as a mix of different species, or combined with other ingredients such as prebiotics to improve performance and health status of fishes [14,19,22–27]. However, the possible risk to transfer antibiotic resistance genes through bacterial probiotics to

pathogenic bacteria is a threat [28,29]. Recently, yeasts have gained interest as promising probiotics to improve fish health [30–36]. The biotechnological importance of yeasts is well-known by their use as starter cultures in the production of high-value functional food with health benefits [37,38]. Moreover, yeasts have been proposed as an alternative for replacing fish meal, being considered a complex protein source in aquafeeds [39,40]. One of the main advantages of yeasts as probiotics supplements is the resistance to antibacterial antibiotics, which makes them suitable for use during antibiotic treatment. *Saccharomyces cerevisiae* and *S. cerevisiae* var. *boulardii* (or *S. boulardii*) isolated from a wide range of sources are extensively studied yeast species as probiotics [41–44]. *S. cerevisiae* var. *boulardii* was recognized as safe (receiving the Qualified Presumption of Safety “QPS” status) by the European Food Safety Authority (EFSA) and the only market is as probiotic products [45]. Moreover, scientific studies have increased and focused on the isolation and characterization of the new non-*Saccharomyces* probiotic species (e.g., *Debaryomyces hansenii*, *Kluyveromyces lactis*, *K. marxianus*, *Torulaspora delbrueckii*, *Pichia fermentas*, *P. guilliermondii*, *P. kudriavzevii*, and *Yarrowia lipolytica*) [46–52]. In this regard, several review articles describing different selection criteria of probiotics have been published in the past several years [53–58].

Several researchers have observed that the administration of yeast probiotics supplements in fish feed improved growth rate [33–35], feed digestion [30,31,36,58], stress tolerance [33], the immune system [31,36], and disease control [30,32,33,35].

The main objective of this study was the assessment of three *Saccharomyces* and non-*Saccharomyces* yeast strains (BB06, OBT05, and MT07) by *in vitro* testing of their functional and safety properties, as promising probiotic candidates in fish feed.

2. Materials and Methods

2.1. Yeast Strains and Culture Conditions

In this study, a BB06 strain (isolated from grapes), OBT05 strain (isolated from barley), and MT07 strain (isolated from grapes), belonging to the Microorganisms Collection of UASMVB (Bucharest, Romania) were used. A commercial probiotic yeast, *S. cerevisiae* var. *boulardii*, was used as an indicator strain. All strains were stored at -20°C in YPD broth (Scharlau, Barcelona, Spain) containing glycerol (30% *v/v*); initially, yeast strains were reactivated in YEPD Agar (Scharlau, Barcelona, Spain) at 26°C for 24 h.

2.2. Yeasts Identification

Yeast strains were identified according to 5.8S-ITS gene sequencing. Briefly, yeast strains were grown in YEPD broth overnight, and cells were recovered by centrifugation at $5000\times g$ for 10 min. The extraction of fungal DNA was performed using a ZR Fungal/Bacterial DNA kit (Zymo Research, Irvine, CA, USA), and finally quantified with SpectraMax® QuickDrop™ (Molecular Devices, San Jose, CA, USA). PCR amplification of the 5.8S-ITS gene was performed in 50 μL of $10\times$ DreamTaq Green Buffer (including 20 mmol MgCl_2), 0.2 mM of dNTPs, 0.5 μM forward ITS1 primer (5'-TCCGTAGGTGAACCTGCGG-3'), 0.5 μM reverse ITS4 primer (5'-TCCTCCGCTTATTG ATATGC-3'), 0.025 U of DreamTaq DNA Polymerase (Thermo Fisher Scientific Baltics, UAB, Vilnius, Lithuania), and 10 μL of fungal template DNA (10–20 ng/ μL). The PCR was performed in a MultiGene thermal cycler (Labnet International, Inc., Cambridge, UK). The PCR program included initial denaturation at 94°C for 2 min followed by 34 cycles (94°C for 1 min, 55°C for 1 min, 72°C for 2 min), and a final extension at 72°C for 7 min. PCR products were detected by electrophoresis on 2% agarose gel dissolved in TBE $1\times$ running buffer (Tris-borate-EDTA) (VWR International, Vienna, Austria), into which was added 0.5 $\mu\text{g/mL}$ ethidium bromide, and visualized using a GelDoc-It Imaging System (Analytik Jena, Upland, CA, USA). Sequencing was performed at the Cellular and Molecular Immunological Application (CEMIA, Larissa, Greece). The generated sequences were then compared with the available sequences in the NCBI database (National Center for Biotechnology Information) using the BLASTN tool (<https://blast.ncbi.nlm.nih.gov/Blast.cgi/>) (accessed on 8 December 2021) to identify at specie level based on percent identity.

2.3. Testing the Influence of Temperature, pH, and Sodium Chloride (NaCl) on Yeast Growth

All tests were performed in sterile tubes containing 10 mL of YEPD broth. Yeast strains were grown in YEPD broth for 24 h (around 10^7 cells/mL). The cells were harvested by centrifugation at $4000 \times g$ for 5 min at 4 °C and resuspended in 0.9% sterile saline solution. The tested temperatures were 14 °C, 20 °C, and 26 °C. The pH was adjusted to the following different levels: 1.5, 2.5, 3.5, 4.5, 5.5, 6.5, and 7.5. The sodium chloride was tested at different concentrations between 0–3% (*w/v*). The inoculated tubes thus prepared were incubated at 26 °C for the pH and NaCl tests. Yeast growth was evaluated after 24 h of incubation by CFU/mL.

2.4. Auto-Aggregation and Hydrophobicity

Auto-aggregation and hydrophobicity activities were assessed using the methods described by Alkalbani et al. [57] with some modifications. Yeast strains were grown in YEPD broth for 48 h. The cells were harvested by centrifugation at $4000 \times g$ for 5 min at 4 °C and then washed twice with PBS 1× solution (phosphate buffered saline, pH 7.2, VWR International, Vienna, Austria) and adjusted to OD₆₀₀ at 0.6 ± 0.05 (A₀). Then, the absorbance (A_t) was measured at time intervals of 0, 2, 4, and 24 h at the OD₆₀₀. The auto-aggregation activity was calculated using the following Equation (1):

$$\text{Auto-aggregation\%} = \left(1 - \frac{A_t}{A_0}\right) \times 100 \quad (1)$$

The affinity of yeast isolates to hydrocarbons was determined using two solvents, hexane (VWR International, Rosny-sous-Bois, France) and xylene (VWR International, Rosny-sous-Bois, France). Cell suspension (3mL) in PBS (pH 7.2) with 1 mL of solvent were mixed for 2 min. After 1 h incubation at room temperature, the aqueous phase was carefully recovered and the absorbance was measured at OD₆₀₀ (A₁). The hydrophobicity percentage was expressed according to the Equation (2):

$$\text{Hydrophobicity \%} = \left(\frac{A_0 - A_1}{A_0}\right) \times 100 \quad (2)$$

2.5. Antioxidant Activity

Antioxidant activity was calculated according to the method reported by Brand-Williams et al. [59] with some modifications. Briefly, the fresh cell suspension was mixed 1:1 with the DPPH (1,1-Diphenyl-2-Picrylhydrazyl) dissolved in 100 μM methanol solution. The suspension was vortexed vigorously for 2 min and then stored at ambient temperature for 30 min in darkness. The samples were centrifuged at $2000 \times g$ for 5 min and the absorbance was measured at 517 nm. The blank solution was prepared using deionized water. The radical scavenging activity was expressed according to the Equation (3):

$$\text{Scavenging rate (\%)} = \left(\frac{A_{\text{DPPH}} - A_{\text{sample}}}{A_{\text{DPPH}}}\right) \times 100 \quad (3)$$

2.6. Yeast Survival Rate to Gastrointestinal Barriers In Vitro

Yeast survival rate to simulated gastrointestinal barriers was assessed using the method described by Diguță et al. [26] with slight modifications. Overnight cell cultures were centrifuged at $2000 \times g$, for 10 min, washed twice, and resuspended with sterile PBS 1× solution. Simulated artificial gastric juice was prepared by suspending pepsin (0.3% *w/v*) in sterile buffer (PBS 1×) with pH adjusted to 2.0. An aliquot (around 10^7 CFU/mL) of isolate was inoculated into 10 mL of simulated artificial gastric juice and then incubated at 26 °C in aerobic static conditions. Over time, an aliquot was taken at 0 min, 1 h 30 min,

3 h, and 24 h and diluted in PBS solution to evaluate cell viability by pour plating in YEPD Agar. The survival rate was defined as Equation (4):

$$\% \text{ viability} = \left(\frac{\log \text{CFU Nt}}{\log \text{CFU Ni}} \right) \times 100 \quad (4)$$

where Ni and Nt denote the log CFU.mL^{−1} at 0 time and after different time intervals, respectively.

Tolerance to bile salts was also assessed *in vitro*. An aliquot of the overnight cell cultures (around 10⁶ CFU/mL) of each strain was inoculated into 10 mL of YEPD broth (pH 8.0) supplemented with 0.3% bile salts, then incubated at 26 °C in aerobic static conditions for 4 h. Over time, an aliquot was taken at 0, 2, and 4 h intervals and diluted in PBS solution to evaluate cell viability by pour plating in YEPD Agar.

2.7. Antibacterial Activity

Antibacterial activity was evaluated against nine indicator pathogenic bacteria including *Bacillus cereus* ATCC 11778, *Escherichia coli* ATCC 25922, *Enterococcus faecalis* ATCC 29212, *Listeria ivanovii* ATCC 19119, *Listeria monocytogenes* ATCC 7644, *Staphylococcus aureus* ATCC 6538 MSSA (methicillin sensible), *Staphylococcus aureus* ATCC 43300 MRSA (methicillin-resistant), *Pseudomonas aeruginosa* ATCC 9027, and *Proteus vulgaris* ATCC 13315 by the cross-streaking method [60]. All reference bacteria were provided by the American Type Culture Collection (ATCC), (Manassas, VA, USA). Briefly, overnight yeast cultures were inoculated by a single streak in the center of the surface of YEPD Agar plates. After incubation at 26 °C for 48 h, the pathogenic strains were inoculated in a streak perpendicular to the yeast strains and incubated again for 24 h at 30 °C. Antibacterial activity was defined as a clear inhibitory zone formed and measured in millimeters (mm).

2.8. Antibiotic Susceptibility

The antibiotic susceptibility of the yeast strains was evaluated using the Kirby Bauer method, according to CLSI [61]. The following thirteen different antibiotics (BioAnalyse, Ankara, Turkey) were used: Ampicillin (AM-10), Cephalexin (CL-30), Chloramphenicol (C-30), Erythromycin (E-10), Lincomycin (L-10), Nalidixic Acid (NA-30), Vancomycin (VA-10), Clotrimazole (CTM-10), Fluconazole (FLU-10), Itraconazole (ITR-10), Ketoconazole (KCA-10), Miconazole (MCL-10), and Nystatin (NS-100). Briefly, an aliquot (100 µL) of each overnight yeast culture was spread onto YEPD Agar plates and then the antibiotic discs were placed on the surface of agar plates. After the incubation period, the diameters of inhibition zones around the discs were measured using a ruler and the results were expressed as sensitive (>15 mm) or resistant (≤15 mm) according to CLSI [61].

2.9. Catalase and Hemolytic Activity

A drop of the overnight yeast culture was mixed with a drop of 3% hydrogen peroxide on a microscope slide. The appearance of bubbles indicates a positive reaction.

Fresh yeast cultures (10 µL) were spotted on the surface of Columbia Agar with Sheep Blood Plus plates (Oxoid, Hampshire, UK) and incubated at 26 °C, for 48 h. *Staphylococcus aureus* ATCC 43300 was used as a positive control for β-hemolysis. Results are expressed as beta (β) hemolysis (complete lysis of the red blood cells which appears as a clear zone around colonies), alfa (α) hemolysis (partial hemolysis which appears as greenish zone around the colonies), and gamma (γ) hemolysis (no hemolysis). Strains that did not produce any change in the medium (γ-hemolysis) were considered safe.

2.10. Conditioning of Yeast by Freeze-Drying Procedure

Yeast conditioning by a freeze-drying procedure was carried out according to the method described by Diguță et al. [26] with slight modifications. The following three different cryoprotective agents were tested during the lyophilization procedure: glucose, maltodextrin, and sucrose having a final concentration of 5% (*w/v*). Cryoprotectant solutions were prepared by dissolving in distilled water and then sterilized by filtration with

Millipore filters with a pore size of 0.22 µm (Merck, Darmstadt, Germany). Distilled water was used as a control.

The yeast cells (stationary phase) were recovered by centrifugation ($4000 \times g$ for 5 min). The cell pellet was washed twice with PBS 1× buffer (pH 6.5), and resuspended into the protective solution. After being frozen overnight at $-20\text{ }^{\circ}\text{C}$, samples were desiccated in a chamber type freeze-dryer (FreeZone6, LABCONCO, 6 Liter Benchtop Freeze Dry System, Kansas, MO, USA) for 16 h at $-55\text{ }^{\circ}\text{C}$ and 0.3 mbar. Freeze-dried yeast strains were rehydrated with PBS 1× buffer. Viability was measured before and after freeze-drying using the plate counting method. Cell viability was expressed as a percentage using the following Equation (5):

$$\% \text{ viability} = \left(\frac{\log \text{CFU Nt}}{\log \text{CFU Ni}} \right) \times 100 \quad (5)$$

Ni and Nt denote the log CFU.mL^{−1} after and before freeze-drying, respectively.

2.11. Statistical Analysis

All of the experiments were performed in triplicate. The results were expressed as the mean ± standard deviation (SD). The CFU/mL results were converted to log₁₀ CFU/mL. Data analysis was conducted using one-way analysis of variance (ANOVA), followed by the Tukey B test. *p* values below 0.05 were deemed statistically significant. Statistical analysis was carried out using IBM SPSS Statistics for Windows version 28 (IBM Corp., Armonk, NY, USA).

3. Results

3.1. Molecular Identification of Yeast Strains

The yeast strains were identified by 5.8S-ITS region sequencing at the specie level. BLASTN analysis was used for a homology search with different 5.8S-ITS sequences deposited in the NCBI database. The 5.8S-ITS region revealed that the strain BB06 showed 100% identity to *Saccharomyces cerevisiae* (*S. cerevisiae*), strain OBT05 was found to have 98.67% identity with *Metschnikowia pulcherrima* (*M. pulcherrima*), and MT07 showed 100% identity to *Torulaspora delbrueckii* (*T. delbrueckii*), respectively.

The sequences were submitted to the NCBI database under the accession numbers listed in parentheses: *Metschnikowia pulcherrima* OBT05 (OL757481), *Torulaspora delbrueckii* MT07 (OL757482), and *Saccharomyces cerevisiae* BB06 (OL757483).

3.2. Influence of Temperature, pH, and Sodium Chloride (NaCl) on Yeast Growth

Different pH values (1.5, 2.5, 3.5, 4.5, 5.5, 6.5, and 7.5) were investigated to assess the capacity of yeast strains to survive at wide pH ranges. In our study, all yeast strains exhibited high tolerance to the lower pH levels, from 1.5 to 3.5, and maintained optimal growth cells at a pH of 4.5–7.5 (Figure 1a). As regards the tolerance to temperature, the experiments were carried out at 14, 20, and 26 °C, the typical temperatures of fishery water. Yeasts showed a high trend toward growth at lower temperatures (Figure 1b), with an optimum at 26 °C. Furthermore, all the yeast isolates had a high tolerance to NaCl, from 1.0 to 3.0% (*w/v*) (Figure 1c).

3.3. Auto-Aggregation and Hydrophobicity Ability

Auto-aggregation and cell hydrophobicity percentages of yeast strains are presented in Table 1. All yeast strains showed auto-aggregation (%) ranging between $45.70 \pm 1.59\%$ and $60.99 \pm 2.77\%$ after 2 h at 26 °C but, by extending the incubation time, this increased significantly, ranging between $73.44 \pm 1.58\%$ and $92.08 \pm 1.49\%$ after 24 h at 26 °C. The strongest auto-aggregation ability, after 24 h, was recorded for *S. cerevisiae* BB06 ($92.08 \pm 1.49\%$), which is significantly higher than the reference *S. boulardii*. A lower auto-aggregation percentage was observed for *M. pulcherrima* OBT05 ($73.44 \pm 1.58\%$) and *T. delbrueckii* MT07 ($74.14 \pm 0.27\%$) after 24 h.

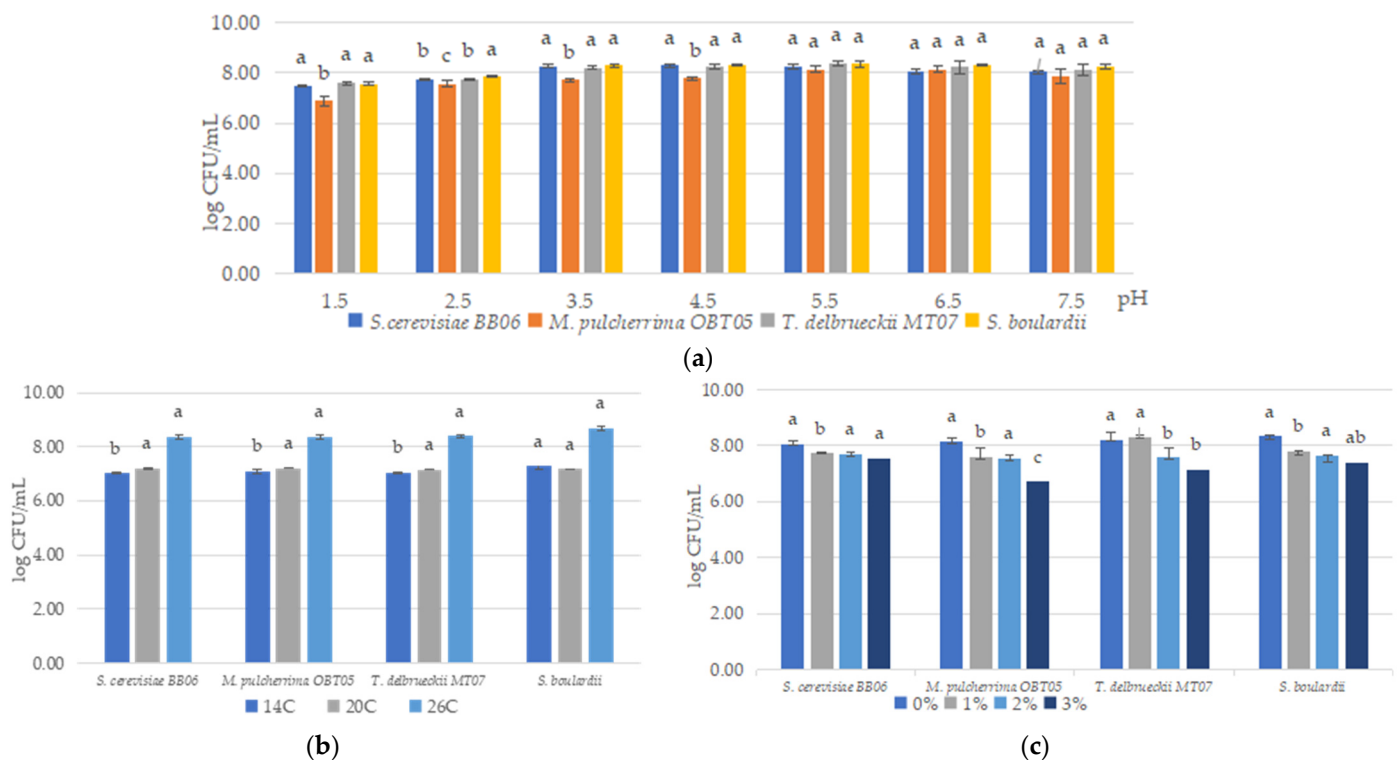


Figure 1. The ability of yeast strains to grow at different abiotic conditions: pH range (a), temperature (b), and NaCl concentration (c). Significant statistical differences ($p < 0.05$) between yeast strains according to the Tukey B test from one-way analysis of variance (ANOVA) have been indicated by different letters.

Table 1. Summarized characteristics and properties of yeast strains: auto-aggregation ability, hydrophobicity, and antioxidant activity.

Yeast Strains	Auto-Aggregation (%)			Hydrophobicity (%)		Antioxidant Activity (%)
	2 h	4 h	24 h	Hexane	Xylene	
<i>S. cerevisiae</i> BB06	60.51 ± 3.03 ^a	81.01 ± 1.35 ^a	92.08 ± 1.49 ^a	53.43 ± 1.09 ^a	24.36 ± 0.36 ^b	55.97 ± 1.62 ^b
<i>M. pulcherrima</i> OBT05	45.70 ± 1.59 ^b	65.88 ± 1.43 ^b	73.44 ± 1.58 ^b	37.76 ± 1.08 ^b	38.08 ± 0.90 ^a	57.14 ± 2.85 ^{ab}
<i>T. delbrueckii</i> MT07	47.24 ± 2.14 ^b	64.68 ± 3.42 ^b	74.14 ± 0.27 ^b	5.93 ± 1.54 ^d	19.03 ± 3.87 ^c	60.61 ± 1.32 ^a
<i>S. boulardii</i>	60.99 ± 2.77 ^a	80.03 ± 0.67 ^a	89.96 ± 1.55 ^a	32.84 ± 3.27 ^c	34.73 ± 0.99 ^a	60.46 ± 0.80 ^a

Results are represented as mean ± SDs of three independent experiments. Significant statistical differences ($p < 0.05$) between yeast strains according to the Tukey B test from one-way analysis of variance (ANOVA) have been indicated by different letters.

Yeast strains revealed low to moderate hydrophobicity in hexane, which ranged between $5.93 \pm 1.54\%$ and $53.43 \pm 1.09\%$, and in xylene, ranging between $19.03 \pm 3.87\%$ and $38.08 \pm 0.90\%$, respectively. *S. cerevisiae* BB06 showed the highest degree of hydrophobicity toward hexane ($53.43 \pm 1.09\%$) compared to reference *S. boulardii* ($32.84 \pm 3.27\%$), and significantly higher than that of the other two yeast strains. Compared with the results reported previously, the hydrophobicity percentage in xylene for *S. cerevisiae* BB06 was lower ($24.36 \pm 0.36\%$), increasing for *T. delbrueckii* MT07 ($19.03 \pm 3.87\%$).

3.4. Antioxidant Properties

The antioxidant activities of yeast cellular suspensions were measured by DPPH assay. The DPPH-free radical-scavenging rate of *T. delbrueckii* MT07 reached $60.61 \pm 1.32\%$, which was similar to reference *S. boulardii* ($60.46 \pm 0.80\%$) and significantly higher than that of the other two strains (Table 1). Moreover, all yeast strains had strong antioxidant properties ($>55\%$) (Table 1).

3.5. Resistance to Gastric Acidity and Bile Salts

The yeast strains were further examined to characterize their survival rates under simulated gastric conditions (pH 2.0 and 0.3% pepsin) (Figure 2a) and growth rates under intestinal fluids (bile salts at 0.3%) (Figure 2b). All yeast strains started the simulation with an average of 7 log CFU/mL.

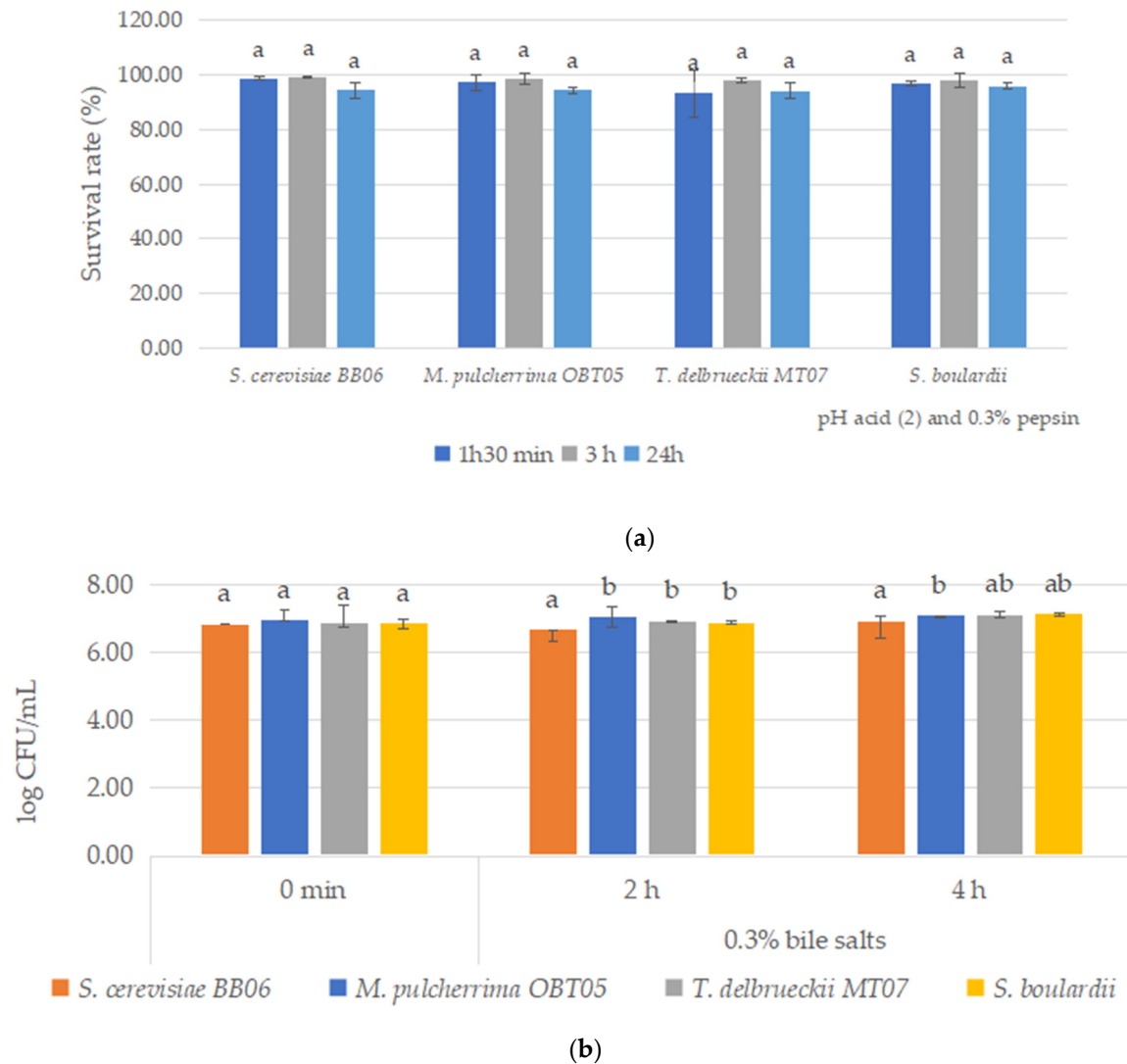


Figure 2. *In vitro* screening of probiotic properties of yeast strains under pH 2.0 and 0.3% pepsin (a) and 0.3% bile salts (b). Results are represented as mean \pm SDs of three independent experiments. Significant statistical differences ($p < 0.05$) between yeast strains according to the Tukey B test from one-way analysis of variance (ANOVA) have been indicated by different letters.

After 90 min of incubation in artificial gastric juice, the four yeast strains showed a high survival rate of between 93.30 and 98.71%; *S. cerevisiae* BB06 was the most resistant, with a survival rate of 98.71% (Figure 2a). After 3 h of incubation, all yeast strains showed an improved tolerance, ranging between 98.01 and 99.32% (Figure 2a). The BB06 strain again exhibited a high rate of 99.32%. However, after 24 h of exposure under simulated gastric conditions, the yeast strains showed a slightly decreased rate of 94.25–95.96%. *S. boulardii* showed a better survival rate of 95.96% (Figure 2a). As regards the tolerance to intestinal conditions, a slight increase of viable cell counts was observed, with 0.09–0.30 log after 4 h of exposure to simulation conditions, which highlighted the high tolerance of all yeast strains at 0.3% bile salts (Figure 2b).

3.6. Antibacterial Properties

The antibacterial properties of yeast strains were explored against the following nine common pathogenic bacteria of fish: Gram-positive (*Bacillus cereus*, *Enterococcus faecalis*, *Listeria ivanovii*, *Listeria monocytogenes*, MSSA, and MRSA *Staphylococcus aureus*), as well as Gram-negative (*Escherichia coli*, *Pseudomonas aeruginosa*, *Proteus vulgaris*). Among the yeast strains used, *S. cerevisiae* BB06 showed high antibacterial activity against all the reference pathogenic bacteria (Figure 3). *M. pulcherrima* OBT05 strain shows relatively low antagonistic activity against several pathogens, namely *Enterococcus faecalis*, *Bacillus cereus*, *Pseudomonas aeruginosa*, *Proteus vulgaris*, and *Listeria monocytogenes*, the greatest inhibitory effect being on *Listeria ivanovii*. The lowest antibacterial activity was presented by the strain *T. delbrueckii* MT07, and against only *Listeria ivanovii*, *Proteus vulgaris*, and *Pseudomonas aeruginosa*. *S. cerevisiae* BB06 presented a higher antagonistic activity than reference *S. boulardii*.

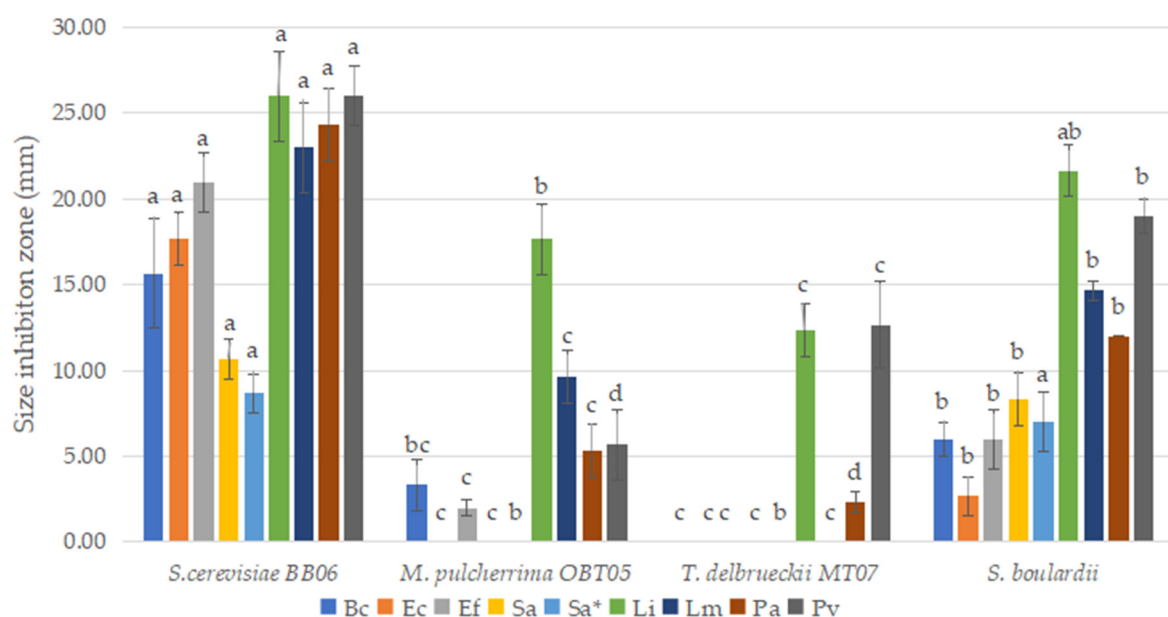


Figure 3. *In vitro* testing of the antibacterial activity of the yeast strains used against *B. cereus* ATCC 11778 (Bc), *E. coli* ATCC 25922 (Ec), *Ent. faecalis* ATCC 29212 (Ef), *L. ivanovii* ATCC 19119 (Li), *L. monocytogenes* ATCC 7644 (Lm), *S. aureus* ATCC 6538 MSSA (methicillin sensible) (Sa), *S. aureus* ATCC 43300 MRSA (methicillin-resistant) (Sa*), *P. aeruginosa* ATCC 9027 (Pa), and *P. vulgaris* ATCC 13315 (Pv). Results are represented as mean \pm SDs of three independent experiments. Significant statistical differences ($p < 0.05$) between yeast strains according to the Tukey B test from one-way analysis of variance (ANOVA) have been indicated by different letters.

3.7. Antibiotic Susceptibility

The antibiotic susceptibility profile of yeast strains to 13 antibacterial and antifungal antibiotics was assessed (Table 2). We found that *S. cerevisiae* BB06, *T. delbrueckii* MT07, and *S. boulardii* showed resistance to all antibiotics used, except nystatin. The *M. pulcherrima* OBT05 strain showed resistance to antibacterial antibiotics and sensitivity to all antifungal antibiotics.

3.8. Catalase and Hemolysis Assay

Concerning catalase activity, all strains were catalase-positive, with *M. pulcherrima* OBT05 and *T. delbrueckii* MT07 exhibiting the highest activity.

Table 2. Safety issues assessment of yeast strains.

Yeast Strains	Catalase Activity	Hemolytic Activity	Antibiotics Susceptibility												
			AM-10	CL-30	C-30	E-10	L-10	NA-30	VA-10	CTM-10	FLU-10	ITR-10	KCA-10	MCL-10	NS-100
<i>cerevisiae</i> BB06	+	Gamma	R	R	R	R	R	R	R	R	R	R	R	R	S
<i>pulcherrima</i> OBT05	++	Gamma	R	R	R	R	R	R	R	S	S	S	S	S	S
<i>delbrueckii</i> MT07	++	Gamma	R	R	R	R	R	R	R	R	R	R	R	R	S
<i>S. boulardii</i>	+	Gamma	R	R	R	R	R	R	R	R	R	R	R	R	S

Legend: +—positive reaction; Gamma (γ) hemolysis; R-resistant; S-sensitive; AM-10 (Ampicillin) CL-30 (Cephalexin), C-30 (Chloramphenicol), E-10 (Erythromycin), L-10 (Lincomycin), NA-30 (Nalidixic Acid), VA-10 (Vancomycin), CTM-10 (Clotrimazole), FLU-10 (Fluconazole), ITR-10 (Itraconazole), KCA-10 (Ketoconazole), MCL-10 (Miconazole) and NS-100 (Nystatin).

Only microbial strains with γ -hemolysis are considered safe, according to EFSA. In our study, all yeast strains showed γ -hemolysis (the greenish or clear area around colonies were not detected), thus strengthening their safety to be used as potential probiotics.

3.9. Conditioning by Lyophilization

Conditioning by lyophilization (or freeze-drying) of yeast strains, using three cryoprotective agents (glucose, maltodextrin, and sucrose in 5% concentration), resulted in obtaining a high percentage of viable yeast cells versus the control (no cryoprotectant), indicating better protection of the cells against stress factors during freeze-drying (Figure 4). High viability (>90%) of *M. pulcherrima* OBT05 and *T. delbrueckii* MT07 strains was observed when the three cryoprotective agents were used (Figure 4). Among the protective substances used, sucrose improved the survival rate of *S. cerevisiae* BB06 and *S. boulardii* (average 85%) more than drying in a medium without cryoprotectants (between 70.25% and 75.87%). Moreover, including only water, the survival rate was higher than 70% for all yeast strains used (Figure 4).

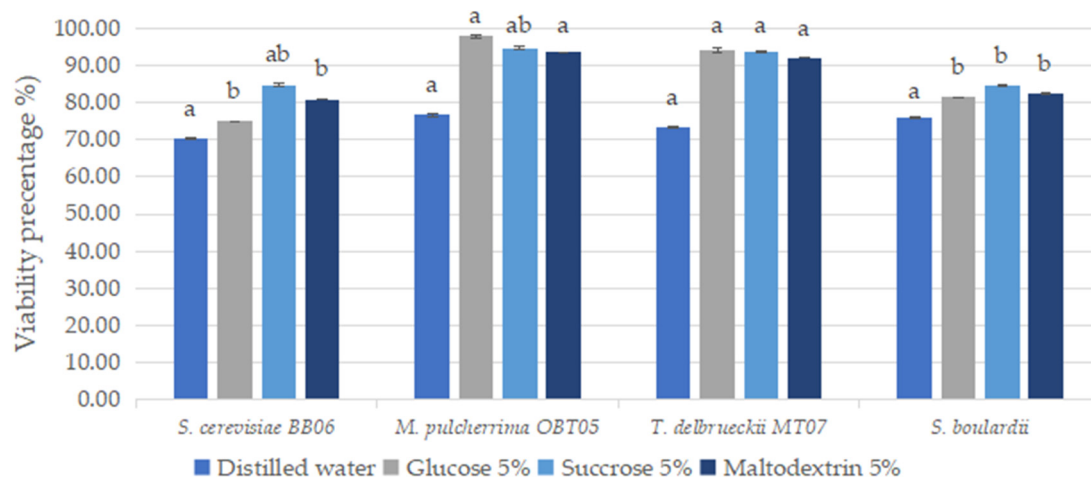


Figure 4. Conditioning by lyophilization of yeast strains with probiotic potential. Results are represented as mean \pm SDs of three independent experiments. Significant statistical differences ($p < 0.05$) between yeast strains according to the Tukey B test from one-way analysis of variance (ANOVA) have been indicated by different letters.

4. Discussion

The biotechnological importance of yeasts is well known by their application as starter cultures in the production of high value functional food with health benefits [37,38,62]. Therefore, there is considerable interest in screening and characterization of new yeasts as potential probiotics. In this study, three yeast strains were isolated from agro-food natural

sources (barley and grapes) and identified through the sequencing of the 5.8S-ITS region. Comparison with sequences deposited in the NCBI database revealed the presence of *Saccharomyces cerevisiae*, *Metschnikowia pulcherrima*, and *Torulaspora delbrueckii*. While *S. cerevisiae* and *S. boulardii* have been intensively studied due to their proven probiotic attributes (reviewed by Łukaszewicz [41]; Palma et al. [42]; Lazo-Vélez et al. [43]; Ansari et al. [44]), *M. pulcherrima* [47,63] and *T. delbrueckii* [47,48,50] have been less investigated.

The next step was to assess *in vitro* the probiotic potential of the yeast strains based on the main selection criteria recommended in various review articles.

We highlighted the ability of yeasts as probiotics to be effective in different environmental conditions such as wide pH ranges, temperature, and salinity variations. In our study, all yeast strains exhibited high tolerance to the lower pH, from 1.5–3.5, and maintained optimal cell growth at a pH of 4.5–7.5. Fishes are ectotherms, which means that their body temperature is influenced by the water temperature in which they are living, whether in the wild or captivity [64,65]. Water temperature can affect the functional activity of probiotics when they are administered as dietary supplements or in rearing water. In our study, it was found that yeast strains can grow at temperatures of 14–20 °C (average 7 log CFU/mL) with optimum growth at 26 °C (average 8 log CFU/mL). Hossain et al. [66] demonstrated the ability of yeast *S. boulardii* to grow at high temperatures of up to 50 °C, with optimum growth at 30 °C. Similar results have been obtained by Fakruddin et al. [67] and Andrade et al. [68]. Salinity stress in aquatic media can affect the survival rate of probiotic bacteria, which limits their application [14]. Yeasts possess certain advantages as compared to probiotic bacteria, such as salt tolerance. Our yeast strains were able to grow and tolerate salt concentrations (1–3%), which supports their use as probiotics in aquatic systems. Previously, Hossain et al. [66] demonstrated the capacity of yeast strains to grow at up to 8.0% NaCl concentration, with a rapid decrease of growth above 3.0% NaCl concentration. Similar results have been obtained by Fakruddin et al. [67] and Andrade et al. [68].

Other relevant probiotic traits have been studied, such as the ability of yeast strains to adhere to epithelial cells (auto-aggregation and hydrophobicity). Yeast strains showed a variable hydrophobic affinity in hexane and xylene and high auto-aggregation ability after extending the incubation time, which is in agreement with previously reported results [66,69].

In addition to functional properties studied for probiotic abilities, it is of interest for fish health to assess the antioxidant capacity. According to their percentage of antioxidant activity, yeast strains have been classified into the following five groups: very low (<20%), low (20–30%), good (30–40%), very good (40–50%), and excellent (>50%) [47]. Based on this classification, the yeasts studied in this work showed excellent antioxidant activity (>55%). Our results are strongly supported by previous studies. Romero-Luna et al. [69] reported that *S. cerevisiae* C41 had excellent antioxidant activity (63.03%), based on the reduction of DPPH radicals. Agarbati et al. [70] reported different *T. delbrueckii* strains possessing high antioxidant activity. However, Fernández-Pacheco et al. [50] reported two *Saccharomyces* strains with antioxidant capacity values of 33.71–32.66%, much lower than our *S. cerevisiae* BB06. In addition, all our yeast strains were positive for catalase. This activity contributes to the defense against reactive species [71].

One of the most desirable properties of probiotics is their antagonistic activity against pathogens. In several studies, the main bacterial pathogens have been identified that are transmitted from fish to humans when improperly cooked or raw fish or contaminated fish products are consumed [10,11]. In our study, *S. cerevisiae* BB06 showed a high broad spectrum of inhibition patterns against the reference Gram-positive and Gram-negative bacterial pathogens (against nine of nine pathogens), followed by *M. pulcherrima* OBT05 (against six of nine pathogens) and *T. delbrueckii* MT07 (against three of nine pathogens), respectively. *S. cerevisiae* BB06 presented high and more broad antagonistic activity than reference *S. boulardii*. Fadahunsi and Olubodun [63] reported that probiotic yeast *M. pulcherrima* showed antibacterial activity against food-borne pathogens such as

Campylobacter jejuni and *Vibrio cholerae*, and different *S. cerevisiae* strains against *Listeria monocytogenes*, *Campylobacter jejuni*, and *Salmonella* sp., respectively. Fakruddin et al. [67] reported that cell lysate of *Saccharomyces cerevisiae* IFST062013 showed better antibacterial activity than the whole cell and culture supernatant whole cells against Gram-positive bacteria (*B. subtilis*, *B. cereus*, *B. polymyxa*, *B. megaterium*, *E. faecalis*, and *S. aureus*,) and Gram-negative bacteria (*E. coli*, *K. pneumoniae*, *S. typhi*, *S. flexneri*, *P. vulgaris*, *P. aeruginosa* and *V. cholerae*). Agarbati et al. [70] reported yeast strains belonging to *Saccharomyces*, *Metschnikowia*, and *Torulaspora* with antimicrobial activity against *Candida albicans*, *E. coli*, *S. aureus*, and *Salmonella enterica*.

A key requirement for potential yeast probiotic strains is to survive in the gastrointestinal tract (GIT). The first challenge is the low acidity in the gastric conditions and our yeast strains successfully survived at pH 2.0 and the presence of 0.3% pepsin (survival rates ranging between 98.01 and 99.32%, after 3 h). We additionally demonstrated (as reported above) that our strains had good growth at 1.5 pH (Figure 1a). After this, bile tolerance is another essential criterion in the characterization of yeast strains as probiotics, because it could allow their growth in the intestinal tract. In our study, all yeast strains had a high ability to tolerate bile salts at 0.3%, after 4 h. Numerous studies have reported the capacity of probiotic yeast strains to tolerate up to 2% bile salts [72–75].

In addition to the studied probiotic properties of the yeast strains, the safety characteristics were evaluated. *S. cerevisiae* BB06, *T. delbrueckii* MT07, and *S. boulardii* showed resistance to antifungal antibiotics, except nystatin. *M. pulcherrima* OBT05 showed susceptibility to all antifungal antibiotics tested. In our study, all yeast strains showed resistance to antibacterial antibiotics, which makes them suitable for use during antibiotic treatment against pathogenic bacteria. No hemolytic activity was detected, which confirms the non-pathogenic character of the yeast strains, which can therefore be considered safe for use as probiotics in fish feed.

The preservation conditioning of probiotic yeasts is a relevant topic to their storage for long periods and maintaining probiotic traits. The most frequently drying methods such as spray-drying, freeze-drying (or lyophilization), vacuum-drying, and a fluidized bed with different upgrades have been used to encapsulate the probiotic preparations and deliver them in the form of dried biomass (reviewed by Frakolaki et al. [76] and Kieps and Dembczyński [77]). Among these techniques, we chose freeze-drying for the preservation of yeast strains in a dry form. In our study, the addition of protective substances such as glucose, maltodextrin, and sucrose (in 5% concentration) protected *M. pulcherrima* OBT05 and *T. delbrueckii* MT07 cells against stress factors during freeze-drying, and were found to be the best cryoprotectants, giving high survival rates (ranging from 91.99% to 97.85%). The survival rates of our yeast strains are much higher than those obtained by Nicolae et al. [78]. In this study, Nicolae et al. [78] reported cells survival rates of 35 and 77% for *S. cerevisiae*, *S. carlsbergensis*, and *Debaryomyces hansenii* mixed with sucrose 10% and gelatin 1.0% after freeze-drying. Arslan et al. [79] studied the effect of different wall materials including carbohydrates and proteins and two temperatures (80 °C and 125 °C) for spray-drying to microencapsulate yeast cells of *S. boulardii*. It was concluded that *S. boulardii* microencapsulated with gelatine and gum arabic displayed greater protection during spray-drying and simulated gastric conditions. Moreover, microencapsulated *S. boulardii* when spray-dried at 125 °C showed higher resistance under *in vitro* gastric conditions.

The promising results obtained in this research study are encouraging, with reference to proceeding with *in vivo* trials to understand the mechanism of action of yeast strains as probiotics. Thus, the use of the *S. cerevisiae* BB06 strain should be established to determine the time required to colonize the gastrointestinal tract of fish and achieve the expected results. Finally, follow-up studies will focus on testing the functional and safety properties of *S. cerevisiae* BB06 to improve fish growth performance, feed digestion, disease control, or improving fish immunity, which will contribute to promote the use of probiotics in aquaculture.

5. Conclusions

Our results showed that the three yeast strains identified based on 5.8S-ITS region sequencing as *Saccharomyces cerevisiae*, *Metschnikowia pulcherrima*, and *Torulaspora delbrueckii* have valuable probiotic attributes in aquatic systems. *In vitro* examination of the influence of environmental conditions (temperature, pH, and salt stress) highlighted the ability of the yeast cells to survive under stressful conditions. High viability in the presence of 0.3% pepsin and low pH (2.0), and 0.3% bile salt, respectively, showed the strong abilities of yeast strains to survive passage through the fish gastrointestinal tract. The ability of yeast strains to respond to oxidative stress was highlighted by the positive results of the catalase test. Yeast isolates also displayed resistance patterns to antibacterial antibiotics and non-hemolytic activity. Overall, all yeast isolates had a strong antioxidant activity (>55%), high autoaggregation (between $73.44 \pm 1.58\%$ and $92.08 \pm 1.49\%$ after 24 h), and different cell surface hydrophobicity values with hexane and xylene (ranging from $5.93 \pm 1.54\%$ to $53.43 \pm 1.09\%$). The obtained results of freeze-drying using sucrose as a cryoprotectant suggested that the yeast strains could be stored as the powdered formula. The BB06 strain showed the best combination of probiotic and healthy properties, which is why it is proposed to be used further for *in vivo* tests by including it in fish feed.

Author Contributions: Conceptualization, F.M. and C.C.; methodology, C.F.D., C.M. and R.C.T.; validation, F.M. and C.F.D.; formal analysis C.M. and C.F.D.; investigation, C.F.D. and R.C.T.; resources, F.M. and C.F.D.; data curation, F.M. and C.F.D.; writing—original draft preparation, C.F.D., C.M. and R.C.T.; writing—review and editing, C.F.D., F.M. and C.C.; visualization, F.M. and C.C.; supervision, C.F.D. and F.M.; project administration, C.M.; funding acquisition, F.M. and C.M. All authors have read and agreed to the published version of the manuscript.

Funding: This research was funded by the University of Agronomic Sciences and Veterinary Medicine of Bucharest—Romania, Research Project 1262/30.07.2021, acronym FEED4FISH in the Competition IPC 2021.

Data Availability Statement: Not applicable.

Acknowledgments: The authors wish to thank Emanuel Vamanu for providing the reference strain *S. boulardii*. Also, special thanks go to Ioan Dopcea for the valuable support in the statistical analysis of data.

Conflicts of Interest: The authors declare no conflict of interest.

References

1. Clavelle, T.; Lester, S.E.; Gentry, R.; Froehlich, H.E. Interactions and management for the future of marine aquaculture and capture fisheries. *Fish Fish.* **2019**, *20*, 368–388. [\[CrossRef\]](#)
2. Deepak, A.; Vasava, R.; Elchelwar, V.; Tandel, D.; Vadher, K.; Shrivastava, V.; Prabhakar, P. Aquamimicry: New an innovative apporoach for sustainable development of aquaculture. *J. Entomol. Zool. Stud.* **2020**, *8*, 1029–1031.
3. Sheng, L.; Wang, L. The microbial safety of fish and fish products: Recent advances in understanding its significance, contamination sources, and control strategies. *Compr. Rev. Food Sci. Food Saf.* **2021**, *20*, 738–786. [\[CrossRef\]](#) [\[PubMed\]](#)
4. Chen, B.Y.; Pyla, R.; Kim, T.J.; Silva, J.L.; Jung, Y.S. Antibiotic resistance in *Listeria* species isolated from catfish fillets and processing environment. *Lett. Appl. Microbiol.* **2010**, *50*, 626–632. [\[CrossRef\]](#) [\[PubMed\]](#)
5. Jamal, M.T.; Sumon, A.A.; Pugazhendhi, A.; Al Harbi, M.; Hussain, A.; Haque, F. Use of probiotics in commercially important finfish aquaculture. *Int. J. Probiot. Prebiot.* **2020**, *15*, 7–21. [\[CrossRef\]](#)
6. Budiati, T.; Rusul, G.; Wan-Abdullah, W.N.; Arip, Y.M.; Ahmad, R.; Thong, K.L. Prevalence, antibiotic resistance and plasmid profiling of *Salmonella* in catfish (*Clarias gariepinus*) and tilapia (*Tilapia mossambica*) obtained from wet markets and ponds in Malaysia. *Aquaculture* **2013**, *372*, 127–133. [\[CrossRef\]](#)
7. Huang, Y.; Zhang, L.; Tiu, L.; Wang, H.H. Characterization of antibiotic resistance in commensal bacteria from an aquaculture ecosystem. *Front. Microbiol.* **2015**, *6*, 914. [\[CrossRef\]](#)
8. Ranjbar, R.; Salighehzadeh, R.; Sharifiyazdi, H. Antimicrobial resistance and incidence of integrons in *Aeromonas* species isolated from diseased freshwater animals and water samples in Iran. *Antibiotics* **2019**, *8*, 198. [\[CrossRef\]](#)
9. Tyagi, A.; Singh, B.; Thammegowda, N.K.B.; Singh, N.K. Shotgun metagenomics offers novel insights into taxonomic compositions, metabolic pathways and antibiotic resistance genes in fish gut microbiome. *Arch. Microbiol.* **2019**, *201*, 295–303. [\[CrossRef\]](#)
10. Novotny, L.; Dvorska, L.; Lorencova, A.; Beran, V.; Pavlik, I. Fish: A potential source of bacterial pathogens for human beings. *Vet. Med.* **2004**, *49*, 343–358. [\[CrossRef\]](#)

11. Ziarati, M.; Zorriehzahra, M.J.; Hassantabar, F.; Mehrabi, Z.; Dhawan, M.; Sharun, K.; Emran, T.B.; Dhama, K.; Chaicumpa, W.; Shamsi, S. Zoonotic diseases of fish and their prevention and control. *Vet. Q.* **2022**, *42*, 95–118. [\[CrossRef\]](#) [\[PubMed\]](#)
12. Nayak, S.K. Probiotics and Immunity: A fish perspective. *Fish Shellfish Immunol.* **2010**, *29*, 2–14. [\[CrossRef\]](#) [\[PubMed\]](#)
13. Tuan, T.N.; Duc, P.M.; Hatai, K. Overview of the use of probiotics in aquaculture. *Int. J. Res. Fish Aquac.* **2013**, *3*, 89–97.
14. Jahangiri, L.; Esteban, M.Á. Administration of Probiotics in the water in finfish aquaculture systems: A review. *Fishes* **2018**, *3*, 33. [\[CrossRef\]](#)
15. Chauhan, A.; Singh, R. Probiotics in aquaculture: A promising emerging alternative approach. *Symbiosis* **2019**, *77*, 99–113. [\[CrossRef\]](#)
16. Hasan, K.N.; Banerjee, G. Recent studies on probiotics as beneficial mediator in aquaculture: A review. *JoBAZ* **2020**, *81*, 53. [\[CrossRef\]](#)
17. Vargas-Albores, F.; Martínez-Córdova, L.R.; Hernández-Mendoza, A.; Cicala, F.; Lago-Lestón, A.; Martínez-Porchas, M. Therapeutic modulation of fish gut microbiota, a feasible strategy for aquaculture? *Aquaculture* **2021**, *544*, 737050. [\[CrossRef\]](#)
18. Yousuf, S.; Tyagi, A.; Singh, R. Probiotic supplementation as an emerging alternative to chemical therapeutics in finfish aquaculture: A Review. *Probiotics Antimicrob. Prot.* **2022**, 1–18. [\[CrossRef\]](#)
19. Ringø, E.; Li, X.; Doan, H.; Ghosh, K. Interesting probiotic bacteria other than the more widely used lactic acid bacteria and bacilli in finfish. *Front. Mar. Sci.* **2022**, *9*, 848037. [\[CrossRef\]](#)
20. FAO/WHO. *Guidelines for the Evaluation of Probiotics in Food*; Food and Agriculture Organization of the United Nations and World Health Organization Working Group Report; FAO: London, ON, Canada, 2002.
21. Hill, C.; Guarner, F.; Reid, G.; Gibson, G.R.; Merenstein, D.J.; Pot, B.; Morelli, L.; Canani, R.B.; Flint, H.J.; Salminen, S.; et al. Expert consensus document: The International Scientific Association for Probiotics and Prebiotics consensus statement on the scope and appropriate use of the term probiotic. *Nat. Rev. Gastroenterol. Hepatol.* **2014**, *11*, 506–514. [\[CrossRef\]](#)
22. Akhter, N.; Wu, B.; Memon, A.M.; Mohsin, M. Probiotics and prebiotics associated with aquaculture: A review. *Fish Shellfish Immunol.* **2015**, *45*, 733–741. [\[CrossRef\]](#) [\[PubMed\]](#)
23. Kuebutornye, F.K.A.; Abarike, E.D.; Lu, Y. A Review on the application of *Bacillus* as probiotics in Aquaculture. *Fish Shellfish Immunol.* **2019**, *87*, 820–828. [\[CrossRef\]](#) [\[PubMed\]](#)
24. Matei, B.; Diguta, C.F.; Matei, F.; Popa, O. Antimicrobial potential of Kombucha bacterial biopolymer. *Sci. Bull. Ser. F Biotechnol.* **2020**, *24*, 133–137.
25. Soltani, M.; Ghosh, K.; Hoseinifar, S.H.; Kumar, V.; Lymbery, A.; Roy, S.; Ringø, E. Genus *Bacillus*, promising probiotics in aquaculture: Aquatic animal origin, bio-active components, bioremediation in fish and shellfish. *Rev. Fish. Sci. Aquac.* **2019**, *27*, 331–379. [\[CrossRef\]](#)
26. Diguță, F.C.; Nițoi, G.D.; Matei, F.; Luță, G.; Cornea, C.P. The Biotechnological potential of *Pediococcus* spp. isolated from Kombucha microbial consortium. *Foods* **2020**, *9*, 1780. [\[CrossRef\]](#)
27. El-Saadony, M.T.; Alagawany, M.; Patra, A.K.; Kar, I.; Tiwari, R.; Dawood, M.A.O.; Dhama, K.; Abdel-Latif, H.M.R. The functionality of probiotics in aquaculture: An overview. *Fish Shellfish Immunol.* **2021**, *117*, 36–52. [\[CrossRef\]](#)
28. Daniali, M.; Nikfar, S.; Abdollahi, M. Antibiotic resistance propagation through probiotics. *Expert Opin. Drug Metab. Toxicol.* **2020**, *16*, 1207–1215. [\[CrossRef\]](#)
29. Li, T.; Teng, D.; Mao, R.; Hao, Y.; Wang, X.; Wang, J. A critical review of antibiotic resistance in probiotic bacteria. *Food Res. Int.* **2020**, *136*, 109571. [\[CrossRef\]](#)
30. Ma, Y.; Liu, Z.; Yang, Z.; Li, M.; Liu, J.; Song, J. Effects of dietary live yeast *Hanseniaspora opuntiae* C21 on the immune and disease resistance against *Vibrio splendidus* infection in juvenile sea cucumber *Apostichopus japonicus*. *Fish Shellfish Immunol.* **2013**, *34*, 66–73. [\[CrossRef\]](#)
31. Navarrete, P.; Tovar-Ramírez, D. Use of yeasts as probiotics in fish aquaculture. *Sustain. Aquac. Tech.* **2014**, *1*, 57196.
32. Sharifuzzaman, S.M.; Austin, B. Probiotics for disease control in aquaculture. In *Diagnosis and Control of Diseases of Fish and Shellfish*; Austin, B., Newaj-Fyzul, A., Eds.; John Wiley & Sons: Hoboken, NJ, USA, 2017; pp. 189–222.
33. Abass, D.A.; Obirikorang, K.A.; Campion, B.B.; Edziyie, R.E.; Skov, P.V. Dietary supplementation of yeast (*Saccharomyces cerevisiae*) improves growth, stress tolerance, and disease resistance in juvenile Nile tilapia (*Oreochromis niloticus*). *Aquac. Int.* **2018**, *26*, 843–855. [\[CrossRef\]](#)
34. Rawling, M.D.; Pontefract, N.; Rodiles, A.; Anagnostara, I.; Leclercq, E.; Schiavone, M.; Castex, M.; Merrifield, D.L. The effect of feeding a novel multistrain yeast fraction on European seabass (*Dicentrarchus labrax*) intestinal health and growth performance. *J. World Aquac. Soc.* **2019**, *50*, 1108–1122. [\[CrossRef\]](#)
35. Banu, M.R.; Akter, S.; Islam, M.R.; Mondol, M.N.; Hossain, M.A. Probiotic yeast enhanced growth performance and disease resistance in freshwater catfish gulsha tengra (*Mystus cavasius*). *Aquac. Rep.* **2020**, *16*, 100237. [\[CrossRef\]](#)
36. Mahdy, M.A.; Jamal, M.T.; Al-Harb, M.; Al-Mur, B.A.; Haque, M.F. Use of yeasts in aquaculture nutrition and immunostimulation: A review. *J. Appl. Biol. Biotech.* **2022**, *10*, 59–65. [\[CrossRef\]](#)
37. Staniszewski, A.; Kordowska-Wiater, M. Probiotic and potentially probiotic yeasts—Characteristics and food application. *Foods* **2021**, *10*, 1306. [\[CrossRef\]](#)
38. Abid, R.; Waseem, H.; Ali, J.; Ghazanfar, S.; Muhammad Ali, G.; Elsbali, A.M.; Alharethi, S.H. Probiotic yeast *Saccharomyces*: Back to nature to improve human health. *J. Fungi* **2022**, *8*, 444. [\[CrossRef\]](#)


39. Glencross, B.D.; Huyben, D.; Schrama, J.W. The application of singlecell ingredients in aquaculture feeds—A review. *Fishes* **2020**, *5*, 22. [[CrossRef](#)]
40. Agboola, J.O.; Øverland, M.; Skrede, A.; Hansen, J.Ø. Yeast as major protein-rich ingredient in aquafeeds: A review of the implications for aquaculture production. *Rev. Aquac.* **2021**, *13*, 949–970. [[CrossRef](#)]
41. Łukaszewicz, M. *Saccharomyces cerevisiae* var. *boulardii*—Probiotic yeast. In *Probiotics*; IntechOpen: London, UK, 2012.
42. Palma, M.L.; Zamith-Miranda, D.; Martins, F.S.; Bozza, F.A.; Nimrichter, L.; Montero-Lomeli, M.; Marques, E.T.A.; Douradinha, B. Probiotic *Saccharomyces cerevisiae* strains as biotherapeutic tools: Is there room for improvement? *Appl. Microbiol. Biotechnol.* **2015**, *99*, 6563–6570. [[CrossRef](#)]
43. Lazo-Vélez, M.A.; Serna-Saldívar, S.O.; Rosales-Medina, M.F.; Tinoco-Alvear, M.; Briones-García, M. Application of *Saccharomyces cerevisiae* var. *boulardii* in food processing: A review. *J. Appl. Microbiol.* **2018**, *125*, 943–951. [[CrossRef](#)]
44. Ansari, F.; Samakkhah, S.A.; Bahadori, A.; Jafari, S.M.; Ziaee, M.; Khodayari, M.T.; Pourjafar, H. Health-promoting properties of *Saccharomyces cerevisiae* var. *boulardii* as a probiotic; characteristics, isolation, and applications in dairy products. *Crit. Rev. Food Sci. Nutr.* **2021**, 1–9. [[CrossRef](#)] [[PubMed](#)]
45. Pais, P.; Almeida, V.; Yilmaz, M.; Teixeira, M.C. *Saccharomyces boulardii*: What makes it tick as successful Probiotic? *J. Fungi* **2020**, *6*, 78. [[CrossRef](#)] [[PubMed](#)]
46. Ochango, H.S.; Gamero, A.; Smith, I.M.; Christensen, J.E.; Jespersen, L.; Arneborg, N. In vitro investigation of *Debaryomyces hansenii* strains for potential probiotic properties. *World J. Microbiol. Biotechnol.* **2016**, *32*, 141. [[CrossRef](#)] [[PubMed](#)]
47. Gil-Rodríguez, A.M.; Carrascosa, A.V.; Requena, T. Yeasts in foods and beverages: In vitro characterisation of probiotic traits. *LWT-Food Sci. Technol.* **2015**, *64*, 1156–1162. [[CrossRef](#)]
48. Rodríguez, P.F.-P.; Arévalo-Villena, M.; Rosa, I.Z.; Perez, A.B. Selection of potential non-*Saccharomyces* probiotic yeasts from food origin by a step-by-step approach. *Food Res. Int.* **2018**, *112*, 143–151. [[CrossRef](#)]
49. Guluarte, C.; Reyes-Becerril, M.; Gonzalez-Silvera, D.; Cuesta, A.; Angulo, C.; Esteban, M.Á. Probiotic properties and fatty acid composition of the yeast *Kluyveromyces lactis* M3. In vivo immunomodulatory activities in gilthead seabream (*Sparus aurata*). *Fish Shelfish Immunol.* **2019**, *94*, 389–397. [[CrossRef](#)]
50. Fernández-Pacheco, P.; Pintado, C.; Briones Pérez, A.; Arévalo-Villena, M. Potential probiotic strains of *Saccharomyces* and non-*Saccharomyces*: Functional and biotechnological characteristics. *J. Fungi* **2021**, *7*, 177. [[CrossRef](#)]
51. Reyes-Becerril, E.; Alamillo, C. Angulo. Probiotic and immunomodulatory activity of marine yeast *Yarrowia lipolytica* strains and response against *Vibrio parahaemolyticus* in fish. *Probiotics Antimicrob. Proteins* **2021**, *13*, 1292–1305. [[CrossRef](#)]
52. Wendy, M.S.; Zachariah, B.C.; Brett, T.H.; Thomas, J.; O'Neill, J.B.; Stephanie, S.B. Evaluation of the ability of *Pichia guilliermondii* to improve growth performance and disease resistance in rainbow trout (*Oncorhynchus mykiss*). *JWAS* **2022**, *3*, 411–423.
53. Shewale, R.N.; Sawale, P.D.; Khedkar, C.D.; Singh, A. Selection criteria for probiotics: A review. *Int. J. Probiotics Prebiotics* **2014**, *9*, 17–22.
54. de Melo Pereira, G.V.; de Oliveira Coelho, B.; Magalhães Júnior, A.I.; Thomaz-Soccol, V.; Soccol, C.R. How to select a probiotic? A review and update of methods and criteria. *Biotechnol. Adv.* **2018**, *36*, 2060–2076. [[CrossRef](#)] [[PubMed](#)]
55. Byakika, S.; Mukisa, I.; Byenkya, Y.; Muyanja, C.; Byenkya Byaruhanga, Y. A review of criteria and methods for evaluating the probiotic potential of microorganisms. *Food Rev. Int.* **2019**, *35*, 427–466. [[CrossRef](#)]
56. Binda, S.; Hill, C.; Johansen, E.; Obis, D.; Pot, B.; Sanders, M.E.; Tremblay, A.; Ouwehand, A.C. Criteria to qualify microorganisms as “probiotic” in foods and dietary supplements. *Front. Microbiol.* **2020**, *11*, 1662. [[CrossRef](#)] [[PubMed](#)]
57. Alkalbani, N.S.; Osaili, T.M.; Al-Nabulsi, A.A.; Olaimat, A.N.; Liu, S.-Q.; Shah, N.P.; Apostolopoulos, V.; Ayyash, M.M. Assessment of yeasts as potential probiotics: A review of gastrointestinal tract conditions and investigation methods. *J. Fungi* **2022**, *8*, 365. [[CrossRef](#)] [[PubMed](#)]
58. Vidakovic, A.; Huyben, D.; Sundh, H.; Nyman, A.; Vielma, J.; Passoth, V.; Kiessling, A.; Lundh, T. Growth performance, nutrient digestibility and intestinal morphology of rainbow trout (*Oncorhynchus mykiss*) fed graded levels of the yeasts *Saccharomyces cerevisiae* and *Wickerhamomyces anomalus*. *Aquac. Nutr.* **2019**, *26*, 275–286. [[CrossRef](#)]
59. Brand-Williams, W.; Cuvelier, M.; Berset, C. Use of a free radical method to evaluate antioxidant activity. *LWT* **1995**, *28*, 25–30. [[CrossRef](#)]
60. Balouiri, M.; Sadiki, M.; Ibsouda, S.K. Methods for *in vitro* evaluating antimicrobial activity: A review. *J. Pharm. Anal.* **2016**, *6*, 71–79. [[CrossRef](#)]
61. CLSI. *CLSI Supplement M100S. Performance Standards for Antimicrobial Susceptibility Testing*, 26th ed.; Clinical and Laboratory Standards Institute: Wayne, PA, USA, 2016.
62. Corbu, V.; Vassu, T.; Csutak, O. *Pichia (Kodamaea) ohmeri* CMGB-ST19-A new strain with complex biotechnological properties. *AgroLife Sci. J.* **2019**, *8*, 77–86.
63. Fadahunsi, I.F.; Olubodun, S. Antagonistic pattern of yeast species against some selected food-borne pathogens. *Bull. Natl. Res. Cent.* **2021**, *45*, 34. [[CrossRef](#)]
64. Djurichkovic, L.D.; Donelson, J.M.; Fowler, A.M.; Feary, D.A.; Booth, D.J. The effects of water temperature on the juvenile performance of two tropical damselfishes expatriating to temperate reefs. *Sci. Rep.* **2019**, *9*, 13937. [[CrossRef](#)]
65. Alfonso, S.; Gesto, M.; Sadoul, B. Temperature increase and its effects on fish stress physiology in the context of global warming. *J. Fish Biol.* **2021**, *98*, 496–1508. [[CrossRef](#)] [[PubMed](#)]

66. Hossain, M.N.; Afrin, S.; Humayun, S.; Ahmed, M.M.; Saha, B.K. Identification and growth characterization of a novel strain of *Saccharomyces boulardii* isolated from soya paste. *Front. Nutr.* **2020**, *7*, 27. [[CrossRef](#)] [[PubMed](#)]
67. Fakruddin, M.; Hossain, M.N.; Ahmed, M.M. Antimicrobial and antioxidant activities of *Saccharomyces cerevisiae* IFST062013, a potential probiotic. *BMC Complement. Altern. Med.* **2017**, *17*, 64. [[CrossRef](#)] [[PubMed](#)]
68. Andrade, R.P.; Oliveira, D.R.; Lopes, A.C.A.; de Abreu, L.R.; Duarte, W.F. Survival of *Kluyveromyces lactis* and *Torulaspora delbrueckii* to simulated gastrointestinal conditions and their use as single and mixed inoculum for cheese production. *Food Res. Int.* **2019**, *125*, 108620. [[CrossRef](#)]
69. Romero-Luna, H.E.; Hernández-Sánchez, H.; Ribas-Aparicio, R.M.; Cauich-Sánchez, P.I.; Dávila-Ortiz, G. Evaluation of the probiotic potential of *Saccharomyces cerevisiae* strain (C41) Isolated from Tibicos by in vitro studies. *Probiotics Antimicrob. Proteins* **2019**, *11*, 794–800. [[CrossRef](#)]
70. Agarbati, L.C.; Marini, E.E.Z.; Ciani, M.F.C. Potential probiotic yeasts sourced from natural environmental and spontaneous processed foods. *Foods* **2020**, *9*, 287. [[CrossRef](#)]
71. Herrero, E.; Ros, J.; Bellí, G.; Cabiscol, E. Redox control and oxidative stress in yeast cells. *Biochim. Biophys. Acta (BBA)-Gen. Subj.* **2008**, *1780*, 1217–1235. [[CrossRef](#)]
72. Czerucka, D.; Piche, T.; Rampal, P. Review article: Yeast as probiotics-*Saccharomyces boulardii*. *Aliment. Pharmacol. Ther.* **2007**, *26*, 767–778. [[CrossRef](#)]
73. Rajkowska, K.; Kunicka-Styczynska, A. Probiotic properties of yeasts isolated from chicken feces and kefir. *Pol. J. Microbiol.* **2010**, *59*, 257–263. [[CrossRef](#)]
74. Syal, P.; Vohra, A. Probiotic potential of yeasts isolated from traditional Indian fermented foods. *Int. J. Microbiol. Res.* **2013**, *5*, 390–398. [[CrossRef](#)]
75. Helmy, E.A.; Soliman, S.A.; Abdel-Ghany, T.M.; Ganash, M. Evaluation of potentially probiotic attributes of certain dairy yeast isolated from buffalo sweetened Karish cheese. *Heliyon* **2019**, *5*, e01649. [[CrossRef](#)] [[PubMed](#)]
76. Frakolaki, G.; Giannou, V.; Kekos, D.; Tzia, C. A review of the microencapsulation techniques for the incorporation of probiotic bacteria in functional foods. *Crit. Rev. Food Sci. Nutr.* **2021**, *61*, 1515–1536. [[CrossRef](#)] [[PubMed](#)]
77. Kieps, J.; Dembczyński, R. Current Trends in the Production of Probiotic Formulations. *Foods* **2022**, *11*, 2330. [[CrossRef](#)] [[PubMed](#)]
78. Nicolae, G.; Dopcea, I.; Nicolae, A.-M.; Stelian, P.; Matei, F. Conservation methods used for yeast isolated from vineyards—Lyophilisation advantage. *Sci. Bull. Biotechnol.* **2010**, *14*, 31–36.
79. Arslan, S.; Erbas, M.; Tontul, I.; Topuz, A. Microencapsulation of probiotic *Saccharomyces cerevisiae* var. *boulardii* with different wall materials by spray drying. *LWT—Food Sci. Technol.* **2015**, *63*, 685–690. [[CrossRef](#)]

Disclaimer/Publisher’s Note: The statements, opinions and data contained in all publications are solely those of the individual author(s) and contributor(s) and not of MDPI and/or the editor(s). MDPI and/or the editor(s) disclaim responsibility for any injury to people or property resulting from any ideas, methods, instructions or products referred to in the content.

Article

Preparation and Characterization of Dextran Coated Iron Oxide Nanoparticles Thin Layers

Gabriel Predoi ^{1,*}, Carmen Steluta Ciobanu ^{2,*}, Simona Liliana Iconaru ² , Daniela Predoi ², Dragana Biliana Dreghici ³, Andreea Groza ³, Florica Barbuceanu ^{1,4}, Carmen Cimpeanu ⁵, Monica-Luminita Badea ^{2,6}, Stefania-Felicia Barbuceanu ⁷, Ciprian Florin Furnaris ¹, Cristian Belu ¹, Liliana Ghegoiu ² and Mariana Stefania Raita ^{1,*}

- ¹ Faculty of Veterinary Medicine, University of Agronomic Sciences and Veterinary Medicine of Bucharest, 105 Splaiul Independentei, Sector 5, 050097 Bucharest, Romania; flori.barbuceanu@yahoo.com (F.B.); ffurnaris@gmail.com (C.F.F.); cristbelu@yahoo.com (C.B.)
- ² Multifunctional Materials and Structures Laboratory, National Institute of Materials Physics, Atomistilor Street, No. 405A, P.O. Box MG 07, 077125 Magurele, Romania; simonaiconaru@gmail.com (S.L.I.); dpredoi@gmail.com (D.P.); monibadea78@gmail.com (M.-L.B.); lilibadea82@yahoo.com (L.G.)
- ³ Low Temperature Plasma Laboratory, National Institute for Laser, Plasma and Radiation Physics, 409 Atomistilor Street, P.O. Box MG 36, 077125 Magurele, Romania; dragana.dreghici@inflpr.ro (D.B.D.); andreeagroza75@gmail.com (A.G.)
- ⁴ Institute for Diagnosis and Animal Health, 63 Staicovici D. Nicolae, Street, 50557 Bucharest, Romania
- ⁵ Faculty of Land Reclamation and Environmental Engineering, University of Agronomic Sciences and Veterinary Medicine of Bucharest, 59 Marasti Blvd, Sector 1, 011464 Bucharest, Romania; carmencimpeanu@yahoo.com
- ⁶ Faculty of Horticulture, University of Agronomic Sciences and Veterinary Medicine, 59 Marasti Blvd., 011464 Bucharest, Romania
- ⁷ Organic Chemistry Department, Faculty of Pharmacy, University of Medicine and Pharmacy, Traian Vuia Street 6, 020956 Bucharest, Romania; stefaniafelicia_barbuceanu@yahoo.com
- * Correspondence: gabrielpredoi2017@gmail.com (G.P.); ciobanucs@gmail.com (C.S.C.); raitastefania@gmail.com (M.S.R.)



Citation: Predoi, G.; Ciobanu, C.S.; Iconaru, S.L.; Predoi, D.; Dreghici, D.B.; Groza, A.; Barbuceanu, F.; Cimpeanu, C.; Badea, M.-L.; Barbuceanu, S.-F.; et al. Preparation and Characterization of Dextran Coated Iron Oxide Nanoparticles Thin Layers. *Polymers* **2021**, *13*, 2351. <https://doi.org/10.3390/polym13142351>

Academic Editors: Dimitrios Bikiaris and Meng-Yi Bai

Received: 2 June 2021

Accepted: 16 July 2021

Published: 18 July 2021

Publisher's Note: MDPI stays neutral with regard to jurisdictional claims in published maps and institutional affiliations.



Copyright: © 2021 by the authors. Licensee MDPI, Basel, Switzerland. This article is an open access article distributed under the terms and conditions of the Creative Commons Attribution (CC BY) license (<https://creativecommons.org/licenses/by/4.0/>).

Abstract: In the present study, we report the synthesis of a dextran coated iron oxide nanoparticles (DIO-NPs) thin layer on glass substrate by an adapted method. The surface morphology of the obtained samples was analyzed by Scanning Electron Microscopy (SEM), Atomic Force Microscopy (AFM), optical, and metallographic microscopies. In addition, the distribution of the chemical elements into the DIO-NPs thin layer was analyzed by Glow Discharge Optical Emission Spectrometry (GDOES). Furthermore, the chemical bonds formed between the dextran and iron oxide nanoparticles was investigated by Fourier Transform Infrared Spectroscopy (FTIR). Additionally, the HepG2 viability incubated with the DIO-NPs layers was evaluated at different time intervals using MTT (3-(4,5-dimethylthiazol-2-yl)-2,5-diphenyltetrazolium bromide) assay. The goal of this study was to obtain a DIO-NPs thin layer which could be used as a coating for medical devices such as microfluidic channel, microchips, and catheter. The results of the surface morphology investigations conducted on DIO-NPs thin layer suggests the presence of a continuous and homogeneous layer. In addition, the GDOES results indicate the presence of C, H, Fe, and O signal intensities characteristic to the DIO-NPs layers. The presence in the IR spectra of the Fe-CO metal carbonyl vibration bonds prove that the linkage between iron oxide nanoparticles and dextran take place through carbon-oxygen bonds. The cytotoxicity assays highlighted that HepG2 cells morphology did not show any noticeable modifications after being incubated with DIO-NPs layers. In addition, the MTT assay suggested that the DIO-NPs layers did not present any toxic effects towards HEpG2 cells.

Keywords: iron oxide; dextran; thin film; glass substrate; polymers; morphology; biocompatibility; glow discharge optical emission spectrometry; MTT assay

1. Introduction

Recently, among the most studied biomaterials due to their special magnetic and biological properties, iron oxide nanoparticles (especially magnetite (Fe_3O_4) and maghemite ($\gamma\text{-Fe}_2\text{O}_3$)) stand out [1,2]. One of the well-known applications of superparamagnetic iron oxide nanoparticles (SPION) is their use as a contrast agent in Magnetic Resonance Imaging (MRI) to visualize liver damage [3]. Previous studies [1] have shown that their unique properties such as high surface area to volume ratios and superparamagnetism (exhibited by particles with a diameter below 30 nm) [4,5] make them suitable for various applications. Therefore, due to their capability to be easily magnetized when they are exposed to the action of an external magnetic field, SPION could be used in various biomedical applications such as: drug and gene delivery [6,7] chelation therapy [8], hyperthermia [9,10], tissue repair [11,12], etc.

The iron oxide nanoparticle's parameters such as shape, size, and properties could be controlled by the synthesis method [1]. SPION can be obtained by various methods of synthesis such as sol-gel, coprecipitation, thermal decomposition, hydrothermal method, etc. [5,13]. Co-precipitation synthesis is among the most used because it is a cheap and efficient method that allows the easy obtaining of superparamagnetic iron oxide nanoparticles [13]. In general, to prevent the agglomeration of nanoparticles and to improve their colloidal stability and biological properties, they are incorporated into polymers (chitosan, dextran, poly(vinyl alcohol)—PVA, gelatin, polyvinylpyrrolidone (PVP), etc.) [6,13–16]. Dextran, $(\text{H}(\text{C}_6\text{H}_{10}\text{O}_5)_x\text{OH})$, is one of the most widely used natural polysaccharides used as a coating for SPION [1]. In addition, dextran has antithrombotic and anticoagulant properties, it is nontoxic, and exhibits a good bioaffinity [1,17–19]. Therefore, the iron oxide–dextran composite (thin films and nanoparticles) are of great interest for biomedical applications, due to their superior biological properties.

A study conducted by A.K. Hauser et al. [20] highlighted that the stability in the PBS (Phosphate buffered saline solution) medium of dextran coated iron oxide nanoparticle is influenced by the amount of dextran used in synthesis. In addition, it was noticed that the synthesis method of dextran coated iron oxide nanoparticles greatly affects the physic-chemical properties of the samples [20]. Therefore, currently iron oxide–dextran compounds (crosslinked iron oxides (CLIO)) are being studied by a large number of researchers around the world, and the results obtained so far are encouraging, indicating that this type of compound could be used as a contrast agent in MRI [3,21]. In general, iron oxide layers can be obtained by various deposition methods (for example: DC-pulsed magnetron, electrodeposition, pulsed laser deposition, chemical vapor deposition, chemical spray pyrolysis technique, etc.) [22]. On the other hand, for the deposition of layers based on iron oxide / polymer, methods such as Matrix Assisted Pulsed Laser Evaporation (MAPLE), dip coating, spin coating, etc. could be used [23,24]. Encouraging results have been obtained by using SPION as a coating for medical devices due to the inhibition of microbial colonization induced by the presence of superparamagnetic iron oxide nanoparticles [25]. Thus, it is of real interest to obtain thin layers of magnetic materials. Previous studies conducted by Prodan and co-workers showed that the antimicrobial activity of iron oxide nanoparticles is influenced on the one hand by the iron concentration and on the other hand by the microbial growth state [26]. Moreover, a good biocompatibility with HepG2 cell line of dextran coated maghemite thin films was noticed [27]. Our previous studies reported the obtaining and characterization of iron oxide–dextran thin films on various substrates by various methods [23,24,27,28]. However, it is not yet fully understood how iron oxide nanoparticles interact with dextran and, on the other hand, further studies are needed to understand how the morphology of the layers influences the biological properties of the dextran coated iron oxides nanoparticles' (DIO-NPs) thin layer. Therefore, on the one hand, iron oxide nanoparticles coated with dextran could be used as a contrast agent, drug carrier, etc. [29], while dextran-coated iron oxide layers could be used to cover prosthetic devices, medical surfaces, etc. [30]. The goal of this study was to obtain a DIO-NPs thin layer which could be used as a coating for medical devices/surfaces.

The novelty of this complex study consists of conducting, for the first time, a study regarding the surface morphology of the DIO-NPs layers for biomedical applications. For this purpose, four microscopy techniques were used (optical, metallographic, SEM, and AFM microscopy) which provided complete information on the surface morphology.

In this context, the main purpose of this study was to investigate the morphology and biocompatible properties of a dextran coated iron oxides nanoparticles (DIO-NPs) thin layer prepared by an adapted method. The morphology of the obtained thin films was analyzed using optical, metallographic examinations, scanning electron microscopy (SEM), and atomic force microscopy (AFM). In addition, Glow Discharge Optical Emission Spectrometry (GDOES) was used in order to study the distribution of the chemical elements into the bulk layer. Information regarding the vibrational properties of a dextran coated iron oxides nanoparticles (DIO-NPs) thin layer were obtained by Fourier-transform infrared spectroscopy (FTIR). Furthermore, the HepG2 viability incubated with the DIO-NPs layers was evaluated at 24, 48, and 72 h using the standard colorimetric MTT (3-(4,5-dimethylthiazol-2-yl)-2,5-diphenyltetrazolium bromide) assay.

2. Materials and Methods

2.1. Materials

In order to develop the dextran coated iron oxide nanoparticles (DIO-NPs) thin layer, the starting materials such as dextran, $\text{H}(\text{C}_6\text{H}_{10}\text{O}_5)_x\text{OH}$, (Dextran from *Leuconos-toc mesenteroides*, MW~40,000, Sigma, Darmstad, Germany), ferric chloride hexahydrate ($\text{FeCl}_3 \cdot 6\text{H}_2\text{O}$, 97%, Sigma Aldrich, Darmstad, Germany), ferrous chloride tetrahydrate ($\text{FeCl}_2 \cdot 4\text{H}_2\text{O}$, $\geq 99\%$, Sigma Aldrich, Darmstad, Germany), sodium hydroxide (NaOH , $\geq 97.0\%$, pellets, Sigma Aldrich, Darmstad, Germany), and hydrochloric acid (HCl solution, 37%, Merck) were purchased. In the synthesis of DIO-NPs and for the rinsing of clusters, we used deionized water. The glass substrate was purchased from Solaronix (Aubonne, Switzerland).

2.2. Thin Layer of DIO-NPs Synthesis

The suspension synthesis and layer preparation were based on an adapted method presented previously [23,31,32]. Ferrous chloride tetrahydrate and chloride hexahydrate were mixed at room temperature and added drop by drop into the dextran solution (20% w/v). The synthesis parameters (adjusting pH, ionic strength, temperature), including the time and rate of adding the base, were carefully monitored and optimized. In the recent study on preparation and characterization of highly stable iron oxide nanoparticles for magnetic resonance imaging [33], it was shown that the slow formation of nanoparticle seeds was followed by a faster formation of cores and a slow formation of stabilized shells. According to Massart studies on preparation of aqueous magnetic liquids in alkaline and acidic media [34], the increase of pH from 4 to 11 of the $\text{FeCl}_2/\text{FeCl}_3$ precursor solution by addition of the NaOH induces the co-precipitation of iron oxide particles. The most important factor of this synthesis was the iron concentration. The $\text{Fe}^{2+}/\text{Fe}^{3+}$ ratio was 0.5. According to previous studies [35–37], the particles obtained with the $\text{Fe}^{2+}/\text{Fe}^{3+}$ ratio between 0.4 and 0.6 are the most effective in biomedical applications. The particles (DIO-NPs) were washed several times to remove the residues. The obtained particles (DIO-NPs) were homogeneous in size and composition according to previous studies [30]. Moreover, previous studies on size-tunable synthesis of stable superparamagnetic iron oxide nanoparticles for potential biomedical applications [38] revealed that the dextran was used as a surfactant, enabling obtained particles to be used directly for biological applications without further surface functionalization. According to past studies [39], at room temperature, the concentration of iron salts is about 0.1 mol/L in terms of magnetite. The resulting suspension obtained was used to realize the DIO-NPs layers. Before the deposition process, the glass substrate was cleaned with ethanol in an ultrasonic bath for 12 min. Using a syringe, 0.2 mL of DIO-NPs suspension was dripped onto the glass substrate ($1 \times 1 \text{ cm}^2$). The glass substrate was rotated during deposition at 1000 rpm for

40 s. The procedure was repeated 5 times. Immediately after coating, the layer was dried in a nitrogen atmosphere for 1 h at 70 °C. The resulting layer was treated at 100 °C under vacuum for 1 h.

2.3. Characterization of DIO-NPs Thin Layer

2.3.1. Optical Microscopy

Optical microscopy was used in order to investigate the surface morphology of the DIO-NPs layers. Thus, for this purpose, a binocular optical microscope with an attached camera from Micros Austria (1.3 MP, Micros Austria, Wien, Austria) was used. The images were recorded at the 40X magnification using Microvisible software. All of the measurements were performed at room temperature. The 3D representation of optical microscopy images of the DIO-NPs layers surface was obtained using ImageJ software [40].

2.3.2. Metallographic Microscopy

An inversed trinocular metallographic microscope OX.2153-PLM, (Euromex, Arnhem, The Netherlands) equipped with an CMEX digital camera (1.3 MP) was used in order to obtain additional information on the morphology of DIO-NPs thin layer. The metallographic images were captured using ImageFocusAlpha software at 20X magnification in ambient conditions. In addition, a 3D representation of 2D metallographic microscopy images of the DIO-NPs layers surface was obtained using ImageJ software [40].

2.3.3. Scanning Electron Microscopy (SEM)

The surface morphology of the DIO-NPs layers and suspension has been investigated by scanning electron microscopy (SEM) with the aid of an Apreo S ThermoFisher Scanning Electron Microscope. Firstly, a drop of DIO-NPs suspension was placed on a double-sided adhesive carbon tape and dried in a vacuum, and then analyzed by SEM. The working voltage and pressure were 10 kV and 10^{-3} Pa. The 2D SEM recorded images have been processed by using the ImageJ software [40]. A 3D surface plot analysis of DIO-NP layers has also been performed. From the 2D image of the DIO-NP layer acquired with 100,000X magnification, the nanoparticles size distribution has been calculated. In addition, 800 particles were measured to establish the mean particle size distribution (D_{SEM}).

2.3.4. Atomic Force Microscopy (AFM)

It is well known that atomic force microscopy is a powerful technique that provides information about the morphology of the samples. Therefore, atomic force microscopy (AFM) was used in order to investigate the morphology of a DIO-NPs thin layer using an NT-MDT NTEGRA Probe Nano Laboratory instrument (NT-MDT, Moscow, Russia). For this purpose, a silicon NT-MDT NSG01 cantilever was used (NT-MDT, Moscow, Russia) coated with a 35 nm gold layer in non-contact mode. The instrument was set to acquire scans of $10 \times 10 \mu\text{m}^2$ and $2.5 \times 2.5 \mu\text{m}^2$ in a non-contact mode with a point number of 512×512 and a frequency of 0.4 Hz. The scanning data used in our study were the image of surface topography (signal Height). The data were acquired on a surface area of $10 \times 10 \mu\text{m}^2$ in atmospheric conditions and at an ambient temperature of 25 ± 1 °C, and data processing was performed with the aid of Gwyddion 2.55 software (Department of Nanometrology, Czech Metrology Institute, Brno, Czech Republic) [41]. The roughness parameters of the 2D surface topography obtained by AFM were also determined using the dedicated “Calculate roughness parameters” of the Gwyddion software. The roughness parameters were determined from the entire $10 \times 10 \mu\text{m}^2$ 2D AFM topography. In addition, the grain size distribution was determined using the statistical analysis of the AFM images. For the determination of the grain size, at least six AFM topographies of $2.5 \times 2.5 \mu\text{m}^2$ and $10 \times 10 \mu\text{m}^2$ were analyzed. The proportion of the grain area was calculated using the following equation:

$$P_i = 0.25 \frac{d_i^2 \pi n_i}{S} \quad (1)$$

where d_i represents the diameter of a given grain, S stands for the area of all grains in the analyzed image, and n_i corresponds to the number of grains of a given size. The distribution plots were fitted using the Gaussian function, and the grain size was determined at the values corresponding to the maxima of the functions.

Before the visualization under microscopes, the samples were dedusted using a compressed air gun.

2.3.5. Fourier Transform Infrared Spectroscopy (FT-IR)

For study of the chemical bonds formed between the dextran and iron oxide nanoparticles, IR spectra analysis of the DIO-NPs layers has been performed. The spectra were acquired in the 400–4000 cm^{-1} wavenumber range in an attenuated total reflection (ATR) mode by using an SP 100 Perkin Elmer FTIR spectrometer (Waltham, MS, USA) with 4 cm^{-1} resolution. The spectra have been acquired in transmittance mode by placing the samples on the diamond-ZnSe crystal plate of the ATR unit inserted into the spectrometer and analyzed by using the Spectrum software version 6.3.5. The spectrum of the DIO-NPs layer was recorded after 32 scans.

2.3.6. Glow Discharge Optical Emission Spectrometry (GDOES)

By Glow Discharge Optical Emission Spectrometry (GDOES), the distribution of the chemical elements into the layer bulk was analyzed. A GD Profiler (Horiba Company, Longjumeau, France) has been used. The procedure and the working parameters were: 650 Pa, 35 W RF power impulse mode at 1 kHz, and a duty cycle of 0.25.

2.3.7. Cell Viability Assay

The biocompatibility of the DIO-NPs layers was investigated using the human hepatoma immortal cell line (HepG2). The HepG2 cell line was derived from the liver tissue of a 15-year-old Caucasian male having a well-differentiated hepatocellular carcinoma and nowadays is the most commonly studied liver cell line due to the advantages of availability and secretion of human proteins [42]. The cytotoxicity of the DIO-NPs against HepG2 cells was assessed using a method previously described in [27]. For the viability assays, the cells were grown in an environment having 5% CO_2 at a temperature of 37 °C, as monolayers, and were seeded at a density of 2.5×10^5 cells/mL and incubated with DIO-NPs layers' different time intervals (24, 48, and 72 h). The HepG2 viability incubated with the DIO-NPs layers was evaluated at 24, 48, and 72 h, using the standard colorimetric MTT (3-(4, 5-dimethylthiazol-2-yl)-2,5-diphenyltetrazolium bromide) assay. The absorbance of the culture medium was quantified with a TECAN spectrophotometer at 595 nm. The data were quantified as previously detailed in [43].

2.3.8. Statistical Analysis

The in vitro experiments were performed in triplicate. The data were presented as mean \pm standard deviation (SD). In addition, the statistical analysis was done using two-sample *t*-tests. Only values of $p \leq 0.05$ were considered statistically significant.

3. Results

By optical microscopy, the polymeric surface texture of the DIO-NPs layers deposited on the glass substrate is revealed at the micron scale. The optical image (40X magnification) of the coating presented in Figure 1a seems to be homogenous, indicating a uniform distribution of iron nanoparticles into dextran. By using the ImageJ software, the optical image of the layer has been processed. Figure 1b presents the 3D representation of the optical image of the DIO-NPs layer's surface.

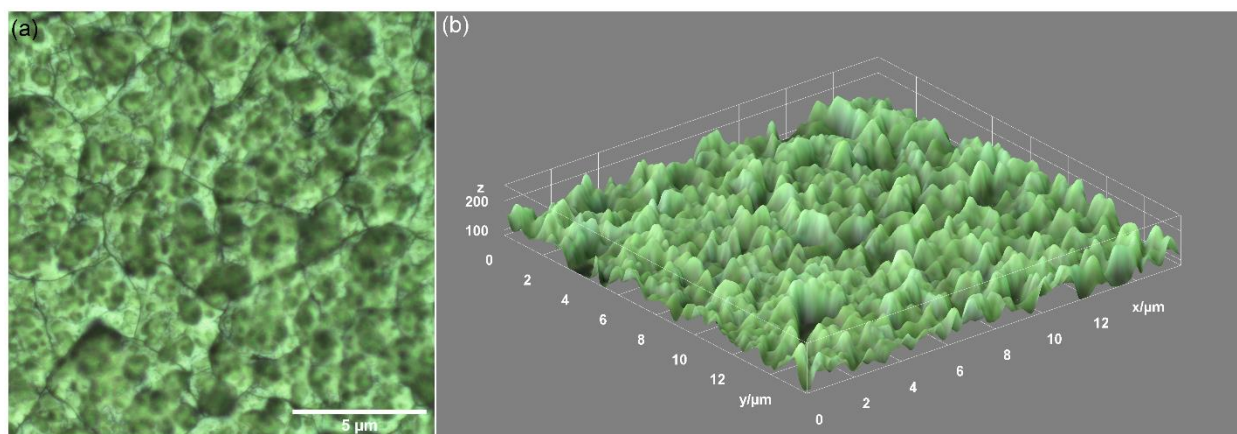


Figure 1. Optical image of DIO-NPs layers acquired with 40X objective (a) and 3D representation of the surface of the DIO-NPs layers (b).

In addition, metallographic microscopy was used to obtain complementary information regarding the surface morphology of the DIO-NPs layers deposited on the glass substrate. The 2D metallographic image of DIO-NPs layers is presented in Figure 2a and the 3D representation of the metallographic image of DIO-NPs layers is also presented in Figure 2b. For this purpose, the 20X objective of the metallographic microscope was used in order to obtain a 2D image of the surface of DIO-NPs layers. For the obtaining of 3D representations of the surface of DIO-NPs layers, ImageJ software [40] was used. Thus, the results presented in Figure 2 suggest that the surface of the studied layers is continuous and homogeneous without noticing the presence of discontinuities or cracks.

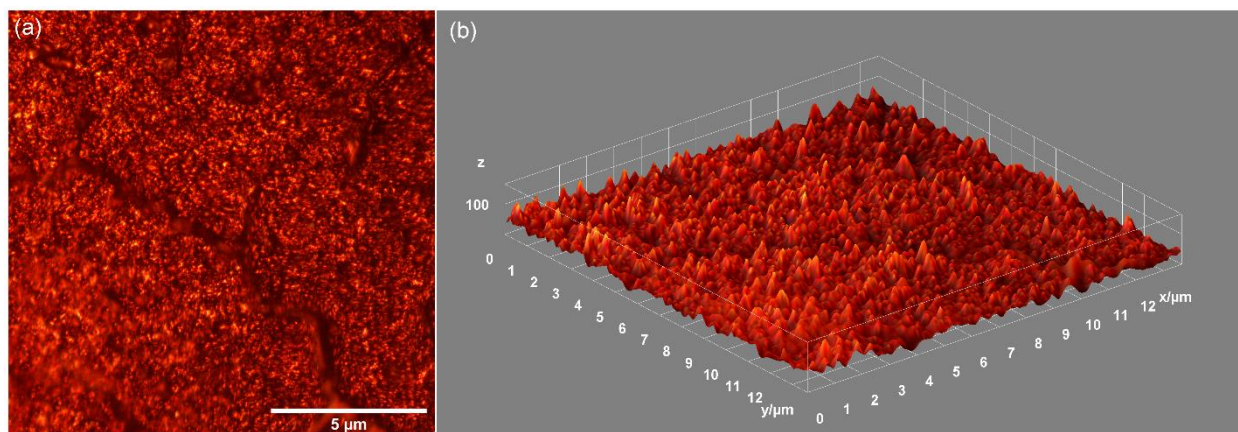


Figure 2. Metallographic microcopy image (20X magnification) of the DIO-NPs layers surface (a) and 3D representation of the surface of the DIO-NPs layers (b).

The SEM micrograph along with particle size distribution of the DIO-NPs suspension are presented in Figure 3. The results of SEM studies conducted on the DIO-NPs suspension revealed that the nanoparticles possess a polyhedral morphology. In addition, in the obtained histogram, it could be observed that the medium particle diameter (D_{SEM}) is 23 ± 3 nm (Figure 3b).

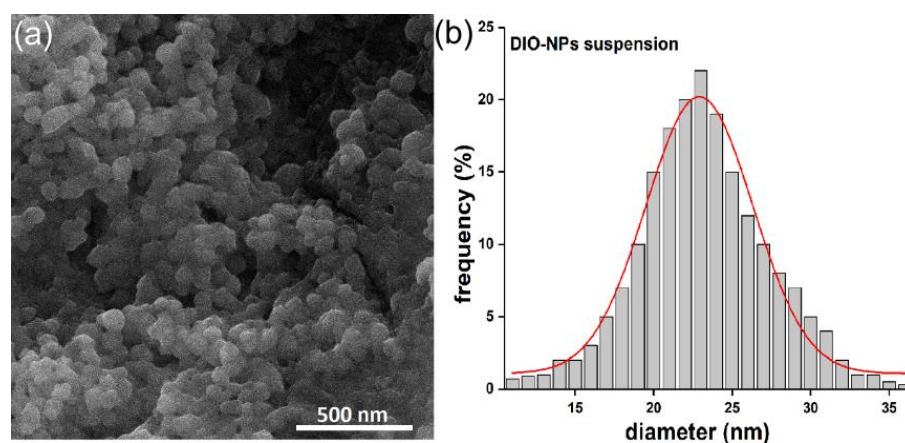


Figure 3. SEM image of DIO-NPs suspension (a) and particle size distribution (b).

The analysis of DIO-NP layers by SEM at two microscope magnifications, namely $10,000\times$ (Figure 4a) and $100,000\times$ (Figure 5a), allowed the disclosure of the DIO-NPs layer surfaces with high accuracy.

On the micron scale, the SEM image from Figure 4a revealed the cobblestone—like structure of the layers. Such surface morphologies are characteristics to dextran layers [26]. The 3D representation of SEM image is presented in Figure 4b and give us the first hint about the embedding of the iron oxide nanoparticles into dextran.

The presence of the iron nanoparticles in dextran is uncovered at $100,000\times$ magnification (Figure 5a), where their uniform and homogenous distribution can be observed, without affecting the cobblestone-like structures. Figure 5b exhibit the 3D plot of the SEM image of the DIO-NP layers. In addition, the particle size distribution of dextran coated iron oxide nanoparticle has been obtained (Figure 5c).

The analyses of the surface morphologies of the layers at different magnifications by SEM technique allowed the disclosure of micron-to nm structure of DIO-NP layers. Therefore, the distribution pattern of iron oxide nanoparticles embedded into dextran has been accurately revealed at $100,000\times$ magnification of the SEM apparatus. The mean nanoparticle size is about $25\text{ nm} \pm 3\text{ nm}$ (Figure 5c). On the micron analysis scale, the surface morphologies of the DIO-NP layers look similar to those observed by optical microscopy (Figure 1a).

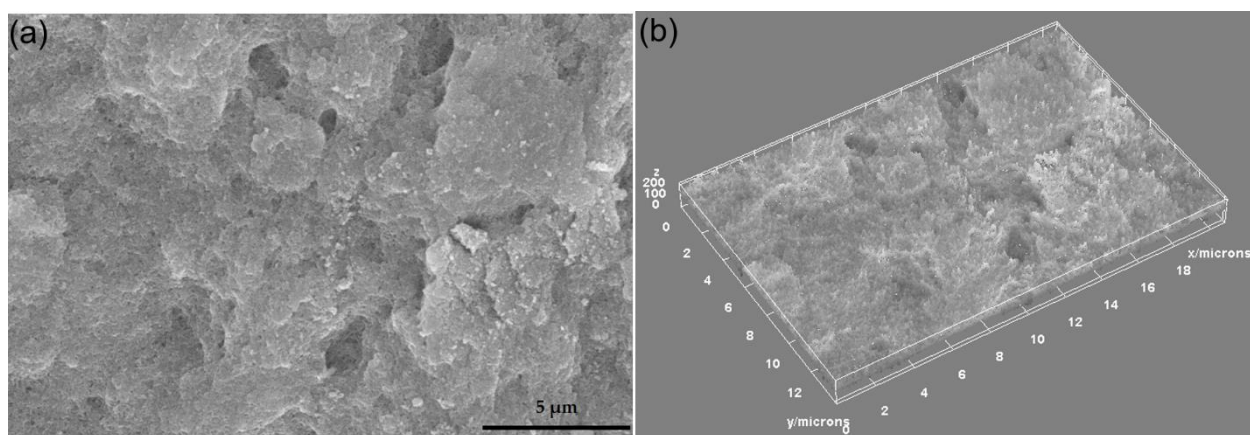


Figure 4. SEM image of DIO-NPs layers at $10,000\times$ magnification (a) and 3D surface plot of SEM image of DIO-NPs layers at $10,000\times$ magnification (b).

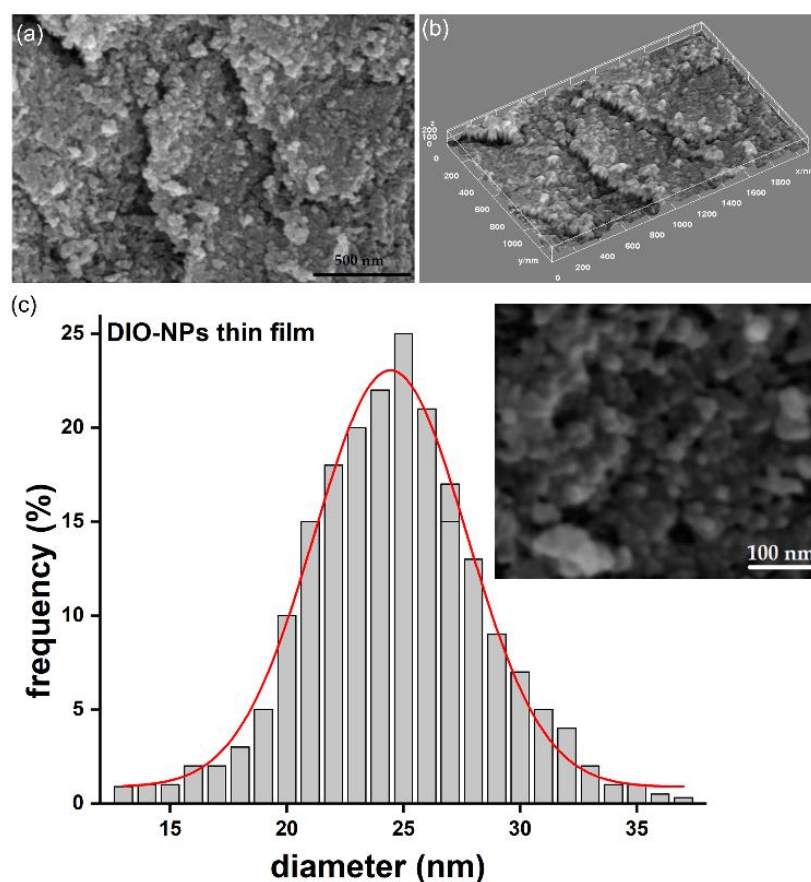


Figure 5. SEM image of DIO-NPs layers at 10,000× magnification (a), 3D surface plot of SEM image of DIO-NPs layers at 10,000× magnification (b) and size distribution of particles from SEM image-inset (c).

In addition, Atomic Force Microscopy was used to study the surface of the DIO-NPs layers deposited on the glass substrate. The results of AFM studies are depicted in Figure 6. The AFM 2D micrograph of the DIO-NPs layers surface is shown in Figure 6a and the 3D representation of the DIO-NPs layers surface is presented in Figure 6b. Both the 2D AFM micrograph and the 3D representation of the surface of the DIO-NPs layers suggest the formation of a continuous and homogeneous layer. The roughness parameters (R_q and R_a) of DIO-NPs layers surface estimated from AFM topography were 23.6738 nm and 19.1050 nm. These results suggest that the surface topography is homogenous and does not present a significant roughness. Moreover, in the AFM images (Figure 6), there is no evidence of the presence of cracks or fissures on the surface of DIO-NPs layers. In addition, the grain size distribution of the DIO-NPs was also determined using six 2D AFM topographies of $10 \times 10 \mu\text{m}^2$ and $2.5 \times 2.5 \mu\text{m}^2$. A representative $10 \times 10 \mu\text{m}^2$ is presented in Figure 6a. Moreover, two of the enlarged $2.5 \times 2.5 \mu\text{m}^2$ AFM sections used for the grain analysis and the grain size plot are also presented in Figure 6b. The sample preparation and the data processing were done using adapted methods of previously suggested methodology [44–48]. Furthermore, the 3D representation of the $10 \times 10 \mu\text{m}^2$ AFM micrograph is also depicted in Figure 6c.

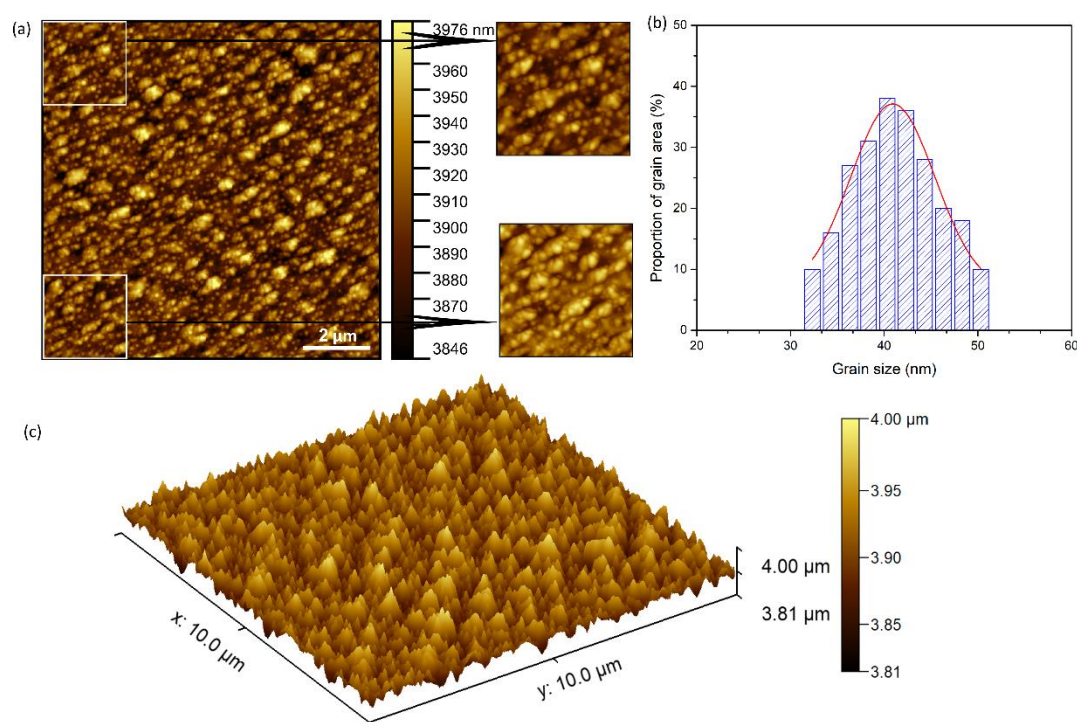


Figure 6. Atomic force microscopy (AFM) topography image of the DIO-NPs layers surface presented in 2D surface (size $10 \times 10 \mu\text{m}^2$) and enlarged areas (size $2.5 \times 2.5 \mu\text{m}^2$) (a), grain size distribution (b) and 3D representation of the surface topography of DIO-NPs layers (c).

Complementary information about the grain size distribution of the DIO-NPs coatings is also determined from the optical microscopy, metallographic microscopy, and scanning electron microscopy. The results are presented in Table 1. The grain size distribution of the optical and metallographic microscopy images was determined using ImageJ software [40], and the results are presented as mean \pm SD. For this purpose, at least three separate sections from the 2D images were analyzed using the “Particle Analyzer” function of the software. The grain size distribution from SEM images was determined by measuring the diameter of the particles and plotting the histogram, and the size distribution from AFM images was determined as previously described by Zubar et al. [47]. The size distribution obtained from the four complementary techniques were in the range of 25–97.5 nm and suggested that the coatings are comprised of a uniform deposited layer of nanometric particles and aggregates of nanometric particles. The particle agglomeration could be attributed to the presence of dextran coating of the iron oxide particles.

Table 1. Grain size of DIO-NPs coatings obtained from different characterization methods.

Characterization Method	Grain Size (nm)
Optical microscopy	97.5 ± 7.8
Metallographic microscopy	72 ± 5.89
Scanning electron microscopy	25 ± 3
Atomic force microscopy	40.95 ± 4.55

Furthermore, additional information regarding the roughness of the DIO-NPs coatings was also obtained using the data from the four complementary techniques (SEM, AFM, optical and metallographic microscopy). The data collected from the SEM, optical, and metallographic microscopy were used to determine the roughness parameters (R_a and R_q). The results are presented in Table 2. The roughness parameters were determined using ImageJ software [40]. On the other hand, the AFM roughness parameters were calculated

using Gwyddion software [41]. The data suggested that the values of the roughness average (R_a) and root mean square (RMS) roughness (R_q) obtained from the four complementary techniques were in the range of 19–114 nm in the case of (R_a) and in the interval of 23–104.5 nm for (R_q). The difference in the results obtained in our study regarding the roughness parameters determination by various techniques could be attributed to the limitation of the instruments in acquiring the images and also to their quality. Nonetheless, the values for the roughness parameters obtained from the four complementary techniques were no higher than 104.5 in the case of R_q and lower than 114.4 for the R_a , which suggested a homogenous and uniform surface with a moderate to minimum roughness.

Table 2. Roughness parameters of DIO-NPs coating's surface obtained from different characterization methods.

Characterization Method Roughness Parameters	Optical Microscopy	Metallographic Microscopy	Scanning Electron Microscopy	Atomic Force Microscopy
R_a	114.367	50.022	110.069	19.1050
R_q	104.548	41.987	104.032	23.6738

Therefore, analyzing the results obtained by the four complementary techniques (SEM, AFM, optical and metallographic microscopy), we can say that the morphology of the surface DIO-NPs layers is continuous and homogeneous without noticing the presence of discontinuities.

The FTIR spectrum of DIO-NPs layers deposited on the glass substrate is presented in Figure 7. The IR bands characteristic to Fe-O bonds, usually manifested in a 550–650 cm^{-1} spectral range [24], appear at 551 respectively 623 cm^{-1} . The IR bands from 726, 891, and 1061 cm^{-1} are characteristic to the structure of dextran [24]. The peak intensity positioned at 766 cm^{-1} is characteristic to α 1, 3 of the glycoside unit in dextran [49]. The stronger bands from 1061 cm^{-1} can be attributed to the C-O-C stretching mode in the ring [50], while the 891 cm^{-1} peak belongs to α -glucopyranose ring deformation modes of the C-O bonds [51]. The IR bands from 1423, 1620 cm^{-1} are attributed to C-H asymmetric bend and H-O-H vibrations, respectively [24,49–52]. The IR bands from 2860, 2926, and 2966 cm^{-1} are specific to symmetric/asymmetric stretch C-H vibrations in the methyl group [51]. The bands from 3275 cm^{-1} are assigned to O-H vibrations [51].

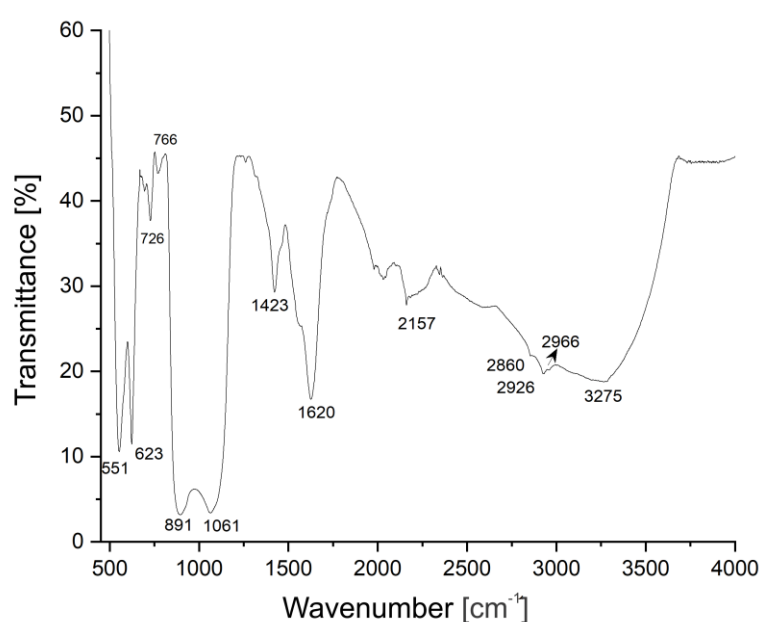


Figure 7. FTIR spectrum of DIO-NPs layers.

The strong IR band from 2157 cm^{-1} is specific to Fe-CO metal carbonyl vibration bonds [53]. Their presence in the FTIR spectrum of DIO-NPs layers proves that the linkage between iron oxide nanoparticles and dextran takes place through carbon–oxygen bonds.

The distribution of iron oxide nanoparticles into the dextran layer was also evaluated from the depth profiles of the C, H, Fe, and O elements, by using the GDOES techniques. In our previous work, we described in detail the working principle of this technique [42].

Figure 8 presents the time dependence of the acquired C, H, Fe, and O signal intensities characteristic to the DIO-NPs layers. The depth profile of O has the highest intensity, as it is included both in the chemical structure of dextran and of the iron oxide nanoparticles. The simultaneous humps observed on the depth profile signal of O, C, and Fe suggest the embedding of iron oxide nanoparticles into dextran. Moreover, the O, Fe, and C signal profiles indicate that the iron oxides are linked to dextran via carbon–oxygen bonds.

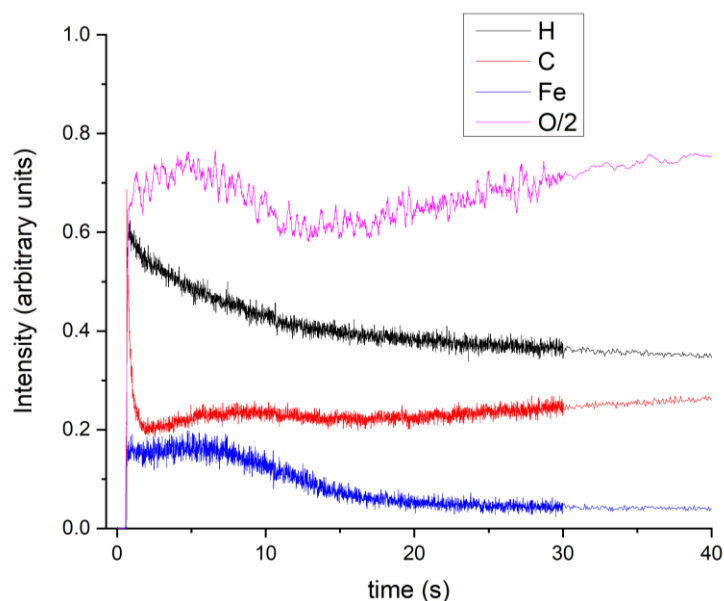


Figure 8. GDOES depth profile of the DIO-NPs layers.

By the GDOES technique, the temporal evolution of the recorded signals expresses the distribution of the elements contained in a layer from its surface up to the substrate interface. In Figure 8, the interface between the DIO-NPs layers and substrate is marked by the decrease of Fe depth profile. The smoothing of the C, H, O, and Fe depth profile signals after 30 s indicates the ending of the measurements.

Therefore, the GDOES results are in good agreement with the results obtained by FTIR studies on the DIO-NPs layers.

The cytotoxicity of the DIO-NPs layers was investigated *in vitro* using a HepG2 cell line. The *in vitro* assays were performed in triplicate and the cell viability of the HepG2 cells incubated with DIO-NPs layers was assessed at three different time intervals (24, 48, and 72 h). The results of the MTT assay, which depicts the HepG2 cell viability after being incubated for different time intervals with DIO-NPs layers, are presented in Figure 9. In addition, a HepG2 cell culture was grown without being incubated with DIO-NPs layers and used as a control. The results of the MTT studies have proven that the HepG2 cells incubated with DIO-NPs layers exhibited a good viability compared to the control for all tested time intervals. More than that, the results of the MTT assay showed that, after 24 h of incubation with the DIO-NPs layers, the HepG2 viability was above 80% with a value of 84% and had an increasing tendency with the increase of the incubation time, reaching a viability of 94% after 72 h of incubation. The results of the *in vitro* assay highlighted that the cell viability of the HepG2 increased with the incubation time. The experiments were performed in triplicate, and the results data were presented as mean \pm SD. More

than that, a statistical analysis was performed using a *t*-test, and all the *p* calculated values were $p < 0.05$.

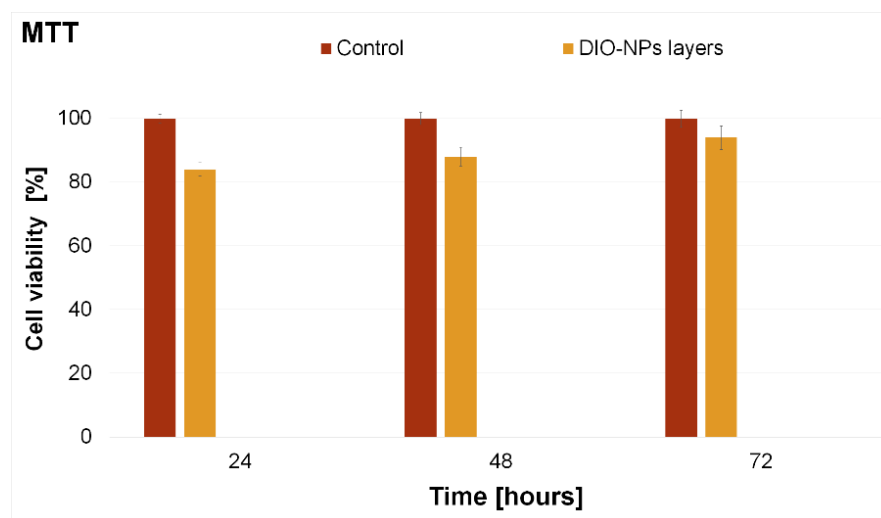


Figure 9. MTT assay of the viability of HepG2 incubated with DIO-NPs layers for 24, 48, and 72 h. The results are presented as means \pm standard error. The data were statistically analyzed using paired and two-sample *t*-tests for means, with $p \leq 0.05$ accepted as statistically significant.

Furthermore, the HepG2 cell morphology and their adhesion and proliferation on the DIO-NPs layers surface were investigated by microscopic visualization. The 2D images of the HepG2 cells incubated on the surface of DIO-NPs layers at three different time intervals are depicted in Figure 10. The 2D images of the HepG2 cells incubated with DIO-NPs layers highlighted that the layers did not exhibit any toxic effect towards the cells for the tested time intervals. Moreover, the microscopic evaluation showed that the evaluated layers did not induce any notable changes in the morphology of the HepG2 cells compared to the control cell culture.

In addition, the 3D representations of the microscopic images of the HepG2 cells adhered on the surface of DIO-NPs layers were obtained using ImageJ software [40] and are depicted in Figure 11. The microscopic visualization and the 3D representation of the microscopic images have proven that the presence of DIO-NPs layers did not affect the morphology of the HepG2 cells or their proliferation rate. The microscopic images depicted the presence of a typical epithelial-like morphology with sizes of approximately $12.35 \mu\text{m}$ for the HepG2 cells incubated with the DIO-NPs for all the tested time intervals (24, 48, and 72 h).

The observations obtained by microscopic visualization are in agreement with the MTT results and highlighted that the investigated DIO-NPs layers present a good biocompatibility towards HepG2 cells and could be further investigated for the development of biomedical devices. The results are also in good agreement with previously reported data regarding the biocompatibility of layers based on iron oxide nanoparticles and iron oxide in various polymeric matrices [27,43]. The toxicity of nanocomposites and their respective coating are usually determined by a high number of factors such as nanoparticles, size, shape, porosity, surface area, wettability, incubation time, concentration, cell line, and, in the case of coatings, the substrate of the coatings as well as the roughness of the surface play an important role [53–57].

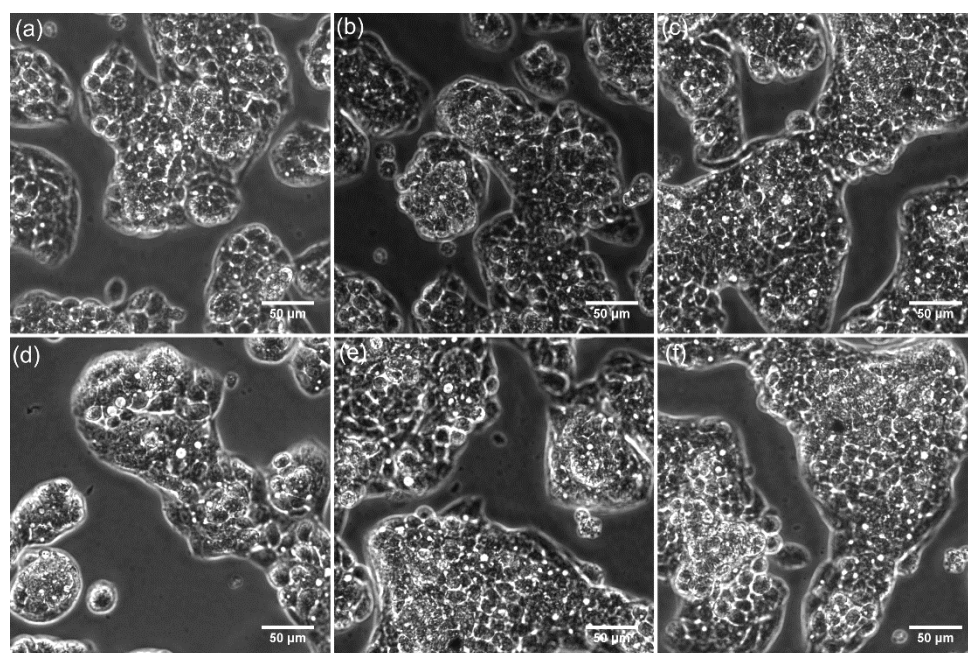


Figure 10. Microscopic images of HepG2 control cells (a–c) at different time intervals (24, 48, and 72 h) and HepG2 cells grown on dextran thin films deposited on glass substrate (d–f) at different time intervals (24, 48, and 72 h).

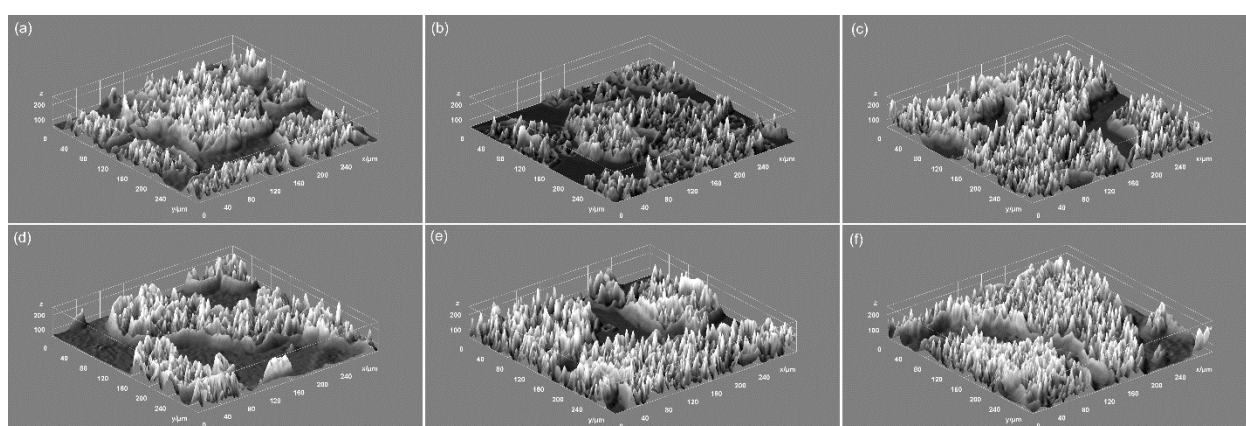


Figure 11. 3D representation of microscopic images of HepG2 control cells (a–c) at different time intervals (24, 48, and 72 h) and HepG2 cells grown on dextran thin films deposited on glass substrate (d–f) at different time intervals (24, 48, and 72 h).

In the literature, the most common mechanism held accounted for the toxicity of iron oxide nanoparticles is the reactive oxygen species (ROS) formation. ROS are defined as highly reactive chemical molecules which appear due to the electron receptivity of O_2 and are usually formed as a natural byproduct of the normal aerobic metabolism of oxygen. In the case of iron oxide nanoparticles uses *in vivo*, ROS have been reported to appear as by-products of the mitochondrial electron transport or to be formed via NADPH oxidase, xanthine oxidase, and nitric oxide synthase [58–62]. Recently, in the literature, numerous papers regarding the cytotoxicity of iron oxide nanoparticle against different cell systems were reported [63–67]. The data reported by these papers have evidenced that a decrease of iron oxide nanoparticle cytotoxicity was observed when dextran and other lipid coatings were employed [59,60,63–70]. In addition, these studies have emphasized that, for very low iron oxide nanoparticle concentrations, there are no significant cytotoxic effects towards the various tested cell types [63,69]. Yu et al. [59] in their study regarding the “Dextran

and Polymer Polyethylene Glycol (PEG) Coating Reduce Both 5 and 30 nm Iron Oxide Nanoparticle Cytotoxicity in 2D and 3D Cell Culture” have concluded that both dextran and PEG coatings could block ROS interaction with the iron oxide nanoparticles which could lead to the prevention of the occurrence of Fenton reaction. In this case, the cell’s antioxidant defense will be capable of neutralizing ROS before being transformed into dangerous hydroxyl radicals [59]. Therefore, there are several papers reporting that a range of iron oxide nanoparticles with particular physico-chemical properties showed low or no toxicity when investigated at different concentrations and under different circumstances, either as solutions, powders, or coatings [23,24,27,43,55,69,70]. Even though each paper has a different approach of the studies, a generalization of the results is difficult, and studies have yet to be conducted in order to better understand and assess the potential toxicological risks involved in using iron oxide nanoparticle systems in biomedical applications. Nonetheless, each study makes a great contribution in the understanding of cellular toxicity mechanisms involved in the use of nanosystems in biomedical applications and expand beyond any doubt our expertise in the development of novel materials and coatings with biocompatible properties.

The previous studies reported in the literature [23,24,27,28] regarding the physico-chemical and biological properties of iron oxide/dextran thin films and suspension on glass/silicon substrate revealed that the deposition method together with their chemical composition influence the properties of the obtained layers. The study conducted by S.L. Iconaru et al. [28] reported the obtaining of magnetic iron oxide nanoparticles doped with dextran (with various concentrations of iron oxide) thin films on glass substrate by the spin coating method. SEM results highlighted that the coatings consist of regular grains with some aggregation [28]. The results of GDOES studies reveal the presence of a coating composed mainly of carbon, iron, and oxygen [28]. In addition, the results of MTT test (using hFOB 1.19 osteoblasts cell line) highlighted a good biocompatibility of the obtained layers. On the other hand, the studies conducted in preparation of iron oxide–dextran nanostructures on glass substrate by a laser technique [24,27] showed that the coatings are continuous and have a granular morphology. In addition, the results of XPS studies revealed the presence of the Fe^{3+} oxides in the samples [24,27]. The MTT assay conducted on the obtained samples using the HepG2 cell line showed their excellent biocompatibility [24,27]. The recent study, conducted by Predoi and coworkers [23], presented the results of complex research conducted on dextran-coated iron oxide nanoparticle solutions and thin films. The thin films were deposited on a Silicon substrate by the spin coating method [23]. Their results showed that the surface of the obtained thin film was uniform and homogeneous. Furthermore, the results of qualitative cytotoxicity assays (HeLa cells), revealed that dextran-coated iron oxide nanoparticle solutions and thin films did not present any toxicity after 24 and 48 h of incubation [23]. Thus, our complex study brings new information about the surface morphology of the layers, thus completing the existing results in the literature, emphasizing once again the biocompatibility of iron–dextran oxide layers. Moreover, the results obtained by optical and metallographic microscopy are presented for the first time, which emphasized the homogeneity and continuity of the layers. In addition, the results of biocompatibility studies (using HepG2 cell line) performed on iron oxide–dextran layers deposited on glass substrate by the spin coating method are presented for the first time.

4. Conclusions

The main purpose of the present research was to obtain iron oxide–dextran (DIO-NPs) thin layers on a glass substrate by an adapted method of synthesis. The SEM results revealed that surface morphology of the samples consists of a cobblestone-like structure. Moreover, the homogeneity and continuity of the DIO-NPs layers were highlighted both by the results obtained by AFM and by those obtained by optical and metallographic microscopy. FTIR and GDOES studies conducted on DIO-NPs layers confirmed the formation of the bonds between dextran and iron oxide nanoparticles. The cytotoxicity assay results

highlighted that DIO-NPs layers did not exhibit any significant toxic effects toward the HepG2 cell line for all the tested time intervals. Furthermore, the cytotoxicity assays on HepG2 cells also revealed that the thin films did not induce any significant morphological changes after 24, 48, and 72 h of incubation. Moreover, the quantitative MTT assay evidenced that the HepG2 cells incubated with DIO-NPs exhibited a high cell viability (84%) after 24 h of incubation. The results indicate the potential utilization of iron oxide–dextran (DIO-NPs) thin layers deposited on glass substrate in biomedical applications.

Author Contributions: Conceptualization, M.S.R., C.S.C., S.L.I., D.B.D., A.G., D.P., F.B., C.C., M.-L.B. and G.P.; methodology, M.S.R., C.S.C., S.L.I., D.B.D., A.G., D.P., F.B., C.C., M.-L.B. and G.P.; software, M.S.R., C.S.C., S.L.I., D.B.D., A.G., D.P., F.B., C.C., M.-L.B. and G.P.; validation, M.S.R., C.S.C., S.L.I., D.B.D., A.G., D.P., F.B., C.C., M.-L.B. and G.P.; formal analysis, M.S.R., C.S.C., S.L.I., D.B.D., A.G., D.P., F.B., C.C., M.-L.B. and G.P.; investigation, M.S.R., C.S.C., S.L.I., D.B.D., A.G., L.G., D.P., F.B., C.C., M.-L.B., S.-F.B., C.F.F., C.B. and G.P.; resources, M.S.R., C.S.C., S.L.I., D.B.D., A.G., D.P., F.B., C.C., M.-L.B. and G.P.; data curation, M.S.R., C.S.C., S.L.I., D.B.D., A.G., D.P., F.B., C.C., M.-L.B. and G.P.; writing—original draft preparation, M.S.R., C.S.C., S.L.I., D.B.D., A.G., D.P., F.B., C.C., M.-L.B. and G.P.; writing—review and editing, M.S.R., C.S.C., S.L.I., D.B.D., A.G., D.P., F.B., C.C., M.-L.B. and G.P.; visualization, M.S.R., C.S.C., S.L.I., D.B.D., A.G., D.P., F.B., C.C., M.-L.B. and G.P.; supervision, M.S.R., C.S.C., S.L.I., D.B.D., A.G., D.P., F.B., C.C., M.-L.B. and G.P.; project administration, M.S.R., C.S.C., S.L.I., D.B.D., A.G., D.P., F.B., C.C., M.-L.B. and G.P.; funding acquisition, C.C. and G.P. All authors have read and agreed to the published version of the manuscript.

Funding: This research was funded by Romanian Ministry of Research and Innovation, Grant No. PN-III-P1-1.2-PCCDI-2017-0134, Contract No. 23PCCDI/2018, and the APC was funded by a grant from the Romanian Ministry of Research and Innovation, through the project “Improvement of Life Quality by Developing New Technologies Based on Efficient Nanoparticles in Water and Soil Decontamination-PN-III-P1-1.2-PCCDI-2017-0134”, Contract No. 23PCCDI/2018.

Institutional Review Board Statement: Not applicable.

Informed Consent Statement: Not applicable.

Data Availability Statement: Data are available on demand from the corresponding author.

Acknowledgments: This research was supported by the Romanian Ministry of Research and Innovation through the PN-III-P1-1.2-PCCDI-2017-0134, Contract No. 23PCCDI/2018. Also, the authors would like to thank to Patrick Chapon (Horiba), for the assistance with GDOES studies and for the constructive discussions.

Conflicts of Interest: The authors declare no conflict of interest.

References

1. Dias, A.M.; Hussain, A.; Marcos, A.S.; Roque, A.C. A biotechnological perspective on the application of iron oxide magnetic colloids modified with polysaccharides. *Biotechnol. Adv.* **2011**, *29*, 142–155. [[CrossRef](#)] [[PubMed](#)]
2. Dutz, S.; Andrä, W.; Hergt, R.; Muller, R.; Oestreich, C.; Schmidt, C.H.; Töpfer, J.; Zeisberger, M.; Bellemann, M. Influence of dextran coating on the magnetic behaviour of iron oxide nanoparticles. *J. Magn. Magn. Mater.* **2007**, *311*, 51–54. [[CrossRef](#)]
3. Nelson, N.R.; Port, J.D.; Pandey, M.K. Use of Superparamagnetic Iron Oxide Nanoparticles (SPIONs) via Multiple Imaging Modalities and Modifications to Reduce Cytotoxicity: An Educational Review. *J. Nanotheranostics* **2020**, *1*, 105–135. [[CrossRef](#)]
4. Brunsen, A.; Utech, S.; Maskos, M.; Knoll, W.; Jonas, U. Magnetic Composite Thin Films of FexOy Nanoparticles and Photocrosslinked Dextran Hydrogels. *J. Magn. Magn. Mater.* **2012**, *324*, 1488–1497. [[CrossRef](#)]
5. Noqta, O.A.; Aziz, A.A.; Usman, I.A.; Bououdina, M. Recent Advances in Iron Oxide Nanoparticles (IONPs): Synthesis and Surface Modification for Biomedical Applications. *J. Supercond. Nov. Magn.* **2019**, *32*, 779–795. [[CrossRef](#)]
6. Matos, J.C.; Gonçalves, M.C.; Pereira, L.C.J.; Vieira, B.J.C.; Waerenborgh, J.C. SPIONs Prepared in Air through Improved Synthesis Methodology: The Influence of γ -Fe₂O₃/Fe₃O₄ Ratio and Coating Composition on Magnetic Properties. *Nanomaterials* **2019**, *9*, 943. [[CrossRef](#)] [[PubMed](#)]
7. Veisheh, O.; Gunn, J.; Zhang, M. Design and fabrication of magnetic nanoparticles for targeted drug delivery and imaging. *Adv. Drug Deliv. Rev.* **2010**, *62*, 284–304. [[CrossRef](#)]
8. Inbaraj, B.S.; Chen, B.-H. In vitro removal of toxic heavy metals by poly (γ -glutamic acid)-coated superparamagnetic nanoparticles. *Int. J. Nanomed.* **2012**, *7*, 4419–4432. [[CrossRef](#)]
9. Usov, N.A.; Nesmeyanov, M.S.; Tarasov, V.P. Magnetic vortices as efficient nano heaters in magnetic nanoparticle hyperthermia. *Sci. Rep.* **2018**, *8*, 1224. [[CrossRef](#)]

10. Soares, P.I.; Laia, C.A.; Carvalho, A.; Pereira, L.C.; Coutinho, J.T.; Ferreira, I.M.; Novo, C.M.; Borges, J.P. Iron oxide nanoparticles stabilized with a bilayer of oleic acid for magnetic hyperthermia and MRI applications. *Appl. Surf. Sci.* **2016**, *383*, 240–247. [\[CrossRef\]](#)
11. Gao, Y.; Lim, J.; Teoh, S.-H.; Xu, C. Emerging translational research on magnetic nanoparticles for regenerative medicine. *Chem. Soc. Rev.* **2015**, *44*, 6306–6329. [\[CrossRef\]](#)
12. Gupta, A.K.; Gupta, M. Synthesis and surface engineering of iron oxide nanoparticles for biomedical applications. *Biomaterials* **2005**, *26*, 3995–4021. [\[CrossRef\]](#) [\[PubMed\]](#)
13. Straczek, T.; Fiejdasz, S.; Rybicki, D.; Goc, K.; Przewoźnik, J.; Mazur, W.; Nowakowska, M.; Zapotoczny, S.; Rumian, S.; Kapusta, C. Dynamics of Superparamagnetic Iron Oxide Nanoparticles with Various Polymeric Coatings. *Materials* **2019**, *12*, 1793. [\[CrossRef\]](#) [\[PubMed\]](#)
14. Reczyńska, K.; Marszałek, M.; Zarzycki, A.; Reczyński, W.; Kornaus, K.; Pamuła, E.; Chrzanowski, W. Superparamagnetic Iron Oxide Nanoparticles Modified with Silica Layers as Potential Agents for Lung Cancer Treatment. *Nanomaterials* **2020**, *10*, 1076. [\[CrossRef\]](#)
15. Predoi, D.; Iconaru, S.L.; Predoi, M.V.; Motelica-Heino, M. Removal and Oxidation of As(III) from Water Using Iron Oxide Coated CTAB as Adsorbent. *Polymers* **2020**, *12*, 1687. [\[CrossRef\]](#)
16. Predoi, D.; Popa, C.L.; Predoi, M.V. Ultrasound studies on magnetic fluids based on maghemite nanoparticles. *Polym. Eng. Sci.* **2017**, *57*, 485–490. [\[CrossRef\]](#)
17. Shaterabadi, Z.; Nabiyouni, G.; Soleymani, M. High impact of in situ dextran coating on biocompatibility, stability and magnetic properties of iron oxide nanoparticles. *Mater. Sci. Eng. C Mater. Biol. Appl.* **2017**, *75*, 947–956. [\[CrossRef\]](#)
18. Qiao, R.; Yang, C.; Gao, M. Superparamagnetic iron oxide nanoparticles: From preparations to in vivo MRI applications. *J. Mater. Chem.* **2009**, *19*, 6274–6293. [\[CrossRef\]](#)
19. Khot, V.M.; Salunkhe, A.B.; Thorat, N.D.; Ningthoujam, R.S.; Pawar, S.H. Induction heating studies of dextran coated MgFe_2O_4 nanoparticles for magnetic hyperthermia. *Dalton Trans.* **2013**, *42*, 1249–1258. [\[CrossRef\]](#) [\[PubMed\]](#)
20. Hauser, A.K.; Mathias, R.; Anderson, K.W.; Hilt, J.Z. The effects of synthesis method on the physical and chemical properties of dextran coated iron oxide nanoparticles. *Mater. Chem. Phys.* **2015**, *160*, 177–186. [\[CrossRef\]](#)
21. Wunderbaldinger, P.; Josephson, L.; Weissleder, R. Crosslinked iron oxides (CLIO): A new platform for the development of targeted MR contrast agents. *Acad. Radiol.* **2002**, *9*, S304–S306. [\[CrossRef\]](#)
22. Hassanien, A.S.; Akl, A.A. Optical characteristics of iron oxide thin films prepared by spray pyrolysis technique at different substrate temperatures. *Appl. Phys. A* **2018**, *124*, 752. [\[CrossRef\]](#)
23. Predoi, D.; Iconaru, S.L.; Predoi, M.V.; Buton, N.; Megier, C.; Motelica-Heino, M. Biocompatible Layers Obtained from Functionalized Iron Oxide Nanoparticles in Suspension. *Coatings* **2019**, *9*, 773. [\[CrossRef\]](#)
24. Ciobanu, C.S.; Iconaru, S.L.; Gyorgy, E.; Radu, M.; Costache, M.; Dinischiotu, A.; Le Coustumer, P.; Lafdi, K.; Predoi, D. Biomedical properties and preparation of iron oxide-dextran nanostructures by MAPLE technique. *Chem. Cent. J.* **2012**, *6*, 17. [\[CrossRef\]](#) [\[PubMed\]](#)
25. Arias, L.S.; Pessan, J.P.; Vieira, A.P.M.; Lima, T.M.T.; Delbem, A.C.B.; Monteiro, D.R. Iron Oxide Nanoparticles for Biomedical Applications: A Perspective on Synthesis, Drugs, Antimicrobial Activity, and Toxicity. *Antibiotics* **2018**, *7*, 46. [\[CrossRef\]](#) [\[PubMed\]](#)
26. Prodan, A.M.; Iconaru, S.L.; Chifiriuc, C.M.; Bleotu, C.; Ciobanu, C.S.; Motelica-Heino, M.; Sizaret, S.; Predoi, D. Magnetic Properties and Biological Activity Evaluation of Iron Oxide Nanoparticles. *J. Nanomater.* **2013**, *2013*, 893970. [\[CrossRef\]](#)
27. Predoi, D.; Ciobanu, C.S.; Radu, M.; Costache, M.; Dinischiotu, A.; Popescu, C.; Axente, E.; Mihailescu, I.N.; Gyorgy, E. Hybrid dextran-iron oxide thin films deposited by laser techniques for biomedical applications. *Mater. Sci. Eng. C* **2012**, *32*, 296–302. [\[CrossRef\]](#)
28. Iconaru, S.L.; Andronescu, E.; Ciobanu, C.S.; Prodan, A.M.; Le Coustumer, P.; Predoi, D. Biocompatible Magnetic Iron Oxide Nanoparticles Doped Dextran Thin Films Produced By Spin Coating Deposition Solution. *Dig. J. Nanomater. Bios.* **2012**, *7*, 399–409.
29. Tassa, C.; Shaw, S.Y.; Weissleder, R. Dextran-Coated Iron Oxide Nanoparticles: A Versatile Platform for Targeted Molecular Imaging, Molecular Diagnostics, and Therapy. *Acc. Chem. Res.* **2011**, *44*, 842–852. [\[CrossRef\]](#)
30. Holban, A.M.; Grumezescu, A.M.; Saviuc, C.M. Magnetite Nanocomposites Thin Coatings Prepared by MAPLE to Prevent Microbial Colonization of Medical Surfaces. In *Eco-Friendly Polymer Nanocomposites. Advanced Structured Materials*; Thakur, V., Thakur, M., Eds.; Springer: New Delhi, India, 2015; Volume 74. [\[CrossRef\]](#)
31. Massart, R. Magnetic Fluids and Process for Obtaining Them. US Patent 4329241, 11 May 1982.
32. Predoi, D.; Valsangiacom, C. Thermal studies of magnetic spinel iron oxide in solution. *J. Optoelectron. Adv. Mater.* **2007**, *9*, 1797–1799.
33. Kovál, D.; Malá, A.; Mllochová, J.; Kalina, M.; Fohlerová, Z.; Hlaváček, A.; Farka, Z.; Skládal, P.; Starčuk, Z.; Jiřík, R.; et al. Preparation and Characterisation of Highly Stable Iron Oxide Nanoparticles for Magnetic Resonance Imaging. *J. Nanomater.* **2017**, *2017*, 7859289. [\[CrossRef\]](#)
34. Massart, R. Preparation of aqueous magnetic liquids in alkaline and acidic media. *IEEE Trans. Magn.* **1981**, *17*, 1247–1248. [\[CrossRef\]](#)
35. Massart, R.; Cabuil, V. Effect of some parameters on the formation of colloidal magnetite in alkaline-medium—yield and particle-size control. *J. Chim. Phys.* **1987**, *84*, 967. [\[CrossRef\]](#)

36. Jolivet, J.P.; Belleville, P.; Tronc, E.; Livage, J. Influence of Fe(II) on the Formation of the Spinel Iron Oxide in Alkaline Medium. *Clays Clay Miner.* **1992**, *40*, 531–539. [CrossRef]
37. Tronc, E.; Belleville, P.; Jolivet, J.-P.; Livage, J. Transformation of ferric hydroxide into spinel by Fe(II) adsorption. *Langmuir* **1992**, *8*, 313–319. [CrossRef]
38. Yu, F.Q.; Yang, V.C. Size-tunable synthesis of stable superparamagnetic iron oxide nanoparticles for potential biomedical applications. *J. Biomed. Mater. Res. Part. A* **2010**, *92A*, 1468–1475. [CrossRef]
39. Gribanov, N.M.; Bibik, E.E.; Buzunov, O.V.; Naumov, V.N. Physico-chemical regularities of obtaining highly dispersed magnetite by the method of chemical condensation. *J. Magn. Magn. Mater.* **1990**, *85*, 7–10. [CrossRef]
40. ImageJ Website. Available online: <http://imagej.nih.gov/ij> (accessed on 10 January 2021).
41. Gwyddion. Available online: <http://gwyddion.net/> (accessed on 20 January 2021).
42. Groza, A.; Surmeian, A.; Diplasu, C.; Luculescu, C.; Chapon, P.; Tempez, A.; Ganciu, M. Physico-chemical processes occurring during polymerization of liquid polydimethylsiloxane films on metal substrates under atmospheric pressure air corona discharges. *Surf. Coat. Tech.* **2012**, *212*, 145–151. [CrossRef]
43. Aden, D.P.; Fogel, A.; Plotkin, S.; Damjanov, I.; Knowles, B.B. Controlled synthesis of HBsAg in a differentiated human liver carcinoma-derived cell line. *Nature* **1979**, *282*, 615–616. [CrossRef]
44. Delvallée, A.; Feltin, N.; Ducourtieux, S.; Trabelsi, M.; Hocheplid, J.F. Direct comparison of AFM and SEM measurements on the same set of nanoparticles. *Meas. Sci. Technol.* **2015**, *26*, 085601. [CrossRef]
45. Cruzier, L.; Delvallée, A.; Ducourtieux, S.; Devoille, L.; Noircler, G.; Ulysse, C.; Taché, O.; Barruet, E.; Tromas, C.; Feltin, N. Development of a new hybrid approach combining AFM and SEM for the nanoparticle dimensional metrology. *Beilstein J. Nanotechnol.* **2019**, *10*, 1523–1536. [CrossRef] [PubMed]
46. Warcholinski, B.; Gilewicz, A.; Kuznetsova, T.; Zubar, T.; Chizhik, S.; Abetkovskaia, S.; Lapitskaya, V. Mechanical properties of Mo(C)N coatings deposited using cathodic arc evaporation. *Surf. Coat. Technol.* **2017**, *319*, 117–128. [CrossRef]
47. Zubar, T.; Fedosyuk, V.; Tishkevich, D.; Kanafyev, O.; Astapovich, K.; Kozlovskiy, A.; Zdorovets, M.; Vinnik, D.; Gudkova, S.; Kaniukov, E.; et al. The Effect of Heat Treatment on the Microstructure and Mechanical Properties of 2D Nanostructured Au/NiFe System. *Nanomaterials* **2020**, *10*, 1077. [CrossRef] [PubMed]
48. Warcholinski, B.; Kuznetsova, T.A.; Gilewicz, A.; Zubar, T.I.; Lapitskaya, V.A.; Chizhik, S.A.; Komarov, A.I.; Komarova, V.I.; Kuprin, A.S.; Ovcharenko, V.D.; et al. Structural and Mechanical Properties of Zr-Si-N Coatings Deposited by Arc Evaporation at Different Substrate Bias Voltages. *J. Mater. Eng. Perform.* **2018**, *27*, 3940–3950. [CrossRef]
49. Predoi, D.; Iconaru, S.L.; Ciobanu, S.C.; Predoi, S.-A.; Buton, N.; Megier, C.; Beuran, M. Development of Iron-Doped Hydroxyapatite Coatings. *Coatings* **2021**, *11*, 186. [CrossRef]
50. Can, H.K.; Kavlak, S.; ParviziKhosroshahi, S.; Güner, A. Preparation, characterization and dynamical mechanical properties of dextran-coated iron oxide nanoparticles (DIONPs). *Artif. Cells Nanomed. Biotechnol.* **2018**, *46*, 421–431. [CrossRef] [PubMed]
51. Coates, J. Interpretation of Infrared Spectra, a Practical Approach. In *Encyclopedia of Analytical Chemistry*; Meyers, R.A., McKelvy, M.L., Eds.; John Wiley & Sons, Ltd.: Hoboken, NJ, USA, 2006. [CrossRef]
52. Predescu, A.M.; Matei, E.; Berbecaru, A.C.; Pantilimon, C.; Drăgan, C.; Vidu, R.; Predescu, C.; Kuncser, V. Synthesis and characterization of dextran-coated iron oxide nanoparticles. *R Soc. Open Sci.* **2018**, *5*, 171525. [CrossRef]
53. Hadjiivanov, K.; Ivanova, E.; Kefirov, R.; Janas, J.; Plesniar, A.; Dzwigaj, S.; Che, M. Adsorption properties of Fe-containing dealuminated BEA zeolites as revealed by FTIR spectroscopy. *Micropor. Mesopor. Mat.* **2010**, *131*, 1–12. [CrossRef]
54. Rahbari, R.; Sheahan, T.; Modes, V.; Collier, P.; Macfarlane, C.; Badge, R.M. A novel L1 retrotransposon marker for HeLa cell line identification. *Biotechniques* **2009**, *46*, 277–284. [CrossRef]
55. Ankamwar, B.; Lai, T.; Huang, J.; Liu, R.; Hsiao, M.; Chen, C.H. Biocompatibility of Fe₃O₄ nanoparticles evaluated by in vitro cytotoxicity assays using normal, glia and breast cancer cells. *Nanotechnology* **2010**, *21*, 075102. [CrossRef]
56. Karlsson, H.L.; Gustafsson, J.; Cronholm, P.; Möller, L. Size-dependent toxicity of metal oxide particles—a comparison between nano- and micrometer size. *Toxicol. Lett.* **2009**, *188*, 112–118. [CrossRef]
57. Villanueva, A.; Canete, M.; Roca, A.G.; Calero, M.; Veintemillas-Verdaguer, S.; Serna, C.J. The influence of surface functionalization on the enhanced internalization of magnetic nanoparticles in cancer cells. *Nanotechnology* **2009**, *20*, 115103. [CrossRef]
58. Rezaei, M.; Mafakheri, H.; Khoshgard, K.; Montazerabadi, A.; Mohammadbeigi, A.; Oubari, F. The cytotoxicity of dextran-coated iron oxide nanoparticles on Hela and MCF-7 cancerous cell lines. *Iran. J. Toxicol* **2017**, *11*, 31–36. [CrossRef]
59. Yu, M.; Huang, S.; Yu, K.J.; Clyne, A.M. Dextran and Polymer Polyethylene Glycol (PEG) Coating Reduce Both 5 and 30 nm Iron Oxide Nanoparticle Cytotoxicity in 2D and 3D Cell Culture. *Int. J. Mol. Sci.* **2012**, *13*, 5554–5570. [CrossRef]
60. Buyukhatipoglu, K.; Clyne, A.M. Superparamagnetic iron oxide nanoparticles change endothelial cell morphology and mechanics via reactive oxygen species formation. *J. Biomed. Mater. Res. Part. A* **2011**, *96A*, 186–195. [CrossRef]
61. Frei, B. Reactive oxygen species and antioxidant vitamins: Mechanisms of action. *Am. J. Med.* **1994**, *97*, S5–S13. [CrossRef]
62. Kehler, J.; Smith, C. Free Radicals in Biology: Sources, Reactivities and Roles in the Etiology of Human Diseases. In *Natural Antioxidants in Human Health and Disease*; Academic Press: San Diego, CA, USA, 1994; pp. 25–62.
63. Wu, X.; Tan, Y.; Mao, H.; Zhang, M. Toxic effects of iron oxide nanoparticles on human umbilical vein endothelial cells. *Int. J. Nanomed.* **2010**, *5*, 385–399. [CrossRef] [PubMed]
64. Soenen, S.J.H.; Himmelreich, U.; Nuytten, N.; De Cuyper, M. Cytotoxic effects of iron oxide nanoparticles and implications for safety in cell labelling. *Biomaterials* **2011**, *32*, 195–205. [CrossRef]

-
65. Hong, S.C.; Lee, J.H.; Lee, J.; Kim, H.Y.; Park, J.Y.; Cho, J.; Lee, J.; Han, D.W. Subtle cytotoxicity and genotoxicity differences in superparamagnetic iron oxide nanoparticles coated with various functional groups. *Int. J. Nanomed.* **2011**, *6*, 3219–3231. [[CrossRef](#)]
 66. Balas, M.; Ciobanu, C.S.; Burtea, C.; Stan, M.S.; Bezirtzoglou, E.; Predoi, D.; Dinischiotu, A. Synthesis, Characterization, and Toxicity Evaluation of Dextran-Coated Iron Oxide Nanoparticles. *Metals* **2017**, *7*, 63. [[CrossRef](#)]
 67. Soenen, S.J.; De Meyer, S.F.; Dresselaers, T.; Velde, G.V.; Pareyn, I.M.; Braeckmans, K.; De Cuyper, M.; Himmelreich, U.; Vanhoorelbeke, K.I. MRI assessment of blood outgrowth endothelial cell homing using cationic magnetoliposomes. *Biomaterials* **2011**, *32*, 4140–4150. [[CrossRef](#)] [[PubMed](#)]
 68. Buyukhatipoglu, K.; Chang, R.; Sun, W.; Clyne, A.M. Bioprinted nanoparticles for tissue engineering applications. *Tissue Eng. Part. C Methods* **2010**, *16*, 631–642. [[CrossRef](#)]
 69. Karlsson, H.L.; Cronholm, P.; Gustafsson, J.; Moller, L. Copper oxide nanoparticles are highly toxic: A comparison between metal oxide nanoparticles and carbon nanotubes. *Chem. Res. Toxicol.* **2008**, *21*, 1726–1732. [[CrossRef](#)] [[PubMed](#)]
 70. Singh, N.; Jenkins, G.J.; Asadi, R.; Doak, S.H. Potential toxicity of superparamagnetic iron oxide nanoparticles (SPION). *Nano Rev.* **2010**, *1*. [[CrossRef](#)] [[PubMed](#)]

STUDIES ON BIODEGRADATION OF TANNED LEATHER

Florentina ISRAEL-ROMING, Evelina GHERGHINA, Gabriela LUȚĂ, Daniela BĂLAN, Alina POPA, Roxana STEFAN, Carmen CÎMPEANU, Călina Petruta CORNEA

University of Agronomical Sciences and Veterinary Medicine Bucharest, Faculty of Biotechnologies, 59, Marasti Blvd., 011464, Bucharest, Romania, www.usamv.ro

Corresponding author email: florentinarom@yahoo.com

Abstract

*Wastes from the leather industry as well as insoluble and hard-to-degrade animal proteins are currently eliminated by incineration, method with high ecological disadvantages. In order to avoid these inconvenients, microbiological and/or enzymatic methods are examined. Leather degradation was performed in two trials: one enzymatic-assisted and the other microbial-assisted. Enzymatic hydrolysis of collagen, the representative protein of leather, was performed with collagenase type IA, with six enzyme concentrations, for up to 10 days. The hydrolysis yield was evaluated by free amino acids determination. Microbial hydrolysis involved 35 bacterial strains belonging to various genera (*Streptomyces*, *Bacillus*, *Pseudomonas*, *Serratia* etc), screened for their ability of growth in minimal medium containing bovine leather, ovine leather or wool as unique carbon or nitrogen sources. Three of these strains: *Bacillus licheniformis* ATCC 14580, *Pseudomonas fluorescens* ATCC 13525 and a new bacterial isolate, designated BN7, were able to grow in the presence of treated leather or wool, visible differences being observed after 10 days of incubation. The best results were obtained with the strain BN7, the level of free amino acids and of the extracellular proteins (as a measure of organic substrate degradation) was rather high (2.22 μ moles amino acids and 61 μ g protein respectively). Amino acids release and extracellular protein synthesis indicates both collagenase and keratinase activity. The degradation of tanned leather was examined microscopically: significant disorganization of leather fibres was observed.*

Key words: bacterial strains, collagenase, keratinase, leather degradation, wool

INTRODUCTION

Leather industries as well as meat industries are important generators of insoluble and hard-to-degrade animal proteins, which are converted in waste with high potential of environmental pollution. Usually, waste from these industries are eliminated by incineration, method with high ecological and sanitary disadvantages [Suzuki et al., 2006]. In order to avoid these inconvenients, microbiological and/or enzymatic methods are examined. It is well known that proteolytic enzymes constitute an important group of commercial enzymes; nevertheless their use in experiments for bioprocessing industrial waste containing animal proteins is well documented. Several experiments were carried out on enzymatic hydrolysis of collagen, the most representative protein of leather waste: the hydrolysis was carried out by collagenases, enzymes that can hydrolyze both native and denaturated collagens [Olde Damnic et al.,

1995, Zerdani et al., 2004]. Other experiments are focused on keratinolytic enzymes useful for degradation of fibrous insoluble proteins in the form of feathers, hair, nails, horn etc, available as agroindustrial by-products [Brandelli, 2008]. In the last ten years, a lot of articles regarding microorganisms able to degrade various types of animal proteins have been published [Brandelli, 2008; Suzuki et al., 2006; Kansoh et al., 2009; Riffel et al., 2003; Gousterova et al., 2005]. It was shown that strains of *Streptomyces* isolated from keratinaceous materials enriched soil were able to degrade human hair, feathers, silk and wool [(Riffel et al., 2003; Kansoh et al., 2009]. Moreover, among *Bacillus* and *Pseudomonas* genera various strains with highly proteolytic activities were identified, potentially useful for biodegradation of insoluble animal proteins [Cai et al., 2008; Tork et al., 2010; Agrahari and Wadhwa, 2010]. Most of the microorganisms isolated from soil presented reduced collagenase activity [Zerdani et al.,

2004] but significant keratinolytic action was detected among some bacterial isolates [Riffel and Brandelli, 2006; Agrahari and Wadhwa, 2010].

This study presents the action of collagenase type IA against sheep and bovine leather, as well as the capability of some mesophilic bacterial strains to synthesize hydrolytic enzymes with collagenolytic and/or keratinolytic activities.

MATERIAL AND METHODS

Culture medium for collagenolytic/keratinolytic enzymes production contained the following constituents (g/L): NaCl 1.0; CaCl₂ 0.05; KH₂PO₄ 0.7; sucrose 3; MgSO₄ 0.91; K₂HPO₄ 2.38, and sheep or bovine leather, and wool 6.0; pH 7.2 [Cai and Zheng, 2009].

Microorganism. 27 strains of *Streptomyces* isolated from compost and seven bacterial strains (*Bacillus subtilis* ATCC6633, *Bacillus licheniformis* ATCC 14580, *Bacillus amyloliquefaciens* BW, *Bacillus spp.* OS15, *Bacillus spp.* OS17, *Pseudomonas fluorescens* ATCC 13525, *Serratia spp.* S1) from the collection of Faculty of Biotechnology, Bucharest, Romania, and a new isolate from soil (designated BN7) were used in experiments.

Free amino acids released by the extent of collagen breakdown were determined using a modification of the Moore and Stein (1948) colorimetric ninhydrin method, by transferring 0.2 ml of sample to test tubes containing 2.0 ml of ninhydrin-ethylene glycol monoethyl ether mixture. After boiling for 30 minutes in a water bath and after cooling, the samples were diluted with 10 ml of 50% n-propanol. The absorbance was determined at 600 nm 15 minutes later. An L-leucine standard curve was used to determine micromoles amino acid equivalent to leucine liberated.

Total soluble protein concentration was determined by the method of Lowry et al. (1951) using bovine serum albumin (BSA) as standard.

Enzyme-assisted leather degradation test was performed using a 2 mg/ml stock solution of bacterial collagenase type IA (Sigma-

Aldrich Chemicals Company). The experiments were carried out with 2 cm² sheep leather samples in 50 mM Tris-HCl buffer pH 7.4 and six IA collagenase concentration levels ranging from 0.05 to 0.6 mg/ml, at 37°C, with shaking (150 rpm), for 10 days. Released amino acids determination was carried out at 48, 72, 96 and 240 hours of reaction.

Microbial-assisted leather degradation test was performed by cultivation in submerged conditions, at 28°C, with shaking (120 rpm) for 10 days. Preliminary screening of microorganisms for proteolytic activity was performed on milk agar plates [Riffel and Brandelli, 2006]. Biochemical determinations consisted in total soluble protein and released amino acids assays carried out at the end of cultivation period.

RESULTS AND DISCUSSIONS

In vitro degradation trial using collagenase (type IA) solution proved the hydrolytic potential when breaking down the collagen from the tanned leather. Because the degradation behaviour is depending on enzyme concentration, six collagenase concentration levels (0.05, 0.1, 0.175, 0.25, 0.3 and 0.6 mg/ml) were tested in order to find out the minimum necessary amount for relevant digestion of the tanned leather. For a longer reaction time (ten days) significant reduction in the degradation of collagen was observed when using 0.1 mg/ml, but for shorter evaluation period (four days) an increased enzyme concentration was needed (at least 0.25 mg/ml) (Fig. 1).

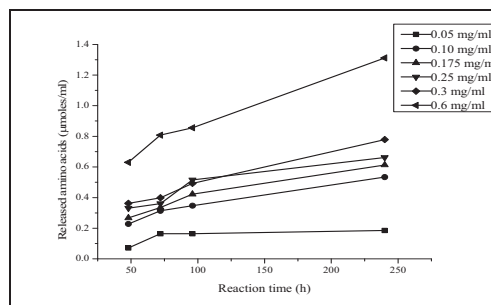


Fig. 1. Leather degradation using six IA collagenase concentrations

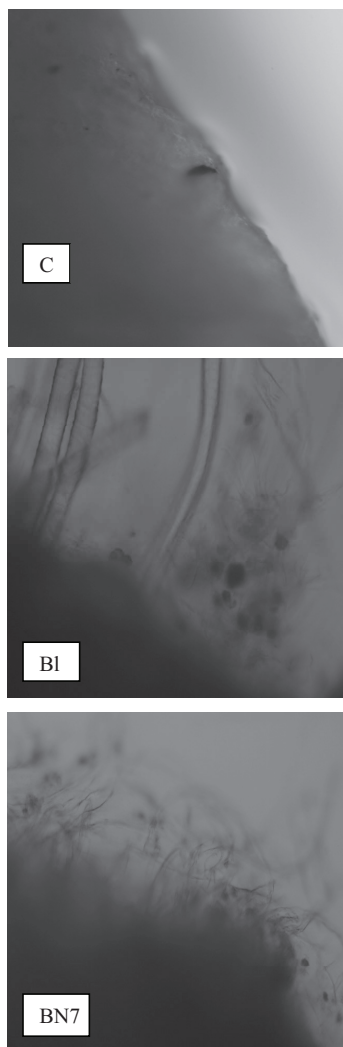


Photo 1. Microscopic examination of sheep pelts: C = control (untreated pelt); B1 = incubation with *B.licheniformis* ATCC14580 for 10 days; BN7 = incubation with the bacterial isolate BN7 for 10 days.

The screening test showed that from the seven bacterial tested strains only the two collection bacteria (*Bacillus licheniformis* ATCC 14580 and *Pseudomonas fluorescens* ATCC 13525) and the new isolate BN7 were able to grow in minimal medium containing leather as sole carbon and nitrogen source. Among streptomycetes, only five strains presented a relatively poor growth in the same medium, but their collagenolytic activity was much reduced. On milk agar plates, the strain

designated BN7 produced clear zone of hydrolysis.

The microscopic examination of sheep or bovine leather fragments incubated with selected bacteria showed significant differences from control. In the control, the edges of the leather fragments were intact, and the aspect was compact (photo 1). After 10 days of incubation with the selected bacteria, the margins structure of sheep leather was modified: it has become more disorganized and both globular and fibrous fragments were released in medium.

The highest degradation, both of sheep leather and of wool samples was observed when the new isolated strain BN7 was used, suggesting the biosynthesis of collagenolytic as well as of keratinolytic enzymes (photo 2).

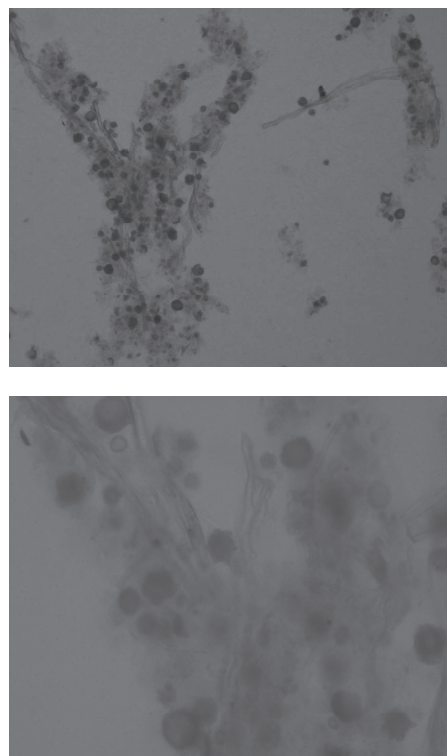


Photo 2. Microscopic aspect (10x and 40x) of degradation fragments resulted after incubation of sheep leather fragments with the bacterial isolate BN7 for 10 days

Similar aspect were observed on bovine pelts treated with the same bacterial strains: the disorganization of the margins and the release

of small fragments are the main actions of the degradative bacteria (photo 3).



Photo 3. Microscopic aspects of bovine pelts incubated for 10 days with the bacterial isolate BN7 (middle and down) comparative with the untreated sample (up)

Biochemical analysis confirmed the microscopic aspects showing high amount of released amino acids after 10 days of cultivation for all the three tested strains, with higher values for bacterial isolate BN7 (Fig. 2). Degradation of sheep leather was, at least, more than twice accelerated than the degradation of bovine leather.

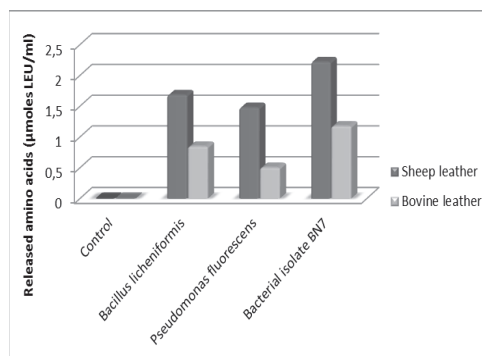


Fig. 2. Degradation of sheep and bovine leather expressed as released amino acids after 10 days of cultivation

Total soluble protein concentration was almost similar for all the tested strains, when acting both on sheep and bovine leather, meaning that enzyme synthesis was quite close (Fig. 3). Though the results obtained for the amino acids released by the action of proteolytic enzymes were totally different. An explanation might be the inhibition produced by the presence of several compounds used for leather processing and acting different, according to the enzyme microbial source.

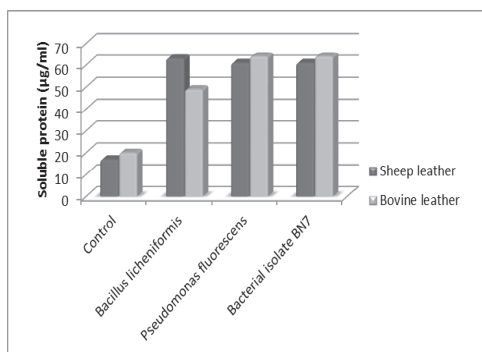


Fig. 3. Degradation of sheep and bovine leather expressed as total soluble protein concentration after 10 days of cultivation

These results suggest that the selected bacteria, and especially *Bacillus licheniformis* ATCC14580 and the new isolated strain BN7 are able to produce increased levels of hydrolytic enzymes, active both on leather and wool.

CONCLUSIONS

The tested strains *Bacillus licheniformis* ATCC 14580, *Pseudomonas fluorescens* ATCC 13525 and the new isolate BN7 can be used for improvement of waste leather biodegradation process. Collagenase activity may be considered as a measure of this degradation process.

ACKNOWLEDGMENTS

This work was supported by Eureka Programme, project **E 5770/2012 - BIOFUR**.

REFERENCES

- [1] Agrahari, S., Wadhwa, N., *Degradation of chicken feather a poultry waste product by keratinolytic bacteria isolated from dumping site at Gahzipur poultry processing plant*, *Internat. J. Poultry Science*, 2010, 9, p.482-489
- [2] Brandelli, A., *Bacterial keratinases: useful enzymes for bioprocessing agroindustrial wastes and beyond*, *Food Bioprocess Technol.*, 2008, 1, p.105-116.
- [3] Cai, C., Lou, B., Zheng, X., *Keratinase production and keratin degradation by a mutant strain of *Bacillus subtilis**, *J. Zheijang Univ. Sci. B.*, 2008, 9, p.60-67
- [4] Cai, C., Zheng, X., *Medium optimization for keratinase production in hair substrate by a new *Bacillus subtilis* KD-N2 using response surface methodology*, *J. Ind. Microbiol. Biotechnol.*, 2009, 36, p.875-883
- [5] Gousterova, A., Braikova, D., Goshev, I., Christov, P., Tishinov, K., Vasileva-Tonkova, E., Haertle, T., Nedkov, P., *Degradation of keratin and collagen containing wastes by newly isolated thermoactinomycetes or by alkaline hydrolysis*, *Letts. Appl. Microbiol.*, 2005, 40, p.335-340
- [6] Kansoh, A. L., Hossiny, E. N., El-Hameed, E. K. A., *Keratinase production from feathers wastes using local *Streptomyces* isolates*, *Australian J. Basic Appl. Sci.*, 2009, 3, p.561-571.
- [7] Lowry, O. H., Rosebrough, N.J., Farr, A. L., Randall, R. J. *Protein measurement with the Folin phenol reagent*, *J. Biol. Chem.* 1951, 193 (1), p. 265–275.
- [8] Moore, S. and Stein, W. H. *A modified ninhydrin reagent for photometric determination of amino acids and related compounds*, *J. Biol. Chem.* 1954, 211, p.907-913.
- [9] Olde Damink, L. H. H., Dijkstra, P. J., Van Luyn, M. J. A., Van Wachem, P. B., Nieuwenhuis, Feijen, P., *J. Changes in the mechanical properties of dermal sheep collagen during in vitro degradation*, *J. Biomed. Mat. Research*, 1995, Vol. 29, p.139-147.
- [10] Riffel, A., Brandelli, A., *Keratinolytic bacteria isolated from feather waste*, *Braz. J. Microbiol.*, 2006, 37, p.395-399.
- [11] Riffel, A., Ortola, S., Brandelli, A., *De-hairing activity of extracellular proteases produced by keratinolytic bacteria*, *J. Chem. Technol. Biotechnol.*, 2003, 78, p.855-859.
- [12] Suzuki, Y., Tsujimoto, Y., Matsui, H., Watanabe, K., *Decomposition of extremely hard-to-degrade animal proteins by thermophilic bacteria*, *J. Biosci. Bioeng.*, 2006, 102, p.73-81.
- [13] Tork, S., Aly, M. M., Nawar, L., *Biochemical and molecular characterization of a new local keratinase producing *Pseudomonas* sp.MS21*, *Asian J. Biotechnol.*, 2010, 2, p.1-13.
- [14] Zerdani, I., Faid, M., Malki, A., *Digestion of solid tannery wates by strains of *Bacillus* spp.isolated from compost in Morocco*, *Internat. J. Agric. Biol.*, 2004, 6, p.758-761.

TOLERANCE TO CADMIUM AND PHYTOCHELATINS SYNTHESIS IN *AGROSTIS TENUIS*

TOLERANTA LA CADMIU SI SINTEZA FITOCHELATINELOR ÎN *AGROSTIS TENUIS*

Carmen CIMPEANU, Irina GREBENIȘAN

Agricultural and Veterinary University, București, România

Corresponding author: Carmen CIMPEANU, e-mail: carmencimpeanu@yahoo.com

Abstract: The paper has as aim the cellular and biochemical identification of some proteins (phytochelatins and iso-phytochelatins) able to bind the cadmium ions. For this, cell suspensions of root callus proceeded from an *Agrostis tenuis* ecotype (harvested from a metalliferous area, polluted with heavy) were obtained. The cell suspensions were treated with different cadmium concentrations. One can ascertain that the *Agrostis* ecotype, from polluted area, has the ability to synthesize phytochelatins and, it manifests an increased tolerance to cadmium ions (solution concentrations of 100 μ M). One can conclude that phytochelatins synthesis has an important role into plant tolerance to cadmium.

Rezumat: Prin prezenta lucrare s-a urmarit identificarea celulara si biochimica a unor proteine (fitochelatine si izo-fitochelatine) capabile de a lega ionii de Cd. Pentru aceasta s-au obtinut suspensii celulare din calus radicular provenit de la un ecotip de *Agrostis tenuis* (recoltat dintr-o zona metalifera, poluata cu metale grele). Suspensiile celulare au fost tratate cu diferite concentratii de Cd. S-a constatat ca ecotipul de *Agrostis* provenit din zona poluata are capacitatea de a sintetiza fitochelatine si, astfel, manifesta o toleranta crescuta fata de ionii de Cd (concentratii ale solutiei de 100 μ M). Se poate concluziona ca sinteza de fitochelatine are un rol important in toleranta plantelor la Cd.

Key words: cadmium tolerance, suspension-cultured cells, phytochelatins, *Agrostis tenuis*

Cuvinte cheie: toleranța la cadmiu, suspensii de culturi celulare, fitochelatine, *Agrostis tenuis*

INTRODUCTION

Hayashi et al. (Murasugi et al., 1981; Kondo et al., 1984) were the first who discovered into yeast cells (*Schizosaccharomyces pombe*) treated with cadmium salts, cadmium-binding peptides. These peptides were named “cadystin” and the identification of their structure emphasized the fact that these peptides are composed from glutathione repetitive units (n) (γ EC)_nG (n=2,3). Similar peptides (γ EC)_nG, with glutathione repetitive number units ranges between 2 and 11 were also found in superior plant (Grill et al., 1985). These peptides, named phytochelatins, contribute to increasing of superior plant tolerance to heavy metal harmful action.

The phytochelatin synthesis starting from GSH and mediated by the phytochelatin-synthetase was demonstrated by Grill et al., 1989, using suspension-cultured cells of *Silene cucubalus*. As results of these *in vitro* experiments, the γ EC dypeptidil-transpeptidase enzyme was isolated and characterized. This enzyme binds the GSH units one of another in order to form phytochelatins (Grill et al., 1989; Loeffler et al., 1989). This enzyme expression is more efficient when is activated by the cadmium ion presence (Grill et al., 1989). Similar enzymatic activities were also reported in other plants (Howden et al., 1995a, 1995b; Chen et al., 1997). Relative recently, the genes for the synthesis of phytochelatin-synthetase from *Arabidopsis* plants (Ha et al., 1999) and from *Triticum aestivum* (Clemens et al., 1999) were isolated. Homeologous genes were also identified in the yeast cells as well as in nematode *Caenorhabditis elegans*. These discoveries suggest the fact that the phytochelatin-synthetase

could has important functions as part of a large variety of organisms (yeasts, plants and invertebrates).

The present paper presents the effect of cadmium on *Agrostis tenuis* root cell growth. It was also tested the effect of cadmium on phytochelatin synthesis in both suspension-cultured cells and root tissues of *Agrostis tenuis*.

MATERIALS AND METHODS

Plant samples

Plant samples (*Agrostis tenuis*) were harvested from a North geographical area of the country: Baia Mare, metalliferous area, strongly and long-term affected by the heavy metal pollution.

To achieve the experiments, suspension-cultured cells from root callus were used.

Suspension-cultured cells were obtained from root callus according to standard protocols (Dodds and Roberts, 1985). Cell suspensions were maintained into sub-cultures in 90 ml liquid Murashige-Skoog medium, into flasks of 300 ml. According to working protocol, a tenth of culture volume was inoculated into a new medium, and the suspension-cultured cell was grown on an agitator at 80 rpm, under conditions of 28 °C and neon light.

Growth experiments

The CdSO₄ solutions (10-100 µM) were sterilized and added into flasks of 100 ml, at 30 ml liquid Murashige-Skoog medium.

To determine the cadmium influence on cell growth, the adding of CdSO₄ solutions was done before to achieve the cell inoculum. The cell suspensions (about 100 mg fresh raw) were inoculated into culture media and grown during 12 days at the temperature of 27°C.

To determine the phytochelatin content, the CdSO₄ solutions were added over the cell suspensions after 3 days of growing into liquid Murashige-Skoog medium, free of Cd ions.

The cell growth was determined by the weighting of fresh raw and dry one at an interval of 2 days, during experiment (12 days).

HPLC analysis to determine the phytochelatin (PCs) and glutathione (GSH) contents

The cell suspensions were extracted at 0°C, with 10% sulfosalicylic acid (SSA), using an acid volume equal to the fresh weight of cell suspension (after method described by Mendum et al., 1990). The extracts were centrifuged at 10,000 g during 1 minute, and the supernatant was maintained 30 minutes at 0°C, before HPLC analysis. The phytochelatin separation was performed in sample 20-µL. The sample was injected in a reverse-phase column and connected at a HPLC pump. The column was eluted with acetonitril linear gradient in 0.1% (w/v) trifluoroacetic acid at a flowing rate of 0.5 ml/minute. The acetonitril gradient was programmed at 0% during 4 minutes, from 0% to 10% in 4 minutes and from 10% to 20% (v/v) in 40 minutes. The elution from a column was derivatized with 75 µM 5,5'-ditiobis (2-nitrobenzoic acid) in 50 mM potassium phosphate (pH=7.6), at a flowing rate of 1 ml/minute and monitored at 412 nm (Grill et al., 1987), using an UV detector. The phytochelatin retention time was identified as adequate to peptides (γEC)nG (n=2-5)(Matsumoto et al., 1990). The phytochelatin content was expressed as millimoles of sulfhydryl equivalent per kilogram fresh

weight of cells, using GSH as standard. The total glutathione content from cell extract was measured by method proposed by Anderson, 1985.

RESULTS AND DISCUSSIONS

Cd ion effect on cells growth

As follows of the performed analyses, one can emphasize the fact that at high concentrations of CdSO_4 (100 μM) the root cell growth is inhibited. It was examined the Cd effect on cell growth from the suspension-cultured cells realized by root callus of the *Agrostis tenuis* ecotype. In the liquid Murashige-Skoog medium culture were added, immediately after the cell inoculation, different Cd ion concentrations. The concentrations of CdSO_4 between 10 and 20 μM (which represent 5.3 and 10.6 ppm Cd respectively) do not inhibit the cell growth, during the 12 days of experiment (Fig.1). This reveals the fact that the root cells from the suspension-cultured cells presents tolerance to effect induced by Cd ions. At higher CdSO_4 concentrations, of 50 μM and 100 μM respectively (which correspond to 26.5 and 53 ppm Cd respectively), the cell growth is initially inhibited. One can ascertain that after 4 days and 8 days respectively (depending on the Cd concentration) the growth rate establishes itself (Fig.1).

The Cd ion effect on the cells growth was compared with a check (*Agrostis* cells from polluted environment, inoculated in culture medium without Cd ion addition).

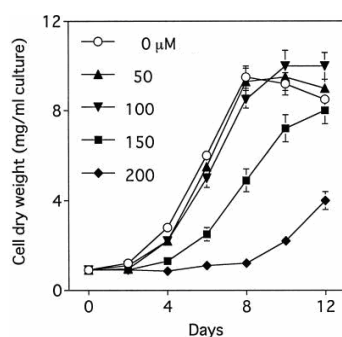


Figure 1. Effect of Cd on growth of suspension-cultured cells of tolerant *Agrostis* (from Baia Mare area). *Agrostis* cells (100 mg) were inoculated in 30 mL of liquid Murashige-Skoog medium and treated with 10 to 100 μM CdSO_4 for 12 days. Cells were collected at a 2-d interval and the dry weights were determined. Data are expressed as means \pm SE (n = 3).

Phytochelatins synthesis into cells

Phytochelatins are heavy- metals complexing peptides which contribute to detoxification processes and confer tolerance to plants, vs. harmful action of metallic ions (Inouhe et al., 1994; Rauser, 1995).

The cells were pre-cultured, during three days, on culture medium without Cd ions. After that, during three days, Cd solutions in different concentrations were added. Under the effect of this treatment, the *Agrostis* cells began to produce phytochelatins (n=2-4)

proportionally with the Cd ion concentration into medium (Figure 2). The phytochelatin presence (n=2-4) into tolerant ecotype cells was detected in high quantities (Figure 3).

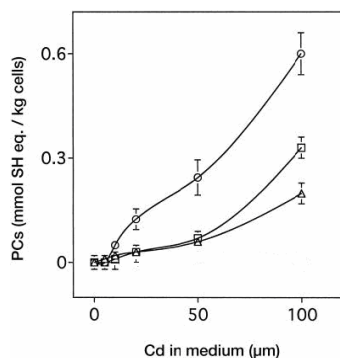


Figure 2. Effects of Cd on the levels of phytochelatin peptides in tolerant *Agrostis* cells. The suspension cells were precultured for 3 d in 30 mL of liquid Murashige-Skoog medium and then treated with various concentrations of CdSO₄ for 3 days. PC peptides (n = 2-4) were determined by the post-column HPLC method. Data are expressed as means ± SE (n = 3).

△, (γEC)₂G; ○, (γEC)₃G; □, (γEC)₄G in tolerant *Agrostis* cells.

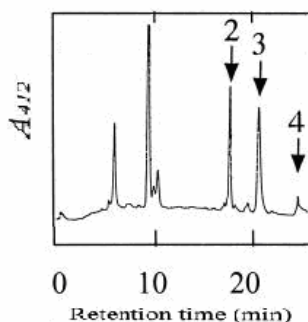


Figure 3. Formations of phytochelatin peptides in suspension cells of tolerant *Agrostis*. The suspension cells of *Agrostis* were precultured for 3 d in 30 mL of liquid Murashige-Skoog medium and then treated with 10 μM CdSO₄ for 3 days. The extracts were analyzed by the post-column HPLC method. Arrows with numbers (n = 2-4) represent the elution times of (γEC)_nG peptides (n = 2-4).

GSH level into cells

GSH represents the substrate for the phytochelatin synthesis. To confirm the fact that the glutathione biosynthesis is involved into phytochelatin synthesis, the GSH total content was determined (Figure 4).

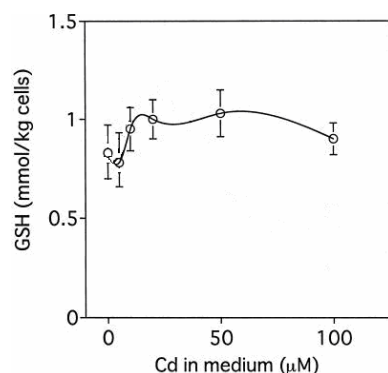


Figure 4. Effects of Cd on the total glutathione contents in tolerant and non-tolerant *Agrostis* cells. The suspension cells were precultured for 3 d in 30 mL of liquid Murashige-Skoog medium and then treated with various concentrations of CdSO₄ for 3 d in the same medium. The total GSH contents in the cells were determined as described in "Materials and Methods." Data are expressed as means \pm SE (n = 3).

In the *Agrostis* cells the Cd presence determines an increase of GSH content, but this increase is not proportionally with the Cd concentration increase, because a part of synthesized GSH is consumed to synthesize phytochelations. It is well known the fact that the Cd ions have a dual effect on GSH metabolism; on one hand, they lead to the GSH level increasing by GSH synthesis increasing, but, on the other hand, they lead to the GSH level diminution by its consumption for phytochelatin synthesis. Other Cd ion effect also occurs in this experiment.

CONCLUSIONS

The suspension-cultured cells of *Agrostis* plants harvested from a polluted area present a high tolerance to Cd ions (Figure 1). These cells develop a high tolerance to 100 μ M Cd solution concentrations. Based on results, one can underline that, the plants grown under strong and long-term pollution (as in Baia Mare area) could develop some defense mechanisms and become tolerant ecotypes.

The biochemical and genetic bases of plant tolerance/resistance to Cd involve both phytochelatin synthesis dependent processes and independent ones (Wagner and Krotz, 1989). This study demonstrated that the *Agrostis* cells from polluted area present efficiency in phytochelatin synthetase activity (Figures 2, 3). These results sustain the idea that phytochelatin synthetase is an essential enzyme which confer to plants tolerance to Cd ion toxic action (Howden et al., 1995b).

The experiments showed that besides phytochelatin, GSH is also involved in plant tolerance to Cd. One can know the fact that GSH could protect plants against heavy-metal toxic action, having anti-oxidative or metal acceptor role (Xiang and Oliver 1998). This study also underlines that the GSH has an important role into detoxification processes of plants contaminated with Cd (Figure 4).

REFERENCES

1. ANDERSON ME (1985) Determination of glutathione and glutathione disulfide in biological samples. *Methods Enzymol* 113: 548-555
2. CHEN J, ZHOU J, GOLDSBROUGH PB (1997) Characterization of phytochelatin synthase from tomato. *Physiol Plant* 101: 165-172
3. CLEMENS S, KIM EJ, NEUMANN D, SCHROEDER JI (1999) Tolerance to toxic metals by a gene family of phytochelatin synthases from plants and yeast. *EMBO J* 18: 3325-3333
4. DELHAIZE E, JACKSON PJ, LUJAN LD, ROBINSON NJ (1989) Poly (γ -glutamylcysteinyl) glycine synthesis in *Datura innoxia* and binding with cadmium. *Plant Physiol* 89: 700-706

- 5.DODDS JH, ROBERTS LW (1985) Cell suspension cultures. In *Experiments in Plant Tissue Culture*, Ed 2. Cambridge University Press, New York, pp 104-112
- 6.GRILL E, WINNACKER E-L, ZENK MH (1985) Phytochelatins: the principal heavy-metal complexing peptides of higher plants. *Science* 230: 674-676
- 7.HA S-B, SMITH AP, HOWDEN R, DIETRICH WM, BUGG S, O'CONNELL MJ, GOLDSBROUGH PB, COBBETT CS (1999) Phytochelatin synthase genes from *Arabidopsis* and the yeast *Schizosaccharomyces pombe*. *Plant Cell* 11: 1153-1163
- 8.HOWDEN R, ANDERSEN CR, GOLDSBROUGH PB, COBBETT CS (1995a) A cadmium-sensitive, glutathione-deficient mutant of *Arabidopsis thaliana*. *Plant Physiol* 107: 1067-1073
- 9.HOWDEN R, GOLDSBROUGH PB, ANDERSEN CR, COBBETT CS (1995b) Cadmium-sensitive, *cad1* mutants of *Arabidopsis thaliana* are phytochelatin deficient. *Plant Physiol* 107: 1059-1066
- 10.INOUE M, NINOMIYA S, TOHOYAMA H, JOHO M, MURAYAMA T (1994) Different characteristics of roots in the cadmium-tolerance and Cd-binding complex formation between mono- and dicotyledonous plants. *J Plant Res* 107: 201-207
- 11.MATSUMOTO Y, OKADA Y, MIN K-S, ONOZAKA S, TANAKA K (1990) Amino acids and peptides: XXVII. Synthesis of phytochelatin-related peptides and examination of their heavy metal-binding properties. *Chem Pharm Bull* 38: 2364-2368
- 12.MENDUM ML, GUPTA SC, GOLDSBROUGH PB (1990) Effect of glutathione on phytochelatin synthesis in tomato cells. *Plant Physiol* 93: 484-488
- 13.MURASHIGE T, SKOOG F (1962) A revised medium for rapid growth and bioassays with tobacco tissue cultures. *Physiol Plant* 15: 473-479
- 14.NUSSBAUM S, SCHMUTZ D, BRUNOLD C (1988) Regulation of assimilatory sulfate reduction by cadmium in *Zea mays* L. *Plant Physiol* 88: 1407-1410
- 15.RAUSER WE (1995) Phytochelatins and related peptides: structure, biosynthesis, and function. *Plant Physiol* 109: 1141-1149
- 16.WAGNER GJ, KROTZ PM (1989) Perspectives on Cd and Zn accumulation, accommodation and tolerance in plant cells: the role of Cd-binding peptide versus other mechanisms. In DH Hamer, DR Winge, eds, *Metal Ion Homeostasis: Molecular Biology and Chemistry*. Alan R. Liss, New York, pp 325-336
- 17.XIANG C, OLIVER DJ (1998) Glutathione metabolic genes coordinately respond to heavy metals and jasmonic acid in *Arabidopsis*. *Plant Cell* 10: 1539-1550.